DOE/BC/10116-26
(DE84009783)

Energy

FOSSIL

FLOW IN POROUS MEDIA, PHASE BEHAVIOR AND ULTRALOW INTERFACIAL TENSIONS: MECHANISMS OF ENHANCED PETROLEUM RECOVERY

1982 Final Report

By
H. T. Davis
L. E. Scriven
W. G. Miller
S. Prager

May 1984
Date Published

Work Performed Under Contract No. AC19-79BC10116

University of Minnesota
Minneapolis, Minnesota

Technical Information Center
Office of Scientific and Technical Information
United States Department of Energy

DISCLAIMER

DISCLAIMER

This report has been reproduced directly from the best available copy.

Available from the National Technical Information Service, U. S. Department of Commerce, Springfield, Virginia 22161.

Price: Printed Copy A19
Microfiche A01

Codes are used for pricing all publications. The code is determined by the number of pages in the publication. Information pertaining to the pricing codes can be found in the current issues of the following publications, which are generally available in most libraries: *Energy Research Abstracts (ERA); Government Reports Announcements* and Index (*GRA* and I); *Scientific and Technical Abstract Reports (STAR);* and publication NTIS-PR-360 available from NTIS at the above address.

FINAL TECHNICAL REPORT: 1982
DOE/DE-AC19-79BC10116

DOE/BC/10116-26
(DE84009783)
Distribution Category UC-92a

DEPARTMENT OF ENERGY
DIVISION OF OIL, GAS, SHALE, AND IN SITU TECHNOLOGY

FLOW IN POROUS MEDIA, PHASE BEHAVIOR AND ULTRALOW INTERFACIAL TENSIONS: MECHANISMS OF ENHANCED PETROLEUM RECOVERY

H. T. DAVIS AND L. E. SCRIVEN, PRINCIPAL INVESTIGATORS
DEPARTMENT OF CHEMICAL ENGINEERING & MATERIALS SCIENCE

W. G. MILLER AND S. PRAGER, SENIOR INVESTIGATORS
DEPARTMENT OF CHEMISTRY

INSTITUTE OF TECHNOLOGY
UNIVERSITY OF MINNESOTA
MINNEAPOLIS, MN 55455

Fred W. Burtch
Technical Project Officer
Bartlesville Project Office

Research performed with partial support from DOE, University of Minnesota departmental funds, and grants-in-aid from Atlantic Richfield Oil and Gas Company, Amoco Production Company, Chevron Oil Field Research Company, Cities Service Company, Exxon Production Research Company, Gulf Research and Development Company, Marathon Oil Company, Mobil Foundation, Schlumberger Technology Corporation and Shell Development Company.

FLOW IN POROUS MEDIA, PHASE BEHAVIOR
AND ULTRALOW INTERFACIAL TENSIONS:
MECHANISMS OF ENHANCED PETROLEUM RECOVERY

CALENDAR YEAR 1982
FINAL TECHNICAL REPOR
DOE/DE-AC19-79BC10116

DEPARTMENT OF CHEMICAL ENGINEERING & MATERIALS SCIENCE
UNIVERSITY OF MINNESOTA

CONTENTS

CONTENTS, CON'T

LIST OF TABLES

LIST OF FIGURES

PAGE

Section I

PAGE

Section II

PAGE

PAGE

PAGE

Section VI

Section VII

PAGE

PAGE

Section XIII

Section XIV

PAGE

FLOW IN POROUS MEDIA, PHASE BEHAVIOR
AND ULTRALOW INTERFACIAL TENSIONS:
MECHANISMS OF ENHANCED PETROLEUM RECOVERY

CALENDAR YEAR 1982
FINAL TECHNICAL REPORT

DOE/DE-AC19-79BC10116

Department of Chemical Engineering & Materials Science
University of Minnesota

ABSTRACT

A major program of university research, longer-ranged and more fundamental in approach than industrial research, into basic mechanisms of enhancing petroleum recovery and into underlying physics, chemistry, geology, applied mathematics, computation, and engineering science has been built at Minnesota. The 1982 outputs of the interdisciplinary team of investigators were again ideas, instruments, techniques, data, understanding and skilled people:

- Forty-one scientific and engineering papers in leading journals, including a definitive scientific article on stress and structure in fluid interfaces.
- Four pioneering Ph.D. theses.
- Numerous presentations to scientific and technical meetings, and to industrial, governmental and university laboratories.
- Vigorous program of research visits to and from Minnesota.
- Two outstanding Ph.D.'s to research positions in the petroleum industry, one to a university faculty position, one to research leadership in a governmental institute.

This report summarizes the 1982 papers and theses and features sixteen major accomplishments of the program during that year. Abstracts of all forty-five publications in the permanent literature are appended. Further details of information transfer and personnel exchange with industrial, governmental and university laboratories appear in 1982 Quarterly Reports available from the Department of Energy and are not reproduced here.

The Minnesota program continues in 1983, notwithstanding earlier uncertainty about the DOE funding which finally materialized and is the bulk of support. Supplemental grants-in-aid from nine companies in the petroleum industry are important, as are the limited University and departmental contributions.

FLOW IN POROUS MEDIA, PHASE BEHAVIOR
AND ULTRALOW INTERFACIAL TENSIONS:
MECHANISMS OF ENHANCED PETROLEUM RECOVERY

CALENDAR YEAR 1982
FINAL TECHNICAL REPORT

DOE/DE-AC19-79BC10116

Department of Chemical Engineering & Materials Science
University of Minnesota

INTRODUCTION

This report summarizes the outputs of the Minnesota research program during all four quarters of 1982. The goals of the program are ideas, instruments, techniques, data, understanding, and skilled people for enhancing the recovery of petroleum in the short term as well as in the longer term, and doing so especially by elucidating basic mechanisms. For then the uncertainties of process design, particularly in scale-up, control and optimization, are reduced, and innovative process development is promoted.

The original focus was surfactant-based chemical flooding, but the approaches taken were sufficiently fundamental that the research, longer-ranged than most industrial efforts, has become quite multidirectional. Many current outputs of the program are basic enough to pertain to petroleum recovery more broadly and to other energy-related technologies.

Scientific Frontiers

At the level of engineering science and underlying physics, chemistry, geology, applied mathematics and computation the program is currently focused on three frontiers:

1. *SCIENCE OF MICROSTRUCTURED FLUIDS AND APPLICATION TO THEIR PHASE BEHAVIOR, INTERFACIAL TENSION, AND RHEOLOGY.* Leading examples of fluid microstructures are the surfactant-based micelles, microemulsions, liquid crystals, vesicles, etc. in chemical flooding formulations. Interfaces are fluid microstructures, and solid surfaces often induce microstructure in adjacent fluid.

Dispersed surfactant regime of ultralow interfacial tension. Applications go back to a 1976 Society of Petroleum Engineers paper in which the Minnesota team brought out that one or both of two distinct regimes of ultralow tension can be active in contending chemical flooding processes. The microemulsion regime was already well identified; the dispersed-surfactant regime they subsequently unraveled. They discovered virtually transparent suspensions of submicroscopic liquid-crystallites and showed that these not only produce ultralow tensions between oil and brine but also cause the mysterious laboratory results that puzzled researchers in the petroleum industry and universities alike. They discovered that the liquid crystals can be converted to vesicles that can pass through sedimentary rock, and with the cooperation of the Petroleum Recovery Research Center (New Mexico) they demonstrated that oil can be recovered from short cores with far less retention of surfactant that is vesiculated — thereby raising a new possibility for consideration by industry.

FLOW IN POROUS MEDIA, PHASE BEHAVIOR
AND ULTRALOW INTERFACIAL TENSIONS:
MECHANISMS OF ENHANCED PETROLEUM RECOVERY

CALENDAR YEAR 1982
FINAL TECHNICAL REPORT
DOE/DE-AC19-79BC10116

Department of Chemical Engineering & Materials Science
University of Minnesota

Microstructural causes of ultralow tension and low viscosity rheology. Current research includes concerted attack on the microstructures and rheologies of both dispersed-surfactant states and microemulsion states by a phalanx of experimental methods. Of special concern are the relations among these still poorly understood states of matter: findings will likely translate into improved formulations for chemical flooding and new ideas for a larger sphere of technologies. The leading hypotheses were put forward by Minnesota researchers at the 1975 and 1976 Gordon Research Conferences and in frequently quoted follow-up letters to *Nature*, the international weekly of science.

Thermodynamics of phase behavior. Another main line of Minnesota research is molecularly based thermodynamic modeling of phase splits and phase equilibria in amphiphile-hydrocarbon-brine systems, whether the amphiphile is a surfactant and the liquids are microstructured, or the amphiphile is merely a solvent such as a low molecular weight alcohol or carbon dioxide. This line can be traced back to a 1977 Gordon Conference and SPE presentation from Minnesota in which not only was a new thermodynamic equation of state put forward for microemulsion systems, but also simple theory and clinching experiments were reported that showed the critical endpoints demanded by thermodynamics are indeed present, despite earlier claims of others that they are not. Also presented at the 1977 Gordon Conference was the interpretation of ultralow tensions as near-critical phenomena, an approach which when published by the chemical physicists Fleming and Vinatieri of Phillips Petroleum Company opened the door to the still vigorous research on microemulsions as near-critical phenomena. One reason for the vigor is that near-critical phenomena are currently prominent in physics research and results there carry implications for microemulsion systems, including those systems being field-tested for enhancing oil recovery.

Theory of interfacial tension. Another, related main line is correlation and prediction of interfacial tensions on the basis of the most effective molecular theory that is available. It was this that led to the near-critical interpretation of ultralow tensions in microemulsion systems. The ideas were based on Minnesota work published in 1975 in *Physical Review* and in 1976 in *Journal of Colloid and Interface Science;* this same work, which amounts to a rigorous version of the early Van der Waals' theory of surface and interfacial tension, also led to 1978 and 1980 American Institute of Chemical Engineers papers on surface tensions and interfacial tensions of hydrocarbons and their mixtures. The Minnesota group has developed the theory further and used it to predict difficult-to-measure tensions in carbon dioxide systems akin to those used in flooding processes — even water-carbon dioxide-hydrocarbon mixtures. They have also published a definitive scientific article on stress and structure in fluid interfaces, a point of departure for additional researches (the article appears as a Supplement to this report).

FLOW IN POROUS MEDIA, PHASE BEHAVIOR
AND ULTRALOW INTERFACIAL TENSIONS:
MECHANISMS OF ENHANCED PETROLEUM RECOVERY

CALENDAR YEAR 1982
FINAL TECHNICAL REPORT
DOE/DE-AC19-79BC10116

Department of Chemical Engineering & Materials Science
University of Minnesota

Scientific instrument development. An accompaniment to these interfacial tension researches has been perfection of the spinning-drop technique and instrumentation for measuring interfacial tensions. The earliest paper from Minnesota appeared in Review of Scientific Instruments in 1977; the latest is in press at this writing. An improved spinning-drop instrument was patented by the University of Minnesota (no manufacturer has materialized, unfortunately). Other new devices and techniques include a convenient multiphase rolling ball viscometer, a systematic guide for interpreting the appearance of dispersed systems, and a fast-freeze cold-stage transmission electron microscopy system for rapidly fixing liquids thermally for structural studies. A new and improved system is the second generation of this novel line.

2. *SCIENCE OF POROUS MEDIA AND CHAOTIC COMPOSITES.* Porous media encompass sedimentary rocks, soil, granular solids and packed beds, and many other materials in nature and technology. A porous medium is a chaotic composite of solid and 'void,' the void always containing fluid of one sort or another. The science of porous media is the science of disordered interspersions of solid with solid as well, and it has roots in the physics of disorder more generally.

Physics of structure and transport -- percolation theory. As more and more petroleum is produced from the porespace of reservoir rock, what remains is increasingly disconnected. The connectivity is the key factor in entrapment of residual oil in waterflooding, and in mobilization of residual oil by low tension processes. This was brought out early by the Minnesota team, at the 1975 Gordon Conference and in an influential letter published by *Nature* in 1977 (delayed by a skeptical London referee). The means of explanation was percolation theory, the relatively new and then little-known theory of transport on disordered networks. Subsequently the Minnesotans have extended and applied this theory to a variety of transport processes in reservoir rock and other porous media, the latest being a predictive theory of capillary pressure and relative permeability, and mechanisms of dispersion or mixing in flow. The approach has been taken up in recent years by others, particularly physicists recruited into petroleum industry laboratories.

Topology of porous media. The connectivity of fluids in porespace is mediated by the connectivity or topology of porespace itself, and it was soon realized that the irregular branching and reconnection of not only the porespace but also the interpenetrating matrix play crucial roles: topology is as important as geometry in chaotic composites. Publicly enunciated at the 1979 DOE Tulsa Symposium on Enhanced Oil & Gas Recovery, this fact has fueled accelerating research. One important recent result is the experimental demonstration of the theoretically predicted close correlation of residual oil

saturation with the topological genus, or holeyness, per unit volume of porous rock.

Geometry of porespace. Though the roles of pore size and shape had long been recognized, the Minnesota researchers were helping delineate these roles by the 1976 Joint Convention on Enhanced Recovery of the Petroleum Society of the Canadian Institute of Mining and the Canadian Society of Petroleum Geologists in Calgary: behavior of oil-water menisci in pores, mobilization of entrapped oil blobs, contrast between packed-sphere, polyhedral, and other types of porespace. The latest developments are the mechanism of oil choke-off in pore throats, and working concepts of subpopulations of pores defined by pore entry criteria. The latter are central in the new theories of capillary pressure, relative permeability, and dispersion in two-phase flow. Underlying these developments is a systematic method of analyzing both the geometry and topology of porespace, a method that will be more practicable with automated image analysis of serial sections of rock samples.

Modeling of structure and transport. Among porespace that have been analyzed at Minnesota are those of synthetic 'rocks' -- actually copper sinters controlled to specifications -- and computer-generated rocks, totally managed though nevertheless chaotic or random in nature. Prominent among the latter are polyhedral porous structures generated from the Voronoi tessellation of space, originally introduced as a rough model of microemulsion microstructure by the Minnesota team at a National Science Foundation Workshop in Cleveland in February 1976. A complementary model, perfectly smooth-walled porous structures generated from the Schwarz-surface division of space, is currently under study as well.

The chaos of real rocks and their porespace has been modeled by Monte Carlo sampling of computer realizations, a powerful technique that came into its own in mathematical physics with the advent of modern computers. By this means the Minnesotans have attacked a variety of transport processes -- conductivity, flow, deformation, microcracking, and fracture -- in a compaign to develop a comprehensive theory. To date most of the research has been with Voronoi-type models. Because only relatively small models can be treated in detail, methods of scaling their behavior up into predictions of core-level and field-level performance have come under increasingly intense study. Effective medium theory is promising, and the latest development in press at this writing, is a combination of that theory with the more recent renormalization approach from statistical physics.

Fluid distribution. In petroleum recovery as in other processes involving immiscible fluids in porespace, the distribution of fluids can be crucial. In many circumstances the distributions are mediated, or even controlled, by the degree to which each of competing fluids "wets" the porewall, as deduced

from responses to one or more tests that have defined wettability syndromes. Over the past several years the basic physics of wetting has been under study at Minnesota, the results appearing in a series of papers in journals of chemical physics, surface and colloid chemistry, and petroleum engineering. The key to wettability syndromes, and apparent contact angles that are sometimes measured, has proved to be the behavior of submicroscopically thin films and pockets of liquid -- behavior associated with what has come to be called disjoining pressure or disjoining potential. A manifestation of intermolecular forces in inhomogeneous fluid, as is interfacial tension too, thin-film behavior falls under the molecular theory and thermodynamics work originally addressed to tension and phase behavior. Recent contributions include papers on the nature of wetting transitions, the dynamics of wetting, and the ways in which residual wetting liquid distributes in porespace of varying roughness.

A novel experimental approach to visualization of fluid distributions is the freeze-fracture cold-stage scanning electron microscopy system developed at Minnesota (in the wake of the transmission electron system for studying microstructured fluids), where applications have been made to not only petroleum and brine in rock, but also drilling fluids, persistent emulsions, and a variety of hydrated porous media. It has been adapted in at least one petroleum industry laboratory.

3. *SUPERCOMPUTER-SCALE THEORETICAL ANALYSES AND MATHEMATICAL MODELING.* The Minnesota group has harnessed applied mathematics, numerical mathematics, and up-to-date scientific computers and computer software and is solving heretofore intractable problems. Modern finite element mathematics has emerged as the workhorse for the two-dimensional and three-dimensional physics and engineering involved. In many cases a supercomputer is needed. Late in 1981 Minnesota became the first university to install a supercomputer, a CRAY-1, to the great advantage of the research group. The group continues to pursue ever more reliable, cost-effective methods, whether on the CRAY-1, the older CDC-74 mainframe computer, or departmental VAX midi-computers. Among the benefits have been uncommon skill in matrix-handling methods, continuation schemes, Schwarz-Wendroff approximation (for integral and integrodifferential systems), stability analysis, and outright innovation in efficiently representing boundary regions and in automatically adapting discretizations to systems with sharp fronts or waves.

One-dimensional chemical flooding simulator. An early version, for laboratory core floods and field streamtube applications, was used in the late 1970's at Intercomp for analysis of laboratory data and for guidance of a two-dimensional simulator in the design competition for the Bell Creek Field Test by DOE and Gary Operating Company. The current effort at Minnesota is on a one-dimensional chemical flooding predictor that relies virtually entirely on theoretically generated or interpolated wetting, flow, dispersion, and phase behavior properties.

FLOW IN POROUS MEDIA, PHASE BEHAVIOR
AND ULTRALOW INTERFACIAL TENSIONS:
MECHANISMS OF ENHANCED PETROLEUM RECOVERY

CALENDAR YEAR 1982
FINAL TECHNICAL REPORT

DOE/DE-AC19-79BC10116

Department of Chemical Engineering & Materials Science
University of Minnesota

Front-tracking methods. Following on the 1976 Gordon Research Conference that highlighted the need for more effective front-tracking for reservoir simulation, particularly of chemical flooding processes, work began at Minnesota on the novel variably-timed flux updating method for controlling numerical dispersion, a troublesome artifact in finite difference computations. That research culminated in a 1980 Society of Petroleum Engineers Paper showing how effective the method can be for two-dimensional simulation, and adding impetus to the trend of incorporating aspects of the method of characteristics into finite difference approximations. More recent research at Minnesota is on adaptive subdomaining for the alternative finite element method, which is under widespread investigation today.

Computation of phase and tension behavior from equations of state. One of the main lines of development at Minnesota is efficient fitting of parameters to experimental data, and calculation of phase splits, phase compositions, and interfacial tensions from thermodynamic equations of state and associated tension equations. Examples are the Peng-Robinson and recent Kleintjen-Konigsveld equations for vapor-liquid and liquid-liquid equilibria, and the screened Flory-Huggins equation for microemulsion systems. Work on the last began in a 1975 research seminar and led to a major paper published in the December 1982 *Society of Petroleum Engineers Journal*. One of the novel features is the attention paid to metastable states that may intrude, and their interpretation in terms of thermodynamic energy surfaces. Further contributions are in preparation which include making use of higher order critical points as well as key features of one- and two-component equilibria in the systematic computation of multicomponent equilibria of greater practical interest.

Molecular theory calculations. Another long-evolving line is the computation of molecular distributions and microstructures from the differential and integral equations of molecular theory, and in certain cases by the Monte Carlo and molecular dynamics approaches. Basic insights from the results, many of them unprecedented in the literature, have informed the researches on surfactant phenomena, phase behavior, interfacial tension, and wetting films. Among the latest outcomes is the discovery, through formidable theoretical calculations (backed by analysis of relatively simpler idealizations), of the factors that determine wetting transitions, which are still a subject of scientific controversy -- and are potentially important to surfactant-based enhanced recovery processes.

Statistical physics of porous media. Here too the Minnesota team is on the frontier of computer applications to challenging problems, from the efficient generation of three-dimensional Voronoi-like tessellations and

FLOW IN POROUS MEDIAL, PHASE BEHAVIOR AND ULTRALOW INTERFACIAL TENSIONS: MECHANISMS OF ENHANCED PETROLEUM RECOVERY

CALENDAR YEAR 1982
FINAL TECHNICAL REPORT

DOE/DE-AC19-79BC10116

Department of Chemical Engineering & Materials Science
University of Minnesota

Schwarz-like divisions of space, to Monte Carlo calculations of percolation properties of the networks of pore-occupying fluids, to finite element analysis of mechanical properties and transport processes. Recent accomplishments are the delineation of the roles and relative importance of topological disorder and geometrical disorder, e.g. porespace connectivity vis-a-vis shape and attendant flow resistance; and the explanation of the anisotropy of dispersion when one or more fluids flow, i.e. the different rates of effective fluid mixing in the average flow direction and at right angles to that direction.

Technological Challenge

Though the approaches taken are fundamental, the research is coordinated and directed to contribute to enhancing petroleum recovery. Ongoing interactions with industrial researchers and engineers have helped ensure relevance from the beginning of the program. Thus the topics at Minnesota that continue to be largely or partly supported by DOE funds are:

1. *the character of porespace and porewalls in oil-bearing sedimentary rocks;*

2. *the distribution of fluids in and displacement of one by another from permeable rocks;*

3. *the strength and transport properties of permeable rocks, especially as influenced by fluid contents;*

4. *the origins and roles of phase behavior and interfacial tensions in chemical flooding processes (carbon dioxide, caustic, surfactant, micellar, etc.);*

5. *the physical chemistry and rheology of microstructured fluids occurring in such processes;*

6. *the mechanisms of ultralow tensions attained in some such processes;*

7. *the molecular design of surfactant/amphiphile systems that have ultralow tensions tolerant to hostile, variable environments;*

8. *the principles of chemical flooding process design.*

FLOW IN POROUS MEDIA, PHASE BEHAVIOR
AND ULTRALOW INTERFACIAL TENSIONS:
MECHANISMS OF ENHANCED PETROLEUM RECOVERY

CALENDAR YEAR 1982
FINAL TECHNICAL REPORT

DOE/DE-AC19-79BC10116

Department of Chemical Engineering & Materials Science
University of Minnesota

The results of this research will continue to give better understanding of why conventional recovery averages only about one-third of original oil-in-place, and of how additional oil can be recovered economically.

Results are reported in scientific and engineering meetings and published in the refereed literature for quality assurance and permanence, as well as the widest dissemination. Preliminary abstracts and preprints of manuscripts are transmitted to DOE/BETC and can be requested from there or University of Minnesota. Abstracts also appear in Quarterly Reports.

Other important outputs are the information transfers during visits of scientists and engineers to Minnesota and the lively 'low tension' seminar held there weekly, and during visits of Minnesota researchers to other laboratories. Visits and seminars are reported in Quarterly Reports.

No less important are the highly qualified engineers and applied scientists produced at Minnesota for energy-related industries, government agencies, and universities. The program is built on research education, primarily of Ph.D. candidates but also of B.S., M.S., and postdoctoral students, in keeping with the mission of the University. The next page is a roster of researchers in the team fulltime or parttime at the start of 1983.

On the following pages, sixteen major accomplishments of the program are reported in detail, and abstracts are appended of the forty-five publications associated with Calendar Year 1982. Many of these publications are cited in the main text of the report.

FLOW IN POROUS MEDIA, PHASE BEHAVIOR
AND ULTRALOW INTERFACIAL TENSIONS:
MECHANISMS OF ENHANCED PETROLEUM RECOVERY

CALENDAR YEAR 1982
FINAL TECHNICAL REPORT
DOE/DE-AC19-79BC10116

Department of Chemical Engineering & Materials Science
University of Minnesota

RESEARCHERS IN FLUID MICROSTRUCTURE SCIENCE, POROUS MEDIA SCIENCE, AND FUNDAMENTALS OF ENHANCING PETROLEUM RECOVERY

David M. Anderson, M.S. Math (1982) Univ. Minn., 3rd-year grad. X-ray scattering measurements of surfactant microstructures; modeling of near-critical phase behavior; theory and computation of smoothly chaotic structures. (Rm 454 AmH)

Jayesh R. Bellare, B.S. Ch.E. (1982) Ind. Inst. Tech., 1st-year grad. Fast freezing, cold-stage transmission electron microscopy of fluid microstructures; materials science of liquid crystalline states; molecular theory, computation of microstructured fluids. (Rm 470 AmH)

*Robert (Bob) E. Benner, B.Ch.E. (1978) Purdue Univ., 4th-year grad. Molecular theory and computation of surface tension, contact angle, fluid microstructures; stability and bifurcation; finite element analysis, numerical methods, vector processing. (Rm 60 AmH)

**Karl E. Bennett, B.S. Ch.E. (1976) Princeton Univ. Ph.D. 1982: to DuPont Engineering Technology Laboratory. Microemulsion phase behavior, phase behavior modeling, viscosity, rheology; instrument development.

H. Ted Davis, Professor and Head, Department of Chemical Engineering & Materials Science; Professor of Chemistry. (Rm 151c AmH)

**Andrew (Andy) H. Falls, B.S. Ch.E. (1978) Cal. Inst. Tech. Ph.D. 1982: to Shell Development Company. Molecular theory, computation of fluid microstructures; finite element analysis of integral equations; contrast mechanisms in electron microscopy; cold-stage transmission electron microscopy of surfactant microstructures.

*Adel A. Heiba, B.S. Ch.E. (1979) Mass. Inst. Tech., 3rd-year grad. Integrated 1-D chemical flooding process simulator; theory and computation of capillary pressure and relative permeability, residual saturation and wettability effects. (Rm 229 AmH)

* Barry D. Hughes, Ph.D. Appl. Math. (1980) Australian Natl. Univ., Postdoc. Univ. Maryland. Research Associate. Theory of stochastic processes, network approximations to porous media, disordered materials; theory of dielectric relaxation. (Rm 457 AmH)

Gary R. Jerauld, B.S. Ch.E. (1980) Rensselaer Poly. Inst., 2nd-year grad. Voronoi modeling of porous rock; transport, strength, and wave propagation, wave attenuation; network and finite element analysis, numerical methods, CRAY-1 and VAX utilization. (Rm 229 AmH)

**Eric W. Kaler, B.S. Ch.E. (1978) Cal. Inst. Tech. Ph.D. 1982: to University of Washington. Theory and practice of x-ray scattering; light scattering; development of U. Minn. x-ray facility; mini- and micro-processor utilization; analysis of microemulsion and liquid crystal microstructures.

Carol F. Kenfield, B. S. Chem. (1980) Sonoma State Univ., 2nd-year grad. Phase behavior, interfacial tensions, and electrical conductivities of microemulsions and of alcohol-hydrocarbon-brine systems. (Rm 454 AmH)

John E. Kerins, Ph.D. Chem. (1981) Cornell Univ., Postdoctoral Researcher. Theory of three-fluid-phase contact line; molecular theory and computation of states of homogeneous and inhomogeneous (microstructured) fluids; CRAY-1 utilization; capillarity in wetting experiments. (Rm 457 AmH)

*Peter K. Kilpatrick, B.A. Chem. (1978) Occidental College, 4th-year grad. Surfactant synthesis and purification; experiments, theory, modeling, and computation of phase behavior of surfactant systems; near-critical phase behavior; applications of nuclear magnetic resonance spectroscopy. (Rm 454 AmH)

Wan Chu Kung, M.S. Physics (1982) Univ. Minn., 3rd-year grad. Molecular theory and computation of phase equilibria and interfacial tension; finite element analysis of integral equations, stability and bifurcation of thermodynamic equilibria; CRAY-1 utilization. (Rm 457 AmH)

Edward H. Loesch, M.S. Botany (1980) Univ. Minn. Associate Scientist. Scanning electron microscopy, cold-stage SEM; energy dispersive x-ray analysis; distribution of liquids and minerals in solvent extraction cruds, coated papers, sedimentary rocks and model systems. (Rm 443 SpSci)

William (Bill) F. Michels, B.S. Ch.E. (1981) Univ. Texas, 1st-year grad. Electrical conductivity, dielectric relaxation and pulsed gradient NMR studies of surfactant-rich fluid microstructures; deformation mechanisms and rheology. (Rm 454 AmH)

Wilmer G. Miller, Professor, Department of Chemistry; Graduate Professor, Department of Chemical Engineering & Materials Science. (Rm 56 KoltH)

Johannes M. Nitsche, Univ. Minn., 2nd-year undergrad. Kleintjens-Konigsveld equation of state, application to polar binary mixtures and extension to ternary mixtures. (Advised by Gary Teletzke) (Rm 50 AmH)

Ludwig C. Nitsche, Univ. Minn., 2nd-year undergrad. Two-phase flow visualization in microflow cell models of porous media; theory of frontal stability in immiscible displacement. (Advised by Gary Teletzke) (Rm 50 AmH)

Angelos T. Papaioannou, D. Eng. (1980) Natl. Technical Univ., Athens, Greece. Postdoctoral Researcher. Experimental studies of phase behavior and rheology of microemulsions; theoretical modeling. (Rm 454 AmH)

***J. Lincoln Paterson, Ph.D. Eng. Phys. (1981) Australian Natl. Univ., Postdoc. Univ. Ottawa. Postdoctoral Researcher. Flow in porous media; experimental studies of dispersion phenomena. (Rm 457 AmH)

Carolyn V. Pesheck, Research Fellow, Department of Chemical Engineering & Materials Science; Director of X-Ray Facility; Director of Undergraduate Research Participation Program. Phase behavior, interfacial tension; near-critical behavior. (Rm 454a AmH)

Stephen Prager, Professor, Department of Chemistry; Graduate Professor, Department of Chemical Engineering & Materials Science. (Rm 230 Smith)

Andrew W. Rabins, Univ. Minn., 3rd-year undergrad. Amphiphile study: phase splits and compositions in ternary and quaternary surfactant-alcohol-hydrocarbon-brine systems. (Advised by Peter Kilpatrick) (Rm 454 AmH)

*Clay J. Radke, Visiting Professor from University of California, Berkeley. (Rm 307 MM)

*Muhammad Sahimi, B.S. Ch.E. (1977) Teheran Univ. Molecular theory and computation of phase behavior and interfacial tension of CO_2-hydrocarbon systems; Monte Carlo studies and percolation theory of dispersion in multiphase flow in porous media; effective medium and renormalization methods. (Rm 229 AmH)

L. E. (Skip) Scriven, Professor, Department of Chemical Engineering & Materials Science; Graduate Professor of Fluid Mechanics. (Rm 151d AmH)

Joshua (Josh) B. Sweeney, B.S. Ch.E. (1980) Univ. Pennsylvania, 2nd-year grad. Cold-stage scanning electron microscopy of fluid-filled porous media; wetting and thin-film distributions in porous media; molecular theory and computation of electrical double layer phenomena. (Rm 440 AmH)

*Gary F. Teletzke, B.S. Ch.E. (1978) Northwestern Univ. Ph.D. 1982: to Exxon Production Research Company. Theory of perfect wetting; molecular theory and computation of thin-film and wetting phenomena; experimental and fluid mechanical theory of wetting, spreading. (Rm 470 AmH)

*E. L. Thomas, Visiting Professor from University of Massachusetts. (Rm 107 MM)

T. Kyle Vanderlick, M.S. Ch.E. (1982) Rensselaer Poly. Inst., 2nd-year grad. Thin-film physics, layering; multicomponent microfluid mechanics, wetting, spreading. (Rm 470 AmH)

Lynda J. Westburg, Univ. Minn., 3rd-year undergrad. Tricritical point study: phase splits and compositions in quaternary alcohol-hydrocarbon-brine systems. (Advised by Carolyn Pesheck) (Rm 454 AmH)

Robert A. Yapel, Univ. Minn., 1st-year undergrad. Electron microscopy, light microscopy and analysis of tar sands. (Advised by E. H. Loesch) (Rm 454 AmH)

Joseph (Joe) A. Zasadzinski, B.S. Ch.E. (1980) Cal Inst. Tech., 2nd-year grad. Transmission electron microscopy of fluid microstructures in surfactant systems; imperfections and rheology of liquid crystalline states; wetting and fluid distributions in porous media. (Rm 470 AmH)

*Departing 1983
**Departed October 1982
***Departed February 1983

Breakdown (March 1983)

Resident Faculty	4	Postdoctoral Researchers	4
Visiting Faculty	2	Doctoral Researchers	12
Research Staff	2	Master's Researchers	1
		Undergraduate Researchers	5

I. FLUID MICROSTRUCTURES OF SODIUM 4-(1'-HEPTYLNONYL)BENZENESULFONATE MIXTURES

Introduction

The literature on aqueous-surfactant and aqueous-hydrocarbon-surfactant systems is rich in proven and suggested microstructures: single phase and multiphase; equilibrium and nonequilibrium. These include, for example, molecular solutions; normal and inverted micelles; microemulsions; lamellar, hexagonal, and cubic ordered phases; dispersions of liposomes and vesicles. Our interest in surfactant microstructures came from studies on ultralow ($<10^{-3}$ mN/m) interfacial tensions between hydrocarbon and water induced by the presence of low concentrations of surfactants. In some sulfonate systems we found that the apparent interfacial tensions (as measured with a spinning drop tensiometer) depends on the order of mixing components (1), on the hydrocarbon drop size (1), and on the length of contact time of hydrocarbon with aqueous surfactant before tension measurement (2) (Figure 1). Through the use of multiple experimental techniques we were able to correlate these unusual observations with the surfactant microstructures present in the aqueous phase prior to tension measurement.

The pure surfactant, sodium 4-(1'-heptylnonyl)benzenesulfonate, SHBS, together with cosurfactants and cosolvents, was used for many of our studies. In this paper we review the microstructures present, their size and their stability in surfactant systems containing SHBS.

Nature of Microstructures in Aqueous SHBS: Phase Behavior

The progressive addition of surfactant to water at temperatures above the Krafft-point typically results in an orderly sequence of microstructures: molecular solution, micellar solution and, eventually, liquid crystalline phases. This occurs both with surfactants having a single hydrocarbon tail (3) and with ones having a short double tail, such as Aerosol OT (4,5) and the di-alkanoyl lecithins (6).

Our early efforts (1,7) yielded a simple temperature-composition phase diagram for SHBS in water. At low concentration at 25°C SHBS dissolves to form a molecular solution. Conductance data show deviation from Onsager limiting law behavior, but no evidence of micellization (2,8). No Krafft boundary is observed to 90°C, yet at all temperatures investigated a lamellar liquid crystalline rather than a crystalline phase is formed (7). The isotropic liquid crystalline biphasic region is very broad; at 25°C a 0.06 wt. % SHBS solution is in equilibrium with the hydrated lamellar liquid crystal (ca. 75 wt. % SHBS; 1 mole SHBS to 7.5 mole H_2O). In the presence of NaCl the equilibrium isotropic phase contains much less SHBS (7).

It was recently proposed that SHBS forms normal micelles of 17 Å radius at 45°C (9,10). Inasmuch as the 45°C conductivity data (9), on which the presence of a cmc is based, are similar to our 25°C data (2), we sought to probe for the existence of a cmc using ^{23}Na nmr. With sodium salts of anionic surfactants the chemical shift of the sodium ion associated with micelles is well known to differ from the shift in molecular surfactant (11). Due to rapid exchange of the Na^{+} from the molecular solution to the micellar environment, the observed chemical shift is a weighted average. Thus the chemical shift

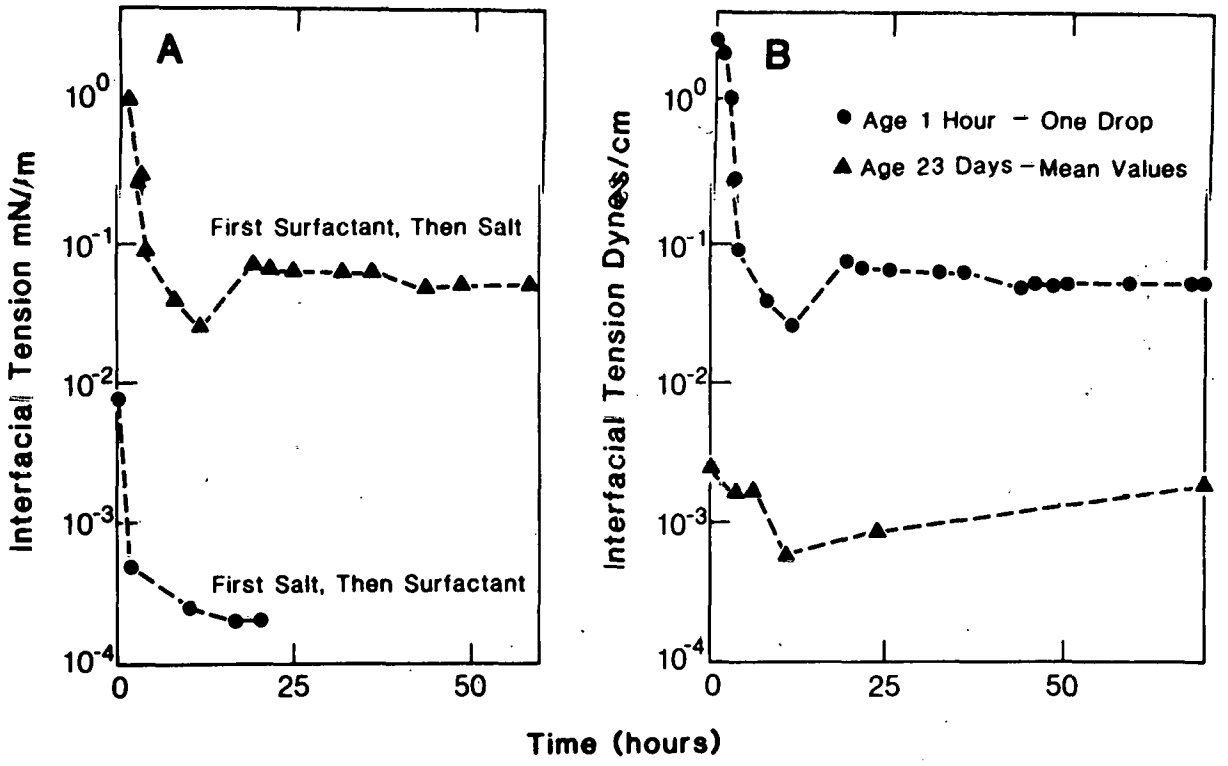

Figure 1. Spinning drop tension measurements against decane of 0.07 wt. % SHBS, 0.3 wt. % NaCl aqueous dispersions as dependent on order of mixing (A) and on contact time before tension measurement (B).

undergoes a rapid change with concentration after the cmc is reached, and has proved to be a reliable method for cmc determination (11). The chemical shift of the sodium ion in a lamellar phase also differs from that in the molecular surfactant solution. The sodium ion is not exchanged rapidly with the sodium in the equilibrium isotropic phase. However, the observed chemical shift changes to that of the lamellar phase shortly after the solubility limit is passed (12). The observed ^{23}Na chemical shift at 47°C for SHBS in water, Figure 2, shows no break when crossing the suggested cmc but does reveal the appearance of the lamellar phase. The continuous smooth change in the chemical shift up to the solubility limit does suggest aggregation, but not classical micelle formation. This is consistent with both the conductivity and neutron scattering data. Thus over a wide range of surfactant concentration, the aqueous SHBS that is contacted with hydrocarbon for tension measurement consists of the liquid crystalline phase dispersed in a aqueous phase devoid of surfactant micelles. The nature of the dispersed liquid crystalline phase is, then, the microstructure of relevance with respect to the observed anomalous tension behavior.

Nature of Microstructures in Aqueous SHBS: The Lamellar Phase

Optical microscopy of aqueous SHBS dispersions between crossed polars shows the birefringence expected of smectic liquid crystal (7). Freeze fracture electron microscopy, Figure 3, reveals clearly its lamellar nature (13). X-ray diffraction, Figure 4, yields a lamellae repeat distance of 33 Å, which

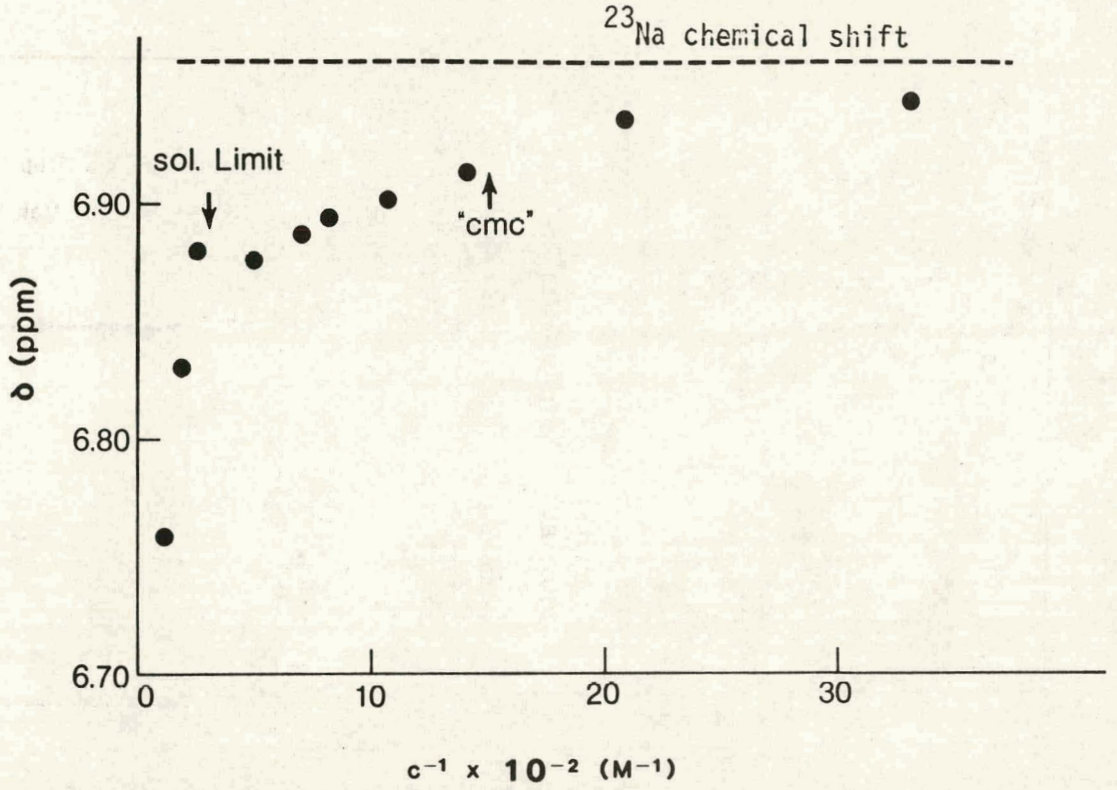

Figure 2. Sodium-23 nmr chemical shift as a function of SHBS concentration at 47°C, compared to the solubility limit and reported (9) cmc. The dashed line is the ^{23}Na chemical shift of NaCl at 47°C.

is independent of added electrolyte up to 5 wt. % NaCl (14).

Differential scanning calorimetry (15), Figure 5, coupled with temperature dependent nmr (7,12,15) and x-ray diffraction (14) data reveals a number of features of the molecular dynamics and thermodynamics of the lamellar phase:

1) the hydrocarbon chain melting occurs at ca. -75°C, while the water between the surfactant bilayers melts over a broad range from -50 to -10°C.

2) the motion of the benzenesulfonate head group is highly anisotropic, and becomes frozen-in at temperatures where the water between bilayers freezes.

3) the x-ray diffraction pattern of the lamellar phase below -50°C indicates that the frozen water is not normal hexagonal ice. The SHBS concentration must be in the biphasic region (< 75 wt. % SHBS) before the normal ice lattice is observed.

4) the ^{2}H, ^{13}C, and ^{23}Na nmr line widths at 25°C indicate the water between bilayers, the sodium ion, and the benzenesulfonate head group are all moving rapidly though anisotropically while the hydrocarbon tails are moving rapidly and nearly isotropically.

The gross features of the lamellar phase are in common with those of long double-tail surfactants. A number of the details are, however, different:

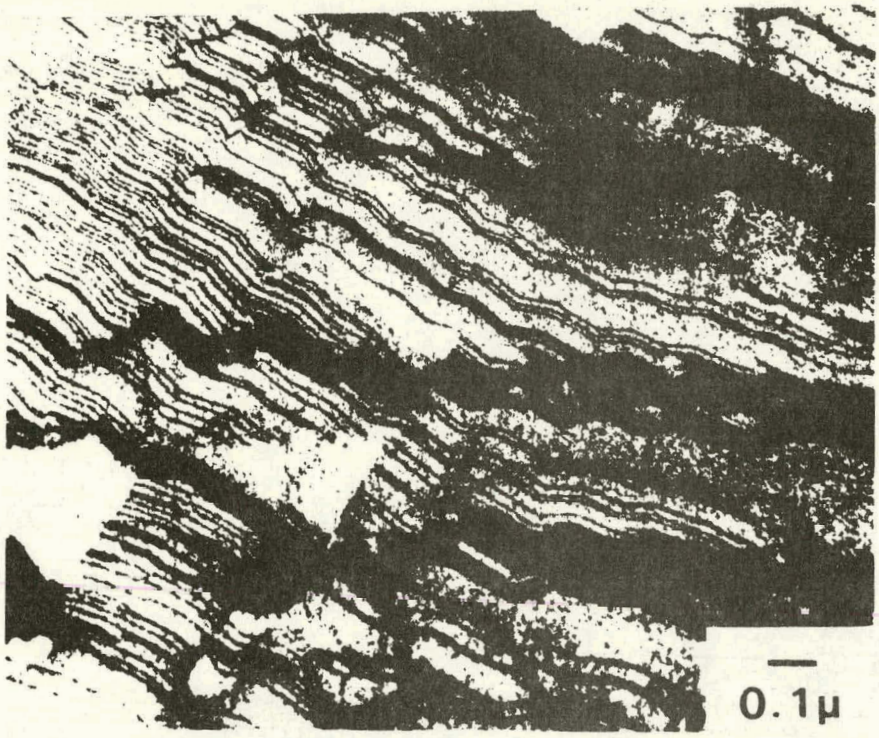

Figure 3. Freeze fracture electron micrograph of a 75 wt. % SHBS smectic phase revealing the lamellar organization.

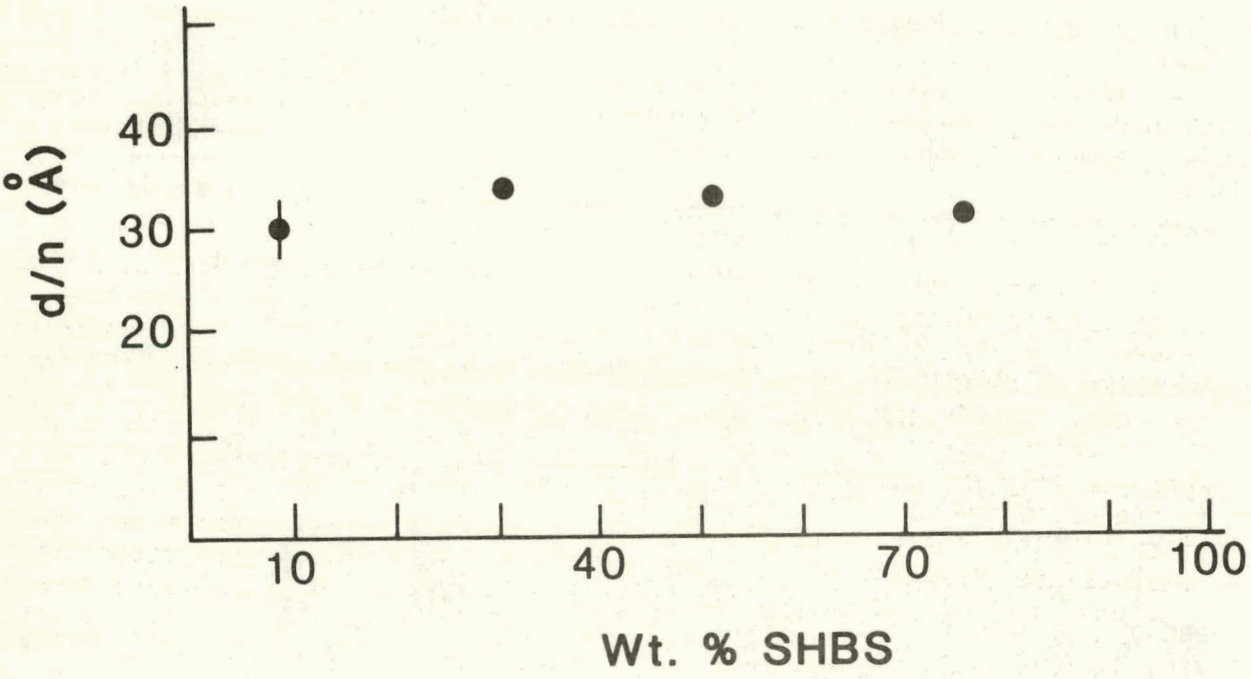

Figure 4. Concentration dependence of the x-ray spacings of SHBS dispersions in water.

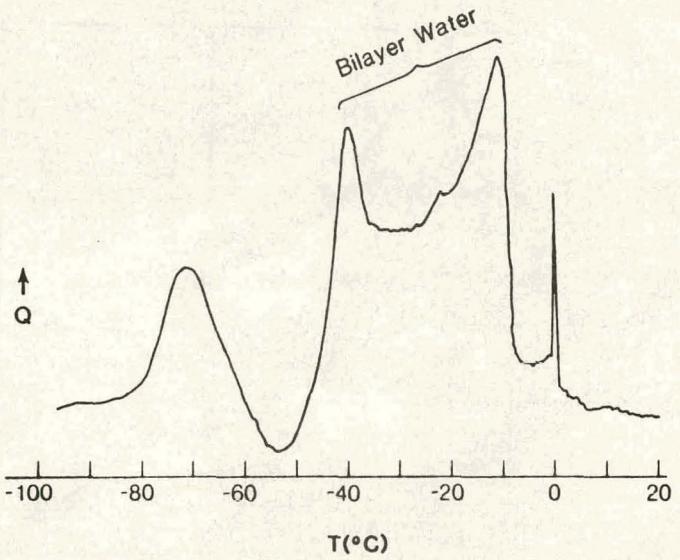

Figure 5. Differential scanning calorimetry of 75 wt. % SHBS. The sharp peak at 0°C is due to a trace of extraneous water.

1) the hydrocarbon chain melting, i.e. the gel-liquid crystalline phase transition, occurs at a temperature below the freezing of the bilayer water, and is the lowest such transition temperature reported. At room temperature the lamellar phase is about a hundred degrees above the gel-liquid crystalline transition temperature.

2) the equilibrium amount of water between surfactant bilayers which contributes only ~ 8 Å to the lamellar thickness, is insensitive to electrolyte (NaCl) concentration, and when frozen is not ice-like. The distance between sulfonate sheets is so small that simple electrostatic theory cannot be used to explain the spacing.

Nature of Microstructures in Aqueous SHBS: Vesicles

Sonication of liquid crystalline dispersions of double-tailed surfactants often produces spheroidal vesicles consisting of a fluid core surrounded by at least one surfactant bilayer of lamella (16). The presence of vesicles in dilute (< 2 wt. %) sonicated dispersions of SHBS was first revealed by fast-freeze cold-stage transmission electron microscopy (17). Further electron microscopy (18) has shown that these vesicle populations have approximately a log-normal distribution of sizes. Quasielastic light scattering measurements (18) indicate that SHBS vesicles have an average diameter of ca. 450 Å in water and that the average vesicle diameter decreases when the vesicles are prepared in 0.3 wt. % NaCl brine or at higher surfactant concentrations (5 or 10 wt. %). A combination of differential scanning calorimetry and nmr results, supported by small-angle x-ray scattering evidence, indicates that most of the vesicles contain a single bilayer (Figure 6) (18).

Vesicles are of scientific importance as, for example, simple models of biological membranes. However, the thermodynamic and kinetic stability of vesicular dispersions has not been fully determined. SHBS vesicles are ideally

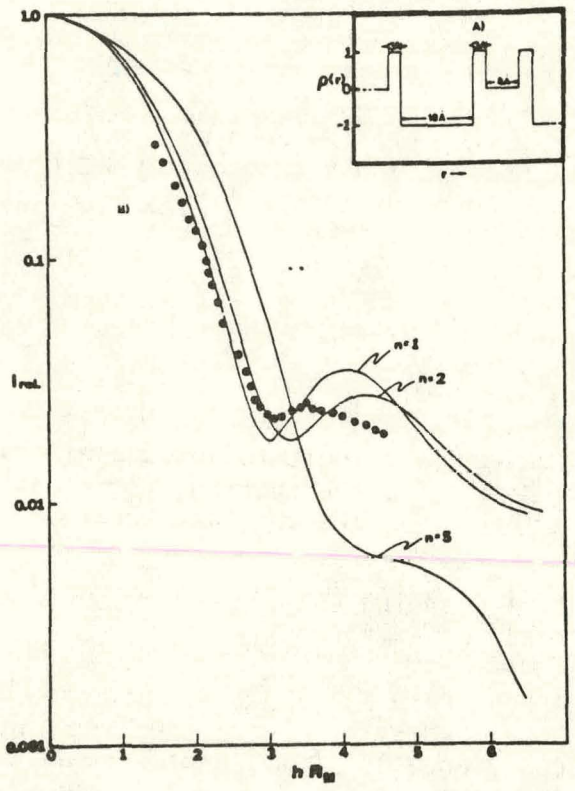

Figure 6. (A) Schematic electron density profile for a SHBS bilayer and water; (B) comparison of the scattered intensity calculated for vesicles with 1, 2, and 5 bilayers (solid lines) with the measured intensity scattered from a 2.0 wt. % vesicle dispersion in water (dotted line).

suited for long-term vesicle stability studies because, unlike most biological vesicle-forming surfactants, SHBS is chemically stable and biologically inert in aqueous solutions at room temperature.

Optical microscopy (17), conductance (17), and light scattering (17,18) measurements along with electron microscopy (18) were used to follow the stability of SHBS vesicle dispersions upon aging. Although vesicles were in some instances found to be stable for months when left undisturbed after sonication, in all cases a reversion to the smectic phase (present as dispersed liquid crystallites) was eventually observed by several techniques. These aging studies, as well as those on phospholipid vesicle dispersions in the literature (19), were carried out in the presence of some dispersed liquid crystallites. Some liquid crystallites remain after sonication, and our attempts to completely remove them failed. Both ultrafiltration and ultracentrifugation were unsuccessful, as was the traditional method of gel permeation chromatography (GPC). Indeed, we showed (18) that flow through a glass bead GPC column actually hastened the reversion of vesicles to liquid crystallites. Thus, it has been impossible to investigate the kinetic stability of an isolated vesicle dispersion in the absence of liquid crystallites. Nonetheless, the reversion of SHBS vesicles to liquid crystallites clearly indicates that these vesicles are not equilibrium structures in water or brine.

Vesicles stability was rapidly altered by osmotic shocks, and by contact with hydrocarbon (8,20). Tension behavior of vesicle dispersions against hydrocarbon differs from that observed with liposome dispersions.(20).

Nature of Microstructures in Aqueous SHBS: Liposomes

The state of the smectic phase depends markedly on sample preparation and history. Sonication of dilute dispersions, as discussed previously, produces vesicles. Mechanical agitation, whether by hand or by a vortex mixer, alters the microstructure even in the bulk smectic phase. Our first indication of this came from ^{2}H nmr studies (21,15), shown in Figure 7, where mechanical agitation changed the spectral line shape of a sample agitated at ambient temperature. Upon standing, even for periods of up to two years, the line shape did not revert to that observed before shaking. However, annealing at 90°C for a few minutes resulted in a return to the original line shape. Similar effects were difficult to observe at lower concentration, where the system is biphasic, as the spectrum was dominated by the water in the equilibrium isotropic phase. We conjectured, however, that even with the single-phase smectic sample, agitation resulted in formation of smaller domains of unknown morphology. Electron microscopy of freeze-fractured, replicated samples shows clearly that this is the case (14). In the nonagitated sample, freeze-fracturing revealed many examples of the fracture plane running through the bilayer plane, as, for example, Figure 3. Upon mechanical agitation the typical micrograph is as in Figure 8, where the fracture plane has run around closed-shell smectic particles, liposomes, rather than through them. Thus in the agitated samples the smectic phase consists of concentric shell liposomes, the mean size of which depends on the agitation history. In the concentrated unshaken samples it is difficult to determine if the much larger particles are closed shell liposomes or planar.

The nmr lineshape is easily understood (14). Annealing at 90°C results in electron micrographs similar to the unshaken material, indicating that the liposome size depends on thermal history as well as mechanical treatment. Similar behavior was observed at lower concentrations, where the system is biphasic. The mean size distribution of the liposomes is highly dependent on sample preparation (14,18) and can be easily altered by even gentle handling techniques. The size distribution can be quite broad with sizes ranging from hundreds of angstroms to hundreds of microns in the same sample.

Effects of Cosolvents and Cosurfactants

The addition of short-chain alcohols to dispersions of SHBS liposomes alters the microstructure. At low alcohol-to-SHBS ratios, the alcohol is incorporated into the lamellar phase and aligns itself with its polar hydroxyl group near the mean plane of surfactant head groups and it short alkyl tail penetrating the hydrocarbon lamellae. This was determined by a combination of centrifugation and ^{13}C nmr (22). The size and number of liposomes are altered, as observed by spectroturbidimetry (2,8). As the alcohol content is increased, the lamellar phase is solubilized into an isotropic phase; the amount af alcohol necessary to completely solubilize the liposomes decreases as the lipophilicity of the alcohol increases in the series n-butanol, n-pentanol, n-hexanol. Conductance data for the isotropic solution (Figure 9A) show marked deviation from Onsager limiting law behavior but no sharp break

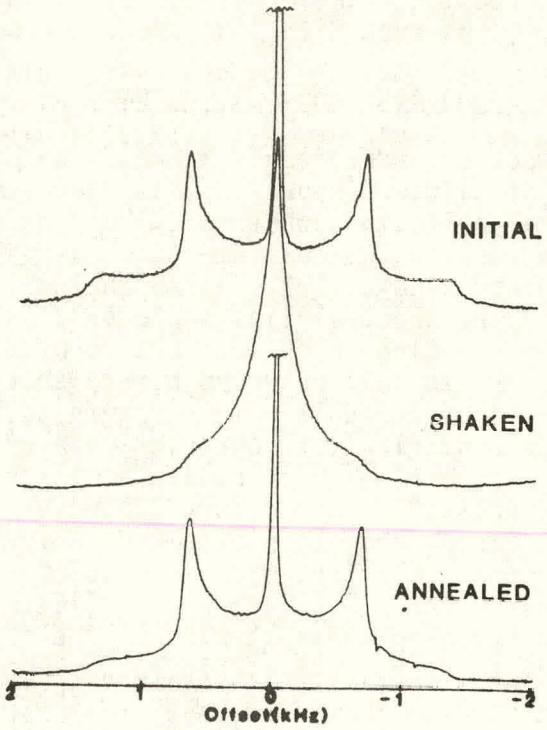

Figure 7. Deuterium nmr spectra at ambient temperature of the hydrated smectic phase (75 wt. % SHBS, 25 wt. % D_2O) before mechanical agitation, after agitation on a vortex mixer, and after heating to 90°C.

Figure 8. Electron micrograph of the hydrated lamellar phase after mechanical agitation.

to indicate the onset of micelles. Low-angle x-ray scattering measurements confirmed the absence of micelles (22).

Addition of the cosurfactant sodium dodecylsulfate (SDS) to a SHBS dispersion in water or brine results in formation of a mixed lamellar phase, as deduced by conductivity, nmr and calorimetry (2,23). These mixed liquid crystals form at weight ratios R of SDS/SHBS below ca. 0.2. At R above ca. 2.0, a single isotropic phase of mixed micelles of SDS and SHBS forms, while for $0.2 < R < 2$ both mixed liquid crystals and mixed micelles are present. Figure 9B shows that the microstructures formed upon solubilization of SHBS lamellar liquid crystalline dispersions by a micelle-forming surfactant are different from those formed upon solubilization by an alcohol.

Quasielastic light scattering measurements indicate that the mixed micelles formed by mixtures of SDS and SHBS are non-spherical in both 0.3 M and 0.6 M NaCl and that the apparent molecular weight of the micelle increases as the ratio R decreases (24).

SHBS-Brine-Hydrocarbon

The phase behavior in the presence of hydrocarbon depends markedly on the components present. With SHBS-H_2O(NaCl)-hydrocarbon, and with SHBS-SDS-H_2O(NaCl)-hydrocarbon formulations which are turbid, frequently opaque, low volume fraction, and of high surfactant content is formed between the water-rich lower phase and the oil-rich upper phase (1,8,23). The microstructures present in this third phase are unknown. It is these systems which display the order of mixing and contact time effects shown in Figure 1. Similar effects have been observed with commercial, multicomponent sulfonates (25).

The occurrence of apparently ill-behaved tension measurements, the appearance of low volume fraction surfactant-rich phase after contact with hydrocarbon, and the presence of liquid crystalline dispersions in the aqueous surfactant phase before contact with hydrocarbon are related. The history dependent tension measurements can be correlated with the size and type of SHBS dispersion in the aqueous phase before contact with hydrocarbon. The dispersed surfactant must reach the surface of the hydrocarbon droplet in the spinning drop measurment. The delivery time depends on the size and density of the particle, and on the flow times in the spinning drop tube. In addition, the dispersed surfactant must spread on the hydrocarbon droplet and produce a thin coat. Thus the order-of-mixing effect is a manifestation of the fact that the SHBS liposomes are less finely dispersed when surfactant. When the third phase was present we found ultralow tensions between oil-rich and water-rich phases (1,2); otherwise, the tension was not ultralow.

SHBS-Brine-Alcohol-Hydrocarbon

When a low molecular weight alcohol is added as a cosolvent, SHBS-alcohol-brine-hydrocarbon mixtures often yield microemulsion phases in equilibrium with excess oil or brine or both (26). These microemulsions can incorporate substantial amounts of both oil and water. They are typically transparent or translucent, isotropic, and have low viscosities. Ultralow interfacial tensions are frequently found between these microemulsions and

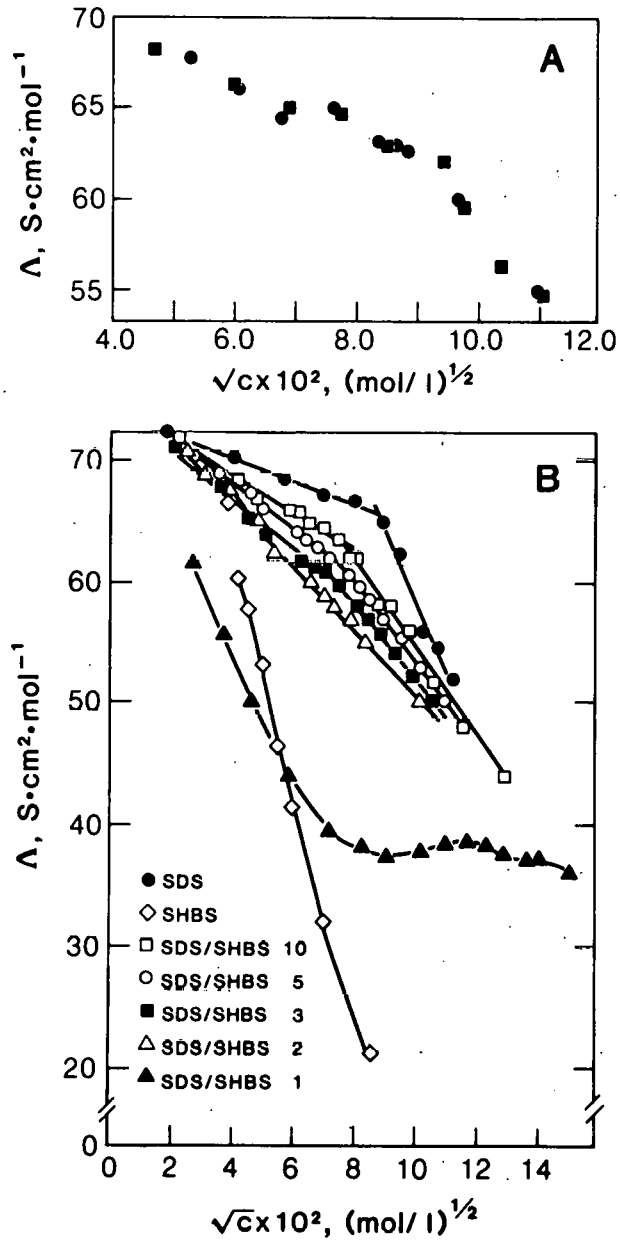

Figure 9. (A) Equivalent conductivity as a function of SHBS concentration for SHBS-NAA-water solutions; (B) Equivalent conductivity as a function of surfactant concentrations for aqueous preparations of SDS and SHBS in different weight ratios.

the excess phases with which they are in equilibrium. Because these tension measurements are made on equilibrium systems, no order-of-mixing or aging effects are observed. There is ample evidence that the ultralow interfacial tension states and the patterns of phase behavior found in microemulsion-forming mixtures such as these result from the nearness of microemulsions to critical points (27-29). However, the microstructure of microemulsions and the way it changes with relative proportions of oil and water remain open questions, particularly for microemulsions containing substantial amounts

of both oil and water.

There is convincing evidence (30) that the addition of small amounts of oil to an aqueous surfactant solution often produces an oil-in-water microemulsion containing surfactant micelles swollen with oil. The analogous water-in-oil microemulsion likewise can contain inverted surfactant micelles swollen with water. Both types of micelles are presumed to be stabilized by surfactant that separates the oil(or water)-rich interiors from the continuous water(or oil)-rich exterior. As appreciable amounts of oil (or water) are incorporated into the microemulsion, the micelles swell; such micellar solutions have been described as equilibrium dispersions of "droplets" (31). This picture of microemulsion microstructure as disjoint "droplets" is viable at low volume fractions of dispersed component. However, at intermediate volume fractions of oil and water it is possible that microemulsions organize into equilibrium bicontinuous structures in which both oil-rich and water-rich regions span the sample (32-40).

Bicontinuous water-oil-surfactant states have been described in detail elsewhere (32,33). One convenient representation of microemulsion structure that can naturally incorporate water/oil, bicontinuous, and oil/water equilibrium microdispersions in the Voronoi model, a random tessellation of space into convex polyhedra filled by water and oil and separated by surfactant sheets. First used by Talmon and Prager (34,35) to build a free energy function for microemulsion systems that predicts phase behavior in qualitative agreement with experiment, it has been extended to model the dynamic and static scattering from a bicontinuous microemulsion microstructure (36) and to represent the electrical conductivity of microemulsions (37). Experimental results show that the representation of a microemulsion as a bicontinuous microstructure is appropriate over a wide range of compositions in both SHBS and other surfactant mixtures (36-41).

Conclusions

1) The temperature-composition phase diagram of SHBS with brine or water is dominated by a large biphasic region in which a lamellar liquid crystalline phase is in equilibrium with a dilute isotropic SHBS solution.

2) The isotropic SHBS solution is not micellar; however, conductance and nmr spectroscopy suggest that non-micellar aggregates are present.

3) The lamellar phase is very fluid, easily deformable, and can be readily dispersed in water to form a broad distribution of closed shell liposomes.

4) The size distribution of liposomes found in dispersions depends markedly on the method of preparation.

5) ^{2}H, ^{13}C, and ^{23}Na nmr indicate that at room temperature the sodium counterions and the sulfonate head group undergo rapid though anisotropic motion in the lamellar phase while the hydrocarbon tail groups move rapidly and nearly isotropically.

6) Sonication of dilute dispersion leads to long-lived, non-equilibrium vesicles which probably consist of a single bilayer.

7) Addition of a suitable alcohol to a liposome dispersion solubilizes the lamellar phase and yields an isotropic phase which is weakly aggregated but not micellar.

8) Addition of a micelle-forming cosurfactant, SDS, produces either mixed liquid crystals, mixed micelles, or both.

9) SHBS, brine, and hydrocarbon combine to produce an opaque, viscous, surfactant-rich third phase.

10) Interfacial tension behavior which is time and preparation dependent correlates with the presence of the viscous third phase and to the nature of the microstructure present in the unprecontacted aqueous surfactant phase.

11) With the addition of a suitable alcohol, SHBS, brine, and hydrocarbon can combine to form a microemulsion phase which solubilizes substantial amounts of both oil and water and which appears from conductance and small-angle x-ray scattering measurements to be bicontinuous.

References Cited in Section I

1. Franses, E. I., Puig, J. E., Talmon, Y., Miller, W. G., Scriven, L. E., and Davis, H. T., J. Phys. Chem. 84, 1547 (1980).

2. Puig, J. E., Scriven, L. E., Davis, H. T., and Miller, W. G., in Interfacial Phenomena in Enhanced Oil Recovery, D. Wason and A. Payatakes, eds., AIChE Symposium Series S-212, 1 (1982).

3. Fontell, K., Mol. Cryst. Liq. Cryst. 63, 59 (1981).

4. Rogers, J. and Winsor, P. A., J. Colloid Interface Sci. 30, 247 (1969).

5. Williams, E. F., Woodberry, N. T., and Dixon, J. K., J. Colloid Sci. 12, 452 (1957).

6. Tausk, R. J. M., Karmiggelt, I., Oudshoorn, C., and Overbeek, J. Th. G. Biophys. Chem. 1, 175 (1974).

7. Franses, E. I., Davis, H. T., Miller, W. G., and Scriven, L. E., in Chemistry of Oil Recovery, R. T. Johansen and R. L. Berg, eds., ACS Symposium Series 91, Amer. Chem. Soc., Washington, DC, 1979, p. 35.

8. Puig, J. E., Ph.D. thesis, University of Minnesota, 1982.

9. Magid, L. J., Shaver, R. J., Gulari, E., Bedwell, B., and Alkhafaji, S., Prep. Div. Pet. Chem., Am. Chem. Soc. 26, 93 (1981).

10. Magid, L. J., Triolo, R., Johnson, Jr., J. S., and Koehler, W. C., J. Phys. Chem. 86, 164 (1982).

11. Gustavsson, H. and Lindman, B., J. Amer. Chem. Soc. 100, 4647 (1978).

12. Blum, F. D., Ph.D. thesis, University of Minnesota, 1981.

13. Costello, M. J. and Gulik-Kryzwicki, T., Biochim. Biophys. Acta 455, 412 (1976).

14. Nietering, K. E., Russo, P. S., Blum, F. D., and Miller, W. G., to be submitted to J. Colloid Interface Sci. (1982).

15. Blum, F. D. and Miller, W. G., J. Phys. Chem. 86, 1729 (1982).

16. Huang, C., Biochemistry 8, 344 (1969).

17. Franses, E. I., Talmon, Y., Scriven, L. E., Davis, H. T., and Miller, W. G., J. Colloid Interface Sci. 86, 449 (1982).

18. Kaler, E. W., Falls, A. H., Davis, H. T., Scriven, L. E., and Miller, W. G., J. Colloid Interface Sci., in press (1982).

19. Larabee, A. L., Biochemistry 18, (1979).

20. Puig, J. E., Franses, E. I., Talmon, Y., Davis, H. T., Miller, W. G., and Scriven, L. E., Soc. Pet. Eng. J. 22, 37 (1982).

21. Franses, E. I. Rose, K., Blum, F. D., Bryant, R. G., and Miller, W. G., in preparation (1982).

22. Kilpatrick, P. K., Blum, F. D., Davis, H. T., Falls, A. H., Kaler, E. W., Miller, W. G., Puig, J. E., Scriven, L. E., and Woodbury, N. A., in Microemulsions, I. D. Robb, ed., Plenum Press, 1982, p. 143.

23. Puig, J. E., Franses, E. I., and Miller, W. G., J. Colloid Interface Sci., in press (1982).

24. Kaler, E. W., Puig, J. E., and Miller, W. G., to be submitted to J. Phys. Chem. (1982).

25. Hall, A. C., Colloids and Surfaces 1, 209 (1980).

26. Bennett, K. E., Phelps, C. H. K., Davis, H. T., and Scriven, L. E., Soc. Petr. Engr. J. 21, 747 (1981).

27. Fleming, III, P. D. and Vinatieri, J. E., AIChE J. 25, 493 (1979).

28. Fleming, III, P. D., Vinatieri, J. E., and Glinsmann, G. R., J. Phys. Chem. 84, 1526 (1980).

29. Davis, H. T. and Scriven, L. E., Soc. Petr. Engr., paper # 9728, Dallas, TX, 21-24 September, 1980.

30. Gulari, E., Bedwell, B., and Alkhafaji, S., J. Colloid Interface Sci. 77, 202 (1980).

31. Zulauf, M. and Eicke, H. F., J. Phys. Chem. 83, 480 (1979).

32. Scriven, L. E., Nature 263, 123 (1977).

33. Scriven, L. E., in Micellization, Solubilization and Microemulsion, K. L. Mittal, ed. Plenum Press, New York, 1977, p 877.

34. Talmon, Y. and Prager, S., Nature 207, 333 (1977).

35. Talmon, Y. and Prager, S., J. Chem. Phys. 69, 2984 (1978).

36. Kaler, E. W. and Prager, S., J. Colloid Interface Sci. 86, 359 (1982).

37. Bennett, K. E., Hatfield, J. C., Davis, H. T., Macosko, C. W., and Scriven, L. E., in Microemulsions, I. D. Robb, ed., Plenum Press, 1982, p. 65.

38. Lindman, B., Kamemka, N., Kathopoulis, T. M., Brun, B., and Nilsson, P-G., J. Phys. Chem. 84, 2485 (1980).

39. Kaler, E. W., Bennett, K. E., Davis, H. T., and Scriven, L. E., J. Chem. Phys., in press (1982).

40. Kaler, E. W., Davis, H. T., and Scriven, L. E., J. Chem. Phys., in preparation (1982).

41. Stilbs, P., Mosely, M. E., and Lindman, B., J. Magn. Resonance 40, 401 (1980).

II. TOWARD UNDERSTANDING MICROEMULSION MICROSTRUCTURE: A SMALL-ANGLE X-RAY SCATTERING STUDY

Introduction

One of many definitions of microemulsion is a thermodynamically stable, optically isotropic liquid phase containing hydrocarbon, water (or brine) and surfactant (1). Usually, though not always, an alcohol or other amphiphilic cosurfactant is necessary for microemulsion formation. It appears that the surfactant, by virtue of its tendency to locate between water-rich and hydrocarbon-rich regions, imposes some intermolecular order in microemulsion; nonetheless, the long-range order remains stochastic, and microemulsions are of low viscosity. The length scale of the inhomogeneities can vary from the size of the surfactant molecule upward (1). The patterns of phase behavior (2-4) in the vicinity of the ultralow tension states observed between hydrocarbon and water phases in multiphase systems containing microemulsion phases have been postulated to arise from the nearness of microemulsions to solution critical points or plait points (5,6). However, the kinds of fluid microstructures present in microemulsions and how they change as the relative amounts of oil and water vary remain open questions, particularly for microemulsions incorporating substantial amounts of both oil and water. These systems are of scientific interest because the microstructure is still a mystery, and they are of industrial importance because they can cosolubilize large amounts of oil and water while producing ultralow interfacial tensions.

There is plentiful evidence (7), particularly from light-scattering and small-angle scattering experiments, that addition of small amounts of oil to an aqueous surfactant solution produces an oil-in-water (o/w) microemulsion containing surfactant micelles swollen with oil. Analogously, the addition of small amounts of water to an oleic surfactant solution can result in water-in-oil (w/o) microemulsions (8) containing inverted surfactant micelles swollen with water. In both cases, the swollen micelles are presumed to be stabilized by surfactant that separates the oil(or water)-rich interiors from the water (or oil)-rich continuous fluid exterior. As appreciable amounts of oil (or water) are incorporated into the surfactant solution, the micelles or inverted micelles swell; such solutions have been described (8) as equilibrium dispersions of microemulsion "droplets".

There seems little doubt that the picture of microemulsion structure as discrete swollen micelles is realistic at low volume fractions of dispersed component. As the volume fraction of oil or water increases, however, the experimental data become much more ambiguous. Several researchers (9-14) have claimed that microemulsion "droplets" simply pack together as their volume fraction increases so that a distinct droplet microstructure persists to high volume fractions ($\phi_D \sim 0.5$). In this view, there is a concentration of swollen micelles above which the microemulsion inverts from an o/w to a w/o swollen micellar structure or vice versa. Such an inversion must be abrupt because o/w and w/o structures are mutually exclusive.

Scriven (15) pointed out the likelihood that at intermediate volume fractions of oil and water, microemulsions organize into equilibrium bicontinuous structures. Such structures contain oil and water domains that are sample spanning and chaotically intertwined; they are again stabilized by sheet-like

surfactant regions in the boundary zones between domains. These sheet-like structures form because surfactants tend strongly to locate between water-rich and oil-rich regions. They are fluid, yet are persistent enough to impose topological order in the microemulsion. Bicontinuous structures may be viewed as fluid analogs of solid porous media such as sponge and sandstone; moreover, they are the only structures known that can allow the often observed *continuous* variation of properties as the microemulsion changes from rich to lean in oil or water.

It is important to recognize that the bicontinuous microemulsion structures envisioned here are not static arrays (such as are likely present in certain classes of viscous isotropic lyotropic liquid crystals) in which the long-range connected networks exist for long times. Rather, because of the fragility of the surfactant-rich sheets with respect to thermal fluctuations the microstructure is dynamic; i.e. oil-rich and water-rich domains continually form and reform, as can be inferred from the fact that microemulsion viscosities do not greatly differ from that of oil or water (16). Aside from the experimental evidence, it is impossible to imagine a *continuous* transition from an entirely o/w to an entirely w/o arrangement without invoking bicontinuous structures at intermediate concentrations. The alternative is a sudden inversion, evidence of which is lacking in our measurements and in careful measurements by others.

The continuous variation of bicontinuous structures, and with lesser fidelity the o/w and w/o swollen micelle morphology, can be qualitatively modeled as a random geometry of oil and water generated by a so-called Voronoi tessellation (17). Talmon and Prager (18) used the Voronoi model to build a free energy theory which predicts phase equilibria patterns similar to those observed experimentally in microemulsion-forming systems. Scattering calculations for both a static and dynamic Voronoi model compare well with experimental results (19). The model also predicts a percolation threshold in electrical conductivity (20) which agrees well with experiment (16). The radioactive tracer diffusion and NMR data of Lindman (21) also indicate that some microemulsions are continuous in both oil and water.

We report here an experimental investigation of microemulsion microstructure using chiefly small-angle X-ray scattering (SAXS) techniques. We have examined dilute microemulsions for which swollen micelle or droplet models are generally accepted, and we have also studied concentrated microemulsions where our data allow us to evaluate critically both bicontinuous models and "droplet" models of the microstructure of microemulsions.

Experimental Materials

The commercial surfactant mixture TRS 10-80 was used as received from the Witco Chemical Company. Analysis of a similar batch (22) showed it to be 79.7 wt. % sulfonate, 9.2 wt. % water and 11.0 wt. % oil with < 0.1 wt. % salt. The surfactant molecular weight is approximately 420. The tertiary amyl alcohol (tAA) and n-octane were reagent grade Aldrich and Phillips products respectively. All brine solutions were made with dried, reagent grade NaCl (Fisher Scientific) and water drawn through a four-stage Millipore cartridge system. The brine salinities are given as g NaCl/100 cm^3 solution. Samples with salinities at or below 1.8 were prepared by mixing equal volumes of brine and surfactant-alcohol-oil stock solution containing 0.40 g TRS 10-80,

0.20 g tAA and 10 ml n-octane. Microemulsions at salinities greater than 1.8 were prepared at a later date using nominally the same recipe. Any variation is due to differences between supposedly identical commercial surfactant samples. All samples were sealed in either ampules or glass pipets, rocked gently at 25°C for at least 24 hours, and then allowed to settle in a water bath at 25° (for one week or until there were no further changes in the volumes or visual appearance of the phases).

Experimental Equipment: Small-Angle X-ray Scattering (SAXS)

Small-angle x-ray scattering patterns were obtained with a Kratky camera modified with an extended flight path to incorporate a TEC Model 210 position sensitive x-ray detector (23). The x-ray source was a fixed-target Siemens Model FK60-20 copper x-ray tube (1.54 Å wavelength) operated at 400 watts with a nickel filter. Approximately 0.2 ml of the microemulsion phase was slowly drawn into a syringe through a 22-gauge needle and then injected into a 1.0 mm diameter glass capillary tube. The sample was maintained at 25°C, and the camera was evacuated to reduce the background scattering. The x-ray patterns were usually obtained in 3 hours with less than 1% counting error for the smallest angles. The scattering from an empty capillary was subtracted from the data after correction for absorption and detector sensitivity. The camera was aligned so that the approximation of an infinite collimation slit was valid, and the collimation effect was removed by the method of Schmidt (24). Only relative scattering intensities were obtained; these are reported as a function of the magnitude of the scattering vector

$$h \equiv \frac{4\pi}{\lambda} \sin \theta$$

where 2θ is the angle between the incident and scattered radiation and λ is the x-ray wavelength.

Experimental Equipment: Viscosity

The viscosity of each microemulsion phase was measured using the multiphase rolling ball viscometer (16,25) in which a 1 mm diameter stainless steel ball (1/6 of pipet diameter) rolls through the liquid phase of interest. The time it takes the ball to traverse a fixed distance is measured electronically and is related to liquid viscosity by calibration with Newtonian oils of known viscosity. All reported viscosities are the average of at least five measurements.

Experimental Equipment: Electrical Conductivity

The electrical conductivity was measured at 25°C in a 3 cm^3 Jones-type conductivity cell connected to a Brinkman E518 direct indicating conductometer operating at 1000 Hz. Samples were transferred to the conductivity cell at approximately 0.2 cm^3/sec through a 13-gauge needle. The conductivity was recorded after it remained constant for at least 4 minutes.

Experimental Equipment: Interfacial Tension

The spinning drop method was used to measure interfacial tensions between the preequilibrated microemulsion phase and the excess oil or brine

phase (26,27). Samples were equilibrated and loaded into the tensiometer in an air box at 25°C to help prevent phase separation. Densities were measured with a Mettler/Paar DMA40 digital density meter and refractive indices with a Bausch and Lomb refractometer.

Experimental Equipment: Compositional Analysis

Water, alcohol and octane concentrations were measured by gas chromatography (GC) on a Porapak-P column operated at 170°C in a Hewlett-Packard model 5730A chromatograph equipped with a Hewlett-Packard model 3390A integrator. Surfactant concentrations were measured by two-phase hyamine titration (28).

Scattering Theory

In the absence of multiple scattering, the intensity of x-rays scattered from an isotropic sample in a SAXS experiment is (29)

$$I(h) = I_e(h)\ \langle(\delta\rho)^2\rangle\ V_s \int_0^\infty \gamma(r)\ \frac{\sin hr}{hr} \cdot 4\pi r^2 dr \qquad (1)$$

where $I_e(h)$ is the intensity of scattering by a single electron, V_s is the scattering volume, $\langle(\delta\rho)^2\rangle$ is the mean square average of the electron density fluctuations and $\gamma(r)$ is the electron density correlation function defined as

$$\gamma(r) \equiv \langle\delta\rho(x)\ \delta\rho(x+r)\rangle\ . \qquad (2)$$

If the x-rays are scattered from electron density variations generated by distinct monodispersed particles, Eq. (1) can be rearranged to

$$I(h) = I_e(h)\ \bar{N}V_p^2\ (\bar{\rho}-\rho_0)^2 P(h)\ S(h,n) \qquad (3)$$

where $\bar{N}$ is the number of particles in the scattering volume, V_p is the particle volume, and $\bar{\rho}-\rho_0$ is the difference in electron density between the particle and the solvent. The structure factor $S(h,n)$ is given by (29)

$$S(h,n) = 1 + n\int_0^\infty (g(r)-1)\ \frac{\sin hr}{hr} \cdot 4\pi r^2 dr \qquad (4)$$

where n is the number density and $g(r)$ is the radial distribution function for the particles. $P(h)$ is the particle form factor, which for a homogeneous sphere of radius R is

$$P(h) = \left[3\ \frac{(\sin(hR) - hR\cos(hR))}{(hR)^3} \right]^2 \qquad (5)$$

Regardless of whether Eq. (1) or (3) is used to describe the scattered intensity, we can obtain a length scale called the apparent radius of gyration R_{ga} defined via the expansion

$$I(h) \cong I(0) \left[1 - \frac{R_{ga}^2 h^2}{3} + \cdots \right] \tag{6}$$

where $I(0)$ is the intensity at zero angle. Both $I(0)$ and R_{ga} depend on microemulsion composition. We have found the measured values of both R_{ga} and $I(0)$ to be sensitive to small random errors introduced in the scattering curve by the desmearing process. More accurate and reproducible values can be obtained by first fitting the uncorrected data to

$$\tilde{I}(h) = \tilde{I}(0) \exp\left(- \frac{\tilde{R}_{ga}^2 h^2}{3} \right) \tag{7}$$

(where the tilde indicates a quantity before collimation correction) and then employing the results relating R_{ga} and $\tilde{I}(0)$ to R_{ga} and $I(0)$ derived by Luzzati.

Another important SAXS quantity is the mean square electron density fluctuation $\langle(\delta\rho)^2\rangle$, also called the invariant, given by (29)

$$\langle(\delta\rho)^2\rangle = 4\pi^2 \int_0^\infty I(h)\, h^2 dh = 2\pi^2 \int_0^\infty \tilde{I}(h)\, h dh \, . \tag{8}$$

The invariant is calculated from the data before collimation correction; Eq. (7) is used to extrapolate the data to $h = 0$. The extrapolation of the data to infinite h is more delicate because the standard assumptions (29) leading to the common result (Porod's law) that $\tilde{I}(h)$ varies as h^{-3} for large h are not in general valid for microemulsions. Instead, when the microemulsion consists of oil-rich and water-rich domains, we have found that an adequate approximation (31) for use in Eq. (8) is simply

$$\lim_{h\to\infty} \left[I(h) \right] = \frac{A}{h^3} + \tilde{I}_b \tag{9}$$

where A is a constant proportional to the specific surface between oil-rich and water-rich domains and $\tilde{I}_b$ is a background intensity arising from intermolecular inhomogeneities in the water-rich and oil-rich domains. $\tilde{I}_b$ is subtracted from the data before the invariant is calculated.

$I(0)$ is in general proportional to the isothermal compressibility of the scattering sample. For the special case of monodisperse particles, Eq. (3) applies and reduces to

$$I(0) = I_e(0)\, (\bar{\rho} - \rho_0)^2 V_p^2 \bar{N} n k T\, \chi_T$$

where χ_T is the osmotic compressibility, i.e.

$$\chi_T \equiv -1/V \left(\frac{\partial V}{\partial \Pi} \right)_T$$

and Π is the osmotic pressure. Normalization of I(0) with the invariant eliminates the electronic density dependence and yields

$$\frac{I(0)}{\langle(\delta\rho)^2\rangle} = \frac{V_p nkT\chi_T}{2\bar{\pi}^2(1-\phi_p)} \qquad (10)$$

where ϕ_p is the volume fraction of particles.

Results: Thermodynamic and Transport Properties

The changes in the relative volumes of microemulsion and excess phases (Fig. 1) as the brine salinity varies are similar to those reported by others (4). In particular, the microemulsion changes from a water-rich lower phase at low salinity to an intermediate density middle-phase and then to an oil-rich upper phase as salinity increases. We denote this phase progression as (32) $\underline{2}$,3,$\overline{2}$, where the numbers give the number of equilibrium phases and the bar indicates whether the microemulsion is the lower ($\underline{2}$) or upper ($\overline{2}$) phase in the two-phase samples. Here, in three-phase samples the microemulsion phase is always intermediate in density and is therefore the middle phase.

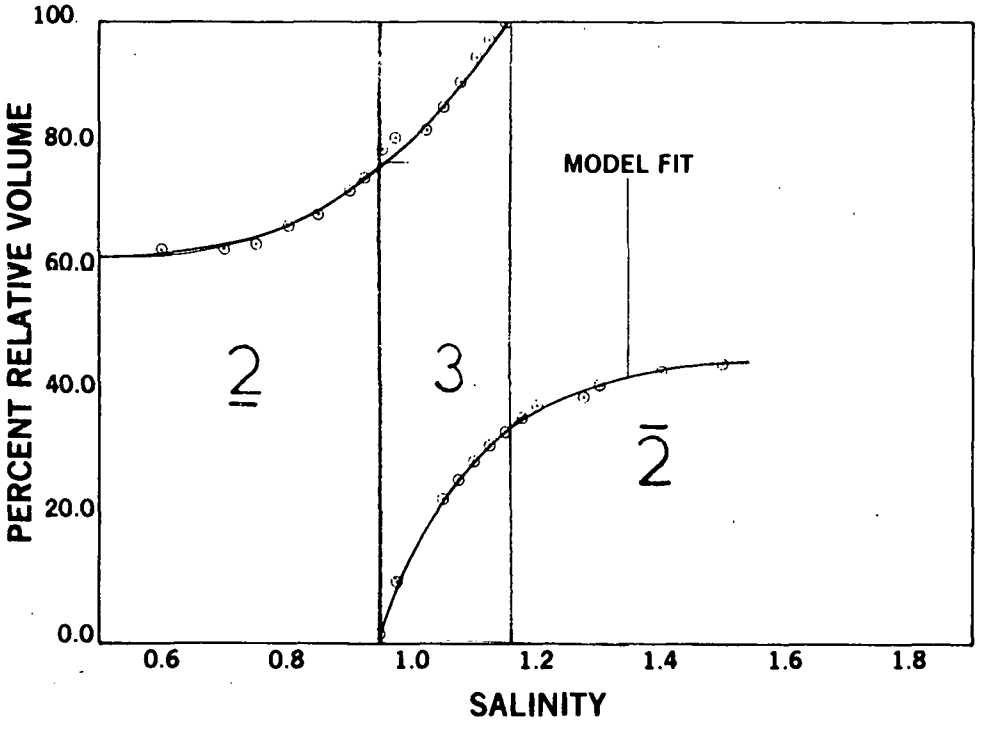

Figure 1. Relative volumes of microemulsions and excess water or oil phases as a function of salinity. The solid lines are least-squares fits to the theoretical equations of ref. 33.

The GC results (Fig. 2) show in detail the shift from water-rich to oil-rich microemulsion as salinity increases. The small differences in oil and

water composition between samples prepared from different surfactant-alcohol-oil stock solutions at 1.8 salinity (Fig. 2A) probably result from differences in composition between the supposedly indentical samples of TRS 10-80. The GC results also show (Fig. 2B) that about 1.0 wt. % tAA is present in the microemulsion phase at all but the lowest salinities. Hyamine titration indicates that negligible surfactant is solubilized in any of the non-microemulsion phases. Combining these results with the phase volume observations (Fig. 1) indicates that the amount of surfactant and alcohol in the microemulsion phase never varies by more that 30% over the entire salinity range and by less than 5% above approximately 1.4 salinity.

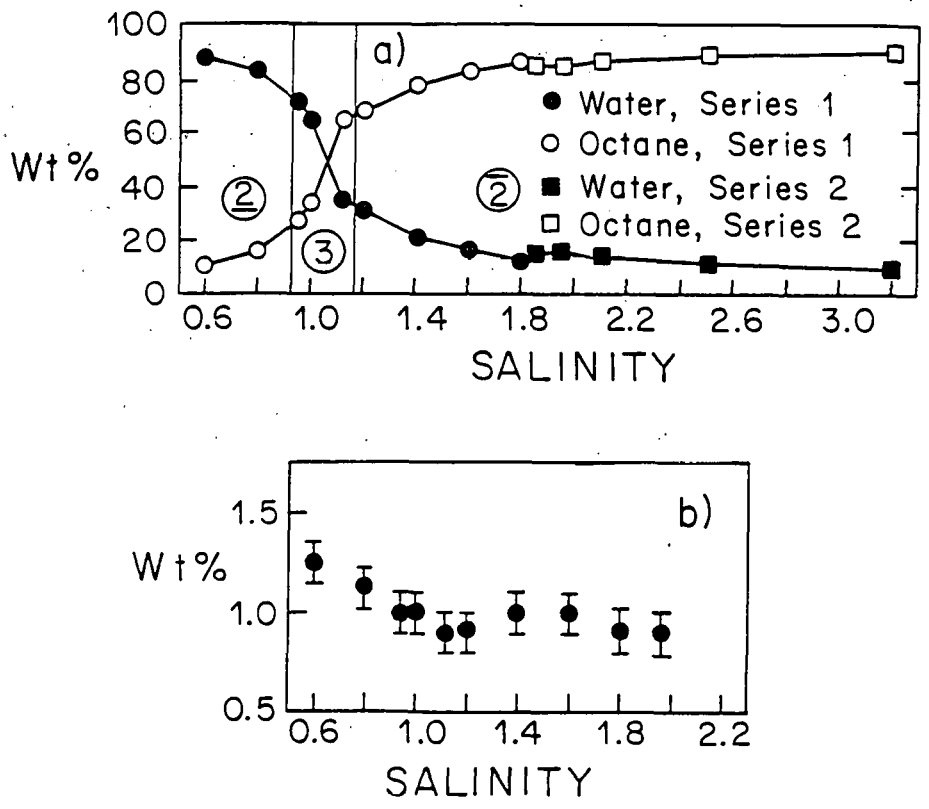

Figure 2. a) Wt. % of water and octane in the microemulsion phase and b) wt. % tert-amyl alcohol in the microemulsion phase as a function of salinity.

The interfacial tensions between the microemulsion phase and the excess oil or water phase are presented in Figure 3. Because of the tendency of the microemulsion phases taken from the three-phase samples to phase separate in the tensiometer due to uncontrollable small temperature fluctuations (less than ± 0.01°C), it was not possible to take reproducible data in the three-phase region.

The viscosities (Fig. 4) and electrical conductivities (Fig. 5) are quite similar to those reported previously (16) for a variety of microemulsion systems. In particular, as the salinity increases, the viscosity (Fig. 4) goes through a sharp maximum, a local minimum and a second maximum. As noted earlier (16) the two maxima do *not* correlate with the $\underline{2}$,3 and 3,$\overline{2}$ phase transitions. At high salinities, the microemulsion viscosity approaches that of the

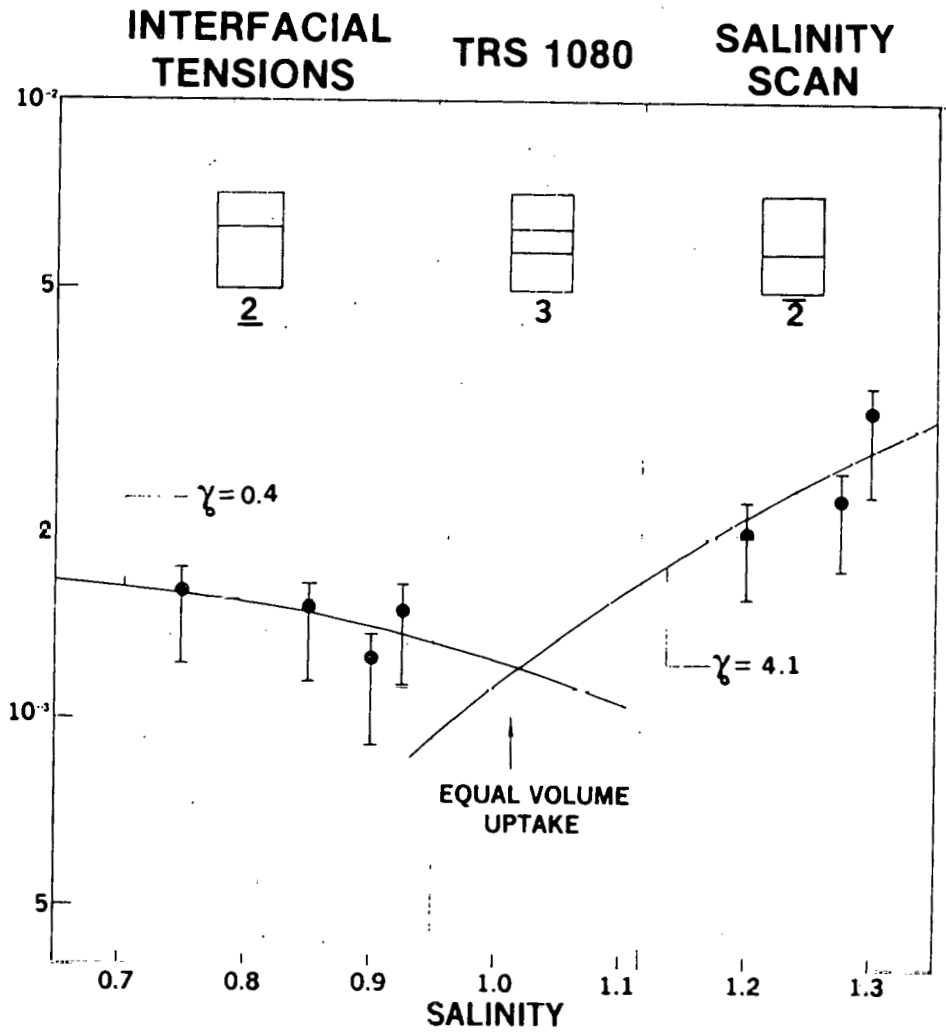

Figure 3. Interfacial tension variation with salinity. The solid lines are least squares-fits to the theoretical equations of ref. 5.

surfactant-alcohol-oil stock solution.

The ratio of the electrical conductivity of these microemulsions to that of the brine used to make the sample increases from less than 0.0007 to 0.9 as the salinity decreases and the volume fraction of brine increases. This ratio is plotted in Figure 5 as a function of the volume fraction brine in the microemulsion. The data points are from microemulsions made from the original surfactant-alcohol-oil stock as well as from microemulsions made with the same recipe but with commercial surfactant stocks that may differ slightly.

Small-Angle X-ray Scattering (SAXS)

A typical microemulsion scattering pattern after correction for the collimation effect (desmearing) is shown in Figure 6. All of the scattering curves decay monotonically with increasing angle. No secondary scattering maxima were

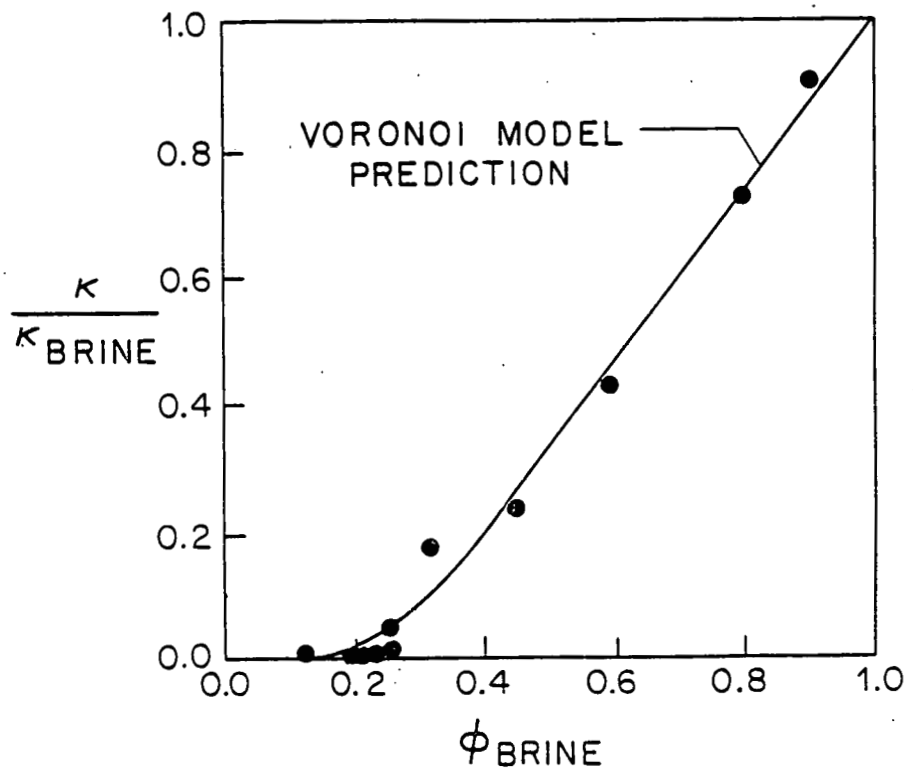

Figure 4. Microemulsion viscosity as a function of salinity.

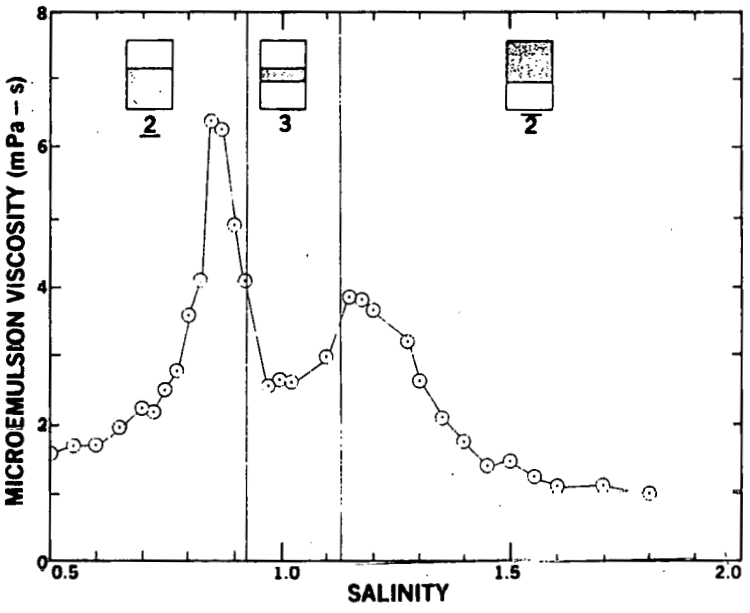

Figure 5. Normalized microemulsion phase electrical conductivity as a function of volume fraction brine. The solid line is the Voronoi model prediction.

ever observed in these samples.

The plot of $\ell n\ \tilde{I}$ vs. h^2 used to determine $\tilde{R}_{ga}$ from the data of Figure 6 is shown in Figure 7, and the variation of R_{ga} with salinity and octane volume fraction is shown in Figures 8A and 8B. The error bars are estimated from duplicate runs of identical samples; the R_{ga} calculated from repeated runs of the same sample are reproducible within the size of the data point. A striking feature in Figure 8 is that the R_{ga} remains nearly constant over a large range of o/w ratios and, in particular, the R_{ga} does not change as the $\underline{2}$,3 and 3,$\overline{2}$ phase boundaries are crossed. The value of R_{ga} for the surfactant-alcohol-octane stock solution sample is 22 ± 3 Å.

As stated above, the Porod region ($h > 0.12$ Å^{-1}) of all of these microemulsions is adequately represented by Eq. (9) (Fig. 9). We note, however, that the scattering intensities are low in this region and thus are quite sensitive to any errors made in the subtraction of background scattering. This problem is particularly acute for microemulsions containing substantial amounts of oil and water because of the difficulty of defining a "solvent" phase, the scattering of which should be subtracted from the microemulsion scattering. For all of the microemulsions in this study, only the scattering from an empty scattering cell is subtracted from the microemulsion scattering curve.

The variation of $I(0)/\langle(\delta\rho)^2\rangle$ with octane volume fraction is shown in Figure 10. The maximum values of $I(0)/\langle(\delta\rho)^2\rangle$ are for samples with the largest R_{ja}.

Discussion: Thermodynamic and Transport Properties

Fleming and Vinatieri (5,33) and others (6,34) have recently proposed theories linking several physical properties of microemulsion, including the ultralow tensions of microemulsions with oil-rich and water-rich phases, to the nearness of critical endpoints. The solid lines in Figures 1 and 3 are least-squares fits of Fleming and Vinatieri's (33) theoretical equations for a near-critical microemulsion model to our phase volume and interfacial tension data. The quality of the fits and the ultralow interfacial tensions measured indicate that this microemulsion system conforms to the "near-critical" concept.

Macroscopic transport properties of microemulsion such as viscosity and electrical conductivity must be related to the microstructure of the microemulsion. Bennett et al. (16) have examined the viscosity and electrical conductivity of several microemulsion formulations, including one nominally identical to the system studies here (any differences are due to variations in the composition of the commercial surfactant). Their results in almost all cases are qualitatively similar to ours (Figs. 4 and 5). In particular, the normalized electrical conductivity ($K = K/K_{Brine}$) remains nearly zero ($K < 0.007$) up to a brine volume fraction (ϕ_B) of between 0.15 and 0.20, above which it increases rapidly with increasing ϕ_B. This behavior accords with a percola-

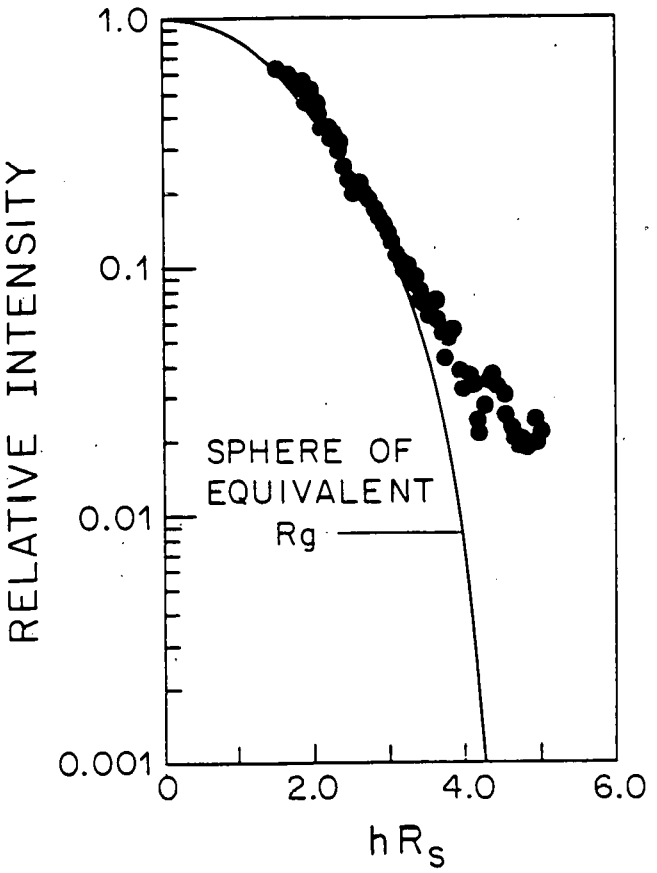

Figure 6. Scattering data from 3.7 salinity microemulsion. The solid curve is the scattering calculated for a sphere (radius R_s) with the same R_g as the microemulsion.

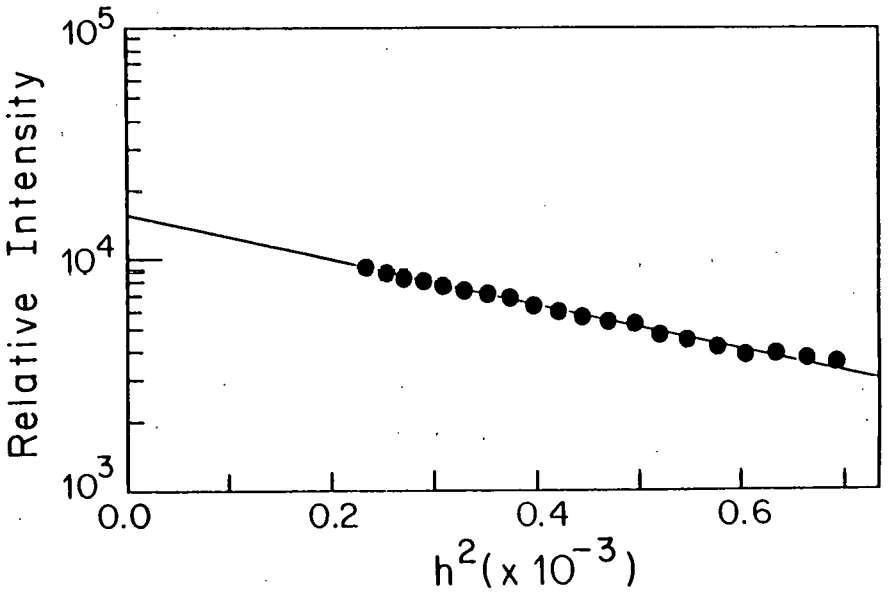

Figure 7. Guinier plot of the data shown in Figure 6.

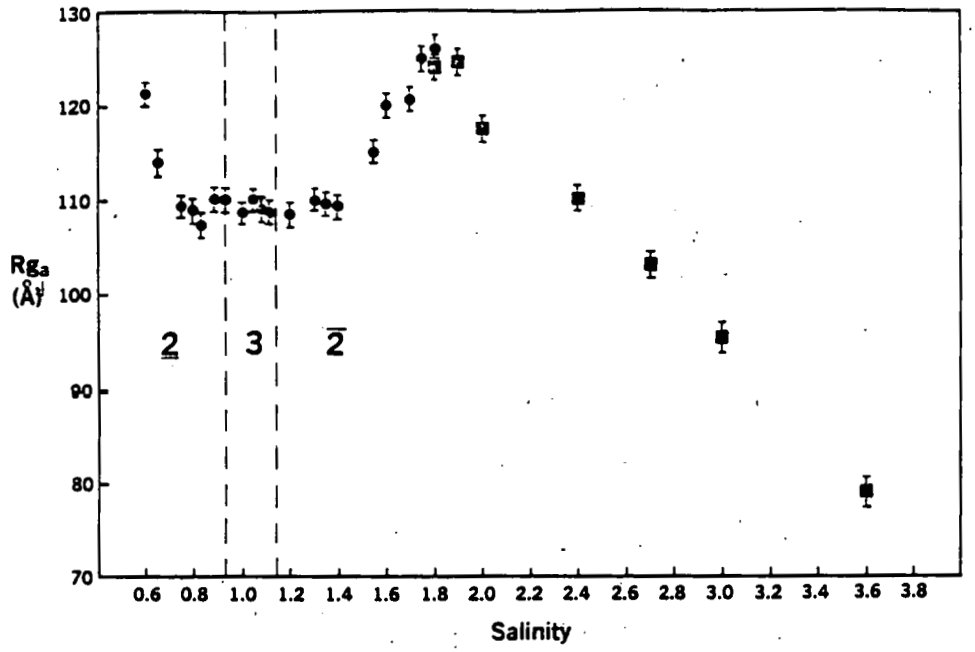

(A)

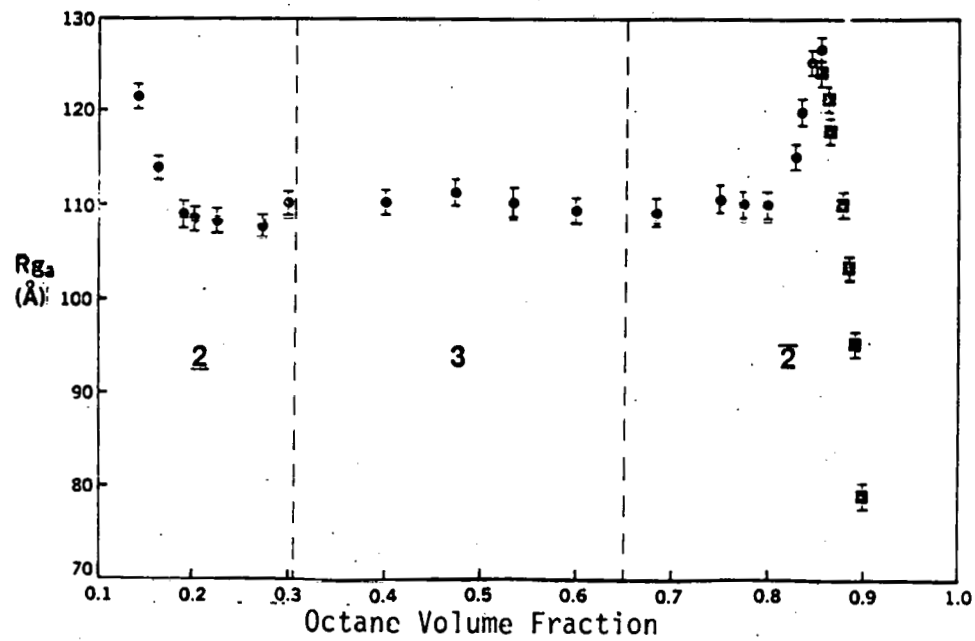

(B)

Figure 8. Variation of the apparent radius of gyration with (A) salinity and (B) octane volume fraction.

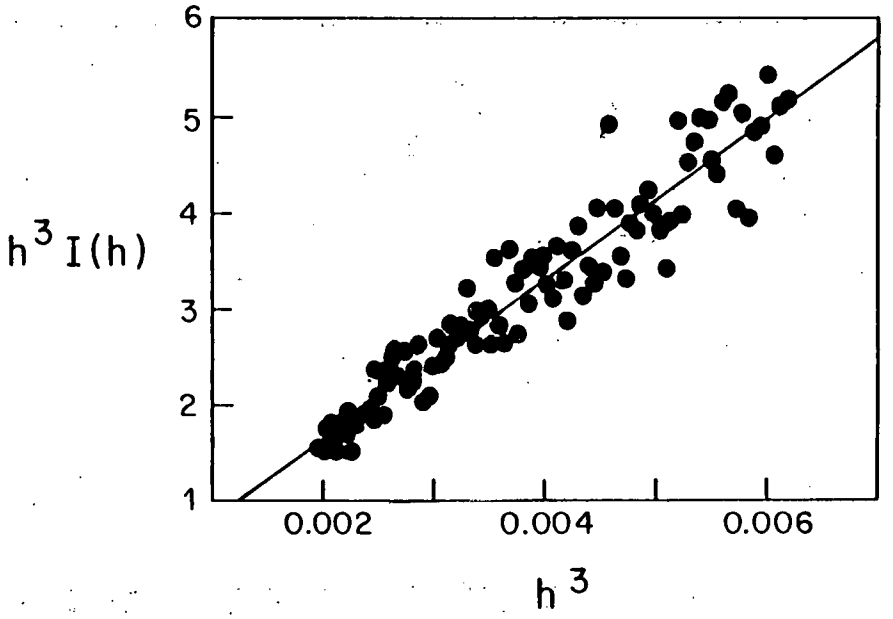

Figure 9. Porod plot for 3.7 salinity. The solid line is a least-squares fit of the data to Eq. (9).

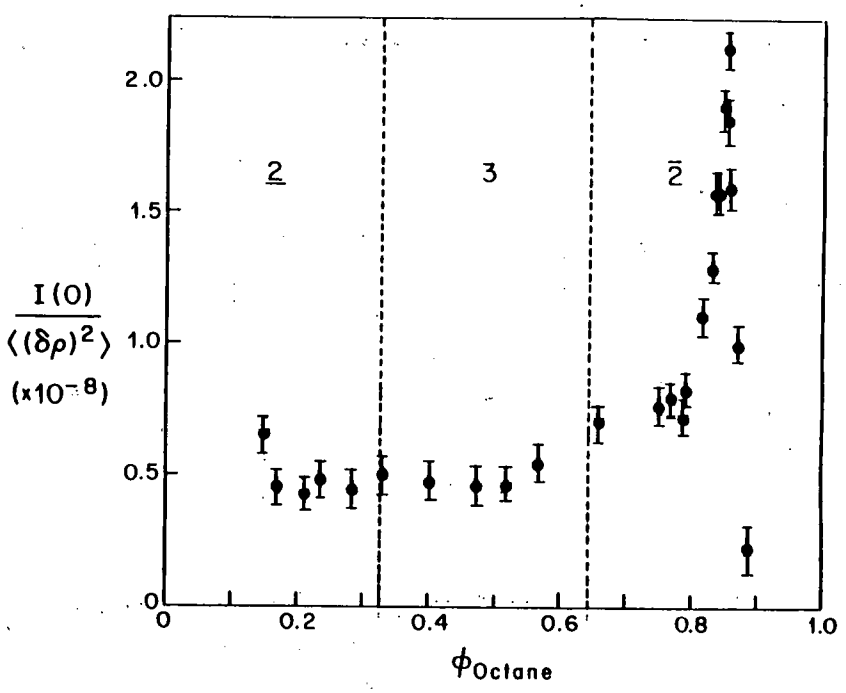

Figure 10. Variation of $I(0)/\langle(\delta\rho)^2\rangle$ with octane volume fraction.

tive mechanism and has been interpreted (16,22) as evidence for a *smooth* transition from an oil-continuous, brine-discontinuous structure to a bicontinuous one in which *both* oil and brine span the sample. This argument can be made more quantitative by means of the electrical conductivities calculated (20) from a Voronoi model of a microemulsion as a random interspersion of brine-rich and oil-rich domains. The data fall near the predictions from that model (solid line in Fig. 5).

An important observation in support of the idea that continuous water-rich domains are present in the microemulsion at all ϕ_B above approximately 0.15 is that the conductivity does not reflect the viscosity undulations (Fig. 4). Because the electrical conductivity depends on the local viscosity around the charge carriers as well as the tortuosity of the conducting path (16), the smooth and monotonic increase of K with ϕ_B in Figure 5 indicates that charge carriers move through water-like channels, the viscosity of which is relatively unaffected by the local morphology of the interspersion. This behavior is consistent with a bicontinuous model in which sample-spanning water channels are available in all microemulsions with ϕ_B greater than approximately 0.15.

Small-Angle X-Ray Scattering (SAXS)

All small-angle scattering measurements of microemulsions reported in the literature have heretofore been interpreted with the aid of Eq. (3), which applies strictly only to systems comprised of monodisperse spheroidal structures in a continuous phase. As demonstrated below this model of microemulsion as monodispersed "droplets" or swollen micelles is difficult to reconcile with the SAXS data over the entire composition region. At the extremes of the salinity scan, however, the swollen micelle and inverted micelle pictures appear to be consistent with the data. We begin with the dilute water-in-oil microemulsions.

Adding surfactant to an apolar solvent often produces an equilibrium solution of inverted micelles (8). Subsequent addition of water leads to an increase in micellar size as water is solubilized in the cores of the inverted micelles. We suspect a similar aggregation process occurs in the commercial-surfactant-alcohol-octane solution, with both water from the surfactant mixture and alcohol being solubilized in the interior of inverted micelles. The measured R_{ga} of 22 Å of this solution confirms the presence of small aggregates—presumably swollen inverted micelles. The addition of brine to the surfactant-alcohol-octane mixture produces a large increase in the apparent radius of gyration, R_{ga}, which continues to increase with increasing brine volume fraction (decreasing octane volume fraction: see Fig. 8). Calculation of a micelle size or shape from the radius of gyration is not straightforward, however, because R_g depends on both the dimensions of the micelle and the distribution of electron density within it. Nonetheless, we can estimate the swollen micelle or droplet dimensions as follows.

With the usual assumptions of monodispersity and negligible interparticle scattering (S(h,n) = 1 in Eq. (3)), R_g is related to the electron density distribution $\rho(r)$ in a spherical structure of outer radius R_M by the equation (29)

$$R_g^2 = \frac{\int_0^{R_M} (\rho(r) - \rho_0)\, r^4 dr}{\int_0^{R_M} (\rho(r) - \rho_0)\, r^2 dr} \qquad (11)$$

where ρ_0 is the electronic density of the solvent. The variation of electronic density with position is shown schematically in Figure 11B. The electron density of the surfactant tails can only be estimated because TRS 10-80 is not a pure surfactant. However, because the electron density of straight-chain hydrocarbon homologs varies little with chain length, the difference in electron density between the surfactant tails and octane (ρ_{oil} = 0.407 mole e^-/cm^3) is small compared to the electron density difference between octane and the core materials (ρ_{water} = 0.556 mole e^-/cm^3, $\rho_{SO_4^{-3}}$ = 1.44 mole e^-/cm^3 (ref. 35), ρ_{tAA} = 0.402 mole e^-/cm^3). We can therefore neglect the contribution of the surfactant tails in Eq. (11). If we also assume that the polar core radius R_c is much greater than the thickness of the regions of high electron density near the head groups (Fig. 11), then R_g very nearly measures the radius of gyration of the polar cores. Eq. (11) then reduces to

$$R_g = (3/5)^{1/2} R_c \ . \qquad (12)$$

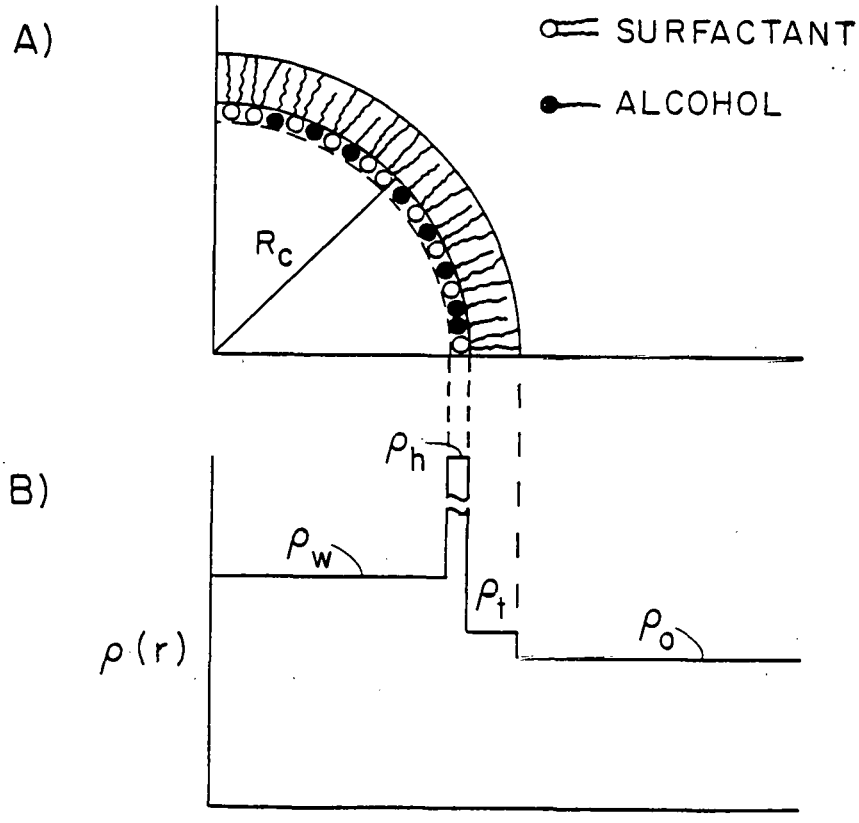

Figure 11. A) Schematic of a swollen inverted micelle. B) Variation of electronic density with position (arbitrary scales).

Analysis of the behavior of R_g with changes in ϕ_c is complicated because a change in composition can change the number, shape and size of the microemulsion "droplets". For purposes of modeling the microemulsion as an equilibrium dispersion of swollen micelles, we assume here that all of the surfactant and alcohol (volume fraction ϕ_{SA}) is at the oil-water interface and that all of the brine (volume fraction ϕ_c) is solubilized in the micelle cores. The volume fraction of the swollen micelles, ϕ_D, is then $\phi_c + \phi_{SA}$.

Experimental constraints on changes in the droplet population in this system are that the total amount of interfacial material (surfactant and alcohol) remains the same in the microemulsion phase and that the total volume of that phase remains approximately constant (Fig. 1) as its composition changes. These constraints imply obvious geometric relationships between the core radius and the core volume fraction ϕ_c. These relationships, together with the assumption of monodisperse spherical droplets, lead to

$$R_c = m\phi_c \quad . \tag{13}$$

Here m is a constant that depends on the area of the surfactant head group, but is difficult to estimate without knowledge of the composition of the surfactant-rich film between the oil-rich and water-rich domains and thus is left as an adjustable parameter. This equation and Eq. (12) predict the observed linear dependence of R_g on volume fraction in the most dilute cases, but fail at ϕ_D above about 0.13 (Fig. 12). This failure is likely due to interparticle scattering.

Accurate representation of the interparticle scattering effect depends on the correct choice of the radial distribution function in Eq. (4). In this model of dilute microemulsion microstructure as inverted water-filled swollen micelles in an oil continuum, electrical repulsions are probably negligible in comparison with hard sphere repulsions, and so a semi-empirical extension of the pair correlation functions derived for hard sphere fluids may be useful. Cebula et al. (11) have demonstrated the utility of such a model in correlating the results of small-angle neutron scattering experiments from microemulsion. Agterof et al. (10) and others (9) have shown that the addition of a van der Waals-type attractive term to the osmotic compressibility predicted by a hard-sphere model leads to a good fit of the microemulsion compressibility as measured with light scattering (see discussion below). We first treat the effect of hard-sphere repulsions alone.

The apparent radius of gyration R_{ga} can be conveniently calculated for hard spheres with the Percus-Yevick (PY) approximation. Rearranging the Ornstein-Zernicke equation (36) yields

$$S(h,n) = \frac{1}{1-n\ C(h,R_{HS})} \tag{14}$$

where $C(h,R_{HS})$ is the Fourier transform of the direct correlation function and R_{HS} is the hard-sphere radius. In the PY approximation (37,38)

$$C(h,R_{HS}) = -32\pi R_{HS}^3 \int_0^1 \frac{\sin(2hR_{HS}x)}{(2hR_{HS}x)} (\alpha + \beta x + \gamma x^3)x^2 dx \ , \qquad (15)$$

with the variables α, β, and γ defined as

$$\alpha \equiv (1 + 2\phi_{HS})^2/(1 - \phi_{HS})^4$$

$$\beta \equiv -6\phi_{HS}(1 + \tfrac{1}{2}\phi_{HS}^2)/(1 - \phi_{HS})^4$$

$$\gamma \equiv \tfrac{1}{2}\phi_{HS}(1 + 2\phi_{HS})^2/(1 - \phi_{HS})^4$$

where ϕ_{HS} is the volume fraction of hard-spheres, i.e.

$$\phi_{HS} \equiv \tfrac{4}{3}\pi R_{HS}^3 n \ .$$

After combining Eqs. (14) and (15) with the form factor for a spherical swollen micelle of radius R_D (Eq. 5), expanding Eq. (3) about the scattering vector $h = 0$ yields

$$R_{ga} = \tfrac{3}{5}R_D^2 - \tfrac{3}{5}R_{HS}^2\left\{\frac{\phi_{HS}(16 - 11\phi_{HS} + 4\phi_{HS}^2)}{(1 + 2\phi_{HS})^2}\right\} \qquad (16)$$

The droplet radius (Fig. 11) is the sum of the core radius and the surfactant tail length t. Thus, with our previous approximation for R_c (Eq. (13)) we have

$$R_D = m\phi_c + t \ .$$

Defining

$$\varepsilon \equiv \left(\frac{\phi_{HS}}{\phi_D}\right)^{1/3} = \frac{R_{HS}}{R_D}$$

allows Eq. (16) to be more compactly written as

$$R_{ga} = R_{ga}(\phi_D;\ m,t,\varepsilon)$$

where m, t, and ε are parameters. We can independently estimate the hydrocarbon tail length from the molecular structure of the surfactant to be of the order of 10 Å; thus only m and ε need to be fit to data. A nonlinear least-squares fit of Eq. (16) to the data below $\phi_D = 0.23$ is shown by the dashed line in Fig. 12 for t fixed at 10 Å. However, neither the fit values of $m = 4100$ or $\varepsilon = 0.88$ nor the quality of the fit are sensitive to values of t chosen between 5 and 20 Å.

The initial rise of R_{g_a} with ϕ_D and the subsequent fall beyond $\phi_D \sim 0.15$ are qualitatively predicted (Fig. 12) by the PY approximation, but the predicted R_{g_a} continues to decrease as ϕ_D increases beyond 0.20 in disagreement with experiment. Also, the scattering curve calculated for the PY hard-sphere model (Eqs. (3,5,14)) fits poorly the data for $\phi_D = 0.17$ (Fig. 13) except at the smallest angles. Agreement for the smallest angles is of course expected since R_{g_a} was determined by fitting theory to experiment in this range. Our results thus indicate clearly that the PY hard-sphere model is inadequate to describe the scattering from these microemulsions at higher volume fractions; this implies either that attractive forces between "droplets" are important at these volume fractions or that the concept of distinct microemulsion droplets is no longer valid. We note that the theory of scattering from interacting polydisperse spheres (39), shows that various distributions of "droplet" sizes could perhaps account for the experimental scattering curve in Fig. 13, but there are at present no physical grounds for selecting a distribution.

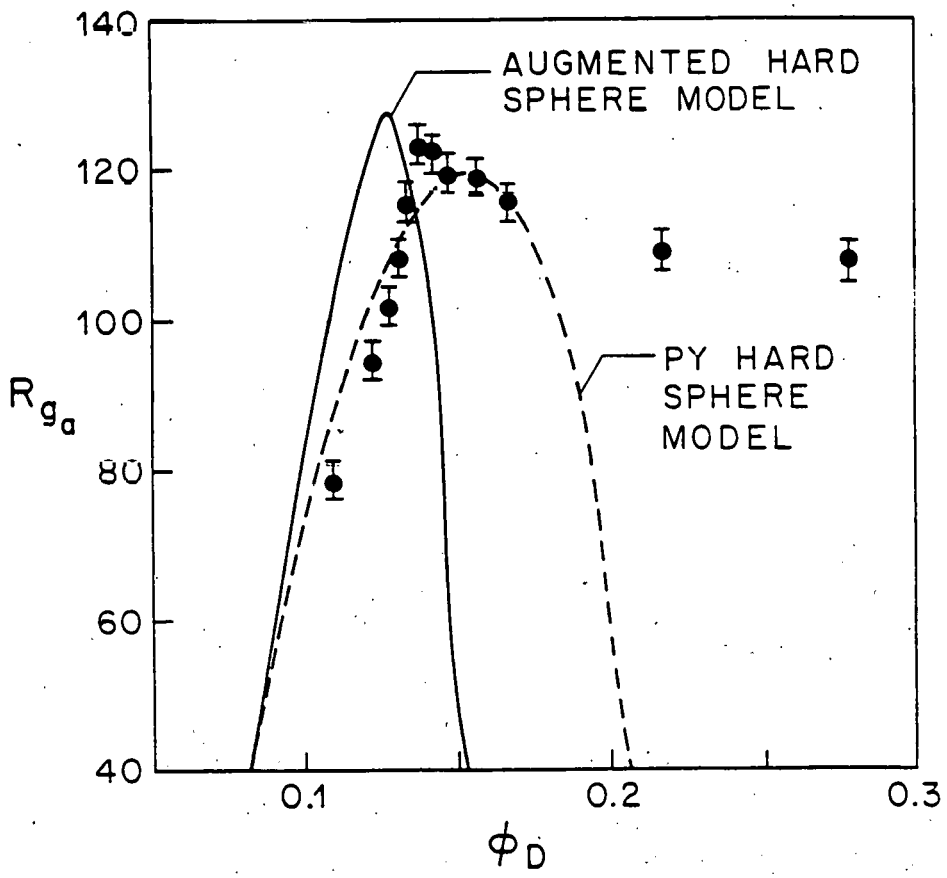

Figure 12. Variation of R_{g_a} at low swollen micelle volume fractions. Dashed line is a fit of the PY model (Eq. (16)) to the data. Solid line is a fit of the attractive hard-sphere model (Eq. (23)).

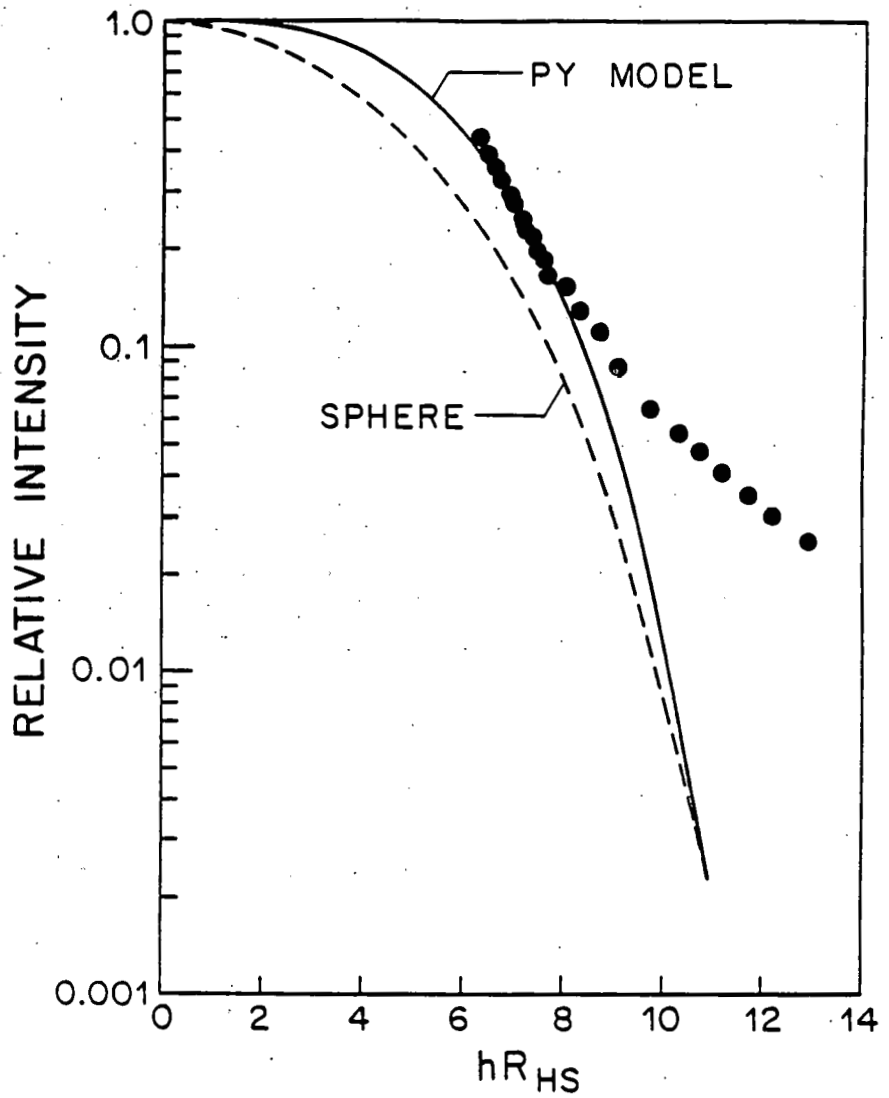

Figure 13. Experimental scattering curve for $\phi_D = 0.17$ (points) with the scattering curves predicted from the PY model (solid curve) and from a sphere of the same apparent R_g.

Before treating the effect of attractive interactions on the R_{ga} model, we find it useful to examine the variation of $I(0)/\langle(\delta\rho)^2\rangle$ with composition. Eq. (10) indicates that $I(0)/\langle(\delta\rho)^2\rangle$ depends on both V_D and ϕ_D. We make the same approximation here as above, namely that the microemulsion consists of "droplets" that are spherical and thus $V_D = 4/3\pi(mR_c + t)^3$. The most accurate representation of hard-sphere osmotic pressure is (40) the combination of the PY hard-sphere compressibility and virial pressure given by Carnahan and Starling (41):

$$\frac{\Pi_{HS}}{nkT} = \frac{(1 + \phi_{HS} + \phi_{HS}^2 - \phi_{HS}^3)}{(1 - \phi_{HS})^3} .$$

Unfortunately, χ_T calculated from this equation of state when combined with the assumed V_D cannot predict the course of the data in Figure 10. However, as mentioned above, Agterof et al. (10) have shown that the addition of an attractive term to the osmotic pressure permits a quantitative fit.

In their theory, a van der Waals-like correction to Π_{HS} is introduced via

$$\Pi = \Pi_{HS} + \Pi_A$$

where the attractive portion of the osmotic pressure Π_A can be semiempirically modelled as

$$\Pi_A = -\left(\frac{kT}{V_D}\right) \frac{B\phi_D^2}{2} .$$

B in principle can be estimated from the weak interaction approximation,

$$B = \frac{4\pi}{kT} \frac{1}{V_D} \int_{2R_{HS}}^{\infty} U_A(r) r^2 dr \qquad (17)$$

where $U_A(r)$ is the attractive portion of the interaction potential between the "droplets". But because knowledge about $U_A(r)$ is lacking, the only option at present is to determine B empirically.

With the attractive interaction approximation, Eq. (10) yields (10)

$$\frac{I(0)}{\langle(\delta\rho)^2\rangle} = \frac{V_D}{2\pi^2} \times \frac{1}{(1-\phi_D)} \times \frac{(1 - \phi_{HS})^4}{[(1+2\phi_{HS})^2 - \phi_{HS}^3(4-\phi_{HS}) - B\phi_D(1-\phi_{HS})^4]} \qquad (18)$$

A least-squares fit of the data up to $\phi_D = 0.5$ of $I(0)/\langle(\delta\rho)^2\rangle$ (ϕ_D; m,ε,B,t) with t again fixed at 10 Å is shown in Figure 14; the fitted parameters are m = 793, B = 20.87 and ε = 1.00. The values of B and ε are in the range of those reported by Cazabat et al. (9) for different microemulsion systems examined with static light scattering techniques.

Although the model fits the data quite well, the origin of the attractive portion of the droplet interaction is not well understood. One possible source of attraction is van der Waals interactions between aqueous droplet cores (10). With this model, the magnitude of B (Eq. (17)) is directly proportional to the Hamaker constant A^H. Unfortunately, there are no estimates available for the value of A^H in this model. Nonetheless, as noted earlier (9,10), A^H calculated from the fitted value of B is over 100 times larger than the value calculated from Lifshitz theory for polystyrene spheres interacting through heptane (42).

The contribution of attractive interactions to the apparent radius of gyration is difficult to evaluate because a complete model of the radial dis-

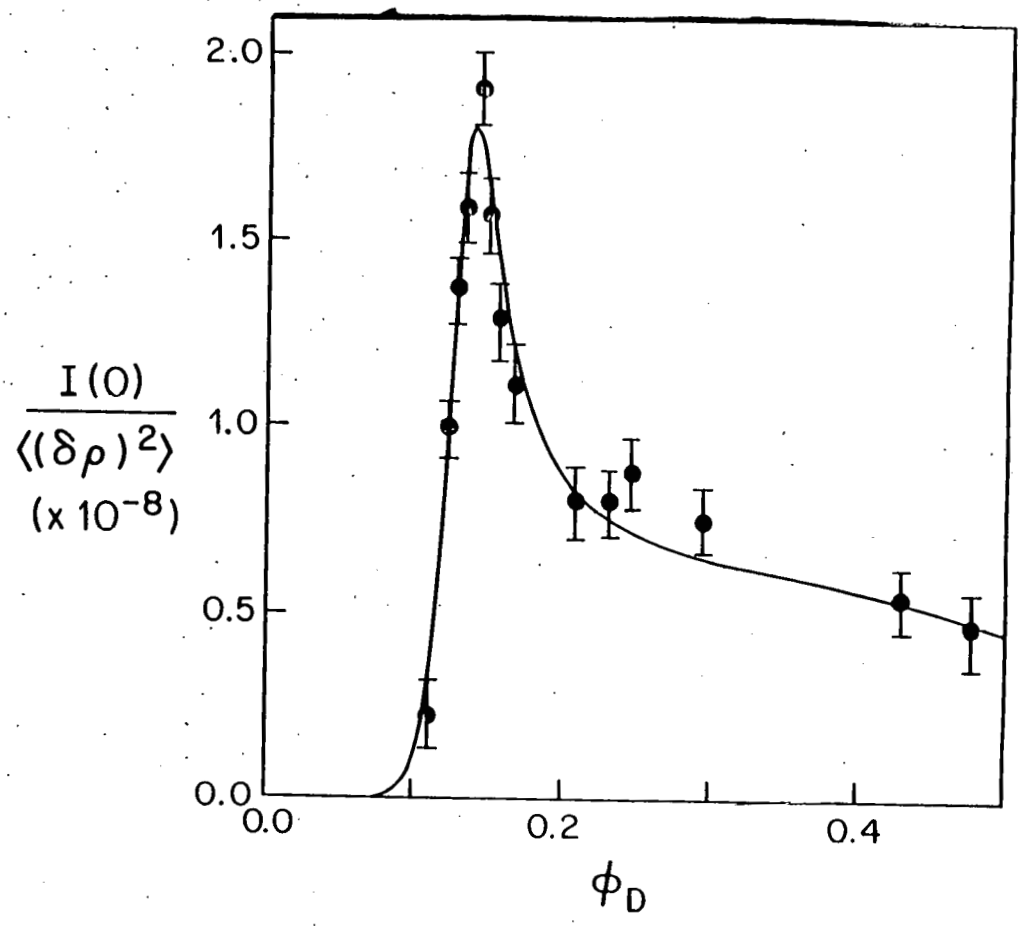

Figure 14. $I(0)/\langle(\delta\rho)^2\rangle$ vs. ϕ_D for ϕ_D less than 0.5. The solid curve is a least-squares fit of the data to Eq. (18).

tribution function is lacking. The effect can be estimated, however. From the Taylor series expansion of Eq. (3) about h = 0,

$$-\frac{2}{3}R_{ga}^2 = P''(0) + \frac{S''(0,n)}{S(0,n)} .$$

Here $S(0,n) = nkT\chi_T$. $S''(0,n)$ is related to the direct correlation function C(r) through Eq. (14), and it follows that

$$R_{ga} = -\frac{3}{2}P''(0) + \tfrac{1}{2}n(nkT\chi_T)C_2 \qquad (19)$$

where $C_2 = 4\pi\int_0^\infty C(r)r^4dr$. If the attractive interactions are again approximated as van der Waals-type corrections to hard-sphere interactions, C_2 is the sum of two terms:

$$C_2 = C_2^{HS} + C_2^A .$$

The first term can be gotten from the PY hard-sphere model (Eq. 15) and the second from the weak interaction approximation of the long-range attractive forces, viz.

$$C_2^A \simeq \frac{4\pi}{kT} \int_{2R_{HS}}^{\infty} U_A(r) r^4 dr \ . \tag{20}$$

With $U_A(r) = A/r^m$, B (Eq. 17) can be evaluated in terms of A and combined with Eq. (20) to yield

$$nC_2^A = B\phi_{HS} \nu R_{HS}^2 \ , \quad \nu \equiv 4\left[\frac{m-3}{m-5}\right] \ . \tag{21}$$

ν is an additional parameter. Then

$$nC_2 = -\phi_{HS} R_{HS}^2 \left[\frac{6}{5} \frac{16 - 11\phi_{HS} + 4\phi_{HS}^2}{(1 - \phi_{HS})^4}\right] \tag{22}$$

which, when combined with Eqs. (10) and (18) in Eq. (19), yields R_{ga} (ϕ_D; m, ϵ, B, t, ν). With the values of m, B and ϵ fit to the $I(0)/\langle(\delta\rho)^2\rangle$ data, this equation cannot account even qualitatively for the form of the observed R_{ga} data. A least-squares fit of the equation to the data ($\nu = 4.8$) is shown as the solid line in Figure 12—a result no closer to predicting the R_{ga} behavior above $\phi_D \sim 0.2$ than the original PY hard-sphere model.

In summary, it appears that though a model of interacting hard spheres can be made to adequately model microemulsion compressibility by adjusting the parameter B, the magnitude of B necessary to fit the data corresponds to a surprisingly large value of the Hamaker constant. The same theory is unable to account for the variation of R_{ga} with composition (Fig. 12), and does not predict the form of the scattering curve.

Alternative microemulsion morphologies are the bicontinuous structures proposed for intermediate volume fractions of oil and water in the microemulsions. Voronoi tessellations have been used to qualitatively model random interspersions of oil-rich and water-rich domains. The scattering curves calculated for the Voronoi tessellation model of bicontinuous microemulsions (19) depend only on the tessellation parameter c (the number of generating points per unit volume) which is itself a function of microemulsion composition and temperature. The model predicts that the apparent radius of gyration varies as

$$R_{ga} = 0.572 \ c^{-1/3} \ . \tag{23}$$

There is as yet no comprehensive theory for the composition dependence of c, and so the dependence of R_{ga} and $I(0)/\langle(\delta\rho)^2\rangle$ on composition cannot presently be quantitatively modelled. We can compare the entire scattering curve, though, fit to data with Eq. (23). Figure 15 shows the agreement between the

scattering curve predicted by the Voronoi theory and a typical scattering curve from a microemulsion incorporating comparable amounts of oil and water. In addition, the Voronoi model predicts

$$\frac{I(0)}{\langle(\delta\rho)^2\rangle} = \frac{3.81}{c} = 20.36\ R_{ga}^3 \qquad (24)$$

for every microemulsion, regardless of composition. The data in Figures 8 and 10 clearly show proportionality between $I(0)/\langle(\delta\rho)^2\rangle$ and R_{ga}; a least-squares fit of all the data (Fig. 16) to Eq. (24) yields an actual R_{ga} exponent of 4.5 instead of the predicted value of 3.0. The hard-sphere models fail to predict any proportionality because they inadequately account for the measured dependency of R_{ga} on composition.

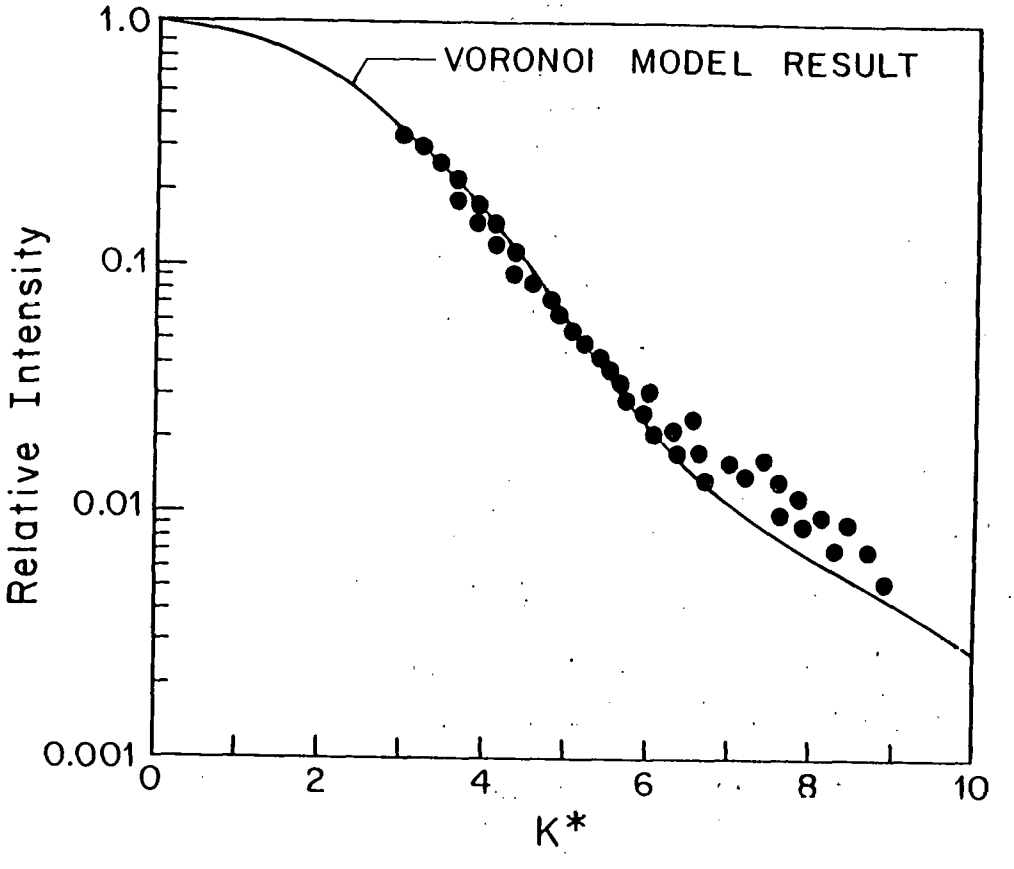

Figure 15. Comparison of the scattered intensity measured for $\phi_{octane} = 0.7$ (dots) with that calculated for the Voronoi model.

It is important to note the electrical conductivity results (Fig. 5) in the light of the scattering results. The percolation threshold of the Voronoi model (ϕ_w ca. 0.16) is very near the point where both the PY and attractive hard-sphere models begin to fail to predict the course of R_{ga} with ϕ_D (Fig. 12). A model admitting bicontinuous structures can explain both the conductivity and scattering behavior above $\phi_D \simeq 0.2$, whereas models relying on discrete, discontinuous droplets cannot.

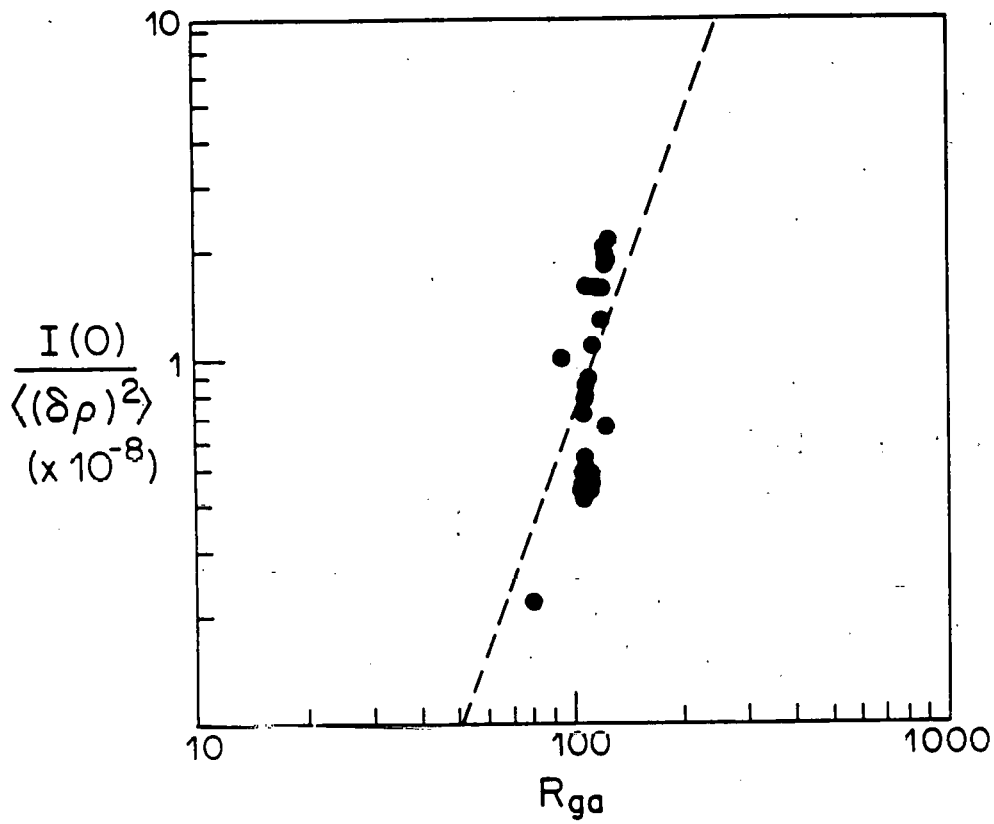

Figure 16. $I(0)/\langle(\delta\rho)^2\rangle$ vs. R_{ga} including all data points. Dashed line is the prediction based on the Voronoi model.

Concluding Remarks

We have presented SAXS, electrical conductivity, viscosity, interfacial tension and compositional data from microemulsions made from the commercial surfactant TRS 10-80, tAA, octane and a progression of NaCl brines. Models based on monodisperse populations of swollen micelles or microemulsion "droplets" adequately represent the SAXS data at low volume fractions of brine. Simple models of the dependence of "droplet" size on volume fraction and the representation of hard-sphere interactions with the PY approximation allow prediction of the scattering behavior up to brine volume fractions near a percolation threshold in electrical conductivity. Above the percolation threshold, addition of an attractive interaction (10) produces a model adequate for the composition dependence of $I(0)/\langle(\delta\rho)^2\rangle$; however, the same level of approximation fails to model R_{ga} above ϕ_D ca. 0.18.

Near the percolation threshold a break in the viscosity curve and changes in the SAXS data as well as the conductivity results support our hypothesis that a bicontinuous microstructure is present. Such a bicontinuous regime is necessary if the surfactant sheets maintain topological order in the microemulsion through a continuous evolution from swollen inverted micelles to swollen micelles. We hypothesize that these bicontinuous states are dynamic and thus are of low viscosity. They are geometrically disordered, yet are topologically ordered because of the surfactant's tendency to form sheets between oil-

rich and water-rich domains. In this view, it is the absence of geometric order that distinguishes microemulsions from ordered, viscous isotropic liquid crystal phases. The hypothesis of persistent topological order in microemulsions is verified by the absence of secondary scattering maxima in the SAXS patterns. The variation of microemulsion viscosity with composition indicates that the rheological properties of the microemulsion are determined by the nature of the surfactant sheets (i.e. by their strength and spacing).

The evidence indicates that bicontinuous structures are present over a broad range of compositions. In the bicontinuous region SAXS and electrical conductivity data are well described with a Voronoi model of a random interspersion of oil and water.

References Cited in Section II

1. Danielsson, I. and Lindman, B., Colloids and Surfaces 3, 391 (1981).

2. Winsor, P. A., Chem. Rev. 68, 1 (1968).

3. Robbins, M. L. in Micellization, Solubilization and Microemulsions, eds. D. O. Shah and R. S. Schechter (Academic Press, New York, 1977) 383.

4. Healy, R. N., Reed, R. L. and Stenmark, D. G., Soc. Pet. Eng. J. 16, 147 (1976).

5. Fleming, P. D., III, and Vinatieri, J. E., J. Colloid Interface Sci. 81, 319 (1981).

6. Davis, H. T. and Scriven, L. E., SPE of AIME 55th Annual Meeting, Paper SPE 9278, Dallas, TX (1980).

7. Gulari, E., Bedwell, B. and Alkhafuji, S., J. Colloid Interface Sci. 77, 202 (1980).

8. Zulauf, M. and Eicke, H. F., J. Phys. Chem. 83, 480 (1979).

9. Cazabat, A. M., Langevin, D. and Pouchelon, A., J. Colloid Interface Sci. 73, 1 (1980).

10. Agterof, W. G. M., Van Zomeren, J. A. J. and Vrij, A., Chem. Phys. Lett. 43, 363 (1976).

11. Cebula, D. J., Ottewill, R. H., Ralston, J. and Pusey, P. N., J. Chem. Soc., Faraday Trans. 1 77, 2585 (1981).

12. Ober, R. and Taupin, C., J. Phys. Chem. 84, 2418 (1980).

13. Bellocq, A. M., Fourche, G., Chabrat, P., Letamendia, L., Rauch, J. and Voucamps, C., Opt. Acta 27, 1629 (1980).

14. Cazabat, A. M., Catney, D., Langevin, D. and Pouchelon, in Scattering Techniques Applied to Supramolecular and Nonequilibrium Systems, eds. S. H. Chen, B. Chu and R. Nossal (Plenum Press, New York, 1977) 787.

15. Scriven, L. E., Nature 263, 123 (1976); in Micellization, Solubilization and Microemulsions, ed. K. Mittal (Plenum Press, New York, 1977) 877.

16. Bennett, K. E., Hatfield, J. C., Davis, H. T., Macosko, C. W. and Scriven, L. E. in Microemulsions, ed. I. D. Robb (Plenum Press, New York, 1982) 65.

17. Meijering, J. L., Philips Res. Rep. 8, 270 (1953).

18. Talmon, Y. and Prager, S., J. Chem. Phys. 69, 2984 (1978).

19. Kaler, E. W. and Prager, S., J. Colloid Interface Sci. 86, 359 (1982).

20. Winterfeld, P. W., Ph.D. thesis, University of Minnesota (1981).

21. Lindman, B., Kamenka, N., Kathopoulis, T., Brun, B. and Nilsson, P., J. Phys. Chem. 84, 2485 (1980).

22. Hatfield, J. C., Ph.D. thesis, University of Minnesota (1970).

23. Kaler, E. W., Ph.D. thesis, University of Minnesota (1982).

24. Schmidt, P. W., Acta Cryst. 19, 938 (1965).

25. Bennett, K. E., Ph.D. thesis, University of Minnesota (1983).

26. Cayias, J. L., Schechter, R. S. and Wade, W. A. in Adsorption at Interfaces, ed. K. Mittal, ACS Symposium Series 8, Amer. Chem. Soc., Washington, DC (1975).

27. Seeto, Y. and Scriven, L. E., Rev. Sci. Inst. 53, 1757-1761 (1982).

28. Reid, V. W., Longman, G. F. and Heinerth, E., Tenside 5, 90 (1968).

29. Guinier, A. and Fournet, G., Small-Angle Scattering of X-rays (Wiley, New York, 1955).

30. Luzzati, V., Acta Cryst. 11, 843 (1958).

31. Luzzati, V., Witz, J. and Nicolaieff, A., J. Molec. Biol. 3, 367 (1961).

32. Knickerbocker, B. M., Pesheck, C. V., Scriven, L. E. and Davis, H. T., J. Phys. Chem. 83, 1984 (1979).

33. Fleming, P. D., III and Vinatieri, J. E., AIChE J. 25, 493 (1979).

34. Pouchelon, A., Chateney, D., Meunier, J. and Langevin, D., J. Colloid Interface Sci. 82, 418 (1981).

35. Reiss-Husson, F. and Luzzati, V., J. Phys. Chem. 68, 3504 (1964).

36. Ornstein, L. S. and Zernicke, F., Physik Z. 19, 134 (1918).

37. Wertheim, M. S., Phys. Rev. Lett. 10, 321 (1963).

38. Ashcroft, N. W. and Lekner, J., Phys. Rev. 145, 83 (1966).

39. Vrij, A., J. Chem. Phys. 71, 3267 (1979).

40. Barker, J. A. and Henderson, D., J. Chem Phys. 47, 4714 (1967).

41. Carnahan, N. F. and Starling, K. E., J. Chem. Phys. 51, 635 (1969).

42. Smith, E. R., Mitchell, D. J. and Ninham, B. W., J. Colloid Interface Sci. 45, 55 (1973).

III. MICROEMULSION PHASE BEHAVIOR: FOUR PHASE PROGRESSION IN FIVE-COMPONENT MIXTURES

In this report we expand upon an earlier observation (1) that some microemulsions formed with an isomerically-pure surfactant show a systematic progression from three phases to four phases, two of them microemulsion phases, to three phases (i.e., a 3,4,3 progression) as temperature or salinity is increased. Previous researchers (2-6) have mentioned the occasional presence of four coexisting liquid phases apparently at equilibrium in microemulsion formulations, but only with multicomponent commercial surfactants for which such occurrences are not unexpected. Furthermore, in only one case (4) was the composition region noted in which four phases were seen.

The surfactant used here was sodium 4-(1'-heptylnonyl)benzenesulfonate (SHBS), also known as Texas No. 1. It was purified (1,7), to remove the chloroform-insoluble impurities which were about 1% of the surfactant as received. To prepare a sample, 1 cm^3 of NaCl brine and 1 cm^3 of surfactant/alcohol/oil stock solution were mixed and sealed in a pipet. The stock solution was prepared from 0.325 g SHBS, 0.650 g secondary butyl alcohol (sBA), and 8.327 g hexadecane (nC_{16}). Samples were thoroughly mixed at each temperature. Phase volumes usually stabilized within two days after mixing. All observations were made through a window in the side of a constant-temperature (± 0.03°C) water bath. Selected measurements of phase volumes, particularly in the four-phase regions, were rechecked after temperature cycling to both higher and lower temperatures than the datum. Details are given elsewhere (1,8). Although phase compositions were not measured in these experiments, analyses in this laboratory and elsewhere (5,6) of mixtures similar in amounts of surfactant, alcohol, oil and brine to those studied here, indicate that only the phase or phases that scatter light contain a significant amount of surfactant.

The SHBS/sBA/nC_{16}/(2.1 g NaCl/100 cm^3 brine) formulation has three equilibrium phases at 18.5°C and four equilibrium phases at 18.8°C. The four coexisting phases are a clear, brine-rich lower phase; a clear, oil-rich upper phase; and two surfactant-rich "middle" phases, the upper one being 1/30th the volume and scattering much more light than the lower one. The relative volume of each equilibrium phase is shown as a function of temperature in Fig. 1. As temperature increases further, the new (upper) surfactant-rich phase grows at the expense of the lower surfactant-rich phase until at 22.5°C the formulation once again has three equilibrium phases. No further phase transitions are observed up to 45°C, the highest temperature studied. Throughout the four-phase region the upper surfactant-rich phase scatters much more light than the lower surfactant-rich phase, suggesting that the two phases have substantially different compositions.

As the salinity decreases to 2.05 and then to 1.95 g NaCl/100 cm^3 brine, the temperature range of four-phase equilibria narrows and moves to higher temperatures, as shown in Figs. 2a and 2b, and the two equilibrium surfactant-rich phases resemble each other more closely. There is a $\underline{2},3,4,3$ progression with increasing temperature at a salinity of 1.95 (Fig. 2b); the $\underline{2},3,\ldots$ mnemonic notation of Knickerbocker *et al.* (9) gives the number of equilibrium phases and, for a two-phase system, indicates whether the surfactant is primarily in the lower, brine-rich ($\underline{2}$) or upper, oil-rich ($\overline{2}$) phase. The $\underline{2},3$ transition at

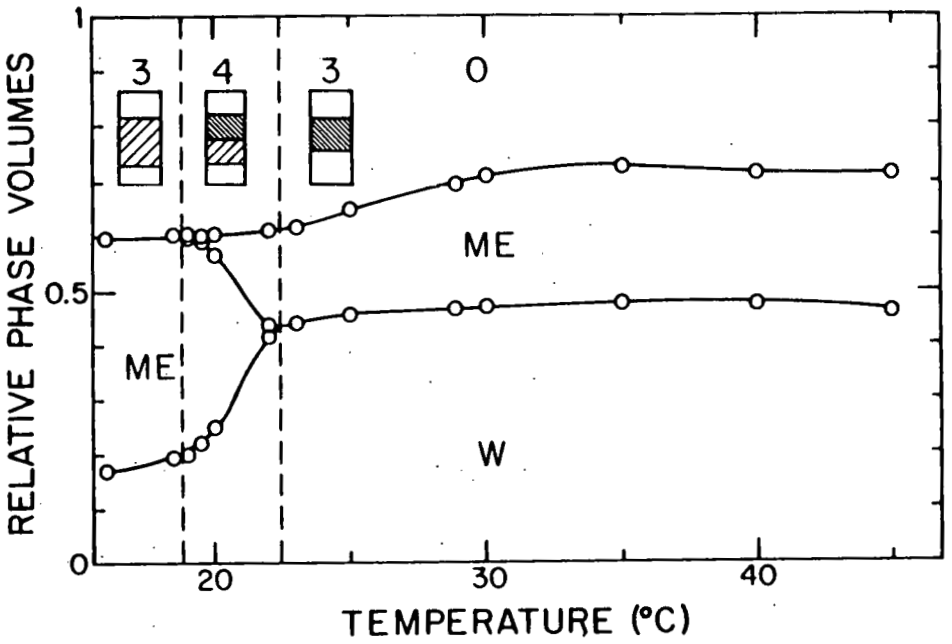

Figure 1. The evolution of a four-phase region with increasing temperature. SHBS/sBA/nC_{16}/(2.1 g NaCl/100 cm^3 brine). The test tubes show the upper oil-rich phase (O), the middle one or two microemulsion phases (ME, shaded), and the lower brine-rich phase (W). The vertical dashed lines mark the temperatures of the 3,4 and 4,3 phase transitions.

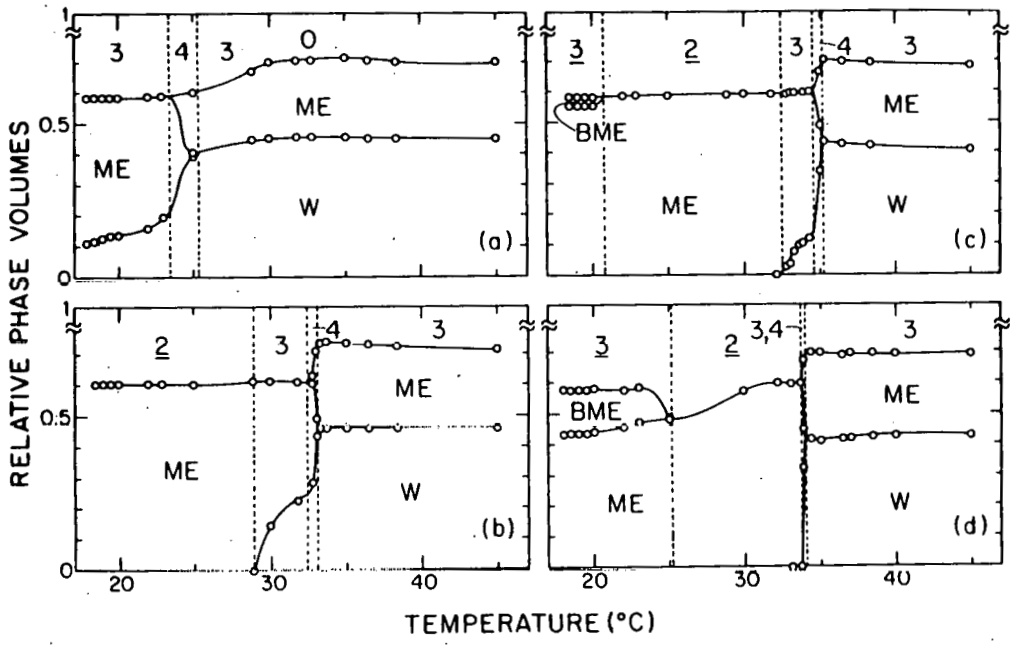

Figure 2. Phase volume progressions vs. temperature: SHBS/sBA/nC_{16}/brine. a) 2.05, b) 1.95, c) 1.90, d) 1.85 g NaCl/(100 cm^3 brine). The vertical dashed lines mark the temperatures of phase transitions. BME means birefringent microemulsion.

29°C is the reverse of the 3,2 transition normally reported with increasing temperature of microemulsions made with an ionic surfactant (3,4).

At a salinity of 1.9 a new phenomenon appears. In addition to the 2,3,4,3 progression, there is a 3 region (3 denoting three equilibrium phases; surfactant-rich lower and middle phases) below 21°C (Fig. 2c). In this region, the middle phase is birefringent, unlike any of the other phases observed in this study. The birefringent middle phase grows in volume and is present over a wider temperature range as the brine salinity is reduced to 1.85, as shown in Fig. 2d. At salinities of 1.9 and 1.85 the temperature range of four-phase equilibria is narrow, and the two surfactant-rich phases are nearly identical in appearance although separated by a sharp, clearly visible interface. The temperatures of the 3,2; 2,3; 3,4; and 4,3 transitions in the above systems are given in Table 1.

TABLE I: Temperatures (°C) at Phase Transitions for SHBS/sBA/nC_{10}/Brine Mixtures

salinity[a]	phase transition				width of four-phase region, °C
	3,2	2,3	3,4	4,3	
2.1			18.8 ± 0.2	22.5 ± 0.4	3.7 ± 0.5
2.05			23.5 ± 0.5	25.4 ± 0.3	1.9 ± 0.6
1.95		29.5 ± 0.5	32.5 ± 0.5	33.2 ± 0.1	0.7 ± 0.5
1.9	21 ± 1	32.5 ± 0.2	34.6 ± 0.4	35.2 ± 0.2	0.6 ± 0.5
1.85	25.2 ± 0.2	33.7 ± 0.1	33.8 ± 0.1	34.2 ± 0.3	0.4 ± 0.4

[a] Units: g of NaCl/(100 cm^3 of brine).

What topological features must a phase diagram have in order to yield the above progressions? Clearly, there must be a four-phase region, i.e., a sequence of four-phase tie tetrahedra, accompanied by contiguous progressions of three-phase tie triangles, binodal lobes with two-phase tie lines, and plait-point curves. To visualize the salient features of these progressions, it is convenient to treat brine as a pseudocomponent and to consider a tetrahedral phase diagram which has brine, oil, alcohol, and surfactant at the vertices and which evolves continuously with changing temperature. One planar slice of this diagram at each temperature suffices for illustration; this slice is chosen (except in Fig. 3c) to contain the mixing-point composition and the tie triangle (or slice of the tie tetrahedron) of interest.

One possible sequence of slices of tetrahedral phase diagrams that would account for the observed 3,2,3,4,3 behavior is shown in Figs. 3a to 3 . Each diagram shows a tie triangle or tie tetrahedron, and indicates the mixing point x as well as the associated phase volumes and appearances. The lower left and right corners of each phase diagram represent brine and oil, respectively. The two-phase regions are not shown because the tie lines generally are not coplanar with the tie triangle.

The overall mixing point of a 3 system lies within a tie triangle defined by an oil-rich phase containing little surfactant and two surfactant-rich phases as shown in Fig. 3a. With increasing temperature the tie triangle sweeps over the mixing point (Figs. 3b and 3c) resulting in a 3,2 transition. (The tie

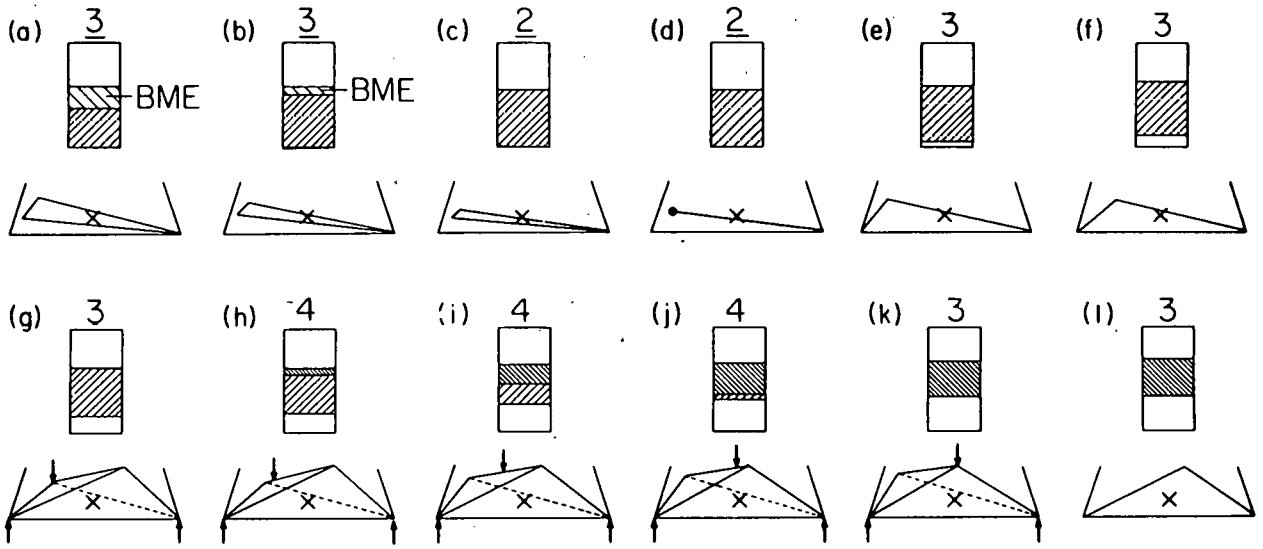

Figure 3. A sequence of phase diagrams that gives 3,2,3,4,3 behavior for the mixing point x, together with the associated phase volumes (shaded regions are microemulsion) and mnemonic notation for the phase counts. The lower left and right corners of the phase diagrams represent brine and oil, respectively. BME means birefringent microemulsion.

triangle and mixing point in Fig. 3c might never be coplanar.) At this stage the tie triangle can either collapse to a critical tie line (10-11) (referred to by some authors as a critical endpoint tie line (12) or a critical endpoint (13)) in a two-phase region (Fig. 3d), i.e., the tie line that terminates in a critical endpoint, and then reemerge from a different critical tie line (not shown), or it can remain open, skipping Fig. 3d. The former possibility is more likely since the first three-phase region has a birefringent phase, but a more detailed scan of mixing points and temperatures would be needed to distinguish unequivocally the possibilities. When the tie triangle once again sweeps over the mixing point (Fig. 3e) there is a 2,3 transition. At some temperature a four-phase region (not shown) forms within the tetrahedral phase diagram but need not enclose the mixing point. With increasing temperature, the tie triangle enclosing the mixing point grows (Fig. 3f) and then becomes one side of a four-phase tie tetrahedron (Fig. 3g). This tetrahedron then sweeps over (Figs. 3h to 3k) and passes by (Fig. 3) the mixing point, generating a 3,4,3 progression; in Figs. 3g to 3k the mixing point (fixed) lies in the plane defined by the tips of the three arrows.

The features of the phase diagram change proportions with changing brine salinity. As salinity falls, the tie tetrahedron most likely narrows down as evidenced by the reduction of the temperature range over which there are four phases (Table 1) and by the approach in appearance of the two microemulsion phases. If this narrowing process continues with decreasing salinity, the tie tetrahedron will collapse to a tie triangle as shown in Fig. 4a. We call the collapsed tetrahedron a critical tie triangle, i.e., a tie triangle in which one of the phases (vertex C in Fig. 4) is critical.

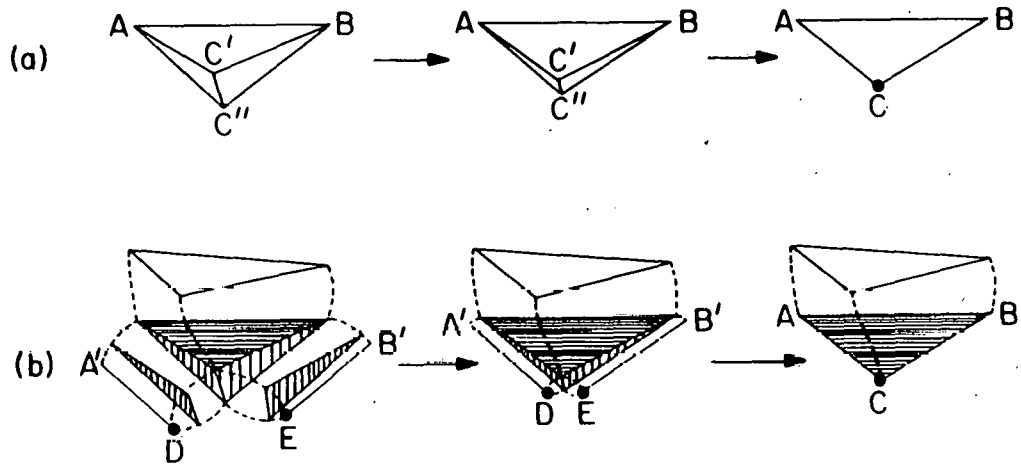

Figure 4. A four-phase tetrahedron collapses to a critical tie triangle (Δ ABC) in a three-phase region. a) Only the four-phase tetrahedron is shown; b) three of the four three-phase regions that surround the four-phase tetrahedron (shaded are shown. The dashed lines are the loci of vertices of the three-phase triangles. A'D and B'E are critical tie lines.

The tie tetrahedron is surrounded by four three-phase regions of which three are shown in Fig. 4b. The two three-phase regions associated with the collapsing sides of the tetrahedron terminate in critical tie lines $\overline{A'D}$ and $\overline{B'E}$. As these two three-phase regions disappear, the critical tie lines become the critical sides $\overline{AC}$ and $\overline{BC}$ of the critical tie triangle, i.e., the collapsed tetrahedron. Simultaneously, critical endpoints D and E (Fig. 4b), which are the two ends of a plait point curve (not shown), and tetrahedron vertices C' and C" (Fig. 4a) merge to form critical vertex C. The collapse of a tie tetrahedron to a critical tie triangle in a three-phase region is analogous to the collapse of a tie triangle to a critical tie line in a two-phase region (Figs. 3a to 3d). The theoretical possibility of such a progression has been remarked elsewhere (13).

The two three-phase regions that do not collapse merge into a single three-phase region containing the critical tie triangle. What would be the topology of the phase diagram if critical tie lines terminated these three-phase regions? Knickerbocker et al. (14) discuss the three possible phase diagrams that result when no four-phase region is present, i.e., when there is a single three-phase region terminating in two critical tie lines. As is discussed elsewhere (8) these three cases give rise to six topologically distinct configurations of three-phase regions and critical tie lines about a tie tetrahedron; an additional twenty-two distinct configurations are possible if the four three-phase regions can terminate in tricritical points or critical tie lines, although not all of these configurations exist immediately after the tie tetrahedron emerges from a critical tie triangle. The other ways in which a four-phase region can

collapse (8,13) — e.g., in a tie line joining two critical points, in a tie line joining a non-critical phase and a tricritical point, or in a tetracritical point — do not change the number of distinct configurations of three-phase regions about the tie tetrahedron.

In summary, there are 3,4,3 and 3,2,3,4,3 phase progressions with increasing temperature in five-component mixtures of SHBS/sBA/nC_{16}/(NaCl brine) over a range of brine concentrations. These progressions can be interpreted with pseudo-quaternary phase diagrams inferred from them. Particularly interesting are the collapse of a four-phase tie tetrahedron to a critical tie triangle and the topology of the progression of phase diagrams.

Four-phase regions have been observed (8) in similar formulations that contain the alcohol diethylene glycol monohexyl ether [$CH_3(CH_2)_5O(CH_2CH_2O)_2H$] instead of sBA. Presumably, fine enough temperature and composition scans would reveal many other microemulsion formulations having regular four-phase progressions.

References Cited in Section III

1. Bennett, K. E., Phelps, C. H. K., Davis, H. T. and Scriven, L. E., Soc. Pet. Eng. J. 21, 747 (1981).

2. Healy, R. N. and Reed, R. L., Soc. Pet. Eng. J., 14, 491 (1974).

3. Healy, R. N., Reed, R. L. and Stenmark, D. G. Soc. Pet. Eng. J., 16, 147 (1976).

4. Anderson, D. R., Bidner, M. S., Davis, H. T., Manning, C. D. and Scriven, L. E., SPE Paper No. 5811, Tulsa, OK, March 22-24, 1976.

5. Reed, R. L. and Healy, R. N., in Improved Oil Recovery by Surfactant and Polymer Flooding, Eds., D. O. Shah and R. S. Schechter (Academic Press, Inc., New York, 1977) 383.

6. Nelson, R. C. and Pope, G. A., Soc. Pet. Eng. J., 18, 325 (1978).

7. Franses, E. I., Ph.D. Thesis, University of Minnesota (1979).

8. Bennett, K. E., Ph.D. Thesis, University of Minnesota (1982).

9. Knickerbocker, B. M., Pesheck, C. V., Davis, H. T. and Scriven, L. E., J. Phys. Chem., 83, 1984 (1979).

10. Vogel, R., Die heterogenen Gleichgewichte, Akademische Verlagsgesellschaft Geest & Portig K.-G. (1937 and 1959).

11. Rossen, W. R., Brown, R. G., Davis, H. T., Prager, S. and Scriven, L. E., SPE Paper No. 10062, San Antonio, TX, Oct 5-7, 1981.

12. Lang, J. C., Jr. and Widom, B., Physica, 81A, 190 (1975).

13. Furman, D., Dattagupta, S. and Griffiths, R. B., Phys. Rev. B, 15, 441 (1977).

14. Knickerbocker, B. M., Pesheck, C. V., Davis, H. T. and Scriven, L. E., J. Phys. Chem., 86, 393 (1982).

IV. THERMODYNAMIC MODELLING OF QUATERNARY SYSTEMS: OIL-BRINE-SURFACTANT-ALCOHOL

Introduction

After secondary oil recovery, a majority of the residual oil is held in place in the reservoir pore space by capillary forces. The strength of the forces is dictated by the interfacial tension between coexisting oleic and aqueous phases. In one method of tertiary oil recovery the capillary forces are reduced by injection of formulations containing surfactant and alcohol which form with oil and brine a microemulsion phase having, under the right conditions, ultralow interfacial tensions against coexisting oil-rich and water-rich phases. When ultralow tensions occur, flooding with the surfactant and alcohol formulation can result in substantial oil recovery (5,6). Whether ultralow tensions occur depends crucially on the equilibrium phase behavior of the surfactant and alcohol mixtures with the reservoir oil and brine (5,7-9).

Although reservoir oil, brine and commercial surfactant are multicomponent substances, it is common to treat the oil-brine-surfactant-alcohol system as a pseudoternary mixture in which the surfactant and alcohol, the oil, and the brine partition as pseudocomponents (1,4,5,7-13). This approach has been quite useful for qualitatively understanding the general patterns of phase behavior, but it suffers the quantitative disadvantage that alcohol and surfactant partition quite differently between oil-rich and water-rich phases and are therefore poor pseudocomponents (3,4). The purpose of this paper is to improve the situation by modelling oil-brine-surfactant-alcohol systems as a quaternary mixture in which surfactant and alcohol are independent components.

Two methods show promise in the correlation and prediction of phase splits and composition data for oil-brine-surfactant-alcohol systems. One method, attractive because of its simplicity and ease of use in reservoir simulation, is to take limited data and interpolate and extrapolate them with a mathematical curve fit which is thermodynamically consistent. This approach has been applied to pseudoternary systems (1,2). The other method, attractive because it is based on the physics of the molecular constituents, is to fit the limited data to the parameters of a free energy equation of state. Taking this approach, a modified version of the Flory-Huggins equation of state has been applied to pseudoternary oil-brine-surfactant systems (14) and succeeds in qualitatively representing phase behavior. We believe the quaternary version of the model will prove useful for quantitative predictions of phase splits and compositions.

The benefits of a thermodynamic equation of state description of phase behavior are many: [1] the free energy of the model dictates the number of phases and the driving force for nucleation of possibly long-lived metastable states, [2] the parameters of the model link directly the phase behavior and the molecular forces between constituent molecules, [3] the topography of the free energy function in composition space is the primary determinant of interfacial tension [see reference 15 and citations therein], and [4] recent experimental (16) and theoretical (17) evidence indicate that the wettability

relations to which fractional flow is so sensitive depend strongly on the free energy topography.

We present here a quaternary version of the Flory-Huggins equation of state modified to account for ternary interactions between amphiphile, oil, and brine and which treats surfactant and alcohol as distinct components. The computational strategy for extracting phase equilibria from a quaternary thermodynamic model relies on known equilibria for binary and ternary systems which then serve as initial guesses for quaternary equilibria. The unfolding of phase behavior is aided by direct computation of the limit of thermodynamic stability — the spinodal surface in a quaternary — and all critical points, which not only pinpoint spots of possible numerical difficulty in attempting to calculate phase equilibria but also determine qualitatively the pattern of global phase behavior which must exist (24).

The computational strategy and methods we describe are rather general and readily extend to quaternary thermodynamic modelling of CO_2-light hydrocarbon-medium hydrocarbon-heavy hydrocarbon systems with state-of-the-art PVT equations of state such as the Redlich-Kwong, Peng-Robinson, and Soave equations.

Thermodynamics of Phase Behavior

In our approach, phase equilibria calculations in multicomponent composition space begin with information about binary edges and ternary faces and proceed by numerical continuation into the desired higher dimensional quaternary phase space. (The advanced reader on heterogeneous phase equilibria is referred to the classical text by Gibbs (18) while the uninitiated may wish to draw first from Prigogine and Defay (19) or Modell and Reid (20).)

Ternary Phase Behavior

The limit of stability of any one-phase state is known as the spinodal. When the composition moves from a stable one-phase state across the spinodal two or more phases must spontaneously separate. In a ternary system at constant temperature T and pressure P, the equation defining the spinodal, curve is given by

$$|\underline{\underline{Q}}| \equiv \begin{vmatrix} \frac{\partial^2 g}{\partial x_i^2} & \frac{\partial^2 g}{\partial x_i \partial x_j} \\ \frac{\partial^2 g}{\partial x_i \partial x_j} & \frac{\partial^2 g}{\partial x_j^2} \end{vmatrix} = 0 \qquad (1)$$

where $|\underline{\underline{Q}}|$ denotes the determinant of the matrix $\underline{\underline{Q}}$, g the molar Gibbs free energy, and x_i and x_j the independent composition density variables for the ternary system (e.g., two mole or volume fractions).

Critical points are those one-phase states on the spinodal curve for which the directional derivative of the spinodal equation along the spinodal curve vanishes:

$$\underline{x}^o \cdot \nabla |\underline{\underline{Q}}| = 0 \quad , \tag{2}$$

where $\underline{x}^o$ is the eigenvector corresponding to the zero eigenvalue of $\underline{\underline{Q}}$. Thermodynamic stability of the critical points is given by the next higher order gradient of $\underline{\underline{Q}}$. Locally stable critical points are those states which satisfy equations (1) and (2) as well as the inequality constraint:

$$(\underline{x}^o \cdot \nabla)^2 |\underline{\underline{Q}}| > 0 \quad . \tag{3}$$

Once the limit of stability along with the critical points and their stability has been calculated, the global phase behavior is qualitatively determined. Multiphase regions are then calculated using chemical potential equations. The chemical potential of species i in an n-component system is given by:

$$\mu_i = g - \sum_{j \neq i}^{n} \left(\frac{\partial g}{\partial x_j}\right)_{x_{k \neq i}} x_j \qquad i=1,\ldots,n \tag{4}$$

The compositions of phases α and β in equilibrium are given by:

$$\mu_i^\alpha = \mu_i^\beta \qquad i=1,\ldots,n \ . \tag{5}$$

The locus of points in composition space determined by equation (5) is called the binodal — it is the locus of the ends of two-phase tie-lines. Similarly, the compositions of three-phase equilibrium are given by:

$$\mu_i^\alpha = \mu_i^\beta = \mu_i^\gamma \quad , \qquad i=1,\ldots,n \tag{6}$$

Three-phase equilibria may arise in one of two ways: either a critical tie-line opens at one endpoint to form a three-phase triangle or a tricritical point opens into a small three-phase triangle (21-24). The equations satisfied by a critical endpoint and a tricritical point are quite different. A critical endpoint lies at the end of a critical tie-line and thus must satisfy the three chemical potential equations (in a ternary system) for two-phase equilibria (equation (5)). In addition, the critical endpoint must satisfy the critical equations (1) and (2). A tricritical point, on the other hand, is a higher order critical point and in addition to satisfying critical equations (1) and (2) must satisfy two additional critical equations and an inequality for local stability:

$$(\underline{x}^o \cdot \nabla)^2 |\underline{\underline{Q}}| = 0 \quad , \tag{7}$$

$$(\underline{x}^o \cdot \nabla)^3 |\underline{\underline{Q}}| = 0 \quad , \tag{8}$$

$$(\underline{x}^o \cdot \nabla)^4 |\underline{\underline{Q}}| > 0 \quad . \tag{9}$$

For a ternary system, equations (7)-(9) are fairly complicated and become truly unwieldy for quaternary systems. However, once the spinodal equation (1) is determined, numerical derivatives of $|\underline{\underline{Q}}|$ may always be taken to obtain equations (7)-(9) to the desired degree of accuracy.

Quaternary Phase Behavior

The spinodal in a quaternary system at constant T and P is a surface, rather than a curve as in a ternary system. The determinant equation defining the spinodal is now third order:

$$|\underline{\underline{Q}}| = \begin{vmatrix} \frac{\partial^2 g}{\partial x_i^2} & \frac{\partial^2 g}{\partial x_i \partial x_j} & \frac{\partial^2 g}{\partial x_i \partial x_k} \\ \frac{\partial^2 g}{\partial x_i \partial x_j} & \frac{\partial^2 g}{\partial x_j^2} & \frac{\partial^2 g}{\partial x_j \partial x_k} \\ \frac{\partial^2 g}{\partial x_i \partial x_j} & \frac{\partial^2 g}{\partial x_j \partial x_k} & \frac{\partial^2 g}{\partial x_k^2} \end{vmatrix} = 0 \tag{10}$$

Critical points satisfy equation (10) and the quaternary form of equation (2). Locally stable critical points must also satisfy the inequality constraint (3).

Chemical potentials of the four components and two- and three-phase equilibria are given by equations (4)-(6) with n=4. Three phase equilibria arise from critical endpoints and tricritical points as in the ternary system but now the possibility for four-phase equilibria, which are not just accidents of symmetry (25) exist. Four-phase equilibria must satisfy

$$\mu_i^\alpha = \mu_i^\beta = \mu_i^\gamma = \mu_i^\delta \quad , \qquad i=1,\ldots,4 \tag{11}$$

Four-phase equilibria can arise in one of four different ways (21,26,27): 1) through a critical tie-triangle where one of the vertices of the three-phase triangle becomes critical, 2) from a doubly critical tie-line where both endpoints of the tie-line are critical, 3) from a critical tie-line where one of the endpoints is tricritical, and 4) from a tetracritical point.

A critical tie-triangle must satisfy the critical equations ((10) and (2)) at one of the vertices and the eight equations (6) for three phase equi-

libria. Thus ten equations must be satisfied for nine independent-composition variables (the 3 composition variables for each of the 3 triangle vertices). Therefore, one of the parameters of the model must be varied continuously to obtain a critical tie-triangle.

A doubly critical tie-line must satisfy the critical equations (10) and (2) at both ends of a tie-line as well as the four equations (5) for two-phase equilibria. Thus eight equations in six composition variables must be satisfied which requires either symmetry which reduces the number of equations to be satisfied or continuous variation to unique values of two independent parameters. A tricritical tie-line also requires simultaneous solution of eight equations in six composition variables.

A tetracritical point must satisfy the four tricritical equations — (10), (2), (7), and (8) — and two additional critical equations:

$$(\underline{x}^{o} \cdot \nabla)^{4} |\underline{\underline{Q}}| = 0 \quad , \tag{12}$$

$$(\underline{x}^{o} \cdot \nabla)^{5} |\underline{\underline{Q}}| = 0 \quad , \tag{13}$$

and a higher order gradient inequality constraint for local stability. This constitutes six equations in three independent composition variables, a degree of freedom deficiency of three. It is clear from this equation and unknown counting that the most common method of a four-phase tetrahedron evolving is through a critical tie-triangle while the rarest method is from a tetracritical point (which has never been observed experimentally).

The Gibbs phase rule modified to account for criticality (18,28) includes an additional term:

$$P + F = C + 2 - 2n \tag{14}$$

where P is the number of phases, F the degrees of freedom, C the number of components, and n the order of the critical point. An "ordinary" critical point is first order, a tricritical point is second order, and a tetracritical point is third order (22,29,30). Table 1 summarizes the ways in which three- and four-phase equilibria can arise in quaternary systems. Of course, Table 1 does not account for special cases of symmetry which introduce constraints on the unknown compositions and thus increase the available degrees of freedom (31). We draw on the most common methods for eruption of three- and four-phase equilibria, critical tie-lines and critical tie-triangles, in illustrating the phase equilibria one observes in the quaternary system.

Thermodynamic Model

The thermodynamic equation of state we used to model ternary surfactant-oil-brine and alcohol-oil-brine and quaternary oil-brine-surfactant-alcohol systems is a modified version of the Flory-Huggins equation of state (see Rossen et al. (14) and references therein for an analysis of the development of the model). In addition to the ordinary entropic ϕ_i ℓn ϕ_i terms, ϕ_i being

Table 1

Three- and Four-Phase Equilibria in Quaternary Systems

$F = C - P + 2 - 2n$ Phase Rule (Modified for Criticality)
$(C = 4)$

Geneses of Three-Phase Regions:

Type	Degrees of Freedom in Quaternary	Fixed T,p
Critical Tieline	$F = 4 - 2 + 2 - 2 = 2$	0
Tricritical Point	$F = 4 - 1 + 2 - 4 = 1$	-1

Geneses of Four-Phase Regions:

Type	Degrees of Freedom	Fixed T,p
Critical Tie-Triangle	$F = 4 - 3 + 2 - 2 = 1$	-1
Double Critical Tie-Line	$F = 4 - 2 + 2 - 4 = 0$	-2
Tricritical Tie-Line	$F = 4 - 2 + 2 - 4 = 0$	-2
Tetracritical Point	$F = 4 - 1 + 2 - 6 = -1$	-3

the volume fraction of component i, and the enthalpic $\alpha_{ij}\phi_i\phi_j$ terms of the Flory-Huggins model, where α_{ij} is the binary energy of interaction parameter, we model those specific interactions of surfactant and alcohol resulting from their amphiphilicity. In particular, along with the usual binary interactions between amphiphile with oil or brine, the model contains ternary interactions representing the amphiphile's tendency to orient itself between oil and brine with its hydrophilic moiety interacting with brine and its lipophilic moiety interacting with hydrocarbon. The simplest embodiment of the ternary interaction is a trilinear term, $-\beta_A\phi_A\phi_O\phi_W$, where β_A is the ternary interaction parameter and ϕ_A, ϕ_O, and ϕ_W are the volume fractions of amphiphile, oil, and brine, respectively. The effect of the ternary interaction on phase equilibria can be strengthened by combining the binary oil-brine interaction term and the ternary oil-brine-amphiphile interaction term into a single exponential enthalpic contribution:

$$\alpha_{WO}\, e^{-\beta_A\phi_A\phi_O\phi_W} \approx \alpha_{WO}\phi_O\phi_W(1-\beta_A\phi_A + \frac{(\beta_A\phi_A)^2}{2} - \ldots) \qquad (15)$$

The first two terms of the Taylor expansion of this exponential term give the binary and trilinear interactions and for small values of β_A, the linear approximation holds. Large values of β_A reflect a strong tendency for amphiphile to orient itself between oil and brine domains which implies the ability

to sheet, that is to form a coherent layer of surfactant molecules all oriented in a particular direction (hydrophilic groups towards brine). It is the essence of this "sheeting" or topological ordering of surfactant (32,33) which is captured with the exponential "screening" of oil and brine by amphiphile.

The quaternary form of the exponentially screened Flory-Huggins (ESFH) equation of state is:

$$g = \frac{\tilde{V}_W n \tilde{g}}{RT} = \phi_W \ell n \phi_W + \frac{m_W}{m_O} \phi_O \ell n \phi_O + \frac{m_W}{m_S} \phi_S \ell n \phi_S + \frac{m_W}{m_A} \phi_A \ell n \phi_A + \alpha_{WS} \phi_W \phi_S$$

$$+ \alpha_{OS} \phi_O \phi_S + \alpha_{WA} \phi_W \phi_A + \alpha_{OA} \phi_O \phi_A + \alpha_{AS} \phi_A \phi_S + \alpha_{WO} e^{-(\beta_S \phi_S + \beta_A \phi_A)} \phi_W \phi_O \quad (16)$$

where g is the dimensionless molar Gibbs free energy of mixing, $\tilde{V}_W$ is the molar volume of water, n the molar density of solution, $\tilde{g}$ the dimensional molar Gibbs free energy, RT has its usual significance, m_W/m_O, m_W/m_S and m_W/m_A are aggregate molecular weight ratios and reflect the relative tendency of oil, surfactant, and alcohol to associate over water, α_{ij} is the binary interaction parameter representing the net difference between i-i, j-j, and i-j interactions (34), β_S and β_A are the screening parameters for surfactant and alcohol, and ϕ_i is the volume fraction of component i. One simplifying assumption which is made to reduce the number of parameters of the model is to set m_W/m_O to unity to reflect no tendency for oil to associate relative to brine. The methods for handling the other parameters are discussed in the following sections.

Numerical Techniques and Computational Algorithm

The solving of equations (1) or (10) and (2) for critical points and of equations (5), (6), and (11) for multiphase equilibria require the simultaneous solution of sets of highly nonlinear equations. This was accomplished by standard Newton iteration. The convergence criterion that $\sum_i |\mu_i^\alpha - \mu_i^\beta|^2 < \varepsilon$, with $\varepsilon = 10^{-20}$, was sufficient. For solutions with one volume fraction $\phi_i < 10^{-5}$, the surrogate variable $u = \ell n \phi_i$ was used to avoid numerical scaling difficulties and to speed convergence.

First-order parametric or compositional continuation was used to track families of critical points and multiphase equilibria through parameter or composition space. By first-order, we mean updating the Newton iteration Jacobian and initial guess solution vector with the previous solution vector plus the increment in the previous two solutions, i.e.,

$$\underline{x}_{i+1}^{(1)} = \underline{x}_i^{(c)} + \Delta \underline{x}_{i,i-1}^{(c)} + \underline{\underline{J}}^{-1}(\underline{x}_i^{(c)} + \Delta \underline{x}_{i,i-1}^{(c)}) \, \underline{f}(\underline{x}_i^{(c)} + \Delta \underline{x}_{i,i-1}^{(c)}) \quad (17)$$

where $\underline{x}_i^{(c)}$ is the converged solution vector for the ith parameter or composition step, $\Delta\underline{x}_{i,i-1}^{(c)}$ is the difference in the converged solution vector for the ith and i-1st parameter or composition steps, the superscripts denote the number of iterations, $\underline{\underline{J}}^{-1}$ is the inverse of the objective function Jacobian matrix, $[\partial f_i/\partial x_j]$, and $\underline{f}$ is the objective function vector.

Using compositional first-order continuation, convergence for multiphase equilibria is typically quadratic with a volume fraction step of 0.005 to 0.01. Convergence either fails or becomes linear when two of the phases approach criticality: either tie-lines approaching a plait point or tie-triangles collapsing as they near a critical tie-line. Using parametric first-order continuation, convergence for multiphase equilibria is usually quadratic for interaction parameter steps of 0.5 to 1.0. Again, convergence either fails or becomes linear as two of the phases in equilibrium become critical. Four-phase tie-tetrahedra are completely determined by fixing the parameter values for a quaternary system and families of tie-tetrahedra must be calculated by parametric continuation. Convergence fails or becomes linear as the tetrahedra collapse in the vicinity of a critical tie-triangle.

Although the computational time required for calculating multiphase equilibria increases tremendously near degenerate critical features like critical points, critical tie-lines, and critical tie-triangles, this expense and effort can be circumvented by calculating the critical features directly. As the computation of critical points only involves the solution of two nonlinear equations, the computer time required is typically an order of magnitude less than that required for multiphase equilibria. Once computed, the critical lines serve as barometers for anticipated numerical convergence difficulties and can thus make multiphase equilibria calculations much more cost-effective.

All ternary and quaternary systems studied had the oil-brine binary edge in common. The two component form of the ESFH model for oil and brine reduces to

$$g = \phi_W \ln\phi_W + \phi_O \ln\phi_O + \alpha_{WO}\phi_O\phi_W \quad . \tag{18}$$

The limit of thermodynamic stability for the binary described by equation (20), is given by

$$\phi_{spinodal} = \frac{1}{2}\left(1 \pm \sqrt{1 - \frac{2}{\alpha_{WO}}}\right) \quad . \tag{19}$$

By first-order continuation, the spinodal curve for a ternary face to which this binary edge is attached is readily calculated. A supplemental calculation of equation (2), performed while tracking the spinodal curve, indicates the nearness to a critical point which is then easily computed. Table 2 outlines the computational algorithm used for tracking spinodal solutions and critical points through ternary and quaternary ESFH solution.

Table 2

Algorithm for Calculating Critical Points in Quaternary System

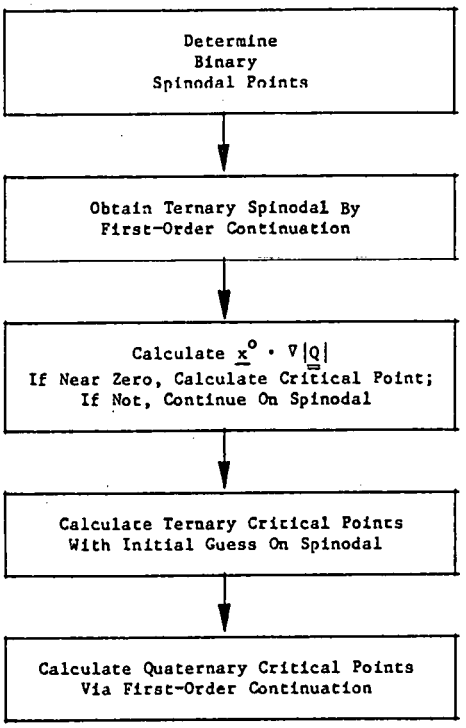

Once the limit of stability and all critical points have been calculated, multiphase equilibria can be found in a similar fashion. The spinodal points on the binary oil-brine edge serve as a good initial guess for the binary miscibility gap. Once it has been calculated, first-order continuation is used to obtain the ternary binodal. Ternary critical points not lying on this binodal indicate the presence of other binodals and possible three-phase equilibria. Binodals can be continued away from critical points using as initial guess compositions along the spinodal equidistant from the critical point. Intersections of binodals then serve as guesses for vertices of three-phase tie-triangles. Once a three-phase equilibrium is obtained for a ternary, parametric continuation to compute families of ternary three-phase equilibria or compositional continuation is easily done to generate fans of quaternary tie-triangles. Fans of tie-triangles are then computed for different quaternary tetrahedra by parametric continuation. The three-phase equilibria can become unstable, in general, in one of two ways: either a tie-triangle collapses into a critical tie-line or it becomes critical and erupts into a tie-tetrahedron. Both cases were explored here and in fact both may occur within the same quaternary tetrahedron, as we see below. Once a four-phase equilibrium has been calculated, by using as initial guess intersecting fans of tie-triangles, families of tie-tetrahedra in parameter space can be computed. Finally, the entire process of compositional and parametric continuation is reversible; once a tie-tetrahedron with desired parameter values has been found, the three-phase equilibria which form its faces may be continued away from it. Table 3 summarizes the algorithm for calculating multiphase equilibria in quaternary phase space.

Table 3

Algorithm for Calculating Multiphase Equilibria

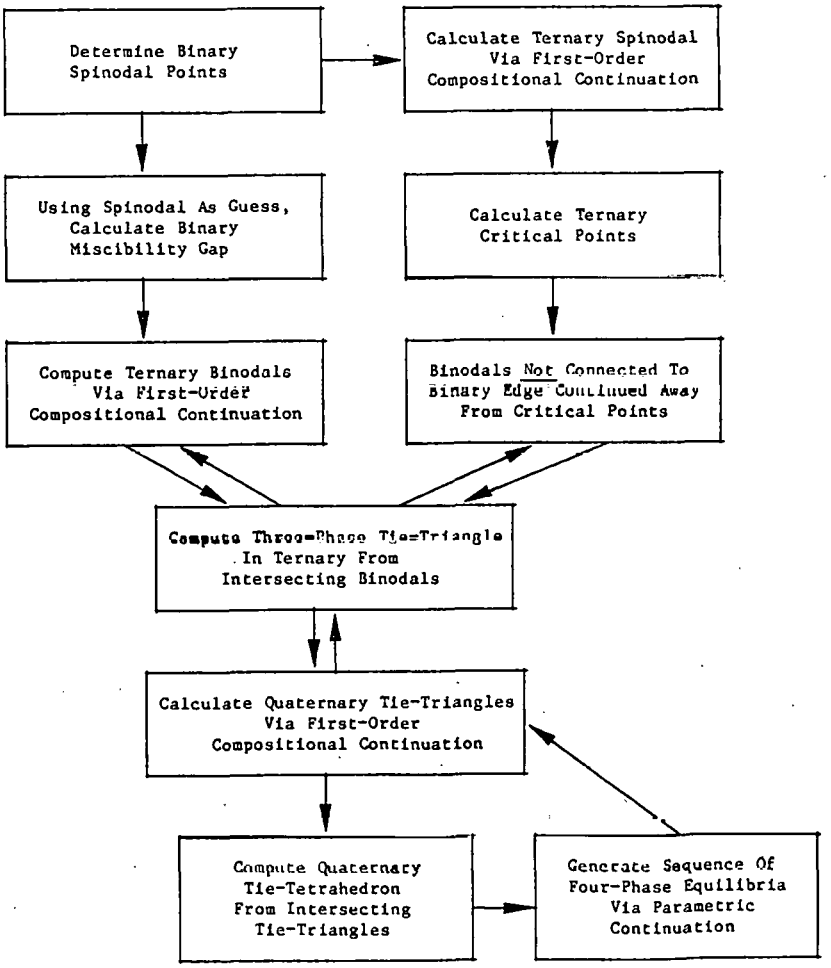

All multiphase equilibria were checked for local stability by noting the sign of the spinodal determinant at tie-line endpoints and tie-triangle and tetrahedron vertices. Global stability can only be ascertained by an exhaustive multidimensional gridpoint search of the g hypersurface to check for non-tangential intersectons of the tangent plane at the points of equilibria. From the observed trends in phase equilibria, we are confident all phase equilibria reported here are globally stable.

Results and Discussion

Selection of Parameters for Model Phase Diagrams

We do not attempt to quantitatively fit the parameters of the model to actual data. Rather, we chose parameter values that illustrate typical be-

havior of oil-brine-surfactant-alcohol systems that are compatible with the physics of the model.

The quaternary version of the ESFH dimensionless free energy of mixing has 10 independent parameters: six binary interaction parameters — α_{WS}, α_{OS}, α_{WA}, α_{OA}, α_{AS}, and α_{WO} — which can be fixed by binary phase equilibria, two screening parameters β_S and β_A, and two aggregate molecular weight ratios, $\varepsilon_S = m_W/m_S$ and $\varepsilon_A = m_W/m_A$. Despite the large number of parameters, several can be fixed within narrow limits by physical considerations and others can be independently fixed by binary or ternary phase equilibria constraints. We outline here first the physical constraints and binary phase equilibria requirements and proceed to ternary phase behavior and, ultimately, quaternary equilibria.

The two aggregate molecular weight ratios, ε_S and ε_A, can be chosen within narrow limits to reflect the relative tendencies of surfactant and alcohol to associate cooperatively in polar and nonpolar media. ε_S must be small to reflect the sheeting tendency of surfactant. For the ternary surfactant-oil-brine case, a value of 0.04 was chosen to yield a low base of the symmetric three-phase tie-triangle. The model of symmetry is chosen for its simplicity and ease of calculation and as the point of departure in generating the typical $\underline{2}$-3-$\overline{2}$ progression (1,5,7-9,23,35,36) of surfactant-oil-brine phase behavior as, for example, salinity is varied. Smaller values of ε_S yield volume fractions of surfactant in excess phases smaller than 10^{-300}, which is the underflow limit on the computer used for phase behavior calculations. ε_A should be larger than ε_S but smaller than unity to reflect alcohol's ability to associate weakly but non-cooperatively. A value of 0.1 was used although phase behavior is relatively insensitive to ε_A and another value between 0.04 and 1 could have been chosen.

Binary interaction parameters were chosen to reflect miscibility or immiscibility of component pairs. Oil and brine are virtually insoluble in each other and, thus, a value of 4.8 for α_{WO} was selected, which yields a binary miscibility gap from $\phi_0 = 0.01$ to $\phi_0 = 0.99$. Increasing α_{WO} slightly pushes ϕ_0 rapidly to zero in the aqueous phase and unity in the oleic phase. When symmetric ternary phase diagrams were desired, the interaction parameter pairs α_{WS}-α_{OS} and α_{WA}-α_{OA} were chosen to be equal. This reflects middle phases in three-phase equilibria where uptake of oil and brine are equal, as for example at so-called optimal salinity. α_{AS} was chosen to roughly approximate surfactant-alcohol repulsion or attraction.

Screening parameters β_S and β_A are chosen to reflect strong and weak screening, respectively. As discussed below, β_S is taken to be 12.5 to give a symmetric three-phase tie-triangle with $\phi_S = 0.10$ in the middle phase. β_A is taken to be very small and positive, 0.3, to reflect weak screening. For modelling different alcohols and surfactants, different values of β_S and β_A must be selected to match desired ternary phase behavior.

Ternary Surfactant-Oil-Brine Base Case

In the earlier pseudoternary modelling with the ESFH equation of state (14), the base case of active amphiphile-oil-brine at optimal salinity was chosen to be a symmetric three-phase tie-triangle with 10 volume % surfactant in the middle and virtually no surfactant in the excess phases ($\phi_S^A = \phi_S^O \cong 10^{-40}$) (Figure 1). The fitting of surfactant volume fraction in middle phase at optimal salinity for experimental systems is easily done by adjusting the screening parameter β_S. Figure 2 shows symmetric three-phase triangles for $\alpha_{WS} = \alpha_{OS} = 0$, $\alpha_{WO} = 4.8$, and $\varepsilon_S = 0.04$ and various values of β_S. Two research groups (37,38) have recently obtained three-phase microemulsion systems in pseudoternary mixtures of brine, oil, and surfactant with no alcohol present. Three-phase equilibria can also be generated holding β_S fixed and varying $\alpha_{WS} = \alpha_{OS}$ simultaneously. Figure 3 shows symmetric three-phase triangles for $\beta_S = 12.5$, $\alpha_{WO} = 4.8$, and $\varepsilon_S = 0.04$ with varying values of $\alpha_{WS} = \alpha_{OS}$.

The typical progression of amphiphile-oil-brine systems from $\underline{2}$-3-$\overline{2}$ phases (1,5,7-9,23,37,38), is readily modelled by altering the symmetric $\overline{b}$ase case through one of the binary interaction parameters, α_{WS} or α_{OS}. For example, increasing α_{WS} corresponds to increasing the salinity of the brine or decreasing α_{OS} to increasing the aromaticity or polarity of the oil. Figure 4 shows a sequence of ternary phase diagrams for $\alpha_{WO} = 4.8$, $\varepsilon_S = 0.04$, $\beta_S = 12.5$, $\alpha_{OS} = 0$, and values of α_{WS} from 0 to -6. This mimics a portion of a salinity scan for an oil-brine-surfactant system without any alcohol.

Ternary Alcohol-Oil-Brine Base Case

The alcohol-oil-brine base case was chosen to mimic a representative small-chain alcohol with n-alkane and brine at equal volume uptake of brine and oil in an alcohol-rich middle phase. The amount of alcohol actually necessary to solubilize equal amounts of oil and brine in experimental systems varies anywhere from 70-80 volume % for some of the small chain monohydric alcohols like ispropanol and isobutanol to about 30 volume % for some of the ethoxylated alcohols like C_8E_3 (39) (triethylene glycol mono-octyl ether). For our base case, we chose a symmetric three-phase tie-triangle with about 52 volume % amphiphile in the middle phase and 20% amphiphile in the excess aqueous and oleic phase. Figure 5 is this equilibrium ternary phase diagram for $\beta_A = 0.3$, $\alpha_{WO} = 4.8$, $\varepsilon_A = 0.1$, and $\alpha_{WA} = \alpha_{OA} = .55$. As mentioned above, phase behavior is relatively insensitive to the values of ε_A. β_A was selected to be 0.3 to elevate the height of the three-phase triangle while still maintaining weak screening. $\alpha_{WA} = \alpha_{OA}$ was taken to be slightly positive to increase the size of the three-phase triangle. Figure 6 shows the effect of fixing $\varepsilon_A = 0.1$, $\beta_A = 0.3$, $\alpha_{WO} = 4.8$ and varying $\alpha_{WA} = \alpha_{OA}$ from .50 to .58. Increasing $\alpha_{WA} = \alpha_{OA}$ further results in the symmetric binodal and its critical point rising to coincide with the three-phase vertex, thus rendering the three-phase equilibrium globally unstable.

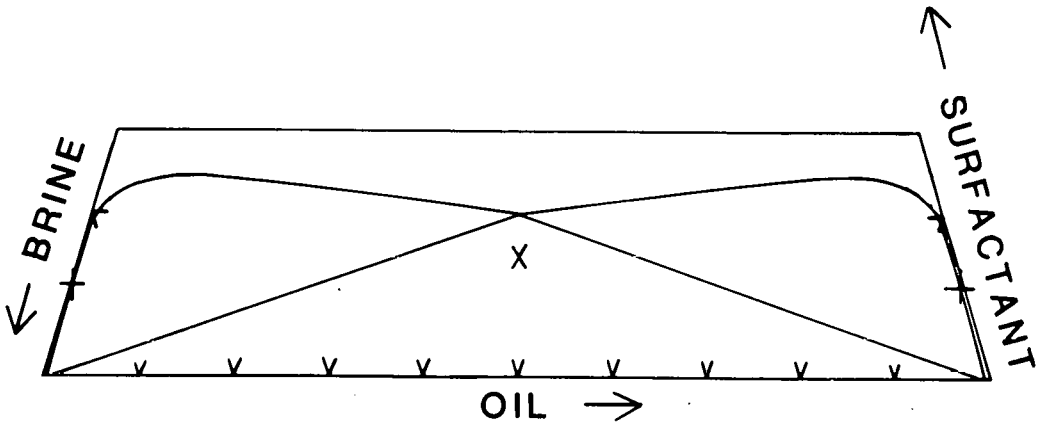

Figures 1 and 4a. Ternary phase diagram of surfactant-oil-brine base case. Parameter values: α_{wo}=4.8, α_{ws}=0, ε_s=0.04, and β_s=12.5. The vertical surfactant composition axis has been expanded to twice that of the oil-brine axis. (The same scale has been used in all surfactant-oil-brine ternary phase diagrams. Also in this and subsequent figures, tick marks denote volume fraction increments of 0.1, +'s denote locally stable critical points, and X's denote locally unstable critical points.)

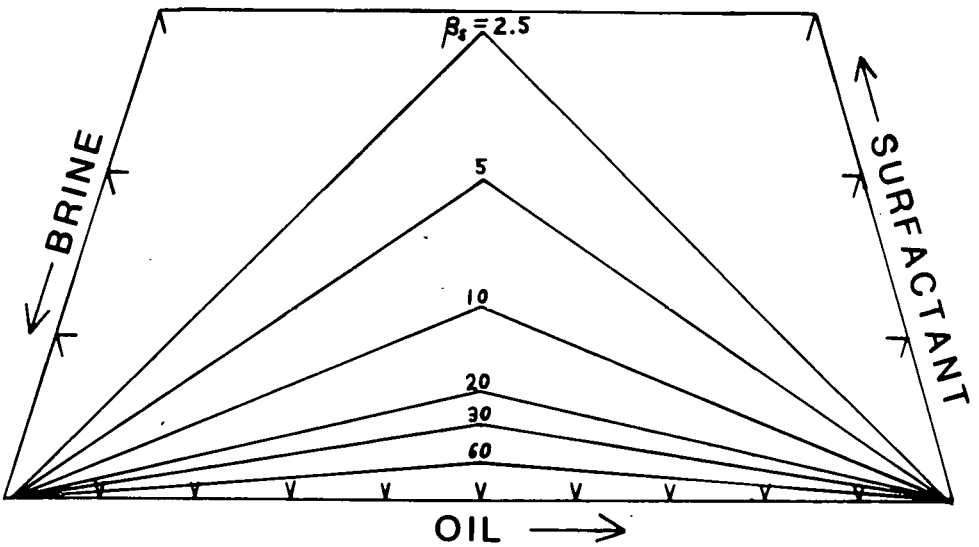

Figure 2. Sequence of symmetric surfactant-oil-brine three-phase tie-triangles for α_{wo}=4.8, α_{ws}=α_{os}=0, ε_s=0.04, and values of β_s varying from 2.5 to 60.

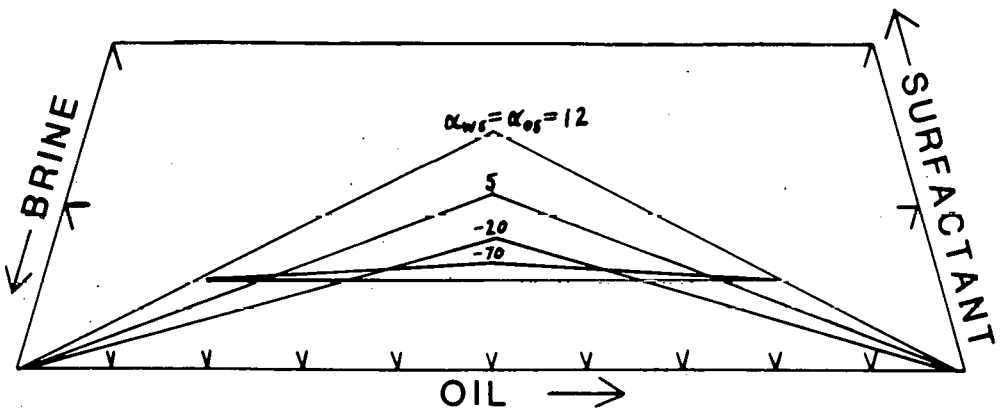

Figure 3. Sequence of symmetric surfactant-oil-brine three-phase tie triangles for α_{wo}=4.8, ε_s=0.04, β_s=12.5, and values of α_{ws}=α_{os} varying from 12 to -70.

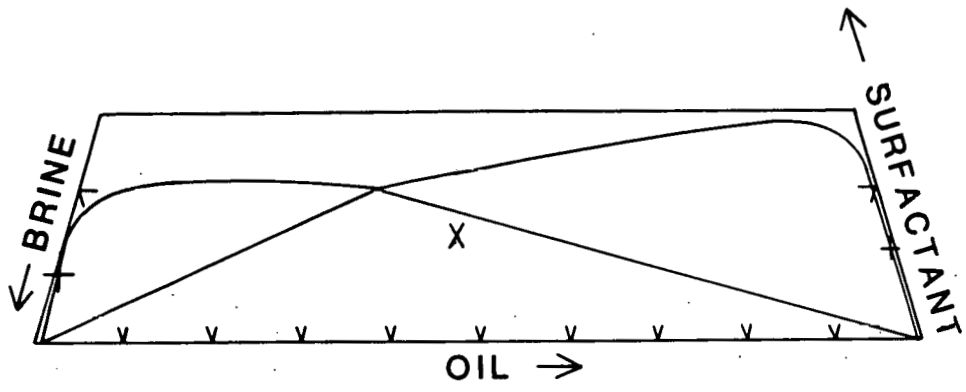

B

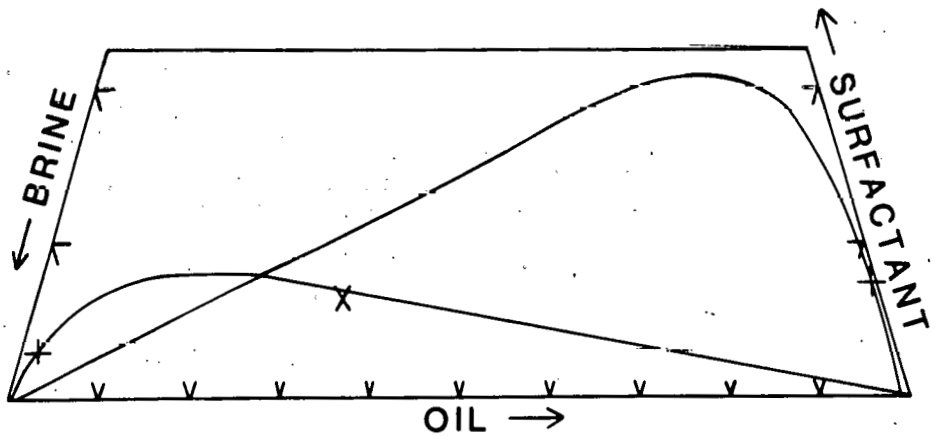

C

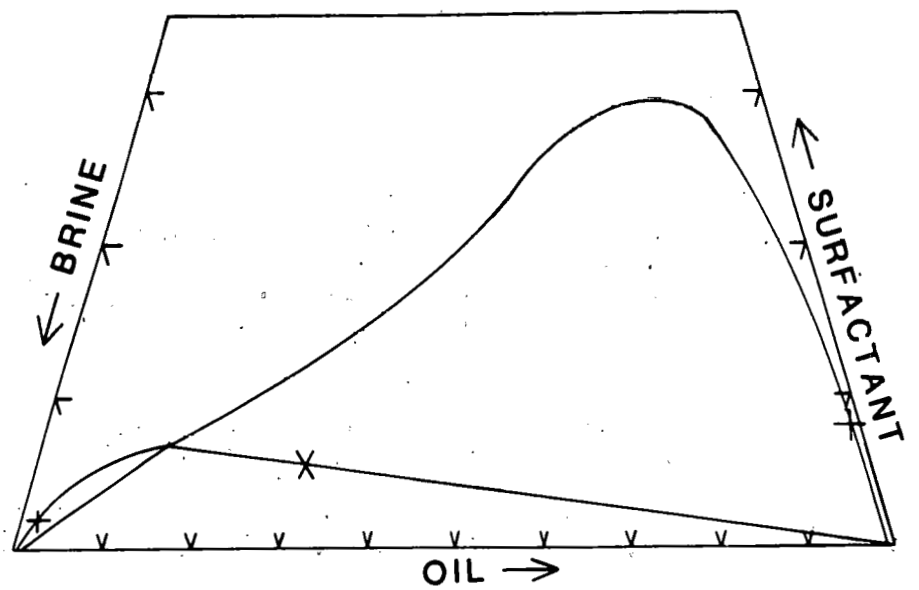

D

Figure 4. Sequence of ternary surfactant-oil-brine phase diagrams for α_{wo}=4.8, α_{os}=0, ε_s=0.04, β_s=12.5, and varying values of α_{ws}: (A) α_{ws}=0, (B) α_{ws}=-2, (C) α_{ws}=-4, (D) α_{ws}=-6.

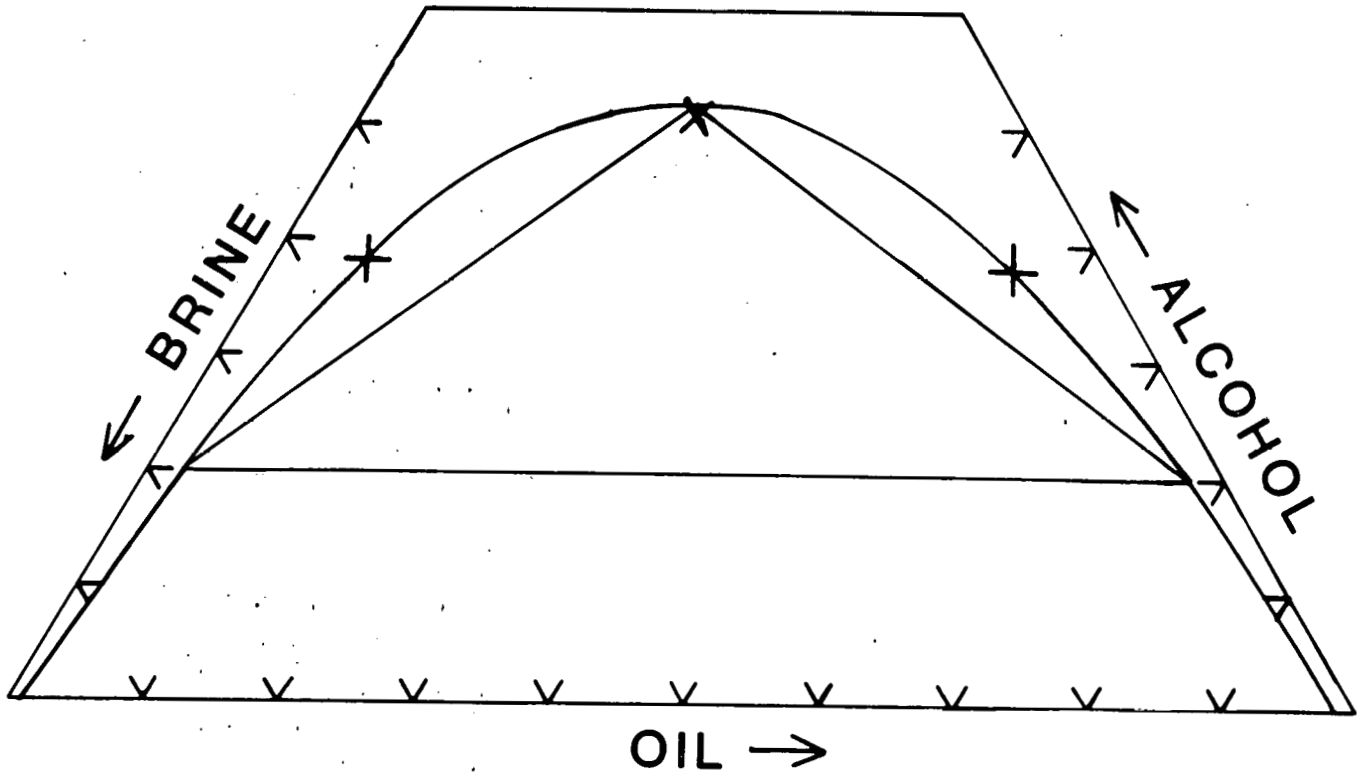

Figures 5 and 7a. Ternary phase diagram of alcohol-oil-brine base case. Parameter values: $\alpha_{wo}=4.8$, $\alpha_{wa}=\alpha_{oa}=0.55$, $\varepsilon_a=0.1$, and $\beta_a=0.3$.

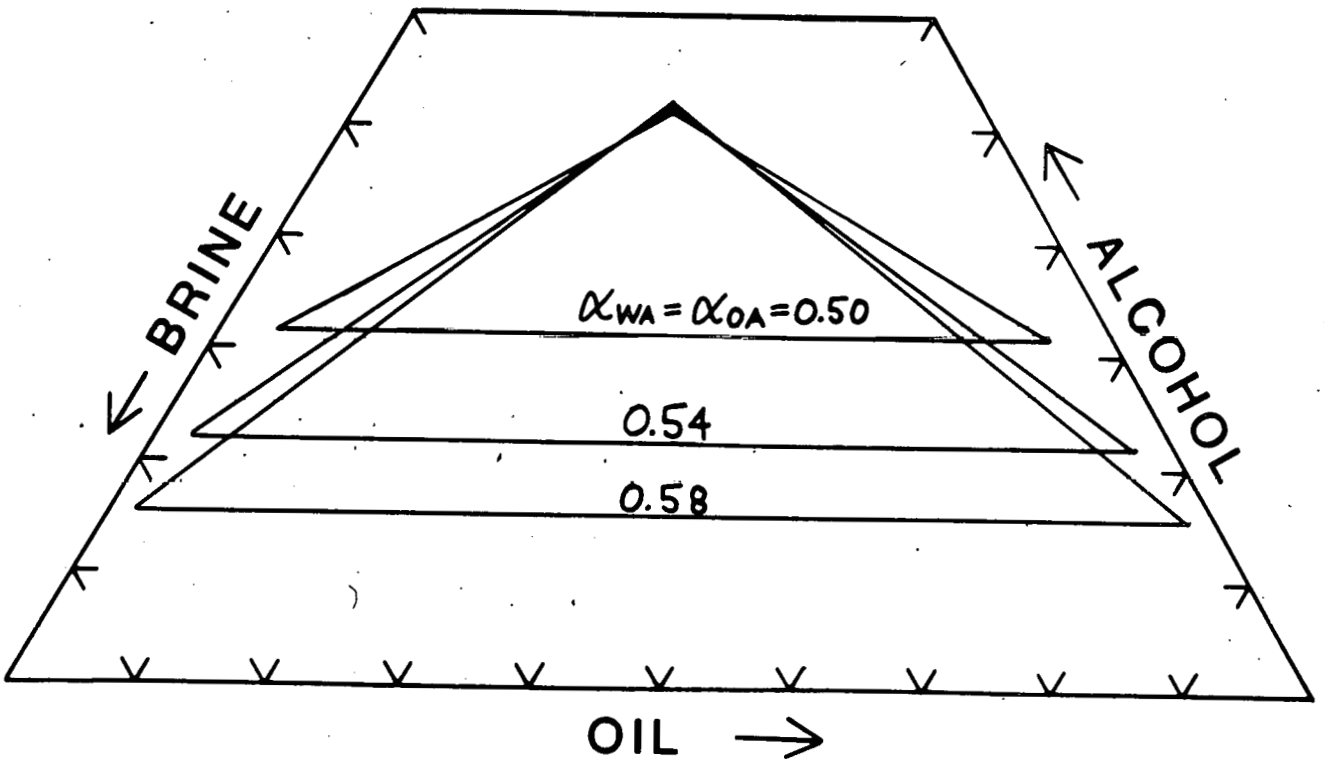

Figure 6. Sequence of symmetric alcohol-oil-brine three-phase tie-trangles for $\alpha_{wo}=4.8$, $\varepsilon_a=0.1$, $\beta_a=0.3$, and values of $\alpha_{wa}=\alpha_{oa}$ varying from 0.50 to 0.58.

Just as α_{WS} and α_{OS} can be made unequal to generate a salinity scan for ternary surfactant systems, so can α_{WA} and α_{OA} be varied to give critical endpoint-to-critical endpoint phase behavior. Figure 7 presents a series of ternary phase diagrams for $\epsilon_A = 0.1$, $\beta_A = 0.3$, $\alpha_{WO} = 4.8$, $\alpha_{OA} = 0.55$ and α_{WA} varying from 0.55 to 0.61. For even larger values of α_{WA}, the tie-triangle collapses to a critical tie-line whereupon the critical point detaches from the globally stable binodal and migrates within the two-phase region to merge with the unstable critical point X (Figure 8). This is the typical avenue for the genesis or collapse of a three-phase region.

Quaternary Phase Equilibria

Armed with knowledge of the desired ternary equilibria, we now address particular examples of quaternary phase equilibria. With the ternary surfactant-oil-brine and alcohol-oil-brine base cases serving as faces of the tetrahedron, the only remaining parameter to fix is α_{AS}, the interaction parameter between alcohol and surfactant. For $\alpha_{AS} = 0$, the symmetric tie-triangles fan through the tetrahedron from both faces but intersect at a common oil-rich, brine-rich tie-line edge. The result is a four-phase equilibrium depicted schematically in Figure 9. The compositions of the four-phase region are given in Table 4. The four-phase region collapses as α_{AS} is made negative, i.e. rendering alcohol-surfactant interactions attractive. For $\alpha_{AS} = -1$, the four-phase region has vanished and the quaternary tetrahedron is filled with a fan of symmetric tie-triangles (Figure 10). The degenerate four-phase equilibrium, or critical tie-triangle (27) from which the tie-tetrahedron springs, occurs at $\alpha_{AS} = -0.8875$. The compositions of its vertices are also given in Table 4.

The case of symmetry is instructive and certainly the obvious point of departure, but asymmetry is the rule. We begin by altering the fan of symmetric tie-triangles through one of the amphiphile-oil or amphiphile-brine interaction parameters, in this case α_{WA}. By choosing α_{WA} such that the tie-triangle on the alcohol-oil-brine face has already collapsed into a two-phase region, we obtain a fan of tie-triangles which begins symmetrically on the surfactant-oil-brine face and then skews before collapsing into a critical tie-line short of the far face of the tetrahedron. In the middle of this fan, a tie-tetrahedron has erupted. The situation has been projected onto a pseudo-ternary diagram with alcohol and surfactant lumped into a single pseudocomponent (Figure 11). With this simple perturbation of the symmetric case, we can begin to appreciate the richness and complexity of phase equilibria in the experimental systems.

The situation just described represents only the beginnings of an approach to modelling the actual experimental situation. We can approach this objective by skewing both ternary faces from symmetry, but in opposite directions. For a parameter set of $\alpha_{WO} = 4.8$, $\alpha_{AS} = -1$, $\beta_S = 12.5$, $\beta_A = 0.3$, $\alpha_{WA} = 0.6$, $\alpha_{OA} = 0.55$, $\alpha_{WS} = -5$, $\alpha_{OS} = 0$, the amphiphile-rich vertices of the three-phase tie-triangles fan from brine-rich on the surfactant-oil-brine

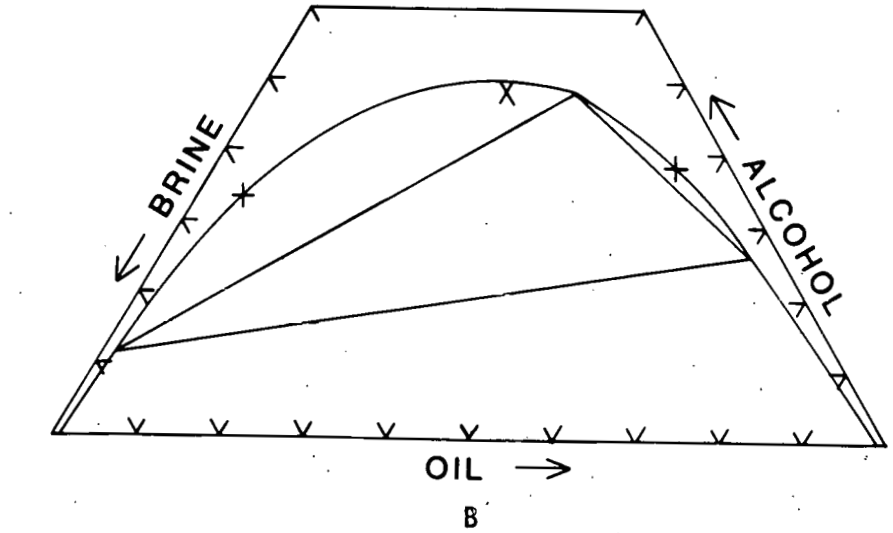

B

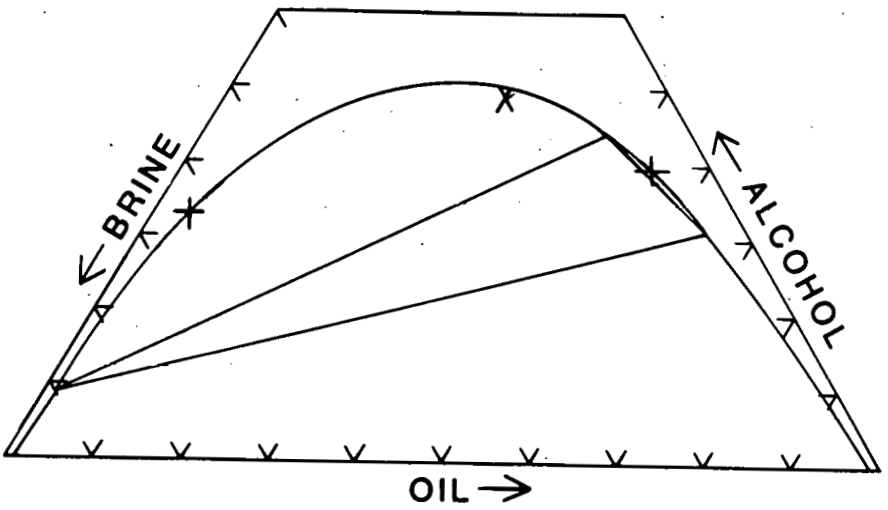

C

Figure 7. Sequence of ternary alcohol-oil-brine phase diagrams for α_{wo}=4.8, α_{oa}=0.55, ε_a=0.1, β_a=0.3, and varying values of α_{wa}: (A) α_{wa}=0.55, (B) α_{wa}=0.59, (C) α_{wa}=0.61.

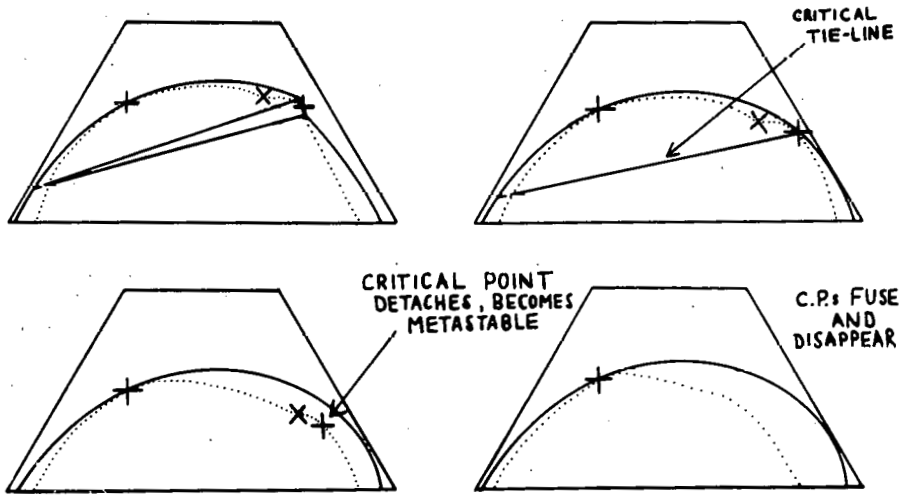

Figure 8. Schematic sequence of ternary phase diagrams showing collapse of a tie-triangle to a critical tie-line and subsequent fusion and disappearance of two critical points. The spinodal curve is given by the dotted line.

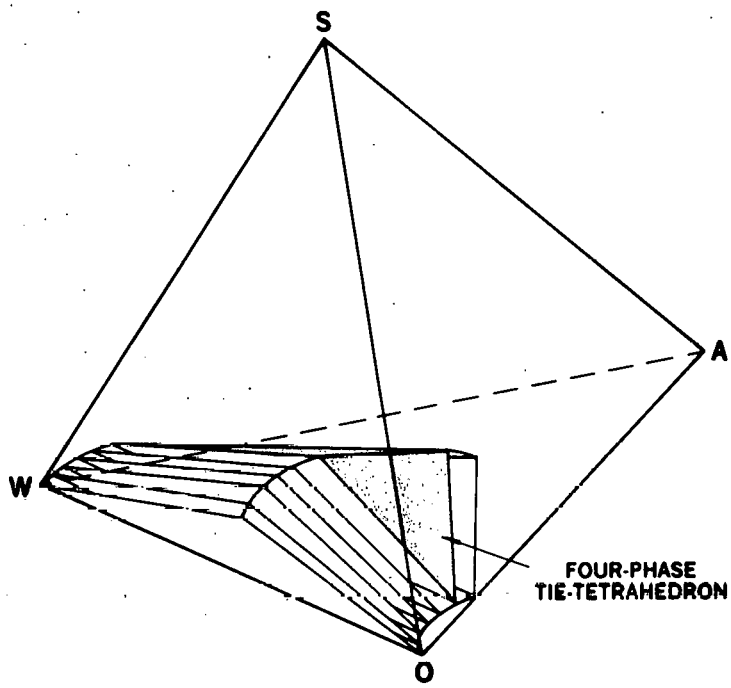

Figure 9. Schematic quaternary oil-brine-surfactant-alcohol phase diagram showing fan of symmetric tie-triangles with intervening four-phase tie-tetrahedron. Parameter values: $\alpha_{wo}=4.8$, $\alpha_{ws}=\alpha_{os}=0$, $\alpha_{wa}=\alpha_{oa}=0.55$, $\alpha_{as}=-0.6$, $\varepsilon_s=0.04$, $\varepsilon_a=0.1$, $\beta_s=12.5$, and $\beta_a=0.3$.

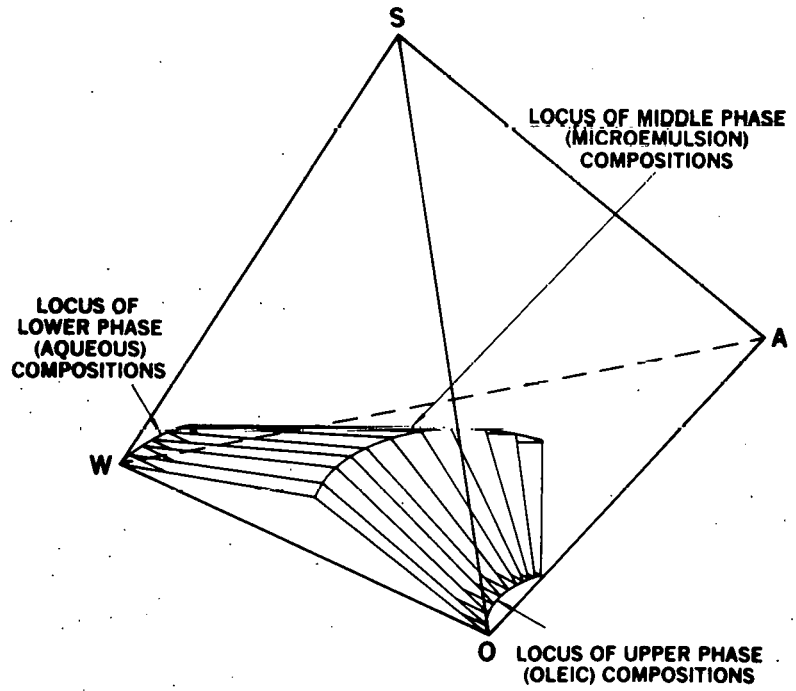

Figure 10. Schematic quaternary oil-brine-surfactant-alcohol phase diagram showing fan of symmetric tie-triangles through entire tetrahedron. Parameter values: $\alpha_{wo}=4.8$, $\alpha_{ws}=\alpha_{os}=0$, $\alpha_{wa}=\alpha_{oa}=0.55$, $\alpha_{as}=-1$, $\varepsilon_s=0.04$, $\varepsilon_a=0.1$, $\beta_s=12.5$, and $\beta_a=0.3$.

Table 4

Compositions of Four-Phase Tie-Tetrahedron
for Symmetric Quaternary Phase Diagram

Parameter Values: $\alpha_{WO} = 4.8$, $\alpha_{WS} = \alpha_{OS} = 0$, $\alpha_{WA} = \alpha_{OA} = 0.55$, $\alpha_{AS} = 0$,
$\varepsilon_S = 0.04$, $\varepsilon_A = 0.1$, $\beta_S = 12.5$, $\beta_A = 0.3$

$\phi_W^\alpha = .7734$	$\phi_S^\alpha = .552 \times 10^{-24}$	$\phi_A^\alpha = .2002$
$\phi_W^\beta = .0264$	$\phi_S^\beta = .552 \times 10^{-24}$	$\phi_A^\beta = .2002$
$\phi_W^\gamma = .2406$	$\phi_S^\gamma = .135 \times 10^{-5}$	$\phi_A^\gamma = .5188$
$\phi_W^\delta = .4248$	$\phi_S^\delta = .0903$	$\phi_A^\delta = .0602$

Compositions of Critical Tie-Triangle
for Symmetric Quaternary Phase Diagram

Parameter Values: $\alpha_{WO} = 4.8$, $\alpha_{WS} = \alpha_{OS} = 0$, $\alpha_{WA} = \alpha_{OA} = 0.55$, $\alpha_{AS} = -0.8875$
$\varepsilon_S = 0.04$, $\varepsilon_A = 0.1$, $\beta_S = 12.5$, $\beta_A = 0.3$

$\phi_W^\alpha = .7805$	$\phi_S^\alpha = .944 \times 10^{-24}$	$\phi_A^\alpha = .1939$
$\phi_W^\beta = .0256$	$\phi_S^\beta = .944 \times 10^{-24}$	$\phi_A^\beta = .1939$
$\phi_W^{critical} = .2836$	$\phi_S^{critical} = .0248$	$\phi_A^{critical} = .4079$

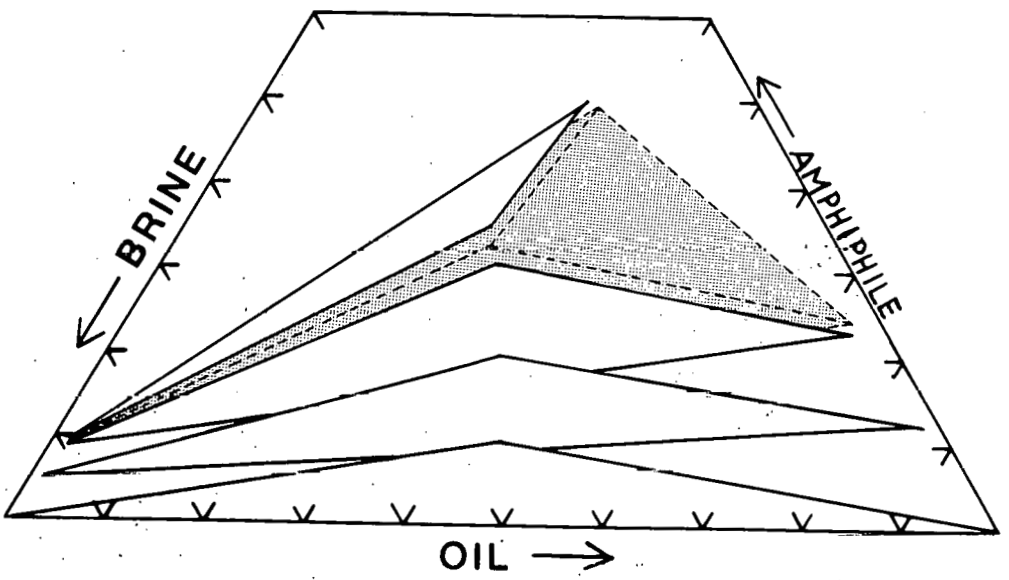

Figure 11. Pseudoternary representation of quaternary oil-brine-surfactant-alcohol phase diagram. Alcohol and surfactant have been lumped as a single pseudocomponent called amphiphile. A skewed four-phase tie-tetrahedron is denoted by the stippled area. Parameter values: $\alpha_{wo}=4.8$, $\alpha_{ws}=\alpha_{os}=0$, $\alpha_{wa}=0.62$, $\alpha_{oa}=0.55$, $\alpha_{as}=-1$, $\varepsilon_s=0.04$, $\varepsilon_a=0.1$, $\beta_s=12.5$, and $\beta_a=0.3$.

face to oil-rich on the alcohol-oil-brine face. This case is closer to the reality of experiment as surfactant and alcohol will, in general, not have the same optimal salinity for the same hydrocarbon.

Just as with the symmetric fan of tie-triangles, this asymmetric fan becomes unstable when α_{AS} is increased, resulting in a four-phase tie-tetrahedron. For $\alpha_{AS} = -0.6$, a stable tie-tetrahedron is present. This is undoubtedly the simplest and likeliest fashion in which four-phase equilibria arises in quaternary oil-brine-alcohol-surfactant systems (27).

Another pattern of quaternary phase behavior worthy of note is the case of two phase equilibria on the ternary amphiphile-oil-brine faces with surfactant partitioning into a brine-rich phase and alcohol residing in an oil-rich phase. The parameters are chosen very near the critical tie-line values on these faces: $\alpha_{WA} = .62$, $\alpha_{OA} = .55$ and $\alpha_{WS} = -12$, $\alpha_{OS} = 0$. Just within the tetrahedron, the two-phase regions soon develop critical tie-lines which open into tie-triangles and begin to fan. The three-phase triangles are only stable over a short compositional distance and soon merge to form a very skewed four-phase tie-tetrahedron. This situation is depicted schematically in Figure 12.

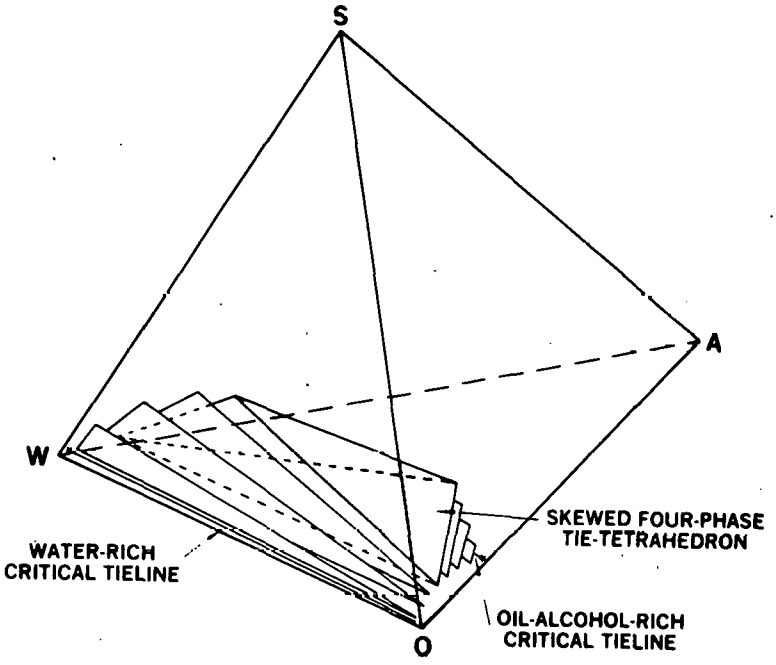

Figure 12. Schematic quaternary oil-brine-surfactant-alcohol phase diagram showing critical tie-line-to-critical tie-line phase behavior with intervening skewed tie-tetrahedron. Parameter values: $\alpha_{wo}=4.8$, $\alpha_{ws}=-12$, $\alpha_{os}=0$, $\alpha_{wa}=0.62$, $\alpha_{oa}=0.55$, $\alpha_{as}=-0.6$, $\varepsilon_s=0.04$, $\varepsilon_a=0.1$, $\beta_s=12.5$, and $\beta_a=0.3$.

Extensions of the Method

The screened Flory-Huggins model described here has been applied to ternary alcohol-oil-brine and surfactant-oil-brine and quaternary alcohol-surfactant-oil-brine systems. However, the computational algorithm and equation of state can be readily modified to treat other quaternary systems.

By choosing two large screening parameters and adjusting amphiphile-brine and amphiphile-oil interaction parameters, the equation of state can model the case of two mixed surfactants with oil and brine: one highly water-soluble and the other oil-soluble. This would find application in the treatment of commercial surfactant systems such as the petroleum sulfonates. By increasing the number of amphiphilic components, the model could be extended to incorporate several distinct surfactants in the mixture, although the computational requirements increase substantially with the number of components.

Another attractive application of the equation of state is to treat electrolyte as a distinct component in the quaternary salt-water-oil-amphiphile systems. Although brine has been reported to behave as a good pseudocomponent (4) in surfactant systems, it has been shown that in alcohol systems (40-43) salt does not partition with water in the same proportions in phases in equilibrium. The interaction parameter between water and salt could be adjusted for salt concentration: α_{WS} should be negative for miscibility at low salt concentrations while positive for immiscibility at higher salt concentrations.

Finally, the computational algorithm appears suitable for treating quaternary CO_2-hydrocarbon systems with a PVT equation of state, such as the Peng-Robinson or Redlich-Kwong equations. Recent CO_2-hydrocarbon thermodynamic modelling efforts (44) have revealed distinctly different binary equilibria for CO_2-propane, CO_2-decane, and CO_2-hexadecane binary mixtures. Thus, a quaternary model may be desirable in CO_2 flooding simulations to capture the effects of light, intermediate, and heavy hydrocarbon components in crude oil.

References Cited in Section IV

1. Bennett, K. E., Phelps, C. H. K., Davis, H. T. and Scriven, L. E., SPE Journal (December 1981) 747.

2. Nelson, R. C. and Pope, G. A., SPE Journal (October 1978) 325.

3. Salter, S. J., paper SPE 7056, presented at the Fifth Symposium on Improved Methods for Oil Recovery, Tulsa, Oklahoma, April 16-19, 1978.

4. Fleming, P. D. III and Vinatieri, J. E., J. Chem. Phys. 66, 3147 (1977).

5. Reed, R. L. and Healy, R. N., in Improved Oil Recovery by Surfactant and Polymer Flooding, eds. D. O. Shah and R. S. Schechter (Academic Press, Inc., New York, 1977) 383.

6. Bragg, J. R., Gale, W. W., McElhannon, W. A., Jr., Davenport, O. W., Petrichuk, M. D. and Ashcroft, T. L., paper SPE/DOE 10862 presented at the Third Joint Symposium on Enhanced Oil Recovery of the Society of Petroleum Engineers, Tulsa, April 4-7, 1982.

7. Healy, R. N. and Reed, R. L., SPE Journal (October 1974) 491.

8. Healy, R. N. Reed, R. L. and Stenmark, D. G., SPE Journal (June 1976) 147.

9. Healy, R. N. and Reed, R. L., SPE Journal (April 1977) 129.

10. Anderson, D. R., Bidner, M. S., Davis, H. T., Manning, C. T. and Scriven, L. E., paper SPE 5811, presented at Improved Oil Recovery Symposium, Tulsa, Oklahoma, March 22-24, 1976.

11. Larson, R. G., SPE Journal (December 1979) 411.

12. Helfferich, F. G., SPE Journal (February 1981) 51.

13. Hirasaki, G. J., SPE Journal (April 1981) 191.

14. Rossen, W. R., Brown, R. G., Davis, H. T., Prager, S. and Scriven, L. E., SPE Journal, in press.

15. Davis, H. T. and Scriven, L. E., Adv. Chem. Phys. 49, 357 (1982).

16. Reed, R. L. and Healy, R. N., paper SPE 8262, presented at the 54th Annual Fall Conference and Exhibition, Las Vegas, Nevada, September 23-26, 1979.

17. Teletzke, G. F., Scriven, L. E. and Davis, H. T., paper SPE 10112, presented at the 56th Annual Fall Conference and Exhibition, San Antonio, Texas, October 4-7, 1981.

18. Gibbs, J.W ., The Scientific Papers of J.W. Gibbs (Dover, New York City, 1961) Volume I, "Thermodynamics".

19. Prigogine, I. and Defay, R., Chemical Thermodynamics, translated by D. H. Everett (Longmans, Green, and Co., New York, 1952).

20. Modell, M. and Reid, R. C., Thermodynamics and its Applications, (Prentice-Hall, Englewood Cliffs, N.J., 1974).

21. Griffiths, R. B., Phys. Review B 12, 345 (1975).

22. Mistura, L., J. Phys. A 9, 2139 (1976).

23. Knickerbocker, B. M., Pesheck, C. V., Davis, H. T. and Scriven, L. E., J. Phys. Chem. 86, 393 (1982).

24. Kilpatrick, P. K., Davis, H. T. and Scriven, L. E., to be published.

25. Meijering, J. L., Philips Res. Rep. 5, 333 (1950) Part I; Philips Res. Rep. 6, 183 (1951) Part II.

26. Furman, D., Dattagupta, S. and Griffiths, R. B., Phys. Rev. B15, 441 (1977).

27. Bennett, K. E., Davis, H. T. and Scriven, L. E., J. Phys. Chem., in press.

28. Zernike, J., Rec. Trav. Chim. Pays-Bas 68, 585 (1949).

29. Bartis, J. T., J. Chem. Phys. 59, 5423 (1974).

30. Griffiths, R. B., J. Chem. Phys. 60, 195 (1974).

31. Scott, R. L., J. Chem. Soc., Faraday Trans. II 73, 356 (1977).

32. Scriven, L. E., in Micellization, Solubilitzation and Microemulsions, ed. K.L. Mittal, (Plenum Press, New York, 1977) 877; Nature 263, 123 (1976).

33. Davis, H. T. and Scriven, L. E., paper SPE 9278, presented at the 55th Annual Fall Conference and Exhibition, Dallas, Texas, September 21-24, 1980.

34. Guggenheim, E. A., Mixtures (Clarendon Press, Oxford, 1952) 29.

35. Puerto, M. C. and Reed, R. L., paper SPE/DOE 10678 presented at the Third Joint Symposium on Enhanced Oil Recovery of the Society of Petroleum Engineers, Tulsa, April 4-7, 1982.

36. Lellan-Cassou, C. and Wade, W. H., University of Texas, private communication.

37. Robbins, M. L., in Micellization, Solubilization, and Microemulsions, ed. K.L. Mittal (Plenum Press, New York, 1977) 713.

38. Knickerbocker, B. M., Pesheck, C. V., Scriven, L. E. and Davis, H. T., J. Phys. Chem. 83, 1984 (1979).

39. Kilpatrick, P. K., Gorman, C. A., Davis, H. T., Scriven, L. E.,and Miller, W. G., to be published.

40. Bellocq, A.-M., Bourbon, D. and Lemanceau, B., J. Dispersion Sci. and Tech. 2, 27 (1981).

41. Wormuth, K. and Kilpatrick, P. K., unpublished results.

42. Puig, J. E., Ph.D. Thesis, University of Minnesota (1982).

43. Pesheck, C. V., Lind, M. I., Scriven, L. E. and Davis, H. T., to be submitted to J. Phys. Chem.

44. Sahimi, M., Scriven, L. E. and Davis, H. T., paper SPE 10268, presented at the 56th Annual Fall Conference and Exhibition, San Antonio, Texas, October 4-7, 1981.

V. INTERPRETING THE APPEARANCE OF DISPERSED SYSTEMS: PART I. MODEL DISPERSIONS OF POLYMER LATEX MICROSPHERES

Introduction

The visual appearance of macroscopically homogeneous liquids is often used as a criterion for initially classifying them as solutions, micellar solutions, microemulsions, macroemulsions, dispersions, etc. (1,2). Simple observations can be useful in studying phase behavior, interfacial tension, and nonequilibrium of dispersed and colloidal systems. Observations can quickly provide qualitative information that is valuable in any screening program. And, most important, they can indicate directions for more detailed scientific investigations.

Various published rules for estimating particle size in nonabsorbing emulsions and microemulsions are shown in Table I. In the phenomenon called Tyndall effect, if a nonabsorbing system is illuminated by white light, it appears blue by scattering light and orange-red by transmitted light (3). This effect has been used extensively to detect Rayleigh scatterers. These are particles with dimensions much smaller than the wavelength of the light used; they are generally smaller than 0.1 μm (3). There seems to be no detailed account of how the reported rules depend on path length of sample, concentration of scatterers, extent of multiple scattering, amount of chromophore absorption, and intensity of light source.

Table I. Literature rules for interpreting appearance of dispersions

a) Prince[1]

Appearance	Tyndall Effect	Average Particle Size (Å)
"dead white"	none	>5000
"white-gray"	weak	1000-3000
"gray-translucent"	strong	100-1400
"clear transparent"	none	<100

b) Griffin[2]

Appearance	Average particle size (Å)
"distinguishable phases"	macroglobules
"milky white"	>10000
"blue-white"	1000-10000
"gray-semitransparent"	500-1000
"transparent"	<500

To evaluate these rules and devise improved ones, we made spectroturbidimetry experiments and visual observations on a series of aqueous dispersions of polymer latex microspheres. Such dispersions are excellent model systems for testing quantitatively theories, equipment, and procedures concerning colloidal particles (4). Latex microspheres of highly uniform size are commercially available in diameters ranging from 0.09 to many micrometers. The particles can remain in stable suspension for weeks and months, although they eventually agglomerate.

In Part I we review briefly the important principles of light scattering, spectroturbidimetry, and spectrophotometry, which form the basis for interpreting visual appearances. We investigate by spectroturbidimetry the three most important scattering regimes, Rayleigh, Rayleigh-Debye-Gans, and Mie, by using appropriate monodisperse particle sizes. We also examine certain single- and multiple-scattering dispersions by light scattering. We use mixtures of monodisperse sizes to simulate size distributions, which are present in most practical systems. Moreover, we test dispersions with added dye to see how the interpretation of spectroturbidimetry and visual appearance must be modified when there is chromophore absorption in addition to scattering. Absorbance measurements enable us to evaluate the visual observations and analyze their pitfalls. We conclude that the previously published rules are not always reliable. We suggest new rules and discuss their limitations. The limitations are fewer if observations are combined with spectroturbidimetry.

In part II we outline simple rules, in guide form, for quick and careful visual observations of surfactant systems (5). We show that the dispersions of polymer latex microspheres are indeed good models of surfactant dispersions. And finally we illustrate the usefulness of the guide by reporting observations of various surfactant systems we examined in the course of studies of phase behavior, interfacial tension, and dispersion stability (6-8).

Theory

Absorption and Scattering

For a parallel light beam of incident intensity I_0 and transmitted intensity I, the transmittance T is defined as I/I_0 and the absorbance A as $-\log_{10}T$. Usually $T < 1$, and hence $A > 0$. The attenuation of incident light is due to chromophore absorption (A_{abs}), or scattering (A_{scat}), or both. The specific absorbance due to chromophore absorption is $\varepsilon \equiv A_{abs}/\ell c$, where c is the molar concentration ($mol.l^{-1}$) and ℓ is the path length (cm). According to the Beer-Lambert law, ε is independent of the concentration and the state of aggregation of the chromophores. Relatively minor deviations can arise from effects of complex formation or variation of solvent polarity (9,10). By contrast, A_{scat}, which measures the total scattering in all directions, depends strongly on particle size and may vary with concentration. In systems in which the chromophores occupy a small volume fraction of the scattering particle or aggregate, the scattering and absorption efficiencies of the particle should not affect each other. Therefore, the absorbances due to scattering and absorption should be additive: $A/\ell c = A_{abs}/\ell c + A_{scat}/\ell c$. Hence, by measuring the total absorbance A and A_{abs} the total scattering can be determined by difference.

Single Scattering

In single scattering, less than about 10% of the incident intensity is scattered (see next subsection). Thus the sample is exposed to virtually the same incident intensity over the whole path length, provided of course that chromophore absorption is also small. For light wavelength λ_o (in vacuo) the scattering intensity $i(\theta)$ at a scattering angle θ depends on λ_o, θ, and the ratio m of the refractive index n_p of the particle or aggregate relative to the refractive index n_o of the surrounding solvent: $m \equiv n_p/n_o$. For spherical particles of diameter d, their dimensionless size is

$$\alpha \equiv \pi d/\lambda \tag{1}$$

where $\lambda = \lambda_o/n_o$.

The scattering intensity and its state of polarization are complex functions of α, λ_o, θ, m, and the state of polarization of the incident light (3). Simple limiting cases that are important for colloidal sizes (< 0.2 μm) are presented below. One can use polarized (e.g. vertically, I_o^V, or horizontally, I_o^H) or unpolarized (I_o^u) incident light and measure either the total scattered intensities (i_V, i_H, and i_u or i_θ, respectively) or vertical or horizontal components of the scattered light.

In the Rayleigh scattering regime, the external field induces a dipole that oscillates in phase with the external field, which is virtually homogeneous over the extent of the scattering particle. Rayleigh scattering occurs when the particle size is much smaller than the wavelength and when the static polarization is established in a time short compared to the period, i.e. when (Ref. 11, p. 75)

$$\alpha << 1 \text{ and } \alpha|m| << 1 \tag{2}$$

Provided $|m| < 2$ and $d < \lambda/10$ these conditions are satisfied adequately in practice. For particles in this regime

$$i_V/I_o^V = 2\,K\,M\,c/r^2 \tag{3}$$

$$i_H/I_o^H = 2\,K\,M\,c\,\cos^2\theta/r^2 \tag{4}$$

and

$$i_u/I_o^u = K\,M\,c(1 + \cos^2\theta)/r^2 \tag{5}$$

where K is an optical constant, $K \equiv 2\pi^2 n_o^2 (dn/dc)^2 (N_A/\lambda^4)$, and M is the molecular weight of the particles, N_A is Avogadro's number, and dn/dc is the specific refractive index increment, $dn/dc \equiv \lim(n-no)/c$ as $c \to 0$ (12).

Equations (3) through (5) apply to suspensions so dilute that the particles scatter independently of each other. As concentration rises, dependent scattering, or interparticle interference, becomes important. The following equation can describe the concentration dependence (12):

$$Kc/R_\theta = 1/M + 2Bc + 3Cc^2 + \cdots \tag{6}$$

where R_θ, the Rayleigh ratio, is defined as

$$R_\theta \equiv r^2 i_u/[I_o^u(1 + \cos^2\nu)] = r^2 i_V/(2I_o^V) = r^2 i_H/(2I_o^H) \tag{7}$$

and B and C are the second and third virial coefficients (12).

If i_T is the fraction of the incident intensity that is scattered, i.e.

$$i_T \equiv (I_o - I)/I_o = 1 - T = \ell(1/I_o) \int_0^\pi 2\pi r^2 i_\theta \sin\theta d\theta \tag{8}$$

and τ is the turbidity $\tau \equiv - \ell n(I/I_o) = - \ell nT$, then $\tau = \ell n(1 - i_T)$ and $\tau = 2.303A_{scat}$. For single scattering, as explained above, $i_T << 1$. It follows that $\tau \simeq i_T$ and

$$R_\theta = (3/16\pi)\tau/\ell \tag{9}$$

Thus by measuring A_{scat}/ℓ for single scattering, the Rayleigh ratio can be determined.

Single scattering from optically isotropic Rayleigh spheres is completely polarized for polarized incident light. The direction of polarization can differ from that of the incident light. With polarized incident light, single scattering from anisotropic or nonspherical Rayleigh particles can, however, be partially unpolarized (13). A useful measure of size, shape, orientation, and extent of multiple scattering is the scattering ratio, which is defined as

$$\rho_u(\theta) \equiv i_H(\theta)/i_V(\theta) \tag{10}$$

For isotropic Rayleigh spheres $\rho_u(90°) = 0$, according to Eqs. (3) and (4). For nonspherical Rayleigh particles $\rho_u(90°) > 0$. For isotropic or spherical particles that are not in the Rayleigh regime $\rho_u(90°) > 0$ in most cases, because the oscillating dipoles are not parallel to the electric vector of the incident light.

In the Rayleigh-Debye-Gans regime each volume element gives Rayleigh scattering and does so independently of the other volume elements (Ref. 11, p. 85). The refractive index differs little from that of the surrounding medium and the phase shift $\alpha|m-1|$ is small, i.e.

$$|m-1| \ll 1 \quad \text{and} \quad \alpha|m-1| \ll 1 \tag{11}$$

Hence α can be larger than 1 if $|m-1|$ is sufficiently smaller than 1. Because of destructive interparticle interference, the Rayleigh ratio, which is independent of angle in Rayleigh scattering, can vary with scattering angle θ; when $d < \lambda/2$, it decreases monotonically over the whole range of angles 0 to 180° (14). A convenient measure of the angular dependence is the dissymmetry

$$Z(\theta) \equiv i(\theta)/i(180° - \theta) \tag{12}$$

In this regime, $Z(\theta) > 1$. Dissymmetry measurements and tabulated calculations (14) can provide the particle size if the particle shape or configuration is known from other evidence.

If neither the conditions (2) nor (11) are satisfied, the scattering is called Mie scattering after Mie's theory, which applies to spheres at any value of m and α. In this regime the scattering intensity is concentrated mainly at small forward angles and can have maxima and minima as angle increases. The turbidity can increase or decrease and have maxima and minima as size increases or as wavelength decreases (15,16).

The wavelength dependence of scattering by a dispersion of particles can be represented by the exponent g defined from $\tau \propto \lambda_o^{-g}$, i.e.

$$g \equiv - d\log\tau/d\log\lambda_o \tag{13}$$

The value of g is a sensitive indicator of the value of the dimensionless size α if the refractive index ratio m is known. It is also important for relating spectroturbidimetry to appearance because it determines the scattering colors. In the Rayleigh regime, the dependence of the turbidity on the wavelength is the strongest (9).

$$\tau = \frac{24\pi^3 c}{N_A} \left(\frac{m^2 - 1}{m^2 + 2}\right)^2 \frac{M n_o^4}{\rho_p^2 \lambda_o^4} \tag{14}$$

Because n_0 and m vary a little with wavelength, g can be slightly larger than 4. In the Rayleigh-Debye-Gans regime, the exponent g is less than 4 and decreases with decreasing wavelength. In the Mie scattering regime g is smaller than 4 and can be negative. The smaller the value of $|m-1|$ the larger the range of α in which the turbidity increases with increasing size, i.e. g is positive (15,16). It is useful to estimate g and determine roughly the scattering by plotting $A\lambda_o^4$ and $A\lambda_o^2$ versus λ_o. For Rayleigh scattering, the product $A_{scat}\lambda_o^4$ is constant or increases slowly. A value of g less than 4 indicates that some or all particles in the dispersion are not Rayleigh scatterers. According to published calculations, if g ranges from 2 to 4 and $m < 1.3$, then α is less than 2.5 (15). Mie scattering is implied when $g < 2$. By analogy to the dissymmetry, which measures the departure of scattering from the Rayleigh limit, the particle dissipation factor is defined as

$$Q \equiv \tau/\tau_o \tag{15}$$

where τ and τ_o are the turbidities in the presence and absence, respectively, of intraparticle interference. Chromophore absorption can depend much more strongly than scattering on wavelength. Whereas the product $A_{scat}\lambda_o^4$ can increase only slightly with decreasing wavelength, $A_{abs}\lambda_o^4$ can increase substantially (recall that the total absorbance $A = A_{scat} + A_{abs}$). Hence when $A\lambda_o^4$ increases strongly with decreasing wavelength, A_{abs} must be significant.

Spectroturbidimetry, plots of A or $A\lambda_o^4$ or $A\lambda_o^2$ versus λ_o, is not as sensitive an indication of sizes as are measurements of the scattering intensity versus angle. In the visible wavelength range, 800 to 350 nm, the scattering parameter $\alpha(\equiv \pi d/\lambda)$ varies less than does the angular scattering parameter $(\pi d/\lambda)\sin(\theta/2)$ in the angular range 30° to 150°, which is commonly scanned. Spectroturbidimetry, however, is affected much less by multiple scattering, i.e. when $A > 0.04$, as explained in the next section. Hence, when $A < 0.04$, measurements of the angular dependence are undoubtedly superior; when $A > 0.04$, spectroturbidimetry is preferable.

Multiple Scattering

As the turbidity τ increases, an increasing fraction of scattered light is scattered repeatedly before it reaches the detector. Dispersed particles are exposed to both the attenuated incident beam and to the scattered light. If the specific turbidity τ/c is independent of concentration, multiple scattering is almost certainly insignificant (11). However, τ/c can depend on concentration because of interparticle interactions (12), even when single scattering prevails. If τ/ℓ is independent of the path length ℓ at a fixed concentration, then multiple scattering is unimportant. Thus the length-dependence criterion is more reliable than the concentration-dependence criterion. Van de Hulst suggests using the turbidity as the criterion: if $\tau < 0.1$ ($A \lesssim 0.04$), single

scattering prevails; if $0.04 \leq A_{scat} < 0.13$, a correction for multiple scattering is needed; and if $A_{scat} > 0.13$, multiple scattering dominates (11).

Multiple scattering redistributes in space the singly-scattered light. The angular dependence of multiply scattered light becomes more uniform with increasing extent of multiple scattering (17). In the Rayleigh-Debye-Gans regime, the dissymmetry (Eq. (12)) increases. Moreover, the degree of depolarization increases as multiple scattering gains in importance (18). The scattering ratio $\rho_u(90°)$ approaches 1, from below or from above, as in certain cases of Mie scattering. This means that the scattering light is mainly unpolarized.

The problem of deducing the particle size from the angular dependence of multiple scattering is difficult to intractable when particle sizes are distributed. Only if there is strong evidence that the particles are of uniform size and shape is it worth the computational effort to match calculations to multiple-scattering data in order to estimate particle size. On the other hand, multiple scattering will affect the turbidity per unit path length τ/ℓ and its wavelength dependence much less than it does the angular dependence. The reason is as follows. If the incident beam is very thin and parallel and if the distance between the sample and the detector is very large, little scattered or rescattered light reaches the detector. The turbidity is then strictly proportional to the path length. The incident beam, however, may have some divergence and it certainly has a finite cross-section. The light scattered at small angles in the cone of acceptance that the detector subtends the sample enhances the measured transmitted intensity and thus introduces an error in the measured absorbance. The error is of course larger the larger the angle of acceptance (19,20).

For small α, corresponding to Rayleigh and Rayleigh-Debye-Gans scattering, the angular distribution of scattered light is quite uniform. The fraction of the total scattered light which reaches the detector is then about equal to f, the fraction (in steradians divided by 4π) of the solid angle subtended by the detector at the center of the sample. If only the angle-of-acceptance error is considered, the measured absorbance A^* is

$$A^* = \log_{10}\{10\text{-}A(1-f) + f\} \qquad (16)$$

where A is the true absorbance.

For the typical absorbance range 0 to 2 of a commercial spectrophotometer and a typical solid angle fraction $f = 0.004$, the relative error in A is less than 7.3%; when $A < 1$ and $f = 0.004$, the error is less than 1.6%. Consequently, at $A < 2$ and $f < 0.004$ in Rayleigh and Rayleigh-Debye-Gans scattering, the turbidity is affected by less than 7.3% at all wavelengths. The error in the wavelength exponent g, which is a 'fingerprint' of the particle-size distribution, is small and often tolerable. The farther the detector is placed from the sample, the smaller the error and the larger the absorbance range that can be interpreted in terms of the single-scattering theory.

In Mie scattering most of the scattered light is concentrated at small

angles. The fraction of the total scattering which reaches the detector is much larger than f. The angle-of-acceptance error is larger for Mie scattering than for Rayleigh-Debye-Gans scattering and can be important even when A < 0.2. As A increases with decreasing wavelength, the asymmetry in the angular distribution of single scattering increases, as in some important cases of Mie scattering. The error in the absorbance may decrease, however, as the extent of multiple scattering increases. Thus the relative error in absorbance depends little on the wavelength, and the wavelength dependence yields a size distribution 'fingerprint' which is almost identical to that when single scattering prevails.

Materials and Procedures

The microspheres used are characterized in Table II. The as-received, ~ 10 wt % latex, dispersions of sizes 0.091, 0.254, 0.325, and 1.10 μm were diluted to stock dispersions of concentrations 500 to 1500 ppm, which were subsequently diluted further. The concentrations of the samples examined were known accurately on a relative but not on an absolute basis. The dependence of absorbance on size and concentration gave no indication that any significant aggregation of microspheres occurred before the measurements. All measured absorbances at 780 to 400 nm were due to scattering. All samples were diluted with an aqueous solution of 0.21 wt % sodium dodecylsulfate (SDS). The absorbance arising from the surfactant was less than 0.001 cm^{-1} at all wavelengths and hence was neglected.

Table II. Features of polymer latex microspheres used

Sample	Nominal Diameter+ (μm)	Standard Deviation (μm)	Latex Material	m≠	dn_o/λ_o		$\alpha = \pi dn_o/\lambda_o$	
					λ_o=780 nm	λ_o=400 nm	λ_o=780 nm	λ_o=400 nm
1	0.091	0.0058	PS[a]	1.20	0.155	0.30	0.48	0.94
2	0.254	0.0025	PS[b]	1.20	0.43	0.85	1.35	1.67
3	0.325	unavailable	PMMA[c]	1.13	0.56	1.08	1.76	3.39
4	1.10	0.0059	PS[a]	1.20	1.88	3.67	5.91	11.53

+: Values, provided by the manufacturer, were almost certainly determined by electron microscopy.

≠: Refractive index of polymer particle relative to water, $m \equiv n_p/n_o$; it depends slightly on wavelength.[21]

a: Polystyrene, from Dow Diagnostics : 0.091μm, lot #2F5R; 1.10μm lot #2F8R.

b: Polystyrene, carboxylate-modified surface, from Dow Diagnostics, lot #6H3K.

c: Poly (methyl methacrylate), from Polysciences, Inc.

The surfactant improved substantially the stability of the dispersions of the 0.091 μm microspheres; no visible particles were observed in such dispersions over more than a month. On standing, the further diluted dispersions of 0.325

μm and 1.10 μm microspheres flocculated and settled faster than the stock dispersions. Moreover, after months a crystalloidal precipitate was seen. This precipitate was visually and microscopically similar to the precipitate observed when only SDS was present. We believe that the precipitate arises from SDS hydrolysis. For these reasons, different concentrations of dispersions of the same particle size were tested the same day and all samples were tested within ten days after dilution.

Cary 14 and Cary 15 spectrophotometers were used. Their important features were identical. The solid angle fraction f subtended by the detector at the sample was less than 0.004. Specific absorbances A/ℓ measured at 1 cm path length were used to calculate absorbances at other path lengths at which the effects of multiple scattering on absorbance were unimportant and hence A was proportional to ℓ. A SOFICA brand light scattering photogoniodiffusometer 42000, Model 701, was used to measure dissymmetries and scattering ratios.

The water-soluble dye used was the sodium salt of methyl red (Eastman Kodak Co.). The aqueous solutions ranged in color from yellow to red, depending on concentration and path length.

For visual observations, cylindrical vials of internal diameter 2 cm were used. They were filled to 6 cm depth so that observations could be made at two different path lengths. Smaller vials of diameter 1 cm were also used; they were filled to 2 cm. Observations were made with normal laboratory illumination with a fluorescent light source. Many of the 2 cm vials were photographed against a black background using Kodak EPT 4 ASA 50 film and a matched Tungsten 3200°K lamp. A uv filter was used in the camera. Among photographs with different exposure times, the one with colors and translucency closest to the visual appearance under the same illumination source was chosen. The exposure time was normally 1/15 s.

The light reaching the eye is a mixture of light scattered from the sample at different scattering angles and that transmitted through the sample; the proportions depend on the relative position of light source, sample, and observer. For this reason, in tables of observations below we use the entry 'color of scattered or transmitted light'. Only if one uses high intensity illumination, a collimated incident beam, and a dark background, and observes a narrow range of scattering angles can one observe solely the scattered light.

Results and Discussion

Dispersions of Microspheres of One Size

We measured the absorbance spectra of the following dispersions: 0.091 μm; 21, 120, and 1300 ppm; 0.254 μm: 18 and 48 ppm; 0.325 μm: 70 and 900 ppm; and 1.10 μm: 4.6, 18, and 65 ppm.

With each size of microspheres the specific absorbance A/c was at all wavelengths independent of concentration within the experimental accuracy. Since the absolute uncertainty in absorbance was about the same in all measurements,

the relative uncertainty was higher the lower the absorbance. With the 0.091 μm microspheres, the maximum variation of A/c with concentration was 5% for absorbances 0.02 to 2; with the 0.254 μm microspheres, the specific absorbances at 48 ppm were about 10% lower than those at 18 ppm at all wavelengths. Since some crystalloidal particles which could contribute to the scattering were seen in the low-concentration sample, it is not certain that the discrepancy is significant. With the 0.325 μm microspheres, the specific absorbances at 900 ppm were similarly 10 to 20% smaller than at 70 ppm. With the 1.10 μm microspheres, the specific absorbance also decreases by 1 to 8% from 4.6 to 18 ppm and by an additional -2 to 7% from 18 to 65 ppm. We report spectra of the specific absorbances at only one concentration for each size — 1300 ppm for the 0.091 μm, 48 ppm for the 0.254 μm, 70 ppm for the 0.325 μm, and 18 ppm for the 1.10 μm microspheres — since the spectra at the other concentrations had the same shape.

Because the spectrum of specific absorbance was the same whether or not there was multiple scattering, we concluded that the effects of multiple scattering and angle of acceptance on absorbance were negligible in our apparatus, for absorbances up to 2 and for particle sizes up to 1.1 μm at least. Hence in these ranges the absorbance is proportional to the path length, with deviations smaller than 20%. For particles having refractive index ratios relatively to water smaller than 1.2, that of the polystyrene spheres used, the scattering is less concentrated in forward angles. Thus we feel that sizes larger than 1.1 μm can be reliably probed by the wavelength dependence of the absorbance measured with commercial spectrophotometers of the sort we employed.

In Fig. 1A we show the absorbance for the four sizes studied. The specific absorbance of the smallest microspheres, d = 0.091 μm, was the smallest and depended most strongly on wavelength. For these microspheres the dimensionless size parameter α ranged from 0.48 to 0.94 (Table II); hence the product αm ranged form 0.58 to 1.05. Because the conditions (2) for Rayleigh scattering did not hold strictly, (or not at all for $\alpha m = 1.05$), we expected that the measured wavelength exponent g would be smaller than 4. Kratochvil (14) gives values of the particle dissipation factor Q, Eq. (15), as 1/1.099 for $d/\lambda = 0.15$ and 1/1.409 for $d/\lambda = 0.30$. We could, therefore, explain for the 0.091 μm microspheres a decrease of about 25% of the product $A\lambda_o^4$ with decreasing wavelength, but in fact we did not observe it: the product $A\lambda_o^4$ versus λ_o was constant, i.e. g = 4 (Fig. 1B). Probably the increase of the refractive index ratio with decreasing wavelength compensated the decrease in Q (16).

We measured light scattering from dispersions of 0.091 μm microspheres at increasing concentration and path length in order to examine the effect of multiple scattering. The results are shown in Table III. At the green and blue wavelengths the dissymmetry was virtually concentration-indpendent up to absorbances of about 0.03, above which it started dropping. At the concentration of 3.25 ppm, the variation of the dissymmetry and the scattering ratio with path length indicates that the observed decrease in dissymmetry and increase in scattering ratio were related to the absorbance, i.e. to the extent of multiple scattering, and not to concentration dependence of scattering. We drew the same conclusion by comparing results at the same concentration and path length but at a second wavelength at which the absorbance was different (the 51.0 ppm entry).

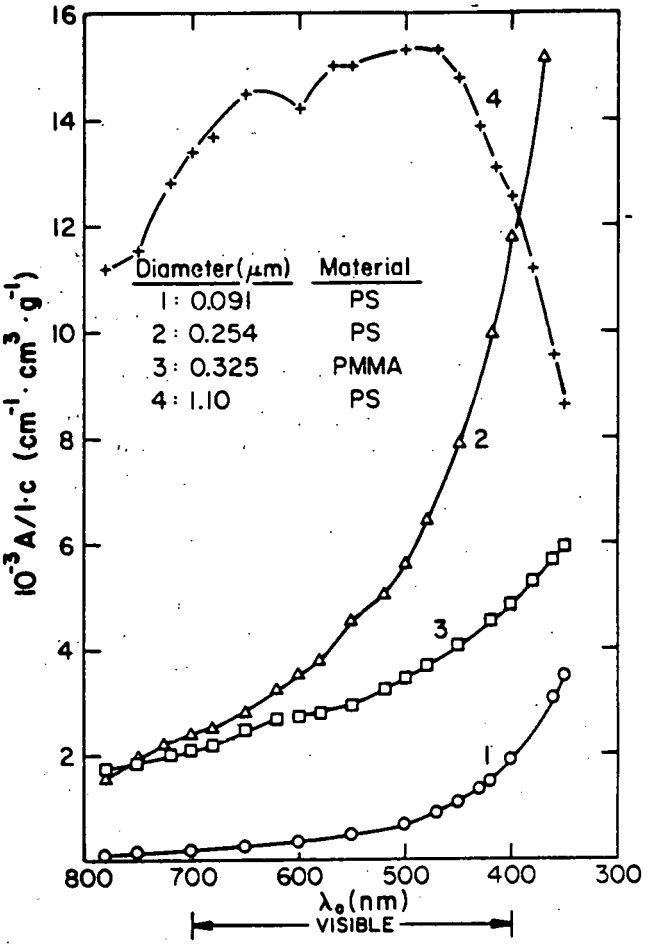

Fig. 1A

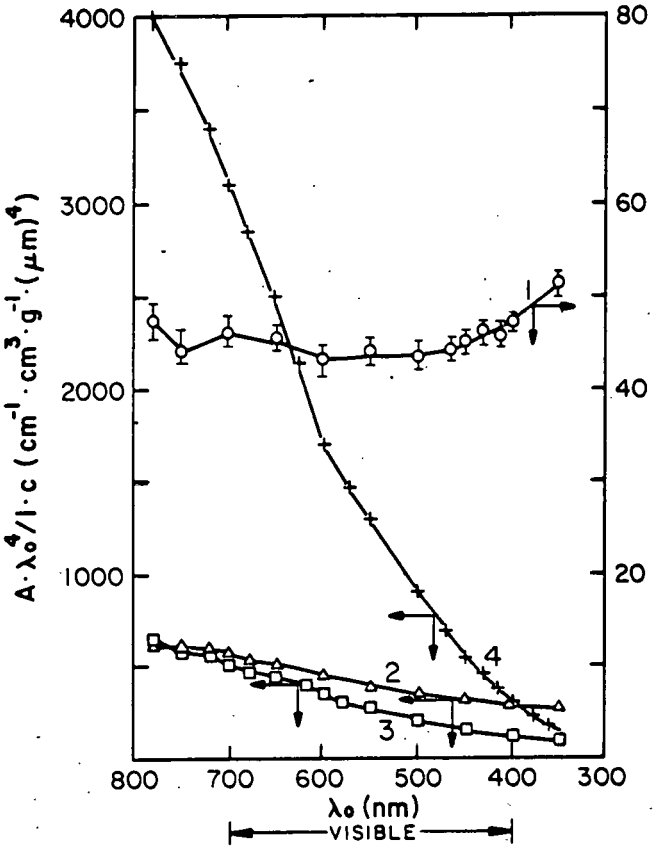

Fig. 1B

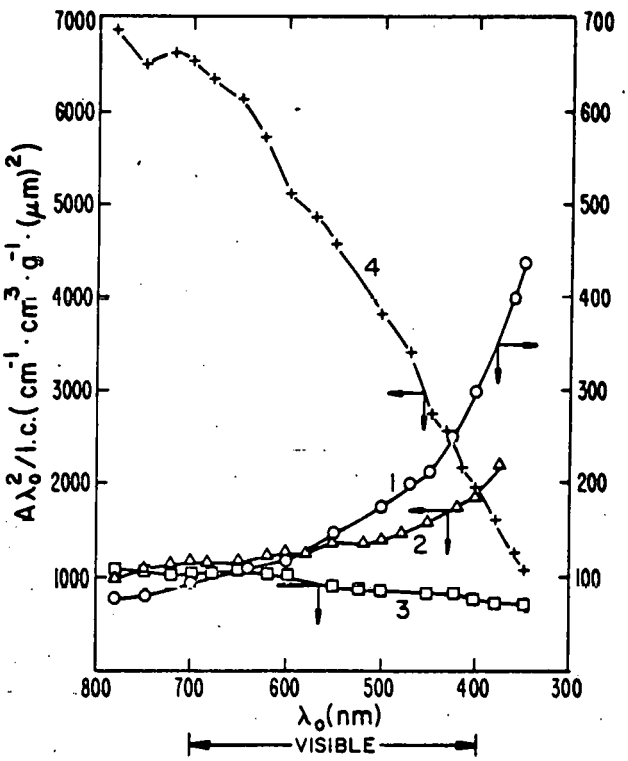

Fig. 1C

Fig. 1A. Absorbance of dispersions of polymer latex microspheres.

Fig. 1B. Wavelength dependence test of specific absorbances of Fig. 1A.

Fig. 1C. Alternate wavelength dependence test of specific absorbances of Fig. 1A.

Table III.Effect of increasing absorbance, i.e. of extent of multiple scattering, on light scattered from polymer 0.091 μm microspheres

Concentration ppm	$A^{\neq}$	λ_o = 546 nm (green) $Z(45)^a$	$Z(30)^a$	ρ_u^b	$A^{\neq}$	λ_o = 436 nm (blue) $Z(45)^a$	$Z(30)^a$	ρ_u^b
2.06	0.0012	1.3_2	1.5_0	0.02_2	0.0029	1.4_0	1.6_0	0.02_2
3.2	0.0018				0.0044		1.5_7	
4.9	0.0021	1.2_6	1.4_3	0.02_5	0.0069	1.3_9	1.5_6	0.02_4
5.5	0.0031				0.0077		1.5_8	
10.8	0.0061				0.0152		1.5_2	
13.8	0.0080	1.2_7	1.3_7	0.02_2	0.0195	1.3_9	1.4_8	0.02_7
20.5	0.0120				0.0288		1.5_2	
51.0	0.029	1.2_5	1.3_5	0.03_5	0.072	1.3_7	1.5_0	0.05
315	0.12	1.2_2	1.2_9	0.09	0.295	1.1_7	1.2_0	0.18
315	0.18	1.1_1	1.2_1	0.11	0.445	1.1_6	1.2_5	0.24

≠: Total absorbance due to scattering: calculated from the specific absorbance A/lc, measured by a spectrophotometer, and the radius of the scattering cell (1.2 cm in most cases).

a: Dissymmetry $Z(\theta) \equiv i(\theta)/i(180 - \theta)$; i is scattered intensity and θ is scattering angle.

b: Scattering ratio ρ_u (90°) $\equiv i_H(90)/i_V(90)$; i_H and i_V are total scattered intensities for horizontally and vertically polarized incident light.

Evidently multiple scattering leads to a more uniform angular dependence of scattering intensity than does single scattering, in agreement with published calculations (17). The scattering ratio at 90°, Eq. (10), which is another sensitive indicator of multiple scattering, increased from its lowest value of 0.02 (which could be an instrumental artifact) to values as high as 0.24 at an absorbance of 0.445 (or a turbidity of 1.02). Multiple scattering is predominant at so high turbidity (11).

If we would interpret the dissymmetry results in terms of single scattering theory (14), we would get diameter values which would appear to decrease with increasing concentration, (Table IV), even though the true value remains 0.091 μm. Moreover, a scattering ratio of 0.11 at 546 nm would imply erroneously a larger diameter of 0.3 μm (18). The conclusion is that when there is multiple scattering, i.e. where A > 0.04, the size cannot be reliably estimated from the angular dependence and the state of polarization of scattered light. On the other hand, the wavelength dependence of absorbance gives a reliable size 'fingerprint', for sizes up to 1.1 μm at least, provided the absorbance does not exceed 2. Moreover, simply decreasing the angle of acceptance by placing the detector as far from the sample as is practicable can increase greatly these limits of applicability of spectroturbidimetry. By increasing the distance

Table IV. Effect of multiple scattering on apparent particle diameter calculated from dissymmetries

λ_o(nm)	Z(45)*	D/λ+	D(μm)≠
546	1.32	0.22	0.088
546	1.22	0.19	0.078
546	1.11	0.14	0.057
436	1.40	0.24	0.078
436	1.37	0.23	0.076
436	1.16	0.16	0.052

* From Table III.

\+ From tables in Kratochvíl.[14]

≠ Nominal sphere diameter was 0.091 μm.

between sample and detector by a factor of 10, the absorbance limit will increase from 2 to 4, because f will decrease by a factor of 100 (see Eq. (16)).

The absorbance of dispersions of the 0.254 μm microspheres increased with decreasing wavelength (Fig. 1A). Since $A\lambda_o^4$ decreased with decreasing wavelength, whereas $A\lambda_o^2$ increased, the exponent g was between 2 and 4 (Figs. 1B and 1C); moreover, because g varied with wavelength, no attempt was made to fit values of g. The wavelength dependence was typical of the Rayleigh-Debye-Gans regime, because the basic conditions (Eq. (11)) for this regime were approximately fulfilled: $m-1 = 0.2$ and $\alpha(m-1) = 0.27$ to 0.53. For these values, which are not much less than one, the deviations from the Rayleigh-Debye-Gans regime are small.

The wavelength exponent of absorbances of 0.325 μm PMMA dispersions was slightly smaller than 2 (Fig. 1C). These microspheres also scattered light in the Rayleigh-Debye-Gans regime. The specific absorbances were smaller than those of the 0.254 μm microspheres, because the refractive index ratio of PMMA is smaller than that of PS (Table II and Ref. 5).

The 1.10 μm particles scattered in the Mie regime at the wavelengths used, because the Rayleigh and the Rayleigh-Debye-Gans conditions were clearly violated; depending on wavelength, α ranged from 5.91 to 11.53, and $\alpha(m-1)$ ranged from 1.18 to 2.31. The wavelength exponent was roughly between 1 and -1. The absorbance maximum (Fig. 1A) occurred at $\lambda_o = 500$ nm. For $m = 1.2$, the calculated absorbance maximum should occur at $\alpha = 7.2$ (15). This implies a value of 0.86 μm for the microspheres' diameter, which was 20% smaller than the nominal diameter determined from electron microscopy by the manufacturer. Inasmuch as there are often discrepancies of 5 to 15% between estimates of diameters from electron microscopy and light scattering (4), we judged that agreement between theory and experiment was good.

The measured specific absorbances (Fig. 1) were consistently lower than the calculated absorbances (15). We did not investigate further this discrepancy, because the absolute concentrations were not known precisely and because the wavelength dependence of the absorbance was primarily used to interpret visual observations of scattering colors (5).

Our observations of dispersions are recorded in Tables V through VIII.

Table V. Observations of aqueous dispersions of polymer latex microspheres of diameter 0.091μm. Relation to spectroturbidimetry (Fig. 1)

SAMPLE			OBSERVATIONS				SPECTROTURBIDIMETRY			
				COLORS					Scattering Events[f]	
Particles Concentration ppm	Path Length cm	Photograph in Fig. #	Appearance[a]	Scattered Light[b]	Scattered or Transmitted[c]	Angular Dependence of Color[d]	Exponent g[+]	Scattering Regime	650 nm	450 nm
0	2	2A	clear	colorless		no	-	-	s	s
21	0.5	-	clear	colorless		no	4	Rayleigh	s	s
21	2	2A	clear	faint bluish	faint bluish	no	4	Rayleigh	s	s-m
117	1	2B	translucent-clear	light bluish	light bluish or light yellowish	mild	4	Rayleigh	s	m-s
117	2	2A	translucent-clear	bluish	bluish or yellowish	mild	4	Rayleigh	s-m	m
1,292	1	2B	turbid-translucent	bluish-white	bluish-white or orange	strong	4	Rayleigh	m	m
1,292	2	2A	translucent-turbid	bluish-white	bluish-white or orange	strong	4	Rayleigh	m	m
1,292	4	-	turbid	bluish-white	bluish-white or orange	strong	4	Rayleigh	m	m
100,000	0.5	-	opaque	milky white		no	indeterminate*		m	m

a: Appearance can be:[5] clear, transparent; translucent, i.e. cloudy or hazy, but one can resolve details by looking at an object through the sample; turbid, i.e. one cannot resolve details by looking at an object through the sample; opaque. By turbid-translucent is meant closer to translucent than to turbid.

b: Sample observed so that detected light was mainly scattered and not transmitted.

c: Sample was placed in different positions relative to the light source so that either scattered or transmitted light be observed from different regions of the sample.

d: Dependence of colors on relative position of source, sample, and observer; related to c.

+: Exponent g defined from $A \propto \lambda_o^{-g}$.

f: Depending on turbidity ($\tau = 2.303A$) in the red, 650 nm, or blue, 450 nm, scattering events are: single, s, if $\tau < 0.1$; single and multiple, s-m, if $0.1 < \tau < 0.3$; multiple and single, m-s, if $0.3 < \tau < 1$; and multiple, m, if $\tau > 1$.

*: Absorbance was so high that wavelength dependence could not be interpreted.

Table VI. Observations of aqueous dispersions of polymer latex microspheres of diameter 0.254μm. Relation to spectroturbidimetry (Fig. 1).

SAMPLE			OBSERVATIONS				SPECTROTURBIDIMETRY			
				COLORS					Scattering Events[f]	
Particles Concentration ppm	Path Length cm	Photograph in Fig. #	Appearance[a]	Scattered Light[b]	Scattered or Transmitted[c]	Angular Dependence of Color[d]	Exponent g^+	Scattering Regime	650 nm	450 nm
18.3	0.2	-	clear	colorless		no	$2 < g < 4$	Rayleigh-Debye-Gans	s	s
18.3	0.5	-	clear	faint bluish	faint bluish	no	"	"	s	s-m
18.3	2	2C	clear	light bluish	bluish or yellowish	minor	"	"	s-m	m-s
18.3	7	-	translucent	bluish	bluish or yellowish	medium	"	"	m-s	m
48.3	2	2C	translucent	bluish	bluish or yellowish	medium	"	"	m-s	m
48.3	7	-	turbid-translucent	gray-bluish		minor	"	"	m	m
463	2	2C	turbid-opaque	gray-white		minor	indeterminate*		m	m
463	6	-	turbid-opaque	gray-white		minor	indeterminate*		m	m
100,000	0.5	-	opaque	milky-white		no	indeterminate*		m	m

Footnotes the same as those of Table V.

Table VII. Observations of aqueous dispersions of polymer latex microspheres of diameter 0.325μm. Relation to spectroturbidimetry (Fig. 1)

SAMPLE			OBSERVATIONS				SPECTROTURBIDIMETRY			
				COLORS					Scattering Events[f]	
Particles Concentration ppm	Path Length cm	Photograph in Fig. #	Appearance[a]	Scattered Light[b]	Scattered or Transmitted[c]	Angular Dependence of Color[d]	Exponent g^+	Scattering Regime	650 nm	450 nm
8.4	2	2D	clear	faint bluish	faint bluish	no	$1 < g < 2$	Rayleigh-Debye-Gans	s	s-m
68	1	-	translucent-clear	light bluish	light bluish	mild	"	"	m-s	m-s
68	2	2D	translucent	light bluish	light bluish or light yellowish	mild	"	"	m-s	m
68	5	-	translucent-turbid	faint bluish	faint bluish or yellowish	mild	"	"	m	m
900	1	-	turbid	gray	gray or yellowish	mild	"	"	m	m
900	2	2D	turbid	gray	gray or yellowish	mild	"	"	m	m
900	5	-	turbid-opaque	white	gray or white	mild	indeterminate*		m	m
100,000	0.5	-	opaque	milky-white		no	indeterminate*		m	m

Footnotes the same as those of Table V.

Table VIII. Observations of aqueous dispersions of polymer latex microspheres of diameter 1.10μm. Relation to spectroturbidimetry (Fig. 1).

SAMPLE			OBSERVATIONS				SPECTROTURBIDIMETRY			
Particles Concentration ppm	Path Length cm	Photograph in Fig. #	Appearance[a]	COLORS Scattered Light[b]	COLORS Scattered or Transmitted[c]	Angular Dependence of Color[d]	Exponent g^+	Scattering Regime	Scattering Events* 650 nm	Scattering Events* 450 nm
4.64	2	3A	clear	light gray		no	$-1 < g < 1$	Mie	s-m	s-m
4.64	5	-	translucent-clear	light gray		no	"	"	m-s	m-s
18.3	2	3A	translucent	gray-white		no	"	"	m	m
18.3	5	-	translucent-turbid	gray-white		no	"	"	m	m
65.3	2	3A	turbid	gray-white		no	"	"	m	m
65.3	5	-	opaque	gray-white		no	"	"	m	m
716	2	-	opaque	gray-white		no	indeterminate*		m	m
716	5	-	opaque	gray-white		no	indeterminate*		m	m
100,000	0.5	-	opaque	milky-white		no	indeterminate*		m	m

Footnotes the same as those of Table V.

Figs. 2 and 3 are photographs of the same samples. A surprising result was that under normal laboratory illumination single scattering could scarcely be detected by the unaided eye. The eye's sensitivity was better in the dark with intense illumination directed toward the sample. For high absorbances, higher than 10 say, most samples looked milky-white, and thus we could obtain no information from their visual appearance alone.

In Rayleigh scattering with absorbances in blue light ranging from 0.05 to 0.2, bluish scattered light was visible and transmitted light was white to yellowish. In order to detect the Tyndall effect, i.e. the bluish colors of scattered light and orange colors of transmitted light in ordinary laboratory illumination, we had to use samples with absorbances in blue light from 0.2 to 2, for which multiple scattering is predominant.

In Rayleigh-Debye-Gans scattering, we saw bluish scattered light and yellowish transmitted light at absorbances of about 0.1 to 1 (Tables VI and VII). The bluish color was less brilliant than the color arising from Rayleigh scattering, because wavelengths other than blue were scattered comparably and decreased the color purity of scattered light. We could see no color in dispersions of Mie microspheres (Table VIII), which is as predicted from the weak wavelength dependence of absorbance.

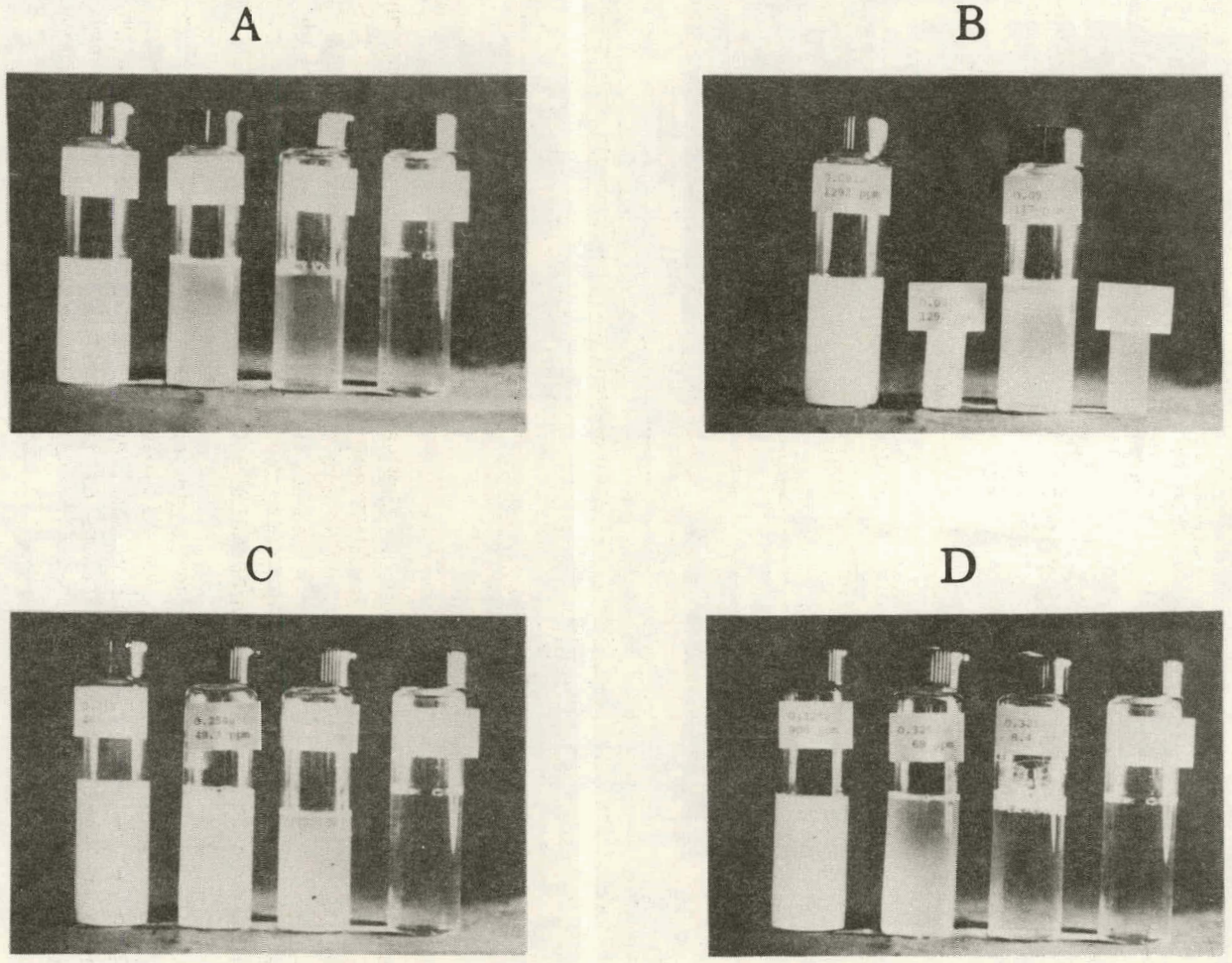

Fig. 2. Photographs of dispersions of polymer latex microspheres. Upper left: 0.091 μm particles of concentrations 1300, 120, 21, and 0 ppm (from left to right); upper right: 0.091 μm, 1300, 1300, 120, and 120 ppm; lower left: 0.254 μm, 460, 48, 16, and 0 ppm; lower right: 0.325 μm, 900, 70, 8 and 0 ppm.

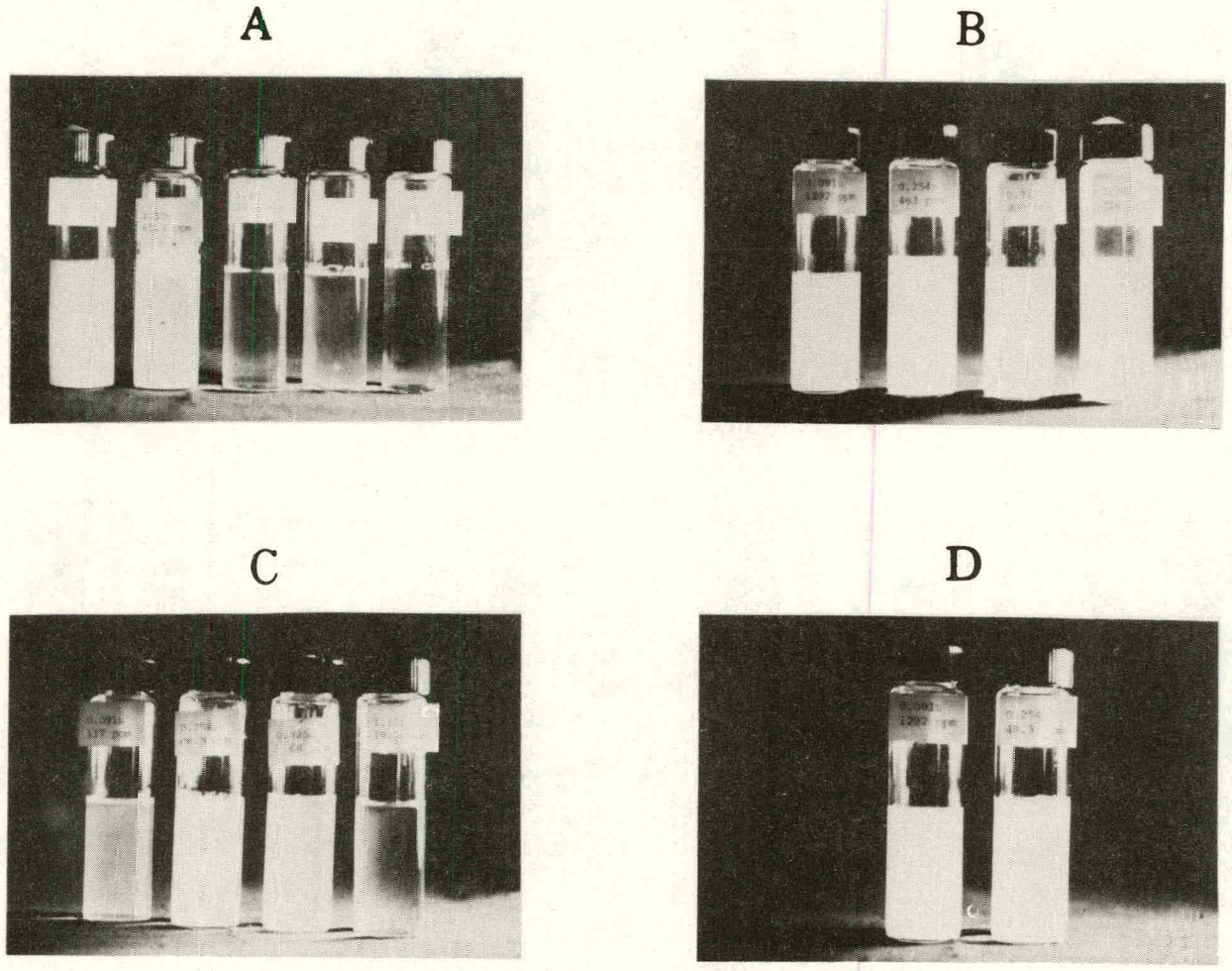

Fig. 3. Photographs of dispersions of polymer latex microspheres. Upper left: 1.10 μm, 720, 55, 18, 4.6, and 0 ppm; upper right: 0.091 μm - 1300 ppm, 0.254 μm - 450 ppm, 0.325 μm - 900 ppm, 1.10 μm - 720 ppm; lower left: 0.091 μm - 120 ppm, 0.254 μm - 28 ppm, 0.325 μm - 70 ppm, 110 μm - 18 ppm; lower right: 0.091 μm - 1300 ppm, 0.254 μm - 48 ppm.

By comparing appearances of dispersions of microspheres of widely different sizes (Fig. 3B), we determined that little information could be obtained at absorbances higher than 3. However, by comparing dispersions with about the same absorbance in the range 0.1 to 1, we could tell that they differed in size. Figure 3D shows that if A > 1, a high concentration of smaller microspheres could give rise to a less brilliant blue than the scattering bluish color arising from larger particles, and thus could lead to the erroneous conclusion that the particle size was larger.

Thus, careful, naked-eye observations of dispersions of monodisperse particles can give qualitative information in agreement with that given by spectroturbidimetry. The latter is surely more reliable and more sensitive.

Dispersions of Mixtures of Microspheres with Different Sizes

Absorbance measurements and visual observations were designed to probe whether one can detect particles of one size in the presence of particles of another size. Spectra of absorbances of three dispersions of pairs of sizes are shown in Fig. 4. Concentrations were chosen so that for path lengths 1 cm and 2 cm absorbances fall in the range 0.1 to 1, which we found to be the best range for observing by unaided eye. The measured absorbances were equal to theory and experiment within 10% to the sum of the absorbances calculated from Fig. 1 and from the particle concentrations. The wavelength exponent for 91 ppm microspheres of diameter 0.091 μm dropped from 4 to about 2 upon addition of just 6 ppm of microspheres of 1.10 μm. Thus one cannot distinguish from g-values alone between a mixture of Rayleigh and Mie particles and Rayleigh-Debye-Gans particles; calculations are necessary. Nevertheless, spectroturbidimetry can readily detect particles of sizes larger than 0.1 μm merely from the wavelength exponent. For the 1.10 μm microspheres, concentrations as low as 6 ppm can be detected.

Visual observations are described in Table IX. Translucency and lack of bluish scattering colors indicated correctly the absence of Rayleigh particles, i.e. indicated particles of sizes larger than 0.1 μm in the sample with the 0.325 and 1.10 μm microspheres.

Dispersions of Microspheres with Dye Added

Absorbance spectra of aqueous methyl red dye with 0.21% SDS added are shown in Fig. 5. The specific absorbance A/c was independent of concentration within experimental precision and it therefore followed Beer's law. The molar absorptivity at the wavelength λ_{max} = 430 nm of maximum intensity was found to be $\varepsilon_{max} = 3.30 \times 10^4$ 1 $mol^{-1} \cdot cm^{-1}$.

Because the absorption peak was wide, the higher the absorbance the more important was the reduction of intensity at wavelengths around the wavelength λ_{max}. Table X shows the percentage of light absorbed for each color band. The perceived color of the samples resulted, of course, from selective reduction of

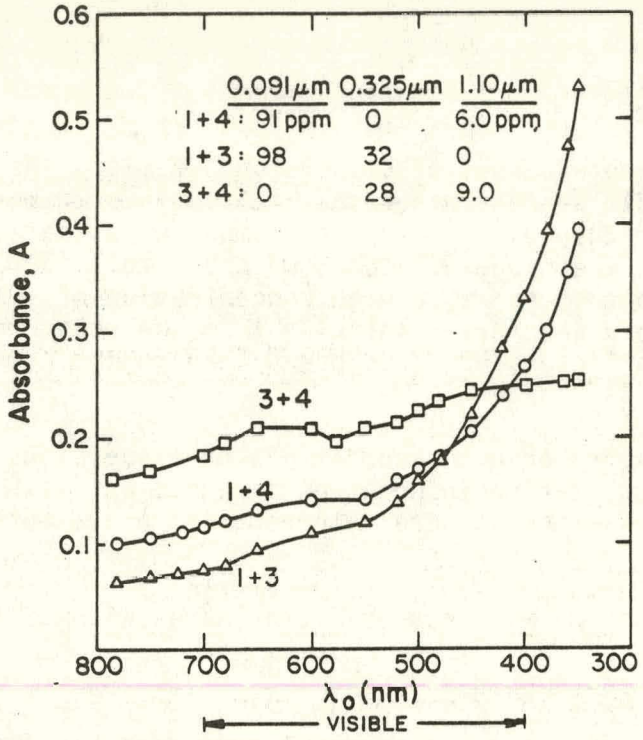

Fig. 4A. Spectra of absorbance, through 1 cm path length, of dispersions of mixtures of microspheres with different size.

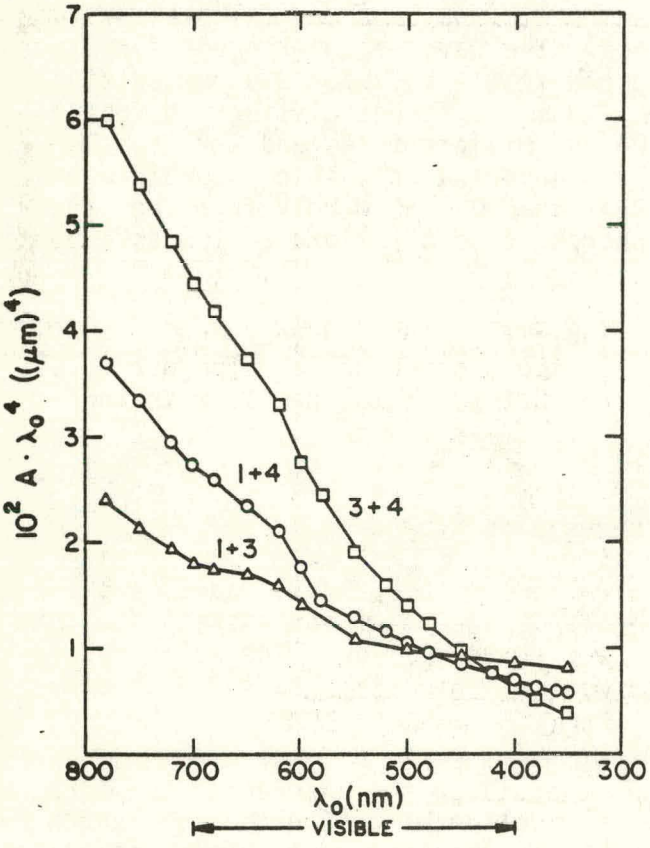

Fig. 4B. Wavelength dependence test of absorbances of Fig. 4A.

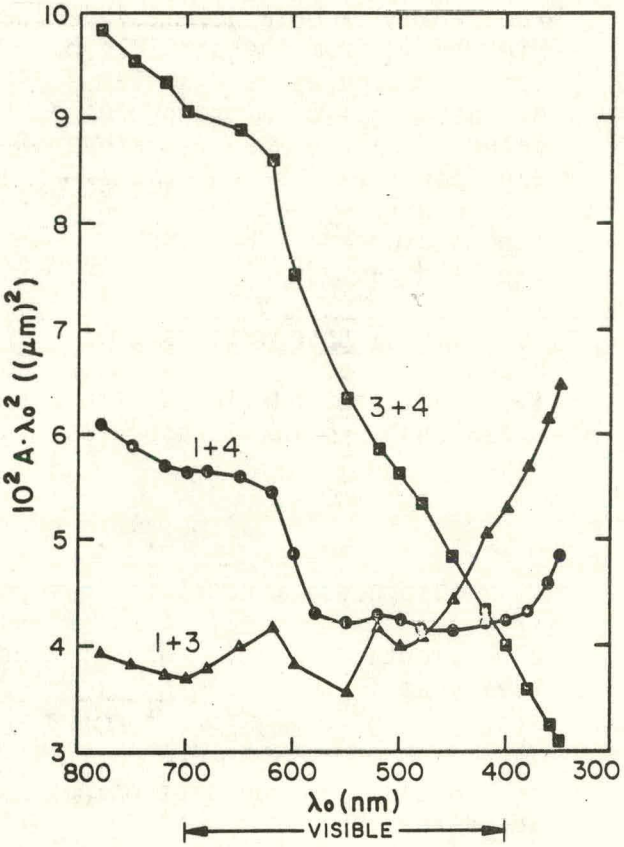

Fig. 4C. Alternate wavelength dependence test of absorbances of Fig. 4A.

Table IX. Observations of aqueous dispersions of mixtures of monodisperse polymer latex microspheres. Relation to spectroturbidimetry (Fig. 4).

SAMPLE				OBSERVATIONS				SPECTROTURBIDIMETRY			
Concentration, ppm			Path Length		COLORS					Scattering Events[f]	
0.091μm	0.325μm	1.10μm	cm	Appearance[a]	Scattered Light[b]	Scattered or Transmitted[c]	Angular Dependence of Color[d]	Exponent g+	Scattering Regime	650 nm	450 nm
91	0	6.0	1	translucent - clear	bluish	bluish or light yellowish	mild	~2(<2)	Rayleigh Debye-Gans	m-s	m-s
91	0	6.0	2	clear-translucent	bluish	bluish or yellowish	medium	~2(<2)	"	m-s	m-s
98	32	0	1	clear-translucent	bluish	bluish or light yellowish	mild	~2(>2)	"	s-m	m-s
98	32	0	2	translucent		bluish or yellowish	medium	~2(>2)	"	m-s	m
0	28	9.0	1	translucent	grayish-faint bluish		minor	~1	Mie	m-s	m-s
0	28	9.0	2	translucent	grayish-faint bluish		minor	~1	Mie	m-s	m

Footnotes the same as those of Table V.

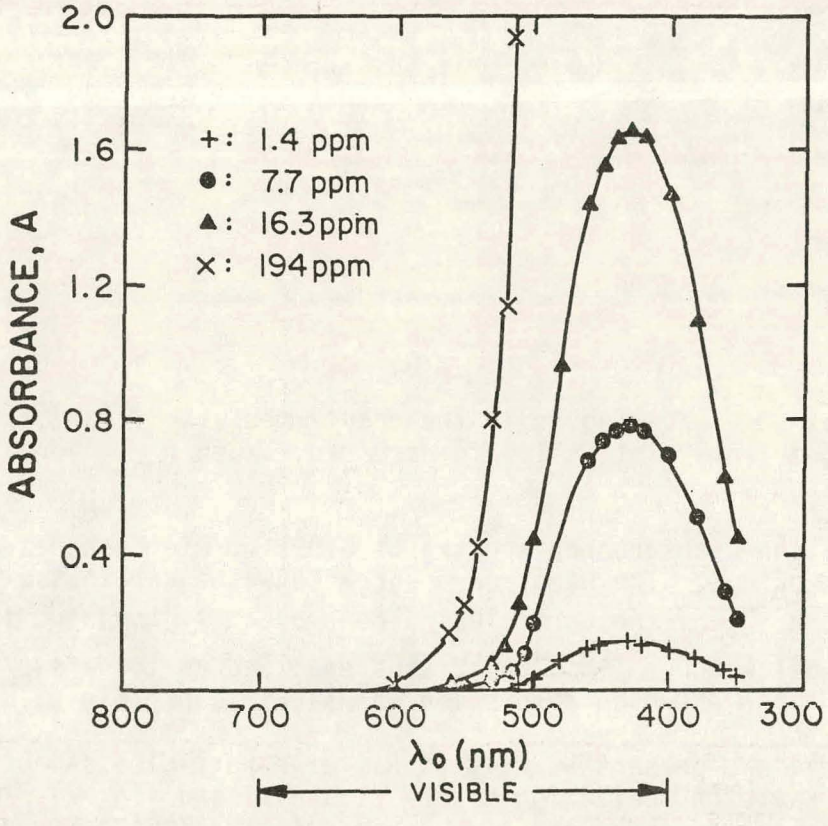

Fig. 5. Spectra of absorbance, through 1 cm path length, of aqueous methyl red dye.

Table X. Colors of clear aqueous solutions of methyl red dye. Relation to absorption spectrum (Fig. 5).

Concentration ppm	Path Length cm	Perceived Color	% pure color absorbed					
			Red	Orange	Yellow	Green	Blue	Violet
0.36	<1	none	<1	<1	<1	<1	1-6	6-8
1.4	0.2	none	<1	<1	<1	<1	1-5	5-7
1.4	0.5	faint yellow	<1	<1	<1	1-4	4-14	14-20
1.4	2*	faint yellow	<1	<1	<1	1-15	15-45	45-50
1.4	5	light yellow	<1	<1	<1	1-35	35-80	80-85
7.7	2*	yellow	<1	<1	<1	1-60	60-97	96-97
7.7	5	yellow	<1	<1	<1	4-90	90-99+	99+
16.3	2*	yellow	<1	<1	1-7	7-87	87-99+	99+
16.3	5	yellow to light orange	<1	<1	3-11	11-99+	99+	99+
194	1	light orange	<1	1-9	9-24	24-99+	99+	99+
194	2*	orange	0-2	2-20	20-84	84-99+	99+	99+
194	5	dark orange	0-5	5-37	37-84	84-99+	99+	99+
2650	0.5	red to orange	0-8	8-50	50-90	90-99+	99+	99+
2650	2	red	0-38	38-90	90-99+	99+	99+	99+
2650	6	dark red	0-75	75-99+	99+	99+	99+	99+

*: Photographs of these samples are shown in Fig. 7.

intensity at some wavelengths in the spectrum of the illuminating source. Colors ranged from faint yellow to dark red. When $A_{max} < 0.05$, no color was discernable.

Fig. 6 shows absorbance spectra of 0.091 μm microspheres with various concentrations of dye. The measured absorbance was equal to the sum of A_{abs} by the dye and A_{scat} by the particles. The product $A\lambda_o^4$ started increasing substantially below 500 nm (Fig. 6B), thus enabling us to detect correctly the wavelength range at which absorption was significant (Fig. 5).

When dye was present as well as Rayleigh particles, absorption colors were mixed with Rayleigh scattering colors (Table XI and Fig. 7). The result of mixing of colors depended on the hue and relative luminosity of the components (5). Because the scattered color varied with the angle between the direction of illumination and the direction of observation, i.e. on the relative position

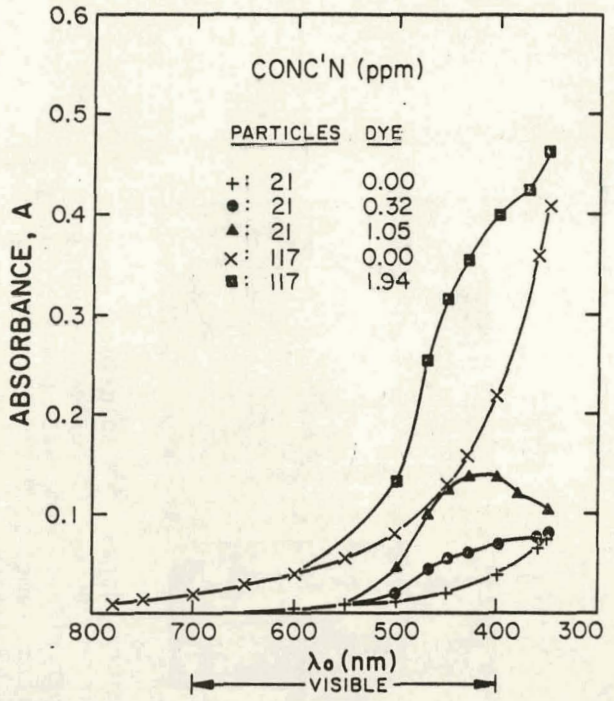

Fig. 6A. Spectra of absorbance, through 1 cm path length, of 0.091 μm polymer latex microspheres in aqueous methyl red dye.

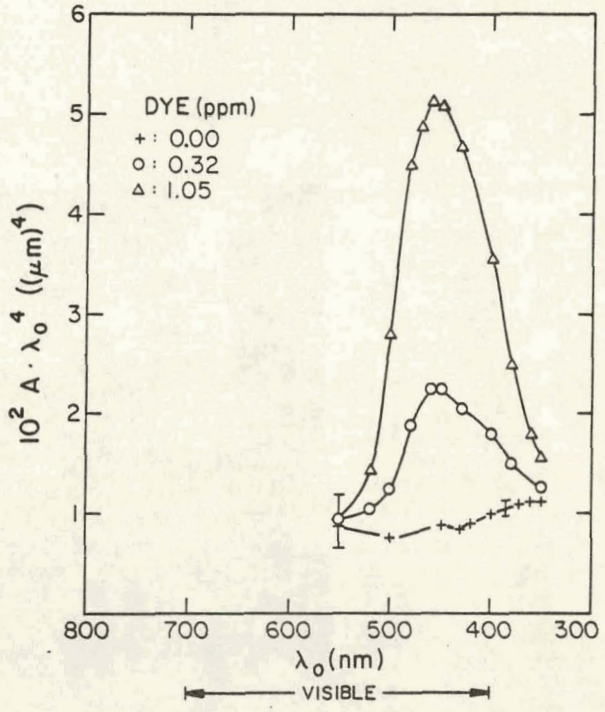

Fig. 6B. Wavelength dependence test of absorbances of dispersions of 0.091 μm microspheres, 21 ppm, in aqueous methyl red dye, Fig. 6A.

Table XI. Observations of aqueous dispersions of polymer latex microspheres with added methyl red dye (Figs. 6 and 7).

Particles		Dye	Appearance		COLORS						
Diameter μm	Concentration ppm	Concentration ppm	Particles With Dye (1)	Particles Only (2)	Dye Only	Scattered Light (1)	Scattered Light (2)	Scattered or Transmitted (1)	Scattered or Transmitted (2)	Angular Dependence Color (1)	Angular Dependence Color (2)
0.091	1179	17	turbid-translucent	turbid-translucent	yellow	orange & green	bluish-white	yellow or orange	bluish-white or orange	strong	strong
0.091	142	173	translucent	translucent	orange	orange	bluish	orange	bluish or yellowish	no	medium
0.091	117	0.36	translucent-clear	translucent-clear	none	light bluish & faint yellowish	bluish	bluish or yellowish	bluish or yellowish	medium	mild
0.091	117	1.94	translucent-clear	translucent-clear	faint yellow	yellowish	bluish	bluish or yellowish	bluish or yellowish	mild	mild
0.091	21	0.32	clear	clear	none	faint bluish	faint bluish	faint bluish or yellowish	faint bluish	mild	no
0.091	21	1.05	clear	clear	faint yellow	faint yellowish	faint bluish	yellowish	faint bluish	mild	mild
0.325	900	1.27	turbid	turbid	faint yellow	yellow	gray	yellow or gray	grayish or yellow	mild	mild
1.10	63	7.2	turbid	turbid	yellow	yellow	gray-white	yellow	gray-white	no	no

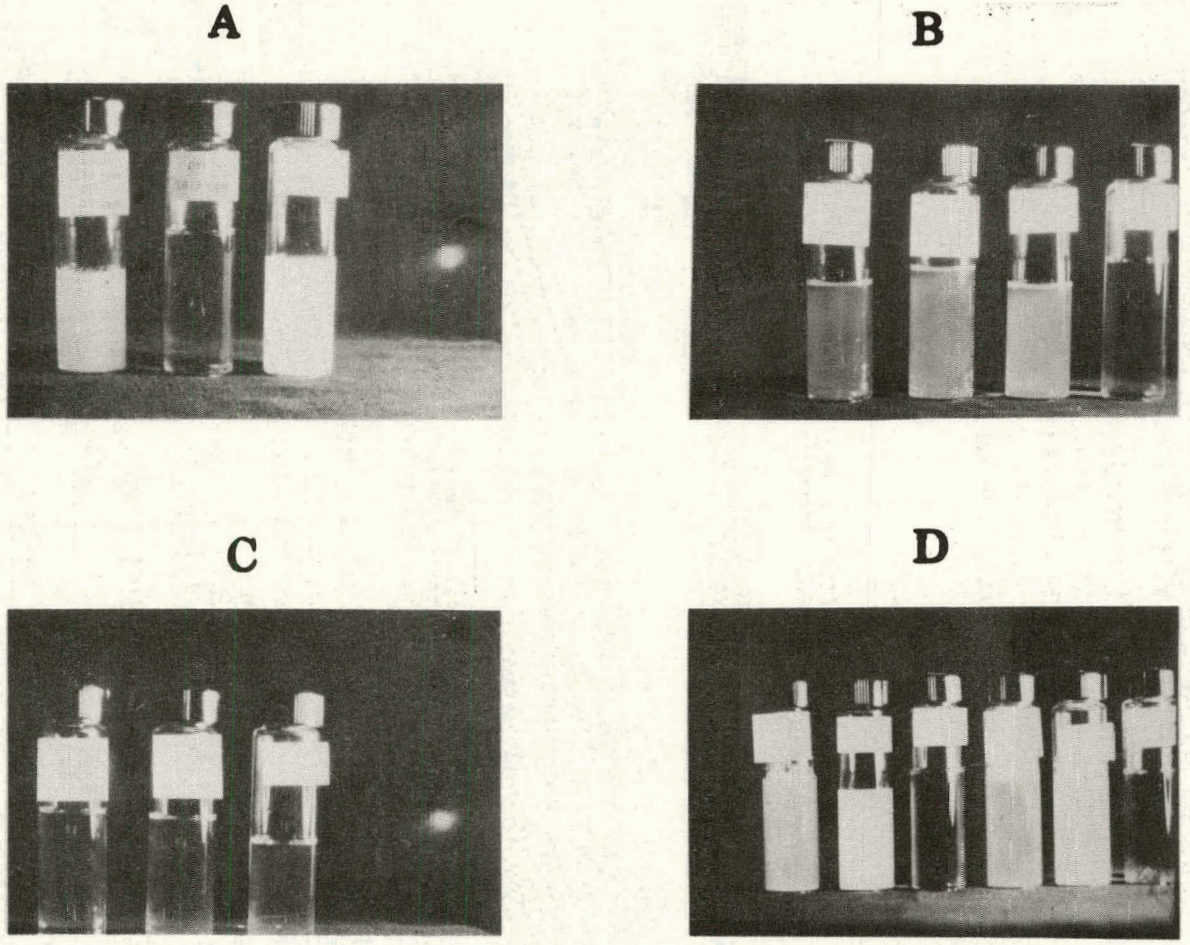

Fig. 7. Photographs of dispersions of polymer latex microspheres, dye solutions, and mixtures of them. Upper left: 0.91 μm particles and dye of respective concentration in ppm 1200-17, 0-16, and 1300-0; upper right: same with concentrations 120-1.9, 120-0.36, 120-0, and 0-1.4; lower left: same, 21-0.32, 21-1.05, and 12-0; lower right: 0.325 μm - 900 ppm with 1.27 ppm of dye, 0.325 μm - 900 ppm with no dye, 1.4 ppm dye with no particles, 1.10 μm - 63 ppm and 7.2 ppm dye, 1.10 μm - 65 ppm, and dye 7.7 ppm.

of light source, sample, and observer, the mixed color depended on this angle. The Tyndall effect was thus affected by the absorption color and was totally suppressed when absorption was sufficiently strong (second entry in Table XI). Also shown in Fig. 7 is a turbid dispersion of 63 ppm, 1.10 μm microspheres with 7.2 ppm dye. Its absorbance spectrum (not shown) has a maximum. Because scattering can cause such maxima (15), the observed maximum does not necessarily imply absorption. The plot (not shown) of $A\lambda_o^4$ versus λ_o decreased monotonically with decreasing wavelength, providing no clue to absorption either. However, the color of the dispersion, yellow and independent of angle, could not be accounted for by scattering alone and thus must have been due to absorption. This was a relatively rare case in which the visual observation was more sensitive than spectroturbidimetry for detecting the absorption.

References Cited in Section V

1. Prince, L. M., in Emulsions and Emulsion Technology, Ed., K. J. Lissant (Marcel Dekker, New York, 1974) 125.

2. Griffin, W. F., in Encyclopedia of Chemical Technology, 2nd ed., Vol. 8 (Wiley, New York, 1965) 117.

3. Kerker, M., The Scattering of Light and Other Electromagnetic Radiation (Academic Press, New York, 1969) Ch. 7.

4. Van den Hul, H. J. and Vanderhoff, J. W., in Polymer Colloids, Eds. R. M. Fitch (Plenum Press, New York, 1971) 1.

5. Franses, E. I., Scriven, L. E., Miller, W. G. and Davis, H. T., J. Amer. Oil Chem. Soc., Part II, accepted (1983).

6. Franses, E. I., Davis, H. T., Miller, W. G. and Scriven, L. E., in Chemistry of Oil Recovery, Eds., R. Johansen and R. L. Berg, ACS Symposium Series 91, American Chemical Society, Washington, D.C. (1979) 35.

7. Puig, J. E., Franses, E. I., Davis, H. T., Miller, W. G. and Scriven, L. E., Soc. Pet. Eng. J. 19, 71 (1979).

8. Franses, E. I., Talmon, Y., Scriven, L. E., Davis, H. T. and Miller, W. G., J. Colloid Interface Sci. 82, 449 (1982).

9. Meehan, E. J., Optical Methods of Analysis, reprinted from Treatise on Analytical Chemistry, Eds. I. M. Kolthoff and P. J. Elving (Wiley, New York, 1964) Part I, Vol. 5, 2707.

10. Cardinal, J. R. and Mukerjee, P., J. Phys. Chem. 82, 1614 (1978).

11. Van de Hulst, H. C., Light Scattering by Small Particles (Wiley, New York, 1957) 6.

12. Tanford, C., Physical Chemistry of Macromolecules (Wiley, New York, 1961) 282, 287.

13. Sudhakar, Y., M.S. Thesis, in progress, Purdue University.

14. Kratochvil, P., in Light Scattering from Polymer Solutions, Ed., M. B. Huglin (Academic Press, London, 1972) 333.

15. Heller, W., and McCarty, H. J., J. Chem. Phys. 29, 78 (1958).

16. Heller, W., Bhatnagar, H. L. and Nakagaki, M., J. Chem. Phys. 36, 1163 (1962).

17. Kortum, G., Reflectance Spectroscopy (Springer Verlag (Engl. transl.) Berlin, 1969) 94.

18. Heller, W. and Tabibian, R., J. Phys. Chem. 63, 2059 (1962).

19. Goulden, J. D. S., Brit. J. Appl. Phys. 12, 456 (1961).

20. Walstra, P., Brit J. Appl. Phys. 16, 1187 (1965).

21. Huglin, M. B. in Light Scattering from Polymer Solutions, Ed., M. B. Huglin (Academic Press, London, 1972) 255.

VI. INTERPRETING THE APPEARANCE OF DISPERSED SYSTEMS PART II. A GUIDE FOR SURFACTANT SYSTEMS

Introduction

Observing fluid surfactant systems with the naked eye is an important factor in screening surfactant systems for many types of applications and for scientific studies. With such observations surfactant systems are classified as solutions, microemulsions, macroemulsions, dispersions, etc., although classification may be no more than tentative.

In Part I (1), we tested certain literature rules (2,3) for interpreting appearances against spectroturbidimetry and light scattering measurements on model dispersions of polymer latex microspheres. We found that those rules are unreliable for correctly interpreting the appearance of many important disperse systems. We suggested more general rules and examined them systematically.

In this paper, we analyze sketchily the perceptions of color and transparency. Based on this analysis and the rules put forward in Part I, we propose a guide for surfactant systems in a step-by-step diagnostic format. We demonstrate the applicability of this guide to certain important surfactant systems we have researched in detail elsewhere (4,6).

Color and Transparency

Light is electromagnetic radiation detectable by the average human eye, i.e., with wavelengths in the range 350 to 780 nm or, for a reasonable sensitivity, in the range 400 to 700 nm. It is well known that ordinary white light (e.g. direct sunlight) can be analyzed by means of a prism into several distinct bands of wavelengths, each of which gives a characteristic sensation called color. A 'spectral' color is one which consists of a narrow band of wavelengths and remains unchanged if analyzed further.

The visible range can be roughly divided into six familiar color bands each of which merges into its neighbors.

λ_o range (nm)	color
400-450	violet
450-500	blue
500-700	green
570-590	yellow
590-610	orange
610-700	red

The human eye can *not* analyze light into its component wavelengths. The sensation induced by a spectral distribution of light - energy distribution per unit wavelength - reaching the eye is an overall one: quite different spectral distributions can give the same senation that a pure spectral color does (see the law of color perception later). For example, a clear brilliant yellow can

be obtained by mixing appropriate amounts of red and green light beams. The perception of color has, therefore, no direct physical meaning but *psychophysical meaning*, which has some *correspondence* to physical qualities (7). A marvelous account of the physics, physiology, and psychophysics of color vision is given by Feynman et al. (8).

What is called *brightness* of a light source corresponds to the *luminance*. Luminance, in turn, is defined as the *radiance* (W/m^2) reaching the eye times the eye sensitivity. The eye sensitivity depends on the wavelength; a (semi-) quantitative measure of it defined for an average observer is called *luminosity*.

What is called *hue*, or main color (if any), corresponds to the dominant wavelength (if any) of the incident radiation. What is called *saturation* of color corresponds to the *purity* or *monochromaticity* of light. Because white, black, and gray have no dominant wavelength, they are not colors in the regular sense and they are called *hueless* or *achromatic*. Of a certain spectral distribution the perceived hue and saturation lumped together are called *chromaticity* (chroma is the Greek word for color). An operational definition of dominant wavelength is that spectral color which would have to be mixed with an appropriate amount of white light in order to match the chromaticity of a given light source. The following degrees of decreasing chromaticity may be distinguished: *brilliant* (spectral color or mixed color matching a spectral color), *bright* (not to be confused with high luminance), *moderate, pale,* and *light*. *Faint* refers to only slight discernible hue.

The theory of color vision of Young and Helmholtz assumes the existence at the retina of the eye, of three cone-nerve combinations each of which has a different spectral response. The response can be considered analogous to that of three photomultipliers with different cathodes and dynode systems receiving the same signal but responding differently (8). The theory seems to lack supporting anatomical evidence but it is simple and adequate. The three cone-nerve combinations give three characteristic stimuli which are "processed" in the brain to give an overall sensation of color.

The fundamental law of color perception states that almost all colors can be produced by a combination of *three* colored sources or lights called *primaries*. These primaries are most conveniently, *but not uniquely,* chosen from the middle and near each end of the visible spectrum, namely red, green, and blue. The amounts of the three primaries needed to produce a particular optical sensation are called the *tristimulus values*, X, Y, and Z (8). The method has been standardized using standard sources and an average response of observers. Given a spectral energy distribution from absorption or scattering, the tristimulus values are calculated and the color predicted. Two ratios of the tristimulus values, x and y ($x \equiv X/(X + Y + Z)$ and $y \equiv Y/(X + Y + Z)$), are sufficient to predict the chromaticity of the source, namely its hue and its saturation, whereas the scale factor characterizes the brightness or luminance. *The response of the eye* to the different wavelengths is different at high light intensities of, say, an average reading room and low light intensities i.e. in the dark. At high light intensities, the average eye has maximum sensi-

tivity at 450 nm and at low intensities at 510 nm (8). The dark-adapted eye has a much higher sensitivity, but its ability to distinguish colors is weaker. Thus the eye has a quite selective and nonlinear response, although, as mentioned previously, there is certain correspondence between physical parameters of spectral distribution and brightness and sensations.

A substance may appear colored if it absorbs or scatters light. Usually the absorption is selective with respect to wavelength. Thus when white light illuminates a solution which absorbs but does not scatter light, the solution appears colored as a result of selective loss of intensity of some wavelengths. However, if the absorbance at some wavelengths is small, about 1 or less, those wavelengths pass through the sample but with a decrease in their intensity. The optical information carried by those wavelengths about an object behind the sample is not 'scrambled' and one can 'see through' the sample. The sample is termed *clear* or *transparent*, whether it is colored or not. There is, of course, a practical limit on the level of transmitted intensity which can still be detected and carry the information conveyed by the intensity incident to the sample. If the absorbance due to absorption over all visible wavelengths is 2 or more, as in a crude oil or in a concentrated aqueous solution of potassium permanganate, then one cannot see through the sample, even if it does not scatter. However, this is not a serious problem in most systems of interest, because they do not absorb strongly at all wavelengths and the absorbance can of course be decreased by shortening the path length. How to interpret observations of some dye solutions in terms of the measured absorbance spectra is explained in Ref. 1.

If the system scatters light, whether it absorbs or not, then depending on the type of illumination and the observation, some of the scattered light will reach the eyes of the observer together with some transmitted light, and the information perceived will be scrambled. If light passes through, the sample looks slightly cloudy or hazy, and one can resolve details of an object by looking at it through the sample, the sample is *translucent*. If one can see an object in outline but cannot resolve details, the sample is *turbid*. If one cannot see anything which lies behind the sample (at its umbra preferably), then the sample is *opaque*.

Light scattered by aggregates or particles carries information about these aggregates or particles. In particular it provides clues about their size and refractive index (1,7). If this information is not excessively 'scrambled' along the path length by subsequent scattering, i.e. if there is not excessive multiple scattering, then the qualitative observations can be interpreted on the basis of the theory of single scattering.

The ability of the eye to detect scattering depends on the background illumination. For ordinary white light, apparent absorbances ($A \equiv \log_{10}(I_0/I)$, where $100\ I/I_0$ is the % transmittance) larger than about 0.05 (transmittances less than 90%) are detected as a slight hue in the case of absorption or as a slight bluishness or haziness in the case of scattering. Larger apparent absorbances are detected more easily and information is more readily interpretable with translucent to turbid samples which have apparent absorbances due to scattering between 0.05 and 2, or better, between 0.1 and 1(1) and absorbance due to absorption no more than 1, averaged over wavelength. Thus

observations of scattering, at ordinary illumination, are possible only when there is substantial multiple scattering (1). The absorbance can be adjusted by decreasing the path length, as by tipping the vial containing a liquid system, or by transferring it to vials with smaller or larger diameter as necessary. We caution against diluting surfactant systems because the microstructure of liquid phases and the distribution of equilibrium aggregates such as micelles or of suspended particles may change in ways that are not apparent and that may remain unknown.

The following examples illustrate important principles of light scattering detailed in Ref. 1:

i. If the refractive index n_s of aggregates or particles equals that of the surrounding medium, there is no scattering.

ii. For a surfactant with $n_s = 1.45$, a dispersion of small surfactant particles of given concentration would scatter 0.0144/0.0009 = 16 times more in water ($n_w = 1.33$) than in hexadecane ($n_h = 1.42$) because according to Eqs. (7) and (8) in Ref. 1,

$$(n_s - n_w)^2 = (1.45 - 1.33)^2 = 0.0144$$

and

$$(n_s - n_o)^2 = (1.45 - 1.42)^2 = 0.0009.$$

Therefore it is crucial to have an estimate of the refractive index difference to interpret visual observations accurately.

iii. Air is transparent, for even fairly long path lengths, because the absorbance is much less than 0.05 at all wavelengths; however, the atmosphere over long distances, e.g. the blue sky, is translucent.

iv. From Fig. 1A, Ref. 1, one gets, with path length 1 cm and monochromatic light of wavelength (in vacuo) $\lambda_o = 436$ nm, an absorbance A = 0.065 for just 0.005 wt% in water of poly-styrene latex microspheres of size 910 Å and apparent molecular weight 200,000,000. This sample looks slightly opalescent. Therefore, very small concentrations of large particles are detectable, and the larger the size the lower the limit of detectable concentrations.

v. Conversely, ordinary pure solvents, molecular solutions, and solutions of small micelles scatter very little and are transparent over path lengths up to 500 cm and more. Huisman (9) measured the following absorbances with wavelength $\lambda_o = 436$ nm and path length 1 cm:

A = 0.000017 for pure water; the sample looks transparent.
A = 0.00022 for 0.5% aqueous SDS with 1.7% NaCl, a solution that contains mostly micelles of molecular weight 35,400 or 123 molecules per micelle. The sample looks transparent. In order to observe opalescence, i.e. to detect scattering visually, a path length of at least 0.05/0.00022 = 230 cm is needed.

vi. Because intensity is proportional to concentration c times molecular weight M, $i \propto cM$, (Eq. (7), Ref. 1), or $i \propto cd^3$ for spheres, a given concentration (in g cm^{-3}) of material dispersed as spherical particles of 500 Å scatters $(500/50)^3 = 1000$ times more than the same concentration dispersed as particles of 50 A diameter. Micellar solutions containing swollen micelles, e.g. oil-swollen micelles in aqueous solution, may have particles large enough — larger than 300 A or so — to produce observable turbidity at concentrations as low as 0.001 g cm^{-3} at a path length of 1 cm.

vii. Some mixtures of non-absorbing materials may appear colored. This is simply the result of the wavelength dependence of scattering. (1,7). This wavelength effect depends on the particle dimensions and the refractive index contrast. The intensity of scattered light also depends on the scattering angle, which is the angle between the direction of observation and the direction of illumination. For this reason, the distribution of light intensity per unit wavelength of light scattered depends on the scattering angle. Since the perception of color depends on that distribution of intensity, different colors can be perceived at different scattering angles. This fact provides us with an easy way to detect Rayleigh and Rayleigh-Debye-Gans scattering. As explained in Ref. 1, in translucent samples the bluishness of scattered light is an indication of small particles, 0.5 μm or less, that fall in the Rayleigh or the Rayleigh-Debye-Gans scattering regimes. Orange-red colors of transmitted light are an indication of small particles, 0.1 μm or less (Rayleigh scattering). If one sees a haziness, and no color, most of the scattering comes from particles larger than 0.5 μm (Mie scattering) (10).

The above rules hold approximately, at best, if the system is turbid or milky (1). Whether turbid or not, interpretation of colors and translucency is more complicated if the sample absorbs light. However, the color of an intrinsically colored sample which also scatters can differ from the intrinsic color and can vary with the scattering angle. Thus the scattering regimes, especially the Rayleigh regime, can be detected even in a colored sample (Figs. 7A and 7B in Ref. 1).

In summary, color — both hue and saturation — and degree of translucency are the important optical porperties of fluid systems. Observations of these properties, if properly interpreted, can provide qualitative information about the state of aggregation or state of dispersion in the fluid.

Procedure and Guide

Observations are more meaningful if the solution, microemulsion, or dispersion of interest is known to be at equilibrium or in metastable equilibrium. Moreover, for concentrated microemulsions, the inferences are less precise (11). The way of preparing the system might govern its final appearance, because it may determine the sizes of dispersed particles or aggregates (Fig. 1, below). It may be advisable to equilibrate two components prior to the addition of the third, the three prior to the addition of the fourth, and so on. If the system appears to change upon further stirring or otherwise

with time, it is desirable to record the changes while waiting as long as necessary for the system to stop changing. Possibilities of ambient temperature variation, evaporative loss, oxidative degradation, light sensitivity, etc., need to be checked.

Distinct layers are identified when they are separated by well-defined interfaces. These interfaces must be carefully detected by several criteria, such as smoothness, shininess, or total internal reflection at some angle, and distinguished from graded phases, flocs, etc. In practice, the presence of interfaces can be obscured by emulsions next to them, by proximity to critical points, or simply by dirt particles. The number of layers is the number of transverse liquid/liquid interfaces plus one.

In counting the number of layers or apparent phases one should take into account the not uncommon reluctance of dispersed phases to settle and coalesce. Centrifugation and ultracentrifugation are important tools for testing this, although a centrifugal field can alter the apparent phase behavior (12). Before accepting an unchanging appearance over days, weeks, or even months as signalling an equilibrium state, one has to try different orders of mixing. If one still has any doubt, one must use heating-cooling cycles or freezing-thawing treatments as checks for the history-independence, which is the hallmark of equilibrium.

One should take pains to avoid introducing dust and other extraneous particles into the system. Vials should be cleaned and filled carefully. It is desirable to avoid fingerprints and labels on the outside of the vials.

For observing a visually homogeneous sample, by which is meant a liquid that appears as a single layer, it is best to fill the vials to a standard height three times the vial diameter, in order that observations can be made at two path lengths differing by a factor of three. For systems with two and three apparent layers, including both transparent and extremely turbid ones, it is useful to observe and same compositions in vials of different diameter, so that the dependence on path lengths can be seen.

The suggested procedure is to answer a sequence of diagnostic questions (Tables I and II). A series of possible answers is listed below and one can underline or mark the most appropriate ones. The implications of each answer are indicated, followed by either another clarifying question or a hint about interpreting the particular observation or series of observations in terms of the number of phases present and the size of particles or aggregates. The observer should record details as called for in the suggested procedure and should be sure to record any additional observations not covered in the guide.

Since the unaided eye is a poor detector of polarization, some instrument is required to determine the state of polarization of scattered light, which can provide clues about particle size, or shape, or both (1). Use of such instruments falls outside the simple rules for quick and careful visual observations with the unaided eye at ordinary laboratory illumination.

Using the Guide in Certain Surfactant Systems

Surfactant dispersions, Fig. 1, can look quite similar to dispersions of polymer latex microspheres. Details of observations and photography are given in Ref. 1. Such comparisons suggest the use of the latex dispersions to standardize observations of translucency and colors by different observers and with varying conditions of illumination.

Moreover, size estimates can be obtained without any measurement at all. In Fig. 1A, the sonicated aqueous dispersion of 1.29 wt% surfactant Texas #1 (sodium p-(1'-heptylnonyl)benzenesulfonate) looks clear to translucent. Its colors are bluish by scattered light and bluish or yellowish by transmitted light (the latter colors are not shown in the photograph). This appearance indicates unequivocally that sizes of the surfactant particles are smaller than 1000A (0.1 μm), and further that the maximum possible number of particles present of sizes larger than 1000 Å is a negligible fraction of the total. By comparing the surfactant dispersion side-by-side with the dispersion of 117 ppm microspheres of size 0.091 μm, it is seen that the scattering is about the same. Thus, the scattering efficiency, A/c, of the surfactant particles is 110 times smaller than that of the 910 Å microspheres. Since in this size range $i \propto (n - n_o)^2$ and $i \propto d^3$ (1), and since $(n - n_o)/c = 0.25\ cm^3\ g^{-1}$ for the polymer microspheres (13) and $(n - n_o)/c = 0.17\ cm^3/g$ for the surfactant (14), the size of the surfactant particles is estimated to be about 270 Å, if the particles are rigid spheres. The estimate is increased slightly to 330 Å, if the surfactant particles are vesicular, i.e. each consists of a fluid-fluid cavity surrounded by a surfactant membrane, as explained in Ref. 6. Even though this estimate ignores interparticle interactions, it is in excellent agreement with the estimate from absorbance measurements, which also ignore such interactions, and both agree with electron microscopy results (6).

Photograph 1B shows that the appearance and scattering colors of the *unsonicated* 1.29% Texas #1 sample are about the same as 990 ppm of 0.325 μm PMMA particles. Thus sonication must have decreased greatly the particle size. Photographs 1C and 1D show how strongly the appearance and thereby the size of dispersed particles depend on order of mixing of Witco's TRS 10-80 (which is a commercial petroleum sulfonate surfactant) and NaCl in water (see also Fig. 3D below). The first-surfactant-then-salt sample exhibits Rayleigh-Debye-Gans type scattering (Fig. 3C). Since, however, the concentrations differ by a factor of 100, the scattering efficiency of the surfactant sample is 100 times less on the average than that of the polymer sample. If the sizes were uniform in the surfactant sample, they would be about 0.08 μm (estimated from $100x(0.15/0.25)^3 x 0.254\ \mu m = 0.08\ \mu m$). But then the sample would look bluish like a Rayleigh dispersion. The conclusion is that the sample contains a substantial amount of large (Mie and Rayleigh-Debye-Gans) particles and that in order to scatter so efficiently the sample must contain a substantial amount of particles smaller than 0.08 μm. Indeed, micron-size particles were detected in the microscope, indicating that Mie scatterers were indeed present; moreover the bluishness is consistent with Rayleigh particles being present also.

Fig. 2 illustrates certain important features of the phase behavior of Texas #1 in water and brine. The 0.029% sample looks transparent and is below the solubility limit which is about 0.06% (4). The 0.096% sample after being shaken looks transparent; closer examination reveals some visible particles which flocculate and settle slowly. The 1.29% sample is a turbid dispersion. Photograph 2B reveals a dramatic dependence of the appearance of dispersions on salinity. Although the particles in 3% brine look solid-like, they are liquid crystalline, as found by polarizing microscopy and ^{13}C nmr, just as are the particles in the more stable dispersions at 0 and 0.3% NaCl (4).

In Fig. 3 samples of aqueous solutions and dispersions of TRS 10-80 are shown. The absorption by the sample is significant at concentrations down to about 0.1 wt% at 2cm path length. The brilliance of the yellow color increases of course with surfactant concentration. In the presence of scattering colors, the absorption color is generally mixed with the scattering colors. Microscopic examination revealed that the 5.07% sample contains a large concentration of Mie particles, which do not produce scattering colors; hence the color is predominantly due to absorption. The same holds for the 0.263% sample in 1% brine, "first salt"; this sample was prepared by dissolving the salt first and then dispersing the surfactant. However, with the same composition but the inverse order of mixing, the particles fall in the Rayleigh or Rayleigh-Debeye-Gans regime, at which blue scattering colors are observed. In this sample, the scattering colors mask to a large extent the absorption color.

Discussion

A detailed guide for interpreting visual observations of surfactant dispersions has been set out. The guide is based on principles of light scattering and spectroturbidimetry and the perceptions of transparency and color; it can be also used for dispersions of other substances. The appearance of surfactant dispersions can be simulated by model dispersions of monodisperse polymer latex microspheres. Because observations can be subjective and the conditions of illumination can vary, comparison with model dispersions helps interpret observations objectively. Using dark background and high intensity illumination can of course improve the sensitivity of visual observations. This aspect remains to be systematically examined.

We believe that following the rules suggested here will help colloid scientists and engineers estimate quickly, simply, and fairly accurately the size range of dispersed particles and thereby to select rationally the research pathway for characterizing dispersions more definitively.

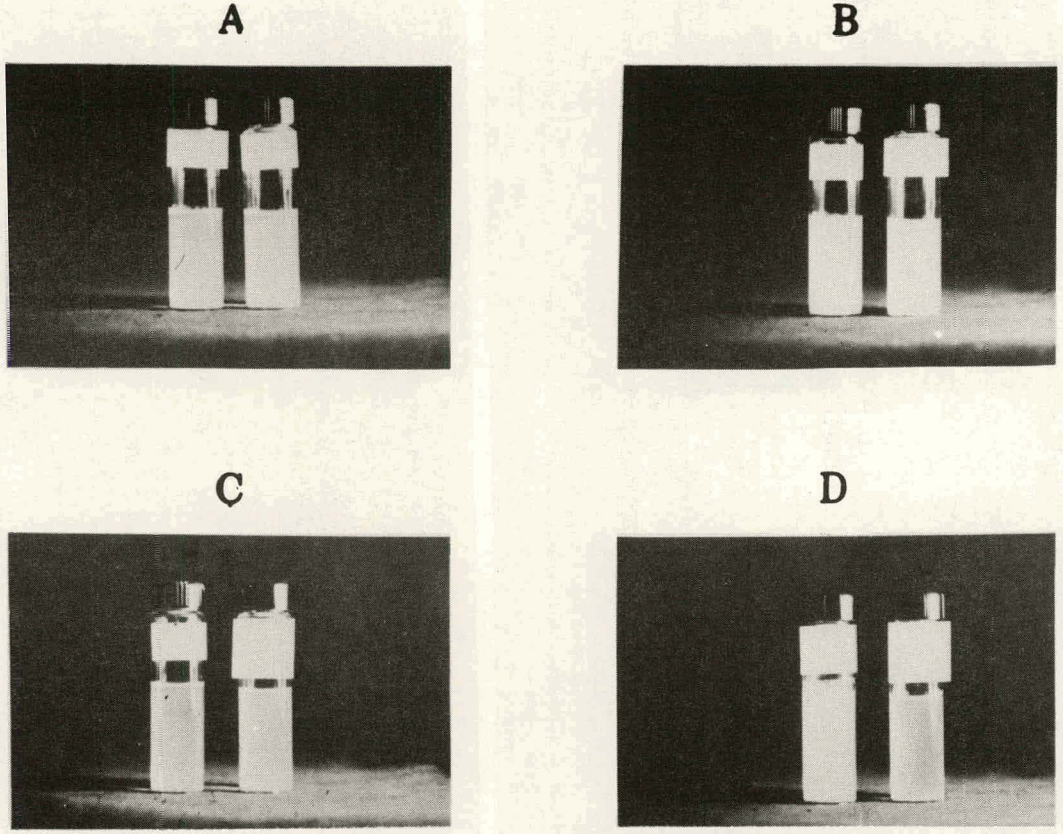

Fig. 1. Photographs of aqueous surfactant dispersions vs. model dispersions of polymer latex microspheres. Texas #1 stands for the sodium 4-(1'-heptylnonyl)benzenesulfonate surfactant (Ref. 4). TRS 10-80™ is the commercial name of the petroleum sulfonate surfactant manufactured by Witco (Ref. 5). All concentrations are w/w. Upper left (from left to right): sonicated dispersion of 1.29% Texas #1 in water vs. a 117 ppm dispersion of 0.091 μm microspheres; upper right: 900 ppm of 0.325 μm microspheres vs. unsonicated 1.29% Texas #1 in water; lower left: 26.7 ppm of 0.254 μm microspheres vs. 0.263% TRS 10-80 in 1.0% aqueous NaCl; this sample was produced by first dissolving the surfactant and then adding aqueous NaCl; lower right: 900 ppm of 0.325 μm particles with 1.27 ppm methyl red dye added vs. the previous TRS 10-80 sample but prepared with the opposite order of mixing (first salt then surfactant).

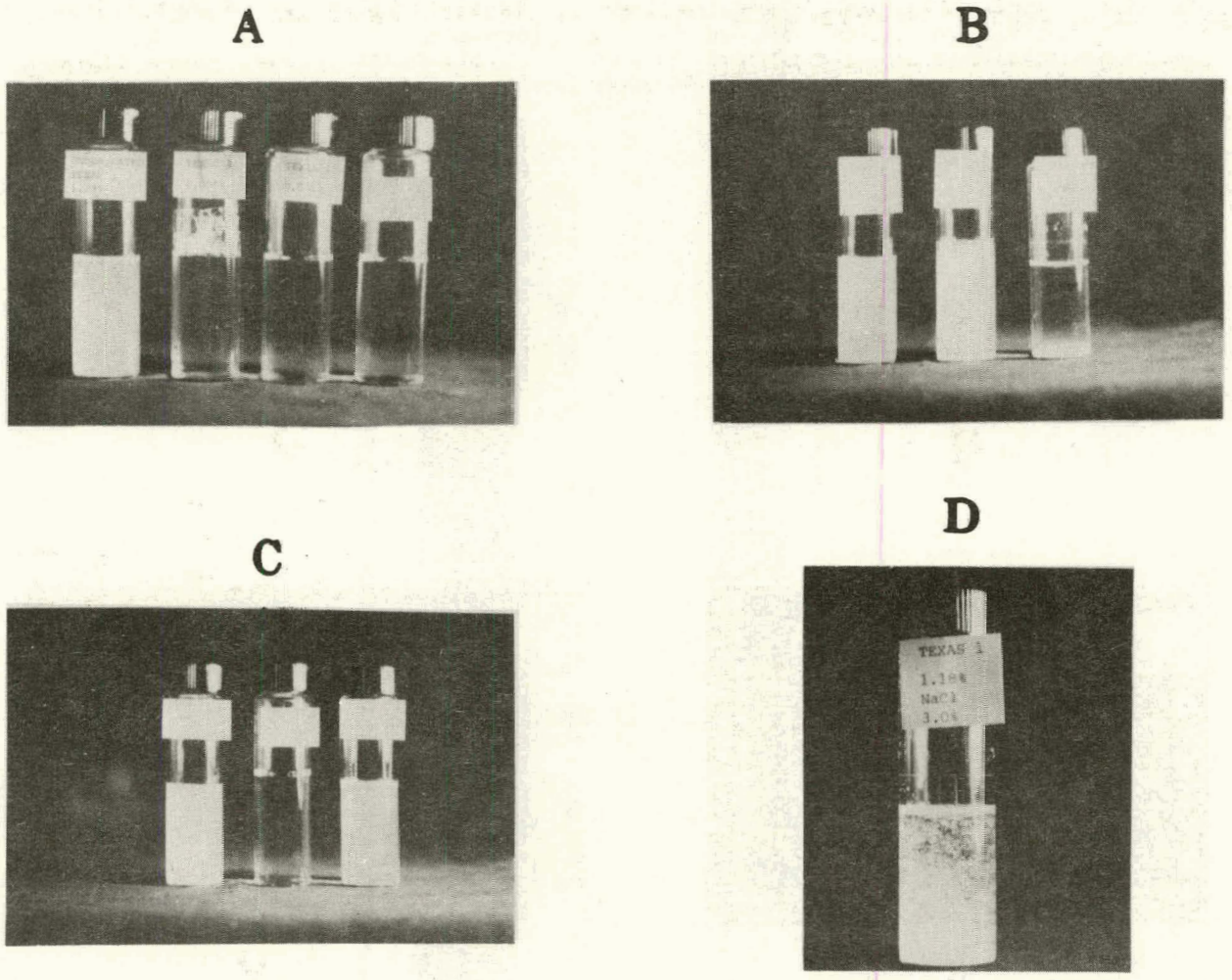

Fig. 2. Photographs of Texas #1 preparations in water and NaCl salt-water. Upper left: 1.29% unsonicated, 0.096%, 0.029%, and 0.0%; upper right: 1.29% - no salt, 0.99%-0.88% salt, and 1.18%-3.0% salt; lower left; 1.29% unsonicated, water (0 ppm), 1.29% sonicated; lower right: 1.18%-3.0% salt.

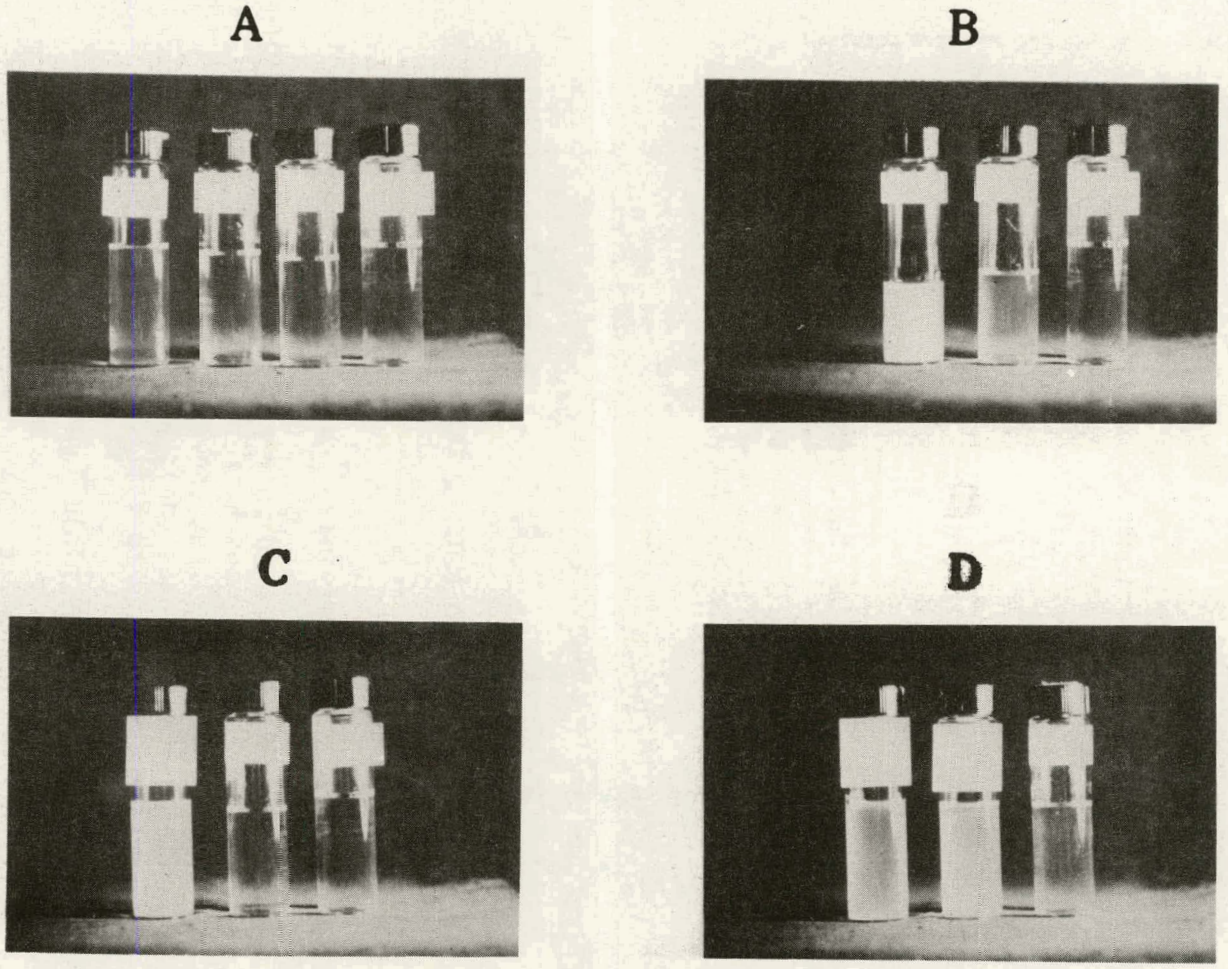

Fig. 3. Photographs of TRS 10-80 preparations in water and salt-water. Upper left: 0.99%, 0.263%, 0.1%, and 0.0%; upper right: 5.07%, 1.316%, and 0.0%; lower left: 0.1% with 1.6% NaCl with surfactant mixed first, 0.1% with no salt, and 0.0%; lower right: 0.263% with 1% salt with salt mixed firt, same with surfactant mixed first, and 0.263% with no salt.

Table I. Diagnostic Guide to Visual and Microscopic Observation of Surfactant Systems

Date:

Name:

A. Report the following information:

I. Materials used: names, overall amounts, composition and appearance, especially color.

II. Procedure of system preparation:

i. order of mixing or layering;

ii. stirring method, apparatus, vessel, time;

iii. thermal treatment and temperature.

III. Visually resolvable particles or droplets:

If no, go to IV.

If yes, estimate amount;

estimate size;

describe (shape, texture, turbidity, color);

sketch position.

IV. Number of visible discernible liquid/liquid transverse interfaces:

Move the eye relative to the level of the sample (vertically). Is there an angle at which there is shininess or total internal reflection? If yes, then there are two or more layers (number of such interfaces plus one); go to V(i). If no, there is one homogeneous layer; go to V(ii).

V. Number of visible discernible *layers*.

i. *If* one, does appearance change upon gentle stirring?

If no, 1 homogeneous layer; go to B.

If yes, 1 homogeneous layer;

any gradient in turbidity? *If* no, go to B.

If yes, two

phases;

sketch system

and go to C.

ii. *If* two or more, sketch system.

B. For *each* homogeneous layer, characterize its appearance.

I. Transparent (or clear); if so, compare with water

in similar vial; is sample

less clear than water?

If yes, scattering indicates that some particles may be present .

If no, use two long (~20 cm) volumetric cylinders and compare with water; is sample less clear than water?

Yes.

If no — one phase but check C.

II. Translucent; is any bluishness (opalescence) detectable by observing sample from different angles?

If no, does it look hazy or foggy?

If yes — Mie scattering; large particles or droplets, size 0.5 μm or more.

If no — moderate size particles, 0.5 μm or less.

If yes, does it look orange-red or yellow to transmitted light?

If no, try sunlight and answer again:

If no, — Rayleigh-Debye-Gans scattering, size 0.1 to 0.5 μm.

If yes, — Rayleigh scattering, size 0.1 μm or less.

If not sure, go to C.

III. Turbid or milky: Can you see details of an object which is placed behind the sample, at its shadow, its umbra rather than its penumbra? The object is to be held at most a few cm from the sample.

If yes, go to C.

If no, use thinner and thinner vials or droppers until you see through: then go to II.

C. *If* layer is inhomogeneous, or appearance changes upon shaking, or homogeneous layer is translucent to milky, it may be a two-(or more) phase dispersion:

Put a drop on a glass slide and observe through the light microscope, at ordinary setup, O.S., and crossed polars, C.P.,(beware of evaporation; use capillary or coverslip). Are any particles discernible?

If no, is there light coming through C.P.?

If yes, increase magnification and repeat. Are any particles visible?

If no, the layer is most probably one phase.

If yes, go to B-II.

**If* yes, report *set-up*, final magnification, size, shape and texture of particles; take a photograph if possible

D. For each homogeneous layer report about its color the following:

hue, e.g. blue, yellow, etc; recall that gray, white, and black are not colors.

saturation, faint, light or pale, moderate, bright, or brilliant. Is color different when the sample is viewed from different angles?

If no, are any of the pure materials used colored?

If no = scattering, go to B-II.

If yes and layer is clear —*no* scattering, go to B-I.

If yes, is any of the pure materials used colored?

If no — certainly scattering, go to B-II.

If yes — scattering, mixed with absorption (consider predicting color based on tristimulus values); fluorescence is possible, too.

Table II. Diagnostic Guide in a Condensed Form

Date:

Name:

A. Report the following information:

   I. Materials used: overall amounts, chemical characterization, appearance, and especially color. Total composition of system — wt% or vol%.

   II. Procedure used for system mixing or layering, stirring details, and thermal treatment and temperature used; keep system isothermal for several hours at least after preparation is completed.

B. Make a sketch of vial indicating dimensions (cm). Record number of well-defined interfaces and layers separated by interfaces. For each layer record whether it is homogeneous or not in appearance. Also record any visible particles present and their location. Also record the layer's appearance, color, homogeneity or color, and the dependence of any color on the direction of observation. Indicate whether any layer becomes more turbid by gentle shaking. Record anything else that seems pertinent.

C. Recapitulate observations. Decide on number of phases, equilibrium or not, with a short description in terms of dominant component, color, appearance, particles, and other scattering features.

References Cited in Section VI

1. Franses, E.I., Scriven, L.E., Miller, W.E. and Davis, H.T., J. Amer. Oil Chem. Soc., Part I, accepted (1983).

2. Prince, L.M., in Emulsions and Emulsion Technology, K.J. Lissant, ed., Marcel Dekker, New York, N.Y., 1974, p. 125.

3. Griffin, W.C., in Encyclopedia of Chemical Technology, 2nd ed., Vol. 8, Wiley, New York, N.Y., p. 117.

4. Franses, E.I., Davis, H.T., Miller, W.G. and Scriven, L.E., in Chemistry of Oil Recovery, R. Johansen and R.L. Berg, eds., ACS Symposium Series 91, American Chemical Society, Washington, D.C., 1979, p. 35.

5. Puig, J.E., Franses, E.I., Davis, H.T., Miller. W.G., and Scriven, L.E., Soc. Pet. Eng. J. 19, 71 (1979).

6. Franses, E.I., Talmon. Y., Scriven, L.E., Davis, H.T., and Miller, W.G., Colloid Interface Sci. 82, 449 (1982).

7. Kerker, M., The Scattering of Light and Other Electromagnetic Radiation, Academic Press, New York, N.Y., 1969, p. 396 ff.

8. Feynman, R.P., Leighton, R.B. and Sands, M., The Feynman Lectures on Physics, Addison-Wesley, Reading, Mass., 1963, Ch. 35.

9. Huisman, H.F., Proc. Kon Ned. Acad. v. Wet. B. 67, 367, 376, 388, 407 (1964).

10. Oster, G., in Physical Methods in Organic Chemistry, A. Weissberger, ed., Interscience, New York, N.Y., 1980, Vol. 1 , Part III, p. 2185.

11. Bennett, K.E., Ph.D. Thesis, University of Minnesota (1982).

12. Rossen, W.R., Davis, H.T. and Scriven, L.E., J. Colloid Interface Sci. (submitted).

13. Huglin, M.B., in Light Scattering from Polymer Solutions, M.B. Huglin, ed., Academic Press, London, 1972, p. 255.

14. Ludlum, D.B., J. Phys. Chem. 60, 1240 (1956).

VII. INTERFACIAL TENSIONS IN SYSTEMS OF THREE LIQUID PHASES

Introduction

In the course of studies of triphasic multicomponent mixtures that contain surfactant and display low interfacial tensions (1-5), we observed how three liquid phases distribute themselves within the rotating, horizontal cylindrical container used in the spinning drop method of measuring interfacial tension (6,7). These observations were subsequently borne out by a simple ternary system, n-butanol-n-hexadecane-water, that splits into three liquid phases at equilibrium at 23°C and atmospheric pressure. By virtue of Gibbs' phase rule the three coexisting phases and interfacial tensions between them are invariant. This system has been described recently as consisting of three liquid phases, but the compositions of the three phases were not reported (8). It can serve as a convenient standard for tension studies of multiphase systems. Within a rapidly spinning tube a variety of arrangements of three phases is possible, depending on interfacial tensions, densities, rotational speed, relative phase volumes, and history of the system. We saw many but not all of the metastable distributions that could arise. Several arrangements are lenticular configurations akin to those seen at nearly flat fluid interfaces (9,10), others are analogous to composite drop configurations (11). The observations reported here are novel and may be useful to other investigators, not only in recognizing three-phase systems in spinning drop experiments, but also in studying the wetting of fluid interfaces, Antonov's rule and the inequalities it separates (12-19). Interfacial tensions are conveniently and accurately measured by the spinning drop method, which is simple and reliable provided full thermodynamic equilibrium is attained. This requires gyrostatic equilibrium (7,20). An advantage is the freedom from interference by a solid wall and uncertainty about the contact angle. The reliability of the often-used capillary-rise method hinges on the experimenters' success in selecting a transparent capillary tube of suitable composition and inside surface finish, and a direction of meniscus motion before measurement, which make the cosine of the contact angle close to unity.

In addition to reporting distributions of three liquid phases in the spinning drop tensiometer, in this paper we record carefully measured tensions and investigate whether Antonov's rule is valid in ternary and quaternary systems that split into three liquid phases. We provide a thermodynamic derivation of Antonov's rule as a limiting case of the triangle inequality and suggest conditions under which the inequality may be reversed.

Experimental

Reagent grade n-propanol (NPA), n-butanol (NBA) and t-butanol (TBA) were obtained from J. T. Baker Chemical Co. or Aldrich Chemicals. The alkanes employed, 99% pure, were obtained from Aldrich Chemicals or Phillips Chemicals. Sodium chloride was certified A. C. S. grade from Fisher Scientific. Laboratory redistilled and deionized water was used.

Components were mixed in sample vials with teflon discs inserted in the screw caps to reduce losses by evaporation, shaken vigorously, and then allowed to equilibrate for one week or more at constant temperature (±0.2°C) before phases were analyzed or tensions measured. Specimens of equilibrium phases were withdrawn with a syringe as detailed elsewhere (21) and analyzed with a

Hewlett Packard 3730 A gas chromatograph employing an 8% Carbowax 1540 on Teflon 6 column or a Poropak P column.

Interfacial tensions were measured in gyrostatic equilibrium (20) with an air-bearing spinning drop tensiometer (7) or with an earlier ball-bearing model (6). Some tensions were cross-checked with a sessile drop tensiometer; in all cases, tensions measured with the two methods agreed within experimental uncertainty. Densities, which are needed to calculate interfacial tension, were determined with a Paar DMA 40 oscillating tube precision digital density meter. Refractive index of the denser phase in the spinning drop tensiometer was measured with a Abbé refractometer from Bausch and Lomb; this refractive index is the magnification factor of the spinning drop (3,5,7,22).

Antonov's Rule and the Triangle Inequality

When three fluid phases coexist in equilibrium, the number of possible interfaces is three. Let the corresponding interfacial tensions be σ_{12}, σ_{23}, and σ_{13}. Let σ_{13} be the largest. Then they must be related by one of the three equations:

$$\sigma_{13} = \sigma_{12} + \sigma_{23} \tag{1}$$

$$\sigma_{13} < \sigma_{12} + \sigma_{23} \tag{2}$$

$$\sigma_{13} > \sigma_{12} + \sigma_{23} \tag{3}$$

The first possibility is known as Antonov's rule. The second possibility, the triangle inequality, is simply a condition of mechanical equilibrium at a contact line between the three fluid phases. This is what is most commonly observed in reality (12-14). The third possibility, the reverse inequality, is not possible at thermodynamic equilibrium (13,14,17,18). Whether this is always true continues to be controversial. Widom (17,18) and others (14,23) have reasoned that either Eq. (1) or (2) must hold because at equilibrium the total free energy of the 1-3 interface could be lowered by the formation of a thin sheath of phase 2 between phases 1 and 3 if the interfacial tensions were related by Eq. (3). In strict terms this contention applies only to systems large enough to be effectively open, and to systems in which capillary pressure effects at curved interfaces do not intrude.

Consider the open system of volume V illustrated in Figure 1. Suppose that upon removing phase 2 completely, no thin film of that phase forms at the interface between phases 1 and 3 when equilibrium is re-established. In this case the Helmholtz free energy of the system is

$$F = f_1 V_1 + f_3 V_3 + \sigma_{13} A + \sum_i \mu_i [N_i - n_i^{(1)} V_1 - n_i^{(3)} V_3] \tag{4}$$

where f_α and V_α are the free energy and volume of phase α, μ_i the chemical potential of component i, $n_i^{(\alpha)}$ the density of component i in phase α, N_i the total number of particles of component i in the system, and A the interfacial area. V_1 and V_3 are defined by dividing the system with a plane placed in the interfacial zone.

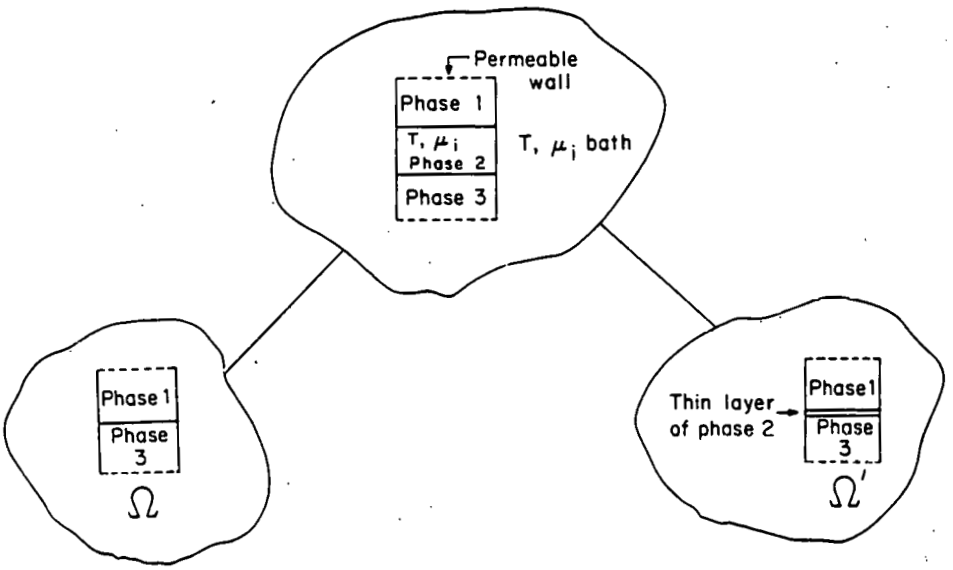

Figure 1. T-μ-V ensemble

Consider next the situation in which a thin layer of phase 2 of volume V_2' forms by recruiting material from phases 1 and 3. Assume that the free energy densities of phases 1 and 3 remain at their original values, f_1 and f_3. Whereas this condition is maintained in an open system at equilibrium, it is obviously violated in closed systems, although the changes may be insignificant if phases 1 and 3 are sufficiently large and the layer of phase 2 is but a thin film. The free energy, F', of this re-equilibrated system is then

$$F' = f_1V_1' + f_2V_2' + f_3V_3' + (\sigma_{12} + \sigma_{23})A + \sum_i \mu_i[N_i - n_i^{(1)}V_1' - n_i^{(2)}V_2' - n_i^{(3)}V_3'] , \quad (5)$$

The thermodynamic potential, $\Omega \equiv F - \sum_i N_i\mu_i$, is, for the system without the thin layer of phase 2,

$$\Omega = f_1V_1 + f_3V_3 + \sigma_{13}A - \sum_i n_i^{(1)}\mu_iV_1 - \sum_i n_i^{(3)}\mu_iV_3 \quad (6)$$

and for the system with the thin layer of phase 2,

$$\Omega' = f_1V_1' + f_2V_2' + f_3V_3' + (\sigma_{12} + \sigma_{23})A - \sum_i n_i^{(1)}\mu_iV_1' - \sum_i n_i^{(2)}\mu_iV_2' - \sum_i n_i^{(3)}\mu_iV_3' \quad (7)$$

$n_i^{(j)}$ denotes the density of component i in phase j. The conditions for phase

equilibrium are of course that the truly intensive variables (field variables), temperature T, pressure p (in the absence of capillary pressure effects), and the chemical potential of each component μ_i are the same in every phase. Now

$$\sum_i n_i^{(j)} \mu_i = f_j + p \quad (j = 1,2,3) \tag{8}$$

and because

$$V = V_1 + V_3 = V_1' + V_2' + V_3' \tag{9}$$

it follows that

$$\delta\Omega \equiv \Omega' - \Omega = (\sigma_{12} + \sigma_{23} - \sigma_{13})A \tag{10}$$

If $\sigma_{13} < \sigma_{12} + \sigma_{23}$, then $\delta\Omega > 0$: the 1-3 interface will not become covered by a thin layer of phase 2 because the resulting system would be at higher thermodynamic potential. However, if $\sigma_{13} > \sigma_{12} + \sigma_{23}$, then $\delta\Omega < 0$: a thin layer of phase 2 will form *spontaneously* between phases 1 and 3 and perfectly wet the interface, so that the *observed* tension will be

$$\sigma_{13}^{\text{obs.}} = \sigma_{12} + \sigma_{23}. \tag{11}$$

This is the sense in which Antonov's rule obtains.

Special consideration is required by closed systems or systems with curved interfaces, both situations being commonly encountered in tension measurements. Suppose phases 1 and 3 are in equilibrium with phase 2 across planar interfaces at T, $\mu_1, \mu_2, \ldots, \mu_c$, c being the number of components of the system. Drawing samples of phases 1 and 3 and contacting them across a planar interface in a closed system will result in some redistribution of the bulk concentrations of 1 and 3 as material is recruited or rejected at system walls and the interface. Chemical potentials change correspondingly. So also does the interfacial tension, according to the Gibbs isotherm:

$$d\sigma_{13} = -\sum \Gamma_i d\mu_i \tag{12}$$

Γ_i is the surface excess of component i at the interface measured relative to some convenient dividing surface. If after readjustment of the contact samples of phases 1 and 3 the chemical potentials are $\tilde{\mu}_1, \ldots, \tilde{\mu}_c$, the tension between 1 and 3 is

$$\tilde{\sigma}_{13} = \sigma_{13} - \sum_i \int_{\mu_i}^{\tilde{\mu}_i} \Gamma_i d\mu_i \ . \tag{13}$$

Thus, if the experimental uncertainty in a tension measurement is ε, then $\tilde{\sigma}_{13}$ will be found equal to σ_{13} as long as the samples of 1 and 3 that are contacted are sufficiently large for a given interfacial area that

$$\left| \sum_i \int_{\mu_i}^{\tilde{\mu}_i} \Gamma_i d\mu_i \right| < \varepsilon \qquad (14)$$

If an interface is curved, Eq. (12) still holds with an appropriate choice of dividing surface, but the chemical potentials are affected not only by the material rearrangement between interface and bulk phases but also by the pressure jump across an interface created by curving it. Again, whether $\tilde{\sigma}_{13}$ is found equal to σ_{13} within experimental precision is governed by the inequality in Eq. (14).

Thus, when in an open system $\sigma_{13} = \sigma_{12} + \sigma_{23}$ owing to perfect wetting, Antonov's rule will be observed experimentally in a closed system if the samples of 1 and 3 that are brought into contact for the measurement are sufficiently large compared to interfacial area and if the radii of curvature of the interface between 1 and 3 are sufficiently large that Eq. (13) is not violated.

Many examples of Antonov's rule as well as numerous instances of the inequality have been documented (12-14,16,19,24-27). The reverse inequality has also been reported—by careful investigators (27-29). The circumstances in which the triangle inequality may be violated, i.e. $\sigma_{13} > \sigma_{12} + \sigma_{23}$, include (i) the time of formation of the thin layer of phase 2 is long compared to the time of experimental observation, (ii) the system otherwise is not in thermodynamic equilibrium, or (iii) in a closed system there is not enough of a component for recruitment to form the thin layer. Moreover, Antonov's rule may be irrelevant to systems in which pressure and chemical potential respond to the centrifugal field in the spinning drop apparatus, or in which curved menisci give rise to capillary pressure effects. These possibilities are discussed in the following sections.

Phase Distributions

Let the three phases be so labeled that $\rho_1 < \rho_2 < \rho_3$. Then the liquid that fills most of the sample tube of a spinning drop apparatus can be either phase 3 or phase 2, and the drop can be either phase 2 or phase 1. The various possible arrangements when three fluid phases are in the spinning tube without a meniscus contacting the tube wall are illustrated in Figure 1. If phases 1 and 2 form separate drops, these must lie on the axis of rotation as in (a). Provided each is more than about four times as long as its equatorial diameter, the ratio of the diameters is necessarily $D_{13}/D_{23} = [\sigma_{13}(\rho_3-\rho_2)/\sigma_{23}(\rho_3-\rho_1)]^{1/3}$. Where three fluid phases intersect in a contact line the Neumann triangle condition of mechanical equilibrium must be satisfied; a necessary requirement is that $\sigma_{ik} < \sigma_{ij} + \sigma_{jk}$; if there were significant line tension the Neumann triangle condition would have to be modified (10). If phase 2 is present at the interface between phase 1 and phase 3, there are four possible types of configurations. These can be grouped as sessile lenses and sessile double drops: (b) - (e) in Figure 2. It must be emphasized that patch lenses are not themselves axisymmetric and perturb the entire system of menisci from axial symmetry. If the third phase is 1 or 3, lenses are still conceivable and may exist under circumstances in which they are metastable. Lenses of phase 1 can be called inwardly pendant lenses: (f) and (g); lenses of phase 3

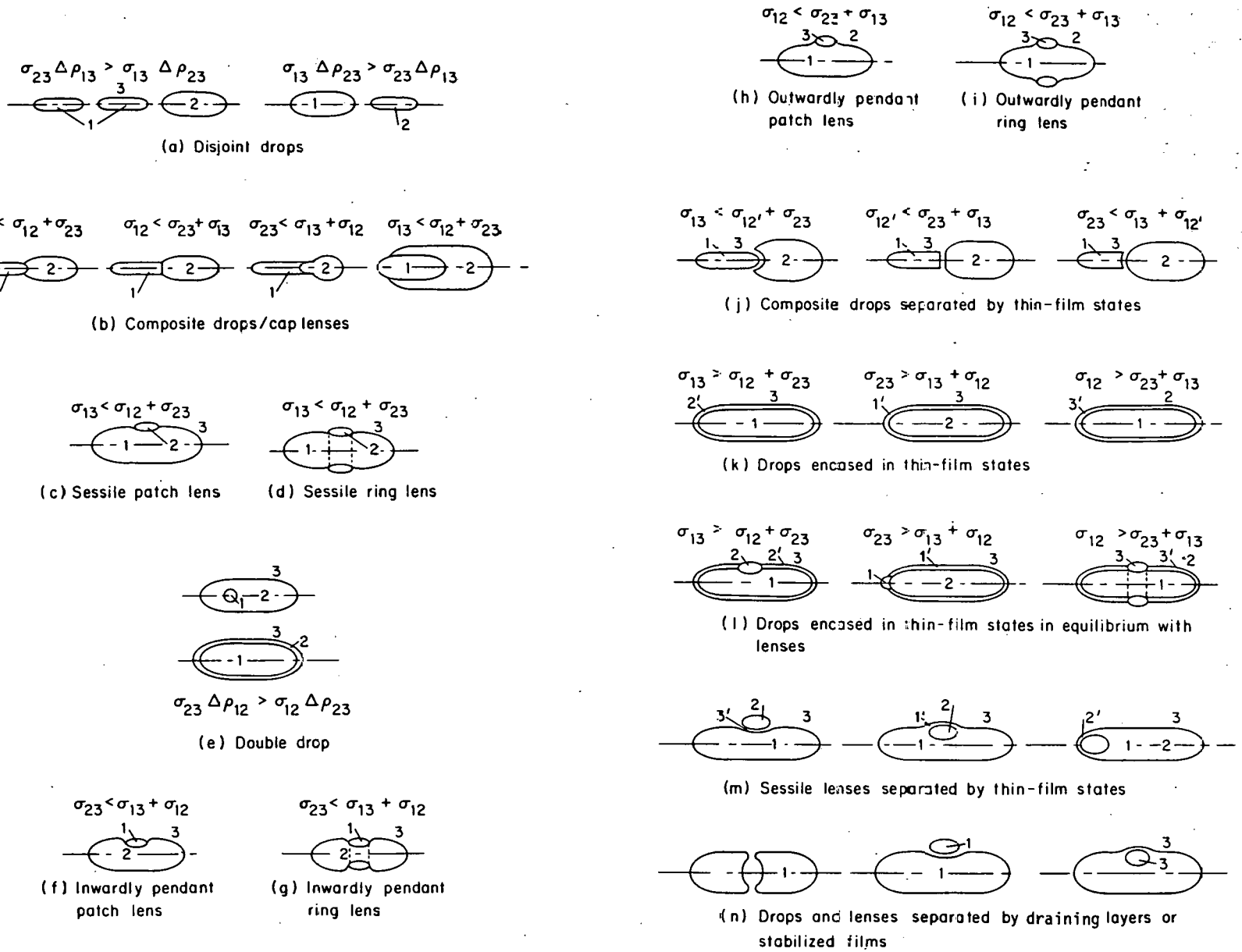

Figure 2. Possible arrangements when three liquid phases coexist in the spimning tube and no meniscus contacts the tube wall.

can be called outwardly pendant lenses: (h) and (i). Where draining films are long-lived, or can be stabilized in metastable equilibrium by means of additives, the configurations (j) and (k) shown in Figure 3 are possible, as are those in (n) too. But the configurations in (j) and (k) can also arise from very thin, inhomogeneous, equilibrium films that are close in composition to the outer liquid. These are denoted by 3' in Figure 2 and are designated thin-film states (31), in contrast to thin layers of a third phase.

Because the term, film, is applied loosely to many configurations, it is useful to distinguish between a thin layer, or what was infelicitously called a duplex film by earlier writers (compare references 12 and 13) and a thin-film state. By a thin layer is meant a film consisting of essentially homogeneous bulk phase bounded by interfacial zones. By a thin-film state is meant a film-like zone across which there are gradients of density or composition at equilibrium, or the homogeneous bulk phase conditions being achieved nowhere in the zone (30,32). This includes interfaces and adsorbed layers between bulk phases. Along the right thermodynamic path a thin-film can thicken into a thin layer of a third phase (32).

The stabilities of the various phase distributions appear to be as follows: When the triangle inequality, i.e. $\sigma_{13} < \sigma_{12} + \sigma_{23}$, holds, the cap lenses of Figure 2(b) are at least metastable. Depending on the relative volumes of phases 1 and 2 and the angular velocity, the minimum energy state may be a cap lens, patch or ring lens, or double drop—a matter that remains to be settled by calculation. When the relative volume of phase 2 is small, the patch lens of (c) is probably at least metastable when it is astride the equatorial plane; however, if it should form sufficiently close to an end of the drop it is probably unstable with respect to sliding toward the rotation axis and there forming a cap lens. When the relative volume of phase 2 is somewhat larger, the axisymmetric patch lens becomes unstable with respect to the axisymmetric ring lens of (d), which is at least metastable when situated at the equator. When the relative volume of phase 2 is still larger, the stable form is almost certainly a cap lens.

The patch and ring lenses of the least dense phase, as indicated in (f) and (g), can be metastable in certain circumstances. As lens volume or angular velocity increases, the interface between 1 and 2 bulges inward and eventually a drop of phase 1 detaches, migrates to the center line, and gives a configuration like (e). Ring lenses might be subject to another mode of instability, viz. break-up into patch lenses, analogous to the instability of a fluid cylinder with respect to break-up into drops. The patch and ring lenses of the densest phase, sketched in (h) and (i), are almost certainly metastable over certain ranges of conditions. As lens volume or angular velocity increase, the interface between 2 and 3 would be expected to bulge outward, become unstable, and discharge a drop of phase 3 to the tube wall. In each case, the limits of stability are a delicate issue, because they are governed by the net of several simultaneous energy changes: surface energies proportional to the areas of the three interfaces, and mechanical potential energies that depend on the location of matter in the centrifugal field.

In cases in which, owing to lack of equilibration, the triangle inequality is reversed, i.e. $\sigma_{13} > \sigma_{12} + \sigma_{23}$, no contact line is possible and the stable distribution is either disjoint drops (a) or double drops (e). As the

relative volume of phase 2 decreases the thickness of the outer layer of a double drop diminishes until the layer becomes an imperceptibly thin layer, and ultimately all that is left is an equilibrium thin-film state (31,32) or interface between phases 1 and 3 when these are on the verge of equilibrium with bulk phase 2, as in (1) in Figure 2.

When Antonov's rule, i.e. $\sigma_{13} = \sigma_{12} + \sigma_{23}$, would hold for a planar interface in an open system, secondary effects probably determine the stable distribution. In fact, when a thin-film state is present, the apparent tension σ'_{13} between phases 1 and 3 is given by $\sigma'_{13} = \sigma_{12} + \sigma_{23} + \delta\sigma_{13}$, where $\delta\sigma_{13}$ is the tension increment, which depends on the chemical potentials, temperature, and curvature of the thin-film, as discussed at Eqs. (13) and (14). How thick a thin-film must be to observe Antonov's rule within experimental precision depends on the particular system, but it can be as little as several molecular diameters for a planar interface (32). When a thin layer of a third phase is present and the drop is at least four times as long as its equatorial diameter, the apparent tension σ'_{13} is given by a formula derived in Appendix A:

$$\sigma'_{13} = \sigma_{12} + \sigma_{23} + \frac{D_2 - D_1}{D_2} K \ , \ K > 0 \qquad (15)$$

where D_2 and D_1 are the equatorial diameters of the outer and inner drops, respectively. Thus the apparent tension diminishes as the layer thins into a thin-film state, the increment $(D_2 - D_1)K/D_2$ eventually melding into $\delta\sigma_{13}$. Antonov's rule is in strict agreement with reality only under those conditions that make $\delta\sigma_{13} = 0$. It will, however, appear to be valid when the increment falls within the experimental uncertainty of tension measurements. For example, for a long drop of 1 mm diameter covered by a 1 micron thick layer of phase 2, $\sigma'_{13} \approx \sigma_{12} + \sigma_{23} + 4 \times 10^{-3}\ \sigma_{12}$.

When the reverse inequality, $\sigma_{12} > \sigma_{13} + \sigma_{23}$, holds, a double drop consisting of phase 1 encased in phase 3 is not possible because it is surely unstable. What seems likely is a thin layer 3' that forms by diffusion, encapsulates phase 1, and is sufficiently thin that the thickness-dependent chemical potentials of a thin-film state are involved. Such a thin-film could exist in stable equilibrium with lens forms within which chemical potentials are influenced by the pressure level, which depends in turn on lens size through the curvature of the interfaces by virtue of the Young-Laplace equation (the pressure level also varies with distance from the rotation axis, and this influences lens location). These possibilities are shown in Figure 2, (l) and (m), along with analogous configurations for the cases $\sigma_{23} > \sigma_{13} + \sigma_{12}$ and $\sigma_{13} > \sigma_{12} + \sigma_{23}$.

In this light the ultimate equilibrium sizes of the mechanically stable drops and lenses in Figure 2 must depend, after diffusional equilibrium is established, on the locations and curvatures of any other drops and wall layers within the spinning tube. Thus attainment of total equilibrium could take a long time, particularly in triphasic systems, where chemical potentials can be comparatively insensitive to composition and therefore affected more importantly than usual by capillary pressure and centrifugal pressure. Indeed, even when we load pre-equilibrated liquids, we observe equilibration

times in 2-mm i.e. spinning sample holders that are typically minutes or tens of minutes for two-phase systems, scores of minutes for three-phase systems, and hours or days when surfactants are present.

What follows are the arrangements fo three liquid phases we observed in spinning drop instruments during studies of multicomponent triphasic systems.

Procedures for Producing or Removing Third Phase

We have seen and photographed configurations such as those in (a) - (f) and (h) in Figure 2. Stable rings as in (g) and (i) probably occur only in a narrow range of circumstances if at all. Direct evidence of thin-film states like those in (j) - (m) requires more instrumentation than we have so far been able to bring to bear on the problem. The draining layers in (n) we have frequently seen between coalescing drops.

Some three-phase configurations can be produced by injecting a small amount of third phase along with the other two in the sample tube before it is spun. It is possible, when the required conditions on tension are met, to inject a drop of phase 1 inside a drop of phase 2 and thereby produce a double drop as in (e). Disjoint drops of phases 1 and 2 can be loaded and, after spin-up, caused to move together to test among (b) - (f). However, it is difficult otherwise to control the motion of an injected drop of phase 1 or 3: a drop of phase 1 tends to "rise" to the rotation axis and of phase 2 to "sink" to the tube wall during spin-up.

Another method is by changing the temperature of the air bath in which the sample tube spins. From a triphasic system pre-equilibrated at the desired temperature, two of the three phases are loaded into the sample tube, the less dense phase as the drop. By changing the temperature in one direction or the other it is then possible to cause the third phase to nucleate and grow. Often this happens at the original interface, with the result that many small patch lenses appear, like those in (c), (f), and (h) of Figure 2. These may coalesce into larger patch lenses, or ring lenses, or into a continuous layer. It is not uncommon when working with a long drop of phase 1 in phase 3 to observe the formation of several sessile ring lenses of phase 2 along the original drop. Near the ends of a drop, precipitating patch lenses of 1 or 2 may slide along the interface until they reach the axis of rotation. As pendant patch lenses grow larger they usually, in our experience, become unstable and either "rise" to the center line, or "fall" to the tube wall if they are of phase 3. Usually we have seen the densest phase, phase 3, nucleate and grow on the tube wall, where a temperature change is first felt, and throughout the bulk of middle phase, from where it merely migrates to the tube wall; however, we have also seen the densest phase precipitate on the interface between middle phase (phase 2) and upper phase (phase 1). Thus nucleation and density relations determine whether a given configuration can be produced by temperature management.

Ternary Test System

C. D. Manning (2) observed that n-butanol-n-hexdecane-water mixtures split at 23°C into three liquid phases over a considerable range of composi-

tion. An advantage of a ternary system is that the three coexisting phases and the respective interfacial tensions are invariant at a given temperature and pressure, as codified in Gibbs' phase rule.

Ternary diagrams were constructed from the results of mixing n-butanol, n-hexadecane, and water in different volume proportions, thermostatting them, vigorously shaking them, and allowing several days at constant temperature (±0.2°C) for final equilibration. The resulting diagram for 23°C is shown in Figure 3 with the direction of movement of the three-phase compositions with an increase in temperature. Analyses of the composition of each phase at the invariant points are given in Table I; densities are given in Table II.

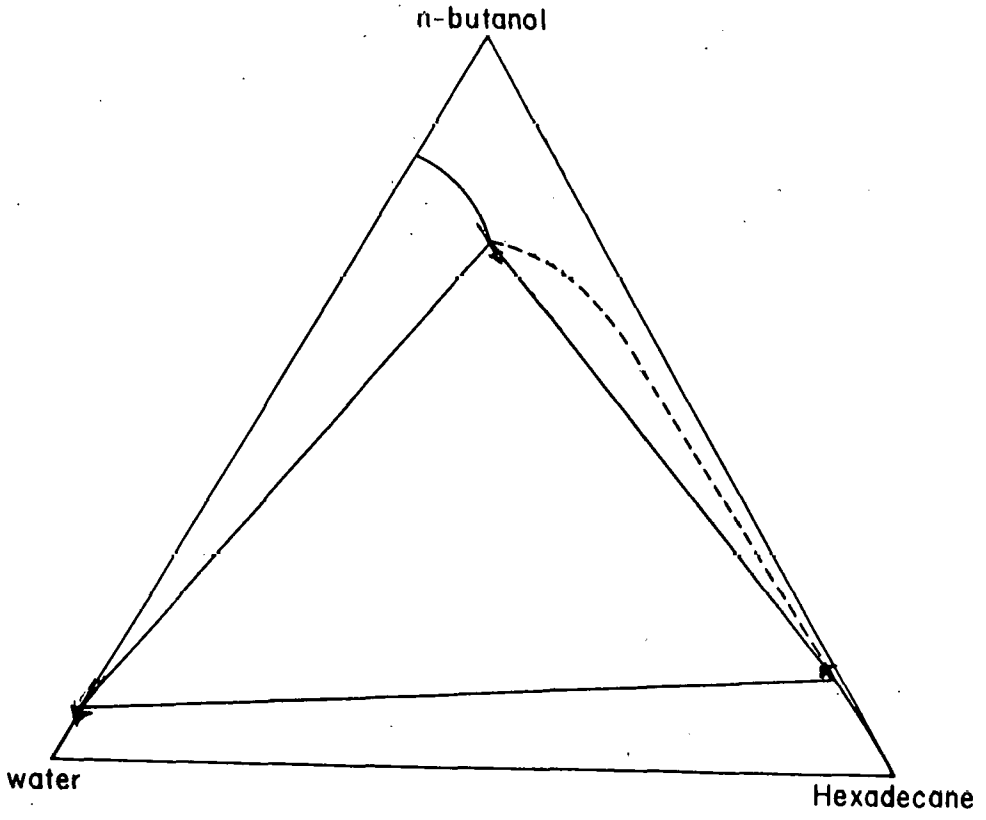

Figure 3. Phase diagram of n-butanol, water and hexadecane in weight percents, at 23°C; the direction of the change in composition of each phase with an increase in temperature is shown by the arrows.

The outcomes of phase formation experiments are summarized in Figure 4. When upper (hexadecane-rich) and middle (n-butanol-rich) phases were loaded and spun in the sample tube, increasing the temperature caused lower (water-rich) phase to precipitate at the tube wall and throughout the middle phase, and no configuration of interest arose. However, in several quaternary alcohol-hydrocarbon-water-salt systems (5) the lower phase formed at the interface between middle phase and upper phase drop as outwardly pendant lenses—Figure 4(a). Moreover, as the amount of lower phase increased the lenses became unstable and eventually "sank" to the tube wall. When lower and middle phases

		18°C	23°C	30°C
UPPER PHASE	water	0.66±0.06	0.75±0.05	0.80±0.04
	n-butanol	11.6±0.1	13.4±0.3	15.4±0.5
	n-hexadecane	87.77±0.05	85.9±0.3	83.8±0.5
MIDDLE PHASE	water	13.24±0.05	12.9±0.1	12.75±0.06
	n-butanol	73.3±0.2	72.1±0.4	70.7±0.3
	n-hexadecane	13.5±0.1	15.0±0.4	16.6±0.3
LOWER PHASE	water	92.49±0.04	92.88±0.04	93.32±0.09
	n-butanol	7.51±0.04	7.12±0.04	6.69±0.09
	n-hexadecane	$<3\times10^{-3}$	$<3\times10^{-3}$	$<3\times10^{-3}$

Table I. Compositions of phases at the invariant point at 18°, 23°, and 30°C.

	18°C	23°C	30°C
UPPER PHASE	0.7791	0.7766	0.7728
MIDDLE PHASE	0.8279	0.8239	0.8167
LOWER PHASE	0.9879	0.9868	0.9852

Table II. Densities of phases in g/cm^3 at invariant point at 18°, 23°, and 30°C.

were loaded in the sample tube, decreasing the temperature brought precipitation of upper phase as patch lenses and some of these appeared to end up as disjoint drops on the rotation axis, both inside and outside the original drop of middle phase. This is shown in Figure 4(b).

More interesting is the outcome of warming a spinning tube loaded with upper and lower phases, shown in Figure 4(c). Middle phase is first observable as patch lenses, *not* as a continuous thin layer around the drop. Thus at supersaturation at which microscopically visible patch lenses can persist, the inequality $\sigma_{13} < \sigma_{12} + \sigma_{23}$ holds. This is in apparent contradiction of Antonov's rule, which, as is shown in the next section, holds for this ternary system. However, Antonov's rule takes no heed of curvature effects. In the experiment, the lens-to-thin-layer transition may take place because the

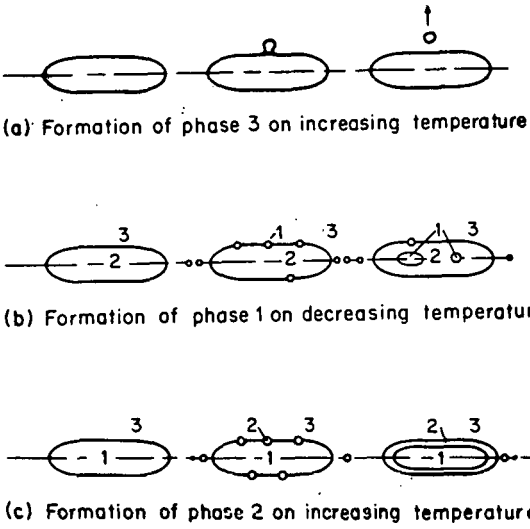

Figure 4. Formation of third phase by changing temperature with two phases in gyrostatic equilibrium inside a spinning tube.

amount of middle phase grows so that a continuous layer takes over from the lenses; alternatively, the transition may take place because the perfect wetting temperature is reached (31). In this case, Antonov's rule should hold above such temperature.

Interfacial Tension Measurements

Interfacial tensions in the ternary system were measured as functions of alcohol concentration. Samples were prepared by vigorous hand-mixing of n-butanol and equal volumes of n-hexadecane and water. Moderately persistent macroemulsions were encountered in specimens of less than 1 vol. % n-butanol; this observation suggests the presence of traces of an interfacially-active impurity. In almost all measurements the tension decreased slightly from the initial value and reached its final, steady value within a hour. Figure 5 records interfacial tension versus n-butanol concentration in the two- and three-phase regions. Tension fell smoothly from 41.9 dyne/cm at 0.05 vol. % to 3.54 dyne/cm at 10 vol. % NBA. Moreover, the two-phase interfacial tension approached that between the lower and upper phases in the three-phase region as the bottom tieline was approached. Interfacial tensions in the three-phase region remained constant with increasing alcohol concentration as required by the Phase rule. Furthermore, they agreed, within experimental error, with Antonov's rule (see Table III).

Antonov's rule was also tested in several quaternary alcohol-hydrocarbon-water-sodium chloride systems in which the three-phase region was traversed by increasing the NaCl concentration. Results are reported in Table IV. Of course, interfacial tensions do not remain constant as the salinity of the system is varied. However, in all the systems examined, Antonov's rule holds within the precision of the measurements throughout the entire three-phase region. It is noteworthy that a thin film of middle phase surrounding a spinning drop of upper phase was frequently seen during measurement of the tension between the upper and lower phases, i.e. σ_{13}. Whenever this film formed, Antonov's rule was valid. Thin films of middle phase be-

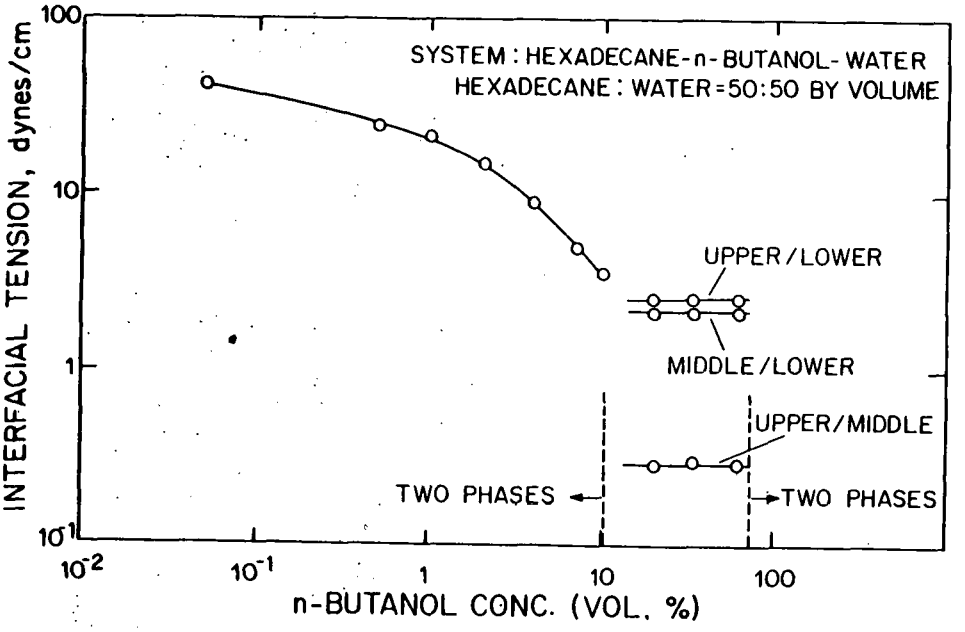

Figure 5. Interfacial tensions in n-butanol-n-hexadecane-water system at 23° C, when water and hexadecane are kept in the ratio 1:1 by volume.

	% uncertainty	% error estimated
σ_{12} = 0.287±0.007	2.4	2.8
σ_{23} = 2.120±0.015	0.7	1.7
$\sigma_{12}+\sigma_{23}$ = 2.40±0.017	0.7	—
σ_{13} = 2.39±0.02	0.4	1.7

Table III. Interfacial tensions at 23°C in the three-phase region of the n-butanol-n-hexadecane-water system. The ranges given are standard deviations.

tween the upper and lower phases in alcohol systems were also detected by Lang et al. (16) while measuring σ_{13} by the capillary rise method; in all these cases, $\sigma_{13} = \sigma_{12} + \sigma_{23}$. This evidence supports the argument given above that a thin layer of phase 2 or a thin-film behaving almost as a layer of phase 2 in the sense that Eq. (14) holds must form at the 1-3 interface whenever Antonov's rule holds.

It is of interest to compare the interfacial tension measurements by the spinning drop method reported here with similar ones made elesewhere with the capillary rise technique (16). So we estimated the precision of the spinning drop method as carried out with the instruments we used. The estimated errors are ±0.0001 cm in apparent drop diameter D_{app} owing to resolution of the microscope; an additional 0.3% because of eccentricity in the sample tube;

SYSTEM: n-PROPANOL-n-OCTANE-BRINE				
Brine conc. cg NaCl/ml	σ_{12} dyne/cm	σ_{23} dyne/cm	$\sigma_{12}+\sigma_{23}$ dyne/cm	σ_{13} dyne/cm
5	0.285±0.007	0.251±0.006	0.536±0.009	0.553±0.012
6	0.248±0.010	0.448±0.009	0.696±0.013	0.691±0.047
7	0.146±0.004	0.628±0.025	0.774±0.025	0.767±0.020
9	0.034±0.002	1.01±0.020	1.044±0.020	1.12±0.050

SYSTEM: n-PROPANOL-n-DODECANE-BRINE				
Brine conc. cg NaCl/ml	σ_{12} dyne/cm	σ_{23} dyne/cm	$\sigma_{12}+\sigma_{23}$ dyne/cm	σ_{13} dyne/cm
10	1.47±0.02	0.384±0.013	1.854±0.024	1.90±0.04
12	1.26±0.045	0.743±0.019	2.003±0.049	2.01±0.05
14	1.18±0.02	1.02±0.02	2.20±0.028	2.05±0.08
16	0.966±0.019	1.30±0.05	2.266±0.054	2.15±0.04
20	0.727±0.008	1.95±0.06	2.677±0.06	2.75±0.044

SYSTEM: t-BUTANOL-n-DODECANE-BRINE				
Brine conc. cg NaCl/ml	σ_{12} dyne/cm	σ_{23} dyne/cm	$\sigma_{12}+\sigma_{23}$ dyne/cm	σ_{13} dyne/cm
3.5	0.083±0.009	0.183±0.008	0.266±0.012	0.275±0.005
4.0	0.176±0.008	0.136±0.003	0.312±0.0085	0.322±0.018

Table IV. Interfacial tensions at 25°C of three-phase alcohol-hydrocarbon-water-sodium chloride systems. The ranges given are standard deviations.

about 0.7% in angular velocity, Ω, in the University of Texas instrument, and less than 0.3% in the air-bearing instrument, as determined by means of an auxiliary frequency counter; 0.00014 g/cm^3 in $\Delta\rho$; and less than 0.02% in the drop magnification factor measured as refractive index η of the denser phase (3,7,22). The error in the basic working formula (20)

$$\sigma = \frac{\Omega^2 D_{app}^3 \Delta\rho}{32\eta^3} \tag{6}$$

is less than 0.1% when drop length-to-diameter ratio L/D is greater than 5, and less than 0.4% when L/D is greater than 4. The total estimated error is plotted in Figure 6, and the particular estimates for the drop sizes employed (reported only for the ternary system) are listed in Table III. (These do not take into account whatever variations of temperature existed in the spinning drop method). The results in Table III show that the statistical measures of uncertainty agree with the independently estimated error of the method.

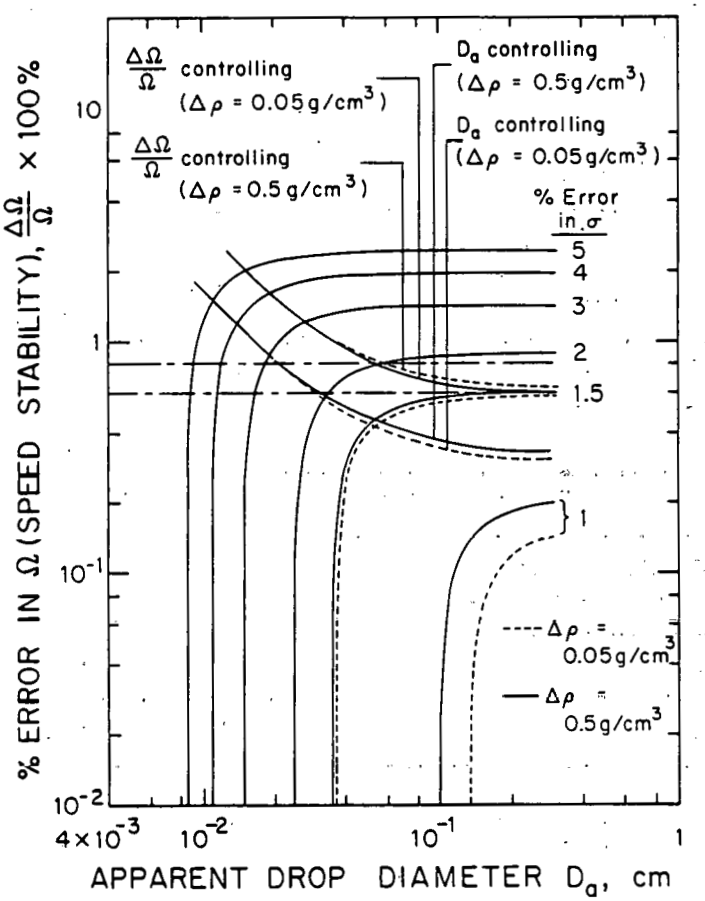

Figure 6. Contours of constant estimated error in tension, on the basis of uncertainties in measuring drop diameter and rotational speed in the spinning drop apparatus, and density difference and refractive index by separate means.

The conclusion is that the precision of the spinning drop method is superior to that readily attainable with the capillary rise method (16), which in addition is prey to uncertainties stemming from wetting phenomena. Moreover, the spinning drop method has advantages for careful studies of triphasic liquid systems as well as for studying the wetting of fluid interfaces, Antonov's rule, and the inequalities it separates.

Appendix A: Derivation of the Formula for Apparent Tension σ'_{13}

A typical profile of half of a spinning drop of phase 1 encased in a thin layer of bulk phase 2, where $\rho_1 < \rho_2 < \rho_3$, is shown in Figure 7.

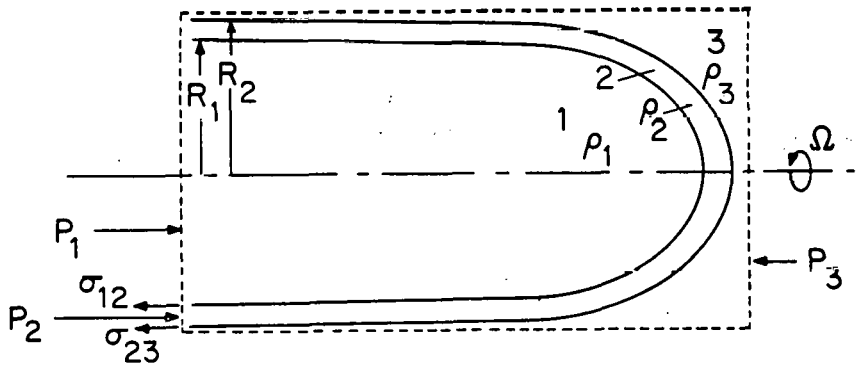

Figure 7. Spinning double drop of phase 1 entirely contained within a thin layer of bulk phase 2 which is surrounded by still denser phase 3 ($\rho_1 < \rho_2 < \rho_3$). The control surface shown cuts the drop at its equatorial phase and encloses the right half.

A control surface passing through the equatorial phase and enclosing the entire half of the drop is relevant. At gyrostatic equilibrium the pressure differences across the two interfaces at radial distance r are, respectively,

$$P_1(r) - P_2(r) = \frac{\Delta\rho_{12}\Omega^2}{2}(R_1^2 - r^2) + \sigma_{12}\left(\frac{1}{R_1} + \frac{1}{R_1'}\right), \quad r < R_1 \qquad \text{(I)}$$

and

$$P_2(r) - P_3(r) = \frac{\Delta\rho_{23}\Omega^2}{2}(R_2^2 - r^2) + \sigma_{23}\left(\frac{1}{R_2} + \frac{1}{R_2'}\right), \quad r < R_2 \qquad \text{(II)}$$

where R_1' and R_2' are the meridional radii of curvature of the 1-2 and 2-3 menisci, respectively, at the equatorial plane. Balancing of forces on the volume within the control surface gives

$$2\pi R_1\sigma_{12} + 2\pi R_2\sigma_{23} = \int_0^{R_1}(P_1 - P_2)2\pi r dr + \int_{R_1}^{R_2}(P_2 - P_3)2\pi r dr. \qquad \text{(III)}$$

Combining these equations, integrating, letting $R_1/R_2 \equiv 1 - \varepsilon$ and $R_1'/R_2' \equiv 1 - \varepsilon'$, neglecting second and higher orders of ε and ε', and substituting $\Delta\rho_{13} = \Delta\rho_{12} + \Delta\rho_{23}$ lead to

$$\sigma_{12} + \sigma_{23} = \frac{\Omega^2 R_2^2 \Delta\rho_{13}}{4} \left(1 - \frac{R_2}{R_2'}\right)^{-1} - \varepsilon K \qquad \text{(IV)}$$

where, for drop length-to-diameter L/D greater than 4,

$$K \approx 2\left(1 - \frac{R_2}{R_2'}\right)^{-1} \left[\sigma_{12} + \frac{\sigma_{12}}{2} \left(1 + \frac{R_2}{R_2'}\right) + \frac{\sigma_{12}}{2} \left(\frac{R_2}{R_2'}\right) \left(1 - \frac{\varepsilon'}{\varepsilon}\right) \right] \qquad \text{(V)}$$

The first term on the right side of equation (IV) is the apparent tension σ_{13}' measured when an imperceptibly thick film of bulk phase is present, i.e. when $R_1 \to R_2$. Plainly this value is greater than $\sigma_{12} + \sigma_{23}$ by the quantity εK. Because εK is small, this inequality may not be obvious experimentally. As $\varepsilon \to 0$, R_1 and R_2 approach a new radius R_3, and we have from (IV) that

$$\sigma_{12} + \sigma_{23} = \frac{\Omega^2 R_3^2 \Delta\rho_{13}}{4} \left(1 - \frac{R_3}{R_3'}\right) = \sigma_{13} \qquad \text{(VI)}$$

which is just the limit as a thin layer of bulk phase 2 is left encapsulating the drop.

When the inner drop of a double drop is optically resolvable, its apparent diameter is not its true diameter, owing to the cylindrical lens effect of the layer of phase 2, the outer annulus of phase 3 and the wall of the sample holder. By ray optics (3,22) it can be shown that the magnification factors for the inner and outer menisci are

$$\frac{D_{1app}}{D_1} = \eta_2 \ , \quad \frac{D_{2app}}{D_2} = \eta_3$$

where D_{1app} and D_{2app} are the apparent diameters and η_2 and η_3 are the refractive indices of the respective phases referred to air. These refractive indices can be measured precisely outside the spinning drop apparatus.

References Cited in Section VII

1. Anderson, D., Bidner, M. S., Davis, H. T., Manning, C. D. and Scriven, L. E., SPE paper 5811 presented at the Society of Petroleum Engineers Symposium on Improved Oil Recovery, Tulsa, OK, March 22-24, 1976.

2. Manning, C. D., M.S. thesis, University of Minnesota (1976).

3. Seeto, Y., M.S. thesis, University of Minnesota (1977).

4. Puig, J. E., Franses, E. I., Davis, H. T., Miller, W. G. and Scriven, L. E., Soc. Pet. Eng. J. 19, 71-82 (1979).

5. Puig, J. E., Ph.D. thesis, University of Minnesota (1982).

6. Cayias, J. L., Schechter, R. S. and Wade, W. H. in Adsorption at Interfaces, K. L. Mittal, ed., ACS Symposium Series 8, 234-247 (1975).

7. Seeto, Y. and Scriven, L. E., Rev. Sci. Inst. 53, 80-84 (1982).

8. Knickerbocker, B. M., Pesheck, C. V., Scriven, L. E. and Davis, H. T., J. Phys. Chem. 83, 1984 (1979).

9. Princen, H. M. in Surface and Colloid Science, Vol. 2, E. Matijevic, ed., Wiley-Interscience, New York, pp. 1-84 (1969).

10. Pujado, P. R. and Scriven, L. E., J. Coll. Interf. Sci. 40, 82-98 (1972).

11. Torza, S. and Mason, S. G., J. Coll. Interf. Sci. 33, 67-83 (1970).

12. Adam, N. K., The Physics and Chemistry of Surfaces, 3rd ed., Oxford University Press, London (1941).

13. Adamson, A. W., Physical Chemistry of Surfaces, 3rd ed., Wiley-Interscience, New York (1976).

14. Davies, J. T. and Rideal, E. K., Interfacial Phenomena, Academic Press, New York (1963).

15. Defay, R., Prigogine, I., Bellemans, A. and Everett, D. H., Surface Tension and Adsorption, Longmans, Green and Co., London (1966).

16. Lang, J. C., Jr., Lim, P. K. and Widom, B., J. Phys. Chem. 80, 1719-1723 (1976).

17. Widom, B., J. Phys. Chem. 62, 1332-1336 (1975).

18. Widom, B., Phys. Rev. Lett. 34, 999-1002 (1975).

19. Bellocq, A. M., Bourbon, D. and Lemanceau, B., J. Disp. Sci. Techn. 2, 27-52 (1981).

20. Manning, C. D. and Scriven, L. E., Rev. Sci. Inst. 48, 1699-1705 (1977).

21. Pesheck, C. V., Lind, M. I., Davis, H. T. and Scriven, L. E., J. Phys. Chem., to be submitted (1983).

22. Seeto, Y., Puig, J. E. and Scriven, L. E., J. Coll. Interf. Sci., to be published (1983).

23. Hemker, D. L., Puig, J. E., Davis, H. T. and Scriven, L. E., Paper No. 11c, 86th National AIChE Meeting, Houston, TX, April 5-9, 1979; also J. Phys. Chem., submitted (1982).

24. Antonov, G. N., J. Chim. Phys. 5, 372-385 (1907).

25. Bartell, F. E., Case, L. O. and Brown, H., J. Am. Chem. Soc. 55, 2769-2776 (1933).

26. Butler, E. B., J. Phys. Chem. 67, 1419-1425 (1963).

27. Donahue, D. J. and Bartell, F. E., J. Phys. Chem. 56, 480-484 (1952).

28. Healy, R. M. and Reed, R. L., Soc. Pet. Eng. J. 14, 491-501 (1974); Trans. AIME, Vol. 257.

29. Collins, S. H., M.S. Thesis, University of Texas, Arlington (1976).

30. Bongiorno, V., Scriven, L. E. and Davis, H. T., J. Coll. Interf. Sci. 57, 462-475 (1976).

31. Teletzke, G. F., Scriven, L. E. and Davis, H. T., J. Coll. Interf. Sci. 87, 550-571 (1982).

32. Falls, A. H., Scriven, L. E. and Davis, H. T., J. Chem. Phys., accepted for publication (1983).

VIII. HOW LIQUIDS SPREAD ON SOLIDS

Introduction

Equilibrium configurations of liquid drops, layers, and films on solid surfaces are described by the augmented Young-Laplace equation (1-3), which represents the balance among capillary pressure, hydrostatic pressure, and disjoining pressure. Capillary pressure is the resultant of surface tension in a curved fluid interface; hydrostatic pressure reflects the action of gravity and other body forces; disjoining pressure stems from the fluid/solid intermolecular forces in very thin liquid films at rest. Liquids are seldom deposited on solids in equilibrium configurations, and when they are not it is often important to know the way in which the liquid flows into its equilibrium state, and the time needed for its meniscus to come to rest.

If initially the liquid appears not to cover the entire surface of the solid, the flow process is commonly called spreading. On the other hand, if initially it does appear to cover the entire surface, the process by which it attains mechanical equilibrium is commonly called surface levelling when in the final state it covers the surface totally, and dewetting when finally there appear to be uncovered areas. These different processes are familiar in everyday experience. Spreading is the topic of this paper. The extension to surface levelling and dewetting is treated elsewhere (4).

Since Hardy's (5) pioneering observations over a half-century ago there have been numerous experimental studies of how liquids spread on solids and several attempts at theoretically describing the various mechanisms involved. But until now no theory that accounts for all known driving forces of spreading has been presented.

In cataloging the mechanisms it is convenient to define three classes of spreading: primary, secondary, and bulk. Primary spreading refers to the way the first molecular layer or so of liquid reaches the solid. In the case of a viscous nonvolatile liquid, primary spreading is by surface diffusion (6-9). If the liquid is volatile or a condensible vapor is present, primary spreading occurs by condensation of an adsorbed film (5).

Secondary spreading refers to the mechanisms by which grow liquid films ranging from several molecules thick up to several microns thick. This action is driven either by a disjoining pressure gradient or by a surface tension gradient. Fluid films thinner than about one micron are inhomogeneous in density or composition and thus are subject to anisotropic stress states peculiar to their microstructure. Disjoining pressure gradients arise from the variation of the aggregate of fluid-solid and fluid-fluid intermolecular forces with film thickness (10). Surface tension gradients arise from either temperature gradients along the solid (11) or composition gradients caused by evaporation of a volatile component (6), or by the composition of the emplaced bulk liquid being different from that of the primary film upon which it is set (5,12,13).

Bulk spreading refers to flow driven by capillarity and gravity, the dominant driving forces of flow in films thicker than a micron.

In this paper we present a theory of the spreading of liquids on smooth, clean solids which accounts for all of the mechanisms just described. The theory is useful for identifying which mechanisms govern the spreading behavior of a given fluid-solid system. We illustrate its application by comparing its predictions with experimental observations of water spreading on glass (14,13) and of oils spreading on high-energy surfaces (6,11). In addition, we use the theory to interpret the results of Deryagin's (15-17) blowing-off experiment for studying thin-film rheology.

Equations of Thin-Film Shape and Evolution

We begin by deriving the equation governing the evolution of the shape of a fluid film thin enough to be subject to forces that originate in fluid microstructure, i.e., special forces which arise when the film's thickness is comparable in magnitude to the range of intermolecular forces (0.1 μm for London-van der Waals dispersion forces, 1 μm or more for electrostatic forces), but thick enough to have essentially the viscosity of bulk liquid. According to the molecular theory of thin-films, these assumptions are valid when a film is thicker than about five to ten molecules (10,18). Later in this section we generalize the equation to films so thin that they have thickness-dependent viscosity. Throughout this paper we restrict our attention to single component fluids on solid substrates.

The anisotropy and nonuniformity of the pressure tensor in a thin-film distinguish a thin-film from bulk fluid. To find the equations of film shape and evolution we follow the strategy of Higgins and Scriven (19), which we have recently generalized to thin-films (10). There are two such equations. The first, which expresses conservation of matter when there is no mass transfer across the interface, is the integral form of the kinematic condition; for flow translationally symmetric in the z-direction it is

$$\frac{\partial h}{\partial t} + \frac{\partial}{\partial x}\int_0^h u\,dy = 0 \quad , \tag{1}$$

and for an axially symmetric flow it is

$$\frac{\partial h}{\partial t} + \frac{1}{r}\frac{\partial}{\partial r}\int_0^h ur\,dz = 0 \quad . \tag{2}$$

The second equation expresses the balance of viscous, inertial, gravitational, capillary, and microstructural fluid forces and momentum fluxes acting on a slice of film of differential thickness in the x- or r-direction, and is an integrodifferential momentum equation. When the liquid film is bounded by gas which exerts negligible shear, for a translationally symmetric flow the equation is (10):

$$\gamma_{LV} h \frac{\partial}{\partial x}(2\mathcal{H}) - \frac{\partial \gamma_F}{\partial x} = \frac{\partial}{\partial t}\int_0^h \rho u dy + \frac{\partial}{\partial x}\int_0^h (\rho u^2 - \rho v^2 + \tau_{yy} - \tau_{xx})dy$$

$$+ \frac{\partial^2}{\partial x^2}\int_0^h \int_y^h (\rho uv - \tau_{xy})dy'dy + \frac{\partial^2}{\partial t \partial x}\int_0^h \int_y^h \rho u dy'dy - \frac{\partial}{\partial x}(\rho g_y h^2/2)$$

$$- \rho g_x h - [\rho uv - \tau_{xy}]_{y=0} \quad , \tag{3}$$

$$2\mathcal{H} = h_{xx}/(1 + h_x^2)^{3/2} \quad ;$$

and for an axially symmetric flow it is

$$\gamma_{LV} h \frac{\partial}{\partial r}(2\mathcal{H}) - \frac{\partial \gamma_F}{\partial r} = \frac{\partial}{\partial t}\int_0^h \rho u dz + \rho \int_0^h \frac{u^2}{r} dz$$

$$+ \frac{\partial}{\partial r}\int_0^h (\rho u^2 - \rho v^2 + \tau_{zz} - \tau_{rr})dz - \frac{1}{r}\int_0^h \tau_{rr} dz$$

$$+ \frac{\partial^2}{\partial r^2}\int_0^h \int_z^h (\rho uv - \tau_{rz})dz'dz - \frac{1}{r}\int_0^h \int_z^h \tau_{rz} + \frac{\partial^2}{\partial t \partial x}\int_0^h \int_z^h \rho v dz'dz$$

$$- \frac{\partial}{\partial x}(\rho g_z h^2/2) - \rho g_r h - [\rho uv - \tau_{rz}]_{z=0} \quad . \tag{4}$$

$$2\mathcal{H} = h_{rr}/(1 + h_r^2)^{3/2} + h_r/[r(1 + h_r^2)^{1/2}] \quad .$$

The quantities in these equations are defined in Fig. 1. The τ_{ij} are the components of viscous stress tensor, γ_{LV} is the liquid vapor interfacial tension, ρ is density, and $\mathcal{H}$ is the mean curvature of the interface. The film tension

$$\gamma_F \equiv \int_0^h (P_{xx} - P_B)dy$$

$$\equiv \int_0^\infty (P_{xx} - P_{yy} + \int_y^\infty \rho \frac{\partial u_e}{\partial y'} dy')dy \quad , \tag{5}$$

where P_{xx} and P_{yy} are components of the pressure tensor and u_e is the interaction potential between fluid and solid molecules, accounts for microstructural fluid forces, i.e. the anisotropy and nonuniformity of the pressure tensor. The velocity field $\underline{v}$, the viscous stress field $\underline{\underline{\tau}}$, the film tension γ_F, and

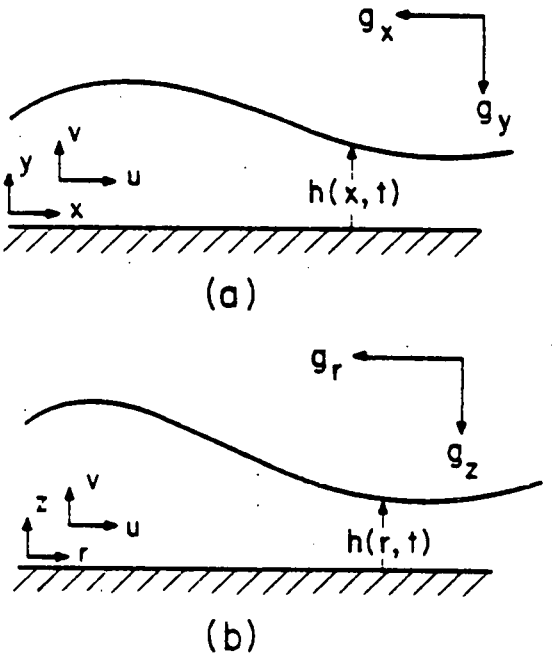

Figure 1. Basic quantities in thin-film: (a) translationally symmetric; (b) axially symmetric.

the interface location h are unknown variables in these equations. To reduce them to equations of interfacial shape and motion in terms of solely the interface location h(x,t) requires specifying constitutive relations for $\underline{\underline{\tau}}$ as a function of $\underline{v}$ and γ_F as a function of h and the velocity field. We use the Newtonian constitutive relation for $\underline{\underline{\tau}}$ and take viscosity to be independent of film thickness. If the thickness varies slowly, i.e. $\partial h/\partial x \ll 1$, the isothermal Gibbs (20) adsorption equation for a single-component planar film

$$d\gamma_F = - \Gamma \, d\mu \quad , \tag{6}$$

where Γ is surface excess mass

$$\Gamma \equiv \int_0^\infty [\rho(y) - \rho_B] dy \quad , \tag{7}$$

can be used to relate changes in film tension to changes in chemical potential μ. Equation (6) is often written in an alternative form that incorporates definitions of film thickness

$$h \equiv \Gamma / \rho_L^S \quad , \tag{8}$$

where ρ_L^S is the density of saturated bulk liquid, and of disjoining pressure, (1,21)

$$\Pi = -\rho_L^S[\mu(h,T) - \mu(h=\infty,T)] \ , \tag{9}$$

If Π depends on h alone, it follows that

$$\frac{\partial \gamma_F}{\partial x} = h\frac{\partial \Pi}{\partial x} = h\frac{\partial \Pi}{\partial h}\frac{\partial h}{\partial x} \ . \tag{10}$$

Therefore, in the small slope approximation the constitutive relation for γ_F is determined once the disjoining pressure function $\Pi(h)$ is known. The dependence of this function on the constitution of the vapor, liquid and solid is sketched in the next section.

Provided $\partial h/\partial x << 1$ so that the small-slope approximation does apply, it is also appropriate to adopt as a first approximation a lubrication-type velocity field, i.e., a locally variable combination of Couette and Poiseuille flow:

$$u(x,y) = F_0(x) + yF_1(x) + y^2F_2(x) \ . \tag{11}$$

The no-slip condition at the solid surface y=0 sets $F_0(x) \equiv 0$. The condition of vanishing shear stress at the interface y=h provides a relationship between $F_1(x)$ and $F_2(x)$. A second relationship between $F_1(x)$ and $F_2(x)$ comes from the integrodifferential momentum equation (3) or (4). Substituting the resulting velocity profile in the integral kinematic condition yields the equation of interfacial shape and motion: for translationally symmetric flows it is

$$\frac{\partial h}{\partial t} = \frac{\partial}{\partial x}\left\{\frac{h^3}{3\eta}\left[-\frac{\partial}{\partial x}(2\mathcal{H})\gamma_{LV} - \frac{\partial \Pi}{\partial h}\frac{\partial h}{\partial x} + \rho g_y\frac{\partial h}{\partial x} + \rho g_x\right]\right\} \ , \tag{12}$$

while for axially symmetric flows it is

$$\frac{\partial h}{\partial t} = \frac{1}{r}\frac{\partial}{\partial r}\left\{\frac{rh^3}{3\eta}\left[-\frac{\partial}{\partial r}(2\mathcal{H})\gamma_{LV} - \frac{\partial \Pi}{\partial h}\frac{\partial h}{\partial r} + \rho g_z\frac{\partial h}{\partial x} + \rho g_r\right]\right\} \ . \tag{13}$$

Here η is viscosity.

The result in both cases is a nonlinear, one-dimensional, parabolic equation for diffusion of film thickness. Evolution of the film profile is described by solutions of either Eq. (12) or Eq. (13), to both of which capillarity contributes a fourth-derivative term because the mean curvature itself contains a second derivative. The quantity in brackets is the volu-

metric flux in the film at position x or r; this flux is the product of the driving forces for flow (capillary pressure, disjoining pressure, and gravitational potential gradients) and the diffusivity of thickness, which in this case is a viscous conductance inversely proportional to viscosity η and strongly dependent on film thickness h.

Equations (12) and (13) are derived by assuming the volumetric flux is related to the driving forces for flow by hydrodynamic laws in the application of which the film viscosity is presumed not to depend on its thickness. As mentioned above, this presumption is not warranted when the film is thinner than about 5-10 molecules. In films approaching molecular dimensions the flow of fluid on the solid is more appropriately considered a surface diffusion process rather than a hydrodynamic one. The continuity equation of a single-component fluid on a solid surface is (22)

$$\frac{\partial \Gamma}{\partial t} = - \nabla_s \cdot \underline{J}_s \quad , \tag{14}$$

where $\underline{J}_s$ is surface excess mass flux relative to a frame of reference in which the solid is at rest and ∇_s is the surface gradient operator. According to linear transport theory (23), the diffusion flux for small gradients in chemical potentials is given by

$$\underline{J}_s = - L_s \nabla_s \mu \tag{15}$$

where L_s is the surface transport coefficient which in general depends on surface excess mass (cf. Eq. (7)). In conventional applications of linear transport theory it is assumed that μ is the local equilibrium chemical potential. Inserting Eq. (15) into Eq. (14) yields

$$\frac{\partial \Gamma}{\partial t} = \nabla_s \cdot (L_s \nabla_s \mu) \quad . \tag{16}$$

Comparing Eq. (16) with Eqs. (12) and (13) in view of the definition of film thickness, Eq. (7), makes it plain that Eq. (16) is uniformly valid for all film thicknesses. In the limit of large h — which is what we have previously called a thick thin-film (10,18) — L_s is given by

$$L_s = \frac{\rho_L h^3}{3\eta} \quad , \tag{17}$$

and μ includes capillary, gravitational, and disjoining contributions:

$$\mu - \mu_o = \frac{1}{\rho_L} [2\gamma_{LV} - \Pi(h) + \rho g_y (h-h_o)\ \rho g_x (x-x_o)] \quad , \tag{18}$$

μ_o is the value of the chemical potential at position x_o.

In the limit of small h — which is what we have previous referred to as an adsorbed film — we assume that capillary and gravitational contributions to the chemical potential can be absorbed in disjoining potential. Then Eq. (16) can be rewritten

$$\frac{\partial h}{\partial t} = \nabla_s \cdot (L_s \frac{\partial \pi}{\partial h} \nabla_s h) = \nabla_s \cdot (D_s \nabla_s h) \quad , \tag{19}$$

where $D_s \equiv L_s \, \partial\Pi/\partial h$ is the surface diffusion coefficient. In the limit $h \to 0$, D_s can be estimated from a simple model in which molecules are imagined to diffuse by hopping from adsorption site to adsorption site on the solid (24).

Between the thick film regime and the submonolayer regime — which is what we previously have referred to as a thin thin-film (10,18), the behavior of L_s or D_s is presently unknown and presents a challenging problem in nonequilibrium molecular theory. In such cases, however, L_s or D_s can be regarded as phenomenological coefficients, the thickness dependence of which can be adjusted to account for experimentally observed flows. This we explore in a subsequent section.

Dimensionless variables are convenient:

$$h' = h/H \quad , \quad x' = x/H \quad , \quad 2\mathcal{H}' = 2\mathcal{H}H \quad , \quad t' = t/T \quad , \tag{20}$$

where H is a characteristic film thickness and T is a characteristic time. In the next section we explain that disjoining pressure can be modeled as

$$\Pi(h) = \sum_{h=1}^{4} \frac{A_n}{h^n} \tag{21}$$

for many fluid-solid combinations. When this is the case,

$$\frac{H^2}{\gamma_{LV}} \frac{\partial \Pi}{\partial h} = \frac{L_1 h_x}{h^2} + \sum_{n=2}^{4} \left(\frac{L_n}{H}\right)^{n-1} \frac{h_x}{h^{n+1}} \quad , \tag{22}$$

where $L_n^{n-1} \equiv nA_n/\gamma_{LV}$ are characteristic lengths of the various types of intermolecular interactions. With these choices Eq. (12) becomes

$$\frac{\eta H}{\gamma_{LV} T}\frac{\partial h'}{\partial t'} = \frac{\partial}{\partial x'}\left\{\frac{h'^3}{3}\left[-\frac{\partial}{\partial x'}(2\mathcal{H}') - \frac{L_1 h'_{x'}}{h'^2} - \sum_{n=2}^{4}\left(\frac{L_n}{H}\right)^{n-1}\frac{h'_{x'}}{h'^{n+1}} + G_y\frac{\partial h'}{\partial x'} + G_x\right]\right\}, \tag{23}$$

where $G_y \equiv \rho g_y H^2/\gamma_{LV}$ and $G_x \equiv \rho g_x H^2/\gamma_{LV}$. The characteristic film thickness H can be chosen equal to one of the L_n, say L_3, and the characteristic time can be chosen $T = \eta H/\gamma_{LV} = \eta L_n/\gamma_{LV}$. With these choices, there are five dimensionless parameters in Eq. (23), three L_n, G_y, and G_x. This simple dimensional analysis indicates that when one contribution to disjoining pressure dominates the others and gravitational driving forces are small, the characteristic time for flows in geometrically similar configurations is proportional to viscosity times a length characteristic of intermolecular forces, divided by interfacial tension. This has been observed in numerous experiments (13).

Elsewhere (10) we examined stationary-state solutions of Eq. (12), i.e., flows for which $\partial h/\partial t = 0$ in a frame of reference fixed with respect to a meniscus moving with uniform velocity U. These flows satisfy the condition

$$\frac{dh}{dt} = \frac{\partial h}{\partial t} + U\frac{\partial h}{\partial x} = 0 \tag{24}$$

Substituting Eq. (24) for $\partial h/\partial t$ in Eq. (12) and integrating leads to the augmented Landau-Levich equation

$$\frac{\partial}{\partial x}(2\mathcal{H}) + \frac{\partial \Pi}{\partial h}\frac{\partial h}{\partial x} = \frac{3U\eta}{\gamma_{LV}}\frac{h-h_\infty}{h^3} + \rho g_y\frac{\partial h}{\partial x} + \rho g_x \tag{25}$$

which governs the deposition of a film of uniform thickness h_∞ by the steady motion of a meniscus in a tube or slot, or by the steady withdrawal of a solid from a bath.

When surface tension gradients are present, as is always a likelihood in multicomponent films, or when the shear stress exerted by the gas at the interface is appreciable, as is the case in Deryagin's blowing-off experiment (to be discussed later), the tangential stress boundary condition at the interface, in small-slope approximation, is

$$\frac{\partial \gamma_{LV}}{\partial x} + \tau_f = \eta\left.\frac{\partial u}{\partial y}\right|_h, \tag{26}$$

where τ_i is the shear stress exerted by the gas on the liquid. Eq. (12) then becomes

$$\frac{\partial h}{\partial t} = \frac{\partial}{\partial x}\left\{\frac{h^3}{3\eta}\left[-\frac{\partial}{\partial x}\left(2\mathcal{H}\gamma_{LV}\right) - \frac{\partial \Pi}{\partial h}\frac{\partial h}{\partial x} + \rho g_y \frac{\partial h}{\partial x} + \rho g_x\right] - \left(\frac{\partial \gamma_{LV}}{\partial x} + \tau_i\right)\frac{h^2}{2\eta}\right\} \tag{27}$$

Thus the outcome is to add to Eq. (12) a convective term in which the convective velocity is proportional to the film thickness times the sum of the surface tension gradient and the interfacial shear stress.

Special versions of Eqs. (12), (13), and (27) have been used previously to study the spreading of liquid drops (25-27), the surface-tension-gradient-driven creep of a liquid up a vertical surface (11) and the blowing-off technique for studying thin-film rheology (15). Several investigators of spreading drops neglect microstructural fluid forces in Eqs. (12) and (13) (25-27). This leads to an unacceptable force singularity at the apparent line of contact where the meniscus seems to intersect the solid surface over which the liquid is moving. These authors use one of two approaches first suggested by Huh and Scriven (28) to remove the singularity. The first, and most popular, approach is to replace the no-slip condition near the apparent contact line with a Navier slip condition in which the slip coefficient distribution near the contact line is specified; others have preferred specifying a slip velocity distribution (29). Of course, such an approach provides no insight into the submicroscopic origins of the apparent slip. The second approach, which is the one used here, is to include microstructural fluid forces in a theory of spreading. This approach was previously attempted by Lopez, Miller and Ruckenstein (25), but they neglected capillarity and considered only a particular type of disjoining pressure function appropriate to nonpolar fluids. We show that capillarity and the form of the disjoining pressure function strongly affect spreading behavior.

Ludviksson and Lightfoot (11) also neglected capillarity and microstructural fluid forces in their analysis of surface tension gradient driven spreading, as did Deryagin (15) in his analysis of the blowing-off experiment. In Sections 5 and 6 we examine how these forces affect the interpretation of their experimental results.

The crux of our theory is the function chosen to describe how local disjoining pressure depends on the local film profile. Before turning to the analysis of specific cases, we review disjoining pressure functions for various substances.

Disjoining Pressure Functions

Disjoining pressure arises in molecular forces and is customarily divided into several contributions. The molecular contribution to disjoining pressure, Π_m, arises in long-range forces between neutral molecules, e.g., dispersion, induction and multipolar electrostatic forces, and is present in all thin-

films. The ionic-electrostatic contribution, Π_e, comes from the compression of electrostatic double layers if present. Finally a third contribution which is often called the structural component, Π_s, accounts for the forces not included in Π_m and Π_e, e.g., hydrogen bonding in water and alcohols and short-range repulsive forces significant in all films of molecular thickness.

Table 1 summarizes the different contributions and lists their approximate dependence on film thickness. The molecular origins and experimental measurements of the functions shown here we have reviewed elsewhere (10). Because the nonadditive interactions between individual contributions are not fully known, the total disjoining pressure in a thin-film is regarded in first approximation as the sum of the individual contributions. Each contribution can be positive or negative depending on the constitution of the three phases involved — the solid and the two fluids. Thus disjoinig pressure can vary with thickness and change signs in a variety of ways. Several representative possibilities have been catalogued by Dzyaloshinskii, Lifshitz and Pitaevskii (30). In this paper we restrict consideration to liquids that completely or perfectly wet the solid surface at equilibrium, i.e., systems for which the equilibrium apparent contact angle is 0°. Mohanty et al. (2) have shown that in such cases the disjoining pressure function is positive for all thicknesses. In addition we consider only disjoining pressure functions which are monotonically decreasing functions of film thickness, i.e., for which $\partial\Pi/\partial h < 0$ for all thicknesses.

Table 1. Contributions to Disjoining Pressure

Component	Origin	Approximate Dependence on h
Molecular Π_m	London-van der Waals dispersion including electromagnetic retardation	A_3/h^3, small h A_4/h^4, large h
Ionic-Electrostatic Π_e	Overlapping of double layers. Surface charge-dipole interaction	Ee^{-Kh} A_2/h^2, water
Structural Π_s	Short range forces. Hydrogen bonding	A_0 ln h A_1/h water

Spreading Liquid Drops: Water Drops on Glass

Marmur and Lelah (12,13) recently reported striking measurements of how drops of water, ethanol, and aqueous surfactant solutions spread on carefully cleaned glass slides in air partially saturated with the vapor of the liquid. Their experiments have antecedents in Hardy's (5) observations. They found that water drops spread faster on smaller surfaces — but as they went to larger glass slides they found the influence of size disappears. When they

placed a drop off-center on a small slide, it spread more rapidly toward the nearer edges of the slide.

The appropriate equation in this case is the film profile equation for axisymmetric flows, Eq. (13), with $g_r = 0$ because the experiments were done on a horizontal nonrotating surface. We obtain initial and boundary conditions by noting firstly that experiments by a number of researchers (31) reveal that a multilayer water film around 1-1.5 nm thick adsorbs on glass at the ambient conditions of Marmur and Lelah's experiment, namely, room temperature and 50% relative humidity; and secondly that a liquid film draped over any sharp edge is made much thinner there by curvature-induced capillary pressure (32), so that there is greatly increased resistance to flow over an edge. We therefore approximate the drop's initial profile as a spherical cap atop a primary film preadsorbed from the ambient vapor. To model Marmur and Lelah's experiments, we took the volume of the sphere-cap to be 0.01 cm^3, the area of its base to be 0.5 cm^2, and the thickness of the primary film to be 1 nm in the calculations reported here. We approximated the resistance to flow over the edge of the slide by requiring that there be no flow across the circular edge at r = L, where L is the size of the slide. The no-flow condition is satisfied by setting equal to zero the first and third r-derivatives of the film profile at r = L,

$$\left.\frac{\partial h}{\partial r}\right|_L = \left.\frac{\partial^3 h}{\partial r^3}\right|_L = 0 \quad . \tag{28}$$

There is also symmetry about the drop's pole, and hence

$$\left.\frac{\partial h}{\partial r}\right|_0 = \left.\frac{\partial^3 h}{\partial r^3}\right|_0 = 0 \quad . \tag{29}$$

These four boundary conditions ensure conservation of the total volume of fluid on the surface, namely

$$V = 2\pi \int_0^L hr\,dr \quad . \tag{30}$$

Indeed, differentiating Eq. (30) with respect to time t and applying the integral kinematic condition Eq. (2) leads to

$$\frac{dV}{dt} = 2\pi \left[\int_0^h ur\,dz \right]_{r=0}^{r=L} \quad . \tag{31}$$

The term in brackets, the difference in volumetric flow rates at r=0 and r=L, vanishes according to conditions (28) and (29), and consequently dV/dt = 0.

We discretized the spatial domain by a standard finite-difference procedure (33) and this led to a set of nonlinear ordinary differential equations

for the time dependence of the interfacial profile. This system was solved by an Adams-Bashforth predictor, trapezoidal-rule corrector scheme described by Gresho et al. (34). The time step size was adjusted as described by Gresho et al. so that at each time step only one Newton iteration was required for convergence. The scheme was started up with a backward-difference corrector to avoid nonphysical oscillations that are characteristic of the trapezoidal rule.

The remaining ingredient of the theory is the function chosen to describe how local disjoining pressure depends on the local film profile. For a water film, we at first took disjoining pressure to be inversely proportional to the square of the film thickness, in accord with the ionic-electrostatic, overlapping double-layer contribution — the contribution well established as dominating the disjoining pressure in water films more than 120 nm thick (31). However, integrating the film-profile equation with this disjoining pressure function produced drop spreading rates much slower than Marmur and Lelah measured. The spreading rate we predicted this way was also independent of the size of the glass slide.

Pashley (31) recently summarized persuasive evidence for disjoining pressure in water films on glass or silica being simply inversely proportional to film thickness up to thicknesses of at least 40 nm, a somewhat anomalous dependence that apparently reflects a hydrogen-bonding-dependent structural contribution. Shown in Figure 2 is the disjoining pressure function we finally employed: inverse dependence on film thickness up to 80 nm, spliced to inverse square dependence above 120 nm. Also shown is a representative curve for a nonpolar liquid such as a hydrocarbon oil on quartz. Integrating the profile equation (13) with it leads to predictions of extremely slow spreading, as we show in the next section.

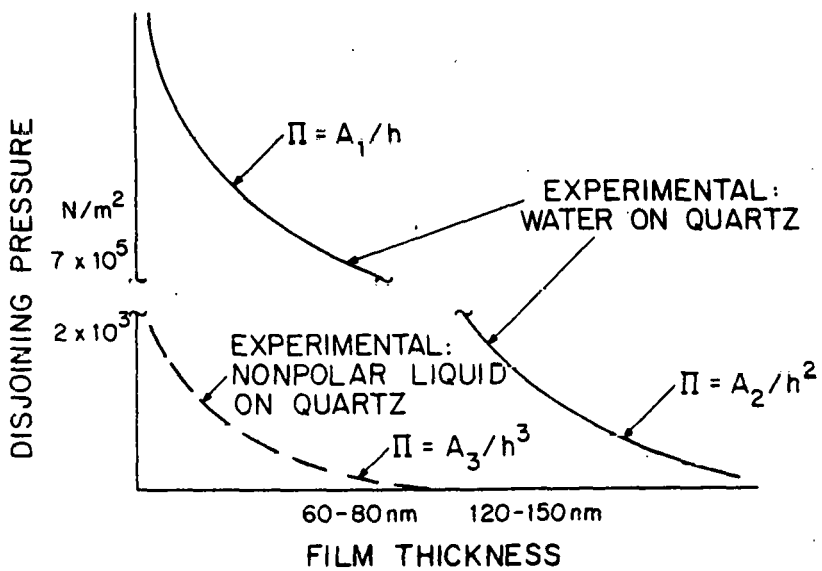

Figure 2. Disjoining pressure functions for water on quartz and for a completely wetting nonpolar fluid.

Our predictions for Marmur and Lelah's drop spreading on a 2-cm slide, which we approximated as circular rather than square, are shown in Fig. 3. A broadening front of secondary thickening (inset) of the 1 nm primary film up to 100 nm races outward from the capillary choke at the drop margin to the capillary arrest at the edge of the plate, reaching the edge in about a second (which corresponds to a diffusivity of thickening of around a square centimeter per second). Thus a primary film conduit of one million times greater conductance for drop spreading is established all the way to the edge of the slide within a second. Then, as the main plot shows, the spreading margin of the drop marches along behind at one-tenth the rate. The two rates and associated time scales come from the switch-over in disjoining pressure dependence at film thicknesses between 80 and 120 nm.

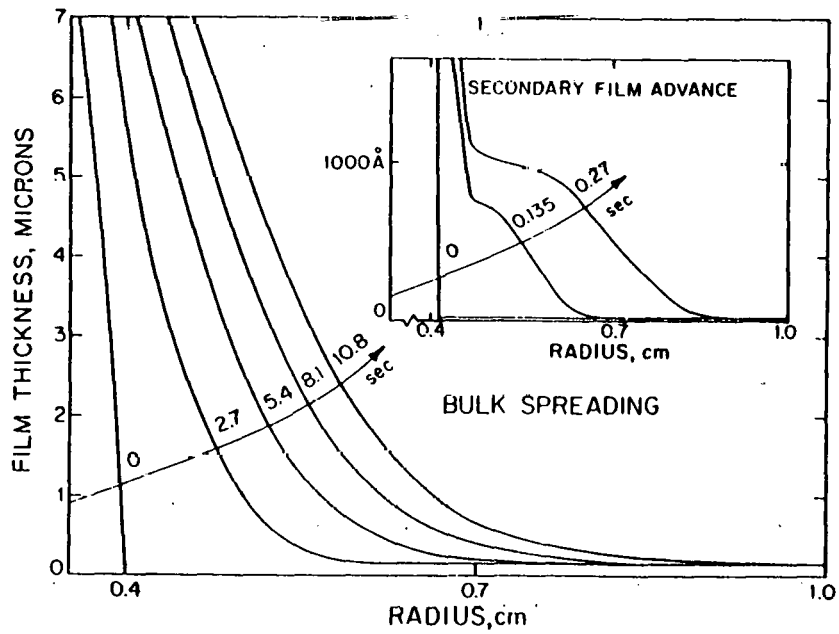

Figure 3. Predicted evolution of film profile at the apparent margin of a water drop on a 2 cm square glass slide.

The effect of slide size is shown in Fig. 4. Marmur and Lelah observed the spreading drops from below the glass slide by means of transmitted light and measured as a function of time the area within a dark ring which they took to be the drop's margin. An optical analysis (35) predicts that the radius of the dark ring closely corresponds to the radial distance from the drop's axis at which the interfacial profile has maximum curvature. Therefore, to compare with Marmur and Lelah's experiment in Fig. 4 we plot as a function of time the area within the point of maximum curvature of the profile, which we took to be the drop margin. Marmur and Lelah observed that the area within the drop margin increases more rapidly on a small slide than on a large one. The theoretical calculation based on separate measurements

of equilibrium disjoining pressure completely accounts for this and also correctly predicts the magnitude of the spreading rate. The theoretical predictions shown in Fig. 4 we found are not significantly affected by reasonable changes in the primary film thickness, the viscosity of the film for thicknesses less than 10 nm, the initial drop profile, or the way in which the two disjoining pressure functions are spliced.

The reason for the size dependence is the secondary film thickening that races outward to the edge and in effect sends back news of the barrier there. Marmur and Lelah found that a paraffin escarpment on the slide has the same effect as the edge. Because the racing is diffusive, and the configuration radially symmetric, its speed falls off with distance. When the slide is 8 cm or more across, the edge barrier is too far from the drop margin for the diffusing secondary film to transmit any appreciable thickness effect back to the drop.

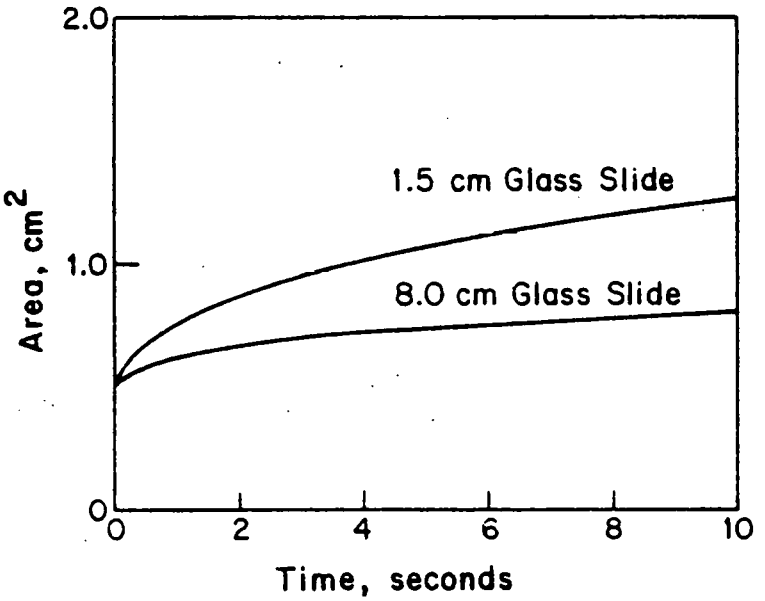

Figure 4. Predicted area of water drop versus time for 1.5 cm and 8.0 cm square glass slides.

Marmur and Lelah (13,14) found that the formula

$$A = 12.0\ V^{0.6}\ t^{0.2} \tag{32}$$

where A is the apparent area of the drop in cm^2, V is the drop volume in cm^3, and t is time in sec, correlated very well the spreading of water drops on large glass slides at long times. This formula can be derived from a simple model which incorporates the physics of the rigorous theory described above. The assumptions of the simple model are that the drop shape is a spherical cap and that the apparent dynamic contact angle at the drop margin depends on

the speed at which the margin advances according to an equation proposed by Friz (36).

The following relationships hold for a shallow spherical cap if $H/R \ll 1$,

$$V \simeq \frac{\pi}{2} HR^2 \quad , \quad \tan\theta = \frac{2H}{R} \quad , \tag{33}$$

and therefore

$$V \simeq \frac{\pi}{4} \tan\theta \, R^3 \quad , \tag{34}$$

where H is the height of the sphere-cap at its axis, R is the radius of its base, and θ is the apparent contact angle, which in general depends on the speed $d\bar{R}/dt$ at which the apparent contact line advances over the solid. If the drop volume remains constant Eq. (34) gives the relationship between $\theta(t)$ and $\bar{R}(t)$.

Standing waves are predicted on the secondary film just ahead of the advancing drop margin. These are similar in appearance to those predicted and observed by Bretherton (37) and Friz (36) in their studies of menisci advancing steadily over preexisting, uniform bulk films. Because the secondary film advances rapidly compared to the apparent drop margin, and because on large surfaces its thickness is nearly uniform, if the contact line speed dR/dt changes slowly with time and if the curvature of the sphere cap is negligible compared to the curvature of the meniscus near the drop margin, it is reasonable to model the dependence of θ on dR/dt with Friz's (36) equation

$$\tan\theta = C\left(\frac{\eta}{\gamma_{LV}} \frac{dR}{dt}\right)^{1/3} \quad , \tag{35}$$

where C depends on the secondary film thickness. Friz found $C = 3.4$ if the preexisting film is thick enough to be unaffected by disjoining pressure. Combining Eqs. (34) and (35) gives

$$V = \frac{\pi}{4} C \left(\frac{\eta}{\gamma_{LV}} \frac{dR}{dt}\right)^{1/3} R^3 \quad , \tag{36}$$

which can be integrated to give R as a function of time:

$$R(t) = \left(\frac{4V}{\pi C}\right)^{0.3} \left(\frac{10\gamma_{LV} t}{\eta}\right)^{0.1} + R_o \quad . \tag{37}$$

At long times $R >> R_o$ and the area of the drop can be approximated by

$$A = \pi R^2 \simeq \pi\left(\frac{4}{\pi C}\right)^{0.6} \left(\frac{10\gamma_{LV}}{\eta}\right)^{0.2} V^{0.6} t^{0.2} \quad , \tag{38}$$

which for C = 3.4 and the parameter values of water, γ_{LV} = 72 dyne/cm, η = 1 cp, is equivalent to

$$A = 15\ V^{0.6}\ t^{0.2} \quad , \tag{39}$$

in good agreement with Marmur and Lelah's correlation, Eq. (32). This is strong theoretical evidence that water drops on glass spread over a thick secondary film. The more rigorous calculation above establishes that the rapid formation of the secondary film is driven by the rather anomalous behavior of the disjoining pressure function of water on glass in the range h < 100 nm. Although the origin of this structural component of disjoining pressure remains to be elucidated (31), the calculations presented here demonstrate the consistency of two recent experiments that show the peculiar behavior of water on silica surfaces.

Spreading Liquid Drops: Oil Drops on Metal

Bascom, Cottington and Singleterry (6) found that carefully purified high molecular weight oils spread on clean metal surfaces at rates on the order of a millimeter per day — several orders of magnitude slower than the rates of a millimeter per sec reported by Marmur and Lelah for water drops on glass. There are several reasons for this difference, which can be understood by examining the film profile equation written in dimensionless form, Eq. (23). The viscosities of the oils are greater than that of water; hence the viscous resistance to spreading of the oils is greater. The surface tensions of the oils are smaller than that of water and therefore the capillary pressure driving force for oil spreading is less. The disjoining pressure function of a nonpolar fluid is drastically different from that of water, as shown in Fig. 2. In particular, the magnitude of the nonpolar fluid function is less at all thicknesses than that of water. Consequently the disjoining pressure driving force is much less when a fluid is nonpolar. Finally, because the relative volatility of the oils is low, unlike water, there is no primary film present on the solid before the oil drop is emplaced. Rather, the first molecules to cover the surface advance from the edge of the drop by surface diffusion, as suggested by Bascom, Cottington and Singleterry (6).

To investigate the spreading of oils (specifically, squalane, the oil most extensively studied) on metals, we use a disjoining pressure function appropriate to a nonpolar liquid on a high-energy surface, i.e., $\Pi(h) = Ah^{-3}$. Assuming that the Hamaker constant, i.e. $6\pi A$, is 20-30 x 10^{-13} erg for metal-metal interactions, and is 5-10 x 10^{-13} erg for fluid-fluid interactions and

using the geometric mean combining rule (Visser 1972) to calculate the Hamaker constant of fluid on solid, we estimate A to be 5-7 x $10^{-13}/6\pi$ erg.

In the limit $h \to \infty$ the hydrodynamic formula for the surface diffusion coefficient is valid; for this disjoining pressure function it is

$$D_s = \frac{A}{\mu h} \quad \text{as} \quad h \to \infty \quad . \tag{40}$$

In the limit $h \to 0$ the surface diffusion coefficient can be estimated from a simple model of molecular hopping from adsorption site to site on the solid (24):

$$D_s = \nu_s \, a_s^2/6 \quad , \tag{41}$$

where a_s is the distance between sites and ν_s is the jump frequency. Now the self-diffusion coefficient of a molecule within bulk liquid is given by the same type of model, in which the fluid structure is modeled as a cubic lattice (24):

$$D_{FF} = \nu_F \, a_F^2/4 \tag{42}$$

where a_F is the distance between putative sites in the liquid (it is often assumed that $a_F = \tilde{v}^{1/3}$, $\tilde{v}$ being the molar volume of the liquid). According to this model the self-diffusion coefficient is related to the viscosity by (24)

$$D_{FF} = \frac{kT}{\eta \, a_F} \quad , \tag{43}$$

which is essentially the Stokes approximation, where k is Boltzmann's constant and T is temperature. From Eqs. (41)-(43) it follows that

$$D_s = \frac{2}{3} D_{FF} \frac{\nu_s \, a_s^2}{\nu_F \, a_F^2} = \frac{2}{3} \frac{kT}{\eta} \frac{\nu_s}{\nu_F} \frac{a_s^2}{a_F^3} \quad . \tag{44}$$

To approximate the surface diffusion coefficient between the extremes of adsorbed molecules and thick film, we use the interpolation

$$D_s = \frac{A}{\eta(h + h_0)} \quad , \tag{45}$$

where

$$h_o \equiv \frac{3}{2}\frac{A}{kT}\left(\frac{\nu_F}{\nu_s}\right)\left(\frac{a_F}{a_s}\right)^2 a_F \quad . \tag{46}$$

Thus Eq. (45) approximates Eq. (40) as $h \to \infty$ and goes over smoothly to Eq. (44) when $h = 0$. In addition, we assume $h_o = a_F$. Then $(\nu_s/\nu_F)^{1/2} a_s$ is found by solving Eq. (46). For squalane at room temperature $\tilde{v} = 0.00201$ cm^3/mole, $a_F = 0.94$ nm, $\eta = 30$ cp (Reference 6), and it is

$$\left(\frac{\nu_s}{\nu_F}\right)^{1/2} a_s = 2.37 \text{ nm} \tag{47}$$

and therefore D_s is 7×10^{-6} cm^2/sec when h=0. Thus this model is consistent with the physically reasonable proposition that the activation energy for hopping is lower on the solid and/or spacing between adsorption sites is larger than the average volume occupied by a liquid molecule in bulk.

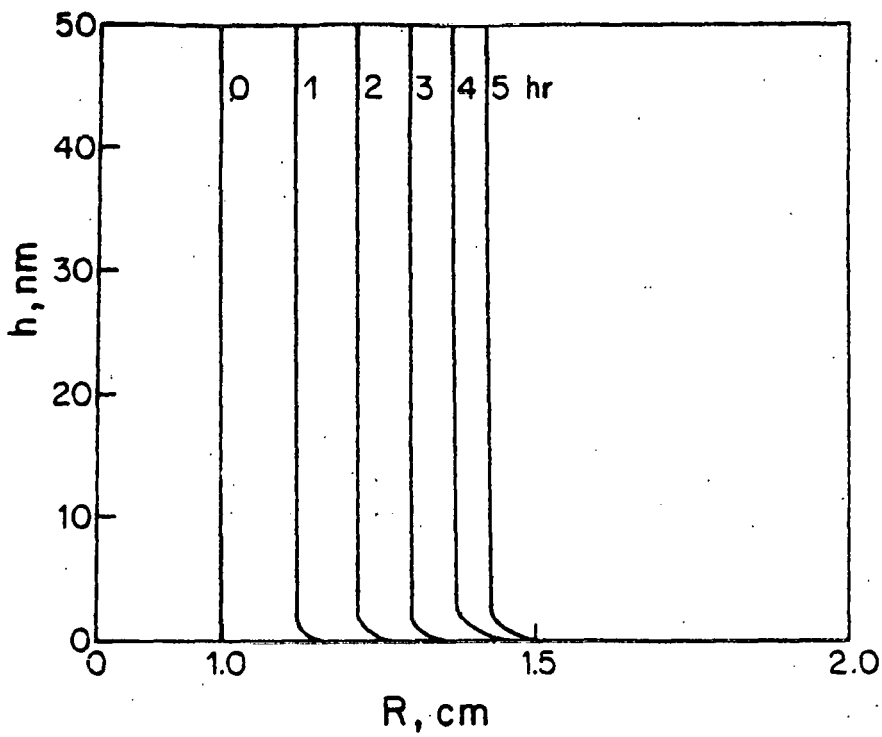

Figure 5. Predicted evolution of film profile at the apparent margin of a squalane drop.

In Fig. 5 are shown the results of calculations with this model of the surface diffusion coefficient. We took γ_{LV} to be 30 dyne/cm, the value for squalane (6). The same initial and boundary conditions were used as described above for water on glass, Eqs. (26) and (29), except that in the present case

we assumed the ambient film to have zero thickness. The calculations predict the formation of a surface diffusion-driven foot at the leading edge of the spreading drop. Such a foot was detected with ellipsometry by Bascom, Cottington and Singleterry (6). We calculated the rate of advance of the point of maximum curvature in the drop profile to be about 5×10^{-5} cm/sec at t = 3 hrs., in good quantitative agreement with Bascom, Cottington and Singleterry's measurements. This rate of drop spreading is limited by the rate of advance of the primary film by surface diffusion — in this case there is no preadsorbed film to aid the flow of fluid away from the drop. This, in conjunction with the smaller disjoining pressure driving force for h < 100 nm, is why oil drops on metal spread so much more slowly than water drops on glass.

Spreading or Contraction Caused by Surface Tension Gradients

Bascom, Cottington, and Singleterry found that the spreading rates of high molecular weight oils could be enhanced by the addition of low molecular weight volatile components. They attributed the enhanced spreading rates to surface tension gradients caused by preferential evaporation of the volatile component from the thinner portions of the liquid film. Ludviksson and Lightfoot (11) found that the spreading rates of oils can be enhanced by surface tension gradients caused by temperature gradients. Surface tension gradients also arise when the composition of an emplaced drop is different from that of an ambient primary film. When the emplaced drop has lower surface tension than the primary film, as for example in the case of an alcohol or aqueous surfactant solution placed on an ambient water film (5,12-14), the surface tension gradient is the main driving force for spreading. When the emplaced drop has higher tension, the surface tension gradient can cause contraction.

Spreading Liquid Drops: Simple Theory

We begin by examining the evolution of the film profile when capillary and disjoining pressure gradients are negligible; in the next subsection we investigate the effects of these driving forces. With them omitted the equation governing the evolution of the shape of a translationally symmetric drop on a horizontal surface when the surface tension gradient, $\partial\gamma_{LV}/\partial x$, is uniform and constant becomes simply

$$\frac{\partial h}{\partial t} = -\frac{h}{\eta}\frac{\partial \gamma_{LV}}{\partial x}\frac{\partial h}{\partial x} \tag{48}$$

This equation can be solved by the method of characteristics, inasmuch as

$$\frac{dh}{dt} = \left(\frac{\partial h}{\partial t}\right)_x + \frac{dx}{dt}\left(\frac{\partial h}{\partial x}\right)_t = 0 \tag{49}$$

along curves in the x-t plane given by

$$\frac{dx}{dt} = \frac{h}{\eta}\frac{\partial \gamma_{LV}}{\partial x} \quad . \tag{50}$$

Thus the drop profile at time t is given by

$$x = x_o(h) + \left(\frac{h}{\eta}\frac{\partial \gamma_{LV}}{\partial x}\right)_t \quad , \tag{51}$$

where $x_o(h)$ is the drop profile at $t = 0$.

According to Eq. (50), larger thicknesses propagate faster. Therefore when $\partial\gamma_{LV}/\partial x$ and $\partial h/\partial x$ have the same sign, i.e., when the thicker regions of the profile have higher surface tension, the profile at long times becomes wedge-shaped, the angle of inclination of the wedge,

$$\left(\frac{\partial h}{\partial x}\right)_t \simeq \frac{\eta}{\left(\partial \gamma_{LV}/\partial x\right)_t} \quad , \tag{52}$$

decreasing with time.

On the other hand, when $\partial\gamma_{LV}/\partial x$ and $\partial h/\partial x$ have opposite signs, i.e., when the thinner regions of the profile have higher tension, the predicted profile becomes a double-valued function of position. This is a physically unacceptable result of neglecting capillary, disjoining and gravitational effects which depend on interfacial inclination and curvature. Analogous multiple-valued profiles are predicted for saturation waves in immiscible fluid displacement in porous media if capillary forces are neglected (38) and for concentration waves in chromatography if convective and diffusive dispersion is neglected (39). Just as in these analogous situations, a physically meaningful result can be obtained by replacing the double-valued solution with a combination of discontinuous and diffusive profiles that satisfy the same mass balance as the unacceptable solution. Here the requisite mass balance across the discontinuity is

$$\int_0^{h_b} u_b\,dy - \int_0^{h_a} u_a\,dy = U(h_b - h_a) \quad , \tag{53}$$

where h_b is the film thickness behind the discontinuity and h_a the film thickness ahead of it. From this follows the velocity of the discontinuity

$$U = \frac{1}{2\eta}\frac{\partial \gamma_{LV}}{\partial x}(h_b + h_a) \quad , \tag{54}$$

which is simply the average of the free surface velocities ahead of and behind it. Correspondingly the position of the discontinuity x_d at time t_d is given by

$$t_d = \frac{-\eta}{(\partial\gamma_{LV}/\partial x)(\partial h/\partial x)_{h_b,t=0}}$$
$$x_d = x_o - \frac{h_b}{(\partial h/\partial x)_{h_b,t=0}} \quad . \tag{55}$$

Examination of these equations shows that the discontinuity begins growing from the minimum film thickness in the profile h_{min}, i.e., $h_a = h_{min}$, and the difference $h_b - h_a$ increases with time. An important special case is when $h_{min} = 0$. In this case the velocity of the discontinuity is

$$U = \frac{h_b(\partial\gamma_{LV}/\partial x)}{\eta} \tag{56}$$

and the discontinuity accelerates with time, eventually approaching a maximum speed of

$$U_{max} = \frac{h_{max}(\partial\gamma_{LV}/\partial x)}{\eta} \quad , \quad t \to \infty \tag{57}$$

where h_{max} is the maximum thickness of the initial profile. Ludviksson and Lightfoot (11) derived analogous equations for surface-tension-gradient-driven spreading up an inclined surface. They started from Eq. (27), neglected capillary and disjoining pressure so that

$$\frac{\partial h}{\partial t} = \left[\frac{\rho g_x h^2}{\eta} - \frac{(\partial\gamma_{LV}/\partial x)h}{\eta} + \frac{\rho g_y}{\eta}\right]\frac{\partial h}{\partial x} \quad , \tag{58}$$

and found that in the special case $h_a = 0$, $g_y = 0$ the discontinuity has constant velocity,

$$U = \frac{3}{16}\frac{(\partial\gamma_{LV}/\partial x)^2}{\eta\rho g_x} \tag{59}$$

and the film thickness just behind the discontinuity is constant at

$$h_b = \frac{3}{4}\frac{(\partial\gamma_{LV}/\partial x)}{\rho g_x} \quad . \tag{60}$$

In the more general case $h_a \neq 0$, $g_y \neq 0$,

$$U = \frac{(\partial\gamma_{LV}/\partial x)}{2\eta}(h_b + h_a) - \frac{\rho g_x}{3\eta}(h_b^2 + h_b h_a + h_a^2) \quad , \tag{61}$$

Such discontinuous profiles obviously violate the small-slope approximation on which the analysis rests. Nevertheless, Ludviksson and Lightfoot observed that a vertically spreading squalane film, driven by a surface tension gradient induced by a uniform temperature gradient, had at its leading edge a fairly sharp transition zone in thickness, the rate of advance of which was well approximated by Eq. (59). Bascom, Cottington, and Singleterry (6) also detected a sharp transition zone at the leading edge of films being pulled upward by a surface tension gradient caused by evaporative depletion of a volatile impurity. Comparison of theory and experiment is more difficult in this case because the surface tension gradient is a complicated function of film thickness, film thickness gradient, composition and time (see Appendix A, p. 166). Nevertheless, inserting Eq. (85) into Eq. (59) leads to the prediction that the vertical spreading rate increases as the derivative of surface tension with respect to composition $\partial\gamma_{LV}/\partial C$ increases, increases as the composition of the volatile component increases, increases as the volatility of the impurity decreases, and decreases with time, all of which agree with Bascom, Cottington, and Singleterry's observations.

Spreading Liquid Drops: Theory Including Capillarity, Disjoining Pressure and Gravitational Potential

The discontinuous film profiles encountered in the preceding subsection are in fact approximations to smoothly varying transition regions, the shapes of which are governed by capillarity, disjoining pressure, and gravity. Here we presume that such a transition or front is a wave of permanent form, i.e. a film profile that is constant in shape and translates at a fixed velocity. Profiles of this type are solutions of Eq. (27) which satisfy the additional condition, Eq. (24). Combined, these two equations give

$$\frac{\partial}{\partial x}\left\{\frac{h^3}{3\eta}\left[-\frac{\partial}{\partial x}(2\mathcal{K}\gamma_{LV}) - \frac{\partial\Pi}{\partial h}\frac{\partial h}{\partial x} + \rho g_y \frac{\partial h}{\partial x} - \rho g_x\right] - \frac{(\partial\gamma_{LV}/\partial x)h^2}{2\eta} + Uh\right\} = 0 \quad . \tag{62}$$

Integrating this gives a third-order ordinary differential equation for film thickness $h(x)$,

$$\frac{\partial}{\partial x}(2\mathcal{K}\gamma_{LV}) + \frac{\partial\Pi}{\partial h}\frac{\partial h}{\partial x} - \rho g_y \frac{\partial h}{\partial x} - \rho g_x = \frac{-3(\partial\gamma_{LV}/\partial x)}{2h} + \frac{3\eta(Uh - q)}{h^3} \quad , \tag{63}$$

where q is the constant volumetric flux. This generalizes Eq. (25) to account for surface tension gradients. The constants U and q are determined by the

conditions that the film thickness approach uniform values h_a ahead and h_b behind the transition zone:

$$h \to h_a \quad \text{as} \quad x \to \infty$$
$$h \to h_b \quad \text{as} \quad x \to -\infty \quad . \tag{64}$$

These conditions lead to the following formulas for U and q:

$$U = -\frac{\rho g_x}{3\eta}(h_b^2 + h_b h_a + h_a^2) + \frac{(\partial\gamma_{LV}/\partial x)}{2\eta}(h_b + h_a) \tag{65}$$

$$q = \frac{\rho g_x h_a}{3\eta}(h_b + h_a) + \frac{(\partial\gamma_{LV}/\partial x)}{2\eta}(h_b h_a) \tag{66}$$

If h_b and h_a are chosen to be the same as the film thicknesses ahead and behind the discontinuity in the solution discussed in the previous subsection, then the velocity of translation of the wave of permanent form is identical to the propagation velocity of the discontinuity [cf. Eq. (59)].

Equation (63) can be solved by quadrature in a manner similar to that we used (10) to solve Eq. (25). Dimensionless variables are convenient:

$$x' \equiv x\sqrt{\rho g_x/\gamma_{LV}} \quad , \quad h' \equiv h\sqrt{\rho g_x/\gamma_{LV}} \quad , \quad (2\mathcal{H}') \equiv 2\mathcal{H}\gamma_{LV}/\rho g_x \quad . \tag{67}$$

When $\Pi(h) = A/h^3$, Eq. (63) becomes

$$\frac{\partial}{\partial x'}(2\mathcal{H}') - \left[\frac{A_o}{h'^4} + \left(\frac{g_y}{gx}\right)\right]\frac{\partial h'}{\partial x'} - 1 = -\frac{3\tau_o}{2h'} + \frac{V_o}{h'^2} - \frac{q_o}{h'^3} \tag{68}$$

Here $A_o \equiv 3A\rho g_x/\gamma_{LV}$, $\tau_o \equiv (\partial\gamma_{LV}/\partial x)/\sqrt{\rho g_x \gamma_{LV}}$, and

$$U_o \equiv \frac{3\tau_o}{2}(h_b' + h_a') - (h_b'^2 + h_b' h_a' + h_a'^2) \quad ,$$

$$q_o \equiv \frac{3\tau_o}{2} h_b' h_a' - h_a'(h'_b + h_a') \quad . \tag{69}$$

We linearize Eq. (68) about $h = h_b$ to obtain initial conditions for starting integration. For small deviations of the film thickness from its asymptotic value h_b, the profile can be expressed as

$$h' = h'_b - \varepsilon h'_1(x) + O(\varepsilon^2) \tag{70}$$

Substituting this in the film profile equation (68) and setting the coefficient of ε to zero, we obtain a linear, third-order ordinary differential equation with constant coefficients for the deviation function $h_1(x)$,

$$h'_{1xxx} - \left[\frac{A_o}{h'^4_b} + \left(\frac{g_y}{g_x}\right)\right] h'_{1x} + \left[-\frac{3\tau_o}{2h'^2_b} + \frac{2V_o}{h'^3_b} + \frac{3q_o}{h'^4_b}\right] h' = 0 \tag{71}$$

This has the form $h'_{1xxx} + Ph'_{1x} + Qh'_1 = 0$ and so its solution is

$$h'_1(x) = Le^{\delta_1 x} + Me^{\delta_2 x} + Ne^{\delta_3 x} \quad , \tag{72}$$

where the δ_k are the roots of the indicial equation

$$\delta^3 + P\delta + Q = 0 \quad . \tag{73}$$

In the instance of a film spreading up a vertical surface for which there is a primary film of negligible thickness far ahead of the advancing front, $g_y = 0$ and $h'_a = 0$. Consequently, $q_o = 0$ and $U_o = 3/2\ \tau_o h'_b - h'^2_b$. If disjoining pressure is negligible at $h = h_b$, Eq. (73) becomes

$$\delta^3 = \left[\frac{2}{h'_b} - \frac{3}{2}\frac{\tau_o}{h'^2_b}\right] \delta \quad . \tag{74}$$

Thus one of the roots, say δ_1, is zero. If $h'_b > 3/4\ \tau_o$, then δ_2 and δ_3 are real and have opposite signs,

$$\delta_{2,3} = \pm \left[\frac{2}{h'_b} - \frac{3}{2}\frac{\tau_o}{h'^2_b}\right]^{1/2} \tag{75}$$

and if $h'_b < 3/4\ \tau_o$, they are imaginary,

$$\delta_{2,3} = \pm i \left[\frac{2}{h_b'} - \frac{3}{2} \frac{\tau_o}{h_b'^2} \right] \quad . \tag{76}$$

Therefore, if $h_b' > 3\tau_o/4$, L and M in Eq. (72) must be set equal to zero to satisfy the boundary conditions (64), and Eq. (72) reduces to

$$h_1'(x) = Ne^{\delta_3 x} \quad , \quad \delta_3 = \left[\frac{2}{h_b'} - \frac{3}{2} \frac{\tau_o}{h_b'^2} \right]^{1/2} \quad . \tag{77}$$

If $h_b' < 3\tau_o/4$, there is no solution satisfying conditions (64) except the trivial one $h \equiv h_b'$.

Three initial conditions for the initial value problem can be found by evaluating at some arbitrary point x^* the expressions for the thickness, slope, and curvature of the asymptotic profile, Eq. (69):

$$\begin{aligned} h' &= h_b' - \varepsilon N e^{\delta_3 x^*} \\ h_x' &= -\varepsilon N \delta_3 e^{\delta_3 x^*} \\ h_{xx}' &= -\varepsilon N \delta_3^2 e^{\delta_3 x^*} \quad . \end{aligned} \tag{78}$$

Because Eq. (68) is translationally invariant, the choices of x^* and εN are irrelevant; different choices give profiles having identical shapes but different vertical positions. We integrated in the positive x-direction using an implicit iteration scheme developed by Hindmarsh (40), details of which are given elsewhere (10). All of the profiles reported here have maximum free surface slope < 0.01. Therefore the small-slope assumption upon which Eq. (27) is based is valid.

The profiles we predicted are to be compared with those measured by Ludviksson and Lightfoot (11) in the two cases they studied: free vertical spreading, and vertical spreading against a barrier. In the former case they found that Eq. (59) predicts spreading rates which average about 10% faster than the measured rates, although they fall within the range of experimental uncertainty. However, the value of h_b' corresponding to Eq. (59) is $h_b' = 3\tau_o/4$ and, as noted at Eq. (77), no solution except $h \equiv h_b'$ is possible for this choice. Moreover, this choice of $h_b = 3\tau_o/4$ is inconsistent with Ludvickson and Lightfoot's measurements. They found that the asymptotic film thickness behind the front was well approximated by $h_b' = \tau_o$. The rate of frontal advance for this choice is

$$U = \frac{1}{6}\frac{(\partial\gamma_{LV}/\partial x)^2}{n\rho g_x} \quad , \tag{79}$$

about 5% slower on average than the measured spreading rates and, like Eq. (59), within the range of experimental uncertainty.

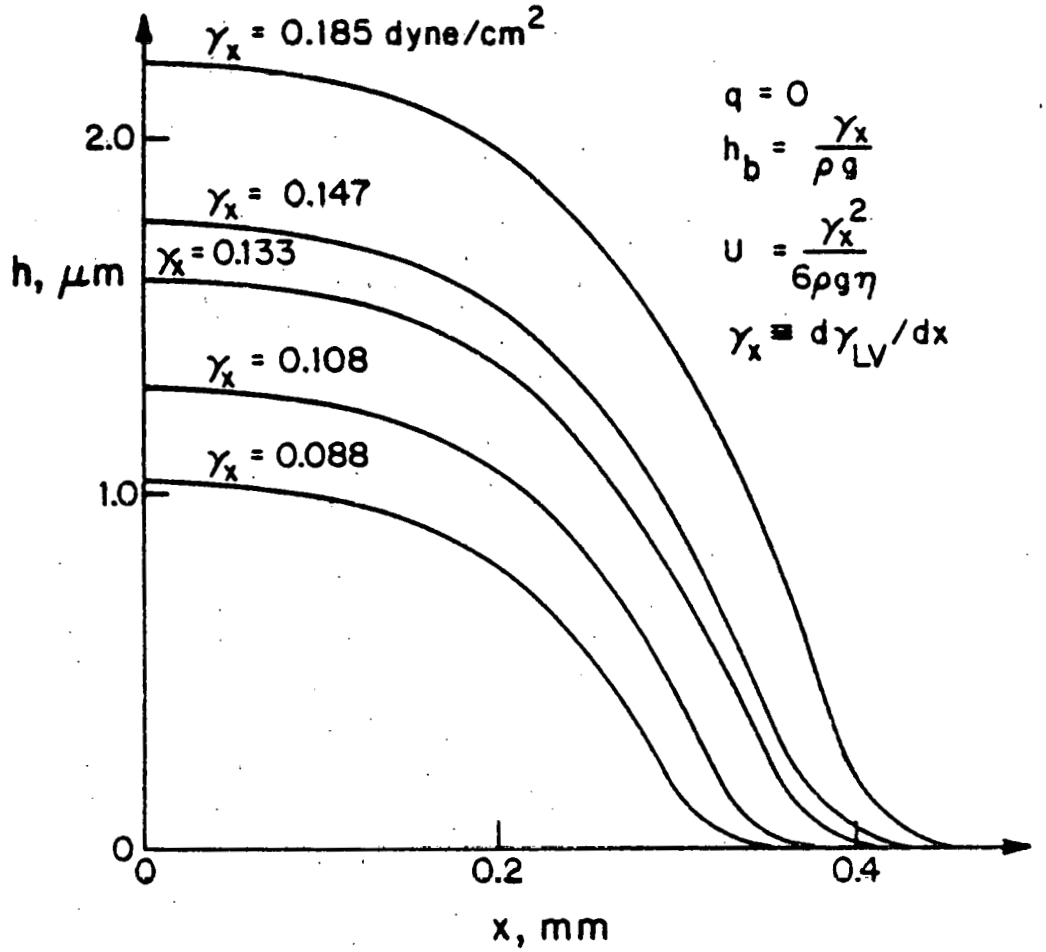

Figure 6. Predicted front shapes for surface-tension-gradient-driven free spreading up a verticle surface.

The profiles calculated for the conditions reported by Ludviksson and Lightfoot are shown in Fig. 6. Although the shapes of the calculated and measured profiles are in qualitative accord, the calculated fronts are about one-third as broad as the experimental ones reported in Fig. 10 of Ludviksson and Lightfoot's paper. This discrepancy cannot be reduced by choosing $h_a \neq 0$; the shape of the profile is not significantly altered until $h_a \simeq 0.1\ h_b$. We are therefore unable to account for the evidently significant difference between the calculated and measured profiles.

The profiles calculated for vertical spreading against a barrier are in much closer agreement with Ludviksson and Lightfoot's measurements, however. In this case U = 0, and we are obligated to choose $h_b = 3\tau_o/2$ according to Eq. (69). The resulting profiles are shown in Fig. 7; they match almost perfectly those reported in Fig. 11 of Ludviksson and Lightfoot's paper.

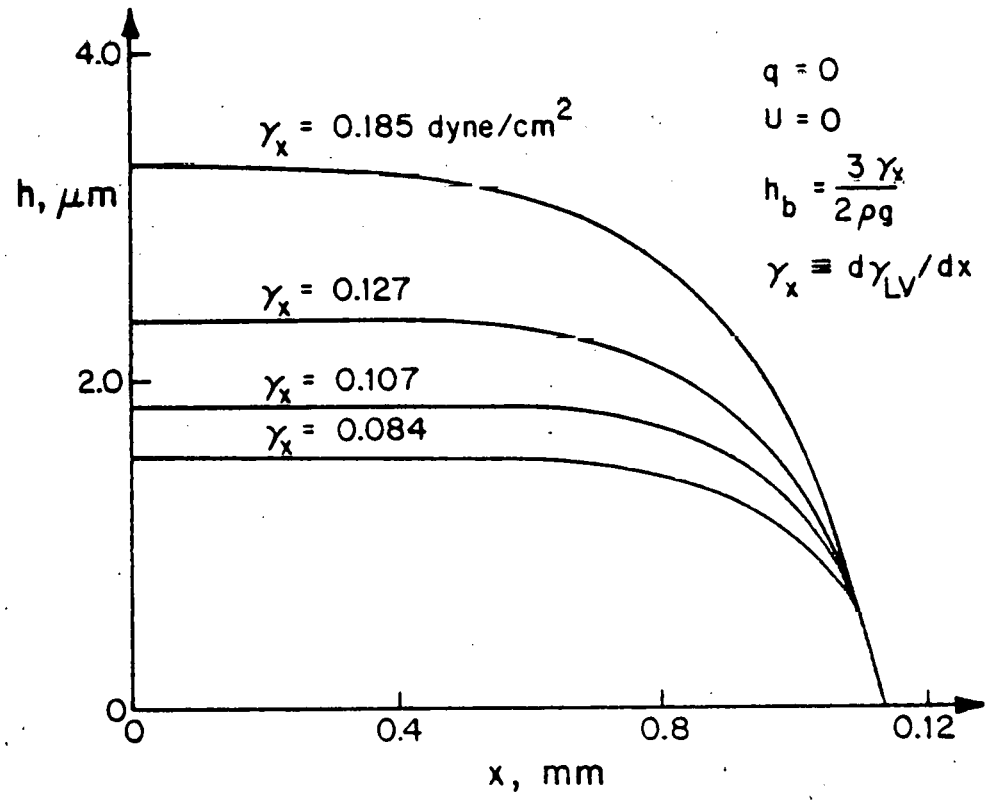

Figure 7. Predicted front shapes for surface-tension-gradient-driven spreading against a barrier.

Analysis of Blowing-Off

Over several decades Deryagin and co-workers reported evidence which they interpreted as indicating anomalous viscosity in thin liquid films. The evidence was drawn from experiments with the so-called blowing-off procedure (15-17). Among the liquids studied were carefully purified mineral oils, polymeric liquids, and solutions of polymers, high molecular weight esters, chlorinated compounds, and silicones on steel, glass, mica or quartz surfaces. Scriven (41) challenged the interpretation Deryagin and co-workers gave to some of their measurements, and proposed several alternative mechanisms which

could account for their observations. More recently, Bascom and Singleterry (42) carefully repeated and extended Deryagin and co-workers' experiments. Noting the similarity of some of the "blowing-off" film profiles to the profiles obtained in their earlier study (6) of oil drops or films spreading under the influence of surface tension gradients, Bascom and Singleterry found that unusual film profiles similar to those obtained by Deryagin and co-workers are associated with flow under surface tension gradients, capillary flow in surface roughness, a very low apparent contact angle of the liquid on the solid, or combinations of these circumstances. To clear up some of the controversy concerning the interpretation of blowing-off experiments, we present in this section an analysis which accounts for driving forces neglected by Deryagin and co-workers, namely capillary pressure, disjoining pressure, and surface tension gradients.

The blowing-off experiment consists of passing a laminar flow of gas over a film of liquid on the lower plane surface of a slit-shaped channel of rectangular cross-section (Fig. 8). The top of the chamber is glass to permit measurement of the evolution of the film profile by interferometry or ellipsometry. If the film thickness is everywhere small compared to the gap width H, the gas flow is unaffected by the presence of the film and the shear exerted by the gas on the film surface is given by Poiseuille's law as

$$\tau_i = \frac{H}{2}\frac{\Delta P}{L} \quad , \tag{80}$$

where ΔP is the pressure difference between the inlet and outlet of the channel and L is the distance between the same.

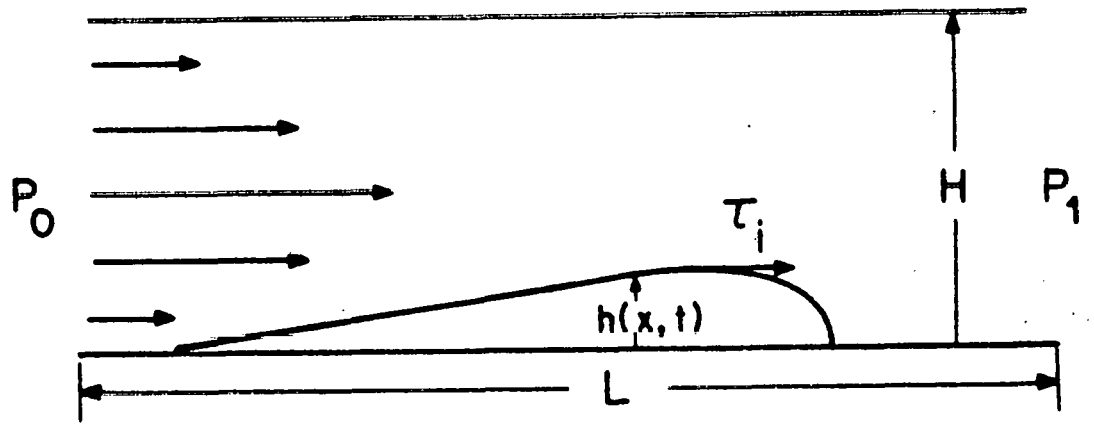

Figure 8. The blowing-off experiment.

When capillary pressure, disjoining pressure, gravitational potential and surface tension gradients are neglected, the equation governing the profile evolution of a film translationally symmetric in the direction perpendicular to the gas flow is

$$\frac{\partial h}{\partial t} = -\frac{h\tau_i}{\eta}\frac{\partial h}{\partial x} \quad . \tag{81}$$

This is the same as Eq. (48) with surface shear stress τ_i substituted for surface tension gradient $\partial\gamma_{LV}/\partial x$. Hence the analysis of both situations is virtually the same. When the initial slope of the profile is positive, as at the upstream side of a translationally symmetric drop (Fig. 9) the profile at long times becomes wedge-shaped, the angle of inclination of the wedge,

$$\left(\frac{\partial h}{\partial x}\right)_t \simeq \frac{\eta}{\tau_i t} = \frac{2L\eta}{H\Delta P t} \quad , \tag{82}$$

decreasing with time. Thus the viscosity of the film η can be deduced from measurements of the slope of the wedge. On the basis of this analysis, Deryagin and co-workers argued that deviations from a constant slope signify variations in viscosity with film thickness.

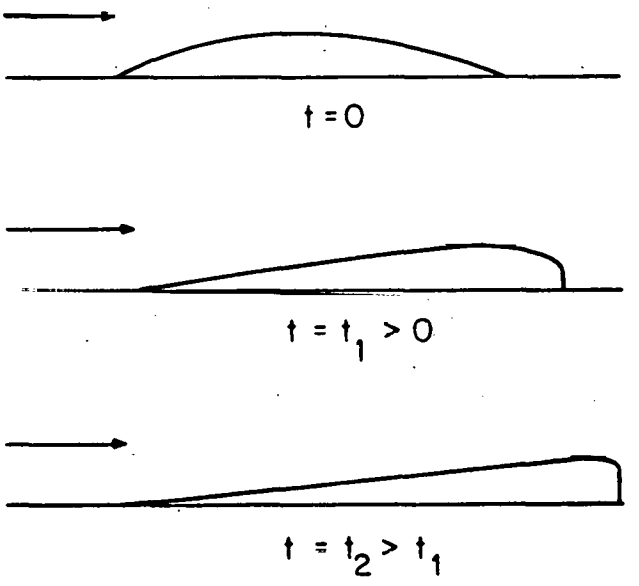

Figure 9. Film profile evolution during blowing-off according to analysis which neglects capillary and disjoining pressure.

When the initial slope of the profile is negative, as at the downstream side of a translationally symmetric drop, the profile develops a discontinuity in film thickness similar to that analyzed in the preceding section. The discontinuity originates at the trailing edge and thickens with time as shown in Fig. 9. In reality, capillary pressure, disjoining pressure, and gravitational potential cause dispersion of the discontinuity; the actual front shapes can be calculated by a procedure analogous to that given in the preceding section.

The effects of capillary pressure, disjoining pressure, and surface tension gradients on the film profiles during blowing-off are revealed by solutions of Eq. (27). We solved this equation by the numerical technique described above. Results are shown in Fig. 10 for the blowing-off of a squalane film with a surface shear stress of 10 dynes/cm^2.

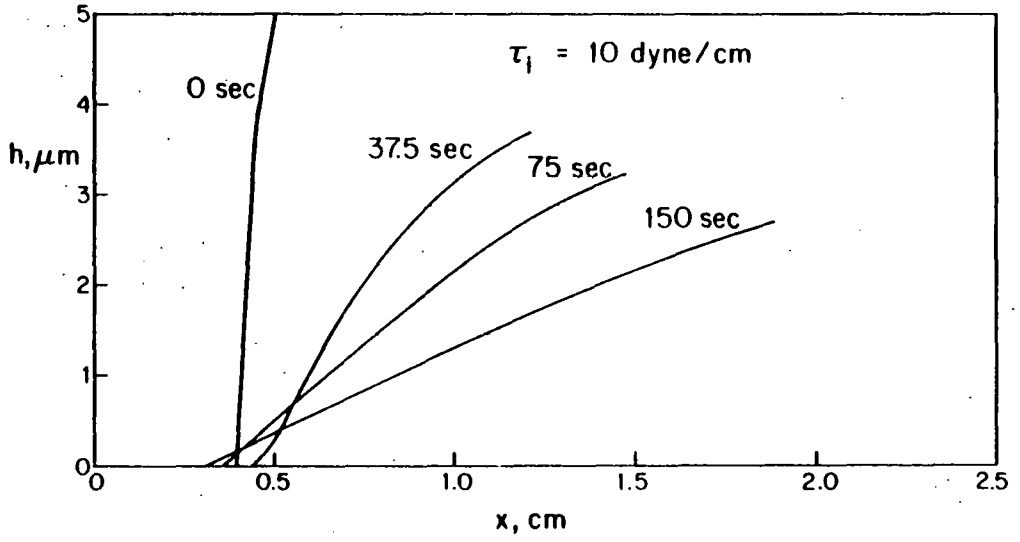

Figure 10. Predicted evolution of film profile during blowing-off of a squalane drop.

The physical properties of squalane were given in a previous section. The initial profile of the upstream end of the film we assumed to be a circular arc having a chord of 1 cm and zenith 5 μm above the chord. Beyond 1 cm downstream of the initial contact line the film was assumed to have a uniform initial thickness of 5 μm. The film profile rapidly became wedge-shaped for film thicknesses larger than several nanometers. The viscosity calculated from the slope of the wedge at several times agreed with the assumed value of 30 cp. Disjoining pressure gradients caused a slight upstream spreading of the apparent contact line and hence deviation from a wedge-shaped profile at small thicknesses. These calculations agree with Bascom and Singleterry's (42) observations of the blowing-off of carefully purified oils. They detected wedge-shaped profiles, but found that the extrapolation of the wedge to h = 0 spread progressively upstream.

Deryagin et al. (17) interpreted certain of the profiles they encountered with silicone liquids as indicating a decrease in viscosity within 2 nm of the surface, an abnormally high viscosity in the zone 2-20 nm, and normal bulk viscosity beyond. Bascom and Singleterry (42) found that similar profiles could be induced by adding volatile impurities to the oil, which presumably caused surface tension gradient driven upstream spreading at the margin of the film. We calculated the evolution of the film profile assuming that at

film thicknesses less than 50 nm a surface tension gradient of 5 dynes/cm^2 was present which opposed a shear stress on the film surface of 100 dynes/cm^2, a typical value for Deryagin's experiments. The profiles so obtained were indistinguishable from those calculated on the assumption that there was no surface tension gradient, i.e., in both circumstances the profiles tended to nearly identical wedge-shapes at long times. Therefore it is not the surface tension gradient alone which causes anomalous profiles. Now such profiles were observed by Deryagin et al. and Bascom and Singleterry only on steel surfaces and only when the film was allowed time to spread between the application of the film and the beginning of blowing or between the cessation of blowing and the measurement of film profile. Measurements during blowing of film profiles on glass surfaces smoother than the steel surfaces used are the only ones directly comparable to the present calculations: these showed little deviation from a wedge shape. Presumably capillary flow in surface roughness produces a primary film which facilitates secondary spreading induced by surface tension gradients.

Bascom and Singleterry (42) also found that liquids having small ($\simeq 1°$) but nonzero equilibrium apparent contact angles on steel gave profiles that deviated from wedge shape at film thicknesses as great as several microns. To examine the effect of contact angle on the evolution of film profile during a blowing-off experiment we chose the disjoining pressure function $\pi(h) = A_3/h^3 - A_2/h^2$, where $A_3 = 0.3 \times 10^{-13}$ erg and $A_2 = 1.2 \times 10^{-7}$ dyne, values that correspond to an equilibrium apparent contact angle of 1° (2). Our calculations revealed that although the film profile becomes convex upwards when film thicknesses are less than about 100 nm, the profile does not deviate from a uniform slope above this thickness. We found that profiles similar to those reported by Bascom and Singleterry can be obtained by assuming a surface tension gradient on the order of 10 dyne/cm, i.e. comparable in magnitude to the shear stress applied to the surface of the film. We can find no grounds for there being such a large surface tension gradient in Bascom and Singleterry's experiments, and thus the reasons for anomalous profiles at film thicknesses greater than a micron remain unresolved.

The analysis presented here points to four conditions that must be achieved in order to insure that blowing-off or similar experiments truly measure thin-film rheology: (1) The equilibrium disjoining pressure function $\pi(h)$ must be known. We have shown that the form of $\pi(h)$ strongly affects the shape of the film profile at film thicknesses less than 10 nm and perhaps as large as 100 nm or even more. (2) The solid surface must be sufficiently smooth to suppress capillary flow in surface roughness (43) and to avoid ambiguities in the optical determination of film thickness when it approaches the magnitude of surface roughness. (3) Measurements of the film profile must be made while the surface of the film is being sheared, in order to avoid rearrangement of the fluid between the cessation of shearing and time of measurement. (4) Surface tension gradients must be suppressed by using only pure liquids or, if impurities are unavoidable, by using a high shear rate. These conditions perhaps could be most easily achieved by doing a dynamic experiment with the Israelachvili's (44,45) apparatus for direct measurement of surface forces. A possible experiment would be to slowly

squeeze a liquid from between crossed cylinders coated with a thin-film of a second immiscible liquid. We suspect that under some conditions the film thickness profile would develop into a wave of permanent form similar to that analyzed in a previous section. Indeed, preliminary observations have shown this to be the case (46). The precise measurement and prediction of such profiles warrants further investigation.

Discussion

The theory put forward here accounts successfully for the various mechanisms of spreading on solids, although in a few of the examples analyzed there are features it does not predict quantitatively. Nevertheless it establishes that macroscopic or bulk spreading behavior, especially the rates of spreading, are governed by the physics of submicroscopic, invisible thin liquid films: the rapidity of formation and thickness of primary films which are precursors of film thickening and observable spreading, the dependence of disjoining pressure on film thickness, and the absence or presence of surface tension gradients.

The theory in its present state is restricted to geometrically smooth, compositionally homogeneous solid surfaces and to situations where the tangent to the liquid surface is little more than slightly inclined to the underlying solid surface. The consequences of heterogeneity of the solid surface are partly indicated by the studies of Johnson and Dettre (47) and Mason and his coworkers (48), but further analysis, particularly of dynamics, is needed. As for films with steeper gradients of thickness, the more general creeping flow version of the theory teaches that their volumetric flux of liquid along the solid surface, which appears in the basic continuity relation, Eq. (1), becomes not only a linear function of the first derivatives of film thickness and of the second derivatives in film curvature, but also a nonlinear function of the same and higher derivatives. Spreading can still be interpreted as a diffusive type of process, however.

The examples considered in the foregoing sections all involve only liquids that perfectly or nearly perfectly wet the solid at equilibrium. But it should be clear that by appropriate choices of disjoining pressure function (Reference 10) the calculations can be extended to situations where the apparent contact angle at equilibrium differs greatly from zero (18).

Measurement of static apparent contact angles, which serve widely as indices of wetting behavior and thus of disjoining pressure functions, is usually plagued by contact angle hysteresis (47,28). Most literature data are visible angles at recently advanced liquid margins, as against recently receded ones — and in contrast to margins that have finally ceased altogether to migrate. The drop spreading rates we predicted for oils on smooth, homogeneous high energy surfaces are mm/hr to mm/day. So here we have one of the factors in contact angle hysteresis (which Fowkes and Harkins (49) found to be absent on the time scale of their measurements of water on clean, smooth glass quartz in a humid atmosphere: compare our predictions of mm/sec in Fig. 3). Of course the roughness and heterogeneity of most surfaces also play

roles, as may also the slow diffusion of surface-active materials, if present, into primary films and onto solid surfaces.

Analysis of the spreading of liquids containing surface-active substances is complicated by the time-dependence of surface tension gradients and disjoining pressure functions. In many instances the initial rapid spread of the margin of a surfactant-containing drop is followed by a slower contraction of the margin (e.g. Harkins (50), Lelah and Marmur (13)). The most likely explanation for the initial spreading is the higher surface tension of the originally present primary film pulling on the margin of the lower tension, surfactant-containing drop. As the drop spreads, surfactant diffuses into the primary film and adsorbs on the solid-liquid and liquid-vapor interfaces, thus modifying the disjoining pressure function, which dictates the contraction of the drop to its equilibrium configuration. This mechanism also is at work any time the liquid in a previously deposited primary film has higher-surface tension than the liquid in an emplaced drop, as in some of the experiments of Hardy (5), Bangham and Saweris (12), and Marmur and Lelah (13,14).

Spreading margins are often not straight or circular as has been assumed here, but instead develop a serrated or saw-tooth appearance, especially when surface tension gradients are present (11,51,13,14). We suspect that such patterns are a hydrodynamic instability; similar "fingering" instabilities of miscible (52) and immiscible (53) displacement fronts in porous media and in Hele-Shaw flow cells (54) are well accounted for by transverse stability analyses of convective-diffusion equations similar in structure to Eq. (27). Such a stability analysis will be the subject of a future publication.

When disjoining pressure is the chief driving force the theory presented here could be quite useful for distinguishing disjoining pressure functions. To make quantitative measurements requires knowing the rheology of thin-film states. Thus the theory could be even more useful as an aid in the design of experiments, such as Deryagin's blowing-off experiment, to probe thin-film rheology when the disjoining pressure function is well established.

Appendix A: Surface Tension Gradients Due to Evaporation of a Volatile Impurity

In small slope approximation the equations governing the evaporation of a volatile component present at small concentration in a nonvolatile liquid film are

$$\frac{\partial C_V}{\partial t} = D_V \frac{\partial^2 C_V}{\partial z^2} \quad , \quad \frac{\partial C_L}{\partial t} = D_L \frac{\partial^2 C_L}{\partial z^2}$$

$$D_L \frac{\partial C_L}{\partial z} = 0 \quad \text{at} \quad z = 0 \quad , \quad D_V \frac{\partial C_V}{\partial z} = D_L \frac{\partial C_L}{\partial z} \quad \text{at} \quad z = h$$

$$C_V = K C_L \quad \text{at} \quad z = h$$

$$C_L = C_0 \quad \text{in} \quad 0 < z < h \quad \text{when} \quad t = 0$$

$$C_V = 0 \quad \text{in} \quad h < z < \infty \quad \text{when} \quad t = 0$$

C_V and C_L are the concentrations of the component in vapor and liquid, D_V and D_L are diffusion coefficients in vapor and liquid, K is the equilibrium partition coefficient, and z is the vertical distance from the solid. The solution of this problem has been given by Lovering (55) and Arcuri and DeBruijne (56). From their solution the derivative with respect to film thickness of the concentration, C_s, of the volatile component at the liquid surface is

$$\frac{\partial C_s}{\partial h} = \frac{C_0}{\sqrt{\pi D_L t}} (1 - p^2) \sum_{n=1}^{\infty} (-p)^{n-1} \, n \, e^{-n^2 h^2 t / D_L} \quad , \tag{83}$$

where

$$p \equiv \frac{1 - \sqrt{D_L}/K \sqrt{D_V}}{1 + \sqrt{D_L}/K \sqrt{D_V}} \quad . \tag{84}$$

Because $\partial C_s/\partial h$ is always greater than zero, the sign of the surface tension gradient

$$\frac{\partial \gamma_{LV}}{\partial x} = \frac{\partial \gamma_{LV}}{\partial C_s} \frac{\partial C_s}{\partial h} \frac{\partial h}{\partial x} \quad , \tag{85}$$

depends on the sign of $\partial \gamma_{LV}/\partial C_s$. If $\partial \gamma_{LV}/\partial C_s > 0$, the surface tension gradient has the same sign as $\partial h/\partial x$ and is a driving force for flow away from thinner regions; but if $\partial \gamma_{LV}/\partial C_s < 0$, which is the more prevalent case, the surface tension gradient has the opposite sign as $\partial h/\partial x$ and consequently is a driving force for flow toward thinner regions. According to Eq. (85) the surface tension gradient increases as $\partial h/\partial x$ increases and as the concentration of the volatile component increases (although not exactly proportionally to C_0, since $\partial \gamma_{LV}/\partial C_s$ generally decreases as C_s increases), decreases as film thickness increases and as volatility $K \sqrt{D_V}/\sqrt{D_L}$ increases, and diminishes with time.

References Cited in Section VIII

1. Deryagin, B. V., Kolloid Zhurnal 17, 205 (1955).

2. Mohanty, K. K., Davis, H. T., and Scriven, L. E., AIChE Preprint 121a, presented at AIChE Annual Meeting, San Francisco, CA, November 25-29, 1979, to be submitted to J. Colloid Interf. Sci.

3. Mohanty, K. K., Ph.D. Thesis, University of Minnesota (1981).

4. Kheshgi, H. S. and Scriven, L. E., to be submitted to Chem. Eng. Sci. (1983).

5. Hardy, W. B., Phil. Mag. 38, 49 (1919).

6. Bascom, W. D., Cottington, R. L., and Singleterry, C. R. in Contact Angle, Wettability and Adhesion, Adv. Chem. Ser. 43, Am. Chem. Soc., Washington, D.C. (1964) 355.

7. Cherry, B. W. and Holmes, C. M., J. Colloid Interf. Sci. 29, 174 (1969).

8. Blake, T. D. and Haynes, J. M., J. Colloid Interf. Sci. 30, 421 (1969).

9. Ruckenstein, E. and Dunn, C., J. Colloid Interf. Sci. 59, 135 (1977).

10. Teletzke, G. F., Davis, H. T. and Scriven, L. E., submitted to J. Fluid Mech. (1982).

11. Ludviksson. V. and Lightfoot, E. N., AIChE J, 17, 1166 (1971).

12. Bangham, D. H. and Saweris, Z., Trans. Faraday Soc. 34, 554 (1938).

13. Lelah, M. D. and Marmur, A., J. Colloid Interf. Sci. 82, 518 (1981).

14. Marmur, A. and Lelah, M. D., J. Colloid Interf. Sci. 78, 262 (1980); Chem. Eng. Commun. 13, 133 (1981).

15. Deryagin, B. V., Strakhovsky, G. and Malysheva, D., Acta Physicochim. USSR 19, 541 (1944).

16. Deryagin, B. V. and Karassev, V. V.,Proc. 2nd Intl. Cong. of Surface Activity, 3, (Academic Press, London, 1957) 531.

17. Deryagin, B. V., Karasev, V. V., Lasygin, I. A., Skorokhodov, I. I., Khronova, E. N., Spec. Trans. Faraday Soc. 1 98 (1970).

18. Teletzke, G. F., Scriven, L. E., and Davis, H. T., J. Colloid Interf. Sci. 87, 550 (1982).

19. Higgins, B. G. and Scriven, L. E., I & EC Fund. 18, 208 (1979).

20. Gibbs, J. W., The Scientific Papers of J. Willard Gibbs Vol. I, Thermodynamics, (Longmans Green, & Co., New York, 1906, 1931, Dover 1961).

21. Deryagin B. V., Proc. 2nd Int. Congr. Surface Activity 2, 153 (1957).

22. Eliassen, J. D., Ph.D. thesis, University of Minnesota (1963).

23. de Groot, S. R. and Mazur, P., Nonequilibrium Thermodynamics, (North-Holland, Amsterdam (1962).

24. Frenkel, J., Kinetic Theory of Liquids (Oxford University Press, Oxford, 1946).

25. Lopez, J., Miller, C. A. and Ruckenstein, E., J. Colloid Interf. Sci. 56, 460 (1976).

26. Hocking, L. M., Quart. J. Mech. and Appl. Math. 34, Pt. 1, 37 (1981).

27. Greenspan, H. P. and McCay, B. M., Studies in Appl. Math. 64, 95 (1981).

28. Huh, C. and Scriven, L. E., J. Colloid Interface Sci. 35, 85 (1971).

29. Dussan, V. E. B., Ann. Rev. Fluid Mech. 11, 371 (1979).

30. Dzyaloshinskii, I. E., Lifshitz, E. M., and Pitaevskii, L. P., Soviet Physics JETP 37, 161 (1960).

31. Pashley, R. M., J. Colloid Interf. Sci. 78, 246 (1980).

32. Philip, J. R., J. Phys. Chem. 82, 1379 (1978).

33. Forsythe, G. E. and Wasow, W. R., Finite Difference Methods for Partial Differential Equations (Wiley, New York, 1960).

34. Gresho, P. M., Lee, R. L. and Sani, R. L., Preprint UCRL-83282, Lawrence Livermore Laboratory, Livermore, CA (1979).

35. Berry, M. V., Adv. Phys. 25, 1 (1976).

36. Friz, G., Zeit. fur angew. Physik 19, 374 (1965).

37. Bretherton, F. P., J. Fluid Mech. 10, 166 (1961).

38. Buckley, S. E. and Leverett, M. C., Trans. AIME 146, 107 (1942).

39. Lake, L. W. and Helfferich, F. G., Society of Petroleum Engineers J. 18, 418 (1978).

40. Hindmarsh, A. C., Lawrence Livermore Laboratory Report UCID-30001, Revision 3, Livermore, CA (1974).

41. Scriven, L. E., Discussion of "Boundary viscosity of polydimethylsiloxane liquids and their binary mixtures," by B. V. Deryagin et al., Spec. Trans. Faraday Soc. 1, 128 (1970).

42. Bascom, W. B. and Singleterry, C. R., J. Colloid Interf. Sci. 66, 559 (1978).

43. Pujado, P. and Scriven, L. E., Journal of Heat Transfer, Trans. ASME 93, (1971).

44. Israelachvili, J. N. and Adams, G. E., J. Chem. Soc. Faraday Trans. I 74, 975 (1978).

45. Israelachvili, J. N., Adv. Coll. and Interf. Sci. 16, 31 (1982).

46. Israelachvili, J. N., Personal Communication (1981).

47. Johnson, R. E., Jr. and Dettre, R. H., in Surface and Colloid Science, vol. 2, ed. E. Matijevic (Wiley, Interscience, New York, 1969).

48. Oliver, J. F., Huh, C. and Mason, S. G., Colloids and Surfaces 1, 79 (1980).

49. Fowkes, F. M. and Harkins, W. D., J. Amer. Chem. Soc. 62, 3377 (1940).

50. Harkins, W. D., The Physical Chemistry of Surface Films (Reinhold, New York, 1952).

51. Tanner, L. H., J. Phys. D.: Appl. Phys. 12, 1473 (1979).

52. Heller, J. P., J. Appl. Phys. 37, 1566 (1966).

53. Nitsche, L. C., Davis, H. T., Scriven, L. E. and Teletzke, G. F., Bull. Amer. Phys. Soc. 27, 1165 (1982).

54. Chouke, R. L., van Meurs, P., van der Poel, C., Trans. AIME 216, 188 (1958).

55. Lovering, T. S., Bull. Geol. Soc. Amer. 47, 87 (1936).

56. Arcuri, C. and deBruijne, D. W. Proc. 5th Intl. Conf. on Surf. Act. Substances, Barcelona, (1968) 61.

IX. DEPENDENCE OF RESIDUAL NONWETTING LIQUID ON PORE TOPOLOGY

Introduction

The microstructure of reservoir rocks strongly influences the transport of momentum, energy, and charge in the solid matrix, in the fluid-filled pore space, and overall. As in most porous media important to science and technology the microstructure consists of a system of interpenetrating, irregularly-shaped pore and grain assemblages. The distributions of sizes and shapes of pores and grains are central ingredients of any accurate characterization of porous media structure. Equally central are the connection patterns of the interpenetrating, network-like pore and grain structures. Connectivity is the subject of topology (1,2). The structure of connection patterns is measured by topological parameters such as the number of alternative paths in the pore clusters or grain clusters. Topological parameters take on added significance when the transport process alters the connection patterns, as for instance the mechanical stresses (momentum flux level) in a solid matrix can reduce matrix connectivity by inducing grain-boundary microcracking (3).

Because topological properties are measures of connectivity they are independent of size and shape, unlike geometric properties. They change only when structures break or fuse in certain ways. Topological properties are also independent of the way a connected structure is regarded as being made up of discrete, though fused, parts. A widely used indicator of connectivity, the coordination number, is not necessarily a topological invariant: in a reservoir rock the average coordination numbers of grains and pores depend on how grains and pores are defined. One of the goals of this paper is to identify and to measure experimentally the proper topological properties on which depend the residual saturation of oil or other nonwetting fluid.

The patterns of connection of the pores and of the rock matrix, however chaotic both may be, are not independent. It is becoming increasingly clear that transport processes through the pore space and through the solid matrix are linked by the interrelationships between not only matrix shape and pore shape, but also matrix topology and pore topology (3). In this paper, we bring out the equivalence relationships between topological parameters of the pore structure and of the solid structure.

The basic properties that should be specified in any detailed study of the microstructure of porous media are size, shape, and topology. Easiest to measure are averages such as volume porosity, surface area per unit volume, and pore size, a length per unit volume. Evaluation of size distributions of three-dimensional irregular structures, however, involves laborious analysis of entire structures. Approximate estimates can be obtained from two-dimensional sections by making assumptions about the shape and topology (4,5). Shapes, i.e. distributions of curvature, are harder to characterize. Exact quantitative expressions have been derived only for regular objects (5). The average shape parameters of irregular objects, such as specific surface area, integral mean and Gaussian curvatures (described below), and certain lengths, are often compared with similar parameters for regular, discrete objects. Metallographers tend to use shape factors that relate a particular linear dimension such as the maximum or minimum length to the average length, surface area, and volume fraction (4,6). Powder technologists define a variety of

shape indexes based on comparisons with spherical or other regular shapes, e.g. roundness, flatness, sphericity, elongation, and bulkiness factor (7). Most shape factors are defined only for isolated, simply-connected closed surfaces. Because multiply-connected surfaces have had comparatively little attention, the shapes in bicontinuous porous media are still hard to characterize. A second goal of this paper is to show that an important shape parameter is in fact a topological parameter.

Over recent decades, a major challenge that has been met quite successfully is the identification of the factors responsible for the entrapment of oil in rocks. At the macroscopic level these include (1) capillary number, which measures the relative influence of capillary forces that hold the oil phase entrapped and of viscous forces or equivalent pressure gradient forces that keep it moving (8,9,10); (2) wettability, which seems intimately related to the apparent contact angle that oil-water interfaces make with the surfaces of the rock, and is now known to depend on thin-film states (11,12); (3) saturation history (13); (4) ratio of oil viscosity to water viscosity (14,15). At the microscopic level the mechanisms of oil phase disconnection (16,17,18) and the mechanism of subsequent mobilization of the trapped fraction (9,19,20), have become clear. Irreducible wetting phase saturations have been found to depend on (1) specific surface area and surface texture (21,22,23); (2) small scale heterogeneities in rock microstructure (24); (3) pore size and shape distributions (24). Within a porous medium, wetting fluid is retained, as has long been known, as pendular rings, surface films, and boluses filling smaller-sized pores. The distribution of residual non-wetting fluid in porous media has been the subject of intense theoretical and experimental research recently (18,25). A thorough investigation of thin-film physics and stability of non-wetting menisci led to the conclusion that residual non-wetting saturations are strongly related to pore geometry and pore topology (18). The controlling geometric features are the distribution of local pore-wall curvatures including pore surface textures.

Experimental investigations relating macroscopic fluid flow behavior to pore space morphology are sketchy and largely qualitative (21,26,27). Wardlaw and Cassan proposed a set of general criteria for relating recovery efficiencies to qualitative estimates of pore connectivities and pore sizes (28). The most extensive work on measurement of pore-size distributions from two-dimensional sections through a three-dimensional porous medium is that of Dullien and co-workers (29-31). These investigators adjust photomicrographic measurements of pore sizes by using various shape factor estimates, and correlate pore size distributions with capillary pressure and relative permeability measurements. However, shape-independent quantitative measurements of pore-sizes can be obtained only by carefully disassembling a sample of rock grain-by-grain, pore-by-pore and recording all of the relevant dimensions and connections. This paper reports such a study of the connectivity structure of several synthetic rocks.

Modeling of fluid flow in porous media began with simple bundle-of-capillary-tubes and sphere-pack concepts that took no account of connectivity but were suited to estimate single phase permeabilities in unconsolidated beds of particles (32). In pioneering research Fatt introduced the concept of connectivity via a regularly coordinated network of capillary tubes (33). Such network models have been used to estimate relative permeabilities, capillary pressures, and formation factors. However, a characteristic network coordi-

nation number, although useful for modeling, is extremely difficult to measure experimentally in porous media as irregular as reservoir rocks.

An approach being developed at the University of Minnesota, the percolation theory of two-phase flow in porous media (10), is followed in this paper to a correlation of pore topology measurements with residual non-wetting saturations after waterflooding. The approach has already been remarkably successful in relating residual non-wetting saturation to the capillary number of displacement (10), in explaining capillary pressure and relative permeability hysteresis (10), in estimating boundary effects on capillary pressure curves (34), and in leading to a theory of relative permeability (35). During the flooding of an initially oil-filled pore space by a wetting fluid, i.e. water, instabilities in interface configurations choke off the necks of oil, in smaller pore throats first, and otherwise break oil connectivity, so that blobs of non-wetting fluid become isolated from the main body of displaced fluid (17,18). Far from every instability produces an isolated blob. In the pore space the locations of breaks are chaotically distributed, and the number of breaks needed on the average to create a blob depends on the connectedness of the pore space. When the wetting phase saturation rises to a critical value the remaining non-wetting phase exists only as disconnected, stranded blobs. This is the residual oil saturation and it is, or is nearly, the percolation threshold of the nonwetting phase. Percolation thresholds in general depend on the connectivity of the structure: the more well-connected a structure, the lower is its percolation threshold. Using percolation theory to explain experimental measurements, we show here that pore topology is as important as pore geometry in setting residual non-wetting saturations.

In order to put fluid displacement experiments under the control of pore morphology it is necessary to fix wettability and capillary number. Capillary number can be maintained at a constant value by using identical fluids and slow rates in experiments, and this we have done. Because controlling the wettability of naturally occurring rocks is difficult, it is advantageous to synthesize porous media of uniform wettability, and this too we have done. Actually the uniform wettability is a natural concomitant of our method of managing pore morphology by controlled sintering of carefully selected granular solids.

Pore Topology

Three-dimensional porous media consist of pore space, parts of which may be accessible from two boundary surfaces and other parts of which may be isolated, and solid matrix that is mostly connected and accessible but may have isolated parts, i.e. loose fines. Pore space and matrix are separated by pore wall, which can be regarded mathematically as oriented surface. Now the topological properties of porous media are invariant under all deformations of pore space and solid matrix, and so different sizes and shapes may be topologically alike. For instance, all the solids in Figure 1(a) are topologically equivalent because they can be continuously deformed into each other. But no such continuous deformation can convert the torus or the equivalent one-holed structure in Figure 1(b) into any of the solids in Figure 1(a), nor the three-holed structure in Figure 1(c) into any of the others.

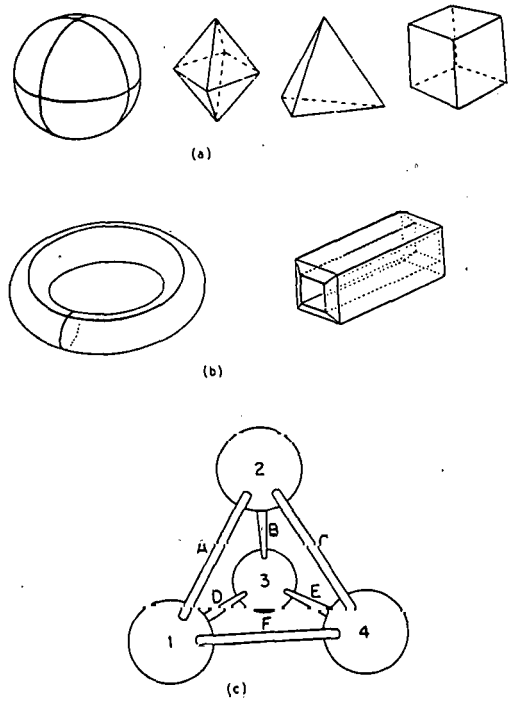

Figure 1. The genus of the solids in (a) is zero, in (b) is one, and in (c) is three.

The fundamental theorem of topology states that two structures are homeomorphic, i.e. topologically equivalent, if and only if their Betti numbers β_i are equal (36-39). The rest of this section is devoted to a geometric interpretation of Betti numbers and their roles in porous media. It sidesteps the mathematical rigors of algebraic topology (38).

The zeroth Betti number β_0 is the number of isolated clusters of disconnected parts in a structure. The four solids in Figure 1(a) are not connected to each other, and so the group as a whole consists of four disconnected clusters; similarly, there are two clusters in Figure 1(b) and one cluster in Figure 1(c).

The first Betti number β_1 is the number of distinct holes through a structure; technically, it is the maximum number of non-intersecting closed curves that can be drawn on the surface of the structure without separating it. Other names for the first Betti number are holeyness and genus. In mathematical literature genus is usual and is denoted by G. Figure 2(a) shows that if a torus is cut along a closed curve ABA, the resulting solid can be deformed into a cylinder; if the cylinder is cut once again along the closed curve CDC, it separates into two disconnected clusters. Thus, the genus of the cylinder is zero whereas that of the torus is one. Similarly, the genus of the tetrahedral structure in Figure 2(b) is three because three of the necks can be cut without increasing the number of clusters. It should be noted that these cuts reduce a multiply-connected structure to one that is simply connected; in the original structure, there are three independent paths between 1 and 2—1A2, 1D3B2, 1F4C2—whereas after the cuts are made there is only one—1D3B2. Thus genus is also a measure of multiplicity of independent paths in

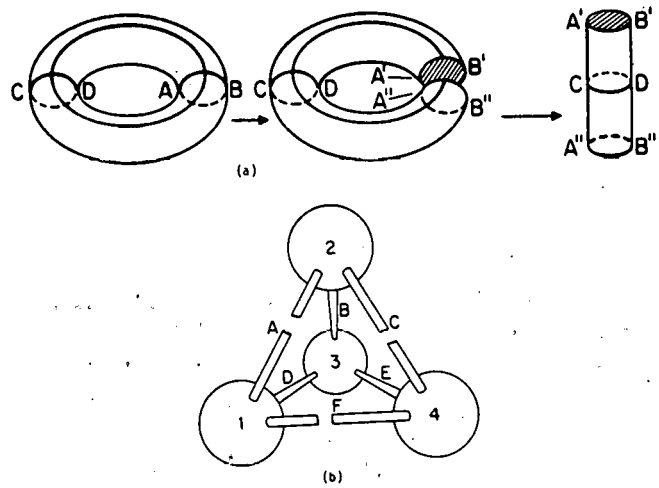

Figure 2. Genus is a measure of the multiplicity of paths in a structure: (a) genus is one; (b) genus is three.

a structure.

The second Betti number β_2 is a measure of the sidedness of a structure. So far the surfaces shown in the figures all bound volumes and so are two-sided—one side of the surface can be regarded as solid material and the other side as pore space. The contrary is illustrated by Moebius strip (Fig. 3(a)): if a normal vector pointing to one side is moved around the continuous strip, it is pointing to the opposite side when it returns to the point it started from, i.e., the surface is one-sided. The topological description of a hollow sphere is the region between two bounding spherical surfaces, one inside the other, on the other sides of which are distinct, i.e. unconnected, regions of space (Fig. 3(b)). It is evident that this hollow sphere cannot be continuously deformed into either a torus or a solid sphere; all three are topologically distinct. The solid shell of a hollow sphere is characterized topologically by $\beta_2 = 1$. Similarly, a solid structure containing n isolated pores has $\beta_2 = n$ because there are n distinct interior regions of space, and so n inside surfaces have to be specified in order to characterize the structure.

In analyzing a porous medium, Betti numbers can be measured of the solid structure, i.e., β_0^S, β_1^S, β_2^S, and of the pore space, i.e., β_0^P, β_1^P, and β_2^P. However, Alexander's duality theorem relates the topologies of pore space and solid matrix (40,41):

$$\begin{aligned} \beta_0^P &= 1 + \beta_2^S \\ \beta_1^P &= \beta_1^S = G \qquad \text{(G is genus)} \\ 1 + \beta_2^P &= \beta_0^S \end{aligned} \tag{1}$$

An obvious corollary is that the sum of distinct regions of pore space and distinct pieces of matrix is independent of the point of view taken:

$$\beta_0^P + \beta_2^P = \beta_0^S + \beta_2^S \tag{2}$$

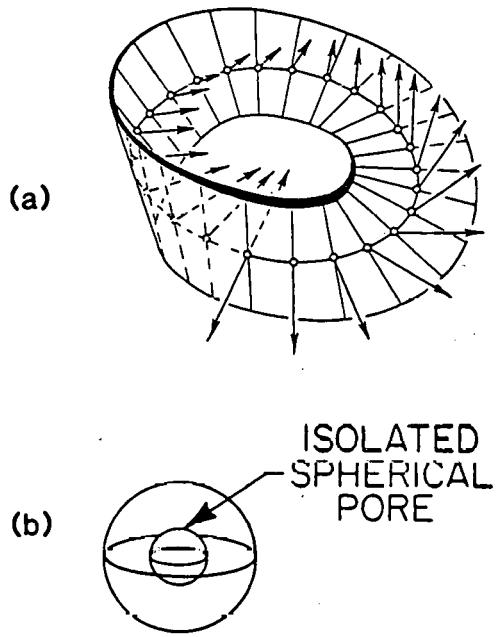

Figure 3. Sidedness of structures: (a) a Moebius strip is a one-sided surface; (b) a hollow sphere has two bounding surfaces, one inside the other.

Thus the topologies of pore space and solid matrix are conjugate; only one need be measured, a very useful circumstance. For instance, the pore space surrounding a solid torus is also doubly connected, and consequently the genus of a solid torus and of the pore space around it are both unity.

In summary, the topology of a three-dimensional porous medium is completely described by its genus or holeyness β_1, which is common to both the pore space and the matrix, by the number of pore clusters β_0^p, and by the number of solid clusters β_0^s. The rest of the Betti numbers follow from Eqs. (1).

These quantities depend on the extent of a porous medium. In media that are locally chaotic but regionally homogeneous their averages over increasingly larger sample volumes become independent of the size of the sample and the location it was taken from, as do the familiar averages known as porosity and permeability. Thus in reservoir rocks there is a range of length scales on which average genus per unit volume G_v, the average number of pore clusters per unit volume β_v^p, and the average number of grain clusters per unit volume β_v^s, are the appropriate measures of topology. In macroscopically homogeneous porous media the corresponding extensive properties, e.g. the total genus (actually its statistical expectation value), are simply proportional to the total volume of sample.

Topological measures per unit volume suffer the seeming deficiency that they depend on the unit chosen for volume. For instance, a lightly consolidated rock consisting of small, well-rounded grains with few grain-to-grain contacts may have the same genus per unit volume as a more heavily consolidated one consisting of large, irregular grains that make many contacts with each other. Therefore it is necessary to choose a natural unit of volume that is appropriate to the local structure that determines the topology of

the porous medium. This is taken up below.

Betti numbers are closely related to incidence matrices that are useful in determining topological structure (42). Pore space can be arbitrarily subdivided, or discretized, into individual pore units, or pore volume elements, and likewise, solid matrix into solid grains, or solid volume elements. A set of surface elements bounds each volume element, a set of lines bounds each surface, and a pair of nodes bounds each line (42). In equivalent network representations (18), volume elements are replaced by zero-dimensional nodes, or points, and surface elements by one-dimensional branches, or lines; this so-called dual representation is convenient in finding the topology of a structure. Incidence matrices—see Ref. 3 for examples—represent the adjacency of elements of different dimension, the matrix entry being zero if elements are not adjacent, and one or minus one (depending on the arbitrarily assigned sense of each element) if they are. For instance, the incidence matrix $\underline{\underline{C}}^{s}_{23}$ represents the adjacency of surface to volume elements in the solid structure, and is identical to $\underline{\underline{\bar{C}}}^{s}_{10}$, the branch-node incidence matrix of the network which is dual. There is, of course, another set of incidence matrices, including $\underline{\underline{C}}^{p}_{23} = \underline{\underline{\bar{C}}}^{p}_{10}$, that relate elements of the pore space. What is fundamental is that if the numbers of i-dimensional elements in a discretization are n_i, and if the ranks of the incidence matrices relating i-dimensional to i + 1-dimensional elements are p_i, then the Betti numbers β_j are given by (37, 40) (note that $\mathcal{r}$ denotes rank)

$$\begin{aligned}
\beta_0 &= n_0 - p_0 \qquad , p_0 \equiv \mathcal{r}(\underline{\underline{\bar{C}}}_{10}) = \mathcal{r}(\underline{\underline{C}}_{23}) \\
\beta_1 &= n_1 - p_0 - (p_1 - 1) \; , p_1 \equiv \mathcal{r}(\underline{\underline{\bar{C}}}_{12}) = \mathcal{r}(\underline{\underline{C}}_{21}) \\
\beta_2 &= n_2 - p_1 - (p_2 - 1) \; , p_2 \equiv \mathcal{r}(\underline{\underline{\bar{C}}}_{23}) = \mathcal{r}(\underline{\underline{C}}_{10})
\end{aligned} \tag{3}$$

With both the pore space and the solid matrix discretized, these equations can be used to determine the topological properties of both. An oft-quoted special case is a genus or holeyness formula,

$$G = \beta_1 = n_1 - n_0 + 1$$

where n_1 is the number of contacts (hence branches in the dual network) between $n_0 = p_0 + 1$ clustered, i.e. connected, particles or pores (hence nodes) —and $p_1 = 1$ because every surface element is bounded by a closed set of lines.

Topology and geometric shape are related by the remarkable Gauss-Bonnet theorem (43). If κ_1 and κ_2 are local principal curvatures of a surface, the local Gaussian curvature is $K = \kappa_1\kappa_2$, which is positive if the local shape is concave or convex and negative if it is saddle-like (44). The integral Gaussian curvature $\mathcal{K}$ of a smooth surface is

$$\mathcal{K} = \int \kappa_1\kappa_2 dS \tag{4}$$

and an extension of this formula covers surfaces with edges and vertices (vertices and curved edges are singular concentrations of Gaussian curvature). The Gauss-Bonnet theorem states that the genus G of a surface is related to its integral Gaussian curvature by

$$\mathcal{K} = 4\pi(1 - G) = 4\pi(1 - \beta_1) \qquad (5)$$

Thus porous media such as reservoir rock, because they are very holey and so have high genus and enormously negative integral Gaussian curvature, must be riddled with pore wall areas that are saddle-shaped. Indeed, every pore throat is such an area—which together with the mechanisms of oil phase disconnection accounts in part for the correlation between residual oil saturation and genus described below.

A second measure of surface shape is the local mean curvature $H \equiv \frac{1}{2}(\kappa_1+\kappa_2)$. The integral mean curvature of a smooth surface is

$$\mathcal{H} = \int \tfrac{1}{2}(\kappa_1+\kappa_2)dS \qquad (6)$$

and there is an extension of this formula too that covers surfaces with edges (which are singular concentrations of mean curvature, whereas vertices have none). An overall measure of pore shape, the integral mean curvature has the dimension of length, in contrast to the lack of dimension of $\mathcal{K}$.

Experimental

Porous Media Synthesis by Sintering

A convenient method of preparing porous media is by sintering, which is the process of heating an unconsolidated bed of particles below their melting point in order to form a coherent porous body. Copper powder was selected as the starting material because (1) it has a so-called high-energy surface, i.e. it is water-wet unlike plastic powders such as teflon which are somewhat easier to work with because of their low melting point; (2) its high thermal conductivity is advantageous for speeding freezing of liquid-filled specimens for scanning electron microscopy studies of oil and water distributions in porous media (45); (3) it has a relatively low sintering temperature of 1000°C (83°C below its melting point) compared with 1600-2000°C for ceramic oxides; and (4) it is available in a variety of forms.

Porous media were synthesized from three different copper powders: (1) spherically shaped grains in the size range 30-90 microns; (2) electrolytically prepared grains of less regular shape in the size range 30-90 microns; (3) electrolytically prepared grains in the size range 250-300 microns. The spherical powder was a product of Cerac, Inc., Menomonee Falls, Wisconsin. As Figure 4(a) shows, not all of the particles were completely spherical. Some were dumbbell-shaped, and others were fusions of small spheres with a larger one, as though the powder was formed by atomization from liquid copper. Even though the particles were 99.5% pure copper, they all had a surface coating of cupric oxide which was removed before starting sintering. The electrolytic copper, which was obtained from Goodfellow Metals, Cambridge, UK, was 99.7% pure with less than 200 ppm of lead and oxygen. Figure 4(b) shows that particle shapes were irregular, and particle surfaces rough. All powders were separated into size classes by using Buckbee-Mears standard micromesh sieves.

Particles with polyhedral shapes were generated by cold compression of spherical powder: see Figure 4(c). Usually parallel dies ¼ inch in diameter

or ½ inch in diameter, one mounted on a ram, were used to apply the compressive stresses. At stress levels of 1.02×10^5psi the copper powder deformed plastically. The presence of any loose powder between the die and ram increased frictional resistance. The height of loose powder was restricted to less than two-thirds of the die diameter. Because the individual compacts were too small to be used in fluid displacement experiments, they served as a source of starting grains of partly or wholly polyhedral shape; i.e. they were broken, resieved, and then sintered to produce a consolidated porous medium.

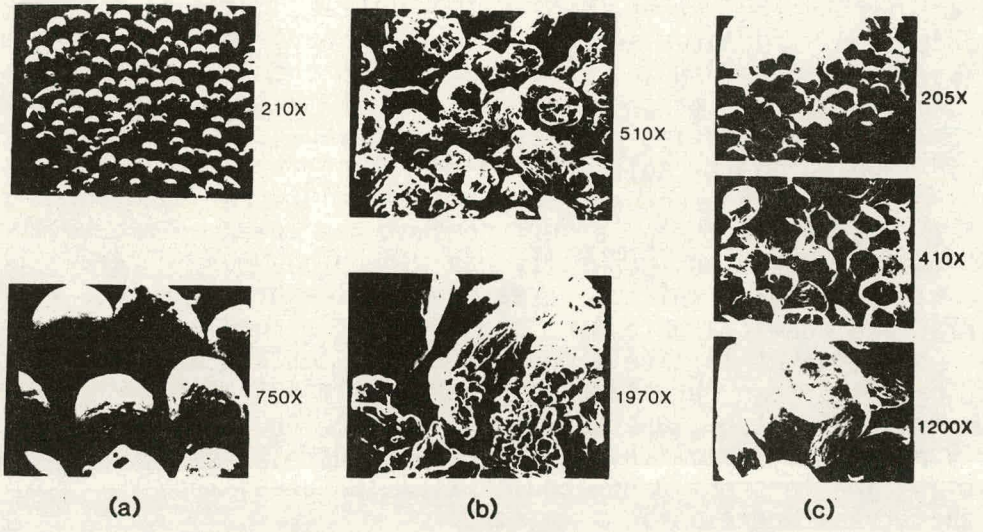

Figure 4. Scanning electron micrographs of powders of copper particles in the size range 30-90 microns: (a) spherical, (b) irregular, (c) polyhedral.

Powders were sintered in a Burrel vertical mount furnace at a temperature of 1000°C ± 5°C under a nitrogen atmosphere. Dry hydrogen gas was introduced for a time at the start of the process, to remove any oxide films on the copper surface.

Microscopy

A Wild stereoscan microscope fitted with a Canon A-1 camera was used for light microscopy. For quantitative measurements of pore morphology, representative planar sections through the porous medium were needed. In order to prevent grain deformation or fracture, the sintered compacts were evacuated and then impregnated with Buehler epoxide resin. After the resin had set, the surface was rough-ground on 100- and 400-grit silicon carbide paper. The final grinding to remove material between successive serial-sections was done with 600-grit silicon carbide powder on a Buehler microcloth. Final surface finishing was done with 1.0 micron and 0.3 micron alumina paste, and this left the copper surface shiny and highly reflective to light.

Displacement Experiments

The Penn State method for measuring relative permeabilities was used because it is fast, accurate, and reliable (46). Saturations were measured

by weighing the test section. The core was evacuated, waterflooded for about 10 pore volumes and then oilflooded for 15-25 pore volumes. Finally water flow was started at a rate corresponding to a capillary number of 2.16×10^{-6}. In all the experiments a white oil, Soltrol 50 from Phillips Petroleum, was used; it is a mixture of aliphatic hydrocarbons in the boiling point range of 116-145°C.

Pore Morphology of Sintered Media

Spontaneous change can be regarded as driven by free energy decrease toward a minimum at equilibrium. In sintering, the dominant free energies are associated with surface areas, surface curvatures, grain boundaries, and crystal imperfection structures in the vicinity of surfaces and grain boundaries (47,48,49). The corresponding contributions to chemical potential provide the driving forces for transport of material in the course of sintering, and during some other compaction processes as in diagenesis of reservoir rock. The chemical potential of solid at and near a surface that has high mean curvature—and which is consequently under a certain strain and hence stress—is generally higher than near a surface that has lower mean curvature. Hence material in convex regions generally has higher chemical potential than material in concave regions, while material in saddle-shaped regions tends to be at intermediate chemical potential and diffuses accordingly. Likewise, the chemical potential of lattice vacancies near a surface of crystalline material that has high mean curvature is generally less than near a surface that has lower mean curvature, and vacancies migrate accordingly. Transport, particularly plastic deformation, is also caused by dislocation movement. Though dislocations are inherently non-equilibrium features, they move in ways that reduce the stress and elastic strain.

In response to these driving forces, the mechanisms of sintering are: (1) vapor phase diffusion, i.e. evaporation and transport through gas to regions of lower chemical potential and partial pressure, where it condenses; (2) surface diffusion, which transports materials from surfaces that are convex to adjacent concave regions; (3) volume diffusion, or vacancy migration; (4) plastic flow by dislocation movement (50). Vapor phase and surface diffusion induce rounding and smoothing of surface contours; this tends to produce surfaces that are locally of minimal area and, as a consequence, uniform mean curvature. For a simply-connected closed surface of zero genus the minimal area may have zero local mean curvature everywhere. Examples of such multiply-connected, minimal surfaces that are periodic are the Schwarz surfaces, which can be regarded as assembled from unit cells of considerable genus (51,52,44).

Sintering proceeds in three stages. At the start, the bed of solid grains is unconsolidated because the point contacts between neighboring grains are incapable of supporting appreciable tensile stress, i.e. point contacts are ineffective and can be discounted here. This unconsolidated bed is characterized topologically by the large number β_0^S of effectively isolated solid grains, a genus of zero, and one connected pore cluster, as shown in Figure 5. As effective necks, i.e. surface contacts capable of supporting tensile stresses, develop between neighboring grains, the packed bed becomes partially consolidated. More and more grains get connected into the solid structure, the number of isolated grain clusters decreases, and so β_0^S falls. Simultan-

eously the genus rises because the holeyness of the solid and pore structures increases: see Figure 5. When the material is fully consolidated, β_0^S is unity.

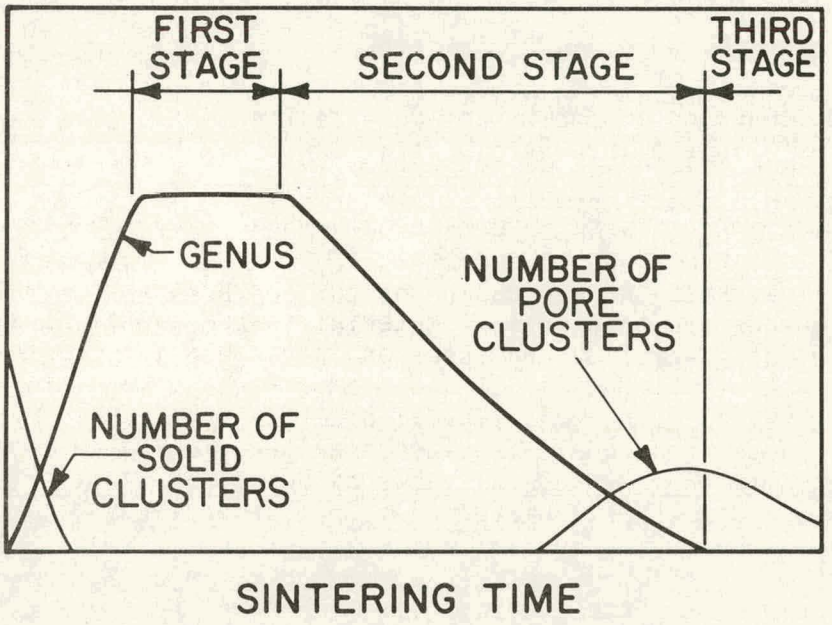

Figure 5. Topological changes during sintering.

First-stage sintering is dominated by changes of geometric shape and size, i.e. surface rounding and smoothing and neck growth. The continued growth of necks reduces the size of pore throats on pore paths. Onset of second-stage sintering is marked by falling genus because grain-neck growth closes pore throats completely. During the second stage, genus continues to fall steadily and some dead-end pores become isolated, while the number of pore clusters β_0^P increases, as indicated in Figure 5. Third-stage sintering is characterized by a genus of zero, and slow reduction in number of isolated pore clusters. The isolated voids are generally small and hardest of all to remove from the solid structure.

Stereological Measurement

If a three-dimensional structure is random, or sufficiently disordered to be approximated as random, its statistical properties can be inferred from measurements made on two-dimensional sections of it. The means of doing this is the theory of stereology (4,5). Evaluating the statistics of topological properties requires a reconstruction of the *three-dimensional* structure. This is a time consuming and laborious task, although it could be automated with a computer-based image analyzer. Certain geometrical properties, however, such as volume fractions, specific surface areas, and specific integral mean curvatures are mathematically related to features on single two-dimensional sections of a specimen. Indeed, a polished section that is extensive enough to be statistically representative suffices for the standard procedure of measuring isotropic and homogeneous structures.

Three-dimensional geometric properties that can be measured from two-

dimensional sections are summarized in Table 1. Surface area per unit volume S_V, which is defined as

$$S_V \equiv \int_V S(v)dv \Big/ \int_V dv \tag{7}$$

is measured by counting the number of intersections N_L that a randomly located test line makes with the interface,

$$S_V = 2N_L \tag{8}$$

Figure 6(a) illustrates the evaluation of surface area per unit volume by counting the number of intersections between five horizontal grid lines and the pore-solid interface.

GEOMETRIC PROPERTY IN 3-DIMENSIONS	STEREOLOGICAL MEASUREMENT ON 2-DIMENSIONAL SECTION
$V_V = A_A = L_L = P_P$	
VOLUME FRACTION V_V	AREAL FRACTION A_A LENGTH FRACTION L_L POINT FRACTION P_P
$S_V = 2N_L$	
S_V SURFACE AREA/VOLUME	N_L - NUMBER OF INTERSECTIONS PER UNIT LENGTH
$\mathcal{H}_V = \pi T_A$	
$\mathcal{H}_V$ - INTEGRAL MEAN CURVATURE	T_A - NUMBER OF TANGENTS PER UNIT AREA
LENGTH OF LINE/VOLUME $L_V = 2P_A$	
CURVATURE OF LINE/VOLUME $C_V = \pi T_V$	
TORSION OF LINE/VOLUME $R_V = \pi I_V$	

Table 1. Stereological measurement of geometric properties of isotropic and homogeneous porous media.

Average mean curvature $\mathcal{H}$ is related to integral mean curvature $\mathcal{H}$ by

$$\mathcal{H} \equiv \mathcal{H}/S = \int_S HdS \Big/ \int_S dS \tag{9}$$

In terms of volume-averaged-integral-mean curvature $\mathcal{H}_V$, this equation is

$$\mathcal{H} = \frac{\int_V H(v)dv}{\int_V S(v)dv} = \frac{\mathcal{H}_V}{S_V} \tag{10}$$

A fundamental relationship that was derived independently by Cahn (53) and Dehoff (54) simplifies the determination of $\bar{\mathcal{H}}$. They showed that irrespective of the shape of the three-dimensional surface, $\bar{\mathcal{H}}$ can be expressed in terms of the easily measured lineal curvature k on a representative two-dimensional section:

$$\bar{\mathcal{H}} = (\pi/2)\ \bar{k} \tag{11}$$

$\bar{k}$ is simply determined by sweeping a test line across the section and counting the number of tangents that the line makes with the pore-solid interface (4). Interfaces concave to pore space form positive tangents; let their number per unit area be T_A^+. Interfaces convex to pore space form negative tangents; let their number per unit area be T_A^-. Then

$$\bar{\mathcal{H}} = 2\pi(T_A^+ - T_A^-)/S_v \tag{12}$$

Regardless of the shape of closed curves in the plane, $(T_A^+ - T_A^-)$ always equals the number of closed curves per unit area. A vertical line which is swept across the square shown in Figure 6(b) forms 37 positive tangents, which lie on the pore-side of the interface, and 43 negative tangents, which lie on the solid-side. Thus, integral mean curvature per unit volume $\mathcal{H}_v$ is -9.9×10^3 cm^{-2}, the average mean curvature $\bar{\mathcal{H}}$ is -26 cm^{-1}.

There are three basic topological parameters that can be evaluated only from successive serial sections through the porous medium: the number of isolated solid grains per unit volume β_v^s, the genus per unit volume G_v, and the number of isolated pores per unit volume β_v^p. A two-dimensional polished section shows interconnected systems of solid cross-sections and pore cross-sections. Some of these cross-sections are isolated in the section, some are multiply-connected, and some end at the boundary, as can be seen in Figure 7, and as can be transcribed into section incidence matrices for computer processing. Some pore cross-sections that intersect the sample boundary may interconnect outside, and if they do they contribute to genus in a way that cannot be found directly (although it could be estimated from measurements on the interior of the specimen). One way to get bounds on genus is to consider two extreme situations: if all paths were to reconnect outside, the genus would be a maximum, G_{max}; on the other hand, if none of the paths were to reconnect outside, the genus would be a minimum, G_{min}.

Each cluster of connected pore or solid cross-sections in a given section is labeled, and identified insofar as possible with a cluster or clusters in the next serial section; this information can be suitably coded into a cluster-cluster incidence matrix to facilitate construction of incidence matrices of the three-dimensional structure from those of the two-dimensional serial sections. The distance between successive serial sections needs to be small enough to allow easy identification of each cluster by its shape and size. But if the distance between sections is too small, few changes in the connectivity structure of clusters will be noticed, and so a large number of sections will have to be analyzed to obtain statistically significant measurements of genus per unit volume (55,56,54). In this work generally 10 to 15 polished sections were taken per mean particle diameter, and typically about 5 to 8 changes in connectivity were observed between successive sections of the size shown in

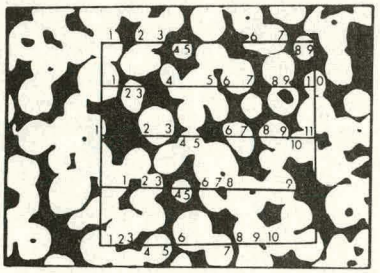

108X

Number of intersections = N_L = 49

$$S_v = 2N_L = \frac{2 \times 49 \times 1 \text{ in.} \times 108}{10 \text{ in.} \times 2.54 \text{ cm}} = 416 \frac{\text{cm}^2}{\text{cm}^3}$$

(a)

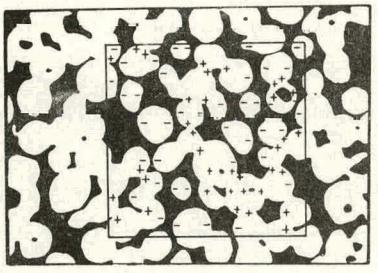

108X

$$T_A^+ - T_A^- = -6$$

$$\overline{\mathcal{H}} = \frac{\mathcal{H}_v}{S_v} = \frac{3.142 \times (-6) \times (108)^2}{4 \times (2.54)^2} \frac{1}{S_v} = -20.48 \text{ cm}^{-1}$$

(b)

Figure 6. Evaluation of surface area per unit volume and average mean curvature by stereological methods.

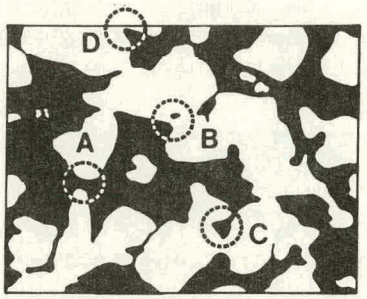

(a)

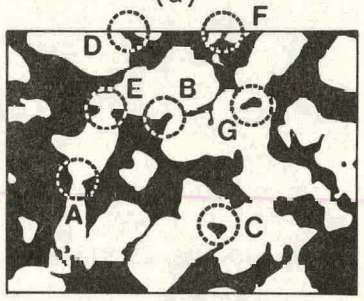

(b)

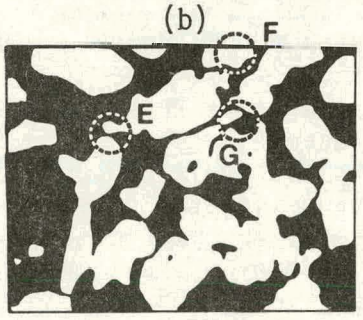

(c)

Figure 7. Topological changes between successive serial sections.

Figure 7. Some topological changes between Figures 7(a) and (b) are: (A) a pore path between two clusters disappears; (B) a pore path between two clusters appears; (C) a deadend pore becomes isolated in the section; (D) a pore path to the boundary appears. Some changes between Figures 7(b) and (c) are: (E) clusters that were connected in Figure 7(a) are now connected by another path; (F) a pore path to the boundary disappears; (G) a pore that was isolated in the section connects to another pore. Some of these changes such as (E) contribute to both G_{max} and G_{min}; others such as (D) contribute only to G_{max}; other such as (A) or (C) do not contribute to G_{max} or G_{min} (55,56). If G_{max} and G_{min} are plotted against cumulative volume of sample analyzed, both curves approach the same constant slope after a sufficient number of serial sections have been analyzed, as shown in Figure 8. This common slope measures average genus per unit volume, which is the property that characterizes pore topology and, by Alexander's duality theorem, Eq. (1), topology of the solid matrix as well.

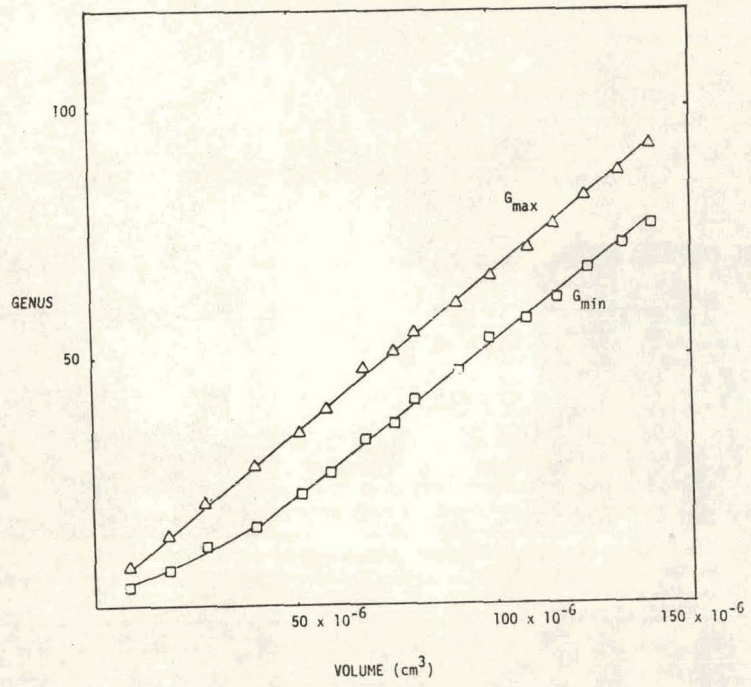

Figure 8. G_{max} and G_{min} vs. volume of sample analyzed.

Pore Morphology

Although quantitative measurements are generally made from polished planar surfaces, valuable qualitative information about pore morphology can be gleaned from fracture surfaces, which are far from planar. Because of their unevenness, fracture surfaces are best viewed by scanning electron microscopes, which usually have much larger depths of field than light microscopes. Scanning micrographs of fracture surfaces of copper powder that has been sintered for only 15 minutes show that the spherical powder is largely unconsolidated, i.e. very few surface contacts have formed: see Figure 9. However, if powder of the same kind is cold-pressed into polyhedral shapes at a stress of 1.02 x 10^5 psi, the average number and area of contacts per particle increases; if this cold-pressed compact is then sintered for 15 minutes, there is extensive growth of necks between particles, as shown in Figure 10. Along the fracture surface the places where these necks have broken, and they do so by ductile failure, show up as large areas of the characteristic honeycomb structure that is associated with dimple formation by microvoid coalescence (58).

As the degree of sintering rises, porosity diminishes, surface roughness disappears, necks grow in size, and solid grains begin to form extended, well-interconnected networks: see Figure 11. If the polyhedral particles formed by cold-pressing to 1.02 x 10^5 psi are first separated and resieved, and then sintered, the fraction of sheet-like pores is reduced and, as Figure 12 reveals, regions of large local mean curvature are absent.

Surfaces of a compact sintered in air are completely covered with flaky cupric oxide, as shown in Figure 13. These highly irregular surfaces illustrate the diversity of porous media that can be synthesized by sintering for

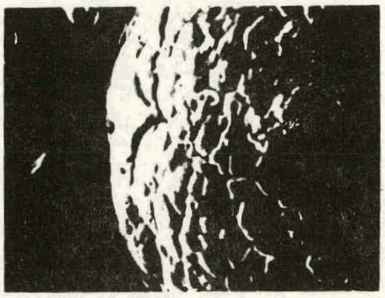

275X

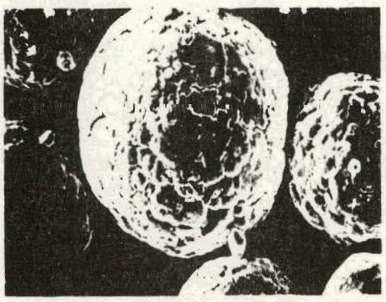

1010X

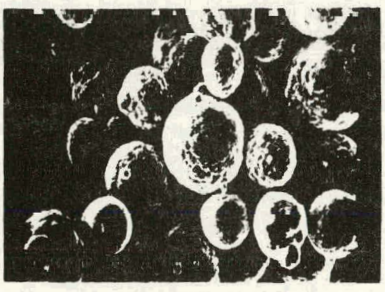

2600X

Figure 9. Spherical copper particles sintered for 15 minutes.

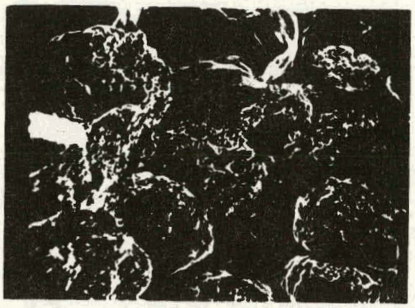

520X

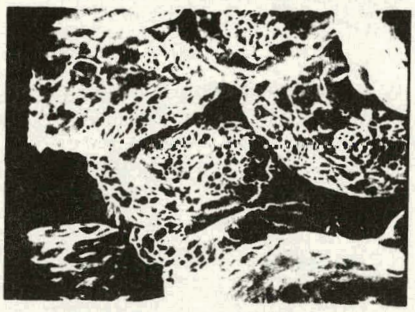

1030X

5000X

Figure 10. Polyhedral particles which are formed by cold-pressing powder of spherical particles, sintered for 15 minutes.

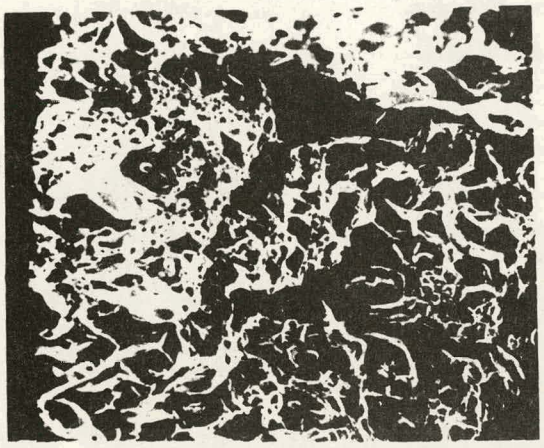

505X

2000X

Figure 11. Polyhedral particles sintered for 2 hours.

Figure 12. Polyhedral particles sintered for 2 hours (after cold pressing, the compact was broken, resieved and then sintered).

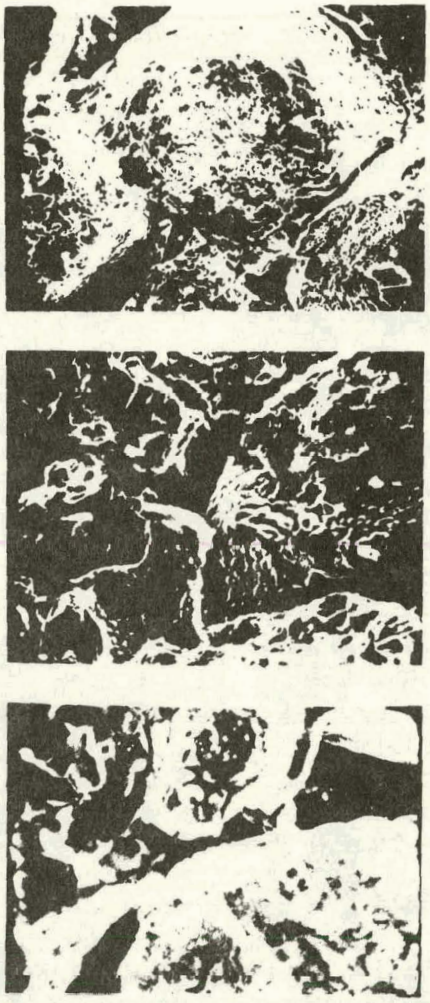

Figure 13. Polyhedral copper particles sintered for 1 hour in air.

use in modeling the morphology of sedimentary rock. Because the oxide film changes wettability, samples sintered in air were not used in fluid displacement studies; all of the samples employed were sintered in nitrogen atmospheres.

Measurements of average topological properties of sintered copper samples are summarized in Table 2. Figure 14 shows that genus per unit volume G_V decreases monotonically with increasing density. Specimens prepared from all three powders of sieve size range 30-90 microns, i.e. an average nominal diameter of 60 microns, were in the second stage of sintering: pore paths had started to close, a process that reduces the genus of solid and pore structures. The solid grains were fully consolidated, and there were no isolated clusters of solid.

Because of surface irregularities such as sharp edges and corners, i.e. regions of high local curvatures, beds of irregular or polyhedral particles pack to higher average number of contacts per particle than do beds of spherical particles (59). Upon sintering, ineffective, point-like contacts between neighboring particles develop into competent surface contacts, and so sinters

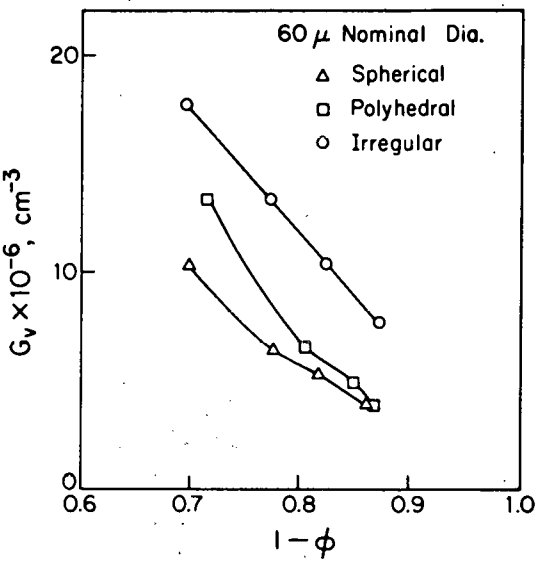

Figure 14. Connectivity, as measured by genus per unit volume G_V, of sintered copper cores.

of irregular and polyhedral particles have higher genus per unit volume than sinters of spherical particles at the same porosity—down to a limiting range. However, most of the G_V stems from slender necks. With increasing degree of sintering, surface rounding smooths out regions of high local mean curvature (cf. Fig. 12), and G_V of sinters of polyhedral particles approaches G_V of sinters of spherical particles. At porosities below 20 percent, isolated pores that are generally quite small begin to appear, i.e. the number of pore clusters increases. Specimens in this range of porosity are near the end of second-stage sintering and would soon have entered third-stage sintering. Surface irregularities promote the formation of small pores that can be isolated easily by grain-neck growth; thus the number of isolated pores per unit volume is higher for irregular and polyhedral particles.

Because isolated pores in effect have zero genus so far as fluid flow is concerned, the values of G_V reported in Table 2 are based exclusively on pores that are accessible in the percolation theory sense, i.e. pores that are each connected to opposite sides of the specimen.

Measured average geometric properties of sintered copper compacts used as cores in this research are summarized in Table 3. Because all the surface roughness and sharp edges of the original powders are smoothed out during the first stage of sintering, in the second stage the specific surface areas S_V no longer depend on the original powder shape and surface texture, as indicated in Figure 15. That is, sinters of spherical, polyhedral, and irregular particles in the size range 30-90 microns have equal specific surface areas at the same porosity (60). Apart from some regions on the irregular ones, the unsintered particles are convex to pore space; because locally both principal curvatures tend to be distinctly negative, the average mean curvature $\bar{\mathcal{H}}$ of unconsolidated particles beds is negative. But as sintering proceeds, saddle-shaped regions appear at the necks that grow at contacts, and in these regions, one principal curvature tends very strongly to be of opposite sign, i.e. positive,

SINTERS OF SPHERICAL PARTICLES

Porosity	$G_V X10^{-6}$ (cm^{-3})	$N_V X10^{6}$ (cm^{-3})
0.302	10.22	0
0.225	6.31	0
0.181	5.29	0
0.141	4.01	0.071

SINTERS OF POLYHEDRAL PARTICLES

Porosity	$G_V X10^{-6}$ (cm^{-3})	$N_V X10^{6}$ (cm^{-3})
0.283	13.4	0
0.193	6.13	0
0.152	4.73	0.103
0.139	3.91	0.12

SINTERS OF IRREGULAR PARTICLES

Porosity	$G_V X10^{-6}$ (cm^{-3})	$N_V X10^{6}$ (cm^{-3})
0.309	17.37	0
0.237	13.21	0
0.182	10.28	0.083
0.129	7.8	0.129

Table 2. Topological properties of sintered copper porous media: genus per unit volume G_V (cm^{-3}), number of isolated pores per unit volume N_V (cm^{-3}). All particles were of 60μ nominal diameter (30-90μ range).

SINTERS OF SPHERICAL PARTICLES

ϕ	S_V (cm^2/cm^3)	$\mathcal{H}_V X10^{-5}$ (cm^{-2})	$\bar{\mathcal{H}}$ (cm^{-1})
0.302	421	-0.099	-24
0.225	367	0.22	60
0.181	310	0.89	287
0.141	263	1.07	406

SINTERS OF POLYHEDRAL PARTICLES

ϕ	S_V (cm^2/cm^3)	$\mathcal{H}_V X10^{-5}$ (cm^{-2})	$\bar{\mathcal{H}}$ (cm^{-1})
0.283	437	-0.061	-14
0.193	336	0.826	246
0.152	281	1.127	401
0.139	272	1.151	423

SINTERS OF IRREGULAR PARTICLES

ϕ	S_V (cm^2/cm^3)	$\mathcal{H}_V X10^{-5}$ (cm^{-2})	$\bar{\mathcal{H}}$ (cm^{-1})
0.309	453	-0.0947	-21
0.237	369	0.413	112
0.182	304	0.899	296
0.129	261	1.18	452

Table 3. Geometric properties of sintered copper porous media: porosity ϕ, surface area per unit volume S_V (cm^2/cm^3), integral mean curvature per unit volume $\mathcal{H}_V$ (cm^{-2}), and average mean curvature $\bar{\mathcal{H}}$ (cm^{-1}). All particles were of 60μ nominal diameter.

and so $\mathcal{H}$ becomes less negative. During first-stage sintering when genus is constant, the pore-solid interface, or pore wall, tends towards a minimal surface that has zero local mean curvature. But the continued growth of necks decreases the cross-section of pore segments, until finally some pore throats —walled by saddle-shaped interface—pinch-off. During the second stage of sintering, pore throat closure reduces genus but increases average mean curvature, as shown in Figure 16.

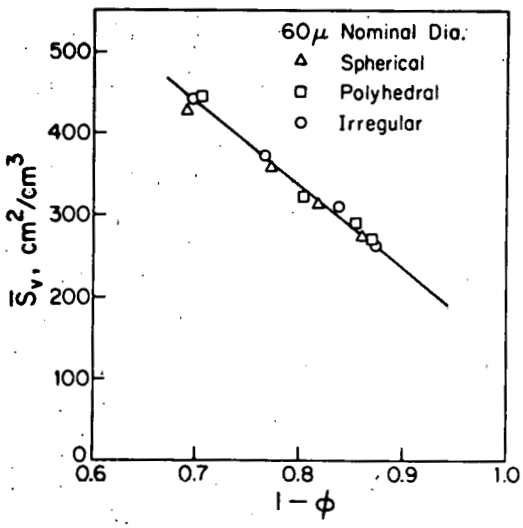

Figure 15. Surface area per unit volume, S_V, of sintered copper cores.

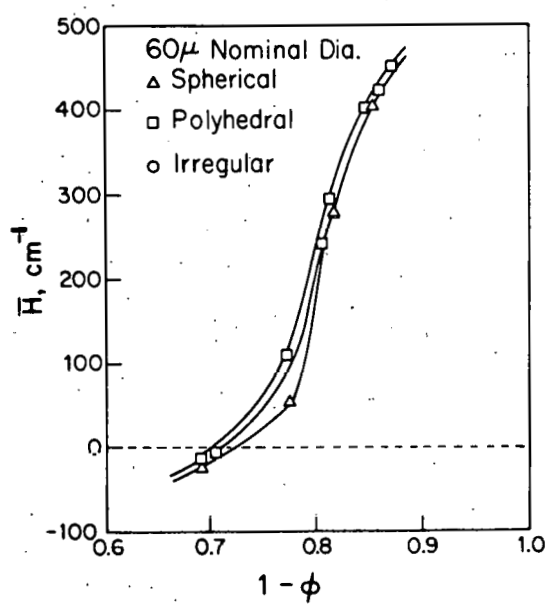

Figure 16. Average mean curvature H of sintered copper cores.

In this study, the sintering times and temperature were deliberately chosen so as to produce cores in the second stage of sintering because such cores can be distinguished topologically by genus per unit volume and number of pore clusters per unit volume; they can of course be distinguished geometrically by porosity. Although other geometrical factors such as specific surface S_v and mean curvature $\bar{\mathcal{H}}$ are needed to characterize more fully the cores, they are nearly the same for spherical, polyhedral, and irregular particle sinters at the same porosity. Surface roughness differences between cores were insignificant because of the surface smoothing during the first stage of sintering.

Because genus per unit volume depends on the underlying scale which is originally set by particle size, the connectivity data collected for sinters of irregular particles in the size range 250-300 microns cannot be compared directly with the data for sinters of various shapes of particles in the size range 30-90 microns. The unit of volume should be a natural one. One candidate is the average current volume per initial particle in the sinter. Another is the average current volume per branch point in the network equivalent to the current pore space, or to the current solid matrix. A third candidate is the volume unit based on the current total mean curvature per unit volume (viz. $\mathcal{H}_v^{-2/3}$). The first candidate has two disadvantages: the significance of the original particle count may diminish as sintering advances; and grain shapes may change drastically during sintering. But within a given shape class, i.e. sinters of particles of different sizes but geometrically similar shapes, the average current volume per initial particle appears to be a reasonable choice. If ℓ_i is the nominal initial particle diameter this unit of volume is proportional to $\ell_i^3/(1-\phi)$ and the corresponding measure of genus is

$$\mathcal{G} \equiv G_v \ell_i^3/(1-\phi) \qquad (13)$$

This quantity is proportional to the genus per particle (the factor would be $\pi/6$ were the particles uniform spheres), which in turn is related to the average coordination $\bar{z}$ of the particles so long as they retain their identities, i.e. $G/n_0 = (\bar{z}/2) - 1$ (n_0 large).

Connectivity changes as measured by $\mathcal{G}$ correlate well with the porosity of the various sinters of irregular particles of 60 micron nominal diameter and 275 micron nominal diameter, as shown in Figure 17.

Residual Non-wetting Saturations of Sintered Media

The disconnection of an originally continuous non-wetting phase is controlled by the instabilities of throat menisci as saturation falls and of head menisci as they move (18). The residual non-wetting fluid resides as disconnected blobs that are held trapped by head menisci in pore throats, although these blobs can be mobilized by greatly increasing capillary numbers (9,19). Although disconnection and mobilization processes depend on the distributions of features of pore space morphology, treating their consequences by percolation theory leads to a two-parameter model of how residual non-wetting saturation depends on capillary number (10). One parameter measures pore-geometry-dependent resistance to passage of the menisci that locally separate two fluid phases. Though this was treated as a limited but adjustable parameter for the

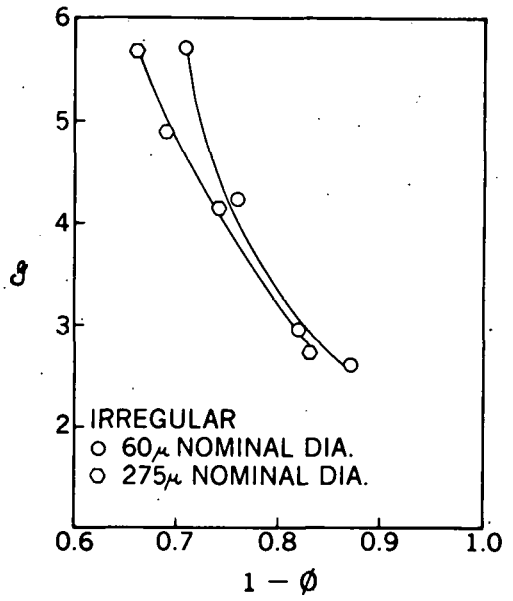

Figure 17. Genus per particle, of sinters of 60μ and 275μ nominal diameter copper powder.

purpose of correlation (10), it is often modeled by means of distribution of pore-throat and pore-body sizes (18,25). The second parameter is essentially a percolation threshold and depends on pore topology, i.e. the connectivity, or genus, which characterize the number of alternative routes of meniscus passage. It too was treated as an adjustable parameter for correlating residual non-wetting saturation. Data are reported here that establish the profound importance of the actual genus of the pore space to the residual saturation of oil.

Measured oil (non-wetting phase) saturation S_{or} plotted as a function of porosity in Figure 18 shows that this zeroth-level measure of pore geometry is not sufficient to characterize the effect of pore morphology on the mechanisms that lead to entrapment of residual oil. As brought out in the last section, during second-stage sintering a number of the average geometrical features are distinguished by porosity alone. Yet sinters of spherical, polyhedral, and irregular particles have different residual oil saturations at identical porosities, and so it is logical to seek the explanation in the topological differences between the sinters. Larson et al. (10) found that in porous sedimentary rocks, the product of porosity ϕ and residual saturation S_{or} is at least approximately equal to the percolation threshold ϕ_c of the network equivalent of the pore space,

$$\phi_c \simeq \phi S_{or} \tag{14}$$

The percolation threshold ϕ_c of the pore space network is a purely topological variable, i.e. it depends only on the genus of the pore structure. If values of ϕS_{or} that were measured for the sintered copper porous media are plotted against genus per unit volume, G_v, the results for all three kinds of particles—spherical, polyhedral, and irregular—fall on the same line, as shown

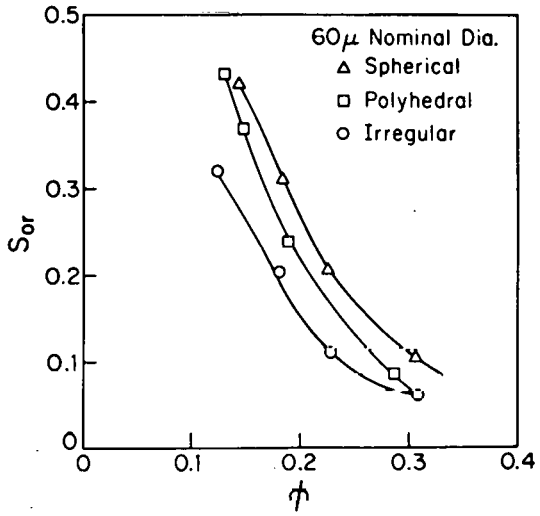

Figure 18. Residual oil saturations of sintered copper cores.

in Figure 19. *The larger the connectivity as measured by* G_v *is, the larger the number of interconnections between pores, the greater the number of alternative routes available for oil drainage, the lower the percolation threshold* ϕ_c*, and the lower the residual oil saturation.* This result is further

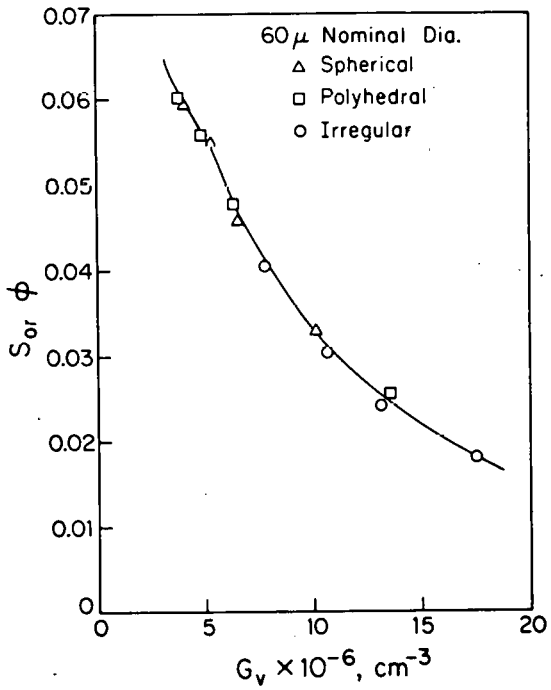

Figure 19. Effective percolation threshold $S_{or}\phi$ of non-wetting phase in cores with different genus per unit volume G_v.

substantiated by plotting ϕS_{or} for sinters of irregular particles against the dimensionless genus : Figure 20. Regardless of the size of the starting particles and pores, increases in genus result in decreases of ϕS_{or}, the percolation threshold of the pore structure. In lightly sintered irregular particles most of the G_v arises from slender necks, as noted above. Although these contributions to G_v could be quite important in setting a wetting phase residual during a non-wetting flood, the substantially smaller G_v corresponding to larger throats and channels presumably control non-wetting residual. Thus there is incentive to measure not just genus in a porous medium, but also the way it is distributed over pore size and shape.

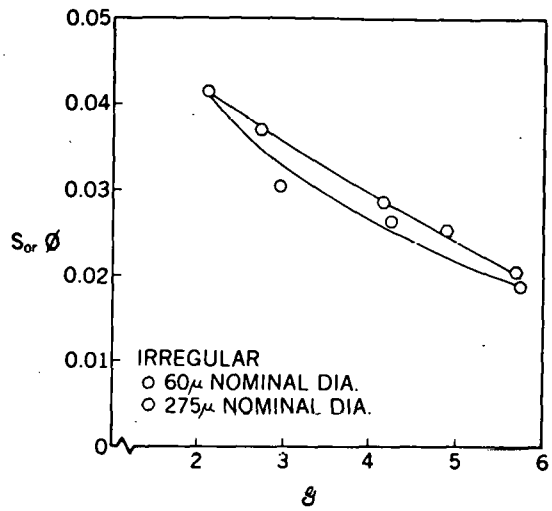

Figure 20. Effective percolation threshold $S_{or}\phi$ of non-wetting phase in cores with different genus per initial particle.

Conclusions

Pore topology, or connectivity structure, is experimentally confirmed to be as important to residual non-wetting saturations in permeable rock as pore geometry is known to be. The topology is described by three counts called Betti numbers, which can be reckoned on a unit volume basis. Of these the genus, or holeyness, per unit volume of porous rock directly affects and correlates well with residual non-wetting saturation. The measurements reported quantify an observation that is often qualitatively stated: residual non-wetting saturations are lower in porous media having well-connected pores than in those having pores that are not well-connected.

Connectivity structure can be designed and controlled by working in the laboratory with synthetic rocks prepared by sintering. Sintering parallels, in many important respects at least, diagenesis of sedimentary rocks. The size and shape distributions of the starting powders and the degree of sintering are the main control parameters. Copper powders offer several advantages, one of which is the ready availability of particles of different sizes and shapes. Pore-wall roughness can also be managed through the sintering process.

Pore topology and matrix topology are directly interrelated; indeed they share the same genus, so that only the genus per unit volume of the pore space

or of the solid matrix need be measured. Moreover, there is a close relationship between this genus and integral Gaussian curvature, a measure of the total curvature of the pore surface which separates pore space from solid matrix.

The topology is inherently three-dimensional and to measure it requires thorough examination of serial sections through samples, or other means of surveying three-dimensionally the rock. Measurement methods are available in the science of stereology. Mathematical methods are at hand for reducing the measurements, in particular through use of incidence matrices and their equivalents. Geometrical and compositional data can efficiently be gathered and reduced at the same time. There is great need for development of appropriately automated, computer-based image analysis of serial sections, in combination with fracture surfaces, for the evaluation of average morphological parameters, their distributions and correlations.

That the approach is feasible for small samples even without computerized facilities is demonstrated in the present work. The techniques employed appear to be as applicable to reservoir rocks as they are to the synthetic rocks actually used.

To arrive at basic, unified understanding of fluid distributions and flows in reservoir rocks and other porous media appears to require detailed study of pore-space morphology and pore-level physics in concert with percolation theory and associated statistical means of relating macroscopic properties, such as residual saturations, to the distributions of microscopic features.

References Cited in Section IX

1. Hilbert, D. and Cohn-Vossen, D., Geometry and the Imagination, Chelsea Press, New York (1952).

2. Courant, R. and Robbins, H., What is Mathematics?, Oxford Univ. Press, London (1941).

3. Pathak, P., Winterfeld, P. H., Davis, H. T. and Scriven, L. E., SPE Paper No. 8846, presented at the First Joint SPE/DOE Symposium on Enhanced Oil Recovery, 20-23 April, 1980; Journal of Petroleum Technology 34, 381-395 (1982).

4. Rhines, F. N. and DeHoff, R. T., Quantitative Microscopy, McGraw-Hill, New York (1968).

5. Underwood, E. E., Quantitative Stereology, Addison Wesley, New York (1970).

6. Fischmeister H. F., Powd. Met. Int. 7 (4), 178 (1975).

7. Beddow, J. K., Vetter, A. F. and Sisson, K., Powd. Met. Int. 8 (2), 69 and 8 (3), 107 (1976).

8. Leverett, M. C., AIME Tech. Publ., 1003 (1938).

9. Melrose, J. C. and Brandner, C. F., J. Can. Pet. Tech. 13 (4), 54-62 (1974).

10. Larson, R. G., Scriven, L. E. and Davis, H. T., Chem. Eng. Sci. 36, 57-73 (1981); Larson, R. G., Scriven, L. E. and Davis, H. T., Chem. Eng. Sci. 36, 75-85 (1981).

11. Owens, W. W. and Archer, D. L., J. Pet. Tech. 23, 873-878 (1971).

12. Teletzke, G. F., Scriven, L. E. and Davis, H. T., SPE Paper 10112, presented at SPE 56th Annual Fall Meeting, San Antonio, TX, 5-7 October 1981.

13. Rathmell, J. J., Braun, P. H. and Perkins, T. K., J. Pet. Tech. 25, 175 (1973).

14. Lefebvre du Prey, E. J., Soc. Pet. Eng. J. 13, 39 (1973).

15. Odeh, A., Trans. AIME 216, 346 (1959).

16. Roof, J. G., Soc. Pet. Eng. J. 10, 85-90 (1970).

17. Strand, S. R., Hurmence, C. J., Davis, H. T., Scriven, L. E. and Mohanty, K. K., to be submitted to Chem. Eng. Sci. (1983).

18. Mohanty, K. K., Ph.D. thesis, University of Minnesota (1981); Mohanty, K. K., Davis, H. T. and Scriven, L. E., SPE Paper 9406 presented at SPE 55th Annual Fall Meeting, Dallas, TX, 21-24 September 1980.

19. Ng, K. M., Davis, H. T. and Scriven, L. E., Chem. Eng. Sci. 33, 1009-1017 (1978).

20. Morrow, N. R., presented at 29th Annual Meeting of Pet. Soc. of CIM, Calgary, June 1978.

21. Morgan, J. T. and Gordon, D. T., J. Pet. Tech., 1199 (1970).

22. Morrow, N. R., Chem. Eng. Sci. 25, 1799 (1970).

23. Mohanty, K. K., Davis, H. T. and Scriven, L. E., in Surface Phenomena in Enhanced Oil Recovery, Shah, D. O., ed., Plenum Press, 595-609 (1981).

24. Morrow, N. R., Bull. AAPG 55, 514-522 (1971).

25. Chatzis, I. Morrow, N. R. and Lim, H. T., SPE/DOE Paper 10681, presented at SPE/DOE Third Joint Symp. on Enhanced Oil Recovery, Tulsa, OK, 4-7 April 1982.

26. Weinbrandt, R. M. and Fatt, I., J. Pet. Tech. 21, 543-548 (1969).

27. Schrank, J. and Hunt, E., Scanning Electron Microscopy/180/1, SEM Inc., AMF O'Hare, IL (1980).

28. Wardlaw, N. C. and Cassan, J. P., Bull. Can. Pet. Geol. 26, 572-585 (1978).

29. Dullien, F. A. L. and Batra, V. K., Ind. Eng. Chem. 62 (10), 25-53 (1970).

30. Dullien, F. A. L. and Dhawan, G. K., J. Coll. Int. Sci. 47, 337-349 (1974).

31. Dullien, F. A. L., Chatzis, I. and El-Sayed, M. S., SPE Paper 6191, presented at SPE 51st Annual Fall Meeting, New Orleans, LA, 3-6 October 1976.

32. Kozeny, J., Sitzungsber Wiener Akad. Abt. IIa, 135, 271 (1927a).

33. Fatt, I., Trans. AIME 207, 144-181 (1956).

34. Larson, R. G. and Morrow, N. R., Powd. Tech. 30, 123-138 (1981).

35. Heiba, A. A., Sahimi, M., Scriven, L. E. and Davis, H. T., SPE Paper 11015, presented at the SPE 57th Annual Fall Technical Conference, New Orleans, LA, 26-29 September 1982.

36. Veblen, O., Analysis Situs, Am. Math. Soc. Coll. Lect. Vol. VI, New York, (1916).

37. Alexandroff, P., Elementary Concepts of Topology, Dover, New York, (1961).

38. Lefschetz, S., Applications of Algebraic Topology, Springer-Verlag, New York (1975).

39. Barret, L. K. and Yust, C. S., Metallography 3, 1-33 (1970).

40. Cairns, S. C., Introductory Topology, Ronald Press, New York (1961).

41. Aleksandrov, P. S., Combinatorial Topology Vol. 1, Graylock Press, Rochester, NY (1956).

42. Pathak, P., Ph.D. thesis, University of Minnesota (1981).

43. Kreyszig, E., Differential Geometry, University of Toronto Press, Toronto, (1959).

44. Scriven, L. E., in Micellization, Solubilization and Microemulsions, Vol. 2, Mittal, K. L., ed., Plenum Press, 877-895 (1977).

45. Pesheck, P. S., Davis, H. T. and Scriven, L. E., to be submitted to Rev. Sci. Instr. (1983).

46. Morse, R. A., Terwilliger, P. L. and Yuster, S. T., Oil and Gas J. 46 (16), 109 (1947).

47. Rhines, F. N., Reutte Plansee Proc. 3rd Seminar, Reutte, Tyrol (1958).

48. Kuczynski, G. C., Trans. AIME 185, 169-178 (1949).

49. Lenel, F. V. and Ansel, G. S., in Modern Developments in Powder Metallurgy, Vol. 1, Hausner, H. H., ed., Plenum Press, New York (1966).

50. Waldorn, M. B. and Daniell, B. L., Sintering, Inst. Chem. Eng., London; published by Heyden and Son, Philadelphia (1978).

51. Schwarz, H. A., Gesammelte Mathematische Abhandlung, Vol. 1, Springer, Berlin (1890).

52. Nitsche, J. C. C., Vorlesungen über Minimalfalchen, Springer-Verlag, Berlin (1975).

53. Cahn, J. W., Trans. Met. Soc. AIME 239, 617 (1967).

54. DeHoff, R. T., Trans. Met. Soc. AIME 239, 617 (1967).

55. DeHoff, R. T. and Aigeltinger, E. H., in Adv. Expt. Tech. in Pow. Met., Vol. 5, Hirschorn, J. S. and Roll, K. H., ed., Plenum Press, New York, (1970).

56. DeHoff, R. T., Aigeltinger, E. H. and Craig, E. R., J. Microscopy 95, 69 (1972).

57. Aigeltinger, E. H. and DeHoff, R. T., Met. Trans. A 6A, 1853-1862 (1975).

58. SEM/TEM Fractography Handbook, McDonnell Douglas Astronautics Co., Huntington Beach, CA, sponsored by Air Force Materials Lab., Metals and Ceramics Information Center (1975).

59. Gray, W. A., The Packing of Solid Particles, Chapman and Hall, London (1968).

60. DeHoff, R. T., Rummel, R. A. LaBuff, H. P. and Rhines, F. N., in Modern Development in Powder Metallurgy, Vol. 1, Hausner, H. H., ed, Plenum Press, New York (1966).

X. PERCOLATION THEORY OF TWO-PHASE RELATIVE PERMEABILITY

Introduction

The concurrent, slow flow of two immiscible fluids such as oil and water through a porous medium can be described by extending Darcy's law to apply to each fluid (1,2,3). That is, the volumetric flux of each phase is proportional to the gradient of mechanical potential (pressure gradient and body force field) acting on that phase and is inversely proportional to its viscosity. The coefficient of proportionality is the Darcy permeability to that phase, a property having the dimension of area. It is usually expressed as the product of a dimensionless relative permeability and the absolute Darcy permeability k of the medium to flow when just one fluid fills the porespace of the medium. Thus the relative permeability to phase j is given by the familiar formula:

$$k_{rj} = \left(\frac{Q_j}{A}\right) \frac{\mu_j}{k} \Big/ \left|\nabla p + \rho_j \underset{\sim}{f}\right| \qquad (1)$$

This definition seems to account for the fluid viscosity in μ_j and the porespace in k, so that the relative permeability might depend solely on the division of the pore volume between the two fluids, i.e. on their saturations S_j — which must sum to unity, so that only one of the two is independent. The situation is much more complicated in reality.

Measured relative permeabilities are found to depend on the saturation histories as well as the saturations of the fluids (4,5), on the porespace morphology (6), on the wetting characteristics of the fluids (7,8), on the ratio of fluid viscosities (9,10), and on the capillary number of flow (11,12). The capillary number indicates the relative importance of viscous stresses exerted by the fluids and the capillary pressures developed in interfaces between them at the pore level. (Moreover, the relative permeability to a phase typically becomes small or altogether negligible when its saturation falls below a value that is distinctly above zero (13)). Further details were reviewed by Larson *et al.* (14, 15,16). While rationales have been advanced for some of this bewildering variety of factors, there has been no sound theory of relative permeability, and quantitative description of multiphase flow through permeable media has rested on experiment alone.

But understanding is increasing of the underlying physical mechanisms and the roles of porespace geometry and topology (17-26), and a qualitative picture has emerged. Each flowing phase occupies its own set of channels, i.e. a continuous connected subspace of the porespace, and in steady two-phase flow there is no movement of the fluid interfaces between the flowing phases (apart from emulsified droplets of one in the other, which are not considered here). If one phase, say water, strongly wets the porewalls, then the set of channels occupied by the nonwetting phase, say oil, consists of sample-spanning clusters of pores that are filled by that phase, apart from thin-film states of low hydraulic conductivity and virtually isolated pendular bodies of the wetting phase. If the two phases locally exert negligible shear stress on each other, then according to the equations of local motion within the porespace, i.e. the Stokes-flow system of equations, the relative permeability of a phase depends solely on the way it is distributed within the porespace. The way a phase is distributed is

controlled by the interplay of porespace morphology, the capillary and normal viscous stresses on its fluid interfaces, the shapes those interfaces take on within the pores, and the stability of the shapes. The shapes actually taken on by the interfaces depend on the proportion of porespace occupied by the phase and the way that proportion was reached, i.e. saturation and saturation history; the reason history enters is that there are multiple shapes that satisfy the demands of the Stokes-flow system — which is made non-linear by the free interfaces (25,26). The shapes also depend on the wettability of the porewalls, which controls the apparent contact angle wherever an interface encroaches on porewall (27,28). The relative importance of capillary and normal viscous stresses in locating interfaces depends on the capillary number. And if the two phases exert appreciable shear stress on each other, then the ratio of their viscosities must also affect their relative permeabilities (29,9).

Most important to the way a phase is distributed in the porespace is the morphology of that porespace. However highly irregular it is, its connectivity, or topology can be represented by a network and its geometry can be represented to a first approximation by recording along the network the radius of the largest sphere that can be locally inscribed within the porespace. Further approximations can also be recorded along the network, as for instance the local resistance to flow through the porespace. Pore bodies and pore throats can be defined in terms of appropriate maxima and minima of largest-inscribed-sphere-radius. All of the volume of a pore body can be assigned to the corresponding network node; alternatively it can be apportioned among the network branches, which represent throats. Elementary branch points within a pore body can be fused into network nodes of coordination greater than three. All of this has been worked out in detail (26, 30). Thus in principle any porous medium can be reduced to a topologically equivalent network and to properties assigned to nodes and branches of that network. For sedimentary rocks and most other porous media the coordination numbers and dimensional properties will obviously be quite chaotically distributed — indeed, virtually randomly distributed.

The intuitive idea of porespace as a network led Fatt (31) and others (32, 33,34) to model two-phase channel flow through a porous medium by (i) choosing a regularly-coordinated network of finite size, (ii) assigning pore radii to nodes and bonds according to some hypothesis about the distribution of pore size and shape, (iii) distributing two phases to a given saturation level according to postulated mechanisms by which one phase would have displaced the other, (iv) calculating flow rate through the channel network occupied by each phase, given a pressure or mechanical potential difference imposed across the overall network, and (v) evaluating the relative permeability from Equation (1). This whole procedure can be repeated for equivalent assignments of pore radii and distributions of phases and statistics of relative permeability can be compiled. This amounts to the Monte Carlo strategy, and it need not be restricted to regularly-coordinated networks (35,36).

There is another approach that leads more directly to accurate estimates of relative permeability, though it sacrifices effects of spatial relationships among parts of the porespace. This approach employs the distributions of relevant features of pore morphology (i.e. no spatial correlations), still incorporates the mechanisms by which the phases compete for porespace, and relies on percolation theory. A statistical approach, its pertinence to relative permeability was explored by Larson (15) but all of the needed ingredients were not clear at

that time. It was, however, successful in explaining the distribution of non-wetting phase in porous media (14,15,37,38) and in accounting for capillary pressures measured when mercury is injected and retracted from porespace (39). In this paper percolation theory is brought fully to bear on relative permeability.

In this work we introduce a disordered bond network as a model of porespace: all germane pore properties are assigned to bonds which are thereby elevated from throat cross-sections (30) to whole pore-segments between branch points. We also introduce the fraction of bonds or throat-segments *allowed* to a given phase, the accessibility function that describes what fraction of allowed bonds are actually *accessible* and therefore occupied by an invading phase, and the conductivity function that describes the distribution of slow-flow hydraulic *conductances* of the bonds or throat-segments.

In the basis of physical arguments we adopt throat radii as the throat-segment occupancy criteria for drainage and imbibition when one of the phases strongly wets the pore walls. From the occupancy criteria we derive general formulas for the saturation-dependent drainage and imbibition relative permeabilities of the two fluids.

For the purpose of illustrating the general formulas we apply them not to a disordered bond network of porespace, but rather to a disordered bond *tree*, i.e. a special kind of network that lacks any reconnections. Though this sort of model would appear to be less appropriate to porespace, it is remarkably successful in fitting experimental measurements of relative permeabilities in reservoir rocks. Its attraction is that accessibility and conductivity functions can be derived analytically for a regularly branching tree, called a Cayley or Bethe tree. We explore the sensitivity of predictions based on these functions to the coordination number of the tree, the throat radius distribution function and the throat-segment conductance and volume functions.

In what follows we find the Bethe tree to be surprisingly effective as a model of porespace morphology and compare tree prediction of relative permeability with those obtained by the Monte Carlo method on a six-coordinated, three-dimensional network. We also discuss extending the theory to account for two-phase relative permeabilities in situations other than where one phase is strongly wetting, as in regimes of intermediate or mixed wettability. Also mentioned are extensions of the theory to three-phase systems.

In the Appendix we give sufficient detail of the theory that others wishing to apply it for different choices of coordination number, pore-throat radius distribution function and the throat-segment conductance and volume functions can do so without difficulty.

Concepts From Percolation Theory

Percolation theory, which was invented by Broadbent and Hammersley (40) seeks by statistical means to describe the morphology of, and transport through, randomly disordered media. As actually developed the theory pertains to network models that consist of branches, or bonds, or links, and nodes, or sites, or junctions. Of all the bonds and sites in a network, those that are actually present in a state under study, or are potentially active in a process, are termed *allowed*. Percolation is defined as the generation of a continuous path of connectedness and thus transport through a randomly allowed set of bonds and

sites of a network. The strict definition refers to a continuous path of infinite extent, i.e. across an unbounded network. Among the quantities covered by percolation theory are the

(1) *accessibility*, measured by the accessible or percolation fraction, the probable fraction of bonds or sites connected to such a continuous path,

(2) *effectiveness*, measured by the *backbone fraction*, the probable fraction of sites or bonds active to transport, i.e. the accessible fraction minus its dead ends,

(3) *equivalent conductivity*, the conductivity of the entire network when the allowed bonds (and possibly allowed sites) have distributed conductances, and

(4) *percolation threshold*, the largest fraction of allowed bonds or sites below which the accessible fraction and equivalent conductivity is zero.

Percolation on regular networks, and on the specializations known as trees, is well reviewed by Shante and Kirkpatrick (41), Essam (42), Kirkpatrick (43) and Frisch and Hammersley (44). Its relevance to flow in porous media is surveyed by Larson *et al.* (14).

Reservoir rocks are so chaotic in their morphology that even if the measurements to define the equivalent networks of representative small samples were feasible, Monte Carlo computations of fluid distributions and relative permeabilities in those networks could be costly (the issue is currently under investigation). An expedient approximation — and a logical preliminary in any case — is to approximate the chaotically coordinated porespace of a sedimentary rock by a regular network or tree of appropriate uniform coordination. This gross approximation of the connectivity, or topology, is only half of the story: the other half is the geometry of the porespace (36), which can be approximated by distributions over the nodes and bonds of a regular network or tree. We employ such distributions here. And for simplicity, as mentioned in the Introduction, we assign all distributed properties of the porespace, in particular pore volume and resistance to flow, to the bonds in the network or tree, which therefore become models of whole pore-segments between branch points of porespace (30). The nodes become essentially zero-dimensional features with no role except as markers of branching. The nodes are supposed to allow the simultaneous passage of any number of phases, and are characterized by the effective coordination number of the porespace locally.

The approximating network or tree, even if it is supposed to be unbounded in extent, must have well-defined inflow and outflow surfaces (or injection and extraction nodes) for the passage of fluid. Portions of networks and a tree satisfying these requirements are depicted in Figure 1.

Of the bonds present a fraction may be *allowed* to occupancy by any fluid. This fraction corresponds to the porosity of the rock, including its isolated porosity, which is inaccessible and hence not active to permeability. Hereafter by porespace we mean accessible porespace. Of that porespace, and therefore of

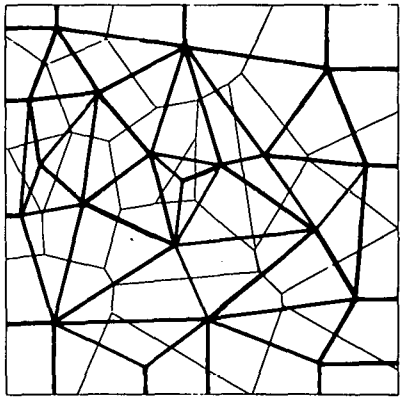

A

Fig. 1(A)—Network generated from Voronoi tesselation.[65]

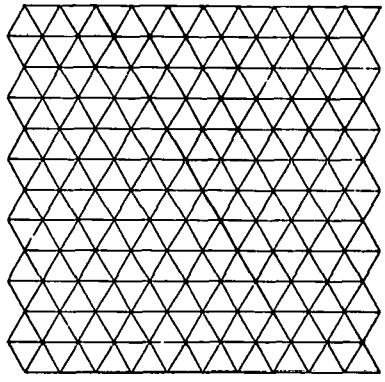

B

Fig. 1(B)—Triangular network.

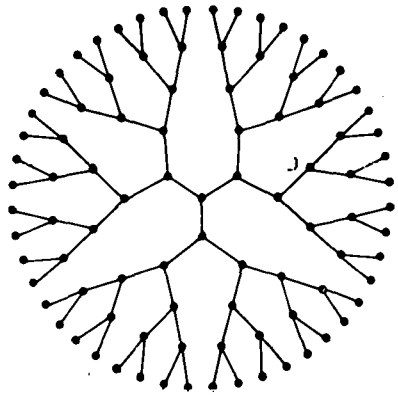

C

Fig. 1(C)—Bethe tree of local coordination number 3.

the bonds of the network representation, an *allowed fraction* X may be assigned to a displacing phase. This fraction is controlled by the physics of displacement, as described in the next section. Whether an arbitrarily chosen pore is occupied by that phase is contingent on the probability that it is, or was, accessible to that phase, i.e. that it is both allowed to the phase *and* is or has been connected to a continuous path or bond-cluster of infinite extent composed or randomly allowed bonds occupied by the phase. Such a path is bound to cross inflow and outflow surfaces and so is called sample-spanning (14-16, 37-39); in the reality of a finite porous medium any path that crosses both surfaces is infinite so far as phase accessibility is concerned. By $X^a(X)$ we denote the relative frequency of occurrence of accessible bonds of the network or tree; this is the percolation fraction, accessible fraction (45) or, as we shall call it herein, the accessibility function, a standard concept in percolation theory.

An accessibility function $X^a(X)$ depends only on network coordination, or topology, and the fraction X of allowed bonds when all is random. Moreover, when the fraction of allowed bonds falls below a critical value X_c, termed the bond percolation threshold, the allowed bonds exist exclusively as isolated clusters of finite extent and correspond to hydraulically isolated, stationary phase. At and above the percolation threshold, a cluster of indefinitely great extent appears, so that the probability that any given allowed bond is part of an infinite cluster approaches unity. Thus

$$X^a(X) = \begin{cases} 0, & X < X_c \\ \\ \to X \text{ as } X \to 1 \end{cases} \qquad (2)$$

Deriving accessibility functions $X^a(X)$ and the associated percolation thresholds X_c is a basic task of percolation theory. In Section 4 we make use of results for certain trees.

The volumes of individual pore segments or bonds are among the geometric quantities that characterize porespace. However, these geometric quantities may correlate strongly enough with throat radius and segment length that they can be represented as a function of the latter, or a more general set of pore parameters $\underline{S}$; then the distribution of volumes V is simply related to the distribution of the parameters $\underline{S}$. In two-phase flow of the sort contemplated here each phase occupies its own set of pore segments, all of which either are connected or were connected at an earlier stage of occupancy. Those that are connected are the clusters of accessible bonds, and those that are not are the isolated clusters, in the language of percolation theory. The total volume occupied by a phase is simply the sum over the segments in which that phase resides; if the distributions of occupied segments in both accessible and isolated clusters can be identified, the summation can be converted to an integration over geometrical parameters $\underline{S}$, as is done in the next section.

The slow-flow volumetric flowrate q through an individual pore-segment or bond is, according to the theory of Stokes flow (46), directly proportional to the difference in pressure Δp between adjacent branch points or nodes (apart from streamwise normal viscous stress, which necessarily vanishes somewhere in the vicinity of each branch point and is not considered here). It is also inversely proportional to the viscosity μ_j of the flowing phase. The proportionality is a conductance g that depends on the shape and size of the pore-segment. If both phases were to occupy significant portions of the same pores g would also depend on the viscosity ratio, a possibility that is not pursued here. Thus for an individual pore-segment or bond,

$$q = g\Delta p/\mu_j \tag{3}$$

Now certain geometric aspects of the pore-segments are germane to relative permeability. If these aspects are characterized by a set of distributed parameters $\underline{S}$, then the distribution of pore-throat conductances can be described by the probability $G(g(\underline{S}))\ dg$ that a pore-segment characterized by $\underline{S}$ has conductance between g and g+dg. In fact the absolute permeability of the porespace is proportional to the hydraulic conductance of the approximating network or tree with the bonds randomly assigned conductances according to $G(g(S))$. Alternatively, in two-phase flow, the permeability of the set of pore-segments occupied by a phase comes only from those in accessible clusters (in fact, only from those in the backbones of such clusters, because dead ends are inactive in flow). That permeability is proportional to the hydraulic conductance of the connected clusters; all other bonds on the network or tree are assigned a conductance of zero. This is a simplification that is possible because we presume that the sites of the network or tree are able to pass more than one fluid simultaneously. We ignore the effects of two-phase crossflow at the nodes. The corresponding random distribution of bond conductances on the *entire* network or tree is

$$G_j(g(\underline{S})) = (1-X_j^*)\delta(g(\underline{S})) + X_j^* G_j(g(\underline{S})) \tag{4}$$

$\delta(g)$ is the Dirac delta function, which is zero if $g \neq 0$ and has unit area. In the case that phase j is the displacing phase, X_j^* and $G_j(g(\underline{S}))$ are, respectively,

the allowed fraction of bonds for that phase and the probability distribution of the conductances of these bonds. The allowed fraction X_j^* appears in Equation (4) even though the displacing phase does not occupy all of the allowed bonds: the reason is that the displacing phase is supposed to occupy all accessible bonds. Alternatively, in the case that phase j is the displaced phase, and can be taken to be disconnecting randomly, X_j^* and $G_j(g(\underline{S}))$ are, respectively, the fraction of bonds occupied by that phase and the corresponding probability distribution of the conductances of those bonds. $G_j(g(\underline{S}))$ is an example of what we shall call a phase-conductivity function. The single-phase conductivity function $G(g(\underline{S}))$ is of course a limiting case of G_j.

To derive mathematically the conductivity, and hence the permeability, of a phase from a phase-conductivity function is a formidable problem. The only available solutions are for Cayley or Bethe trees, and these are employed in what follows. But even without a solution one feature is plain: if there is no sample-spanning cluster of bonds occupied by a given phase, i.e. if $X_j^* < X_c'$, the permeability of that phase is zero.

The equivalent conductivity of an approximating network or tree having a random distribution of bond conductances of the form $G_j(g(\underline{S}))$ is proportional to the permeability of the phase. The proportionality constant depends only on the structure and not on the occupancy of the approximating network or tree. Hence its value is irrelevant to *relative* permeabilities, which are determined by equivalent conductivity ratios.

Statistical Theory of Relative Permeability

From here on we restrict consideration to a pair of incompressible Newtonian fluids, one of which strongly wets the pore surfaces and therefore always coats them if only as a thin-film of negligible hydraulic conductance (47). We suppose that fluid displacements are at low enough capillary numbers that the competition between local mechanical potential gradient and capillary forces together with pore-shape-controlled interface instabilities govern the distribution of the two phases in the porespace. Thus as wetting-phase saturation falls, which is often called "drainage," we have the nonwetting phase occupying first those pore-segments that have the widest throats and are on the verge of accessibility. And similarly as wetting-phase saturation rises, which is often called "imbibition," we have the wetting phase occupying first those pore-segments that have the narrowest throats (25). Notwithstanding the ubiquity of thin-films of wetting fluid we suppose that each throat-segment, or bond, is filled with one phase or the other, at least so far as relative permeability and saturation are concerned.

The independent geometric parameters characterizing the configuration of pore-segments we take to be one: throat radius r. It measures the maximum magnitude of capillary pressure of a head meniscus passing through the throat, and it relates directly to the capillary pressure responsible for throat takeover by wetting phase through collar growth and choke-off (25). Parametrizing porespace so simply not only enables us to lay out the theory, but also leads to accurate correlations of relative permeability data, as described in what follows. Moreover, the theory can be systematically enlarged to account for additional parameters should they prove necessary and measurements of them become available. Throat-radius parametrizations have been common in the literature since Fatt's pioneering work (31).

Geometrical disorder we incorporate in a normalized distribution function $\alpha(r)$ of throat radii over bonds of the network chosen to approximate the topology of porespace. Throat-segment volume V and conductance g we idealize as being perfectly correlated with throat radius, i.e.

$$V \equiv V(r) \quad \text{and} \quad g \equiv g(r) \tag{5}$$

Thus the probability distribution function for pore-throat segment hydraulic conductances is

$$G(g(r)) = \alpha(r) \left| \frac{dr}{dg} \right| \tag{6}$$

Here $G(g(r))$ is the previously described single-phase conductivity function. The absolute permeability of the porespace is proportional to the equivalent conductivity of the approximating network or tree with a random distribution of bond conductances given by Equation (6). The theory can be systematically enlarged to incorporate pore volume and conductance distributions depending on several pore parameters $\underline{S}$, though at considerable cost in complexity.

Drainage Relative Permeabilities

Consistently with the typical experimental procedure (48,49) for measuring relative permeabilities as wetting fluid w is incrementally displaced by nonwetting fluid n, we consider the range of saturations from porespace totally occupied by wetting phase down to the fractional filling at which wetting fluid loses its hydraulic connectivity across the sample, i.e. the "irreducible" wetting phase saturation (which is actually slowly reducible owing to the slight flow conductivity of the persistent thin-film states on the pore walls, but this conductivity can be regarded as not hydraulic).

As the key parameter of stage of displacement we have the capillary pressure between the flowing fluids, which translates into the minimum throat radius r_d through which head menisci can penetrate, and nonwetting fluid thereby displace wetting fluid (25). As a stand-in for capillary pressure we adopt r_d as the throat-segment or bond occupancy criterion (the intimate link between capillary pressure and relative permeability will be developed in another paper — Heiba *et al.* to be published). A given stage of drainage is parametrized by a particular value of r_d: at that stage all throat-segments of *larger* radius are allowable to nonwetting phase, but that phase will have entered only those that are accessible. The fraction of throat-segments or bonds that is allowed is

$$X_d \equiv \int_{r_d}^{\infty} \alpha(r)dr \tag{7}$$

while that actually occupied by the nonwetting phase during drainage is

$$X_{n,d} \equiv X^a(X_d) \quad , \tag{8}$$

where $X^a(\ )$ is the accessibility function of the approximating network or tree.

As described at Equation (4), the nonwetting phase drainage conductivity function $G_{n,d}(g(r))$ corresponds to that random distribution of bond conductivities which is gotten by assigning a conductance of zero to all bonds that are not allowed to occupancy by the displacing nonwetting phase. That is, zero conductance is assigned to throats of radius less than r_d. Thus

$$G_{n,d}(g(r)) \equiv (1 - X_d)\delta(g(r)) + X_d G_{n,d}(g(r)) \tag{9}$$

where $G_{n,d}(g(r))\, dg$ is the probability that a bond allowed to occupancy by the nonwetting phase has conductance between g and g+dg. In this case the allowed conditional conductance probability is

$$G_{n,d}(g(r)) \equiv \alpha_{n,d}(r) \left| \frac{dr}{dg} \right| \tag{10}$$

where $\alpha_{n,d}(r)\, dr$ is the probability that a bond allowed to occupancy by nonwetting fluid during drainage has radius between r and r+dr. Because the nonwetting phase is allowed to all bonds with radius greater than r_d,

$$\alpha_{n,d}(r) = \begin{cases} \dfrac{\alpha(r)}{X_d} & , \quad r \geq r_d \\ 0 & , \quad r < r_d \end{cases} \tag{11}$$

The relative permeability of the nonwetting phase during drainage $k_{rn,d}$ is the equivalent conductivity of the approximating network or tree with the random distribution or bond conductances given by Equation (9), divided by the equivalent conductivity of the network or tree having the random distribution of bond conductances given by Equation (6).

As the nonwetting fluid invades to higher saturation, the capillary pressure between the phases climbs, the head menisci penetrate smaller throats, and the wetting phase loses porespace. It also loses interconnections. Because throats of all sizes are supposed to be randomly distributed in space, the remaining wetting phase presumably occupies randomly placed bonds that constitute the fraction $X_{w,d} \equiv 1 - X_{n,d}$. As described at Equation (4), the phase conductivity function of the displaced wetting phase during drainage $G_{w,d}(g(r))$ corresponds to the random distribution of bond conductances obtained by assigning a conductivity of zero to all bonds not occupied by the wetting phase. Thus

$$G_{w,d}(g(r)) \equiv (1 - X_{w,d})\delta(g(r)) + X_{w,d} G_{w,d}(g(r)) \tag{12}$$

where $G_{w,d}(g(r))\, dg$ is the probability that a bond containing wetting phase has conductance between g and g+dg. This occupancy-conditional conductance probability $G_{w,d}(g(r))$ given by

$$G_{w,d}(g(r)) = \alpha_{w,d}(r) \left| \frac{dr}{dg} \right| \tag{13}$$

where

$$\alpha_{w,d}(r)\,dr \equiv \begin{cases} \dfrac{1 - \dfrac{X_{n,d}}{X_d}}{1 - X_{n,d}}\ \alpha(r)\,dr \quad , & r \geq r_d \\ \dfrac{1}{1 - X_{n,d}}\ \alpha(r)\,dr \quad , & r < r_d \end{cases} \tag{14}$$

is the probability that a bond containing wetting phase during drainage have radius between r and $r+dr$. The relative permeability of the wetting phase during drainage $k_{rw,d}$ is the equivalent conductance of the approximating network or tree having the random distribution of bond conductances given by Equation (12) divided by that given by the single-phase conductivity function defined in Equation (6).

The drainage process is said to terminate when the stage is reached at which the wetting phase loses hydraulic conductivity between the surfaces of the sample. This happens when $X_{w,d}$ falls past X_c, the bond percolation threshold of the network chosen. At any $X_{w,d} < X_c$ the remaining bonds occupied by wetting phase form clusters of finite size and the network permeability to wetting phase is zero. Higher capillary pressures cannot displace wetting phase hydraulically, and so nonwetting phase can penetrate no further. The radius of the smallest throat, $r_{d,c}$, penetrated by nonwetting phase at the termination of drainage follows from

$$1 - X_{w,d} = 1 - X_c = X^a(X_{d,c}) \quad ,$$

$$X_{d,c} \equiv \int_{r_{d,c}}^{\infty} \alpha(r)\,dr \tag{15}$$

At a stage of drainage characterized by r_d the volume fraction of porespace occupied by wetting phase, i.e. the wetting phase saturation $S_{w,d}$, is

$$S_{w,d} = \frac{X_{w,d} \int_0^{\infty} \alpha_{w,d}(r)V(r)\,dr}{\int_0^{\infty} \alpha(r)V(r)\,dr} \tag{16}$$

Here $X_{w,d}$ is the previously defined number fraction of pores containing wetting phase; $\int_0^{\infty} \alpha_{w,d}(r)V(r)\,dr$ is the average volume of a pore-throat segment

containing wetting phase; and $\int_0^\infty \alpha(r)V(r)\,dr$ is the average volume of all pore-throat segments. $\alpha_{w,d}(r)\,dr$ is the probability that a pore-throat segment containing wetting phase have radius between r and r+dr: it is defined in Equation (14). Plainly Equation (16) is the volume weighting of the number fraction of pores containing wetting phase.

Imbibition Relative Permeabilities

Consistently with the typical experimental procedures (48,20) for measuring relative permeabilities as nonwetting fluid is incrementally displaced by wetting fluid, we consider the range of saturations from porespace containing only the hydraulically irreducible wetting phase saturation up to the fractional filling at which nonwetting fluid loses its connectivity across the specimen, i.e. the irreducible or residual nonwetting phase saturation (which is actually reducible by raising the capillary number sufficiently that trapped nonwetting fluid is mobilized, but what is treated here is the low capillary number regime).

In order to avoid algebraic complications that only obscure the development and contribute little to accuracy we assume that the asymptotic equality given in Equation (2) for the bond accessibility function of the approximating network or tree, i.e.

$$\lim_{X \to 1} X^a(X) = X \qquad (2)$$

holds for $X \geq 1 - X_c$. For the various network models of porespace topology considered in what follows this approximation is excellent. With this approximation Equation (15) becomes a more compact definition of $r_{c,d}$, the smallest throat penetrated by nonwetting pahse during drainage

$$X_c = \int_0^{r_{d,c}} \alpha(r)\,dr \qquad (15')$$

A consequence of this assumption is that when the displaced wetting phase loses its hydraulic conductivity during drainage, the wetting phase occupies all pore-throat segments with radius less than $r_{d,c}$ and the nonwetting phase occupies all the rest.

Again the key parameter of stage of displacement is the capillary pressure between the flowing fluids, which translates into the largest throat radius r_i that wetting phase can invade through advance of head menisci or flow into collars that choke off the nonwetting phase (25). At a stage of imbibition parametrized by a particular value of r_i all randomly placed throat-segments of *smaller* radius are allowable to occupancy by wetting phase. The allowed fraction of bonds is

$$X_i = \int_0^{r_i} \alpha(r)\,dr \qquad (17)$$

The actual fraction of bonds occupied by the advancing wetting phase $X_{w,i}$ is merely the fraction of accessible bonds having radius less than r_i, plus all previously occupied bonds of radius less than $r_{d,c}$. Thus

$$X_{w,i} = X_c + \frac{X^a(X_i)}{X_i}(X_i - X_c) \tag{18}$$

Clearly if $r_i \leq r_{d,c}$ no new bonds are allowed to occupancy by wetting phase and $X_{w,i} = X_c$.

As described at Equation (4), the wetting phase imbibition conductivity function $G_{w,i}(g(r))$ corresponds to the random distribution of bond conductivities obtained by assigning a conductance of zero to all bonds not allowed to occupancy by invading wetting phase, i.e. those that have a throat radius greater than r_i. Thus

$$G_{w,i}(g(r)) \equiv (1-X_i)\delta(g(r)) + X_i G_{w,i}(g(r)) \tag{19}$$

where $G_{w,i}(g(r))\,dg$ is the probability that a bond allowed to occupancy by the wetting phase has conductance between g and g+dg. The allowed-conditional conductance probability $G_{w,i}(g(r))$ is given by

$$G_{w,i}(g(r)) \equiv \alpha_{w,i}(r) \left| \frac{dr}{dg} \right| \tag{20}$$

where $\alpha_{w,i}(r)\,dr$ is the probability that a bond allowed to occupancy by wetting fluid has radius between r and r+dr. Because the wetting phase is not allowed to advance into bonds with radius greater than r_i,

$$\alpha_{w,i}(r) \equiv \begin{cases} \dfrac{\alpha(r)}{X_i}, & r < r_i \\ 0, & r \geq r_i \end{cases} \tag{21}$$

The relative permeability of the advancing wetting phase $k_{rw,i}$ is the conductivity of the approximating network or tree having the random distribution of bond conductances given by (19) divided by the equivalent conductivity of the network or tree having the single phase distribution of conductances defined in Equation (6).

As the wetting fluid invades to higher saturation the nonwetting fluid is disconnected by choke-off in larger and larger throats, and by snap-off events as head menisci move through other large throats (25). Because throats of all sizes are supposed to be randomly located through the porespace, the remaining

nonwetting fluid presumably occupies randomly placed bonds that constitute the fraction $X_{n,i} \equiv 1 - X_{w,i}$. Thus as described at Equation (4), the phase-conductivity function of the displaced nonwetting phase during imbibition, viz. $G_{n,i}(g(r))$, corresponds to the random distribution of bond conductances obtained by assigning a conductivity of zero to all bonds not occupied by the nonwetting phase. Therefore

$$G_{n,i}(g(r)) = (1 - X_{n,i})\delta(g(r)) + X_{n,i}G_{n,i}(g(r)) \tag{22}$$

where $G_{n,i}(g(r))\,dg$ is the probability that a bond containing nonwetting phase has conductivity between g and g+dg. The occupied conditional conductance probability $G_{n,i}(g(r))$ is given by

$$G_{n,i}(g(r)) \equiv \alpha_{n,i}(r) \left| \frac{dr}{dg} \right| \tag{23}$$

where

$$\alpha_{n,i}(r)dr \equiv \begin{cases} 0 & r < r_{c,d} \\ \dfrac{[1 - \dfrac{X^a(X_i)}{X_i}]\alpha(r)}{[1 - X_{w,i}]} & , \; r_{c,d} \le r < r_i \\ \dfrac{\alpha(r)}{[1 - X_{w,i}]} & , \; r \ge r_i \end{cases} \tag{24}$$

is the probability that a bond containing nonwetting phase during imbibition has radius between r and r+dr. The relative permeability of the nonwetting phase during imbibition $k_{rn,i}$ is the equivalent conductance of the approximating network or tree having the random distribution of bond conductances given by Equation (22) divided by that given by the single-phase conductivity function defined in Equation (6).

The imbibition process is said to terminate at the stage at which the nonwetting phase loses connectivity between the surfaces of the sample. This happens when $X_{n,i}$ falls past X_c, the bond percolation threshold of the network. The radius of the largest throat, $r_{i,c}$, occupied by wetting phase at the termination of imbibition, i.e. at nonwetting residual saturation, is given by (cf. Equation (15))

$$1 - X_{n,i} = 1 - X_c = X^a(X_{i,c}) \quad ,$$

$$X_{i,c} = \int_0^{r_{i,c}} \alpha(r)\, dr \tag{25}$$

Of course with the previously used assumption that

$$\lim_{x \to 1} X^a(X) = X \tag{2}$$

holds for $X \geq 1 - X_c$, Equation (25) may be simplified to (cf. Equation (15'))

$$X_c = \int_{r_{i,c}}^{\infty} \alpha(r)\, dr \tag{25'}$$

Another corollary of this assumption is that when the nonwetting phase loses its hydraulic conductivity during imbibition, the nonwetting phase occupies all pore-throat segments with radius greater than $r_{i,c}$ and the wetting phase occupies all the rest.

At a stage of imbibition characterized by a given r_i the volume fraction of porespace occupied by nonwetting phase, i.e. the nonwetting phase saturation $S_{n,i}$, is (cf. Equation (15))

$$S_{n,i} = \frac{X_{n,i} \int_0^{\infty} \alpha_{n,i}(r) V(r)\, dr}{\int_0^{\infty} \alpha(r) V(r)\, dr} \tag{26}$$

where $\alpha_{n,i}(r)\, dr$ is the probability that a pore-throat segment containing nonwetting phase has radius between r and r+dr: it is defined in Equation (24). Of course, the corresponding wetting phase saturation $S_{w,i}$ is given by

$$S_{w,i} = 1 - S_{n,i} \tag{27}$$

Application of the Theory

The major difficulty in calculating from the theory the dependence of relative permeabilities on saturation is the evaluation of the bond accessibility function $X^a(X)$ needed at Equations (8) and (18) and the network conductivities called for after Equation (6), and at (9), (12), (19) and (22). For large three-dimensional networks — highly interconnected as porespace is — the only way known of estimating these quantities is by Monte Carlo simulation on large computer-generated samples. Simplifying matters a little is that bond accessibility functions have been computed and tabulated for many regular networks (49) and for a randomly irregular network (50). But whereas the accessibility functions depend solely on the network coordination or topology, the conductivities depend heavily on the distributions of bond conductances. Thus separate Monte Carlo estimates of conductivity would have to be repeated for each of the phase conductivity functions defined at Equations (6), (11), (12), (19) and (22).

Then the statistical theory has nothing useful to add to the Monte Carlo approach described in the Introduction; moreover, that Monte Carlo strategy need sacrifice nothing of the spatial relationships among parts of the porespace.

A promising alternative is the effective medium strategy (43,51-53) which, it is now clear, can be combined with the Monte Carlo approach to good advantage (54). However, effective medium theory in its present state, and with reasonable computation effort, gives in the vicinity of the percolation threshold poor estimates of conductivities, or permeabilities, on three-dimensional networks.

Bethe Tree Approximation to Porespace

There is yet another alternative which would seem to be less promising but which has in fact been much used in statistical physics of disordered media, and has succeeded remarkably in explaining basic aspects of multiphase flow in porous media (14,15,37-39,55). That is to model the porespace with a Cayley or Bethe tree, an endlessly branching structure that totally lacks reconnections. Lacking reconnections, its topological structure is trivial; it is completely characterized by the local coordination number, Z, i.e. the number of bonds that join at each interior node (56). This tree system has been called a Bethe lattice, or an infinite Cayley tree or a Bethe tree by various authors (14,56-58). A portion of a Bethe tree of local coordination number 3 is shown in Figure 1c. The attraction of Bethe trees is that their accessibility functions (45,60) and, most importantly, their conductivities for distributed bond conductances (58,59) have been worked out theoretically and can be calculated from expressions that are in closed form. For example, the accessible bond fraction of a Bethe tree with local coordination number Z is (57)

$$X^a(X) = \begin{cases} X\left[1 - \dfrac{X^*}{X}\right]^{(2Z-2)/(Z-2)} & , \quad X \geq X_c \\ 0 & , \quad X \leq X_c \end{cases} \tag{28}$$

where X is the concentration of allowed bonds and X^* is the root of the equation

$$X^*(1-X^*)^{(Z-2)} - X(1-X)^{(Z-2)} = 0 \tag{29}$$

that vanishes as $X \to 0$ and $X \to 1$. X_c is of course the bond percolation threshold of the Bethe tree, which is (57)

$$X_c = \frac{1}{(Z-1)} \tag{30}$$

After Stinchcombe (58) the conductivity of a Bethe tree can be defined as that between an arbitrarily chosen site — the inflow surface — and all points on a distant enclosing surface — the outflow surface. For this definition the conductivity σ of a Bethe tree of local coordination number Z having a random distribution of bond conductances G(g) follows from

$$\sigma = -Z\ C'(0) \tag{31}$$

Here C(X) is the generation function that is defined by the nonlinear integral equation (58)

$$\int_0^\infty e^{-tx} C(x)\ dx \equiv \int_0^\infty dg\ G(g) \left[\frac{1}{t+g} + \right.$$

$$\left. + \frac{g^2}{(t+g)^2} \int_0^\infty \exp\left[- \frac{gt}{g+t} x \right] [C(x)]^{(Z-1)}\ dx \right] \tag{32}$$

subject to the boundary condition C(0) = 1. Because of the nonlinearity of Equation (32) there is currently no known closed form expression for C'(0) in terms of G(g) and Z. For the calculations of relative permeability in this paper we have used approximations to Equation (33) to obtain C'(0) (see Appendix).

Sample Results and Sensitivity Study

An accurate test of the model proposed for drainage and imbibition relative permeabilities requires that detailed statistical information be available on the shapes, sizes and hydraulic conductances of pores, as well as on the topology of porespace. Optical methods of the type used recently by Pathak and coworkers (60) hold promise of being able to provide such information if they can be sufficiently automated for image analysis.

Lacking such information we have restricted attention to (1) Bethe trees of local coordination numbers 5-7 as models of porespace topology, and to (2) the following two unimodal distributions of pore-throat radii:

$$\alpha(r) = 2re^{-r^2} \quad , \quad r \geq 0 \quad , \tag{33-a}$$

a Rayleigh distribution, and

$$\alpha(r) = \begin{cases} 0 & r < 1 \\ 2(r-1)e^{-(r-1)^2} & r \geq 1 \end{cases} \tag{33-b}$$

a displaced Rayleigh distribution (see Figure 2). The latter frequency distribution is more strongly weighted to larger pore-throat segments.

Plausible correlations of volumes and conductances with throat radius can be gleaned from geometrical models of pores. The difficulty with a one-parameter characterization of local properties of porespace is of course that volume and conductance both depend on a measure or distance between the branch points that

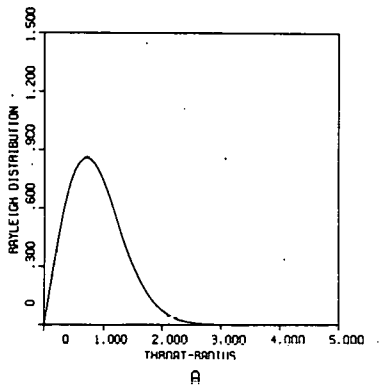

Fig. 2(A)—Rayleigh throat-radius distribution function.

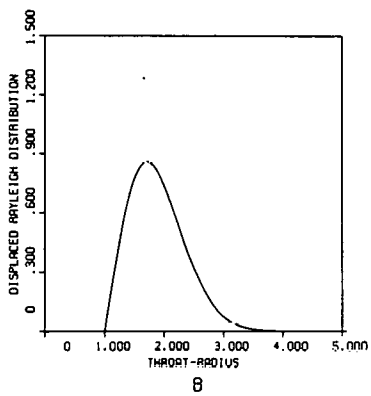

Fig. 2(B)—Displaced Rayleigh throat-radius distribution function.

define pore bodies, besides different moments of the distribution of pore radii between the branch points. These dependences are highly sensitive to the degree of consolidation of the porous medium. By way of example, in the extreme of cylindrical throat-segments of radius r and totally independently distributed distances between branch points, $V(r) \propto r^2$ and $g(r) \propto r^4$. In contrast, in the extreme of sheet-like pores of halfwidth r and two other dimensions that are completely uncorrelated, $V(r) \propto r$ and $g(r) \propto r^3$. From this sort of order-of-magnitude analysis we, for now, restrict attention to models of pores in which

$$V(r) \propto r^{\nu} \quad , \quad 1 \leq \nu \leq 2 \quad ; \tag{34-a}$$

and

$$g(r) \propto r^{\mu} \quad , \quad 3 \leq \mu \leq 4 \tag{34-b}$$

Theoretical predictions of drainage and imbibition relative permeabilities are plotted on Figures 3-6 using Bethe trees of coordination numbers 5-7 as approximations to porespace topology, the throat-radius distributions given by Equations (33-a) and (33-b), and various combinations of the exponents ν and μ appearing in Equations (34-a) and (34-b). The kinks in the curves as drawn are artifacts of the computer graphics. The accessible bond functions $X^a(X)$ required to define the phase conductivity functions called for at Equations (12) and (22) and to calculate the corresponding wetting phase saturations (cf. Equations (16) and (26)) were obtained by solving Equations (28) and (29). The numerical procedure for estimating tree conductivities from Stinchcombe's defining integral equation (cf. Equations (31) and (32)) is described in the Appendix.

Figure 7 shows representative drainage and imbibition relative permeabilities as measured by Talash (48) for oil and water in a core of water-wet Berea sandstone. Despite the considerable range of inputs into the theory, all of

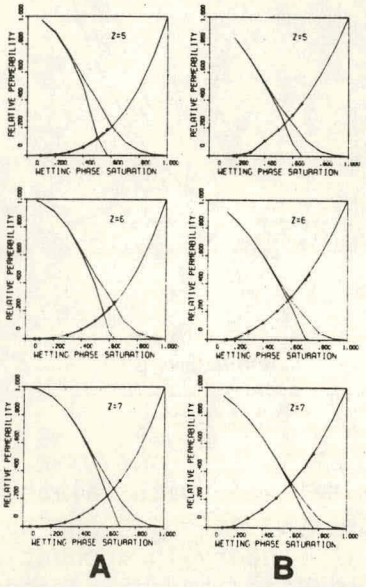

Fig. 3—Predicted permeabilities for $V \propto r$ and $g \propto r^4$, using (A) the Rayleigh, and (B) the Displaced Rayleigh throat-radius distribution functions. (The imbibition wetting phase relative permeabilities are highlighted by the decorations appearing in the figures.)

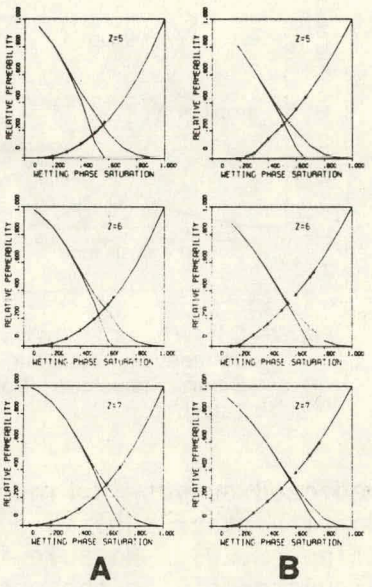

Fig. 4—Predicted relative permeabilities for $V(r) \propto r$ and $g(r) \propto r^3$.

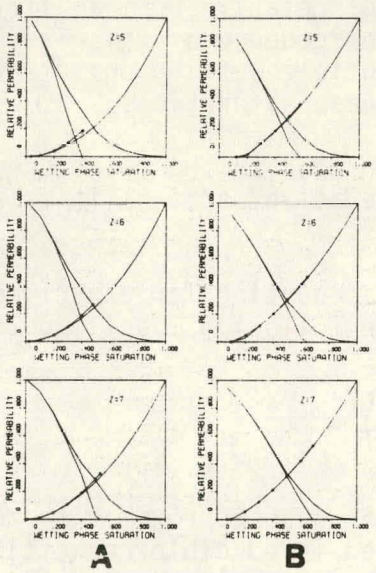

Fig. 5—Predicted relative permeabilities for $V(r) \propto r^2$ and $g(r) \propto r^4$.

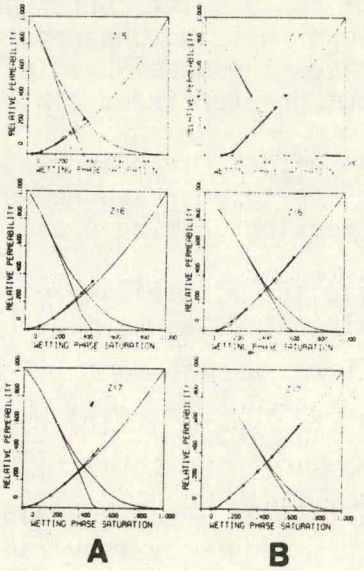

Fig. 6—Predicted relative permeabilities for $V(r) \propto r^2$ and $g(r) \propto r^3$.

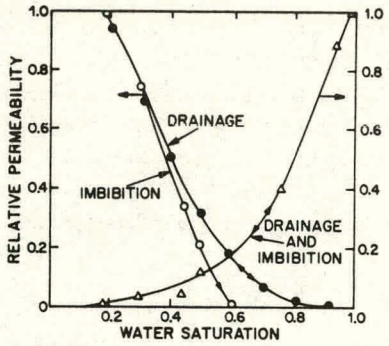

Fig. 7—Oil-water relative permeability data for a Berea Sandstone (from Talash[48]).

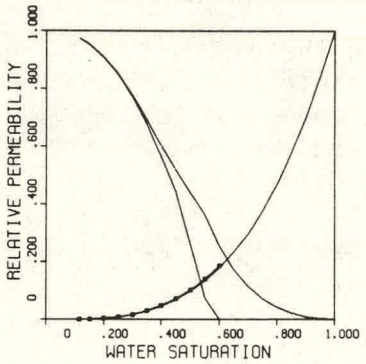

Fig. 8—A fit of Talash's relative permeability data.

the predicted curves in Figures 3-6 agree qualitatively with Talash's data as they do with other published data for two-phase systems where one phase is strongly wetting (8,20). Notable is the success of the theory in accounting for the lack of hysteresis in the wetting phase permeabilities and its presence in the nonwetting phase permeabilities.

Comparison of the cases plotted in Figures 3-6 reveals that:

(1) An effect of increased coordination number Z of the Bethe tree model is to decrease the predicted hydraulically irreducible saturations of both the wetting and nonwetting phases. This accords with the experimental data of Pathak *et al.* (60) on the correlation of irreducible saturations with connectivity as measured by the genus per unit volume of the porespace.

(2) An effect of an increase in the exponent, ν, in the relation $V(r) \propto r^{\nu}$ is to shift corresponding values of relative permeability to lower wetting phase saturation. A consequence of this is that as ν rises the model predicts lower irreducible wetting phase saturations but greater irreducible nonwetting phase saturations.

(3) An effect of an increase in the exponent μ in the relation $g(r) \propto r^{\mu}$ is to decrease nonwetting phase relative permeabilities while increasing wetting phase permeabilities.

To illustrate the flexibility of the model in accounting for experimental data, a fit of Talash's data was made by assuming the following model inputs

$$\alpha(r) = 2re^{-r^2} \quad , \quad V(r) \propto r^{\nu} \quad , \quad g(r) \propto r^4 \quad ,$$

and a Bethe tree of local coordination number 5 as an approximation to porespace topology and fixing ν by requiring the predicted irreducible nonwetting phase saturation to be 40% — the same as that obtained by Talash: see Figure 8. The resulting value of ν is 0.84313. The fit is quite good in view of the fact that only one parameter was adjusted.

Discussion: The Bethe Tree as a Model of Porespace Topology

In the preceding we illustrated theoretical predictions of drainage and imbibition relative permeabilities using Bethe trees of coordination numbers 5-7 as models of porespace topology. In view of the clear differences between the irregular, highly connected three-dimensional topology of porespace and that of the Bethe tree, a question that naturally arises is to what extent the apparent qualitative successes of theory are fortuitous. And, more importantly, what physical interpretation is to be given to the coordination number Z of a Bethe tree approximation to porespace topology?

Insight into these questions is obtained by comparing tree predictions of accessibility and conductivity — and hence of saturation-dependent relative permeabilities — with those obtained by Monte Carlo simulation on presumably more realistic three-dimensional networks. In this regard accumulated experimental and theoretical evidence suggests that aside from a shift in bond percolation threshold X_c, the accessible bond fraction $X^a(X)$ and normalized conductivity $(K(X)/K(1)$ of three-dimensional networks and Bethe trees, at least those having the following well-studied percolation like bond conductivity distribution function

$$G(g) = (1-X)\delta(g) + \delta(g-1) \quad , \tag{35}$$

are qualitatively similar (14,15,49,50,56-59,61,62). An illustration of this is provided in Figure 9, where we have plotted $X^a(X)$ and $K(X)/K(1)$ (for the distribution of bond conductances given by Equation (35)), as predicted by a Bethe tree of local coordination number 5 (X_c = .25) and the six-coordinated three-dimensional simple cubic network ($X_c \approx .25$)(43).

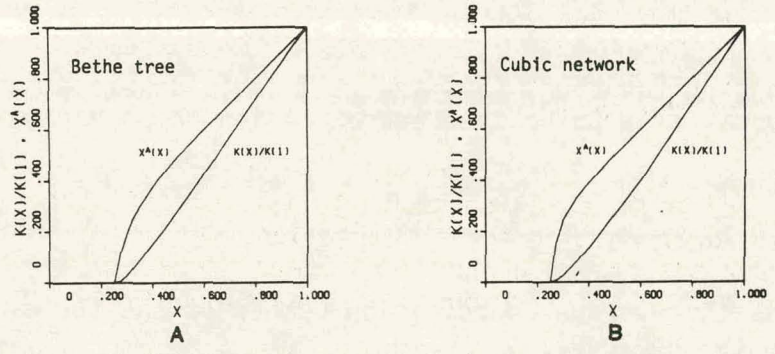

Fig. 9. — Normalized conductivity K(X)/K(1) and accessible bond fraction $X^a(X)$.

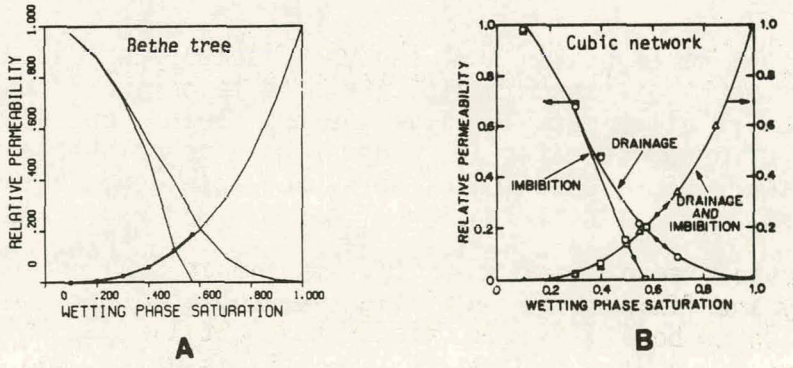

Fig. 10 — Relative permeability predictions.

Although a theoretical explanation of why the Bethe tree works so well in mimicking the predictions of bond accessibility and equivalent conductivity of three-dimensional networks is not yet available, a useful consequence of it is that the Bethe tree can be used to estimate cheaply the Monte Carlo predictions of relative permeability on a three-dimensional network having the same percolation threshold. An illustration of this is provided in Figure 10 where we have plotted the relative permeability predictions of a Bethe tree (Z=5) and a simple cubic network for the throat radii distribution function $\alpha(r) = 2re^{-r^2}$ and the following functional correlations for throat-segment volume V and hydraulic conductance g,

$$V(r) \propto r \quad \text{and} \quad g(r) \propto r^4 \quad .$$

[For a description of the Monte Carlo procedure required to estimate relative permeabilties on the cubic network the reader is referred to Sahimi *et al.* (63)].

A quite accurate approximation to the bond percolation threshold X_c of regular and irregular networks is

$$X_c = \frac{d}{(d-1)\bar{Z}} \tag{36}$$

where $\bar{Z}$ is the average coordination number of the sites and d is the dimensionality of the network (41,50). Alternatively the bond percolation threshold of a Bethe tree of local coordination number Z is

$$X_c = \frac{1}{(Z-1)} \tag{37}$$

By rearranging Equations (36) and (37) it is possible to interpret Z (the coordination number of a Bethe tree approximation to porespace topology) as being

$$Z = \frac{\bar{Z}}{1.5} + 1 \tag{38}$$

where $\bar{Z}$ is the average coordination number of the three-dimensional approximation to porespace topology.

Conclusions

In this paper statistical concepts, some of which are borrowed from the percolation theory of random media, are used to derive formulas for the drainage and imbibition relative permeabilities of two fluids, one of which strongly wets the surfaces of a porous material. Inputs used to calculate relative permeabilities are a network representation of porespace topology, or its Bethe tree approximation, a statistical distribution of pore-throat radii and functions relating the volume and hydraulic conductivity of a pore-throat segment to its radius.

A number of physical assumptions have been used in developing the formulas for relative permeabilities. These assumptions are conveniently separated into two categories. The first is that the morphology of porespace is adequately represented by a random disordered-bond network or tree. The second regards the

effects of capillarity on the spatial distribution of a strongly wetting and nonwetting fluid in porespace. Taken together these assumptions have yielded predictions of relative permeability that are in close qualitative agreement with data typical of two-phase systems where one phase is strongly wetting.

What is currently being explored (64), is whether or not the representation of porespace morphology by a random disordered-bond network or tree can with more complex mechanisms of assigning fluid distributions, yield similarly good predictions of two-phase relative permeabilities in regimes where one phase is no longer strongly wetting. If this turns out to be the case profitable extensions of the theory presented in this paper can be made to three-phase systems.

Appendix A: The Bethe Tree as a Model of Porespace Morphology—Theory

Stinchcombe (58) develops an exact, although implicit, power-series expansion from which the conductivity σ of a Bethe tree of local coordination number Z can be determined. To order $(Z-1)^{-4}$ this expansion yields the following estimate:

$$\sigma = -Z\, C'(0) \tag{A1}$$

where C'(0) is approximated as the root of

$$\begin{aligned} 0 = \int dg\, G(g)[\tau(g)-C'(0)] + (Z-1)I_{210}a_2^o\,[1 \\ + (Z-1)I_{220}] + (Z-1)I_{310}a_3^o + I_{410}[\tbinom{Z-1}{2}(a_2^o)^2 \\ + (Z-1)a_4^o] + \tbinom{Z-1}{2}I_{510}a_2^o a_3^o + \tbinom{Z-1}{3}I_{610}(a_2^o)^3 \end{aligned} \tag{A2}$$

Here G(g) is the random distribution of bond conductances,

$$\tau(g) = \frac{g(Z-1)C'(0)}{[g-(Z-1)C'(0)]} \tag{A3}$$

$$a_n^o = \int dg\, G(g)[\tau(g)-C'(0)]^n/n! \tag{A4}$$

and

$$I_{mno} = \frac{m!}{[n-1]!} \int dg\, \frac{G(g)g^2[\tau(g)-C'(0)]^{n-1}}{[g-(Z-1)C'(0)]^{m+1}} \tag{A5}$$

From Stinchcombe's work (on a more specialized conductance distribution than of interest here) it appears that for $Z \geq 5$, the solution of the expansion (A2) provides an accurate estimate of σ.

In calculating relative permeabilities from the phase conductivity functions developed in this paper, our estimates of tree conductivity were obtained by solving (A2) for C'(0) when G(g) had the general percolation-like form (cf. Equation (4))

$$G(g) = (1-X)\delta(g) + XG(g) \tag{A6}$$

Equation (A2) was solved by the Regula Falsi method. The integrals appearing in Equation (A2) were evaluated numerically. An initial guess to C'(0) was obtained by finding the root of

$$0 = \int dg\, G(g)[\tau(g)-C'(0)] \tag{A7}$$

Stinchcombe estimates that the value of C'(0) obtained from Equation (A7) is of order of accuracy $(Z-1)^{-1}$.

For G(g) having the percolation-like form given by Equation (A6), the implicit power-series expansion yielding Equation (A2) is slowly converging from $|X-X_c| < 1/Z$. In this near-percolation region we used the following asymptotic estimate to tree conductivity (58,59).

$$\sigma = \frac{2Z}{(Z-2)} \cdot .761 \left[\int_0^\infty \frac{G(g)}{g}\, dg\right]^{-1} \left(\frac{X-X_c}{X_c}\right)^2 \tag{A8}$$

provided that σ estimated from Equation (A8) was less than that estimated from Equation (A1). A problem arose when calculating near percolation estimates of conductivity for wetting phase when the Rayleigh distribution of pore-throat radii $\alpha(r) = 2re^{-r^2}$ was used. This occurred because in these cases the integral

$$\int_0^\infty \frac{G(g)}{g}\, dg$$

diverged. In these situations our estimates of tree conductivity were obtained from Equations (A1) and (A2).

References Cited in Section X

1. Hassler, G. L., U.S. Patent 2,345,935 (April 4, 1944).

2. Muskat, M. and Meres, M. W., Physics 7, 346-363 (1936).

3. Leverett, M. C. and Lewis, W. B., Trans. AIME 142, 107-116 (1941).

4. Johnson, E. F., Gassler, D. P. and Naumann, V. D., Trans. AIME 216, 370-376 (1959).

5. Naar, J., Wygal, G. R. and Henderson, J. H., Soc. Petrol. Eng. J. 2, 13-17 (1962).

6. Morgan, J. T. and Gordon, D. T., J. Pet. Tech. 22, 1194-1208 (1970).

7. Owens, W. W. and Archer, D. L., J. Pet. Tech. 23, 873-878 (1971).

8. McCaffery, F. G. and Bennion, D. W., J. Can. Pet. Tech. 13, 42-53 (1974).

9. Odeh, A. S., Trans. AIME 216, 346-353 (1959).

10. LeFebvre du Prey, E. J., Soc. Petrol. Eng. J. 13, 39-47 (1973).

11. Leverett, M. C., Trans. AIME 132, 149-171 (1939).

12. Taber, J. J., Soc. Petrol. Eng. J. 9, 3-12 (1969).

13. Richardson, J. G., Kerver, J. K., Hafford, J. A. and Osoba, J., Trans. AIME 195, 187-196 (1952).

14. Larson, R. G., Scriven, L. E. and Davis, H. T., Chem. Eng. Sci. 36, 57-73 (1981).

15. Larson, R. G., M.S. thesis, University of Minnesota, Minneapolis (1977).

16. Larson, R. G., I & EC Fund. 20, 132-137 (1981).

17. "Fluid Distributions in Porous Systems - A Preview of the Motion Picture," Stanolind Oil and Gas Co. (1952); subsequently reprinted by Pan American Petroleum Corp. and Amoco Production Co.

18. Chatenever, A. and Calhoun, J. C., Trans. AIME 195, 149-156 (1952).

19. Kimbler, O. K. and Caudle, B. H., Oil and Gas J. 55 [50], 85-88 (1957).

20. Raimondi, P. and Torcaso, M. A., Soc. Pet. Eng. J. 4, 49-55 (1964).

21. Stalkup, F. I., Soc. Pet. Eng. J. 10, 337-348 (1970).

22. Craig, F. F., Jr., The Reservoir Engineering Aspects of Water Flooding, H. L. Doherty Memorial Fund of AIME, New York (1971).

23. Colonna, J., Brissaud, F. and Millet, J. L., Soc. Pet. Eng. J. 12, 28-38 (1972).

24. Morrow, N. R. and McCaffery, F. G., in Wetting, Spreading and Adhesion, ed. J. F. Padday, Academic Press, London (1978).

25. Mohanty, K. K., Davis, H. T. and Scriven, L. E., Paper SPE 9406 presented at SPE 55th Annual Fall Meeting, Dallas, Sept. 21-24, 1980.

26. Mohanty, K. K., Ph.D. thesis, University of Minnesota, Minneapolis (1981).

27. Mohanty, K. K., Davis, H. T. and Scriven, L. E., in Surface Phenomena in Enhanced Oil Recovery, ed. Dinesh O. Shah, Plenum Publishing Corp. (1981).

28. Teletzke, G. F., Scriven, L. E. and Davis, H. T., J. Colloid and Interface Science 87, 550-571 (1982).

29. Yuster, S. J., Proc. Third World Petrol. Congress 2, 437 (1951).

30. Mohanty, K. K., Davis, H. T. and Scriven, L. E., to be submitted.

31. Fatt, I., Trans. AIME 207, 144-181 (1956).

32. Singhal, A. K. and Somerton, W. H., Institut Français du Petrole 32, 897-920 (1977).

33. Lin, C. Y. and Slattery, J. C., AIChE J. 28, 311-324 (1982).

34. Payatakes, A. C., Tien, C. and Turian, R. M., AIChE J. 19, 58-67 (1973).

35. Winterfeld, P. H., Scriven, L. E. and Davis, H. T., J. Phys. C: Solid State Phys. 14, Z2361-2376 (1981).

36. Pathak, P., Winterfeld, P. H., Davis, H. T. and Scriven, L. E., Paper SPE 8846 presented at SPE/DOE Symp., Tulsa, April 20-23, 1980.

37. Larson, R. G., Davis, H. T. and Scriven, L. E., Chem. Eng. Sci. 36, 75-85 (1981).

38. Larson, R. G., Scriven, L. E. and Davis, H. T., Nature 268, 409-413 (1977).

39. Larson, R. G. and Morrow, N. R., Powder Technology 30, 123-138 (1981).

40. Broadbent, S. R. and Hammersly, J. M., Proc. Camb. Phil. Soc. 53, 629-641 (1957).

41. Shante, V. K. S. and Kirkpatrick, S., Adv. Phys. 20, 325-357 (1971).

42. Essam, J. W., Phase Transitions and Critical Phenomena, ed. C. Domb and M. S. Green, Academic Press, London, 197-270 (1972).

43. Kirkpatrick, S., Rev. Mod. Phys. 45, 574-588 (1973).

44. Frisch, H. L. and Hammersly, J. M., J. Soc. Indust. Appl. Math. 11, 894-918 (1963).

45. Larson, R. G. and Davis, H. T., J. Phys. C: Solid State Phys. 15, 2327-2331 (1982).

46. Happel, J. and Brenner, H., Low Reynolds Number Hydrodynamics, Prentice-Hall, Englewood Cliffs, NJ, 1965.

47. Teletzke, G. F., Scriven, L. E. and Davis, H. T., Paper SPE 10112 presented at SPE 56th Annual Meeting, San Antonio, Oct. 4-7, 1981.

48. Talash, A. W., Paper SPE 5810 presented at the Improved Recovery Symp. of the Soc. of Petrol. Engrs. of AIME, Tulsa, March 22-24, 1976.

49. Frisch, H. L., Hammersly, J. M. and Welsh, D. J. A., Phys. Rev. 126, 946-948 (1962).

50. Winterfeld, P. H., Ph.D. thesis, University of Minnesota, Minneapolis (1981).

51. Blackman, J. A., J. Phys. C: Solid State Phys. 9, 2044-2071 (1975).

52. Ahmed, G. and Blackman, J. A., J. Phys. C: Solid State Phys. 12, 837-853 (1979).

53. Sahimi, M., Hughes, B. D., Scriven, L. E. and Davis, H. T., submitted to J. Chem. Phys. (1982).

54. Scriven, L. E. and Davis, H. T., talk presented at Ninth U.S. National Congress of Applied Mechanics, Ithaca, New York, June 21-25, 1982.

55. Levine, S., Reed, P. and Shutts, G., Powder Technology 17, 163-181 (1977).

56. Ziman, J. M., Models of Disorder, Cambridge University Press, Cambridge 1976).

57. Fisher, M. E. and Essam, J. W., J. Math. Phys. 2, 609-619 (1961).

58. Stinchcombe, R. B., J. Phys. C: Solid State Phys. 7, 179-203 (1974).

59. Heinrichs, J. and Kumar, N., J. Phys. C: Solid State Phys. 8, L510-516 (1975).

60. Pathak, P., Davis, H. T. and Scriven, L. E., Paper 11016 presented at SPE 57th Annual Technical Conference and Exhibition, New Orleans, Sept. 26-29, 1982.

61. Kogut, P. M. and Straley, J. P., J. Phys. C: Solid State Phys. 12, 2151-2159 (1979).

62. Hughes, B. D., Sahimi, M., Scriven, L. E. and Davis, H. T., to be submitted to J. Chem. Phys.

63. Sahimi, M., Heiba, A. A., Hughes, B. D., Davis, H. T. and Scriven, L. E., Paper 10969 presented at SPE 57th Annual Technical Conference and Exhibition, New Orleans, Sept. 26-29, 1982.

64. Heiba, A. A., Davis, H. T. and Scriven, L. E., to be submitted.

65. Jerauld, G. R., Ph.D. thesis, University of Minnesota, Minneapolis, 1984.

XI. DISPERSION IN FLOW THROUGH POROUS MEDIA

Introduction

The Phenomenon of Dispersion

Continuous fluid can be regarded as a continuum of very small fluid particles that retain their identities as they flow, just as do tracer particles added to the fluid. In steady flow through a disordered porous medium, the *transit time*, or *first passage time*, of a fluid particle between entrance and exit planes depends on the path it follows through the porespace. A population of particles passing the entrance plane at the same instant will be dispersed upon arrival at the exit plane, that is, the population will arrive there with a distribution of transit times. Thus a solute concentration front that enters transverse to the macroscopic mean flow will spread in the mean flow direction as it passes through the medium. The first passage time distribution, or the related spreading of a concentration front, is a measure of *longitudinal dispersion* in a porous medium.

Likewise, a population of particles passing simultaneously through a restricted area of the entrance plane will not follow entirely the mean flow to the exit plane, but will be dispersed in the transverse directions as well, that is the population will have a wider distribution of exit locations than of entrance locations. Thus a concentration front that enters parallel to the mean flow will spread laterally on the way to the exit plane. The distribution of exit locations, or the related spreading of a concentration front, is also connected to transit times and is a measure of *transverse dispersion* in a porous medium.

Mechanisms of Dispersion

Dispersion originates in flow. Two basic mechanisms drive dispersion in macroscopically homogeneous, microscopically disordered porous media, and they arise in the chaotic nature of the pore-level, or microscopic, velocity field forced on flowing fluid by the irregularity of the porespace. The first mechanism is *kinematic*: streamtubes divide and rejoin repeatedly at the junctions of flow passages in the highly interconnected porespace. The consequent tangling and divergence of streamlines is accentuated by the widely varying orientations of flow passages and coordinations of junctions (i.e. the number of passages that come together in each suitable defined locale of the porespace (1)). The result is a wide variation in not only the lengths of streamlines that traverse the system, but also the downstream transverse separations of streamlines that anywhere pass close together. The second mechanism is *dynamic*: the speed with which a given flow passage is traversed depends on the flow resistance or hydraulic conductance of the passage, its orientation, and the local pressure field—especially its deviation from the macroscopic mean pressure gradient causing flow. The two mechanism conspire to produce a broad distribution of first passage times and of accompanying exit locations.

Dispersion is more complicated when more than one fluid phase is present in a porous medium. Each phase by its mere presence denies porespace to the other and consequently alters the streamlines, pressure field, and local traverse times of the other phases. Dispersion in each of the phases depends on the porespace occupied by that phase. As the fraction of porespace held, i.e. the phase saturation, falls that phase ultimately loses its continuity because of disconnections brought about by capillary instabilities. Before that stage its remaining streamtubes grow sparse and tortuous, and increasing amounts of it are immobilized as isolated blobs or ganglia scattered through the porespace. Once its continuity disappears the phase occupies only isolated clusters of pore segments, or in other words its saturation lies beneath a percolation threshold. The effects of this phenomenon on dispersion are brought out later in the paper.

Effects of Diffusion

A constant companion of the basic dispersion process is molecular diffusion. It modifies the effects of the two basic mechanisms, and not only by the primary mechanism of moving material from one streamline to another, but also by the usually weaker streamwise diffusion of material relative to mass-average velocity. The solid matrix of a porous medium of course acts locally as a separator of streamlines and thus as a barrier to diffusion.

Where the local streamlines are perpendicular to existing concentration gradients the rates of diffusion are unaffected by flow ($\underset{\sim}{v}\cdot\nabla c = 0$ in the convective diffusion equation, so that at steady state $\nabla\cdot\underset{\sim}{D}\nabla c = 0$), as when streamtubes of different composition rejoin in a cylindrical passage so that they and all their streamlines run parallel to the next junction. However, differences in speed along those streamlines can tilt concentration gradients away from perpendicularity and thereby induce convective enhancement of diffusion—or diffusion-modified convective transport, as in the familiar phenomenon of Taylor dispersion (2) in tubes. Where local streamlines are parallel to existing concentration gradients, the rates of diffusion can be most affected by flow (i.e. $\underset{\sim}{v}\cdot\nabla c/|\underset{\sim}{v}||\nabla c|$ is at its maximum in the convective diffusion equation) and this is likeliest where streamlines converge or diverge strongly, as in the familiar sharpening action of stretching flow on streamwise concentration gradients.

Thus the modification of dispersion by diffusion depends on porespace morphology and its effects in turn depend on local flow field and concentration fields. At one extreme there is negligible convective spreading and negligible molecular diffusion within distinct flow passages of relatively slowly varying cross-section that can be regarded as elongated pore-throat segments; but there is intense convective diffusion, i.e. thorough mixing, in intervening spaces of rejoining and redividing streamtubes that can be regarded as distinct pore bodies having comparatively little volume. Though no more than an approximation to certain real situations, this extreme case leads naturally to a picture of porespace discretized into a network of branches, with unidirectional, uniform-speed flow in each branch and complete or partial mixing in each junction node.

Molecular diffusion, by moving material into and out of stagnant regions of fluid (dead-end pores, closed recirculating eddies, trapped fluid phases, and the like) and adsorbed states on porewalls, can give rise to temporary residences of solute that also modify basic, convective-driven dispersion. The same is true of chemical reactions that consume or produce a constituent.

Network Approximation

The idea of representing a porous medium as a network is not new (3-5). Only recently, however, has a mathematical process been divised for systematically reducing a porous medium to an equivalent network (1,6,7). With this method, the topology (pore connectedness, coordination) of the porespace is represented by a network of bonds (pore-throat segments) and nodes (pore-body segments) that run everywhere along paths of porespace; and the geometry (pore sizes and shapes) is represented by the radius of the largest sphere that can be inscribed in the porespace for each point along the network paths. Pore bodies and pore throats can be defined in terms of local maxima and minima of the radii of the largest inscribed sphere. All of the volume of a pore body segment can be assigned to the corresponding network node; alternatively it can be assigned to the neighboring network bonds representing pore throat segments. Although the simplest procedure generates elementary nodes of coordination three (three bonds connected to every node), obvious criteria can be used to lump nearly overlapping nodes together into network nodes of coordination greater than three. Details are given elsewhere (1,6,7); what is important to the present work is that any porous medium can, in principle, be represented by a topologically equivalent network with geometrical (and material) properties assigned appropriate to the nodes and bonds.

Macroscopic Modeling

Conventional modeling of dispersion in disordered porous media is based on the *macroscopic* convective-diffusion equation,

$$\frac{\partial c}{\partial t} + \underset{\sim}{\bar{v}}\cdot\underset{\sim}{\nabla} c = \nabla\cdot(\underset{\approx}{D}\cdot\underset{\sim}{\nabla} c) = D_L \frac{\partial^2 c}{\partial x^2} + D_T \nabla_2^2 c \,, \qquad (1)$$

where $\underset{\sim}{\bar{v}}$ is the macroscopic mean, or Darcy-level velocity; c is the macroscopic mean, or Darcy-level concentration; x is the mean flow direction; and ∇_2^2 is the Laplacian in transverse directions. A Darcy-level quantity is the local quantity averaged over a porespace large enough to encompass numerous pore throats and bodies (8). Dispersion is said to be *macroscopically diffusive* when Eq. (1) holds. The idea is to account for dispersion as anisotropic diffusional spreading of mean concentration, the diffusion-like constants being the longitudinal or streamwise dispersion coefficient D_L (in the direction of mean flow) and the transverse dispersion coefficient D_T (in directions perpendicular to mean flow). This approach is phenomenological and provides no insight into how D_L and D_T depend on pore-level morphology. It also presupposes that relative to macroscopic mean flow, fronts of macroscopic mean concentration are dispersed as though by diffusion in an anisotropic continuous medium (as represented by the term $\nabla\cdot(\underset{\approx}{D}\cdot\nabla c)$ in the equation). As have a number of other investigators, we seek the conditions in which Eq. (1) is valid.

Because of the chaotic nature of the flow passages and streamlines they enforce, statistical models of dispersion are natural. Molecular diffusion can be rationalized as the outcome of kinematically random walks (9). Dispersion in porous media has been treated analogously by Scheidegger (10), de Jong (11), and Saffman (12). The randomness of dispersion is inherent in the static morphology of the porespace, however. Consequently the concepts of percolation theory (13) are appropriate. These we point out can be joined with the idea of a continuous-time random walk first developed by Montroll and Weiss (14) and generalized by Scher and Lax (15) in connection with stochastic transport in disordered solids and impurity conduction in semiconductors. We are investigating this approach currently and will report the results in a future publication (16). The marriage of random walks and percolation theories has appeared in other contexts, e.g. hopping transport on a lattice (17-19).

Simulation - A Mesoscopic Approach

In this paper we employ Monte Carlo simulation—experiments by computer—to shed light on the mechanisms of dispersion. We report the results of Monte Carlo simulations of permeability, relative permeabilities, dispersion coefficients and dispersivities, tracer or tagged particle distribution, and transit time distribution for one- and two-phase flow in chaotic porous media represented by square and cubic networks of pore throat segments of distributed capacity and flow resistance. Though we focus on dispersion caused by disorder at the pore level, the concepts and methods can be applied to that caused by macroscopic heterogeneities in permeabilities. Several authors (20-23) have investigated macroscopic one-phase flow dispersion in a porous medium. The present paper reports research that is a preliminary to developing a formal theory of purely convective dispersion and of diffusion-modified dispersion.

Percolation theory concepts have not previously been used to study dispersion in flow through porous media. Scheidegger and coworkers (24,25) proposed a Cayley tree (a network without closed loops) as a model of porous media in order to study dispersion. However, a network lacking closed loops cannot be used to study longitudinal dispersion and it could account for transverse dispersion only in extreme cases. Torreli and Scheidegger (26) proposed a random network, but they reported no results. Simon and Kelsey (27,28) employed random networks to model a miscible displacement process in porous media, but they did not study dispersion. To the best of our knowledge our simulation of dispersion in one- and two-phase flow with a percolation view is the first of its kind.

Distributions and Dispersion Coefficients

If there were no dispersion in steady, unidirectional flow in the x-direction in a macroscopically homogeneous porous medium, a tracer particle released at location (x_o,y_o,z_o) at time zero would be convected by the mean flow in time t to the location $(x_o + \bar{v}t,y_o,z_o)$, where $\bar{v}$ is mean flow velocity. With dispersion, however, the tracer particle, which is convected through pore throats and pore bodies, arrives at some location (x,y,z) after the same time. The squared derivations of the actual particle position from the hypothetical one are

$$S_x^2 \equiv (x - x_o - \bar{v}t)^2,\ S_y^2 \equiv (y - y_o)^2,\ S_z^2 \equiv (z - z_o)^2 . \qquad (2)$$

We define in terms of these quantities for many tracer particles the following dispersion coefficients

$$D_\xi \equiv \langle S_\xi^2/2t \rangle \quad , \quad \xi = x,y,z \ . \tag{3}$$

The pointed brackets, $\langle \cdots \rangle$, indicate an appropriate average over some population or concentration profile of injected tracer particles. Although one usually defines D_ξ by averaging a spatial distribution at a fixed time t (long enough for $\langle S_\xi^2/2t \rangle$ to be independent of time), one can alternatively define D_ξ by a temporal average for a fixed displacement $\xi - \xi_0$. In general these two definitions may yield different dispersion coefficients, in which case the concept of a dispersion coefficient may not even be useful. We show below, however, that they are the same if the dispersion is macroscopically diffusive, i.e., if Eq. (1) is valid.

Because x is the flow direction, D_x is also denoted by D_L, the longitudinal dispersion coefficient and D_y and D_z are denoted by D_T, the transverse dispersion coefficient ($\xi = y$ or z). Because dispersion is flow driven, we expect *a priori* that the longitudinal and transverse dispersion coefficients are different.

Relevant to this study are the tracer particle distribution function $P(\xi - \xi_0, t)$ and transit time distribution function $Q(\xi - \xi_0, t)$, where ξ denotes x, y, or z. $P(\xi - \xi_0, t)d\xi$ is the probability that a particle beginning in the plane at ξ_0 will be in a plane between ξ and $\xi + d\xi$ at time t. $Q(\xi - \xi_0, t)dt$ is the probability that a particle beginning in the plane at ξ_0 will cross, for the first time, a plane at ξ between t and $t + dt$. These distributions are related by the partitioning principle (29)

$$P(\xi - \xi_0, t) = \int_0^t P(\xi - \xi_1, \ t-\tau) Q(\xi_1 - \xi_0, \tau) d\tau \ . \tag{4}$$

This equation can be understood with the following argument. Let $\xi_0 < \xi_1 < \xi$ and consider a random walk from ξ_0 to ξ that passes through the point ξ_1. The displacement of the tracer particle from ξ_0 to ξ can be decomposed into two independent stages: In the first stage, the tracer particle arrives at ξ_1, for the first time, a time τ after it left ξ_0. In the second stage, the particle leaves ξ_1 and arrives at ξ (not necessarily for the first time) after a time $t-\tau$. Inclusion of all intermediate times τ yields Eq. (4). The distribution Q can be gotten from P by employing the Laplace transform. The result is

$$Q(\xi - \xi_0, t) = \mathcal{L}^{-1}\left\{ \hat{P}(\xi - \xi_0, \lambda) / \hat{P}(0, \lambda) \right\} \ , \tag{5}$$

where

$$\hat{P}(\xi - \xi_0, \lambda) \equiv \int_0^\infty e^{-\lambda t} P(\xi - \xi_0, t)dt \ , \tag{6}$$

and $\mathcal{L}^{-1}$ denotes the inverse Laplace transform.

If the dispersion process is *diffusive*, i.e. if it obeys the convective-diffusion equation, then for a particle population injected at the plane ξ_0 at t=0, the location probability density function $P(\xi - \xi_0, t)$ obeys the Gaussian (normal) distribution,

$$P(\xi - \xi_0, t) = (4\pi D_\xi t)^{-1/2} \exp\left[-(\xi - \xi_0 - \bar{v}_\xi t)^2 / 4D_\xi t\right] \ , \tag{7}$$

from which it follows (with the aid of Eq. (5)) that

$$Q(\xi - \xi_0, t) = (\xi - \xi_0)(4\pi D_\xi t^3)^{-1/2} \exp\left[-(\xi - \xi_0 - \bar{v}_\xi t)^2 / 4D_\xi t\right] \ . \tag{8}$$

From these it also follows that the D_ξ can be computed equivalently as a spatial or temporal average if the dispersion process is diffusive:

$$D_\xi = \int_{-\infty}^{\infty} P(\xi - \xi_0, t)(S_\xi^2 / 2t)d\xi = \int_0^\infty Q(\xi - \xi_0, t)(S_\xi^2/2t)dt \ . \tag{9}$$

Calculating the dispersion coefficients by temporal averaging of $S_\xi^2/2t$ is consistent with experimental determination of dispersion coefficients by monitoring at some downstream position the concentration in an emerging concentration front versus time since it was injected.

Concepts From Percolation Theory

In this work we consider one-dimensional mean flow in networks tantamount to square or cubic lattices. The mean flow is parallel to one of the pore axes. If the pores vary in radius, then the local flow will be complicated, with many different flow paths of varying flow rates, the paths giving rise to both kinematic and dynamic dispersion. This dispersion is geometrically driven, since in these regular networks there would be no dispersion if all the pores were identical. On the other hand, if certain fractions of the pores of the regular network are eliminated chaotically, then the remaining pores, even if identical, will provide a variety of flow paths giving rise to kinematic dispersion. Dispersion in this case is topologically driven. In a disordered porous medium, didpersion is a result of combined geometrical and topological disorder, imposed by the porosity and the subpopulation of immiscible phases in multiphase flow. An advantage of computer simulations is that both types of disorder can be investigated separately or in combination.

As the natural language for describing topological disorder is that of percolation theory, we outline in this section those concepts of the theory that are pertinent to the work presented below. Percolation theory of regular networks has been reviewed by several authors (13,30). Its relevance to flow in porous media is now well established (31-34).

Of all the bonds or sites in any given network it is convenient to designate a subset as *allowed* bonds or sites. The allowed bonds or sites are those remaining after others have been removed from consideration. For our purpose disallowed bonds will be removed either by setting their radii equal to zero or by reserving them for a second phase in two-phase flow. With enough allowed bonds, a continuous paths of connectedness and thus transport of allowed bonds will span the network. Percolation quantities of interest here are the

(1) *accessibility*, measured by the *accessible* or *percolation fraction*, the probable fraction of network bonds or sites connected to such a continuous path,

(2) *effectiveness*, measured by the *backbone fraction*, the probable fraction of bonds or sites active to transport, i.e., the accessible fraction minus its deadends.

(3) *percolation threshold*, the largest fraction of allowed bonds or sites below which the accessible fraction is zero. Allowed bonds are either accessible, or isolated in clusters of allowed bonds surrounded by disallowed bonds. Below the percolation threshold all allowed bonds are isolated.

A closely related quantity of interest is the *effective conductivity*. It is the conductivity of the entire network when allowed bonds have distributed conductances and the disallowed bonds have zero conductances. Effective conductivity of a network is not a concept of percolation theory but it is closely associated with the theory and its value ought to be zero below the percolation threshold.

In Figure 1 the accessible and backbone bonds are shown in a square network from which the fraction 0.425 of bonds have been disallowed. The isolated

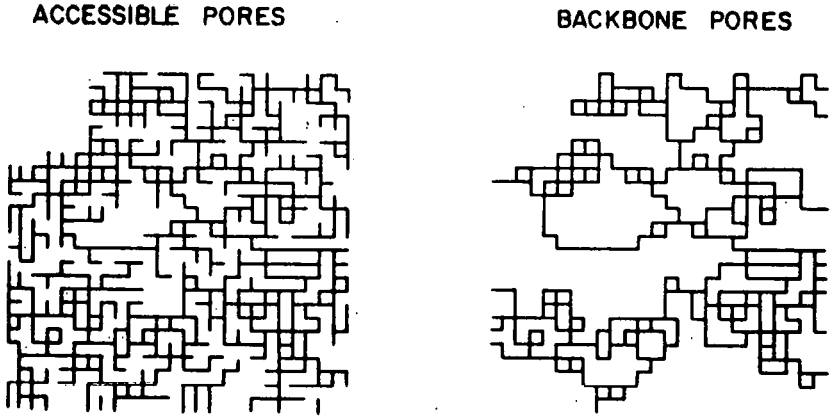

Figure 1. A square network with a fraction 0.425 of bonds removed at random.

allowed bonds are not shown. It is striking that so many of the accessible bonds are deadends and therefore inactive to flow. Also, the backbone is composed of tortuous flow paths involving *links* and *mazes*. Links are the bonds such that if one is cut, the backbone breaks into two parts and the remaining multiply-connected bonds aggregate together in mazes. Each maze is connected to the rest of the backbone by only a few bonds. This picture of backbone near the percolation threshold has been shown by Stanley (35) and by Coniglio (36,37) to be accurate so far as transport is concerned.

As the percolation threshold is approached the backbone paths become more and more tortuous. Since flow in allowed bonds occurs only in the backbone bonds, the topological structure of the backbone plays a major role in driving dispersion in disordered porous media. The distribution of fluids in the backbone is spatially non-uniform because of the random topology of the backbone and because of the many deadend bonds that are connected to it but are not part of it.

A modification of the usual isotropic percolation process is the *directed percolation process* in which a directionality constraint plays a fundamental role. Although implicit in the pioneering work of Broadbent and Hammersley (38), the problem of directed percolation has attracted much attention only in recent years. In this problem, network bonds may be randomly accessible, and each bond is *directed* so that connectivity or information can flow in only one direction along the bond. In this sense, a directed bond is equivalent to a diode in an electrical network (see Figure 2). The directed percolation problem has application in diverse disciplines such as irreversible chemical reaction (39), Markov processes with branching, recombination, and absorption (40), gelation in a flowing solvent (41), hopping transport in an electric field (42), and even galactic evolution (43).

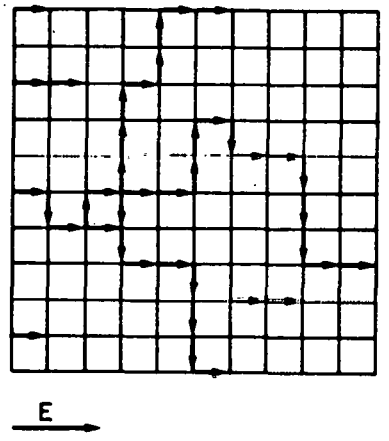

Figure 2. Directed percolation on a square network; the applied field is denoted by E.

In the dispersion process simulated here, most of the bonds parallel to the macroscopic average pressure drop, ΔP, carry flow in that direction and are so directed; only a small fraction of bonds carry flow counter to ΔP. Tracer particles are not allowed to move *relative* to the local flow in network

branches: the effect of the physical process of streamwise diffusion is excluded by our simulation. The effect on the conclusions reached from the network simulation is negligible we believe. To the extent that streamwise diffusion and backflow can be neglected the dispersion process can be interpreted as a directed percolation process. A more physical picture of the process is one in which few or none of the bonds are oriented in the direction of ΔP, and backsteps are allowed with some probability which depends on the orientation of the network. No work has been done on this modification of the directed percolation process and so we ignore the rarely occurring backflows in our use of percolation theory to gain a qualitative picture of the transport process. (However, backflow is allowed in our simulations.)

In the directed percolation problem discussed in the literature the direction of bonds is preassigned. The dispersion process simulated here is a *partially directed* percolation problem because the direction of only those bonds parallel to the macroscopic flow is known *a priori*. Although the bonds in transverse direction are also directed by virtue of the flows they carry their directedness is random and depends heavily on the geometry and topology of the network; thus there is no average orientational order in the transverse directions (see Figure 3).

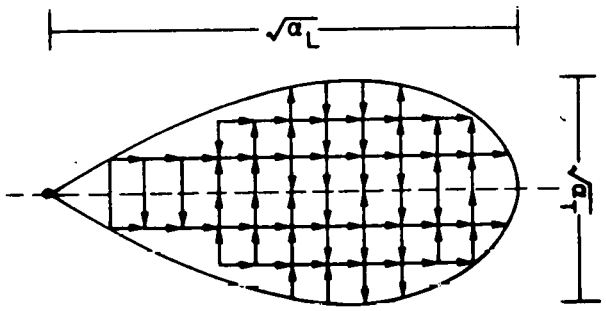

Figure 3. The applied field induces anisotropy in the directed percolation problem.

Strictly speaking the percolation theory that has been developed up to now applies to systems that are effectively infinite in size. Evidently one cannot simulate an infinite network. However, as long as the sample is large compared to the correlation length, ξ, of the backbone, simulation results for flow and dispersion will well approximate those of a large system. The correlation length can be quantified by defining $G(\underset{\sim}{r}-\underset{\sim}{r}')$, the probability that bonds at $\underset{\sim}{r}$ and $\underset{\sim}{r}'$ are allowed and belong to the continuous path of accessible bonds; near the percolation threshold, $G(\underset{\sim}{r}-\underset{\sim}{r}')$ has the asymptotic form (44)

$$G(\underset{\sim}{r}-\underset{\sim}{r}') \sim \exp(-|r-r'|/\xi) \ . \qquad (10)$$

As the percolation threshold is approached (as more bonds are disallowed), the correlation length ξ increases without bound. For example, if allowed bonds are chosen at random, then near the percolation threshold the correlation length obeys the scaling law

$$\xi \propto \ell_o (X - X_c)^{-\nu} , \tag{11}$$

where X is the fraction of allowed bonds, X_c the percolation threshold, ℓ_o a scale factor, and ν the *correlation length critical exponent*. The value ν is believed to depend only on dimensionality of the system for isotropic percolation. In two dimensions $\nu = 4/3$ and in three dimensions $\nu = 0.8$ In directed percolation the scale factor and critical exponent depend on direction. Because a particular direction is picked out, there is a global anisotropy in cluster shapes as the percolation threshold is approached (see Figure 3). The longitudinal correlation length diverges as

$$\xi_L \propto \ell_{oL} (X - X_c)^{-\nu_L} , \tag{12}$$

and the transverse correlation length diverges as

$$\xi_T \propto \ell_{oT} (X - X_c)^{-\nu_T} . \tag{13}$$

Redner and Coniglio (46) obtained an excellent approximation to ν_L and ν_T given by

$$\nu_L = c(d+9)/4(d+2) , \tag{14}$$

$$\nu_T = c\ 7/4(d+2) , \tag{15}$$

where d is the dimensionality of the network ($d = 2,3$) and c is a constant that depends only on the dimensionality of the network ($c = 2.55$ in two dimensions and $c = 2.15$ in three dimensions). From Eqs. (14) and (15) it is apparent that $\nu_L > \nu_T$ and thus the correlation length diverges faster in the longitudinal than in the transverse direction.

In what follows, we shall see that the correlation lengths ξ_L and ξ_T behave similarly to the dispersivities α_L and α_T ($\alpha_\xi \equiv D_\xi/\bar{v}$) which also have dimensions of length. Thus, the correlation lengths may have more significance to dispersion than just determining sufficent sample size for experiment or simulation.

Monte Carlo Simulation Procedure

Overview

We have simulated dispersion in four-coordinated, two-dimensional networks that resemble square lattices and six-coordinated, three-dimensional networks that resemble cubic lattices. In these the orientations of the branches are totally ordered into two or three directions. The branches, or bonds, represent pore-throat segments in which flowing fluid is supposed to spend virtually all of its time; these are linked by nodes or sites representing pore-junction bodies of vanishingly small residence time. Simulation with randomly distributed coordinations, orientations, and dimensions derived from Voronoi tessellations of space (47,48) are projected the results will be reported in a future publication.

To investigate dispersion, we inject a tracer particle into the network at a randomly chosen node in the plane $x=0$ and monitor its motion through the network. The path along which the particle travels depends not only on the geometry and topology of the network, but also on microscopic events within bonds and nodes. In the present work we neglect the velocity distribution within each bond (i.e. the tracer particles are assumed to move as in plug flow). We assume that converging streams are completely mixed at nodes and that a particle arriving at a node leaves into one of the attached bonds with a conditional probability proportional to the fraction of the flow rate departing from the node through that bond. Thus, if q_i is volumetric flow rate in a bond i that transports fluid from the node, the conditional probability that the tracer leave through bond i is $q_i/\Sigma q_j$, where Σq_j is the total volumetric flow rate leaving (and hence entering ^{j}to) the j^{j} node. Such conditional probabilities are of course branch-branch transition probabilities for complete mixing at the node.

The nodal mixing, which depends ultimately on molecular diffusion, creates a homogeneous (one-step) Markov process, because with complete mixing the exit state of the tracer particle depends only on the node at which it has arrived and not on its travel history (see e.g. Papoulis (49)). In effect the tracer particle has no memory, whereas with partial mixing at nodes, it has a finite memory, i.e. only a few previous steps are important and the correlation between the successive displacements of the particle is finite. Montroll (50), who studied the excluded volume effect in polymer chains, showed that provided the correlation coefficient between the components of the position of the j-th and that of k-th displacement decays more rapidly than $c/S^{1+\varepsilon}$ (where $S = |j - k|$) as $S \to \infty$, where c is a constant and ε is an arbitrarily small positive constant, the multistep Markov process can still be treated as the case without any correlations: the asymptotic (long time) results are the same as those for a system lacking correlations. The effect of correlations shows up only in the rate of convergence of the process to the asymptotic regime. Now as nodal mixing weakens, that rate must ultimately appear in macroscopically appreciable distances. Nevertheless we expect that the diffusive behavior shown by the Monte Carlo simulations of dispersion in single- and two-phase flow reported below will prove representative of the process in such porespaces and actual flow situations as can be realistically modeled by extensive network discretizations.

Details of the Simulation

The sequence of calculations in our Monte Carlo method is as follows:

(1) The effective radii of pore throat segments, or bonds, are distributed at random (by means of a pseudo-random number generator subroutine) from a qualitatively representative distribution. Here we employ a Rayleigh distribution (Figure 4)

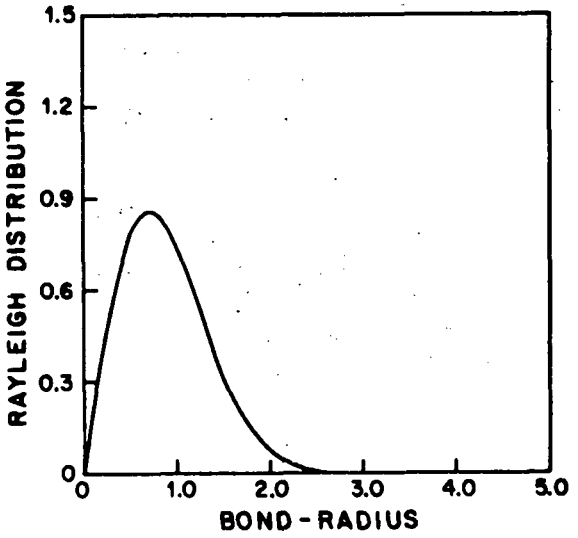

Figure 4. The Rayleigh distribution [Eq. (16), with $\alpha = 1$] used here as a model distribution of pore-throat radii.

$$f(R) = 2\alpha^2 R e^{-\alpha^2 R^2} \tag{16}$$

where α is a characteristic pore radius. This distribution mimics the pore size distributions determined by several investigators (e.g. Thomas *et al.* (51)). Heiba *et al.* (34) used the same distribution in their theory of relative permeabilities and observed good agreement between their predictions and experimental data.

(2) The flow cross-sections of the pore segments are taken to be circular or of low aspect ratio, so that in the Stokes flow (creeping flow) that prevails each bond's flow resistance is proportional to the inverse fourth power of its effective radius (as in Hagen-Poiseuille flow). Moreover the contribution of each segment to total volume of porespace we take proportional to its effective radius. Therefore the pore conductance g is chosen to be

$$g = \frac{R^4}{8\mu\ell}, \qquad q = g\Delta P \tag{17}$$

where ℓ is the pore length and μ is the viscosity of fluid. For simplicity we take ℓ to be a constant.

(3) The steady-state pressure distribution in the entire network is computed. This is done by solving a standard Kirchhoff law formulation in which the flowrate q_i in each bond is the product of the pressure difference Δp_i between its nodes and its hydraulic conductance, as in Eq. (17). Then problem of flow through the random network reduces to a set of linear equations

$$\underset{\approx}{A}\,\underset{\sim}{P} = \underset{\sim}{b} . \tag{18}$$

$\underset{\sim}{P}$ is a column vector whose elements are nodal pressures. $\underset{\sim}{b}$ is a column vector arising from the boundary conditions, which are constant pressures P_1 and P_2 imposed at the entrance and exit planes of the network ($x=0$ and $x=L$, respectively) and matched conditions on the opposed faces in the y-direction and on those in the z-direction (so-called periodic conditions). The entries of the matrix $\underset{\approx}{A}$ are conductances

$$A_{ij} = \begin{cases} 0 & \text{if } i \text{ and } j \text{ are not connected nodes} \\ -\dfrac{R_{ij}^4}{8\mu\ell} & \text{if } i \text{ and } j \text{ are connected nodes and } i \neq j \\ \displaystyle\sum_{k\in\{i\}} \dfrac{R_{ik}^4}{8\mu\ell} & \text{if } i=j \end{cases} \tag{19}$$

Here $\{i\}$ means the set of nearest neighbors of node i and R_{ij} is the effective radius of the bond connecting it to node j. For two-phase flow regimes Eq. (18) must be solved separately for each phase, A_{ij} being set equal to zero for all bonds occupied by other than the chosen phase.

(4) From the pressure distribution and effective pore radius the average velocity of flow in each bond is calculated and the permeability to the chosen phase is determined. That permeability is the product of the total volumetric flow rate across the entrance or exit plane and the viscosity of the phase, divided by the total cross-section of the network and the imposed pressure difference per unit length.

(5) Tracer particles are injected into the network at random at the plane $x=0$. Each particle performs a random walk according to the transition probability law that was laid down above. At each step the travel time of the particle across the current bond is computed from

$$t = 8\left(\frac{\ell}{R}\right)^2 \frac{\mu}{\Delta P} , \tag{20}$$

where ΔP is the pressure drop across the bond. For simplicity we took all bonds to be of the same length so far as travel time is concerned. Then the transit (first passage) time T_i of each tracer

particle is the total time it takes to cross the system from $x=0$ to $x=L$, L being the length of the system.

(6) For each transit time T_i the corresponding average transit velocity $\bar{v}_i$ in the mean flow direction

$$\bar{v}_i = \frac{L}{T_i} \tag{21}$$

is calculated.

(7) The transit time of each tracer particle to travel between a pair of transverse planes of specified separation is recorded and the dispersion quantities $S_y^2/2T$ and $S_z^2/2T$ are computed. Of course the average particle velocity in transverse direction is zero.

(8) After injecting a population of N tracer particles one at a time and recording their $\bar{v}_i$'s the average particle velocity $\bar{v}$ is computed from

$$\bar{v} = \frac{1}{N} \sum_{i=1}^{N} \bar{v}_i \, . \tag{22}$$

(9) The dispersion coefficients are calculated from

$$D_x = \frac{1}{2N} \sum_{i=1}^{N} S_x^2(T_i)/T_i \tag{23}$$

$$D_y = \frac{1}{2N} \sum_{i=1}^{N} S_y^2(T_i)/T_i \tag{24}$$

$$D_z = \frac{1}{2N} \sum_{i=1}^{N} S_z^2(T_i)/T_i \tag{25}$$

The average transit (first passage) time $\bar{T}$ is also found:

$$\bar{T} = \frac{1}{N} \sum_{i=1}^{N} T_i \tag{26}$$

We chose the number of tracer particles N by increasing N until the averages $\bar{v}$, D_x, D_y, and D_z no longer changed appreciably, the criterion being $\left|\frac{E_N - E_{N+n}}{E_N}\right| < \varepsilon$, where E_N is any of the quantities defined by Eqs. (22)-(25), ε is a small preassigned number, 5×10^{-2} in this study, and n is a small integer usually chosen to be ten. In the case of the cubic network with flow in the x-direction the further criterion $\left|\frac{D_y - D_z}{D_y}\right| < \varepsilon$, was used. When these criteria were met, we

chose the time T_f at which the distribution of tracer particle location is calculated. T_f has to be long enough that diffusive behavior if present becomes evident, yet short enough that few particles cross the system in less time. We took T_f to be about $0.6\ \bar{T}$. For a constant overall flow rate Q this corresponds to displacement of 60% of the pore volume (which is given by $Q\bar{T}/AL$ where A is the cross sectional area of the system).

(10) The longitudinal and transverse positions of the tracer particles at time T_f were determined and from them the dispersion coefficients and the probability density $P(\xi,T_f)$ for $\xi = x, y$ or z.

(11) The entire procedure was repeated for several network realizations, i.e. for several assignments of effective bond radii, and then the desired statistics—means and standard deviations—were compiled. The number of realizations was ultimately chosen on the basis of these statistics and computational costs.

Plainly the Monte Carlo strategy is one of constructing realizations that constitute a statistically representative sample from an indefinitely large population. To do this in the case of dispersion in networks requires a large, efficient computer. We employed the Cray-1 computer of the University of Minnesota Computer Center. Calculation of a pressure field took about 4.5 CPU seconds for a 50×50 square network and about 3.3 CPU seconds for a 10×10×10 cubic network calculations. In the case of the 17×17×17 cubic network almost all of the memory of the computer, 10^6 words, was used.

One-Phase Flow Systems

Dispersion in Square and Cubic Networks

At the outset we can dispose of the question of how the results depend on the size of the network employed. Figure 5a shows how the permeability of the square network varies with its size. The permeability of the 15×15 network is the average of 20 realizations and that of other sizes shown in Figure 5a is the average of 5 realizations. There is little difference between the result for the 50×50 network and that of the 60×60 one; moreover, they differ only by about 15% from the permeability of the 40×40 network. Figure 5b shows how the dispersion coefficients D_L and D_T depend on the network size; they follow the same pattern as the permeability. Based on these results we chose the 50×50 square network for more extensive calculations.

The tracer particle distribution $P(x,t)$ for the position x of the tracers in the direction of flow is presented in Figure 6 and for transverse direction in Figure 7. We judged whether the process is diffusive by determining, on the basis of the chi-squared test of goodness of fit whether P is Gaussian, whether Q is derived from a Gaussian P, and whether spatial and temporal averages of $S_\xi^2/2t$ are equal. We compared the sample distributions in Figures 6 and 7 with the Gaussian distribution, Eq. (7) using the average values of D_L and D_T for the longitudinal and transverse cases. The Gaussian distribution fits the longitudinal result (Figure 6) with approximately 85% confidence and the transverse result (Figure 7) with 90% confidence.

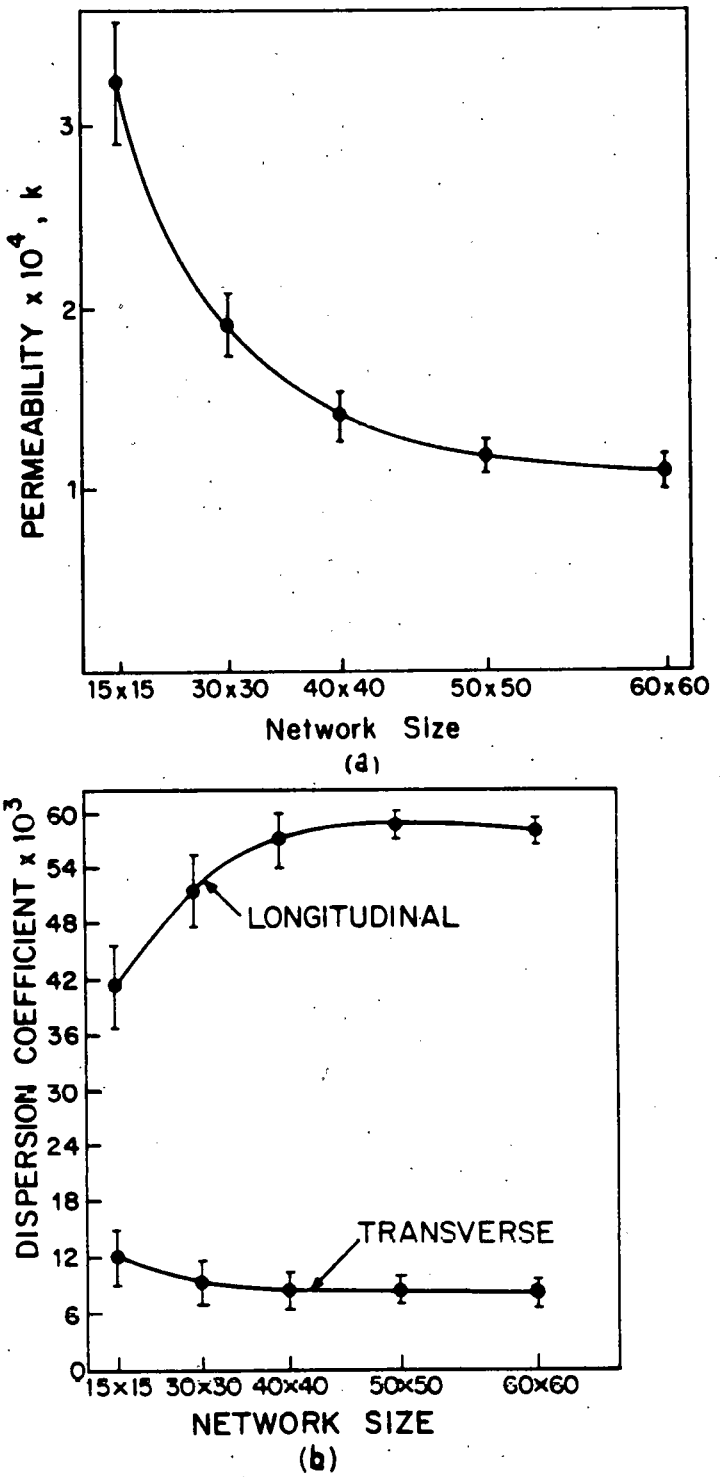

Figure 5. Square network: effect of network size on (a) permeability, and (b) dispersion coefficients.

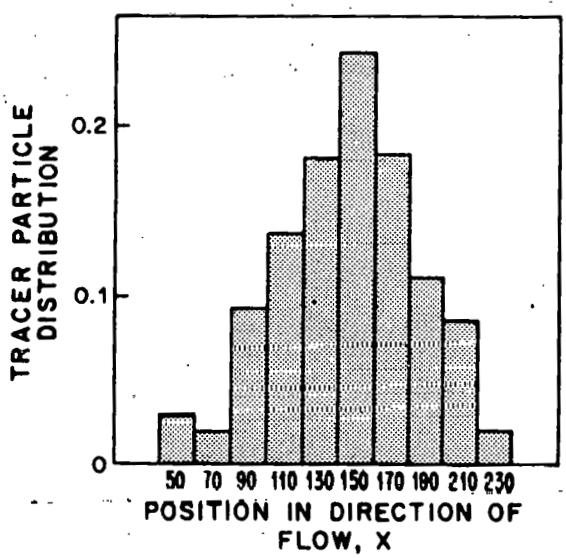

Figure 6. One phase flow in a square network: longitudinal tracer particle distribution at fixed time.

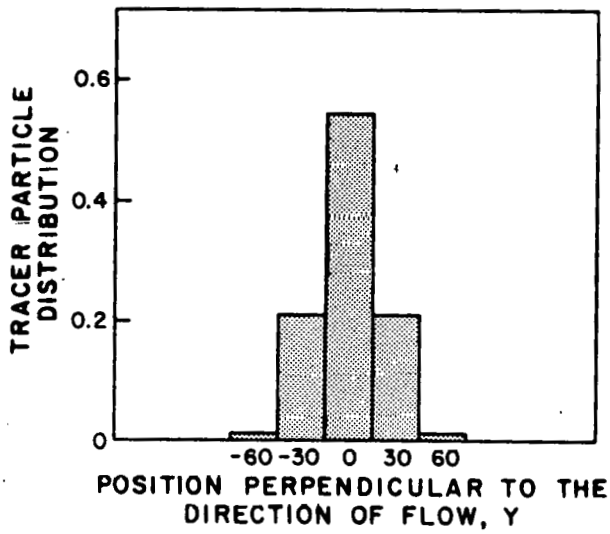

Figure 7. One phase flow in a square network: transverse tracer particle distribution at fixed time.

The average displacement of a tracer particle in the transverse direction is zero. On the other hand the average of the longitudinal positions of the tracer particles is about 28 bond lengths. This is expected because the time at which the positions of particles were recorded is about 60% of the average transit (first passage) time across the system, and so the mean longitudinal position of tracer particles must be about 60% of the 50-bond total length of the medium. Figure 8 is a histogram of the transit time distribution function $Q(L,t)$ of the tracer particles. Because the tracer particle distribution is approximately normal, this should be an exponentially decaying distribution with a long tail (compare Eq. (8)), as it is with 90% confidence. The spatial and temporal averages of $S_x^2/2t$ agree with each other to within 10% as do also those of $S_y^2/2t$. We conclude from this that the dispersion process in single-phase flow simulated here is diffusive, and thus the dispersion coefficients can be identified as effective diffusion coefficients in the macroscopic convective-diffusion Eq. (1).

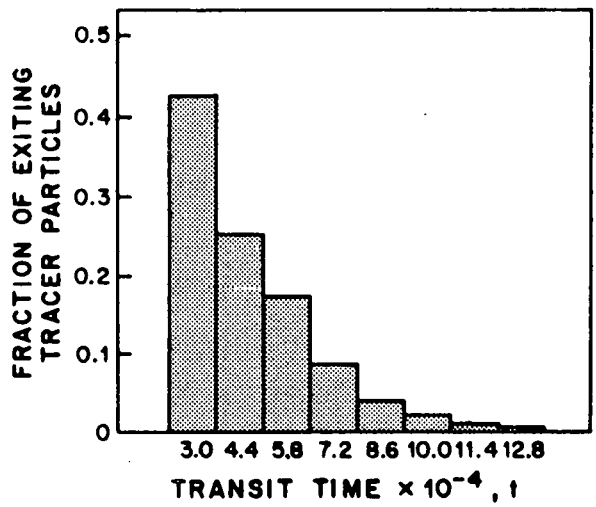

Figure 8. Square network: transit time distribution for one phase flow.

The ratio $\langle|v_x|\rangle/\langle|v_y|\rangle$ where $\langle|v_\xi|\rangle$ is the average particle speed in the ξ-direction, we found to be about 1.95±0.12. This suggests that on average, the transition probability for a displacement in the longitudinal direction is twice as large as that of the transverse direction. The ratio of D_L/D_T was found to be 6.88±0.33.

It is noteworthy that the ratio of the Darcy velocity v_d to the average tracer particle velocity $\bar{v}$ is $v_d/\bar{v}$ = 1.95±0.13. We interpret this to mean that in transit across the network the particle spends on the average half of its time moving in the transverse direction. This is supported by the fact that the ratio n_x/n_y, where n_ξ is the average number of displacements in the ξ-direction, is 1.95±0.15, which is the same as $\langle|v_x|\rangle/\langle|v_y|\rangle$ as it should be. Thus even though the average time spent in a transversely directed bond is twice as large as that spent in a longitudinally directed bond (since $\langle|v_x|\rangle/\langle|v_y|\rangle \cdot 2$), on average only half of the total transit time is spent in bonds of the former orientation.

We also studied dispersion in cubic lattice-like network. Again, we first computed the permeability and the dispersion coefficients as functions of network size, with the results shown in Figure 9. On the basis of these results, and because the flow calculations for the cubic network are so costly, we decided to make most of simulations on the 10X10X10 network. Although there appears to be a slight size effect, we estimate that results for this network are representative of large systems. Each point in Figure 9 represents the average over five realizations, except for the permeability and dispersion coefficients of the 5X5X5 network, which represent averages over 30 realizations.

Injection of about 700 tracer particles in each of the five network realizations sufficed to give convergent values of dispersion coefficients, average particle velocity, and average transit time; whereas for the square network about 1500 particles were required. The lesser number required reflects the diversity of particle paths in three dimensions. The longitudinal dispersion coefficient D_L and the average particle velocity $\bar{v}$ in fact stabilized after only about 250 tracers had been injected, but D_y and D_z converged on each other more slowly.

The ratio $v_d/\bar{v}$ was found to be 2.85±0.35, which supports our conjecture that this ratio must be about three for a large cubic network. The ratio D_L/D_T we found to be about 6.8±0.2, which differs scarcely at all from the value 6.88±0.33 that was found for the square network.

The tracer particle distributions in the cubic network are recorded in Figure 10 and the transit (first passage) time distribution Q(L,t) is shown in Figure 11. The values of D_L and D_T obtained by temporal averaging of $S_x^2/2t$ and $S_y^2/2t$ were used to construct Gaussian distributions which were tested against the simulated distributions with the standard chi-squared test. The result was that the longitudinal distribution can be accepted as a normal distribution with 80% confidence, while the transverse distribution is a normal one with 95% conficence. D_L calculated from the sample was used to construct a transit time distribution Q(L,t), Eq. (8), which was then tested against the transit time distribution from the sample. The simulated distribution fits the theoretical one with 85% confidence. The longitudinal distribution P(x,t) was also determined for the 17X17X17 network as shown in Figure 12. The chi-squared test showed that it is normal with 90% confidence. Dispersion coefficients as calculated by spatial and temporal averaging of $S_\xi^2/2t$ for $\xi = x,y,z$ agreed with each other to within 10%. We conclude from this study that for the process simulated, dispersion is diffusive in the square and cubic networks.

Dispersion and Flow in Defective Square Networks

The dispersion investigated above is caused by the random geometry of the porespace—the dynamical mechanism—in regular networks. In this section we examine the effect of varying the topology of the porespace in the absence of any geometrical variations. We assign the same radius, the average of the pore size distribution in Eq. (16), to all bonds in the square network. With identical bond radii flow is one dimensional and the dispersion coefficients are zero. To create topological disorder we remove at random a fraction of the bonds of the network, i.e. we assign zero radius to them. Then, even

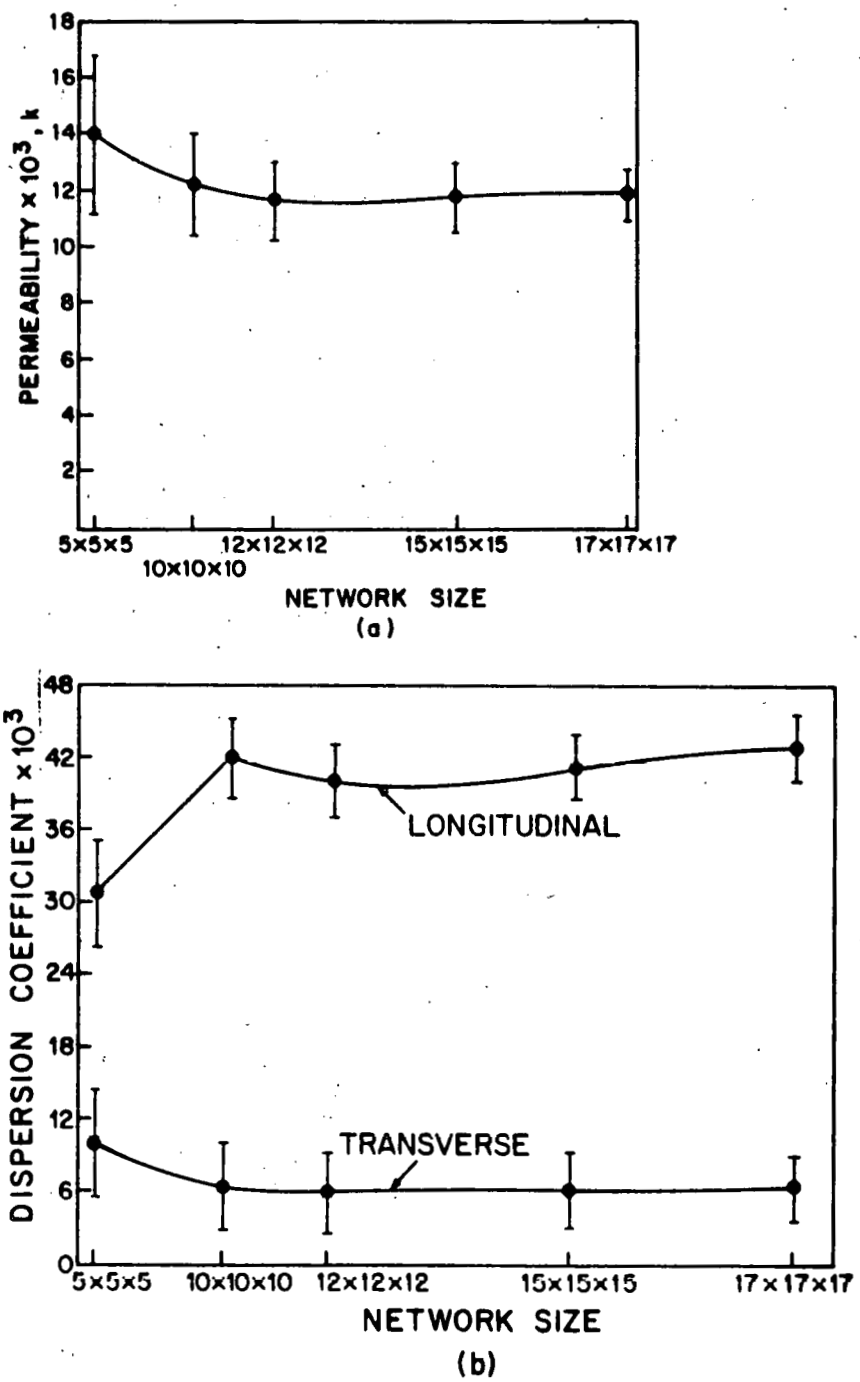

Figure 9. Cubic network: effect of network size on (a) permeability, and (b) dispersion coefficients.

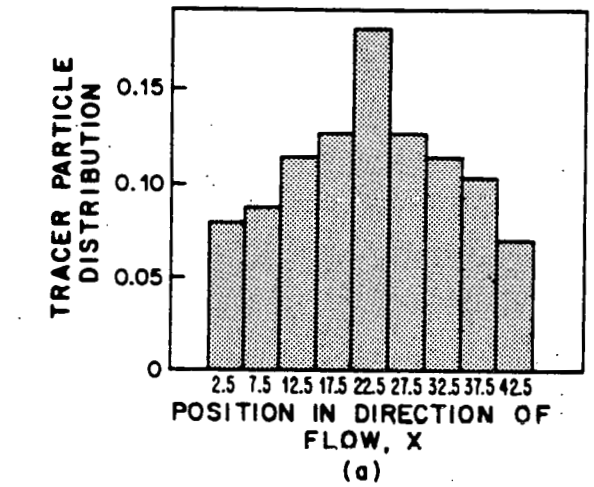

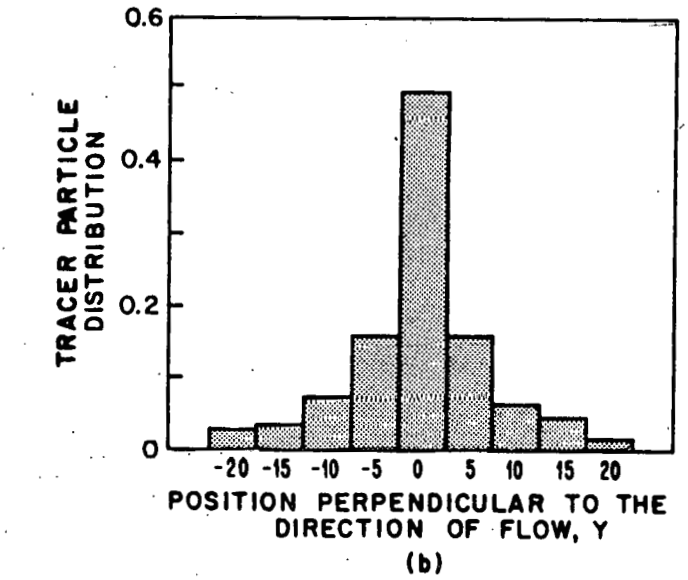

Figure 10. Cubic network: distribution of tracer particle positions at fixed time for one phase flow.

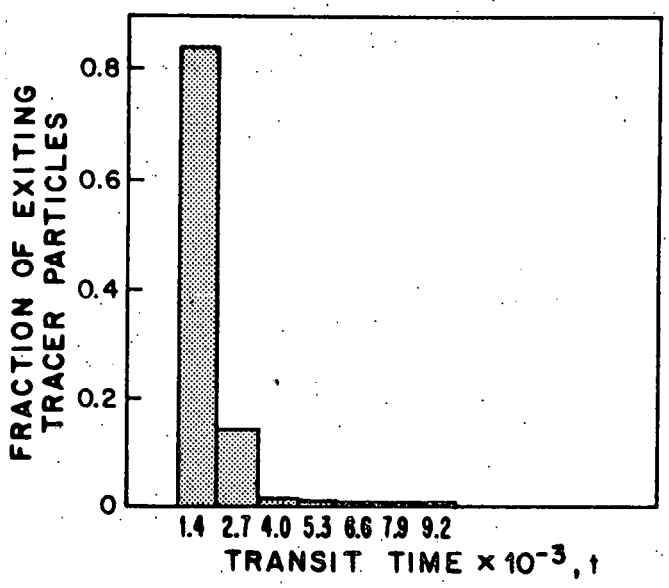

Figure 11. Cubic network: transit time distribution for one phase flow.

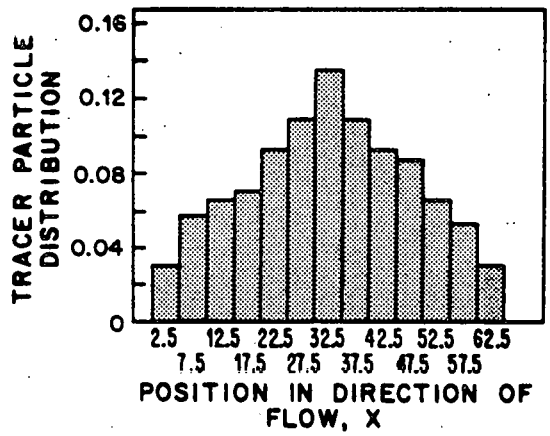

Figure 12. Tracer particle distribution for the largest cubic network used (17x17x17).

though the bonds that are allowed to flow are equivalent, kinematically driven dispersion results from the random topology of the network. Random removal of bonds isolates some bonds and makes others *deadends*, i.e. although they are connected to the sample spanning cluster, they do not participate in transport. Thus only a subset of allowed bonds is active in transport. This subset of bonds is called the *backbone of transport* in the language of percolation theory. A precise definition of the backbone of the sample-spanning cluster is that it is the largest biconnected component of the defective network. A set of network sites is said to be biconnected if every pair of sites can be linked by at least two distinct conducting paths (if they are connected by only one path, then at least one of the sites is isolated).

The percolation threshold of the partially directed square network was found by Redner (52) to be about 0.55. Our 50x50 square network has a slightly lower percolation threshold of about 0.53. To investigate dispersion we began by assigning zero radius (infinite hydraulic resistance) to 0.45 of bonds and a single effective radius to the rest of the bonds; then we make tracer particle experiment on five different realizations of the network. Next we raised the fraction of allowed bonds to 0.60 and repeated the procedure, and continued to larger fractions of allowed bonds. The resulting dispersivities $\alpha_\xi \equiv D_\xi/\bar{v}$ are shown in Figure 13. They decrease with rising fraction X of allowed bonds and vanish when all bonds are present—and have the same hydraulic resistance. Thus in the absence of any geometrical variation in the porespace, the dynamic mechanism of dispersion is inactive but purely topological irregularity of the porespace can give rise to dispersion by the kinematic mechanism. Also shown in Figure 13 are the dispersivities of the same network when the effective radii of the allowed bonds are randomly distributed according to Eq. (16). Plainly the topology is just as important as the geometry. Indeed, while dispersivities of a fully connected and uniform square lattice-like network are zero when it is aligned with the imposed field, the dispersivities of a fully connected network with the random geometry of a pore size distribution are not zero.

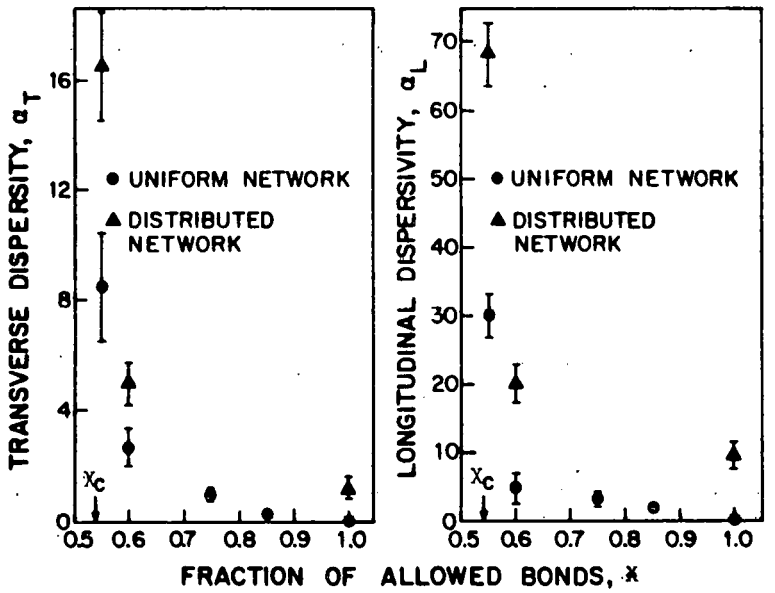

Figure 13. Dispersion in a defective square network, with only a fraction X of the bonds open to flow.

The dispersivities of the partially directed network that arise from the random topology of the backbone can be quantified near the percolation threshold. As was discussed in the section of percolation concepts, for directed percolation the sample-spanning cluster of allowed bonds is anisotropic near the percolation threshold and therefore there are two relevant length scales, $\xi_\parallel$ and $\xi_\perp$, both of which diverge. For a partially directed square network we find from Eqs. (14) and (15) that the critical correlation length exponents are

$$\nu_L = 1.753 , \tag{27}$$

$$\nu_T = 1.115 . \tag{28}$$

That the longitudinal correlation length diverges faster than the transverse correlation length is understandable because randomly directed bonds in transverse direction impose a sort of random walk that causes ξ_T to diverge more weakly than ξ_L. For the dispersion process near the percolation threshold there are also two relevant length scales, the longitudinal dispersivity α_L and the transverse dispersivity α_T, and they both increase as the threshold is approached. Consequently we conjecture that when the dispersivities α_L and α_T arise in random topology of the backbone of the network, then

$$\alpha_L \sim \xi_L , \quad \alpha_T \sim \xi_T , \tag{29}$$

near the percolation threshold. From Figure 13 the ratio of longitudinal dispersivities at 0.55 and 0.6 of bonds is found to be 7.2. This ratio is 8.4 if we use Eq. (29). From Figure 13 the ratio of the transverse dispersivities at 0.55 and 0.60 of bonds is found to be 3.37, while Eq. (29) yields a ratio Of 3.97. The agreement between the two pairs of ratios is good, in the light of the statistical fluctuations of our simulations near the percolation threshold.

For the case of dispersion caused by the random geometry as well as topology of the backbone near the percolation threshold, the exponents ν_L and ν_T remain the same, apparently because they depend only on the topology of the network; the prefactors in Eq. (29) would be expected to depend on the geometry (pore size distribution) of the backbone. Computations to find out if a similar relation holds for the cubic network are not yet available.

Dependence of Dispersion Coefficients on Average Velocity

Because the network flow is a linear process, when the overall pressure drop is changed, the pressure difference between the extremities of each bond of the network changes in proportion, and so also do all the velocities and flow rates. Hence the ratios between flow rates in different bonds that connect to the same node remain unchanged and so the transition probabilities are invariant. Consequently the dispersion coefficients are proportional to the mean velocity in our simulations (of multiphase as well as single-phase flow in the networks):

$$D_L = \alpha_L \bar{v} \tag{30}$$

$$D_T = \alpha_T \bar{v} \tag{31}$$

Some classical experimental works on single-phase flow dispersion are those of Harleman et al. (53), Brigham et al. (54) and Blackwell (55). Experimental data have been correlated with

$$D_L = \frac{D}{F\phi} + \alpha_L \bar{v}^{\beta_L} , \tag{32}$$

$$D_T = \frac{D}{F\phi} + {}_T\bar{v}^{\beta_T} \qquad (33)$$

The first terms on the right sides of Eqs. (32) and (33) are supposed to represent an effect of molecular diffusion, D being the diffusion coefficient, F a formation electrical resistivity factor, and ϕ the fractional porosity. Various values of the exponents β_L and β_T have been reported and it seems likely that they depend on the porous medium. The largest and smallest values of β_L were claimed by Legaski et al. (56): 1.28 and 1.13 respectively. Nevertheless β_L is usually set equal to unity for use in the convective-diffusion equation. Harleman et al. (53) reported the smallest value β_T, 0.7; Hassinger et al. (57) claimed the largest value, unity; Blackwell (55) reported β_T to be about 0.97. For use in the convective-diffusion equation β_T is also taken to be unity. Thus there is fair agreement between experiments and our model of the longitudinal dispersion coefficient. The apparently mildly nonlinear dependence of D_L on $\bar{v}$ may stem from an effect of molecular diffusion that is absent from the network approximation employed here. A prominent candidate is Taylor-like dispersion within streamtubes (2).

Reported experimental values of the ratio D_L/D_T vary from 3 to 61.5 (58), though most authors say it is between 10 and 24 as found by Blackwell (55). The predictions of our square and cubic network models are somewhat lower and of the many possible reasons the directional regularity and orientation of the networks we employed are leading candidates.

Two-Phase Systems

Distribution of Two Fluid Phases

Dispersion in single-phase flow in porous media is an important phenomenon, but our chief purpose in studying it is to lay groundwork for investigation of dispersion in multiphase flow, which is not only more complicated and scientifically interesting but also more important technologically. In this section we first describe the relevant aspects of steady two-phase flow, and then present the results of Monte Carlo simulation of dispersion in each of the phases.

Ordinarily when two immiscible fluids are flowing each occupies its own set of passages, i.e. continuously connected subspaces of the porespace. When the flow is steady there is no movement of the interfaces between the fluids. The way these are located, and thus the way the phases are distributed, is controlled by the interplay of the morphology of the porespace, the capillary and normal viscous stresses on the interfaces, and the stability of the shapes the interfaces try to assume in response. The shapes actually taken by the interfaces depend on the saturations, the volume fractions of phases occupying the pores, and the way those saturations were reached. Saturation history enters because there are multiple sets of shapes that satisfy the demands of pore morphology, capillarity, and Stokes flow, demands that transcribe into nonlinear equations set (59). That a fluid phase loses its continuity as its saturation falls was pointed out in the discussion above of mechanisms of dispersion.

We consider the distinct occupancies of porespace by fluids in the drain-

age process—falling saturation of wetting phase—and in the imbibition process —rising saturation of the wetting phase. In slow flow, the wettability, capillarity and pore morphology (network coordination number and bond radii in our model) determine what space is occupied by invading and retreating phases (1). Our simulations are restricted to strongly wetting and non-wetting phases. Thus, following others (3,34,60) we assume that in drainage the non-wetting phase preferentially invades accessible large pores and in imbibition the wetting phase preferentially invades accessible small pores.

A representative drainage fluid distribution can be created by assigning non-wetting phase to all pore segments that belong to sample-spanning, continuously connected paths of pores having minimum radii (here approximated by effective radii) greater than a given value R_d. The value of R_d is set by the desired saturation. Of the *allowed* pores, i.e. the population of pore segments with radii greater then R_d, only the *accessible or sample-spanning fraction* is filled with non-wetting phase. Segments of radius larger than R_d yet isolated by virtue of connections to segments smaller than R_d are excluded to non-wetting phase in drainage. As the saturation of non-wetting phase rises in drainage, some pore regions containing wetting phase become surrounded by non-wetting phase. In slow flow these isolated regions remain unchanged as non-wetting phase saturation rises further. A saturation is finally reached at which wetting phase is totally isolated; this is the characteristic residual saturation, or percolation threshold, of wetting phase.

A representative imbibition fluid distribution can be created by beginning with a sample containing continuous non-wetting phase together with wetting phase at its residual saturation and then assigning all added wetting phase to all the pore segments that belong to sample-spanning, continuously connected paths of pores having radii less than a given value, R_i, which is fixed by the desired saturation. Wetting phase then resides in two types of space: the accessible fraction of *allowed* pore segments, allowed pore segments being the population with radius less than R_i, and those segments not in the accessible fraction that were left isolated (apart from thin-film connections of negligible hydraulic conductance) at the end of the drainage process. As the wetting phase saturation climbs in imbibition, regions of isolated non-wetting phase begin to appear until finally non-wetting phase exists only in isolated blobs, i.e. its residual saturation (percolation threshold) has been reached. The accessible pore space and residual saturation in each of the two processes can be found directly from Monte Carlo simulations. This approach was followed by Fatt (3) and again by Lin and Slattery (60) in their work on network relative permeabilities. Alternatively drainage and imbibition fluid distributions can be created by means of the percolation theory of Heiba et al. (34) with a consequent reduction of costs of at least one order of magnitude. This is the approach we employed.

Heiba et al. (34) showed that during drainage and imbibition processes the subdistributions of porespace accessible to and occupied by the two phases are different. The pore segment size distribution of the subset of porespace occupied by either phase differs from the overall distribution, which is active in one-phase flow. The key parameter defining the stage of displacement in both drainage and imbibition is the capillary pressure between the flowing phases. As *drainage* proceeds, the current value of capillary pressure determines the minimum effective bond radius R_d of pores into which non-wetting

phase can penetrate and thereby displace wetting fluid. Thus a given stage of drainage is parametrized by a particular value of R_d—at that stage all bonds of larger radius than R_d are allowed to non-wetting phase, but that phase has entered only those bonds which are accessible (i.e. are connected to the sample surfaces by continuous paths of allowed bonds as described in the section on percolation concepts). The fraction of bonds that are allowed to non-wetting phase is then

$$X_d = \int_{R_d}^{\infty} f(R)dR \ , \tag{34}$$

and the fraction of these bonds that are accessible and thus occupied by the non-wetting phase is

$$X_{nw,d} = X^A(X_d) \ , \tag{34}$$

where $X^A(X_d)$ is the accessibility or percolation fraction of the network. Because the non-wetting phase can occupy only bonds of radius greater than R_d, the distribution of the radii of the bonds that are allowed to the non-wetting phase is (34)

$$f_{nw,d}(R) = \begin{cases} \dfrac{f(R)}{X_d} \ , & R \geq R_d \\ 0 \ , & R < R_d \end{cases} \tag{35}$$

Therefore *to simulate dispersion in the non-wetting phase during drainage*, a fraction $1-X_d$ of bonds is chosen at random and assigned zero radius, the radii of the remaining bonds being distributed according to $f_{nw,d}(R)$.

As the non-wetting phase saturation increases, the capillary pressure between the phases climbs, the menisci penetrate smaller pore segments, and the wetting phase loses porespace. Because the radii of the bonds are distributed at random, the fraction of bonds that are occupied by the wetting phase during drainage is $X_{w,d} = 1 - X_{nw,d}$. The distribution of the radii of the bonds that are occupied by the wetting phase is (34)

$$f_{w,d}(R) = \begin{cases} \dfrac{1 - \dfrac{X^A(X_d)}{X_d}}{1 - X^A(X_d)} f(R) \ , & R \geq R_d \\ \dfrac{1}{1 - X^A(X_d)} f(R) \ , & R < R_d \end{cases} . \tag{36}$$

The explanation of this is as follows. A fraction $1 - X^A(X_d)$ of all bonds is

occupied by wetting phase. This fraction can be decomposed into two parts: all bonds of radius less than R_d (the fraction $1-X_d$); and the non-accessible fraction of bonds of radius greater than or equal to R_d (the fraction $X_d - X^A(X_d)$). Because the radii distributions for $R < R_d$ and $R \geq R_d$ are $f(R)/(1-X_d)$ and $f(R)/X_d$ respectively, Eq. (36) follows. Thus *to simulate dispersion in the wetting phase during drainage*, the fraction $1-X_{w,d} = X^A(X_d)$ of bonds is assigned zero radius at random and the radii of the remaining bonds are distributed according to $f_{w,d}(R)$. The drainage process is terminated when the wetting phase loses its connectivity. This happens when $X_{w,d}$ falls below the bond percolation threshold of the network. Obviously the radius $R_{d,c}$ of the smallest bond penetrated by the non-wetting phase during drainage is given by

$$X_c = \int_0^{R_{d,c}} f(R)dR \ , \tag{37}$$

where X_c is the bond percolation threshold of the network.

During *imbibition* the current value of capillary pressure determines the maximum effective radius R_i of pores that wetting phase can invade. Consistent with typical experimental procedure (61,62) for measuring relative permeabilities as non-wetting fluid is displaced by wetting phase, we consider just the range of saturations that extends from porespace containing only the hydraulically irreducible wetting phase saturation to the fractional filling at which non-wetting phase loses its connectivity across the network. Thus a given stage of imbibition is parametrized by a particular value of R_i —at that stage all bonds of smaller radius than R_i are allowed to wetting phase. The fraction of such bonds is given by

$$X_i = \int_0^{R_i} f(R)dR \ . \tag{38}$$

However, only a fraction $X_{w,i}$ of these bonds is occupied by the wetting phase, specifically the fraction of accessible bonds having radius smaller than R_i, plus all previously occupied bonds of radius less than $R_{d,c}$. Thus $X_{w,i}$ is given by

$$X_{w,i} = X_c + \frac{X^A(X_i)}{X_i}(X_i - X_c) \ . \tag{39}$$

In imbibition the distribution of radii of bonds that are open to wetting phase is (34)

$$f_{w,i}(R) = \begin{cases} \dfrac{f(R)}{X_i} & R < R_i \\ 0 & R > R_i \end{cases} \tag{40}$$

Thus *to simulate dispersion in wetting phase during imbibition*, a fraction $1-X_i$ of bonds is assigned zero radius and the radii of the remaining bonds are distributed according to $f_{w,i}(R)$.

As the wetting phase invades to higher saturation the non-wetting phase is either totally disconnected and thereby isolated, or it is pushed out of the medium. Because bonds of all sizes are supposed to be randomly located in the network, the remaining non-wetting phase occupies randomly placed bonds that constitute the fraction $X_{nw,i} = 1 - X_{w,i}$. Then by an argument similar to the one presented for the wetting phase during drainage, it follows that the distribution of the radii of the bonds occupied by non-wetting phase during imbibition is given by (34)

$$f_{nw,i}(R) = \begin{cases} 0 & , \quad R < R_{c,d} \\ \dfrac{1 - \dfrac{X^A(X_i)}{X_i}}{1 - X^A(X_i)} f(R) & , \quad R_{c,d} \leq R < R_i \\ \dfrac{1}{1 - X^A(X_i)} f(R) & , \quad R \geq R_i \end{cases} \tag{41}$$

Thus *to simulate dispersion in the non-wetting phase during imbibition*, a fraction $1-X_{nw,i}$ of bonds is chosen at random and assigned zero radius, the radii of the remaining bonds being distributed according to $f_{nw,i}(R)$. The imbibition process terminates at the saturation at which the non-wetting phase loses connectivity between the surfaces of the network, i.e. becomes isolated. This happens when $X_{nw,i}$ falls below X_c, the bond percolation threshold of the network.

The percolation accessibility functions X^A for square and cubic networks employed in this study were evaluated from simple Monte Carlo simulations of random removal of bonds from the network; after each removal the fraction of accessible bonds was counted. Excellent agreement was found between our results for the accessibility functions and those given by Mohanty et al. (63) and Kirkpatrick (64).

Once the fluid distributions are defined on a network realization there are two single-phase problems to be solved in the same way as when only a single phase occupied the porespace. If one of the phases is below its percolation threshold (residual saturation) the solution for it is, of course, no flow rates in the branches of the subnetworks occupied by each phase. Then there are sets of Monte Carlo experiments with individual tracer particles to carry out. The results for each phase, wetting and nonwetting, at various saturation levels in both drainage and imbibition, are treated just as in the case of one-phase flow. In effect, the phases exclude each other from subpopulations of pore segments and reduce thereby the average coordination number of the random network occupied by each phase. Across the interface between the phases there may be momentum transfer by viscous action, but this possibility

we neglect becuase the corresponding effect of viscosity ratio on relative permeability seldom seems to be large. Accordingly we compute the hydraulic conductance to each phase independently. In the network approximation we allow the two fluids to cross at network nodes without interference. We did not consider the possibility of partitioning of the tracer particles between phases, i.e. we allowed no mass transfer between different phases.

Dispersion and Flow in Square and Cubic Networks

Because a bicontinuous structure cannot exist in two-dimensions (65), we were restricted in the case of the square lattice-like network to simulating only the invading phase in the drainage and imbibition processes. That is, we could calculate the quantities of interest only for the wetting phase during imbibition because the non-wetting phase is discontinuous, and for the non-wetting phase during drainage because then the wetting phase is disconnected. Of course there is no such limitation in three-dimensions. Another shortcoming of two-dimensional networks is their relatively high percolation threshold, which in most cases leads to unrealistically high predictions of residual saturation.

The calculated relative permeabilities for the 10X10X10 cubic network are shown in Figure 14; for comparison Talash's (61) experimental data and the theoretical calculation of Heiba et al. (34) on a Cayley tree of five-fold coordination are also shown. The coordination number of the Cayley tree was chosen to be five to give it the same bond percolation threshold (about 0.25) as the cubic network. The agreement between the three figures is striking: all the features of wetting and non-wetting phase relative permeabilities reported for Berea sandstone are reproduced rather nicely—including not only the shapes of the curves but also the lack of hysteresis in wetting phase relative permeability and its presence in non-wetting phase relative permeability. Our findings also agree with those of Lin and Slattery (60), and in the case of non-wetting phase relative permeabilities, with data of Raimondi and Torcaso (62).

From our Monte Carlo simulations of dispersion in two-phase systems we conclude that the dispersion phenomenon is diffusive. There is, however, a practical problem in carrying out Monte Carlo simulations near a percolation threshold. Because there are large fluctuations, it takes substantially more realizations to reduce the variances of the simulated quantities to an acceptable level. For example, near the percolation threshold 20 realizations of the 50X50 square network and 40 realizations of the 10X10X10 cubic network were required to simulate dispersion in the non-wetting phase during drainage and reduce the variance of the quantities of interest to 10% of their averages. The range near the percolation threshold where large fluctuations are observed is much wider for the non-wetting phase during drainage than for the wetting phase during imbibition; the reason is that the non-wetting phase resides in the large pores during drainage, and so to reach a given saturation many fewer pore segments need to be filled by the non-wetting phase than the number of pore segments that have to be filled by the wetting phase during imbibition to achieve the same saturation. Thus saturation of the non-wetting phase fluctuates widely among realizations. Figure 15 shows the longitudinal distribution of tracer particles and the transit time distribution in the wetting phase during imbibition at $S_w = 0.57$ in the cubic network. The chi-

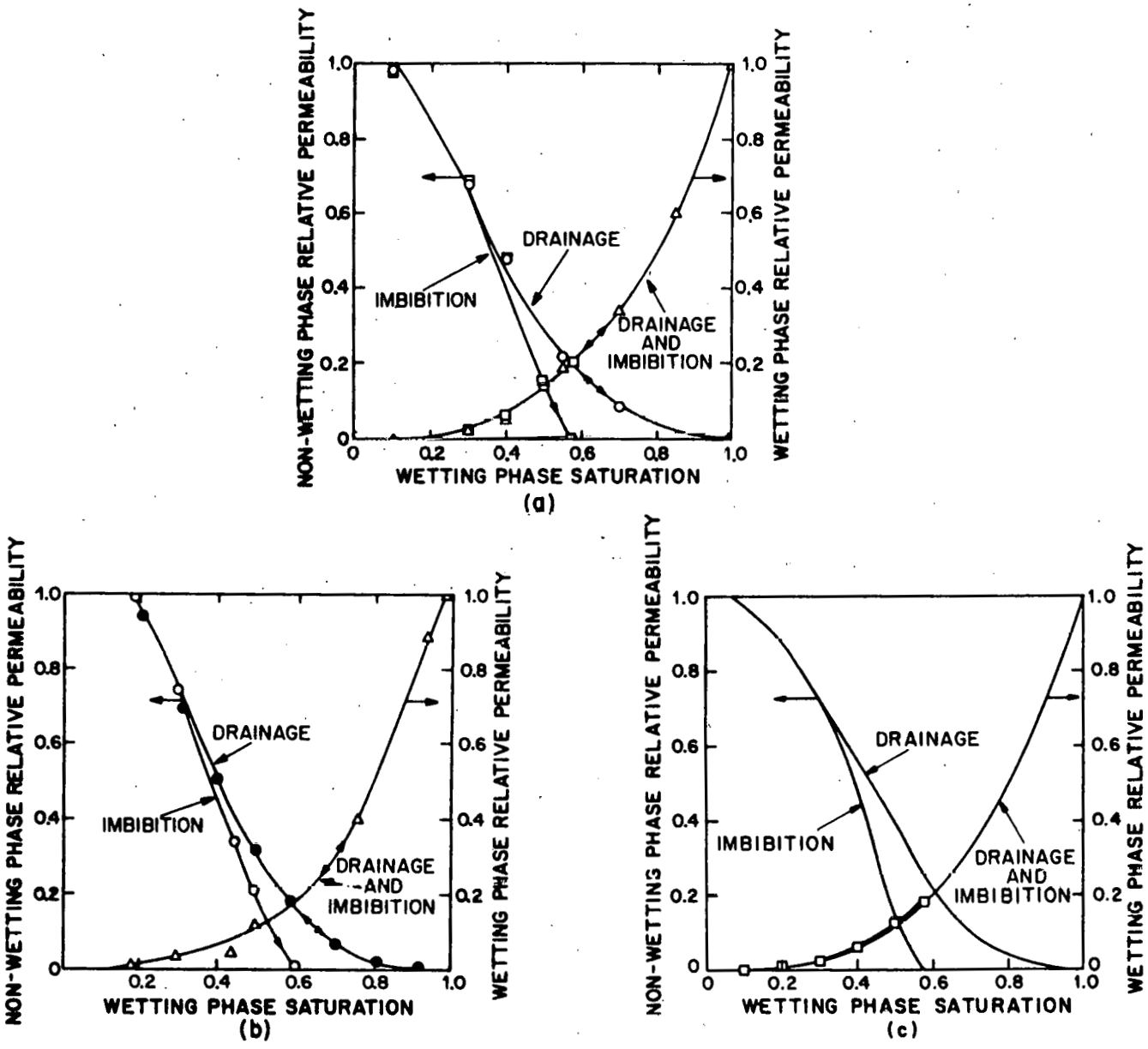

Figure 14. Relative permeabilities for two phase flow: (a) simulation on a cubic network (this paper), (b) experimental data of Talash (61), (c) Cayley tree model of Heiba et al. (34), with coordination number 5.

squared test established that the tracer particle distribution can be accepted as a normal distribution with 75% confidence, while the transit time distribution fits Eq. (8) with 80% confidence. Both distributions are the accumulation of 15 realizations. In Figure 16 we present longitudinal and transverse distribution of tracer particles in the non-wetting phase during drainage at saturation $S_{nw} = 0.3$ in the cubic network. Both of these distributions are Gaussian with approximately 80% confidence. The mean of the transverse distribution of tracer particles deviates a little from zero, which would be the mean if the distribution were perfectly normal. This appears to be a network size effect that diminishes as more realizations are included or if a much larger network is used. The simulated dispersion process on a square lattice also is diffusive. Fewer realizations were needed of the 50X50 square network than of the 10X10X10 cubic network because the former contained 5000 bonds compared with 3000 bonds in the latter.

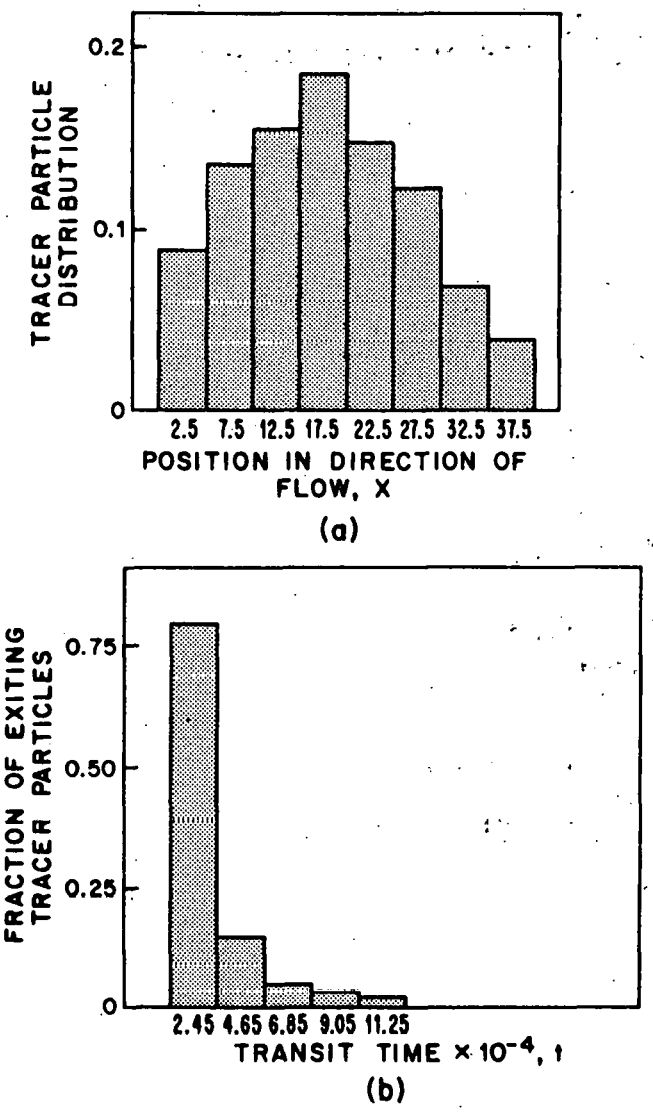

Figure 15. Two phase flow in a cubic network: imbibition at wetting phase saturation $S_w = 0.57$: (a) longitudinal tracer particle distribution at fixed time for the wetting phase, (b) transit time distribution for the wetting phase.

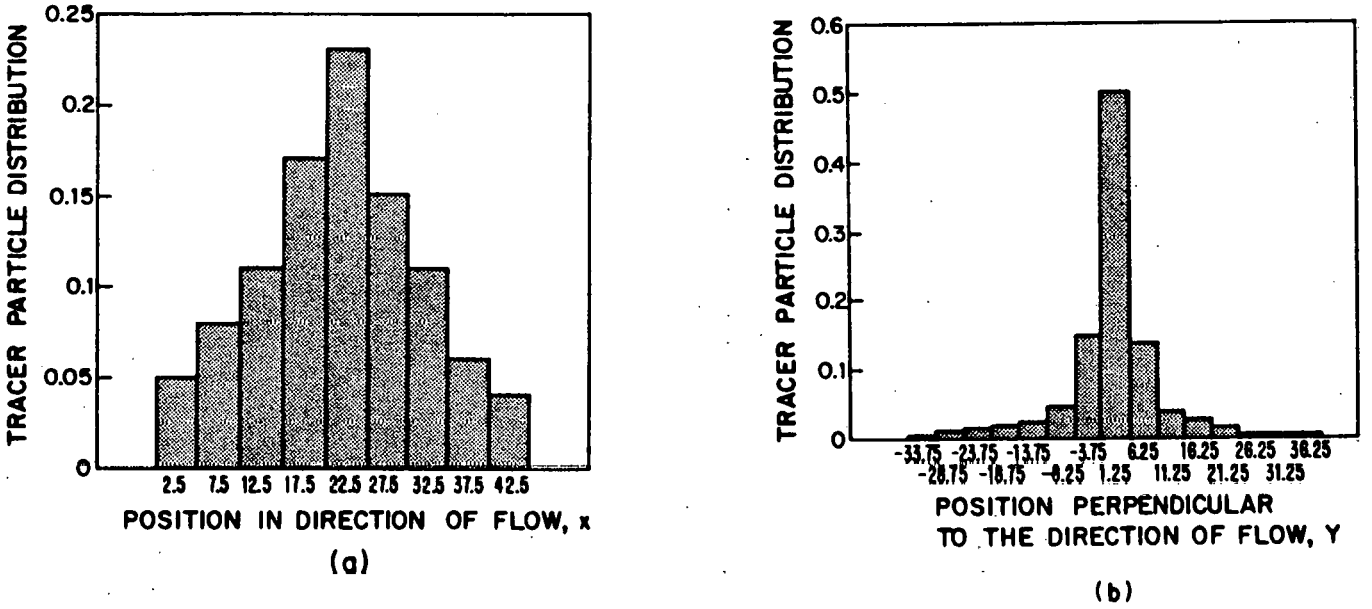

Figure 16. Two phase flow in a cubic network: drainage at non-wetting phase saturation $S_{nw} = 0.3$: (a) longitudinal tracer particle distribution (b) transverse tracer particle distribution for dispersion in the non-wetting phase.

Because the flow of each of the phases is a linear process we converted the dispersion coefficients D_ξ to dispersivities $\alpha_\xi \equiv D_\xi/\bar{v}$ just as in the case of single-phase flow. As functions of saturation these dispersivities have some striking features. Figure 17 depicts the longitudinal and transverse dispersivities of the non-wetting phase during drainage on the square network.

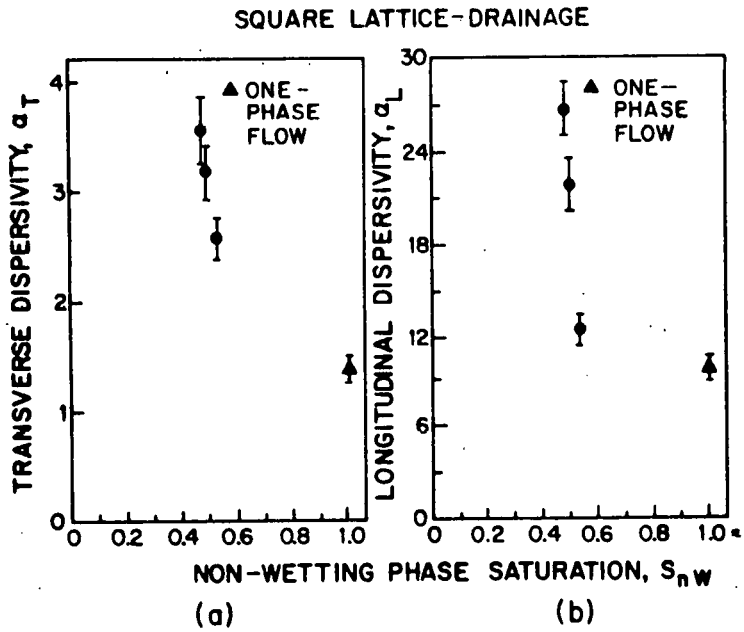

Figure 17. Two phase flow in a square network; dispersion in non-wetting phase during drainage: (a) transverse dispersivity (b) longitudinal dispersivity.

As the wetting saturation falls and the residual saturation (which is about 0.31) is approached, both dispersivities rise. The reason lies in the backbone structure. Figure 1 shows the bonds that are accessible to the non-wetting phase (i.e. have radii greater than R_d) during drainage. The fraction of these bonds is 0.575 which is quite close to the percolation threshold of the network. Among them are many deadend bonds. Also shown is the backbone of the porespace, which is obtained by removing the deadend bonds. Plainly there are three basic elements in the structure of the backbone: *nodes*, *links*, and *mazes*. As the percolation threshold is approached, the backbone of the subporespace occupied by the phase becomes increasingly tortuous. Numerous mazes, most of them containing large numbers of loops, appear which provide alternative paths for tracer particles. These evidently are highly effective in dispersing a concentration front of tracer particles. Moreover, the tortuosity of the backbone, which is defined as the ratio of the backbone fraction of the phase to the hydraulic conductance of the phase, increases without bound as the percolation threshold is approached (66). Pike and Stanley (67) showed that in this limit even the length of the *shortest* path between opposed boundaries of the network diverges. Increasing tortuosity comspires with the mazes and their associated loops to broaden the distribution of transit times: the dispersivities grow larger as a result. The longitudinal dispersivity rises faster than the transverse one because, as discussed above, the length scale over which transport is highly non-uniform grows faster in the direction of the macroscopic pressure drop, to which the directed bonds are parallel, than in transverse directions, where the flow in the bonds is randomly directed and so produces a sort of random walk that restrains the rise of transverse dispersivity.

The dispersivities of the wetting phase during imbibition in the square network are shown in Figure 18. While the qualitative trends are the same as in Figure 17 the numerical values are different. Of course the dispersivities of the two phases differ because they occupy different subpopulations of bonds. The dispersivities of the wetting phase during imbibition and drainage in the cubic network are shown in Figure 19. Comparing these with the relative permeability to the wetting phase during imbibition and drainage, as shown in Figure 14a, reveals a striking feature: each relative permeability is the same in the two processes whereas there is hysteresis in the dispersivities, i.e. they depend on the saturation history. The picture of the backbone near the percolation threshold is instructive. As can be seen, the sample-spanning backbone contains several mazes that are connected as parallel flow paths in the main structure by links of low hydraulic conductance. The contribution of these mazes to the relative permeability of the wetting phase is small. On the other hand, travel times of tracer particles along flow paths through these mazes are long and diverse, so that they can contribute substantially to the dispersivities. According to the theory of Stanley (35) and Coniglio (36,37) the number of links per maze along the backbone falls as the percolation threshold is approached. Evidently this leads to heightened dispersivities; the inference is that mazes connected in simple series by one link per maze yield the most effective dispersing structure of a network.

The dispersivities of the non-wetting phase during drainage and imbibition in the cubic network are presented in Figure 20. Qualitatively these differ little from the dispersivites of the wetting phase (cf. Figure 19). That the dispersivities of both phases in the cubic network are smaller than

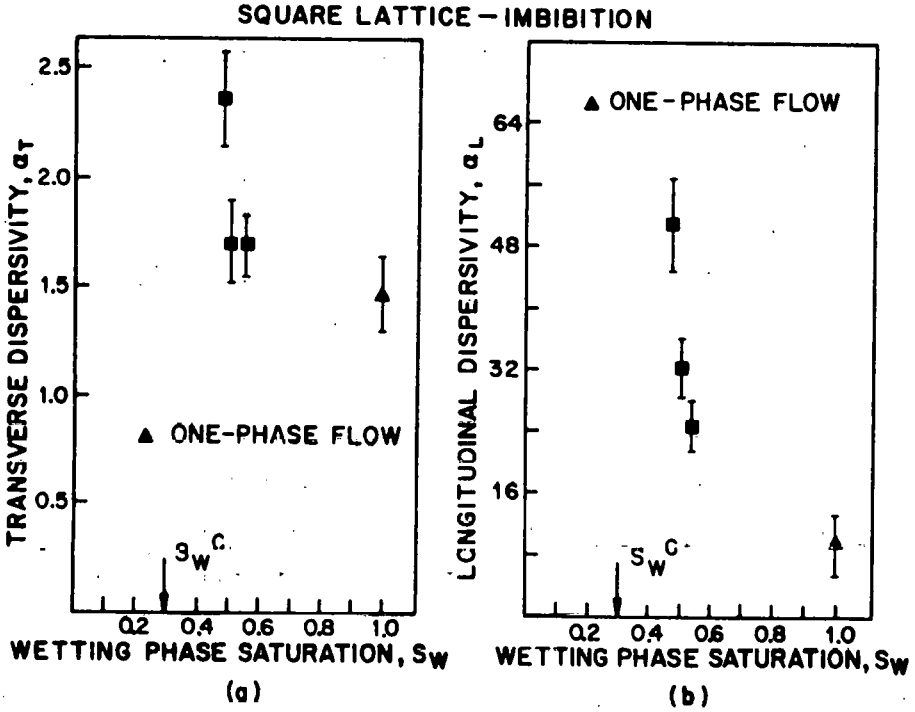

Figure 18. Two phase flow in a square network; dispersion in wetting phase during imbibition: (a) transverse dispersivity (b) longitudinal dispersivity.

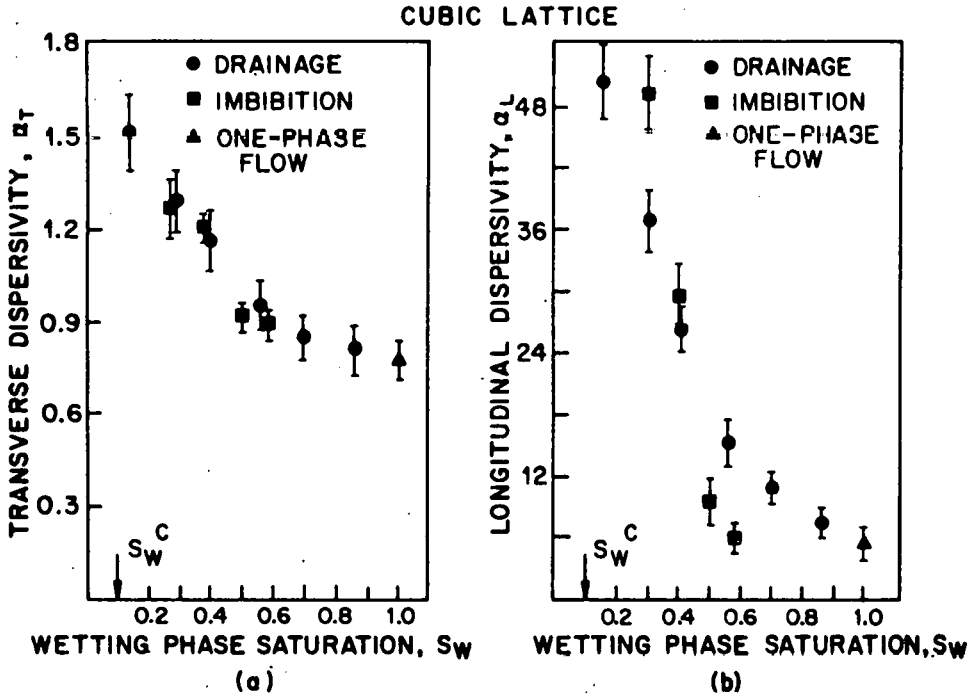

Figure 19. Two phase flow in a cubic network; dispersion in wetting phase for both drainage and imbibition: (a) transverse dispersivity, (b) longitudinal dispersivity.

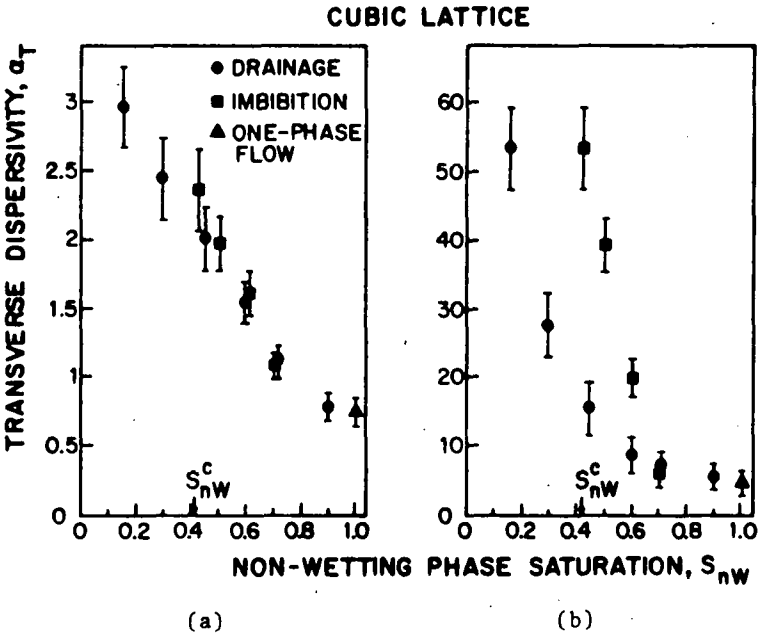

Figure 20. Two phase flow in a cubic network; dispersion in non-wetting phase for both drainage and imbibition: (a) transverse dispersivity, (b) longitudinal dispersivity.

in the square network bears comment, because one might think that in three dimensions there are more diverse paths that tracer particles can take, which should lead to greater dispersivities. However the link-and-maze structure intervenes, in a way that can be rationalized with the concept of fractal dimension introduced recently in percolation theory (68). If the sample-spanning cluster at the percolation threshold had the full connectivity of a three-dimensional network, one would expect that near the percolation threshold the mean numbers S(x) of nodes (or bonds) belonging to a cluster would follow the power law

$$S(x) \sim [\xi(x)]^3 \tag{43}$$

But from Eq. (11) one knows that $\xi \sim (x-x_c)^{-\nu}$ so that

$$S(x) \sim (x-x_c)^{-3\nu} . \tag{44}$$

Now the available numerical estimates (69) show that the exponent that characterizes the behavior of S(x) near the percolation threshold is considerably less then 3ν. Indeed, it has been shown that

$$S(x) \sim \xi^{-d_e} , \tag{45}$$

where d_e is not an integer but is about 2.02 for the cubic and about 1.7 for the square network (35,69). Such a non-integer exponent is called the *effective* or *fractal cluster dimensionality*. In this sense, then, removing bonds and approaching the percolation threshold reduces the dimensionality of the system. Moreover, inasmuch as dispersivities α_L and α_T appear to follow closely the correlation lengths ξ_L and ξ_T, the numerical values of ν_L and ν_T

are probably relevant. From Eqs. (14) and (15) we find that

$$\text{in three dimensions } \nu_L = 1.29,\ \nu_T = 0.7525; \tag{46}$$

$$\text{in three dimensions } \nu_L = 1.753,\ \nu_T = 1.115\ . \tag{47}$$

We see that lower dimensionality is associated with higher rate of divergence of the correlation lengths, just as found here in the case of the dispersivities.

There are only a few experimental data with which to compare our prediction of dispersion in two-phase flow, namely the measurements by Coats and Smith (70), Thomas et al. (51), Raimondi and Torcaso (62), Baker (71), Delshad et al. (72), Stalkup (73), and Salter and Mohanty (74). The general trend is that the longitudinal dispersion coefficient in a given phase increases as the saturation of that phase falls. For comparison we present in Figures 21 and 22 the longitudinal dispersion coefficient of the wetting and non-wetting phases during imbibition and drainage in the cubic network. The pattern is the same as that of experimental data. Shuler (75) found that the longitudinal dispersion coefficient in the wetting phase at a given saturation follows the same velocity trend as per Eq. (32). Moreover our predicted longitudinal dispersivities of both wetting and non-wetting phases agree qualitatively with the experimental data of Salter and Mohanty (74). No experimental data appear to be available with which to compare our predicted transverse dispersion coefficients and dispersivities.

The Effects of Delays

The two basic mechanisms of dispersion, kinematic and dynamic, in no way depend on molecular diffusion, which is a modifying factor chiefly because it moves materials from one streamline to another. In creeping flow through many common types of porespace there can be local, steadily recirculating fluid into and out of which dissolved or suspended materials can diffuse. In two-phase flow there may be diffusional exchange between the immiscible fluids, and portions of one of them may be immobilized as trapped blobs. It is not uncommon for dissolved materials to suffer reversible adsorption on parts or all of the porewalls, and for suspended materials to be impeded in their motion by the porewalls. In all these cases the transit time distribution of the corresponding tracer particles is further broadened by the variable delays they suffer. We have made preliminary studies of two delaying factors: deadend paths of pore segments that communicate with the flowing fluid by molecular diffusion; and adsorbing walls that hold tracer particles temporarily or even permanently. Deadend paths can be prevalent and particularly important when two phases are present.

Deadend Paths

The deadend pores shown in Figure 1 are stagnant peninsulas into and out of which tracer particles in the flowing fluid can diffuse, but not flow in response to the applied field. Goddard et al. (76) concluded from electrical conductivity and diffusion experiments that the non-wetting phase has a dendritic structure, i.e. deadends connected to the backbone, and that a considerable fraction of the non-wetting phase contributes little or nothing

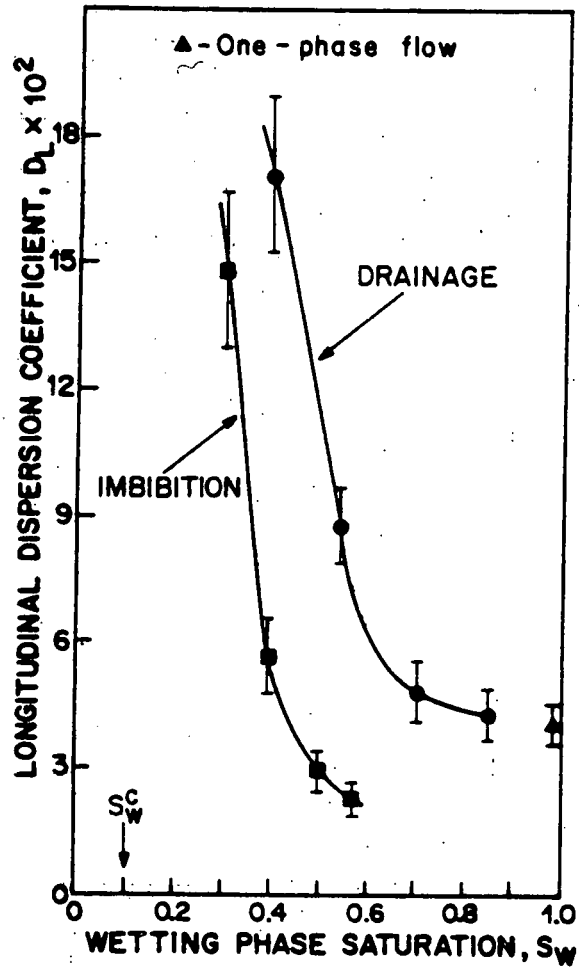

Figure 21. Two phase flow in a cubic network: longitudinal dispersion coefficient in wetting phase.

to its conductivity. Their picture accords with the one developed above. Immobilized blobs of a second fluid can cause an effect similar to that of deadend parts as is evident in the well-known work of Stalkup (73).

Coats and Smith (70) and Baker (71) constructed models of dispersion, starting from the one-dimensional convective-diffusion equation, but adding a term to account for the possible mass transfer equilibrium between flowing fluid and what they termed deadend pores. Stalkup's (73) model replaced equilibrium with mass transfer coefficients to account for rate-limited exchange. The effects of deadend paths on dispersion coefficients can be estimated by assigning a probability for diffusion into a deadend path whenever one is encountered by a tracer particle in Monte Carlo simulations. We chose to make the probabilities for diffusion into a deadend path or remaining with the flowing fluid proportional respectively to the total cross-sectional areas of deadend pores and active pores meeting at the network node. The residence time t_D over which a tracer particle entering a deadend path remains in the immobile fluid there is a distributed quantity and the breadth of the statistical distribution depends on the length of the deadend path. For our purpose it sufficed to assign to all deadend pores the same residence time

distribution; we chose the classic probability density function

$$\theta(t_R) = \frac{1}{\tau_R} e^{-t_R/\tau_R} . \qquad (48)$$

We selected τ_R so that the mean residence time is relatively large (40% specifically) compared to the mean transit time in order to render the effects of the deadend path clearly detectable. The argument is that if the tracer particles spend comparatively large intervals in the deadend paths, the distribution of transit times is substantially altered and so also the spreading of tracer particles and hence the apparent dispersion coefficients.

For these particular choices we found that deadend pores filled with *wetting phase* affect the apparent dispersion coefficients scarcely at all: their values differ negligibly from those in the absence of any diffusion into the deadend pores. For deadend pores filled with the non-wetting phase we found in contrast that apparent dispersion coefficients are significantly altered, as shown by the dashed lines in Figure 22. The apparent longitudi-

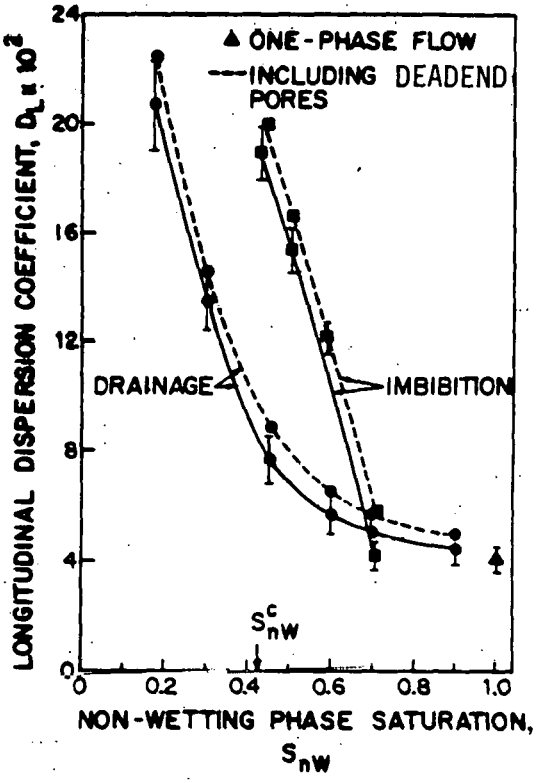

Figure 22. Two phase flow in a cubic network: longitudinal dispersion coefficient in non-wetting phase.

nal dispersion coefficient is higher when there is diffusion into the dead-end pores. This can be attributed to the broadened distribution of transit times. From these preliminary results it is not possible to draw definite conclusions, but our findings to date accord with experiments of Handy (77) who observed that for the wetting phase the apparent fraction of deadend pores is very small except close to the irreducible wetting phase saturation. The work of Goddard et al. (76) indicates that there is similarly a relatively large fraction of deadend pores filled with the non-wetting phase near its residual saturation. In Figure 23 we present the fraction of dead-end bonds filled with the wetting or non-wetting phase during imbibition and drainage. The range of wetting phase saturation over which a relatively large fraction of deadend bonds is filled with that phase is much narrower than the range for the non-wetting phase. This figure and the work of Handy (77) and Goddard et al. (76) indicate that the pattern of the effect of dead-end paths in our limited investigation has more to do with two-phase fluid distribution than with the specific choice of the residence time distribution $\theta(t_R)$.

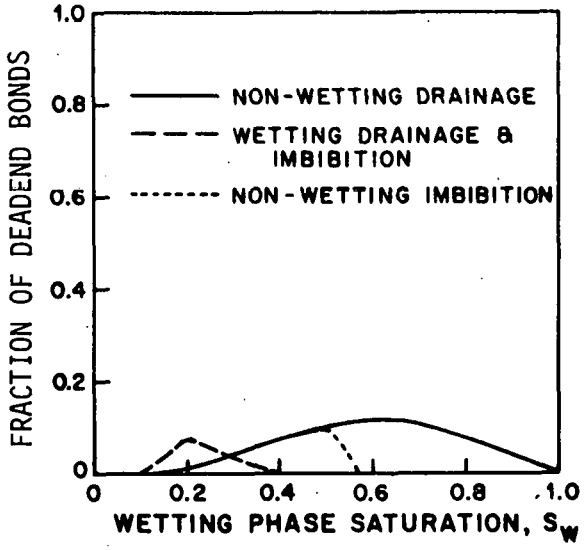

Figure 23. Fraction of deadend bonds during drainage and imbibition (cubic network).

Adsorption

If a tracer particle druing its passage through the porespace is adsorbed on the porewalls its exit from the medium is delayed. If the adsorption is irreversible its transit path is terminated, and so in terms of the transit time distribution an irreversible adsorption is similar to an irreversible chemical reaction. To study the effect of reversible adsorption we adopted a distribution of waiting times to represent the random interval a moving particle must wait to reach a wall and be adsorbed. We chose again an exponentially decaying distribution:

$$\gamma(t_w) = \frac{1}{\tau_w} e^{-t_w/\tau_w} , \qquad (49)$$

which physically means that the longer the tracer particle waits after last entering the flow, the less probable that it will be adsorbed, because it will cross the medium before reaching an adsorbing wall. Once adsorbed, the tracer particle will spend some time on the wall before it is released into the flow to continue its journey. So a probability density function for holding times on the wall is needed. Again we chose an exponentially decaying distribution:

$$\delta(t_H) = \frac{1}{\tau_H} e^{-t_H/\tau_H} . \qquad (50)$$

Two values of τ_w were used. One was selected so that the mean waiting time was short (5% specifically) compared to the mean transit times. The second corresponded to a long mean waiting time (about 50%) of the mean transit time). τ_H was chosen so that the mean holding time was about 2% of the mean transit time. Calculations were carried out for single-phase flow in the 10X10X10 cubic network.

The results indicate that when the mean waiting time τ_w is long, reversible adsorption has, as expected, little effect on the apparent dispersion coefficients. But when the mean waiting time is short, we observed that the reversible adsorption delays the development of diffusive dispersion. That is, the distance into the network at which the distribution of tracer particle locations was Gaussian to a given level of confidence was greater with adsorption than without.

Further investigation of the effects of deadend pores and adsorption is in progress. Of particular interest are residence time, waiting time, and holding time distributions that prevent dispersion in their presence from ever becoming diffusive.

Summary and Conclusions

For representing pore-level flow in a chaotic porous medium the network approximation of porespace is appropriate and leads to a set of linear equations that is readily solved for flow rates and velocities in the branches of the network, so that experiments by computer simulations are feasible. For cases of diffusive mixing of solute or tracer particles at pore junctions and no appreciable diffusion between, the network approximation is further appropriate for representing dispersion in flow. Square and simple cubic networks of variable pore segments, so oriented that the average flow is in one of the pore directions, are instructive idealizations of chaotic porespace and useful precursors not only to more realistic models, but also to formal theory.

Once flow rates and velocities in the branches of a network realization are known, the average permeability and the distribution of transit times across the network can be determined from Monte Carlo experiments in which randomly introduced tracer particles are tracked as they are convected through the network. The distribution of tracer particle locations at a given average displacement can likewise be determined. From these data the nature of particle dispersion can be identified and if it is diffusive, dispersion coefficients and dispersivities can be evaluated.

The results of Monte Carlo simulations show that dispersion is indeed diffusive in the cases simulated so far; that is, the dispersion process can be described macroscopically with the convective diffusion equation in which appear Darcy velocity, macroscopic average concentration, and longitudinal (mean flow direction) and transverse dispersion coefficients. The latter take the role of molecular diffusivity and invest it with flow-derived anisotropy. Longitudinal dispersivity (dispersion coefficient divided by mean flow velocity) is found to be an order of magnitude greater than the dispersivity in transverse directions, in agreement with laboratory experiments. However, both are found to be independent of mean flow velocity, whereas in reality the longitudinal dispersivity is commonly observed to rise gently with increasing mean flow velocity. This suggests that Taylor-type dispersion within streamtubes may be significant, a possibility that is under study.

The Monte Carlo experiments are computer experiments, which of necessity must be totally defined and therefore are made with precisely controlled porespace connectivity, or topology, and size and shape, or geometry. These are the structural factors that govern the two basic mechanisms of dispersion. The two mechanisms are the kinematic and the dynamic and the results illuminate their dependence on porespace structure.

When two fluid phases are present and compete for the porespace, flow and dispersion in each of them depend heavily on their distribution. That distribution depends on porespace morphology, capillarity and viscous flow, and saturation history in ways that are understood well enough to formulate occupancy rules of the phases. While the rules can be employed in Monte Carlo simulations to find fluid distribution functions, they can also be used with the new percolation theory of fluid distributions in slow two-phase flow, which requires less computation and appears to predict the functions well. Once these functions are available, flow and dispersion in each phase can be determined in the same way as when a single fluid occupies all the porespace.

The results of Monte Carlo simulations of two-phase systems agree qualitatively or better with available data and show that dispersion is again diffusive; that the dispersivities depend on the phase, its saturation and saturation history; and that as a phase saturation falls to its residual level, or percolation threshold, the dispersivities increase, the longitudinal one more rapidly than the transverse one. From percolation theory and the simulations it is clear that this behavior near residual saturation arises because the backbone of the subnetwork occupied by the near-threshold phase becomes an increasingly tortuous assemblage of simple linking paths and small interposed mazes. The latter evidently are highly effective dispersers.

Dispersion in the network approximation of porespace is virtually the same as what is known as a directed percolation process and there appears to be a close connection between dispersivities, which have the dimension of length, and the correlation lengths of the directed percolation process, a matter warranting further investigation.

Finally, some limited Monte Carlo experiments with simple representations of the effects of deadend paths within a phase and of reversible adsorp-

tion on the porewalls demonstrate that the approach developed here can be extended to study the influence of such delay mechanisms on the dispersion process.

References Cited in Section XI

1. Mohanty, K. K., Ph.D. thesis, University of Minnesota (1981).
2. Taylor, G. I., Proc. Roy. Soc. 219, 186-203 (1953).
3. Fatt, I., Pet Trans. AIME 207, 144-159 (1956).
4. Rose, W., Illinois State Geol. Survey, Circular 237, 1-31 (1957).
5. Dodd, C. G. and Kiel, O. G., J. Phys. Chem. 63, 1646-1652 (1959).
6. Mohanty, K. K., Davis, H. T. and Scriven, L. E., Proc. Roy. Soc., to be submitted (1982).
7. Cohen, M. H. and Lin, C., Lecture Notes in Physics, Vol. 154, 74-84 (1982).
8. Whitaker, S., AIChE J. 13, 420-427 (1967).
9. Chandrasekhar, S., Rev. Mod. Phys. 15, 1-89 (1943).
10. Scheidegger, A. E., J. Appl. Phys. 25, 994-1001 (1954).
11. De Jong, G. J. Trans. Am. Geophys. Union 39, 67-74 (1958).
12. Saffman, P. G., J. Fluid Mech. 6, 321-349 (1959).
13. Essam, J. W., Rep. Prog. Phys. 43. 833-912 (1980).
14. Montroll, E. W. and Weiss, G. H., J. Math. Phys. 6, 167-181 (1965).
15. Scher, H. and Lax, M. Phys. Rev. B7, 4491-4501, B7, 5402-4519 (1973).
16. Sahimi, M., Hughes, B. D., Davis, H. T. and Scriven, L. E., J. Fluid Mech., to be submitted (1982).
17. Pike, G. E. and Seager, C. H., Phys. Rev. B10, 1421-1434 (1974).
18. Odagaki, T. and Lax, M., Phys. Rev. Lett. 45, 847-850 (1980).
19. Sahimi, M., Hughes, B. D., Scriven, L. E. and Davis, H. T., J. Chem. Phys., in press (1983).
20. Warren, J. E. and Skiba, F. F., Soc. Pet. Eng. J. 4, 215-230 (1964).
21. Heller, J. P., Proc. of the 2nd International symposium on Fundamentals of Transport Phenomena in Porous Media, International Association of Hydraulic Research, Guelph, Canada, 1-26 (1972).
22. Schwartz, F. W., Water Resour. Res. 13, 743-752 (1977).

23. Smith, L. and Schwartz, F. W., Water Resour. Res. 16, 303-313 (1980).

24. Liao, K. H. and Scheidegger, A. E., Int. Ass. Sci. Hydro. Bull. 14, 137-145 (1969).

25. Torelli, L. and Scheidegger, A. E., J. Hydro. 15, 23-35 (1972).

26. Torelli, L. and Scheidegger, A. E., Pure and Appl. Geophys. 89 32-44 (1971/VI).

27. Simon, R. and Kelsey, F. J., Soc. Pet. Eng. J. 11, 99-112 (1971).

28. Simon, R. and Kelsey, F. J., Soc. Pet. Eng. J. 12, 345-351 (1972).

29. Montroll, E. W. and West, B. J., in Fluctuation Phenomena, Montroll, E. W. and Lebowitz, J. L., eds., North-Holland, Amsterdam, 61-175 (1979).

30. Stauffer, D., Phys. Rep. 54, 1-74 (1979).

31. Larson, R. G., Scriven, L. E. and Davis, H. T., Nature 268, 409-413 (1977).

32. Larson, R. G., Davis, H. T. and Scriven, L. E., Chem. Eng. Sci. 36, 57-73 (1981).

33. Larson, R. G., Davis, H. T. and Scriven, L. E., Chem. Eng. Sci. 36, 75-85 (1981).

34. Heiba, A. A., Sahimi, M., Scriven, L. E. and Davis, H. T., SPE 11015, presented at the 57th Annual Fall Meeting of Society of Petroleum Engineers, New Orleans, LA, September 26-29, 1982.

35. Stanley, H. E., J. Phys. A 10, L211-L220 (1977).

36. Coniglio, A., Lecture Notes in Physics 149, Castellani, C., Di Castro, C. and Peliti, L., eds., Springer-Verlag, Heidelberg, 51-55 (1981).

37. Coniglio, A., Phys. Rev. Lett. 46, 250-253 (1981).

38. Broadbent, S. R. and Hammersley, J. M., Proc. Camb. Phil. Soc. 53, 629-641 (1957).

39. Schlögl, F., Z. Phys. 253, 147-161 (1972).

40. Grassberger, P. and Sundmeyer, K., Phys. Lett. 77B, 220-222 (1978).

41. Lubensky, T. C. and Vannimenus, J., J. Physique Lettres 43, L337-L381 (1982).

42. Van Der Mar, M., Schuchardt, R. and Keiper, R., Phys. Stat. Sol. (b) 110, 571-580 (1982).

43. Schulman, L. E. and Seider, P. E., J. Stat. Phys. 27, 83-118 (1982).

44. Kirkpatrick, S., AIP Conference Proceedings, 40, 99-116 (1978).

45. Stauffer, D., Lecture Notes in Physics 149, Springer-Verlag, Heibelberg, 9-25 (1981).

46. Redner, S. and Coniglio, A., J. Phys. A 15, L273-L278 (1982).

47. Winterfeld, P. H., Ph.D. thesis, University of Minnesota (1981).

48. Winterfeld, P. H., Scriven, L. E. and Davis, H. T., J. Phys. C.: Solid State Phys. 14, 2361-2376 (1981).

49. Papoulis, A., Probability, Random Variables, and Stochastic Processes, McGraw-Hill, New York (1965).

50. Montroll, E. W., J. Chem. Phys. 18, 734-743 (1950).

51. Thomas, G. H., Countryman, G. R. and Fatt, I., Soc. Pet. Eng. J. 3, 189-196 (1963).

52. Redner, S., Phys. Rev. B25, 5646-5655 (1982).

53. Harleman, D. R. F., Mehlhorn, P. F. and Rumer, R. R., Proc. ASCE, J. Hyd. Div., HY2 (1963).

54. Brigham, W. E., Read, P. W. and Dew, J. M., Soc. Pet. Eng. J. 1, 1-8 (1961).

55. Blackwell, R. J., Soc. Pet. Eng. J. 2, 1-8 (1962).

56. Legaski, M. W. and Kate, D. L., Soc. Pet. Eng. J. 7, 43-50 (1967).

57. Hassinger, R. C. and von Rosenberg, D. U., Soc. Pet. Eng. J. 8, 195-204 (1968).

58. Nunge, R. J. and Gill, W. N., Ind. Eng. Chem. 61, 33-49 (1969).

59. Mohanty, K. K., Davis, H. T. and Scriven, L. E., SPE 9046, presented at the 55th Annual Fall Meeting of Society of Petroleum Engineers, Dallas, TX, September 21-24, 1980.

60. Lin, C-Y. and Slattery, J. C., AIChE J. 28, 311-322 (1982).

61. Talash, A. W., SPE 5810, presented at the Improved Recovery Symposium of the Society of Petroleum Engineers, Tulsa, OK, March 22-24, 1976.

62. Raimondi, P. and Torcaso, M. A., Soc. Pet. Eng. J. 4, 49-55 (1964).

63. Mohanty, K. K., Ottino, J. M. and Davis, H. T., Chem. Eng. Sci. 37, 905-924 (1982).

64. Kirkpatrick, S., Rev. Mod. Phys. 45, 574-588 (1973).

65. Ziman, J. M., Models of Disorder, Cambridge University Press, Cambridge (1979).

66. Larson, R. G. and Davis, H. T., J. Phys. C. 15, 2327-2331 (1982).

67. Pike, R. and Stanley, H. E., J. Phys. A. 14, L169-L177 (1981).

68. Mandelbrot, B. B., Fractals: Form, Chance and Dimension, Freeman, San Franscisco (1977).

69. Gefen, Y., Aharony, A., Mandelbrot, B. B. and Kirkpatrick, S., Phys. Rev. Lett. 47, 1771-1774 (1981).

70. Coats, K. H. and Smith, B. D., Soc. Pet. Eng. J. 4, 73-84 (1964).

71. Baker, L. E., Soc. Pet. Eng. J. 17, 219-227 (1977).

72. Delshad, M., MacAllister, D. J., Pope, G. A. and Rouse, B. A., SPE 10201, presented at the 56th Annual Fall Meeting of the Society of Petroleum Engineers, San Antonio, TX, October 5-7, 1981.

73. Stalkup, F. E., Soc. Pet. Eng. J. 10, 377-348 (1970).

74. Salter, S. J. and Mohanty, K. K., SPE 11017, presented at the 57th Annual Fall Meeting of the Society of Petroleum Engineers, New Orleans, LA, September 26-29, 1982.

75. Shuler, P. J., Ph.D. thesis, University of Colorado at Boulder (1978).

76. Goddard, R. R., Gardner, G. F. H. and Wyllie, M. R. J., paper presented at the 3rd Congress of the European Federation of Chemical Engineering, Institution of Chemical Engineers, London, June, 1962.

77. Handy, L. L., Trans. Am. Inst. Mining Met. Petrol. Engr. 216, 382 (1959).

XII. IMAGING VESICULAR DISPERSIONS WITH COLD-STAGE ELECTRON MICROSCOPY

Introduction

A vesicle consists of a closed spherical shell of one or more surfactant bilayers surrounding an aqueous fluid core. An aqueous vesicular dispersion can be formed by sonicating a liquid crystalline phase that is dispersed in aqueous solution (1). Vesicular dispersions are translucent, bluish, and contain mostly spherical particles which are 10 to 100 nm in diameter. Liquid crystalline dispersions, on the other hand, are turbid, grayish, and contain numerous irregular crystallites which are larger than 0.25 μm. Vesicles serve as model membranes for biochemical research (2,3) and are candidates for drug delivery in the human body (4) and for surfactant delivery in oil reservoirs (5). Such applications help motivate research on vesicular systems, which also raise important scientific questions.

Vesicles can be studied with many physicochemical techniques including light-scattering, x-ray scattering, nuclear magnetic resonance spectroscopy, and differential scanning calorimetry (DSC). However, because a model must be used to interpret data from them, these methods can only indirectly reflect structure in a dispersion. In contrast, microscopy directly images the state of aggregation, the shape, and the size distribution of particles in a dispersion. Because the size of vesicles is on the order of scores of nanometers, electron, not light, microscopy is the only means of imaging vesicular dispersions. Electron microscopy, unfortunately, places severe restrictions on samples. For the transmission electron microscope (TEM), samples must be thin; the thickness of a typical noncrystalline biological sample is limited by mass-thickness-scattering to about 0.2 μm. In addition, liquid samples must be fixed, that is, their vapor pressures must be dropped below the pressure maintained in the microscope ($< 10^{-6}$ torr).

A liquid system can be fixed either chemically, by adding reagents and drying, or thermally, by rapid cooling; in both cases its original state is altered, the extent of which determines the value of electron microscopy for microstructural analysis. The goal in sample preparation is, of course, to limit structural changes during fixation. Any changes that do occur must be understood so that the appearance of the original system can be reconstructed from images of the altered sample. Because there is always a possibility of introducing artifacts during fixation, it is necessary to vary systematically the sample preparation method before drawing any conclusions about the microstructure in a liquid system. Furthermore, it is desirable to contrast and compare the results of at least one other sample preparation method as well as evidence from less direct probes such as light-scattering and x-ray scattering; DSC is often a useful aid in interpreting images of thermally-fixed specimens.

To begin, we point out the advantages and difficulties of the methods commonly used to prepare vesicular systems for the TEM. We then describe a new technique for elucidating structure in vesicular dispersions: fast-freeze, cold-stage microscopy which can be combined with *in situ* freeze-drying. We apply these techniques to aqueous vesicular dispersions and interpret the images of frozen, hydrated systems by the dynamical theory of electron diffrac-

tion. Finally, we identify some of the artifacts that can confuse interpretation of the images of both frozen, hydrated and freeze-dried specimens.

TEM Preparation Methods

In early work, negative staining followed by drying was used to fix vesicle systems. Horne and Whittaker (6) used potassium phosphotungstate to stain synaptic vesicles without prior fixation. Staining was followed by drying which, they claimed, formed "a glass of electron-dense phosphotungstate in which the subcellular particles show up as areas of relatively low electron density." Finean and Rumsby (7) pointed out that structure can change during evaporation and that fixation by osmium tetroxide or potassium permanganate before drying is essential to prevent artifacts. Nevertheless, Horne et al. (8) and Bangham and Horne (9) asserted that the setting of phosphotungstate glass suppresses structural artifacts during drying; they published micrographs that were corroborated by x-ray scattering. Papahadjopoulos and Miller (10) described negative staining, with ammonium molybdate, and drying but did not address artifacts of specimen preparation. Later on, Glauert and Lucy (11) concluded that phospholipid systems are unaffected by drying but can be altered by stain. Talmon (12) recently showed that staining and drying some amphiphilic systems can actually produce "bilayered" structure in them. Johnson et al. (13) addressed vesicle collapse upon drying. Another variant of the stain-dry method incorporates a heavy-metal salt (14) or oxide (15) inside the vesicle. This method may also suffer drying artifacts.

Vesicles have been fixed by chemical reaction, e.g., with osmium tetroxide the reagent, as in the work of Miyamoto and Stoeckenius (16), who compared the results with those from staining and drying. They found that the sizes of vesicles fixed with osmium tetroxide were in accord with light-scattering observations from unfixed samples but differed from the sizes of vesicles that were stained and dried. Their study argues for fixing vesicular systems with osmium tetroxide prior to drying them.

Aqueous vesicular dispersions have been fixed thermally as well as chemically. Taylor (17) viewed lipopolysaccharide vesicles, frozen in liquid nitrogen, with cold-stage microscopy. Forge et al. (18) froze dispersions of egg lecithin vesicles, placed on copper support discs, in liquid Freon 22. They prepared thin replicas of the frozen specimens and examined them in the electron microscope. Van Venetie et al. (19) also applied the freeze-fracture-replication method to vesicular dispersions but froze their samples by spraying them into liquid propane (20). Cooling rates in the spray-freeze method (> 5000 K/s (19)) are higher than those in standard freezing techniques (about 800 K/s (21)). Recently, we showed that thin, frozen vesicle samples can be imaged directly with fast-freeze, cold-stage transmission electron microscopy (22-24). In this technique, which is described in the next section, cooling rates are on the order of 10^4 K/s (25,26).

Like chemical fixation, thermal fixation is subject to artifacts, most notably those due to phase separation or solute redistribution during solidification. It appears, however, that thermal fixation preserves microstructure

in dilute, aqueous vesicular dispersions: vesicles do not agglomerate in TEM samples prepared with either freeze-fracture-replication (18,19) or fast-freeze, double-film techniques (22-24). Instead, vesicles homogeneously distribute inside single ice crystals and do not concentrate at grain boundaries. Furthermore, variable-temperature ^{23}Na nuclear magnetic resonance spectra and DSC thermograms indicate that surfactant in vesicles remains in single bilayers even when the sample is frozen slowly (at 5 K/s in DSC) (24). Thus, thermal fixation is apt to preserve vesicle structure.

Frozen, Hydrated Specimens: Preparation and Materials

Thin, frozen, hydrated (i.e., undried) specimens for cold-stage microscopy are prepared by trapping a thin layer (ideally less than 0.5 μm thick) of liquid deposited from a syringe between two polyimide film-covered electron microscope grids. Polyimide films, 20 40 nm thick, are used as substrates because they are wet by either oleic or aqueous phases and are radiation resistant (27). The specimen "sandwich" is frozen by plunging it into liquid nitrogen and is stored under the cryogen until it is transferred into the microscope. Preparation of polyimide films and specimens as well as observations of well-characterized systems of plasticized latex spheres have been detailed previously (28).

Fast-frozen, thin sample films are not of uniform thickness. Capillary forces, hydrodynamic forces, and quite possibly disjoining pressure effects (29) produce areas of uneven thickness while the sample is drained before it is frozen. Moreover, particles can be fractionated by size during sample preparation so that the distribution of vesicle sizes in a frozen sample may not accurately reflect the distribution in the unfrozen dispersion.

After they are made, frozen samples are transferred into a JEOL JEM 100CX electron microscope cooling-holder (EM-SCH) equipped with a special cold-stage transfer module (CSTM) (22). The CSTM permits transfer of the holder which contains the frozen specimen into the electron microscope without excessive heating of or frost depositing onto the specimen. The CSTM has been modified recently (30).

Once in the microscope, the frozen, hydrated sample on the cold-stage is kept at about 100K by using liquid nitrogen as the coolant for the stage. Of late, the cooling holder has been altered to contain a controllable heater near the specimen tip (30); this allows the specimen temperature to be maintained anywhere between 100 and 300K for long periods of time without introducing thermally-induced instability. Micrographs in this paper were recorded in the conventional transmission mode with 100 kV electrons.

Vesicles dispersed in doubly-distilled water were prepared from bovine brain lecithin and from a synthetic double-tailed surfactant, sodium 4-(1'-heptylnonyl) benzenesulfonate (SHBS) of molecular weight 404.6. The lecithin was L-α-phosphatidylcholine prepared chromatographically by the Sigma Chemical Company. SHBS was obtained from the University of Texas and purified by extractions with chloroform and a 95:5 (v:v) solution of isobutanol and water

(31). Sodium chloride, cesium chloride, and uranyl acetate (UA) were certified A.C.S. from Fisher Scientific.

Aqueous liquid crystalline dispersions of the amphiphiles were sonicated until they turned opalescent (15-30 minutes) in either a Cole-Parmer Ultrasonic bath, model 8845-3, or a Buchler 75-1980 Ultramet III. The water bath temperature was maintained below 310K. Microscope specimens were prepared within ten minutes after sonication was halted.

Stained vesicular systems were prepared either by adding stain solution to the dispersion before sonication or by allowing the sonicated dispersion to equilibrate with the stain solution through a semipermeable membrane. Stain was not added directly to a vesicular dispersion because osmotic pressure differences may rupture vesicle bilayers (32).

Contrast in Frozen, Hydrated Vesicular Dispersions

Interpreting micrographs requires understanding the electron-optic contrast mechanisms which produce intensity variations in an image. Here we outline the dynamical theory of electron diffraction (33) which is used below to analyze TEM images of frozen, hydrated vesicular dispersions.

Contrast in focussed images of unstained, dried vesicle systems is low because the mass densities of vesicles and the films used to support them are nearly equal. Stains enhance mass-thickness contrast. Positive stains increase electron scattering from vesicle bilayers by replacing the counterion which is ionically bound to the amphiphile with a heavier one. Negative stains, on the other hand, increase the mass density of the continuous phase relative to that of the vesicle bilayers. Negative stains are excluded from amphiphile head groups by charge.

Staining a dispersion also heightens the contrast factor for x-rays scattered from vesicles. Adding stain to a system, however, can change the microstructure and phase behavior of the surfactant dispersion (24) and affect vesicle size. For example, 1 wt% SHBS sonicated in distilled water forms vesicles that have a z-averaged diameter, according to quasielastic light-scattering measurements, of 45 nm; the z-averaged particle diameter in a 1% SHBS, 1% UA dispersion as measured by small angle x-ray scattering (SAXS) is, however, 25 nm. Thus data from stained vesicular dispersions should always be compared to that from unstained ones at comparable ionic strengths.

Phase contrast can sometimes be used to image structures that display low mass-thickness contrast. Phase contrast is increased by under-focussing the image. Optimum defocus for a particular structural detail can be estimated from transfer theory (34). These techniques have been used recently to elucidate structure in unstained lamellar block copolymers with small intrinsic density differences between the phases (35).

In the double-film technique, dilute, aqueous vesicular dispersions freeze into crystalline solid; vesicles become encased in ice grains, the

crystal structure of which is hexagonal (36). The ice matrix also contains grain boundaries, stacking faults, and dislocation defects which have been identified in pure ice samples (26,36). Because densities of organic molecules and ice differ little, TEM image contrast from unstained biological material embedded in crystalline ice must be due primarily to diffraction contrast (17). In passing through a crystalline solid, an electron beam splits into transmitted and diffracted parts. The intensities of the two parts vary inside the crystal and depend on depth in the crystal, crystallographic orientation of the sample, crystal lattice defects, and inclusions or strain fields. Contrast, which is defined as the difference between the intensities from the background and the inclusion divided by the background intensity, results from excluding various beams with an aperture inserted in the back focal plane of the microscope's objective lens. When the transmitted beam is selected, a "bright-field" image is formed. When a diffracted beam is selected, a single-beam "dark-field" image is formed.

Amplitude contrast in images from an ideal, focussed microscope, that is, one in which the microscope transfer function (34) is unity inside the objective aperture and zero otherwise, is accounted for by the dynamical theory of electron diffraction (33). The two-beam approximation to the theory, in which diffuse small-angle scattering and weakly excited Bragg reflections are neglected, provides qualitatively correct explanations of TEM images. Calculations from the two-beam theory best describe experimental images that are formed when only a single diffracted beam is strongly excited. Unfortunately, true two-beam conditions cannot be obtained in the microscope because the geometrical conditions for diffraction of high-energy electrons are nearly satisfied for a number of reflections simultaneously.

The theoretical treatment of the contrast of a vesicle embedded in ice follows that of an inclusion (37) or a void (38,39) in a crystalline metal. The contrast variation throughout the projected image of the inclusion is obtained by applying the equations of the dynamical theory (33) to a series of columns in the crystal, each passing through a different cross-sectional thickness of the inclusion. To calculate intensity distributions in TEM images of frozen vesicular dispersions, ice absorption lengths, vesicle extinction and absorption distances, specimen and vesicle thicknesses, and Bragg deviation parameters are needed. The ice normal absorption length, $\xi_0'^{ice}$, scales intensity in the calculated image. Contrast profiles are more sensitive to the ratio of the anomalous absorption length to the diffracted beam extinction distance, $\xi_g'^{ice}/\xi_g^{ice}$, which is a strong function of temperature, the diffraction vector $\underset{\sim}{g}$, and objective aperture size (40).

Absorption lengths in ice have not been measured; extinction distances and absorption lengths inside a vesicle are even more difficult to obtain because radiation damage intrudes. As a result, we treat unstained vesicles as amorphous inclusions ($\xi_g^{ves} = \infty$, with $\xi_0'^{ves} = \xi_0'^{ice}$) in ice that are described by absorption parameters characteristic of crystalline materials ($\xi_0'^{ice}/\xi_g^{ice} =$

$\xi_g'^{ice}/\xi_g^{ice} = 10$). To describe stained systems, we decrease $\xi_o'^{ves}$ to $\xi_o'^{ice}/3$. With these parameters, calculated contrast profiles explain TEM images of frozen vesicular dispersions.

Experimental Results and Discussion

Structure in Frozen, Hydrated Vesicular Systems

Fig. 1a is a micrograph of a 1% SHBS, 0.1% NaCl sonicated dispersion. The spherical particles, 25 to 90 nm in diameter, are vesicles lying within a single ice crystal. The larger particle in Fig. 1a is a liquid crystallite; even after prolonged sonication, a few liquid crystalline particles remain in the dispersion. These crystallites can bias the average vesicle size measured by light-scattering or small angle x-ray scattering (24). Fast-freeze, cold-stage TEM determines the presence of small (< 0.5 μm) liquid crystalline particles in a dispersion even when visual observations, spectroturbidimetry, light-scattering, and x-ray scattering cannot.

Fig. 2 is an image from an unstained, frozen, hydrated specimen of 0.08% bovine lecithin sonicated in distilled water. Vesicles appear either dark (A) or light (B) against the ice in which they are embedded, depending on the thickness of the ice crystal and its orientation. Long-ranged strain fields produce local variations in the orientation of ice crystal planes. The appearance of a vesicle changes as the local Bragg condition varies. The difference is negative versus positive contrast and can be understood with the dynamical theory of electron diffraction: Fig. 3, called a rocking curve (41), shows the calculated variation in contrast at the center of a vesicle's TEM image as the Bragg conditions of the crystal containing the particle change. The profile in Fig. 3 is for a vesicle located midway through an ice crystal of uniform thickness. Depending on the diffracting conditions, the center of the image appears dark (negative contrast) or light (positive contrast).

Some vesicles in Fig. 2 (at (C) for instance) appear as a bright inner area surrounded by a dark ring. This too can be explained by diffraction contrast theory. Fig. 4 shows the contrast calculated for the projected image of a vesicle. Close to its edges, this particle displays negative contrast. Near its center, the image is lighter.

Although unstained vesicles can be imaged by cold-stage microscopy (22-24), their contrast in thicker sample areas (> 0.25 μm thick) is usually low. (Structures producing contrast levels below about 10% are invisible in a micrograph.) Stain increases electron-scattering from vesicles and enables features that are invisble in unstained dispersions to be imaged. Fig. 5, which is a $(10\bar{1}0)$ dark-field image of a frozen, hydrated specimen of a 1% SHBS dispersion sonicated in 1% UA solution, is an example. $(10\bar{1}0)$ is standard hexagonal crystal lattice notation (42) and denotes the diffracted beam used to form the dark-field image. The ice crystal in Fig. 5 contains a UA-stained SHBS liquid crystalline particle (A) and numerous stacking fault fringes (B) (26). The alternating intensity extrema (C), called "thickness fringes" (41),

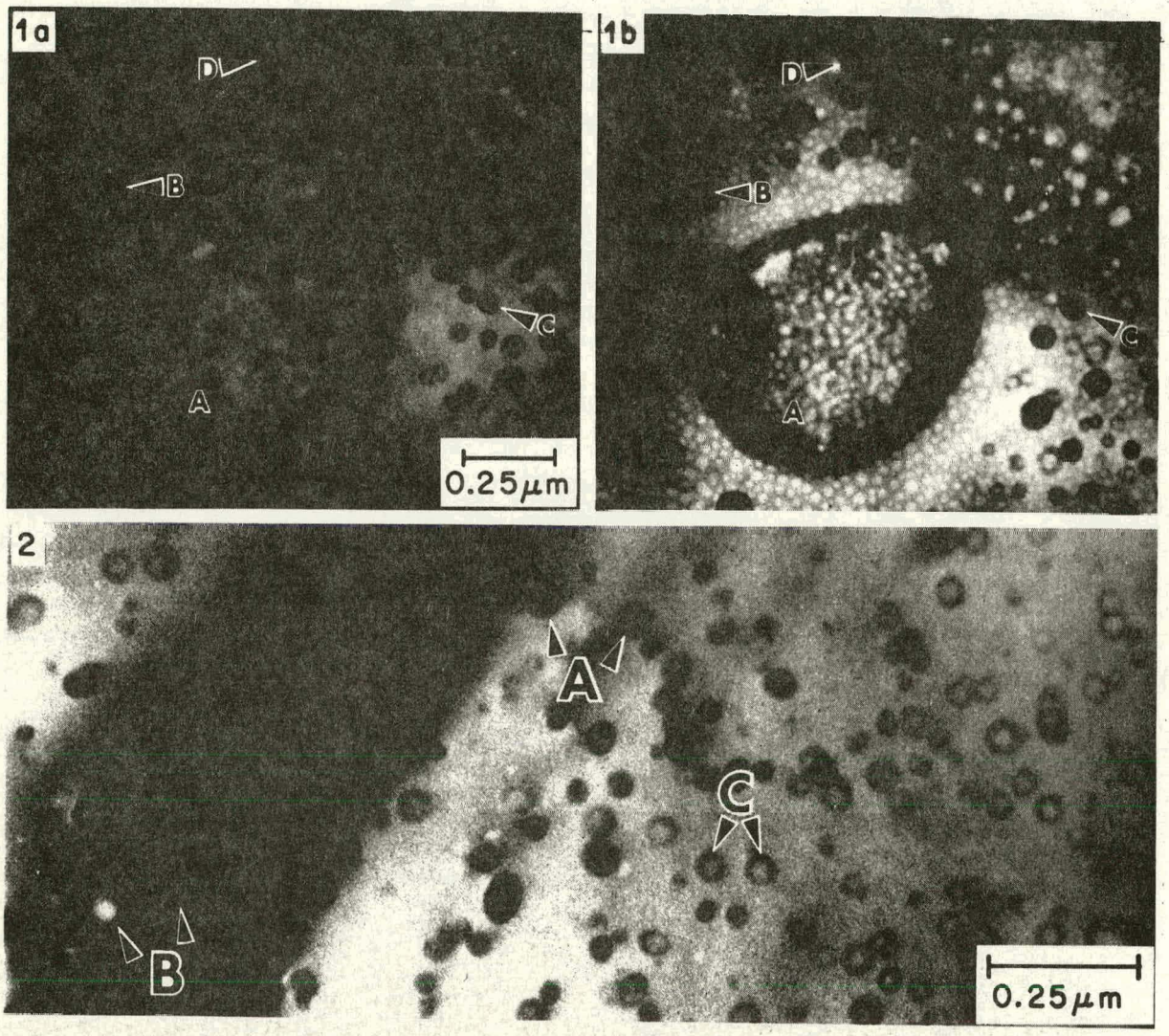

Fig. 1. a. Bright-field micrograph of an unstained, frozen vesicular dispersion of 1% SHBS in 0.1% NaCl brine. A large liquid crystallite (A) is present in the dispersion. b. Area in a after receiving an additional electron dose of $4 \cdot 10^3$ C/m^2. During radiolysis some vesicle images (e.g., at B) expand, others (C) get areas of lower contrast on them, and some appear lighter (D) or disappear.

Fig. 2. Bright-field micrograph from an unstained, frozen, hydrated vesicular dispersion of bovine phosphatidylcholine. Vesicles display both negative contrast (e.g., at A) or positive contrast (B) over the ice matrix. Some vesicles (C) appear as a bright inner area surrounded by a dark ring.

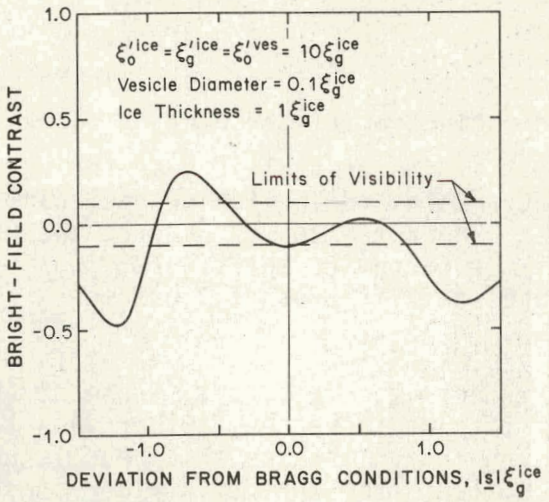

Fig. 3. Calculated bright-field contrast at the center of the image of a vesicle located midway through an ice crystal as a function of the deviation of the ice crystal from the exact Bragg diffracting condition. Vesicles change their contrast as the diffracting conditions vary and can appear either dark or light.

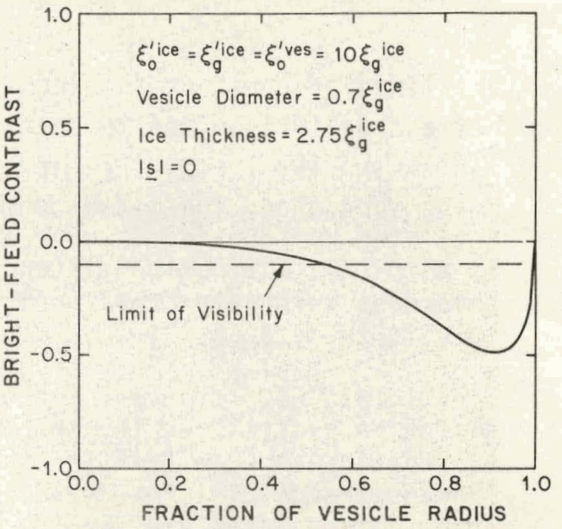

Fig. 4. Calculated variation in bright-field contrast throughout the image of a vesicle. The inside of the vesicle is brighter than its edges.

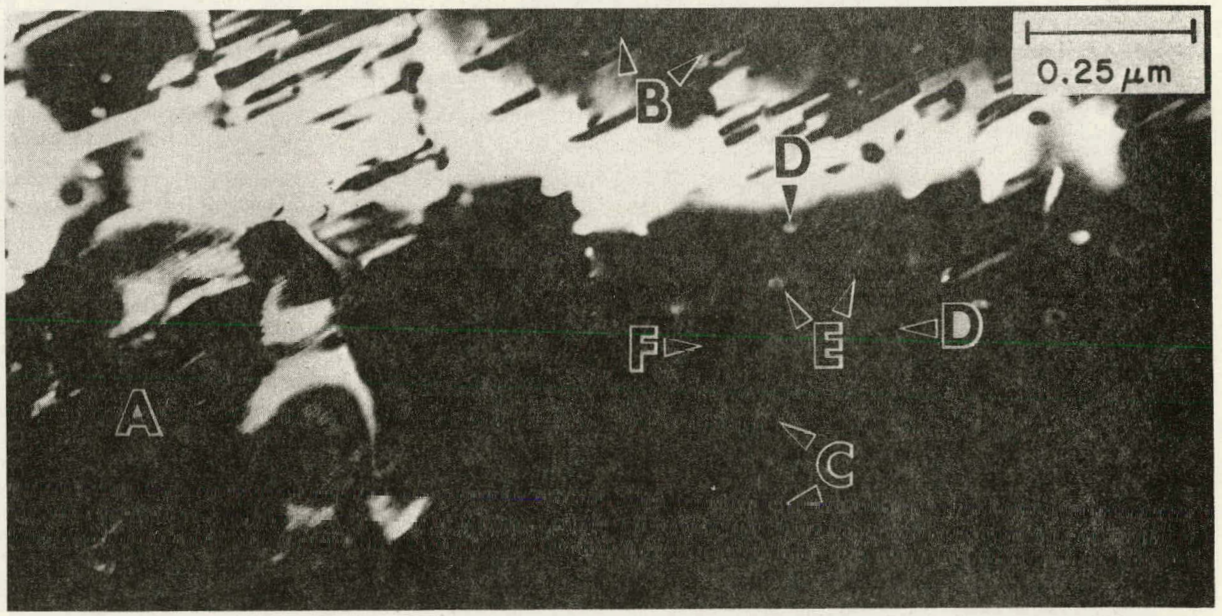

Fig. 5. $(10\bar{1}0)$ dark-field image of a frozen, hydrated 1% SHBS dispersion sonicated in 1% uranyl acetate. A liquid-crystalline particle (A), stacking faults (B), and thickness fringes (C) are visible. Vesicle contrast depends on the ice thickness (D), vesicle depth within the crystal (E), and vesicle size (compare E, F).

are lines of constant thickness in the crystal. The difference in thickness between one fringe and the next is one extinction distance, ξ_g^{ice} (equal to 200 nm for the (1010) reflection (26)). If the crystal is near the exact Bragg condition, the total thickness at a point in the ice crystal can be estimated by counting thickness fringes. Near the top of Fig. 5, the matrix is thin (< 1 extinction distance). At the bottom of the figure, the crystal thickness is greater than 1 μm. Because stain is present, vesicles are visible in these areas.

In Fig. 5, some vesicles of nearly the same size, e.g., those at (D), differ in contrast as the thickness of the ice increases. Other vesicles, at (E) for instance, differ in contrast even though the ice thickness is uniform. The appearance of larger vesicles (F) differs from that of smaller ones (E). These contrast features can be understood with the dynamical theory. Fig. 6 shows calculated bright-field and dark-field contrast profiles for the center of the image of a vesicle located midway through ice crystals of increasing thickness. The contrast may be negative (dark) or positive (light). In thicker crystals, vesicle contrast is low. Figs. 7 and 8 illustrate that the appearance of the vesicle center is a function of both its size and position in a crystal of uniform thickness.

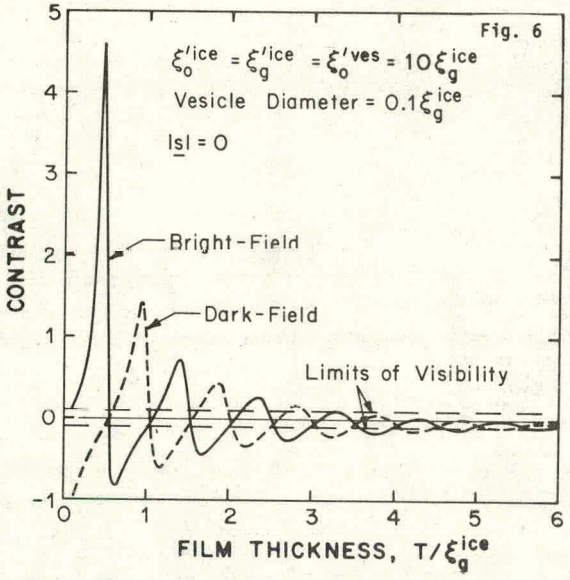

Figure 6. Bright-field and dark-field contrast profiles for the image of a vesicle located in the middle of ice crystals of increasing thickness. Vesicles appear dark or light, depending on the thickness of the crystal in which they are embedded.

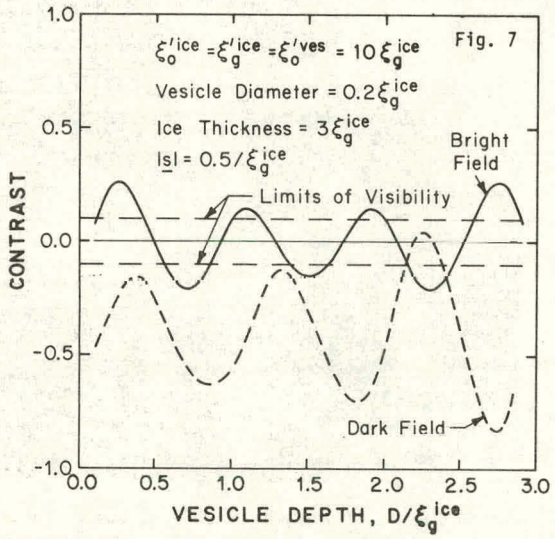

Figure 7. Contrast profiles for the images of vesicles as a function of their size in an ice crystal oriented at the exact Bragg condition, $|s|=0$.

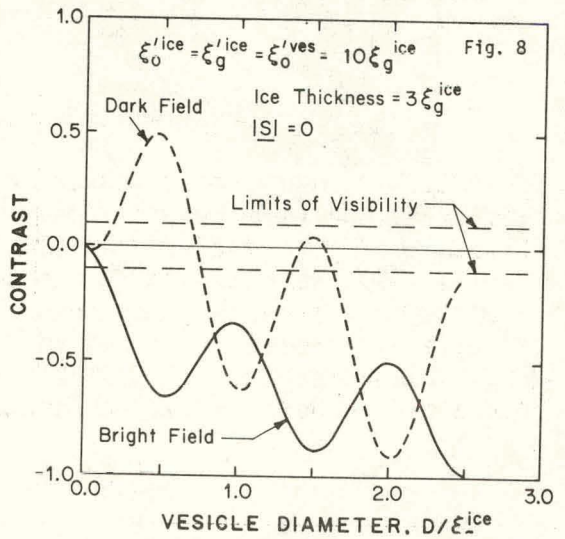

Figure 8. Contract at the center of the image of a vesicle as a function of the particle depth in a uniform ice crystal.

In SHBS systems, uranyl acetate behaves as a positive stain. The density of vesicle bilayers increases when uranyl groups (UO_2^{++}) replace Na^+ counterions that are ionically bound to negatively charged surfactant head groups. Other stains may be better suited to SHBS systems. For example, CsCl can be used instead of NaCl in SHBS-brine systems, or Na^+ in SHBS can be replaced with Cs^+. Cesium not only serves as a positive stain but is akin to the ions in SHBS systems. For cationic amphiphiles, the I^- ion can play a similar role. Fig. 9 is an example from a CsCl-stained SHBS vesicular system.

Bands of contrast are seen around some of the particles in Fig. 9. These are similar to the contours which surround polystyrene spheres and small liquid crystallites in ice (26). Crystals which precipitate from freezing aqueous uranyl acetate, sodium chloride, and cesium chloride solutions also produce contours in the ice around them (26). The contrast bands are sensitive to tilt and sometimes display lines along which there is no contrast (37). The bands therefore are likely caused by strain fields created by differential expansion of ice and the inclusion when the sample solidifies.

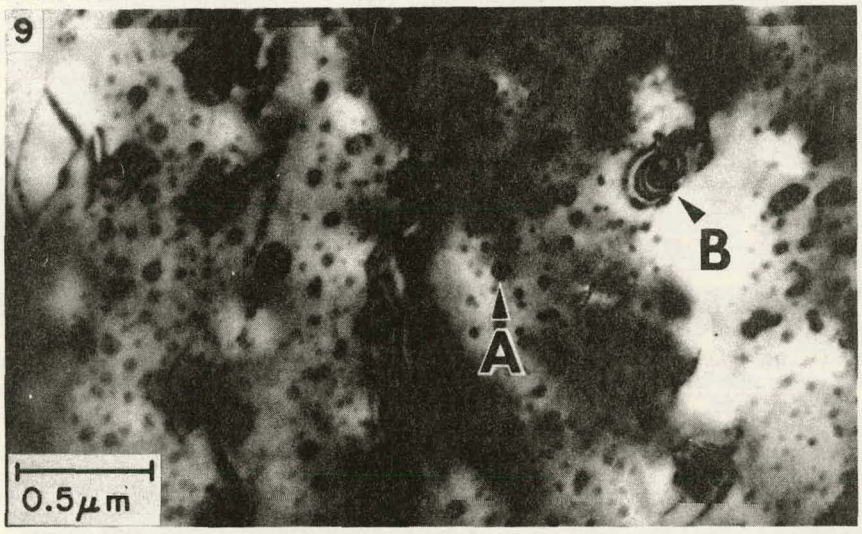

Fig. 9. Bright-field transmission electron microscope image of a frozen, hydrated 1% SHBS, 0.1% CsCl brine vesicular dispersion. Numerous stained vesicles are present (A). Some particles induce strain fields in the ice matrix that produce bands of contrast (B) in the image.

Effects of Radiolysis on Frozen, Hydrated Systems

Radiation by the electron beam modifies the morphology of frozen specimens. Talmon (43) recently reviewed this topic. During irradiation of pure hexagonal ice, cavities form (36,44) and mass is lost (27). Frozen oleic phases lose their crystallinity and crosslink when bombarded by high-energy electrons (25) as do other crystalline biological (45) and polymeric (46) materials. Frozen, hydrated vesicular samples also suffer radiation damage. Fig. 10a shows a 1% SHBS, 1% UA vesicular dispersion which received the minimum electron dose needed to locate, focus, and record its image (approximately

$3 \cdot 10^2$ C/m^2 at this magnification). Fig. 10b is the same area after it received $3 \cdot 10^3$ C/m^2. During radiolysis, some particles (A), that were invisible in Fig. 10a, were revealed.

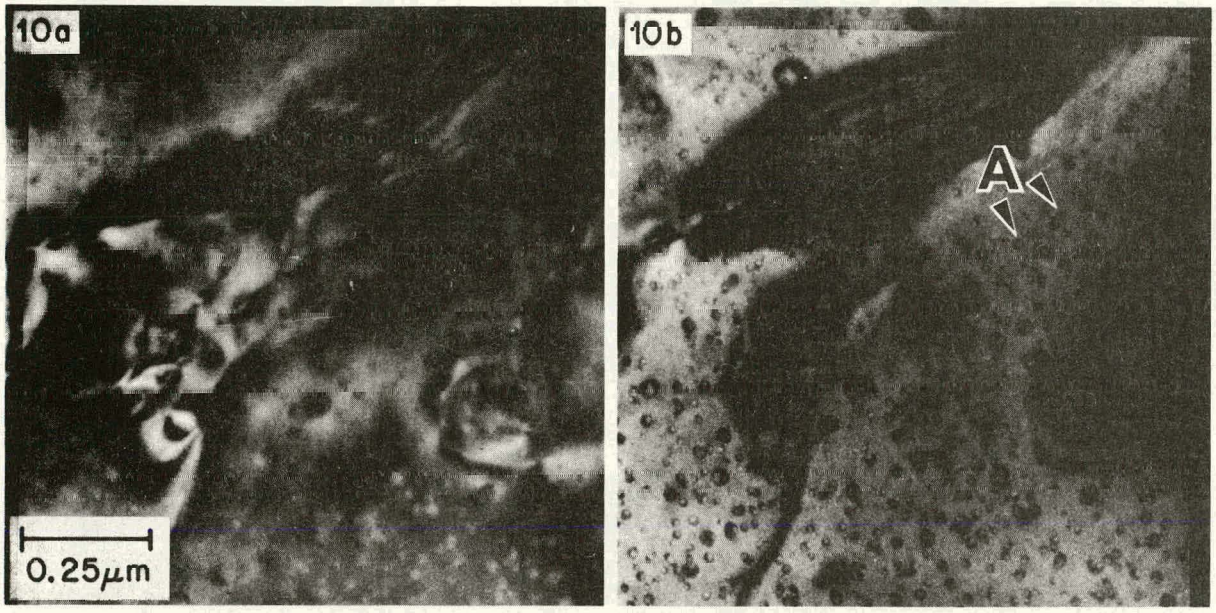

Fig. 10. a. Bright-field image of a 1% SHBS, 1% uranyl acetate vesicular dispersion that was recorded with about $3 \cdot 10^2$ C/m^2. b. Area in Fig. 10a after receiving $3 \cdot 10^3$ C/m^2. During radiolysis some vesicles (A) were revealed.

There are at least three mechanisms which can account for vesicles being "exposed" by radiolysis: (1) when mass is lost, the ice crystal shifts to a new orientation for which the contrast of inclusions is greater (Fig. 3); (2) when mass is lost, the specimen thins and vesicles of previously low contrast in thick crystals reveal themselves (Fig. 6 shows a particle to be invisible when the ice crystal thickness is above $4\xi_g^{ice}$.); (3) vesicles physically expand — possibly because they are attacked by the free radicals that are generated in ice when it is irradiated — the contrast of larger vesicles often being greater than that of smaller ones (Fig. 7).

All of these mechanisms may contribute to vesicles being revealed during radiolysis. Images of vesicles in ice do appear to expand while being irradiated (24). Fig. 1b is an example. During radiolysis, many vesicle images, e.g., at (B) in Fig. 1b, expand. Areas of lower contrast also form on vesicles (C) and some particles appear lighter (D) or disappear as the sample is irradiated.

Diffraction contrast theory can explain vesicle images expanding if the cause is thinning of ice. Fig. 11a shows how the contrast varies over the projected area of a vesicle image in a thick ice crystal. Due to insufficient contrast, this particle appears to be only 60% of its actual size. Fig. 11b shows the contrast profile for the same vesicle in a thinner crystal. The

inclusion now appears to have a diameter of 80% of the actual value. Figs. 11a and 11b also show that stained vesicles display greater contrast in thick ice crystals than do unstained ones. Although a vesicle image can appear smaller than the particle itself, an in-focus image of an inclusion that does not produce a strain field in the crystal cannot be larger than the particle actually is.

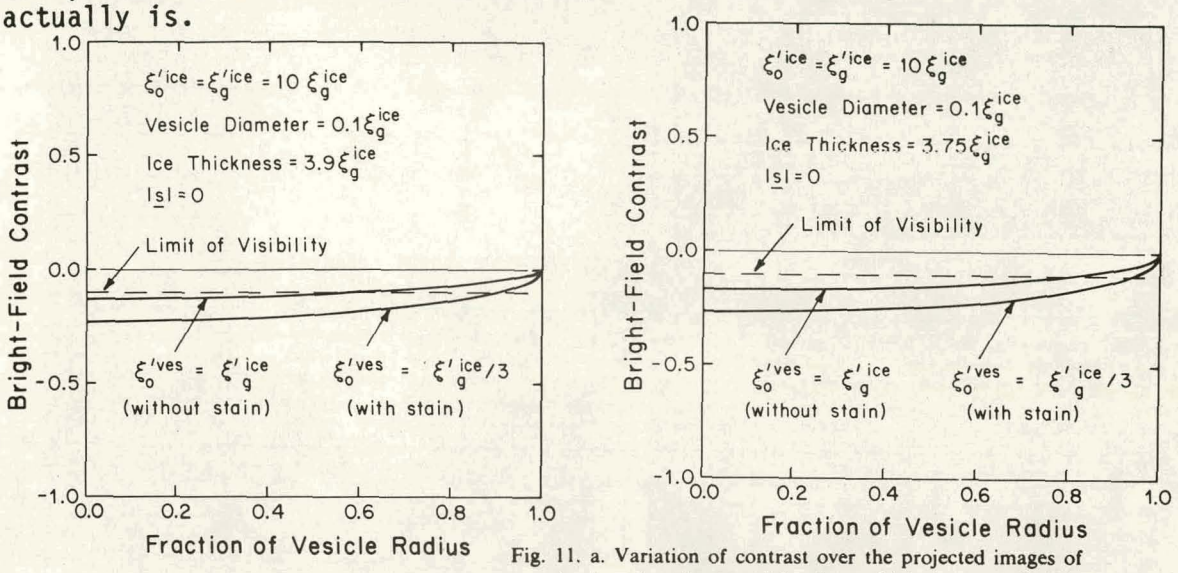

Fig. 11. a. Variation of contrast over the projected images of unstained and stained vesicles in a thick ice crystal. The unstained vesicle appears to have a diameter of only 60% of its actual value. b. Appearance of vesicles with and without stain in a crystal thinner than the one in a. More of the unstained vesicle is visible in the thinner crystal.

So far, it has not been possible to determine which mechanism accounts for the effects of radiation on frozen vesicular dispersions. However, the distributions of vesicle sizes in micrographs imaged with minimum radiation dose agree best with SAXS measurements from unfrozen samples (24). In addition, vesicle boundaries in TEM images are always well defined, even in images formed with minimum radiation dose (cf. those vesicles visible in Figs. 10a and 10b). This suggests that vesicles in frozen, hydrated specimens physically expand during radiolysis.

Structure in Stained, Freeze-Dried Vesicular Dispersions

One advantage of cold-stage microscopy is that drying artifacts (12) are avoided. Fig. 12 shows an air-dried, sonicated 0.07% bovine lecithin, 0.1% UA dispersion. The contrast fringes in Fig. 12 are not restricted to well-defined particles. These structures differ from those in a thermally-fixed sample (cp. Fig. 12 with Figs. 2 and 13a).

A frozen, hydrated specimen can also be freeze-dried in situ, as Heide and Grund (47) have demonstrated. This is done by elevating the sample temperature to about 198K. At this temperature, ice sublimes slowly in the microscope because its vapor pressure is $9 \cdot 10^{-4}$ torr (48). As ice sublimes from thin specimen areas, small holes, which are hexagonal in shape, first form and enlarge gradually as additional material leaves. Within a few min-

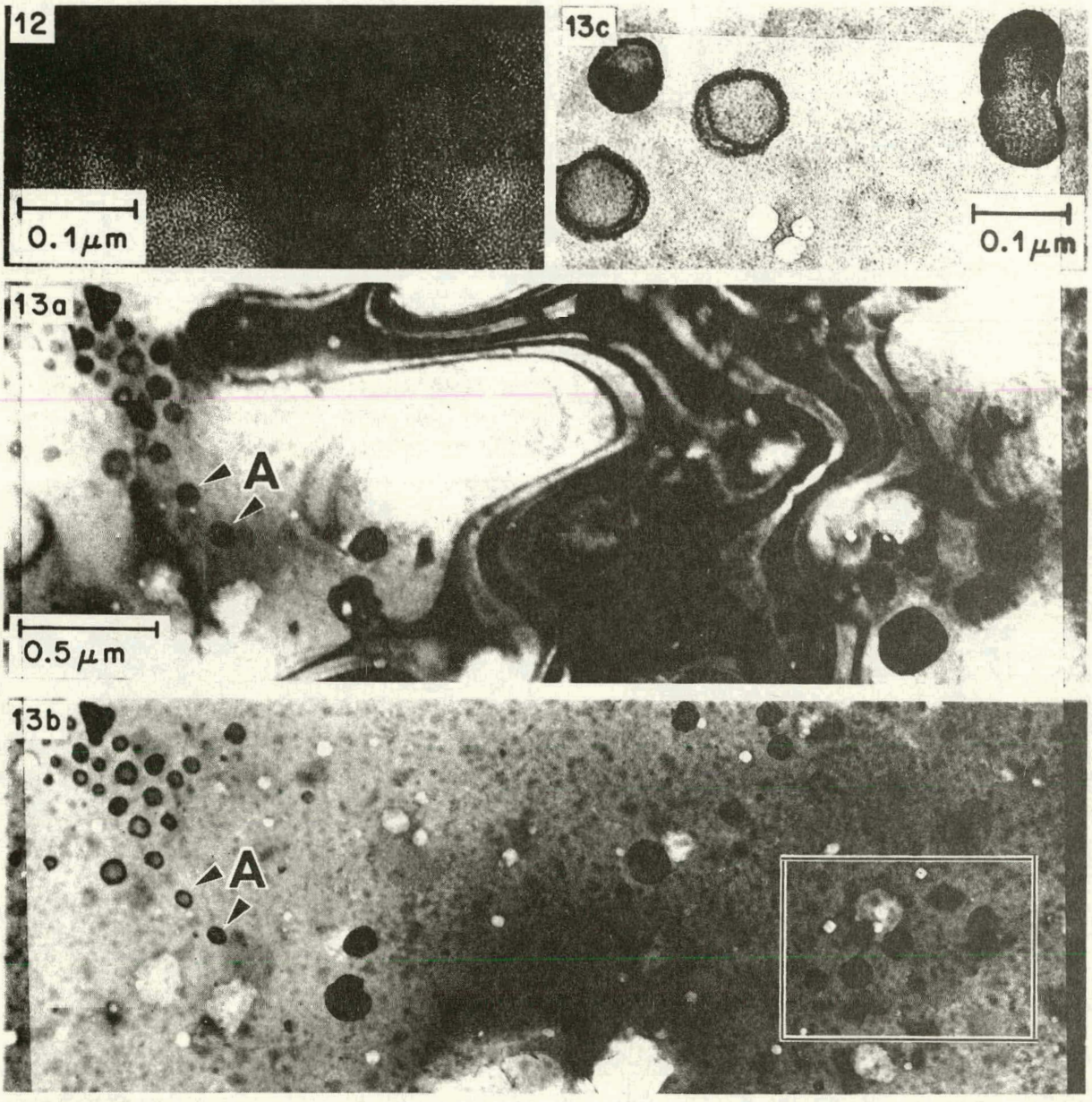

Fig. 12. Air-dried 0.07% bovine phosphatidylcholine, 0.1% uranyl acetate vesicular dispersion imaged with the objective lens defocussed −1.1 μm. Drying produces structure (A) not present in thermally fixed specimens.

Fig. 13. a. Bright-field micrograph of a sonicated 0.07% bovine phosphatidylcholine, 0.1% uranyl acetate dispersion in the frozen, hydrated state. b. Same field of view as in a after the sample has been freeze-dried in the microscope at 198 K. Vesicles are smaller after freeze-drying (compare those at A). c. Enlarged view of part of b.

utes, all of the volatile material is gone and a freeze-dried vesicular dispersion remains. Structures in thin areas stay in their positions during freeze-drying and do not change further when they are warmed to room temperature in the microscope.

Figure 13a shows a sonicated 0.07% bovine lecithin, 0.1% UA dispersion in the frozen state, imaged with minimum radiation. Fig. 13b is the same field of view after in situ freeze-drying at 198K. Structure in the freeze-dried specimen matches that in the frozen, hydrated state. However, vesicles such as those at (A) shrink during freeze-drying as do other frozen, hydrated biological materials (cf. Boyde and Franc (49)).

Some of the objects in Fig. 13 are likely to be liquid crystalline particles which survived sonication of the dispersion; compare Fig. 14 which shows a hydrated/freeze-dried pair of bright-field micrographs from an unsonicated 0.07% bovine lecithin, 0.1% UA dispersion. The micrograph of the frozen, hydrated sample, Fig. 14a, reveals a structural pattern indicative of the Dupin cyclides (50) prevalent in both biological and synthetic smectic, lyotropic liquid crystallites (51,52). The freeze-dried sample, Fig. 14b, lacks evidence of the cyclide.

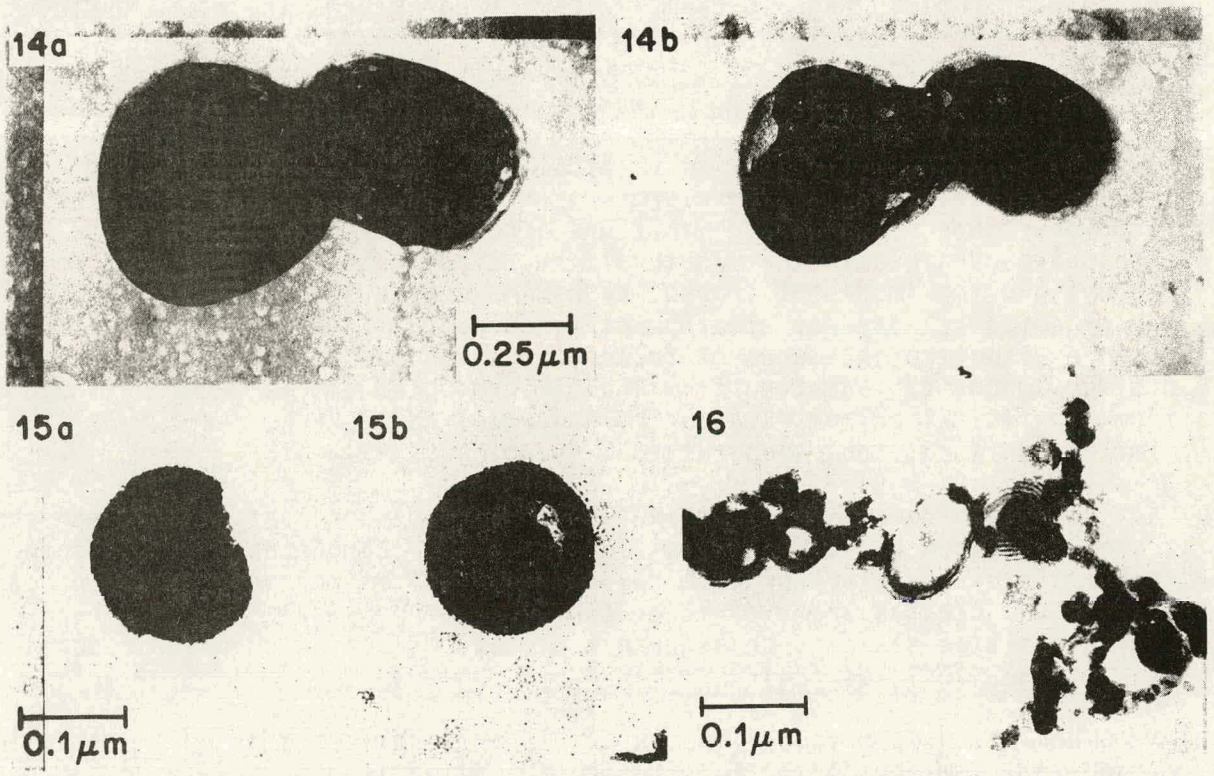

Fig. 14. a. Transmission electron microscope bright-field image of an unsonicated, frozen, hydrated 0.07% bovine phosphatidylcholine, 0.1% uranyl acetate liquid-crystalline dispersion. b. Area in a after it has been freeze-dried in situ at 198 K.

Fig. 15. a. Micrograph of a freeze-dried particle in a 0.07% bovine phosphatidylcholine, 0.1% uranyl acetate dispersion. Stage tilt is −20°. b. Area a, stage tilt +45°.

Fig. 16. Structure from a thick area of a frozen, hydrated 0.07% bovine phosphatidylcholine thin, 0.1% uranyl acetate vesicular dispersion that was freeze-dried in situ.

Ice is the main source of the free radicals that damage a frozen, hydrated specimen during radiolysis (43). Because ice is lost, a freeze-dried sample is less sensitive to radiation damage and can be imaged at higher magnifications. Fig. 13c is an in-focus, high magnification micrograph of part of Fig. 13b. The irregular particle on the right-hand side of Fig. 13c displays mass-thickness contrast fringes that follow the outer particle contour. The spacing of these fringes and those on similar particles is about 3.6 nm but whether the fringes represent surfactant bilayers cannot be decided because the freeze-drying process may have altered them.

Fig. 15 shows the same freeze-dried vesicle at two tilt angles: -20° (Fig. 15a) and +45° (Fig. 15b). The apparent diameter of the vesicle (its projection onto the image plane) changes. This and tilt experiments on other particles suggest that vesicles collapse slightly when the volatile components in the dispersion sublime. Radiation damage prevents imaging frozen, hydrated vesicles at magnifications as high as those of Fig. 13c or Fig. 15.

Structure in thicker regions of frozen, hydrated specimens is not always preserved during freeze-drying. In thicker areas, ice appears to leave the sample along a receding front which can sweep material along with it. This action agglomerates vesicles and moves them away from their original positions in a sample. Fig. 16 exemplifies the structures that form during freeze-drying of thicker sample areas.

Conclusions

Fast-freeze, cold-stage microscopy reveals structure in aqueous vesicular dispersions. The method makes unstained vesicles of natural or synthetic amphiphiles visible in their natural, hydrated state. The contrast mechanisms responsible for images of frozen, hydrated vesicle systems are explained by the dynamical theory of electron diffraction (33). Measurements of average vesicle diameters in images of frozen, hydrated samples that have received a minimum amount of radiation from the electron beam are in accord with those from quasi-elastic light-scattering and small-angle x-ray scattering from similar, unfixed, room temperature dispersions (24).

Radiation damage and positive stains enhance contrast in TEM images of frozen, hydrated vesicular dispersions but both change vesicle structure. Radiolysis by the electron beam causes images of vesicles embedded in ice to enlarge and creates areas of lower contrast on them. On the other hand, adding positive stains such as uranyl acetate or cesium chloride reduces the size of SHBS vesicles (24).

When stain is present, vesicular dispersions freeze-dried *in situ* can be viewed in the microscope. *In situ* freeze-drying is preferred over conventional freeze-drying methods because samples are fixed at higher cooling rates, the freeze-drying process can be observed as well as controlled, and images of the specimen in the hydrated and dried states can be compared. In thin specimen areas, structure in freeze-dried vesicular dispersions resembles that in the frozen, hydrated state although vesicles shrink and sometimes partially collapse when they are freeze-dried. Thereafter, warming to room temperature

does not affect them.

Vesicle samples for cold-stage microscopy are affected by radiolysis, stain, and freeze-drying. The mechanisms responsible for changes brought about by fixing and irradiating aqueous vesicular dispersions are not yet clear but must be understood before images of complex structured fluids such as micellar solutions and microemulsions can be fully interpreted.

References Cited in Section XII

1. Huang, C.-H., Biochemistry 8, 344 (1969).
2. Papahadjopoulos, D., ed., Ann. New York Acad. Sci. 308, 1 (1978).
3. Deguchi, K. and Mino, J., J. Colloid Interface Sci. 65, 155 (1978).
4. Finkelstein, M. and Weissman, G., J. Lipid Res. 19, 289 (1978).
5. Puig, J. E., Franses, E. I., Talmon, Y., Davis, H. T., Miller, W. G. and Scriven, L. E., Soc. Pet. Eng. J. 22, 37 (1982).
6. Horne, R. W. and Whittaker, V. P., Z. Zellf. 58, 1 (1962).
7. Finean, J. B. and Rumsby, M. G., Nature 197, 1326 (1963).
8. Horne, R. W., Bangham, A. D., and Whittaker, V. P., Nature 200, 1340 (1963).
9. Bangham, A. D. and Horne, R. W., J. Mol. Biol. 8, 660 (1964).
10. Papahadjopoulos, D. and Miller, N., Biochim. Biophys. Acta 135, 624 (1967).
11. Glauert, A. M. and Lucy, J. A., J. Microsc. 118, 401 (1969).
12. Talmon, Y., J. Colloid Interface Sci., submitted for publication.
13. Johnson, S. M., Bangham, A. D., Hill, M. W. and Korn, E. D., Biochim. Biophys. Acta 233, 820 (1971).
14. Skarnulis, A. J., Strong, P. J. and Williams, R. J. P., J.C.S. Chem. Comm., 1030 (1978).
15. Mann, S., Skarnulis, A. J. and Williams, R. J. P., J.C.S. Chem. Comm., 1067 (1979).
16. Miyamoto, V. K. and Stoeckenius, W., J. Membrane Biol. 4, 252 (1971).
17. Taylor, K. A., J. Microsc. 112, 115 (1978).

18. Forge, A., Knowles, P. F. and Marsh, D., J. Membrane Biol. 41, 249 (1978).

19. Van Venetië, R., Leunissen-Bijvelt, J., Verkleij, A. J. and Ververgaert, P. H. J. Th., J. Microsc. 118, 401 (1980).

20. Bachman, L. and Schmitt, W. W., Proc. Nat. Acad. Sci. USA 68, 2149 (1971).

21. Van Venrooij, G. E. P. M., Aertsen, A. M. H. J., Hax, W. M. A., Ververgaert, P. H. J. Th., Verhoeven, J. J. and Van der Vorst, H. A. Cryobiology 12, 46 (1975).

22. Talmon, Y., Davis, H. T., Scriven, L. E. and Thomas, E. L., Rev. Sci. Instr. 50, 698 (1979).

23. Talmon, Y., Davis, H. T., Scriven, L. E. and Thomas, E. L., in Proc. 7th European Cong. on Electron Microscopy, eds. P. Brederoo and W. dePriester, Vol. II (Elsevier-North Holland, New York, 1980) 718.

24. Kaler, E. W., Falls, A. H., Davis, H. T., Scriven, L. E. and Miller, W. G., J. Colloid Interface Sci., in press.

25. Talmon, Y., Ph.D. Thesis, University of Minnesota (1979).

26. Falls, A. H., Ph.D. Thesis, University of Minnesota (1982).

27. Talmon, Y., Davis, H. T., Scriven, L. E. and Thomas, E. L., J. Microsc. 117, 321 (1979).

28. Talmon, Y. and Miller, W. G., J. Colloid Interface Sci. 67, 284 (1978).

29. Buscall, R. and Ottewill, R. H., in Specialist Periodical Report, Colloid Science, ed. D. Everett, Vol. 2, (The Chemical Society, London, 1975).

30. Perlov, G. and Talmon, Y., Rev. Sci. Instr., submitted for publication.

31. Franses, E. I., Ph.D. Thesis, University of Minnesota (1979).

32. Puig, J. E., Ph.D. Thesis, University of Minnesota (1982).

33. Howie, A. and Whelan, M. J., Proc. Roy. Soc. London A 263, 217 (1961).

34. Hanszen, K.-J., in Advances in Optical and Electron Microscopy, eds. R. Barer and V. E. Cosslett, Vol. 4, (Academic Press, London, 1971) 1.

35. Handlin, D. L. in Proc. 39th Annual EMSA Meeting ed. G. W. Bailey, (Claitor, Baton Rouge, 1981) 338.

36. Falls, A. H., in Proc. 40th Annual EMSA Meeting, in the press (1982).

37. Ashby, M. F. and Brown, L. M., Phil. Mag. 8, 1649 (1963).

38. Van Landyut, J., Gevers, R. and Amelinckx, S., Phys. Stat. Sol. 10, 319 (1965).

39. Rühle, M. R., in Radiation Induced Voids in Metals, eds. J. W. Corbett, and L. C. Ianiello, L. C., U. S. Atomic Energy Commission,Oak Ridge, TN (1972).

40. Humphries, C. J. and Hirsch, P. B., Phil. Mag. 18, ser. 8, 115 (1968).

41. Thomas, G. and Goringe, M. J., Transmission Electron Microscopy of Materials, (Wiley, New York) 141, 239.

42. Nicholas, J. F. (1966) Acta Cryst. 21, 880-881.

43. Talmon, Y., J. Microsc. 125, 227 (1982).

44. Unwin, P. N. T. and Muguruma, J., Phys. Stat. Sol. (a) 14, 207 (1972).

45. Cosslett, V. E., J. Microsc. 113, 113 (1978).

46. Grubb, D. T., J. Mat. Sci. 9, 1715 (1974).

47. Heide, H. G. and Grund, S., J. Ultrastruct. Res. 48, 259 (1974).

48. Washburn, E. W., ed., International Critical Tables of Numerical Data, Physics, Chemistry and Technology, Vol. 3, (McGraw-Hill, N.Y., 1928) 210.

49. Boyde, A. and Franc, F., J. Microsc. 122, 75 (1981).

50. Friedel, M. G., Annales de Physique 18, 273 (1922).

51. Kléman, M., Williams, C. E., Costello, M. J. and Gulik-Krzywicki, T., Phil. Mag. 35, 33 (1977).

52. Zasakzinski, J., private communication, 1982.

XIII. MULTICOMPONENT PHASE BEHAVIOR IN AN EXTERNAL FIELD: SYNOPSIS OF PH.D. THESIS OF W. R. ROSSEN

The material reported here is taken from W. R. Rossen's Ph.D. thesis which is available through University Microfilm International at the University of Michigan.

Solution thermodynamics governs the design and economics of countless chemical processes including those for chemical flooding for enhanced oil recovery (1-3). The free energy function not only controls phase behavior, i.e. the number and compositions of equilibrium phases, but influences other factors important to process design as well: transport properties, (4,5) interfacial phenomena (6-8) and metastable equilibria. This dissertation describes an equation of state for microemulsions of surfactant, oil and water used in chemical flooding processes and an experimental technique, equilibrium ultracentrifugation, to supplement phase behavior data in the fitting of such a model. The development of the experimental technique led to four separate topics discussed herein: 1) the theory of multicomponent, multiphase equilibrium in an external, e.g. centrifugal, field. 2) the theory of approach to equilibrium in an external field. 3) the practice of equilibrium ultracentrifugation to obtain thermodynamic data. 4) auxiliary experiments to determine the compressibility of mixtures studied by equilibrium ultracentrifugation.

An equation of state is a mathematical expression for the free energy g^o of a mixture as a function of its composition, temperature and pressure. At fixed temperature and pressure this function for a ternary mixture can be plotted as a surface above the composition plane as in Figure 1. Tangent

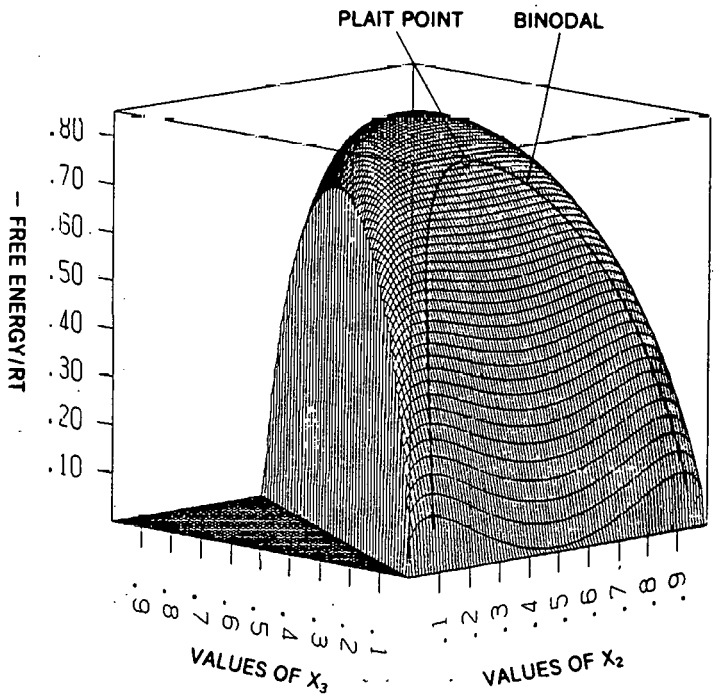

Figure 1. Inverted free energy surface of a ternary regular solution (ref. 9) with parameter values $\alpha_{12} = 3$, $\alpha_{13} = \alpha_{23} = 0$.

planes to this surface intersect the vertical axes corresponding to the pure components at the values of the chemical potentials μ_i^o. Planes which are tangent at two or more points identify phases which are in equilibrium.

Chapter II describes the Screened Flory-Huggins (SFH) equations of state for microemulsions which account both for the aggregation of surfactant into sheets and the separation of oil and water by surfactant into separate domains:

$$\tilde{v}_W n\, g^o / RT = \phi_W \ell n \phi_W + \frac{\tilde{v}_W}{\tilde{v}_O} \phi_O \ell n \phi_O + \frac{\tilde{v}_W}{\tilde{v}_S} \phi_S \ell n \phi_S + \alpha^*_{WO} \phi_W \phi_O + \alpha_{WS} \phi_W \phi_S + \alpha_{OS} \phi_O \phi_S \cdot \qquad (1)$$

Here n is the molar density of the solution, ϕ_W, ϕ_O and ϕ_S are the volume fractions of water, oil and surfactant, $\tilde{v}_W/\tilde{v}_O$ and $\tilde{v}_W/\tilde{v}_S$ are parameters which account for the relative size of such aggregates of each component as form, and the α_{ij} are binary interaction parameters. The success of the SFH models rests upon the idea that the oil-water interaction parameter α^*_{WO} decreases as surfactant concentration increases because surfactant separates oil and water domains. In the Linearly Screened Flory-Huggins (LSFH) model, α^*_{WO} is replaced by $\alpha_{WO}(1 - s\phi_S)$; in the Exponentially Screened Flory-Huggins (ESFH) model, α^*_{WO} is replaced by $\alpha_{WO} \exp(-s\phi_S)$. These equations of state predict the type of phase behavior observed in microemulsion systems (10); a sample phase diagram corresponding to "optimal salinity" (1) from the LSFH model is shown in Figure 2. Here a middle-phase microemulsion in equilibrium with nearly pure oil and brine solubilizes equal amounts of oil and brine with only a small concentration of surfactant.

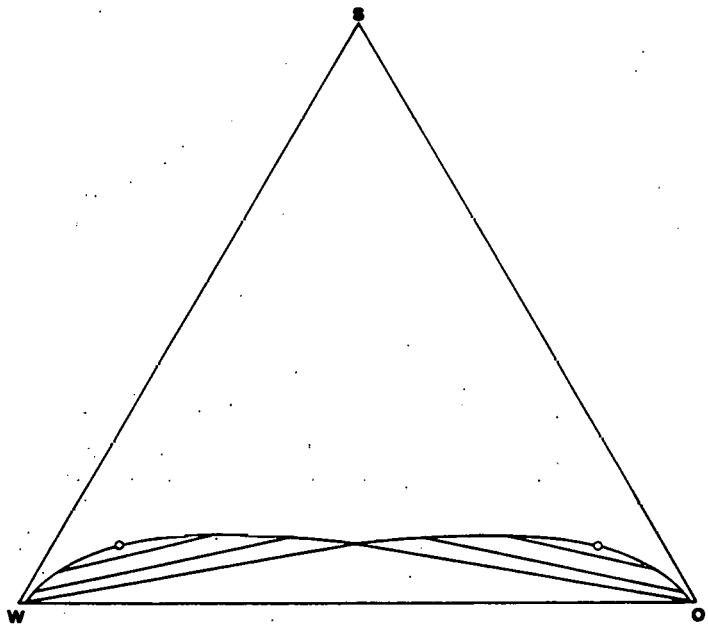

Figure 2. Phase Diagram of the Linearly Screened Flory-Huggins (LSFH) solution model. Parameter values employed are $\tilde{v}_W/\tilde{v}_O = 1$, $\tilde{v}_W/\tilde{v}_S = 0.01$, $\alpha_{WO} = 4.8$, $\alpha_{WS} = \alpha_{OS} = -31.35$, $s = 7.29$.

The LSFH model relates many familiar properties of microemulsions to solution thermodynamics. The low-relief topography of the free-energy surface in the three-phase region (Figure 3), typical of near-critical mixtures, contributes to low interfacial tensions, slow equilibration and large changes in phase compositions in response to small changes in experimental conditions.

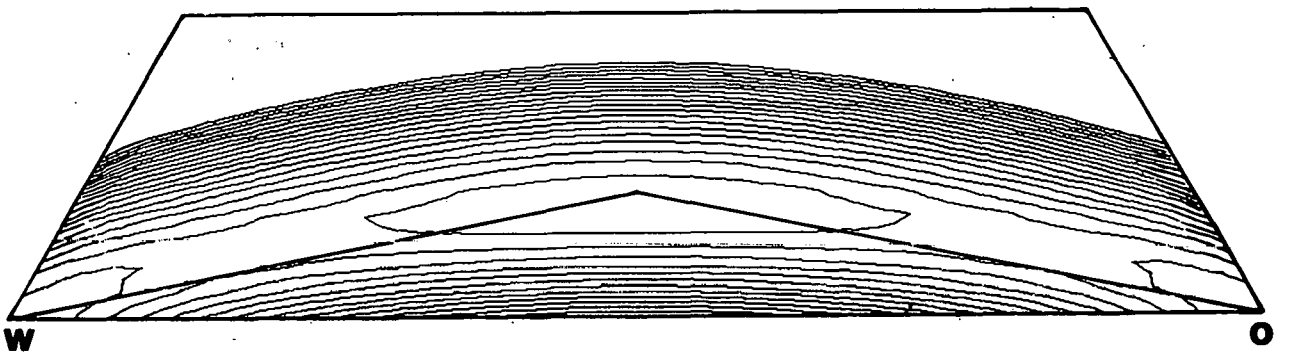

Figure 3. Contour plot of the free energy surface relative to the plane of the three-phase equilibrium. $\tilde{\nu}$ Parameter values are as in Fig. 2. Contours are plotted at intervals of 0.04 $RT/n\tilde{v}_{ij}$.

Figure 4 identifies metastable phases and metastable two-phase equilibria within the stable multiphase regions of Figure 2. These equilibria are stable until a completely new phase nucleates. The existence of metastable states may explain why microemulsion phase behavior is so sensitive to the way in which the samples are prepared.

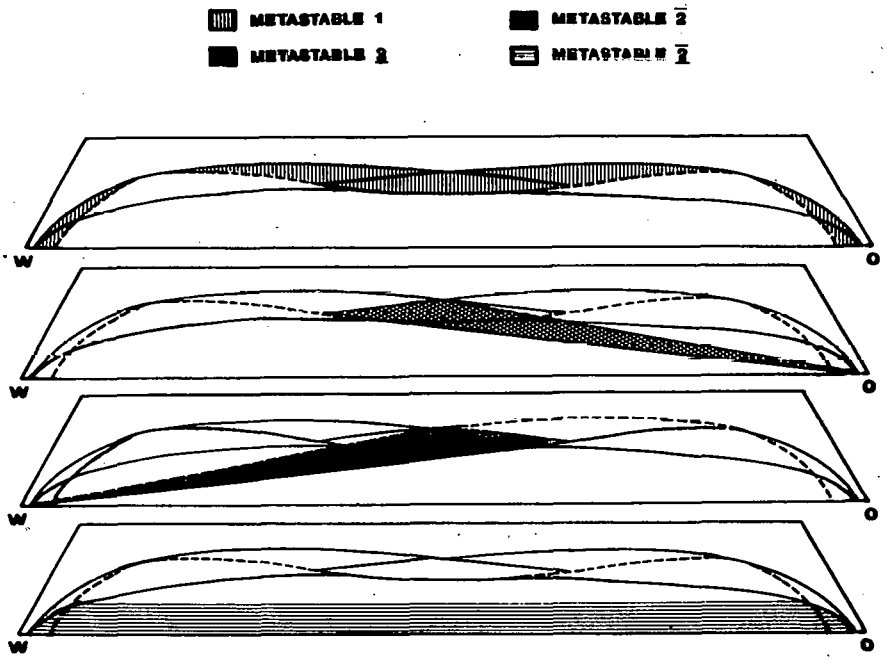

Figure 4. Regions of metastable one- and two-phase equilibria in the LSFH solution of Fig. 2. In region $\underline{2}$ surfactant partitions primarily into the lower, brine-rich phase; in $\bar{2}$, primarily into the upper, oil-rich phase; and, in $\underline{\bar{2}}$, equally between brine-rich and oil-rich phases. In region 1 the mixture is metastable as one phase.

Systematically changing one or more parameters from those of Figure 2 produces a progression of phase diagrams that mimic those produced in the laboratory by varying, e.g. salinity (2,10). Figure 5, for instance, models surfactant's increasing affinity for oil, reflected in the decreasing value of α_{OS}, as salinity increases. For an overall composition of 0.05 volume fraction surfactant and equal fractions of oil and water the lever rule gives the phase volumes pictured. The factor $\sqrt{\Delta\omega_{max}}\, d$ relates the free-energy surface to interfacial tension (7) and indicates a partly thermodynamic basis for low interfacial tensions when the microemulsion phase contains equal amounts of oil and brine. Parameter sequences like Figure 5 can be fit to laboratory data; the resulting phase diagram sequence can then be fit to simpler correlations (10) for use in reservoir simulators.

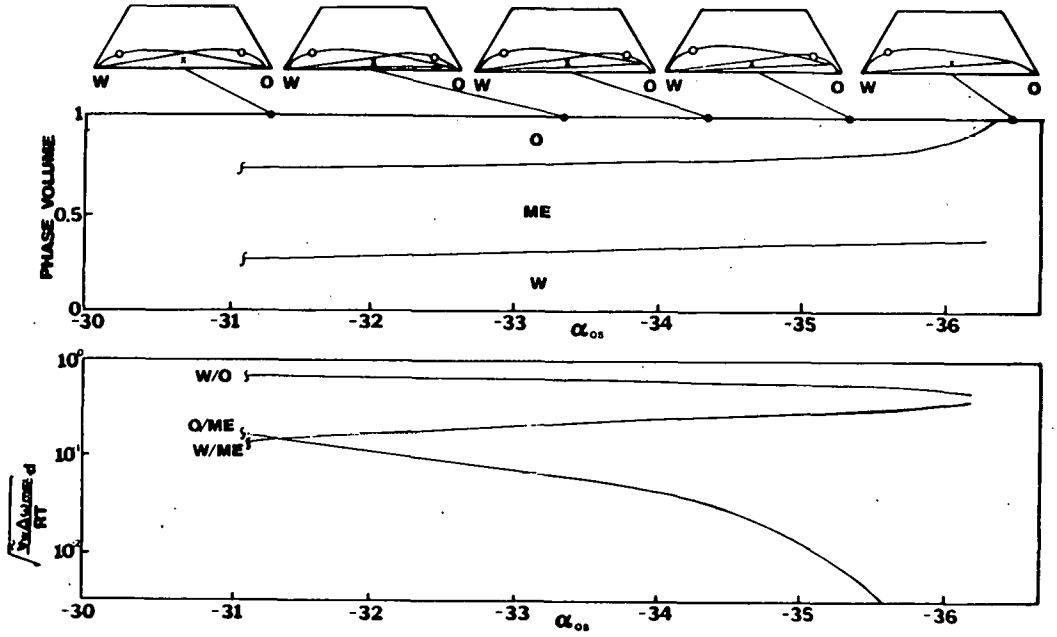

Figure 5. Variation in α_{OS} mimicking the right-hand side of a salinity scan. Parameter values except α_{OS} are as in Fig. 2.

Equilibrium ultracentrifugation can give the thermodynamic data for fitting such an equation of state. Chapter III presents the theory of multicomponent, multiphase equilibrium in an external field such as a gravitational or centrifugal field. Bulk material in such a field is stratified so as to maintain uniform chemical potential μ_i for each component:

$$\mu_i = \mu_i^o\,(T,p,\underline{x}) + M_i\,\Psi\,, \qquad i = 1, \ldots, m\,. \tag{2}$$

In the field the field-free chemical potential μ_i^o, a function of only local temperature, pressure, and composition, is augmented by the potential energy, i.e. molecular weight M_i times external potential Ψ. In a centrifugal field $\Psi = -\omega^2 r^2/2$, where ω is angular velocity in rad sec $^{-1}$. A more convenient form of Eq. 2,

$$\mu_i^o\,(T,p^o,\underline{x}(\psi)) = \mu_i - \int_{p^o}^{P(\psi)} \tilde{v}_i\, d\,p - M_i(\psi - \psi^o)\,, \quad i = 1,\ldots,m\,, \tag{3}$$

where pressure is determined by the condition of hydrostatic equilibrium

$$p = p^o - \int_{\psi^o}^{\psi} \rho \, d\psi \, , \qquad (4)$$

relates the field-free chemical potential at atmospheric pressure p^o to the field induced composition profile $\underline{x}(\psi)$ and the volumetric properties of the mixture: density ρ and partial molar volumes $\bar{v}_i$. Here ψ^o is ψ at the meniscus, where $p = p^o$. Equation 3 gives the change in field-free chemical potential with composition across the stratified sample, data which can be fit to an equation of state (11,12). The sharper is the gradient of composition in the sample, the wider the range of compositions represented and the more information gained about the equation of state.

Sharp equilibrium composition gradients result from large differences in density between components in solution, large molar mass of components or their aggregates in solution and solution nonideality, reflected in flat free energy surface like that of near critical mixtures and microemulsions. Sharp gradients thus indicate solution nonideality as well as colloidal particle mass and therefore inferring colloidal structure from sedimentation-equilibrium data (13-17) is problematic. Because microemulsions and near-critical molecular solutions have sharp equilibrium gradients in the field, however, they are ideally suited to ultracentrifugation to determine their equation of state.

The number of interfaces separating distinct phases can be more, the same, or fewer in a field-stratified sample than in the same sample at 1 g. The phase behavior of near-critical and colloidal mixtures is especially easily distorted because they stratify so greatly in the field. Figure 6 shows the field-free phase diagram of a ternary regular solution with many phase boundaries and plait points; the phase boundaries are distorted beyond recognition by even a moderate centrifugal field. These findings impugn for near-critical and colloidal mixtures the widespread practice of centrifugation to determine field-free phase behavior (18-22).

Nonideal solutions mimic colloidal mixtures in their approach to equilibrium or sedimentation velocity as well as in their sedimentation equilibrium. The same thermodynamic factors which lead to sharp equilibrium gradients -- large differences in density between components, large molecular or aggregate mass, and solution nonideality -- promote sharp sedimentation fronts as well. Therefore the sharp sedimenting fronts usually associated with colloids need not indicate colloidal particles in solution. In addition, because the transport coefficients of a nonideal molecular solution increase without bound near a plait point, the velocity of sedimenting fronts in near-critical molecular solutions can match that of colloids as well. The sedimentation behavior of two molecular solution models presented in Chapter IV illustrates the similarity between colloidal and nonideal-solution sedimentation. Sedimentation patterns in these model solutions match those thought to indicate interspersed oil-in-water and water-in-oil micellar regimes (23), but which are shown to occur in concentrated solutions of any type. From the velocities of the sedimenting fronts in these model solutions we deduce micelle sizes by the standard assumptions used in analysis of colloidal sedimentation -- velocity data (23) -- even though there are no micelles in these solutions. The inferred

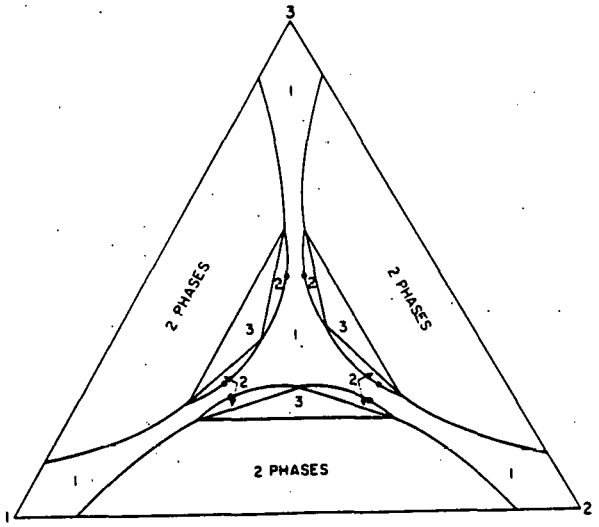

Figure 6. a) Field-free phase diagram of a regular solution (ref. 9). Parameter values employed are $\alpha_{12} = \alpha_{13} = \alpha_{23} = 2.66$.

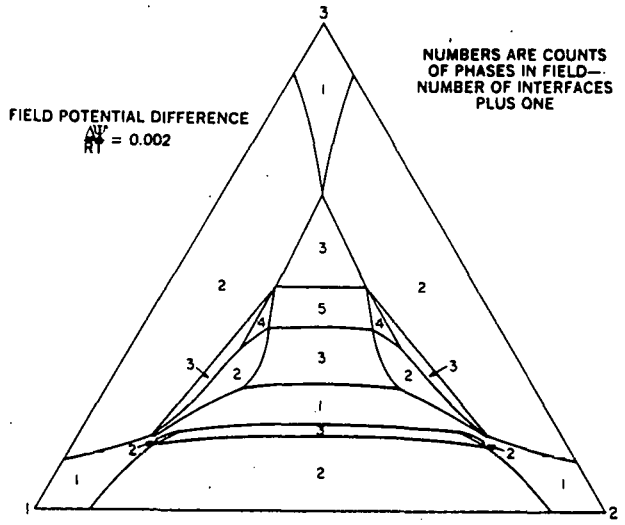

Figure 6 (cont.). b) Field-induced phase boundaries. Field potential difference $\Delta\psi/RT = 0.002$ corresponds to a 1 cm cell in a 50,000 g field. Additional parameter values employed are $M_1 = 150$ g gmol^{-1}, $M_2 = 250$ g gmol^{-1}, $M_3 = 200$ g gmol^{-1}, $v_1 = v_2 = v_3 = 200$ cm^3 gmol^{-1}.

micelle sizes, shown in Table 1, appear deceptively reasonable. In sedimentation velocity as in sedimentation equilibrium, colloidal structure cannot be inferred from sedimentation data alone, contrary to some attempts (18, 23, 24).

	REGULAR SOLUTION			SCALED EQUATION OF STATE		
		MICELLE RADIUS, Å			MICELLE RADIUS, Å	
$T - T_c$	APPROX. s, 10^{13} SEC	ASSUMING UN-HINDERED SETTLING	ASSUMING HINDERED SETTLING	APPROX. s, 10^{13} SEC	ASSUMING UN-HINDERED SETTLING	ASSUMING HINDERED SETTLING
60°	0.45	5.3	33	0.5	5.6	34
30°	0.51	5.7	35	0.73	6.8	42
15°	0.55	5.9	36	1.07	8.3	57
7.5°	0.55	5.9	36	1.6	10	62
3°	0.55	5.9	36	2.9	13	83
0	0.55	5.9	36	∞	∞	∞

For details of these molecular solution models see Chapter IV.

Table 1. APPARENT MICELLE SIZE IN MODEL SOLUTIONS

Chapter V returns to equilibrium sedimentation, specifically the determination of the field-free chemical potentials μ_i from the experimentally determined equilibrium stratification of a multicomponent solution in a centrifugal field. Three systems of oil and water with amphiphile are examined: in one case the amphiphile is a short-chain alcohol; in another, an ethoxylated alcohol; and in the third a long-chain polyethoxylated alcohol similar in some respects to surfactants used in enhanced oil recovery (25).

Equilibrium behavior in the field is determined by preparative ultracentrifugation, fractionation and chemical analysis of fraction. Advantages of the ultracentrifugation technique are that it is ideally suited to near-critical mixtures, that it probes the one-phase region denied to liquid-liquid equilibrium data, that it relates the chemical potentials at many compositions in a single experiment, and that it can accommodate an unlimited number of nonvolatile components. The accuracy of the technique is demonstrated by direct comparison of experimentally determined chemical potentials to published data for a simple mixture and by careful analysis of the sources of experimental error.

The power of the technique applied to near-critical mixtures is shown in Figure 7: in this case Eq. 3 relates chemical potentials throughout a composition profile which spans nearly the entire phase diagram. Remaining problems with the experimental technique are slow equilibration, remixing of the sample before fractions are obtained, and the lack of an adequate model for co-relating required auxiliary volumetric data; these problems and their solutions are discussed in detail in Chapter V. Particular attention is paid to the issue of remixing of the sample before and during fractionation, an important consideration in any scheme for fractionating an inhomogeneous sample.

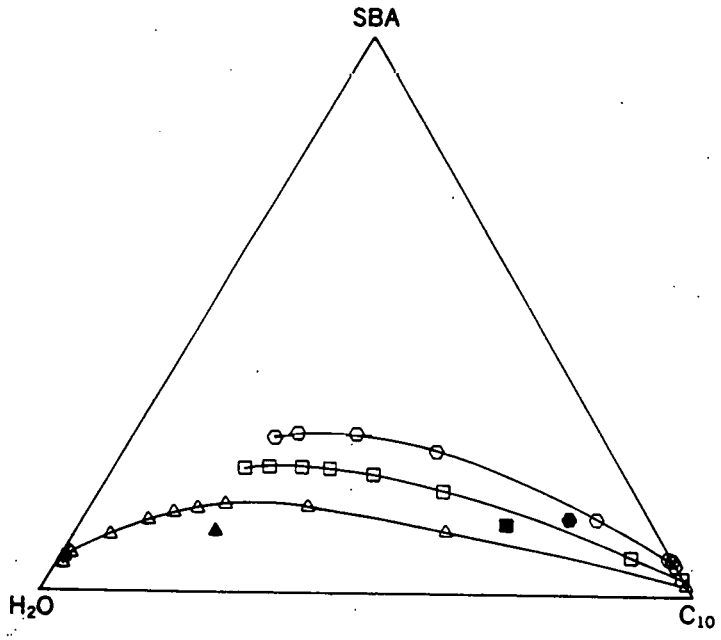

Figure 7. Field-induced equilibrium composition profiles of samples of the system pentaethyleneglycol ($C_{12}E_5$)/sec-butyl alcohol (SBA)/n-decane (C_{10})/ water plotted on a surfactant-free weight % composition diagram. Open symbols represent fractions of the field-stratified samples. Filled-in sysmbols represent the initial compositions.

Chapter VI describes compressibility experiments conducted with Prof. James P. Kohn, of the University of Notre Dame, using a novel device of his construction described here for the first time. Systems studied include the oil/water/amphiphile mixtures examined by ultracentrifugation as well as the microemulsion phase from a salinity scan of commercial surfactant with oil and brine (26). Compressibility data are required for analyzing sedimentation-equilibrium results and also for predicting the effect of high pressures on microemulsion phase behavior, an important topic to enhanced oil recovery processes (27-29). To a first approximation, the compressibility of the amphiphile/oil/water mixtures we examined is linear in volume-fraction composition, and the compressibility of oil and water in solution is that of the pure components.

References Cited in Section XIII

1. Reed, R. L., and Healy, R. N., Improved Oil Recovery by Surfactant and Polymer Flooding, D. O. Shah and R. S. Schechter, ed., Academic Press, Inc., New York (1977), 383-437.

2. Larson, R. G., Soc. Petr. Eng. J. (Dec.), 411-422 (1979).

3. Larson, R. G., Davis, H. T., and Scriven, L. E., J. Petr. Technol. 34, 243-258 (1982).

4. De Groot, S. R., and Mazur, P., Nonequilibrium Thermodynamics, North-Holland Publishing Co., Amsterdam (1962).

5. Bird, R. B., Stewart, W. E., and Lightfoot, E. N., Transport Phenomena, Wiley, (1960), 563-572.

6. Davis, H. T., and Scriven, L. E., Adv. Chem. Phys. 49, 357-454 (1982).

7. Davis, H. T., and Scriven, L. E., Soc. Petr. Eng. paper 9278, presented at the 55th Annual Fall Conference and Exhibition, Dallas, TX, Sept. 21-24 (1980).

8. Fleming, P. D. III, and Vinatieri, J. E., J. Phys. Chem. 84, 1526-1531 (1980).

9. Meijering, J. L., Philips Res. Rep. 5, 333-356 (1950); Part II, Philips Res. Rep. 6, 183-210 (1951).

10. Bennett, K. E., Phelps, C. H. K., Davis, H. T., and Scriven, L. E., Soc. Petr. Eng. J. (Dec.) 747-762 (1981).

11. Pedersen, K. O., Z. Physik. Chem. A 170, 41-61 (1934); Chem. abstr. no. 28-7107.

12. Cullinan, H. T., Jr., and Lenczyck, J. P., I & EC Funda. 8, 819-822 (1969); Lenczyck, J. P.: Ph.D. Thesis, State University of New York at Buffalo (1970).

13. Waugh, D. F., J. Phys. Chem. 65, 1793-1797 (1981).

14. Anacker, E. W., Rush, R. M., and Johnson, J. S., J. Phys. Chem 68, 81-93 (1964).

15. Ottewill, R. H., Stour, C. C., and Walker, T., Farad. Soc. Trans. 63, 2796-2802 (1967).

16. Jorpes-Friman, M., Finn. Chem. Lett. 240-244 (1979).

17. Doughty, D. A., J. Phys. Chem 83, 2621-2628 (1979).

18. Smith, G. D., Donelan, C. E., and Barden, R. E., J. Colloid Interface Sci. 60, 488-496 (1977); Keiser, B. A., Varie, D., Barden, R. E., and Holt, S. L., J. Phys. Chem 83, 1276-1280 (1979); Lund, G., and Holt, S. L., J. Am. Oil Chem. Soc. (August) 264-267 (1980).

19. Chan, K. S., and Shah, D. O., Surface Phenomena in Enhanced Oil Recovery, D. O. Shah, ed., Plenum Press, New York (1981), pp. 53-72.

20. Lang, J. C., and Morgan, R. D., J. Chem. Phys. 73, 5849-5861 (1980).

21. Shinoda, K., and Kunieda, H., J. Colloid Interface Sci. 42, 381-387 (1973).

22. Fontell, K., J. Colloid Interface Sci. 44, 318-329 (1973).

23. Hwan, R. N., Miller, C. A., and Fort, T. Jr., J. Colloid and Interface Sci. 68, 221-234 (1979).

24. Dwiggins, C. W., Jr., and Bolen, R. J., J. Phys. Chem. 65, 1787-1788 (1961).

25. Kilpatrick, P. K., University of Minnesota: work in progress.

26. Bennett, K. E., Hatfield, J. C., Davis, H. T., Macosko, C. W., and Scriven, L. E., Microemulsions, I. D. Robb, ed., Plenum Publ. Corp. (1982), 65-84.

27. Puerto, M. C., and Reed, R. L., Soc. Petr. Eng. paper 10678, presented at the SPE/DOE Third Joint Symposium on Enhanced Oil Recovery, Tulsa, OK, April 4-7, 1982.

29. O'Connell, J. P., and Walker, R. D., presented at the AIChE Annual Spring Meeting, Houston, April 5-9, 1981.

XIV. ELECTRON MICROSCOPY AND MOLECULAR THEORY OF MICROSTRUCTURED FLUIDS: SYNOPSIS OF PH.D. THESIS OF A. H. FALLS

The material reported here is taken from A. H. Fall's Ph.D. thesis which is available through University Microfilms International at the University of Michigan.

Introduction

Microstructure and its effect on physical properties in solids is well recognized. Research on the morphology of semi-solid polymer systems, however, is not as advanced. In contrast, supramolecular order in liquid and semi-liquid systems is scarcely understood. Even less well known is the relation between the microstructure and the phase behavior and physical properties of structured liquids.

Unfortunately, no single experiment can directly determine fluid microstructure. Consequently, results from many techniques must be combined to build a circumstantial case for a microstructural assignment. At the same time, theories must also be developed to understand the molecular origins of supramolecular order in liquids. A successful theory can interpret, explain, and predict macroscopic fluid properties. This thesis describes two experimental and theoretical studies that are part of the research program at the University of Minnesota which seeks to understand fluid microstructure.

Part I: Fast-Freeze, Cold-Stage Transmission Electron Microscopy of Surfactant Microstructures

A surfactant, or surface-active agent, is an amphiphile, that is, it consists of both polar (hydrophilic) and nonpolar (lipophilic) moieties. In either polar or nonpolar solvents surfactants associate preferentially to form long-lived, supramolecular structures, which are types of fluid microstructures, the theory of which is the subject of Part II. Other examples of fluid microstructures are fluid-fluid interfaces, fluid-solid interfaces, thin films, and small drops and bubbles. Figure 1 depicts several simple surfactant microstructures. The goal of Part I of this thesis is to advance cold-stage electron microscopy to where it can identify the types of aggregates present in surfactant/water/oil systems. As such, the morphologies of ice and of frozen brines and surfactant solutions, the knowledge of which underlies successfully interpreting images of complex systems, are examined. Thereafter, images of surfactant microstructures, including aqueous liquid crystalline and vesicular dispersions, micellar solutions, and microemulsions, are presented. To explain these, theories of contrast in transmission electron microscope images of frozen, hydrated specimens are developed, the effects of electron beam radiolysis are identified, and artifacts of staining and freeze-drying samples are analyzed. Specimen cooling rates, which influence the degree of rearrangement in freezing samples and therefore the value of cold-stage microscopy for microstructural analysis, are measured with thin-film thermocouples.

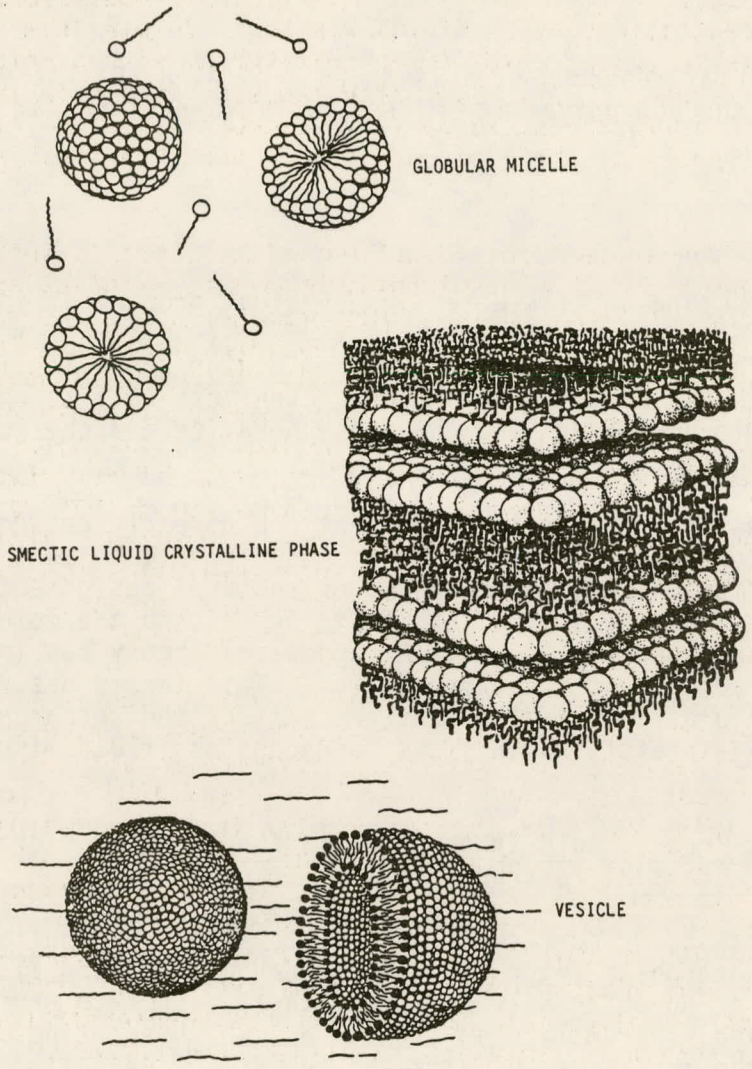

Figure 1. Conceptual drawings of simple surfactant microstructures.

A surfactant with a single, straight-chain hydrophobic "tail" aggregates into micelles when it is above a critical concentration in water. A micelle (Fig. 1) consists of a surface of high surfactant concentration that encloses an isolated, unholey, and persistent subvolume. Double-tailed surfactants, however, form micelles only when their hydrophobic moieties are sufficiently short (1). Instead, depending on temperature, naturally-occurring, double-tailed surfactants such as lecithins phase separate from an aqueous solution into a lamellar liquid crystalline phase as the concentration of surfactant increases. Liquid crystals (Fig. 1) are composed of microscopic domains in which the amphiphile is partially ordered into thermally-fluctuating, repeating, parallel layers with solvent intercalated. Synthetic, double-tailed surfactants also associate in dispersed, lyotropic mesophases at low concen-

trations in water. For example, sodium 4-(1'heptylnonyl)benzenesulfonate (SHBS) at concentrations between 0.06 wt% and ~ 75 wt% in water at 298 K forms a hydrated smectic phase, which is in equilibrium with a molecular solution of surfactant monomer (2,3). Sonicating aqueous dispersions of phospholipids or of synthetic surfactants causes vesicles to arrange (4-7). A vesicle (Fig. 1) is a spherical shell of one or more surfactant bilayers surrounding a fluid core.

When combined in certain proportions with water, hydrocarbons, and, often, salts and alcohols or other cosolvents, both single-tailed and double-tailed surfactants form microemulsions. A microemulsion is a thermodynamically stable, optically isotropic, single equilibrium phase that contains aqueous, nonaqueous, and amphiphilic components (8). Microemulsions display unusual phase behavior by incorporating oleic and aqueous components, normally immiscible with one another, into a stable, optically isotropic phase. They also strongly scatter electromagnetic radiation, show diverse rheological behavior, and exhibit ultralow interfacial tensions (as low as 10^{-4} dyne/cm) against both aqueous and oleic phases which contain less surfactant. This latter property, along with their phase behavior, makes microemulsions important in enhanced oil recovery, where they can be used to mobilize and solubilize residual oil that is trapped by capillary forces in reservoirs (9).

Unfortunately, the constitution and physical properties of microemulsions are system-specific. This has led to controversy, not only over defining microemulsions (Hatfield (8) compiled a compendium of definitions), but over models of supramolecular order in them. A simplified oil-water-amphiphile phase diagram (Fig. 2) intimates the complexity of microemulsion structure. Near the limits of the one-phase region called microemulsion, most researchers agree that the microstructure is in small, nearly monodisperse aggregates such as oil-in-water or water-in-oil swollen micelles (10,11). On the other hand, in systems near the middle of the hypothetical diagram, where roughly equal volumes of oil and water are solubilized by surfactant, the picture of structure is muddled — several microstructures have been proffered, including oil-in-water and water-in-oil micelles existing simultaneously (12), a "pea soup" or hodgepodge of microstructured fragments (13), and bicontinuous structures (14,15). Bicontinuous structures also break down naturally into discrete, polydisperse globular entities.

Despite continued theoretical and experimental research on microemulsions, their microstructure remains unresolved. Recent theoretical work at the University of Minnesota, however, demonstrates that phase behavior (16), electrical conductivity (8,17,18), and scattering of electromagnetic radiation (19) in microemulsions can be explained by Voronoi and Voronoi-like decorated tessellations, or subdividings of space, which incorporate both discrete and bicontinuous structures.

Many experimental methods probe fluid structure. However, results from physicochemical techniques such as conductimetry, nuclear magnetic resonance spectroscopy (NMR), differential scanning calorimetry (DSC), light-scattering, and x-ray scattering can only reflect fluid microstructure. These are indirect because a model must be used to interpret data from them. In contrast,

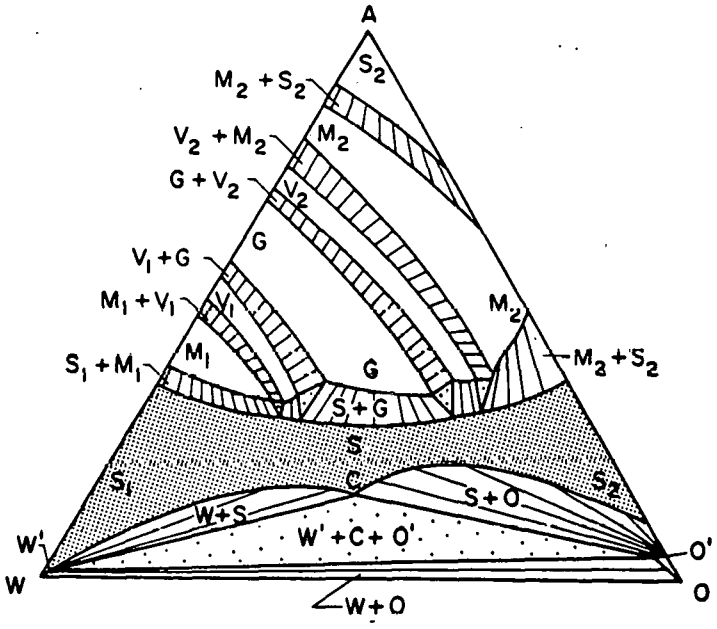

Fig. 2. Hypothetical water-oil-amphiphile phase diagram. Figure after Scriven (1977). Single-phase microemulsion region is stippled.

microscopy directly images microstructure. Consequently, at the University of Minnesota electron microscopy is an integral part of research aimed at elucidating supramolecular order in microemulsions.

J. C. Hatfield pioneered work in electron microscopy of microemulsions at Minnesota. Because liquid systems for microscopy must be fixed, Hatfield prepared microemulsions by spraying them into liquid propane at 88 K. Freezing was followed by fracturing the sample. After components were allowed to sublime from the fracture surface, a thin, platinum/carbon replica was made and examined in the electron microscope. It soon became clear, however, that freeze-fracture-replication microscopy of microemulsions is beyond standard techniques for biological specimens or mesophases: freezing and shearing samples alter their microstructures!

The goal in preparing samples for electron microscopy is, of course, to limit structural changes during fixation. Rearrangements that do occur must be understood so that the appearance of the original system can be reconstructed from images of the altered sample. Because there is always a possibility of introducing artifacts during fixation, it is imperative to vary systematically the sample preparation method before assigning a microstructure to a liquid system. Furthermore, it is desirable to contrast and compare the results of at least one other sample preparation method as well as evidence from less direct probes.

To corroborate freeze-fracture-replication microscopy of microemulsions, Talmon (20) developed a fast-freeze, cold-stage microscopy system. The idea is to capture a layer of sample between two polyimide film-covered grids and to freeze the assembly by plunging it into a cryogen. The frozen sample is put into a JEOL 100CX cooling-holder and transferred into the microscope where its temperature is maintained at 100 K. Although cooling rates in this double-film technique appear to exceed those in standard spray-freeze methods (21), they nevertheless may be insufficient to fix microemulsions of as low viscosity as are of primary interest in applications. An added problem in cold-stage microscopy is the sensitivity of frozen microemulsions to an electron beam. Talmon (20) proved that microemulsions crosslink when irradiated; it is not yet known whether this alters morphology.

Understanding and eventually overcoming cooling-induced and radiation-induced artifacts present challenges to cold-stage microscopy of microemulsions. A key is to perceive the microscopy of structured fluids that are less sensitive than microemulsions to preparation and irradiation — dispersed liquid crystalline and vesiculated surfactant, in particular. Talmon demonstrated that these systems could indeed be imaged with cold-stage microscopy.

Part I of this thesis describes analyzing and using the cold-stage microscopy system to elucidate the morphology of surfactant microstructures. In cooperation with Prof. Y. Talmon, now at the Technion — Israel Institute of Technology, much of the cold-stage equipment has been redesigned. These changes, instigated during summer visits to Minnesota by Prof. Talmon and a trip I took to the Technion, have been elaborated by Perlov et al. (22). A major difference is that the cooling-holder has been altered to contain a controllable heater near the specimen tip. This allows the specimen temperature to be maintained between 100 K and 300 K without introducing thermally-induced motion. It also permits in situ freeze-drying of a sample. The cold-stage transfer module (CSTM) has also been modified to exclude cold nitrogen vapors from contacting the stage O-ring and to allow a specimen to be transferred into the holder while under liquid nitrogen. The modified CSTM keeps the temperature of a specimen below 123 K when it is transferred into the electron microscope; 123 K is the lowest temperature reported for the amorphous to cubic phase transition in ice (23).

Liquid samples must be frozen quickly to insure that their microstructures remain unchanged during solidification. In this thesis, cooling rates in freezing specimens are characterized by measuring the thermoelectric response of thin-film/wire thermocouples plunged into boiling nitrogen. These temperature probes, which have a configuration akin to the double-film samples, cool at a rate of 5000 K/s between 273 K and 173 K. These rates are in accord with Talmon's (20) calculations which show that cooling rates are about 10^4 K/s, owing to film-boiling heat transfer at the specimen/cryogen interface. Riehle's (24) correlations confirm Talmon's estimates. All of these cooling rates are below 10^5 K/s, which is the lowest estimate of the rate required to vitrify water (25). Instead, the crystal structure of ice specimens that are prepared with the double-film technique is hexagonal (26).

Many microstructured fluids contain appreciable amounts of water. Exam-

ples are aqueous dispersions of liquid crystalline phases that lower interfacial tensions between oil and water (3) and aqueous vesicular dispersions which model membranes in biochemical research (27,6) and can recover oil from reservoirs (28). Others include micellar solutions and, of course, microemulsions. To understand structures that arise in the cold-stage microscopy of these systems, it is essential to understand the morphology of ice. Consequently, the microscopy of ice and dilute concentrations of solutes in ice is treated in this thesis.

A sample of water does not freeze into a perfect crystalline matrix. Instead, ice crystals, separated by grain boundaries, form with differing crystallographic orientations. Moreover, ice samples contain lattice defects, including dislocations. Figure 3 shows nonbasal screw dislocations in ice. These defects were indexed from their selected-area diffraction pattern, geometry, and appearance. Cold-stage microscopy indicates that this slip system, heretofore unconfirmed experimentally, operates in hexagonal ice. Nonbasal dislocations have been observed with etch-replication microscopy (29) but their slip planes cannot be identified with this technique (30). More common in hexagonal ice are basal dislocations, which have been confirmed by x-ray topography (31). Figure 4 is an example. This research (26) won an Electron Microscopy Society of America Presidential Award.

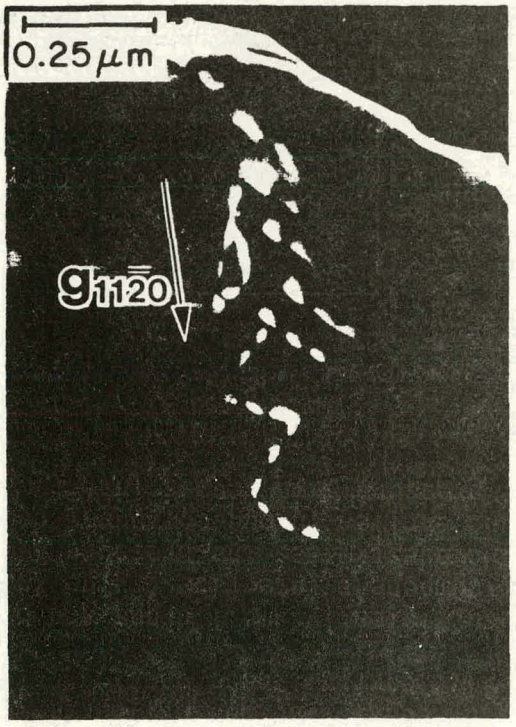

Fig. 3. (11$\bar{2}$0) dark-field transmission electron microscope image of nonbasal dislocations from the (10$\bar{1}$0)[1$\bar{2}$10] and (0$\bar{1}$10)[$\bar{2}$110] slip systems in hexagonal ice. Film orientation: [33$\bar{0}$2].

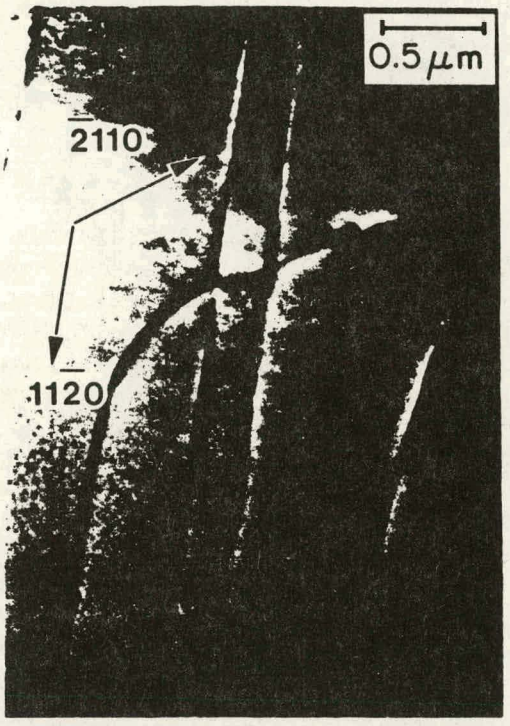

Fig. 4. Bright-field image of (a/3)<11$\bar{2}$0> screw dislocations in the ice basal plane.

When samples of dilute, aqueous dispersed surfactants are prepared with the double-film technique, aggregates embed within ice. To explain transmission electron microscope images of these frozen, hydrated structures, diffraction contrast theories are developed. For example, images of frozen, hydrated liquid crystalline particles display moiré fringes. Talmon et al. (32,33) thought these striations, seen on some of the crystallites in Fig. 5, to result from electrons interacting with an ice lattice overlapping frozen surfactant lamellae. However, selected-area diffraction and dark-field microscopy coupled with contrast theory prove that moiré fringes on frozen liquid crystallites originate from electrons diffracted twice by slightly misoriented ice grains.

The microscopy of frozen, aqueous vesicular dispersions was approached in like fashion. Figure 6 illustrates micrographs from vesicular dispersions of four surfactant systems: SHBS; L-α phosphatidylcholine, a naturally-occurring, bovine brain lecithin; SHBS mixed with sodium dodecylsulfate (SDS) and sodium chloride; and TRS 10-80, a commercial surfactant. Vesicles appear either dark or light against the ice in which they are embedded. The difference is negative versus positive contrast and can be explained with the

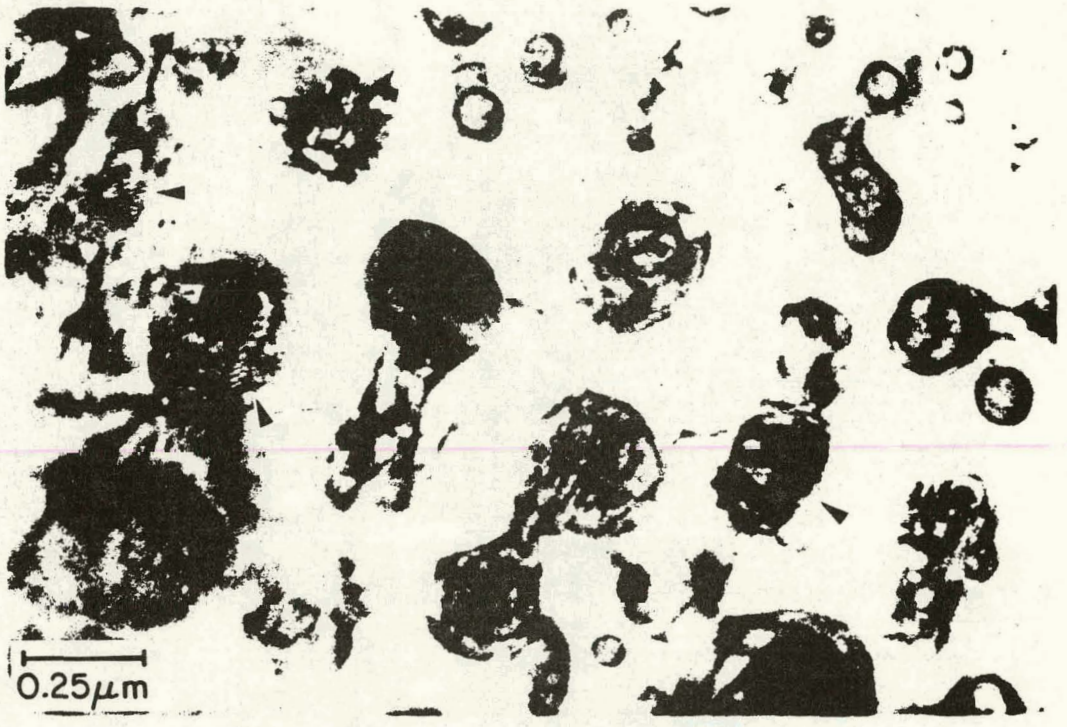

Fig. 5. Micrograph from a frozen aqueous dispersion of 1.19 wt % n-pentanol and 0.697 wt % SHBS. Striations on the crystallites (arrows) are moire fringes formed by electrons scattered from misoriented ice domains.

dynamical theory of electron diffraction (34). Figure 7, called a rocking curve, shows that the appearance of vesicles changes as diffracting conditions in the ice surrounding them vary. Depending on the local Bragg conditions, the center of a vesicle can appear dark (negative contrast) or light (positive contrast).

Supported by contrast theory, cold-stage microscopy, combined with quasi-elastic light-scattering, small-angle x-ray scattering, DSC, NMR, and freeze-fracture-replication microscopy, all performed at Minnesota, is used to characterize aqueous dispersions of surfactants. It confirms the existence of Dupin cyclides (35,36) in dispersed lyotropic liquid crystalline phases (37) and helps show the effects of alcohols on the latter. The method proves that a few large liquid crystallites survive sonication of a dispersion; these aggregates severely bias the measurement of vesicle sizes by quasi-elastic light-scattering (38) and cannot be removed by gel permeation chromatography or ultrafiltration (Fig. 8). Cold-stage microscopy also documents vesicles reverting to liquid crystallites as vesicular dispersions age and helps prove that vesicles are not equilibrium aggregates in water or in brine (38).

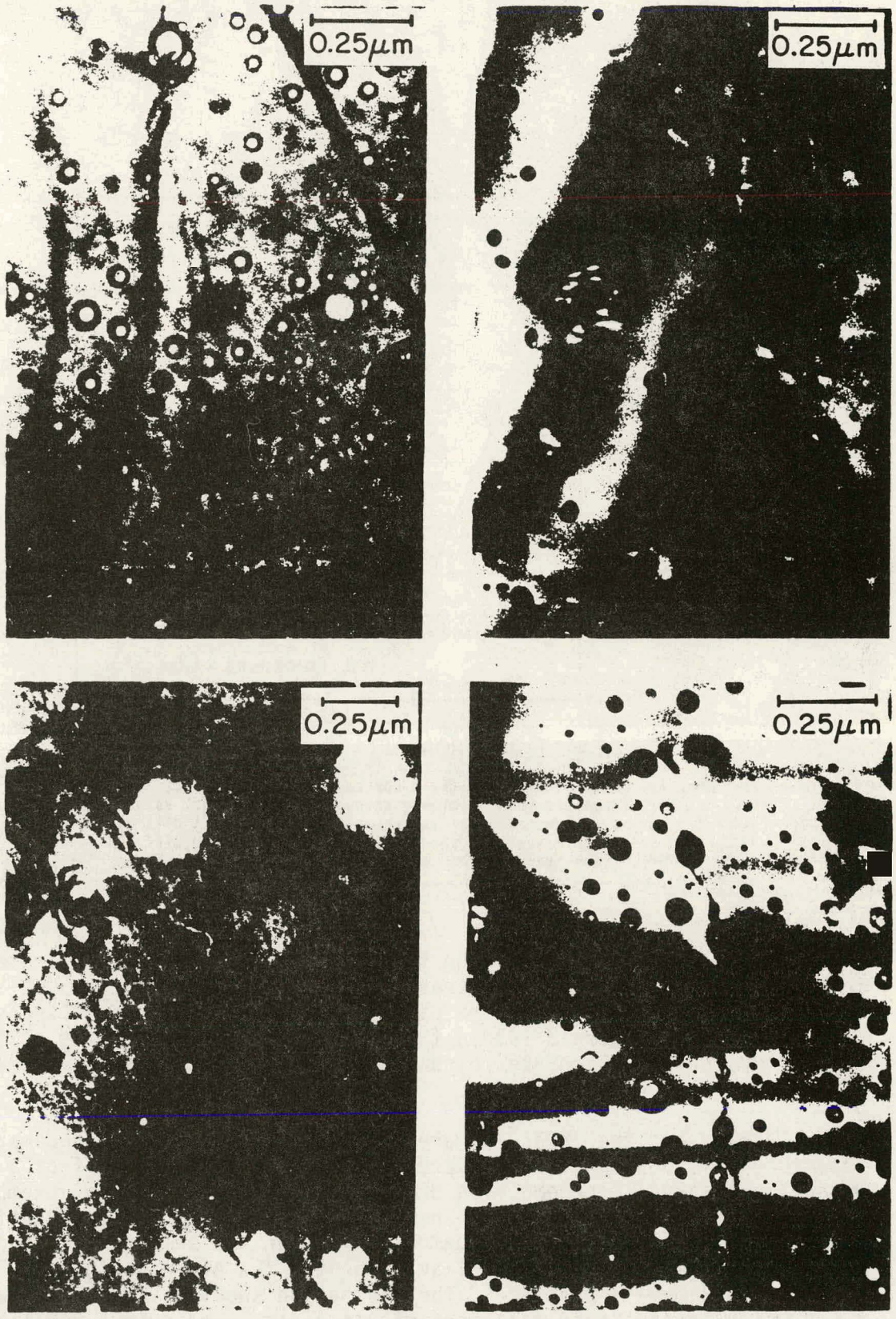

Fig. 6. Bright-field images of frozen aqueous dispersions of surfactants. Clockwise from upper left: 2 wt % SHBS; 0.07 wt % SHBS, 0.02 wt % SDS, 0.3 wt % NaCl; 1 wt % TRS 10-80; 0.07 wt % bovine lecithin, 0.1 wt % uranyl acetate.

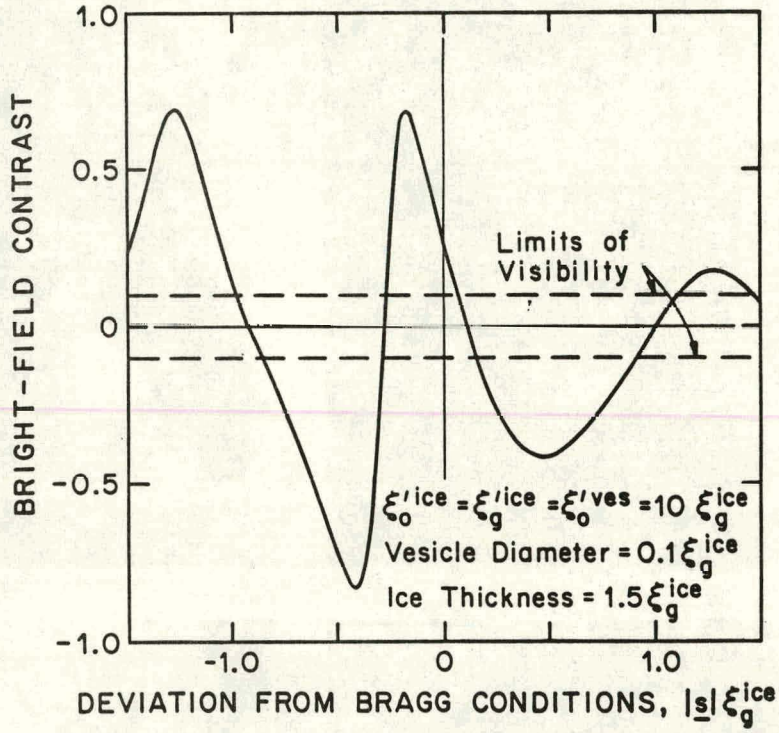

Fig. 7. Calculated bright-field contrast at the center of the image of a vesicle located midway through an ice crystal as a function of the deviation of the crystal from the exact diffracting condition. Vesicles change their contrast as the diffracting conditions vary and can appear either light or dark.

The effects of radiolysis on frozen vesicular dispersions are also examined. Radiolysis increases contrast in vesicle images and changes their structure and size. To overcome radiation damage, vesicular dispersions are stained and then freeze-dried in the microscope. Freeze-drying eliminates volatile materials which are responsible for free radicals that damage a specimen (39).

Staining and freeze-drying are ways to overcome radiation damage to frozen microemulsions and they too are investigated. Figure 9, from a freeze-dried, lower-phase microemulsion stained with cesium chloride, exemplifies the findings. Cesium chloride, an ionic salt, partitions preferentially into the aqueous domains of the microemulsion. When the sample is freeze-dried, the volatile material sublimes leaving behind the stain, which should mark where aqueous domains resided. The micrograph shows a few large, dark structures which appear to be contained within a sample-spanning, web-like matrix. The volume fraction of aqueous components that were in this microemulsion, as measured by volume uptake, is about 16%, just where electrical conductivity shows water domains becoming continuous.

Fig. 8. Micrograph of a 5 wt % SHBS vesicular dispersion. The latter was filtered through a 0.05 μm Millipore filter. Liquid crystalline particles that previously survived sonication also endure filtration. The crystallites, however, elongate while passing through the small, tortuous filter.

Does Fig. 9 accurately represent the supramolecular order in microemulsions? — perhaps, but probably not. Although the large, dark structures in Fig. 9 resemble the "micellar aggregates" in published micrographs (40) from microemulsions of the same system with slightly higher volume fractions of water, scattering techniques give no indication of their presence. Scattering methods, of course, cannot detect large aggregates if they are in low concentration. Nevertheless, it is likely that cooling rates in the double-film technique are insufficient to capture the structure of such low viscosity microemulsions and that the features in Fig. 9 result from phase separation or component redistribution during solidification.

Because of successes with vesicular dispersions (21), staining and freeze-drying hold promise in the microscopy of microemulsions. Next to be tried should be adding ionic stains to microemulsions which have discontinuous water domains (e.g., water/Aerosol-OT/isooctane systems, which remain a single phase at temperatures as low as 188 K (10). The aqueous domains of such systems are apt to freeze-in before the continuous oil phase does, thereby eliminating freezing artifacts. If this proved successful, oil domains in water-continuous microemulsions could likewise be stained with organo-metallic compounds.

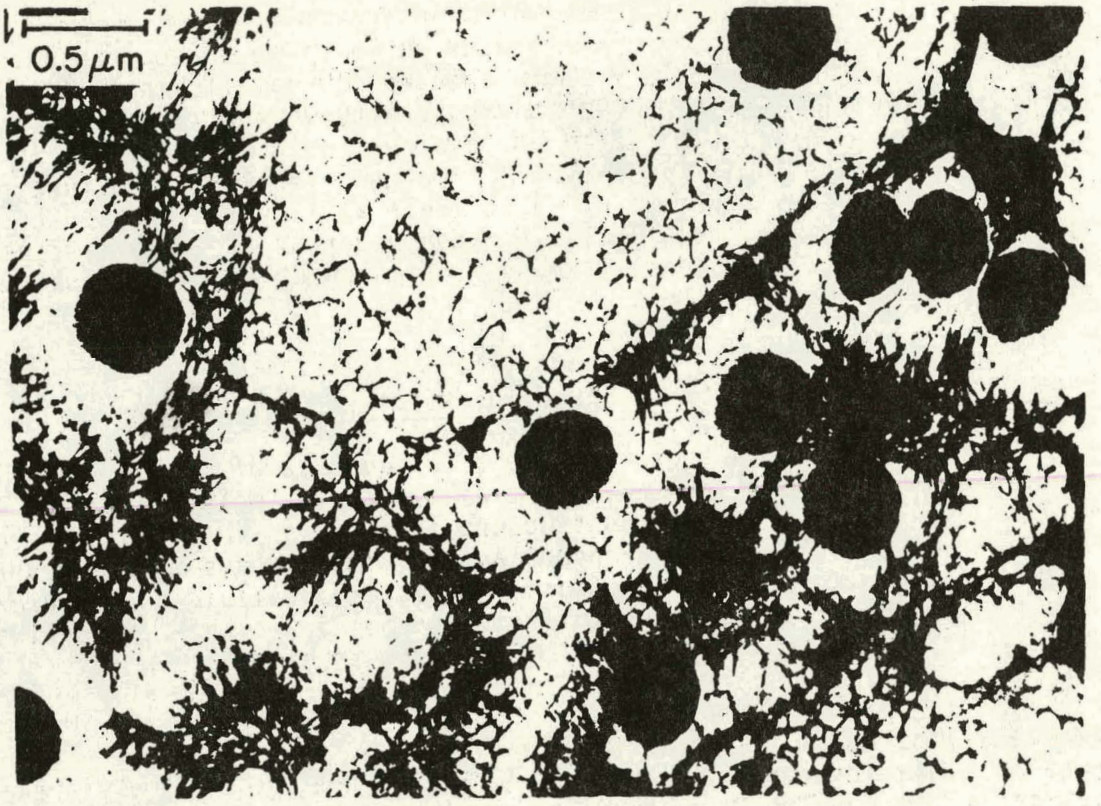

Fig. 9. Bright-field image of a freeze-dried 79.5% toluene, 8.4% n-butanol, 4.2% SDS, 7.9% (1% aqueous CsCl) lower-phase microemulsion.

At the same time, efforts should be continued to raise fast-freeze cooling rates. Analysis can start by using the thin-film/wire thermocouples described herein to investigate freezing in other cryogens or cold vapor jets. Other possibilities include trying emulsion jet (41), jet (42), and spray-freeze techniques (43), both of which are reported to vitrify water.

Cold-stage microscopy of two basic systems, ice and vesicular dispersions, is now well understood. Dislocation and stacking fault defects in ice, however, could be more readily classified if the cold-stage equipment at the University of Minnesota were improved; P. R. Swann (44) recently unveiled a cold-stage which permits tilt about two separate axes. A cold-stage elongation holder would also benefit deformation studies on both ice and polymer systems at low temperatures. Moreover, additional research is needed on radiation damage to frozen, hydrated specimens, a subject not treated broadly in this thesis, especially since Dubochet recently recanted his earlier measurements (45,25) which showed that cooling specimens to 4 K reduces radiation damage. The variable-temperature cold-stage developed by Perlov et al. (22) permits systematic study of radiolysis of ice and frozen, hydrated specimens at temperatures between 100 K and 300 K. Such a study could prove invaluable in learning how to arrest electron beam damage in frozen microemulsions.

Dispersed liquid crystalline phases still raise unanswered questions which microscopy can address: Where are the ice domains that give moiré fringes on frozen, hydrated liquid crystallites? What is the role of disclination and dislocation defects in causing liquid crystallites to deform plastically (as evidenced in Fig. 8)? How does the microstructure of dispersed mesomorphic phases influence their ability to lower interfacial tensions at oil-water interfaces? Already underway are freeze-fracture-replication and cold-stage microscopy studies by J. A. Zasadzinski to help resolve these questions.

Part II: Molecular Theory of Fluid Interfaces

Macroscopic fluid properties are a consequence of microscopic fluid structure. Interfacial phenomena are controlled by what are called fluid microstructures. A fluid microstructure is a region in a fluid where densities and/or compositions vary appreciably over distances on the order of the range of intermolecular interactions. Examples are fluid-fluid interfaces, fluid-solid interfaces, thin films, small drops and bubbles, micelles, microemulsions, foams, gels, and the like. All of these arise in physiological, biological, and chemical products and processes, including enhanced oil recovery. The goal of Part II of this thesis is to continue to develop a comprehensive molecular theory which describes supramolecular structure in liquids. The ultimate aim is molecular engineering: for a particular application, a set of efficient chemicals. As of now, such is beyond the ability of molecular theory. Consequently, this work focuses on developing models and new tools of computational mathematics to treat fluid interfaces.

Early theoretical work on interfacial phenomena dates to Young (46) and Laplace (47) who enunciated the conditions for mechanical equilibrium in interfaces. Gibbs (48) later developed a comprehensive thermodynamic theory of nonuniform systems in which an interface is represented by surface-excess quantities assigned to mathematical surfaces within the interfacial zone. Following Gibbs, Rayleigh (49) and van der Waals (50) viewed a fluid interface as a molecular transition between a pair of equilibrium phases.

Modern free energy theories of inhomogeneous fluid (for a review, see 51) are based on van der Waals' ideas, with statistical mechanics providing an expression for the free energy of nonuniform fluid. Of special interest because of its simplicity is gradient theory, which was begun by van der Waals and made rigorous by Bongiorno et al. (52) at the University of Minnesota and independently by Yang et al. (53). The adequacy of gradient theory and alternative approximations were studied by others in the Minnesota group (54-58).

Carey (58), following earlier work at Minnesota, helped develop gradient theory from a momentum balance approach and investigated the thermodynamic stability of inhomogeneous fluid. He also demonstrated how to obtain the inputs to gradient theory semiempirically — from approximate equations of state and experimentally-measured surface tensions. The results proved astonishing: predictions of surface tensions of hydrocarbons and their mix-

tures (59,60) and even water (61) to within a few percent of experimental values, along with insights into the molecular origins of low tensions and surface activity (62). All this Carey accomplished while using rudimentary, although clever, analytical techniques to solve the nonlinear boundary value problems posed by gradient theory.

This thesis is one of several to grow from Carey's; those by G. F. Teletzke (63) and R. E. Benner (64) are others that comprise the first generation. The work here began with developing new tools of computational mathematics to handle the gradient theory equation for structure in one-component spherical drops, an equation which Carey could not manage with finite difference techniques owing to a mathematical singularity at the origin of the microstructure. These tools, which are forged from finite element basis functions and modern matrix methods and continuation procedures, quickly developed into a modern numerical functional analysis. It is especially well-suited for calculating properties of fluid microstructures from either gradient theory (65-68) or related integral theories (65). It has also proven a boon for determining uniform fluid correlation functions from integral equation models such as the Percus-Yevick (69) and hypernetted chain (70-74) theories (75), even yielding solutions for metastable and unstable fluid where the meaning of physics has yet to be established. Unstable uniform fluid functions, however, are essential to theories of inhomogeneous fluid.

The computer-aided analysis is described at length and used to solve directly the gradient theory equations for component density profiles in single-component and binary fluid-fluid interfaces. Other approaches have been taken in the statistical physics literature. For example, Telo da Gama and Evans (76,77), instead of solving the gradient theory equations directly, forced component density profiles to conform to ad hoc hyperbolic tangent forms. Figure 10 shows how serious an error this is when the functions are nonmonotonic. Not only do hyperbolic tangent function fits misrepresent the density profiles but the interfacial tension calculated from them exceeds that from the true solutions by over 50%!

The approximate density functional model (78), an integral equation theory, is also used to predict the structure of one-component spherical interfaces. Results from it are found to be in accord with those from gradient theory. Consequently, gradient theory is used to describe and analyze the density and stress distributions in microscopic spherical drops. Figures 11-13 display some of the findings. Figure 11 shows density profiles predicted by gradient theory in one-component spherical drops. The thermodynamic parameter used to control drop size is the density n_B of the homogeneous bulk vapor phase surrounding the drop. Density distributions in larger drops are similar to that in the planar interface at the same temperature. As the drop size decreases, the density in the liquid interior at first increases, as expected from the classical Young-Laplace equation. However, below a characteristic drop size, the density at the drop center begins to fall as the size of the microstructure decreases further. These predictions indicate that the classical Young-Laplace equation breaks down for drops smaller than about ten molecules wide (Fig. 12), a discovery now backed by molecular dynamics simulations (K. E. Gubbins, private communication). However, contrary to the usual

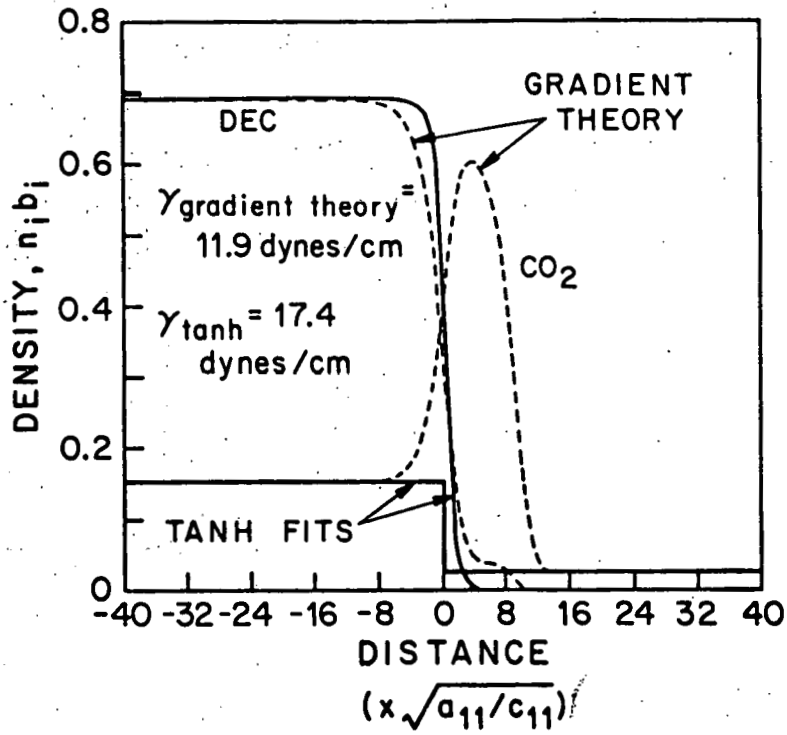

Fig. 10. Hyperbolic tangent and gradient theory density profiles in a CO_2-decane planar interface. The hyperbolic tangent function fits produce an interfacial tension 50% larger than that from the gradient theory profiles.

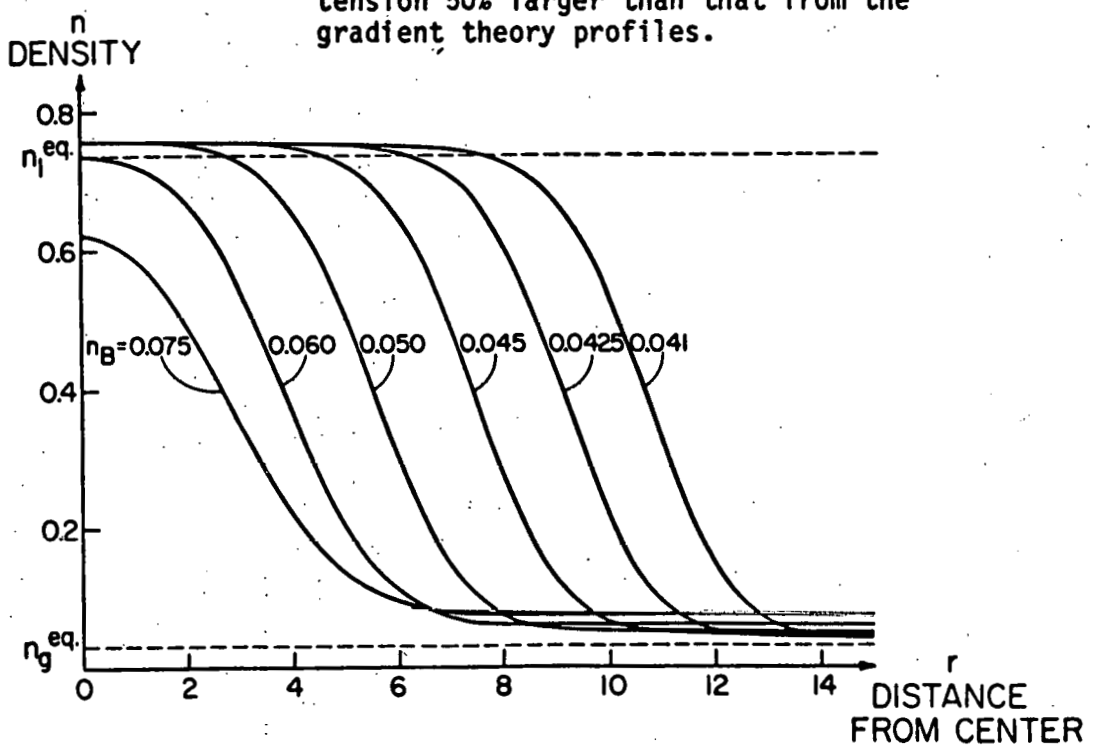

Fig. 11. Density profiles predicted by gradient theory for a series of one-component drops. Density and distance are in dimensionless units.

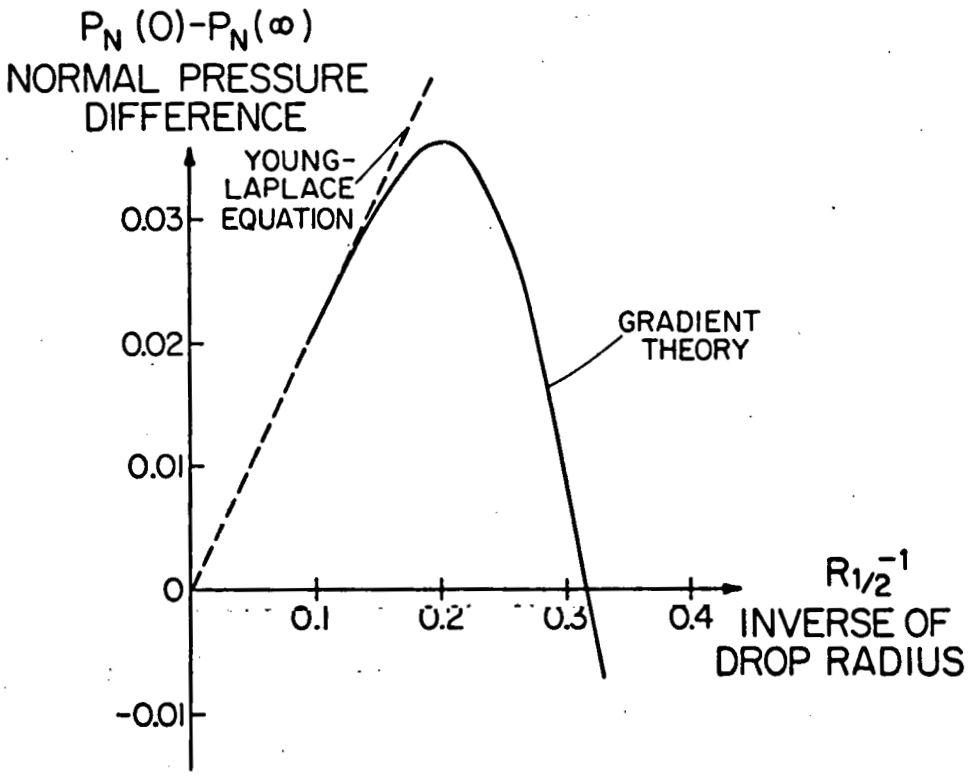

Fig. 12. Comparison of normal pressure differences across one-component interfaces computed by Young-Laplace equation and gradient theory.

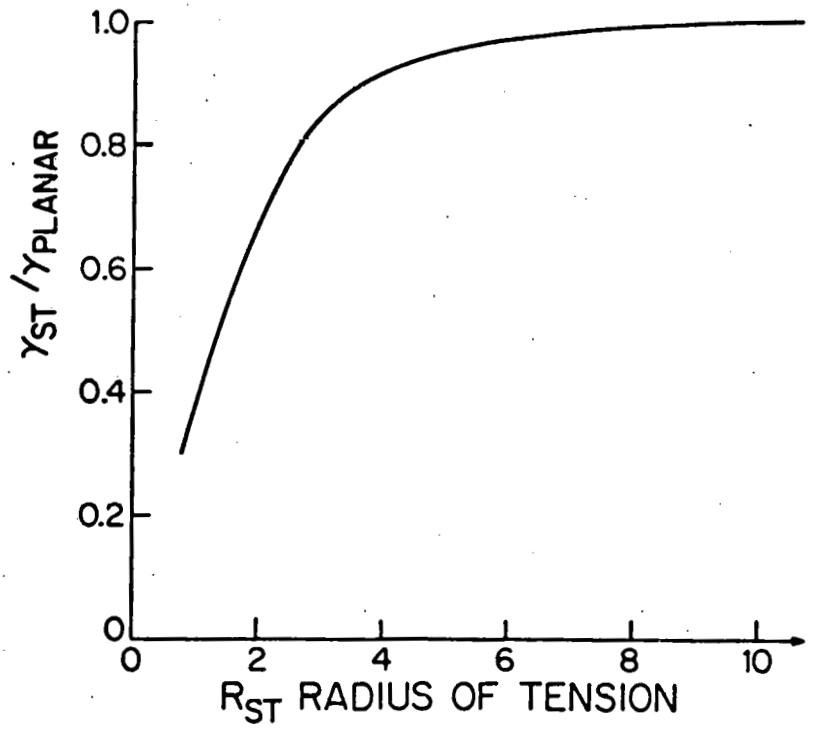

Fig. 13. Dependence of interfacial tension on curvature in one-component drops.

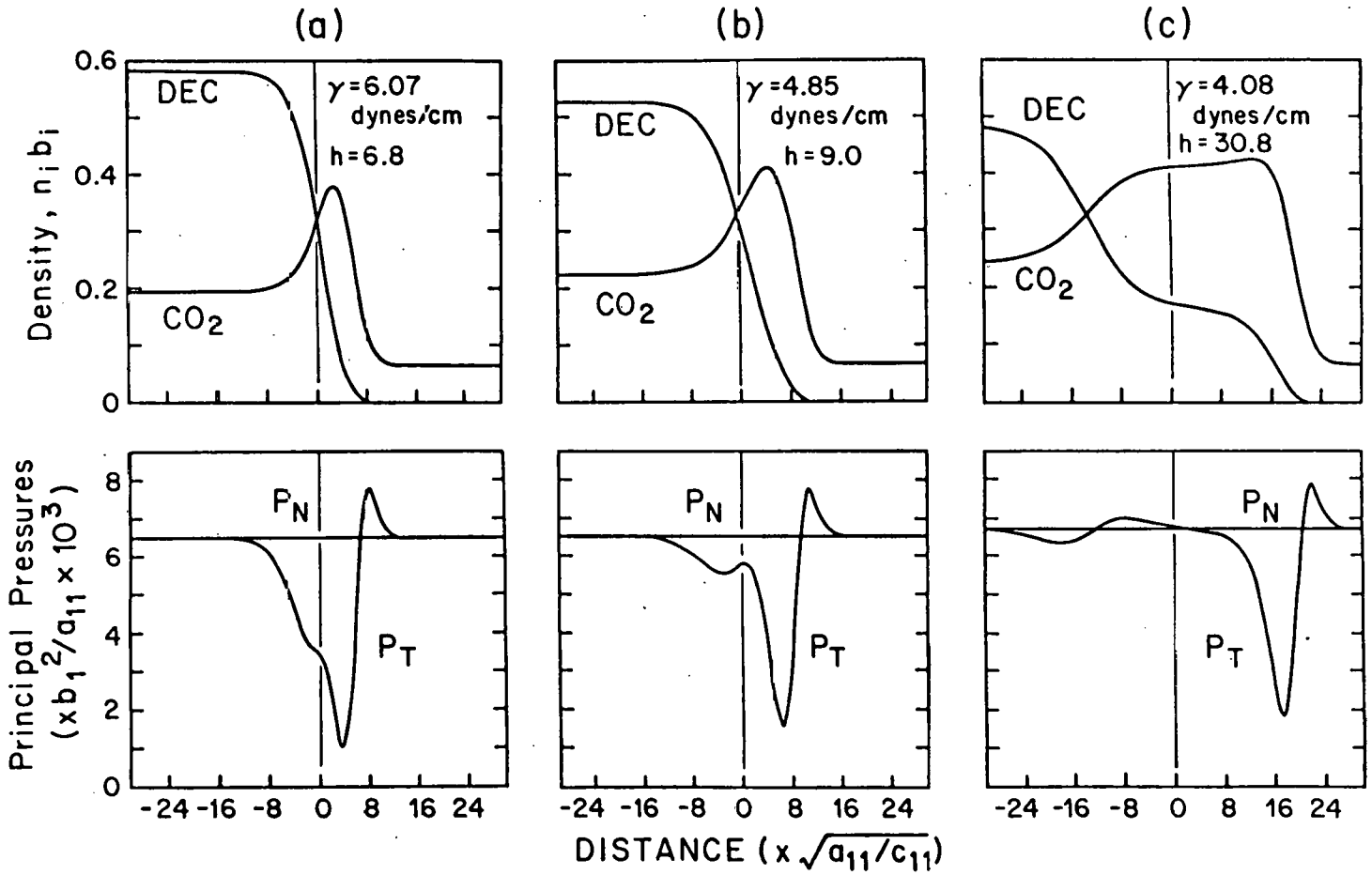

Fig. 14. Structure in liquid-vapor CO_2-decane planar interfaces at a temperature above the perfect-wetting transition temperature. As the bulk-phase densities of the interfaces approach a three-phase region (left-to-right), an adsorbed layer of a second liquid phase grows continuously into a thick film. Densities, distance, and principal pressures are in dimensionless units.

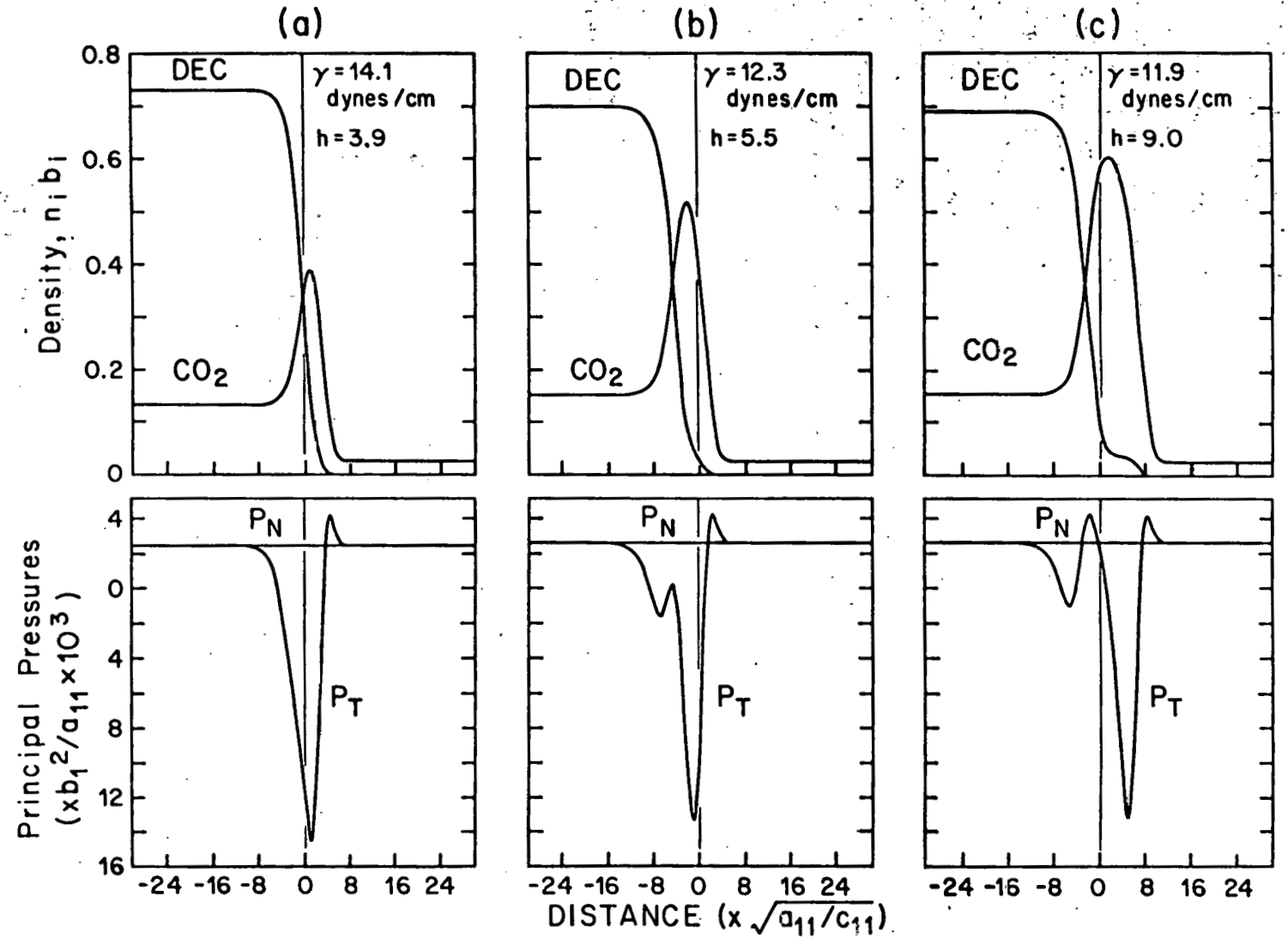

Fig. 15. Density and principal pressure profiles in liquid-vapor interfaces of CO_2 and decane below the perfect-wetting transition temperature. As the three-phase region is approached, the adsorbed layer grows, but not into a thick film of a second liquid phase.

estimate of the curvature dependence of surface tension (79,80), the interfacial tension of even very small one-component drops (say, three or four molecules wide) deviates little from the tension of a planar interface (Fig. 13).

Gradient theory is also used to predict component density and principal pressure (the negative of principal stress) profiles in flat and curved interfaces formed in carbon dioxide and decane mixtures. CO_2/hydrocarbon interfaces are of practical interest in supercritical extraction processes (81) and enhanced oil recovery (82-84). In some cases (e.g., the ones in Fig. 14), the component density (and total density) profiles are far from monotonic, with CO_2 being prominently surface active. In composition regions near where a perfect-wetting third phase arises, the composition and pressure profiles are especially structured, a thin-film appearing which is akin to a phase which perfectly wets and almost separates two distinct interfaces (Fig. 14c). This precursor to the third phase gives rise to Antonov's rule (85,86) for the interfacial tension between the two phases that are nearly in equilibrium with the third, perfect-wetting phase. Below a perfect-wetting transition temperature, such thin-films do not arise near compositions of the three phase region (see Fig. 15). Other theoretical and experimental studies of the wetting properties of coexisting phases, performed at Minnesota (62,67,87-89) and elsewhere (90-94), confirm these wetting patterns.

Curvature of sufficiently small drops and bubbles significantly affects adsorption at multicomponent interfaces. The Young-Laplace equation as traditionally applied overestimates the pressure jump across the interface in some cases (as found earlier in one-component drops) but, as Fig. 16 shows, underestimates the pressure jump across interfaces related to perfect-wetting structures.

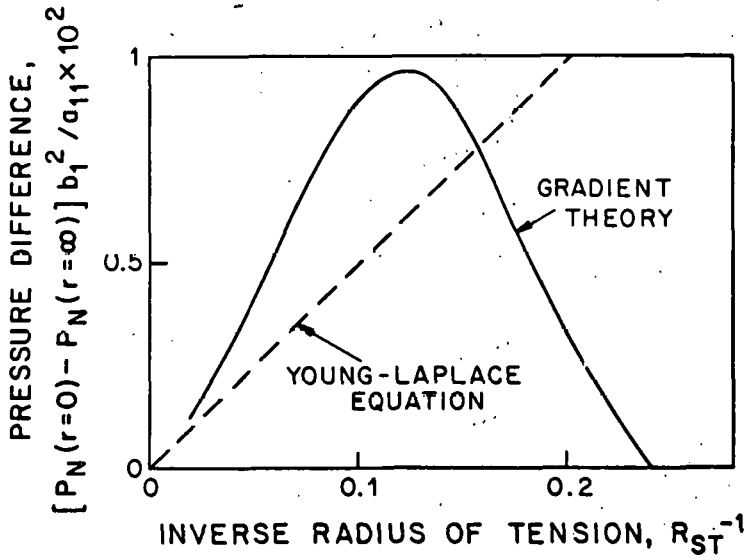

Fig. 16. Comparison between normal pressure differences computed by the Young-Laplace equation and gradient theory in binary spherical microstructures.

Although gradient theory predicts that thin-films form on liquid substrates, it misrepresents their thickness, disagreeing with asymptotic analysis of integral equations describing fluid structure (95), with Lifshitz theory of dispersion forces in thick films (96,97), and with ellipsometry measurements (94). This issue is not investigated in this thesis, but it is likely gradient theory is inadequate simply because it effectively truncates long-ranged fluid interactions. Research, which W. C. Kung has already started at Minnesota, should check the validity of gradient theory for multicomponent interfaces by comparing its predictions with those of integral models.

The spherical structures explored in this thesis are thermodynamically unstable with respect to uniform fluid distributions. However, many spherical microstructures of practical interest, such as micelles and swollen micelles, are thermodynamically stable aggregates. Carey (58) derived the gradient theory equations governing the stability of equilibrium fluid microstructures. Future research should aim at using these to determine the inputs to gradient theory which make spherical microstructures thermodynamically stable. Such should prove key to understanding the origins of complex supramolecular order in liquids and predicting its consequences.

References Cited in Section XIV

1. Tausk, R. J. M., Karmiggelt, J., Oudshoorn, C. and Overbeek, J. Th., G. Biophys. Chem. 1, 175 (1974).

2. Franses, E. I., Ph.D. thesis, University of Minnesota (1979).

3. Franses, E. I., Puig, J. E., Talmon, Y., Miller, W. G., Scriven, L. E. and Davis, H. T., J. Phys. Chem. 84, 1547 (1980).

4. Huang, C.-H., Biochem. 8, 344 (1969).

5. Kunitake, T. and Okahata, Y., J. Amer. Chem. Soc. 99, 3860 (1977).

6. Deguchi, K. and Mino, J., J. Colloid Interface Sci. 65, 155 (1978).

7. Hargreaves, W. R. and Deamer, D. W., Biochemistry 17, 3759 (1978).

8. Hatfield, J. C., Ph.D. thesis, University of Minnesota (1978).

9. Larson, R. G., Davis, H. T. and Scriven, L. E., J. Pet. Tech. 34, 243 (1982).

10. Zulauf, M. and Eicke, H.-F., J. Phys. Chem. 83, 480 (1979).

11. Gulari, E., Bedwell, B. and Alkhafaji, S., J. Colloid Interf. Sci. 77, 202 (1980).

12. Bellocq, A. M., Biais, J., Clin, B., Lalanne, P. and Lemanceau, B., J. Colloid Interf. Sci. 70, 524 (1979).

13. Winsor, P. A., Chem. Rev. 68, 1 (1968); in Liquid Crystals and Plastic Crystals, eds. G. W. Gray and P. Winsor (Ellis Horwood, Chichester, 1974) Vol. 1, 199.

14. Scriven, L. E., Nature 263, 123 (1975).

15. Scriven, L. E., in Micellization, Solubilization, and Microemulsions, Mittal, K. L., ed. (Plenum, New York, 1977) 877.

16. Talmon, Y. and Prager, S., J. Chem. Phys. 69, 2984 (1978).

17. Winterfeld, P. H., Ph.D. thesis, University of Minnesota (1980).

18. Bennett, K. E., Ph.D. thesis, University of Minnesota, in progress (1982).

19. Kaler, E. W. and Prager, S., J. Colloid Interf. Sci. 86, 359 (1982).

20. Talmon, Y., Ph.D. thesis, University of Minnesota (1979).

21. Falls, A. H., Davis, H. T., Scriven, L. E. and Talmon, Y., Biochim. Biophys. Acta, in press (1982).

22. Perlov, G., Falls, A. H. and Talmon, Y., Rev. Sci. Ins., submitted (1982).

23. König, H., Z. Kristallogr. 105, 279 (1943).

24. Riehle, U., Ph.D. thesis, Eidgenössischen Technischen Hochscule, Zürich.

25. Dubochet, J., Booy, F. P., Freeman, R., Jones, A. V. and Walter, C. A., Ann. Rev. Biophys. Bioeng. 10, 133 (1981).

26. Falls, A. H., in Fortieth Annual Proceedings of the Electron Microscopy Society of America, ed G. W. Bailey (Claitor's, Baton Rouge, 1982) 552.

27. Papahadjopoulos, D., ed., Ann. New York Acad. Sci. 308, 1 (1978).

28. Puig, J. E., Franses, E. I., Talmon, Y., Davis, H. T., Miller, W. G. and Scriven, L. E., Soc. Pet. Eng. J. 22, 37 (1982).

29. Sinha, N. K., Phil. Mag. [ser. 8] 36, 1385 (1977).

30. Fletcher, N. H., The Chemical Physics of Ice (University Press, Cambridge, 1970) 25, 196.

31. Webb, W. W. and Hayes, C. E., Phil. Mag. [ser.8] 16, 909 (1967).

32. Talmon, Y., Davis, H. T., Scriven, L. E. and Thomas, E. L., Rev. Sci. Ins. 50, 698 (1979).

33. Talmon, Y., Davis, H. T., Scriven, L. E. and Thomas, E. L., in Proceedings of the Seventh European Congress on Electron Microscopy, eds., P. Brederoo and W. dePriestor (Seventh European Congress on Electron Microscopy Foundation, Leiden, 1980) Vol. 2, 718.

34. Howie, A. and Whelan, M. J., Proc. R. Soc. A 263, 217 (1961).

35. Dupin, Ch., Applications de Géométrie et de Méchanique (Paris, 1822)) 200.

36. Maxwell, J. C., Quart. J. of Math. 9, 111 (1867).

37. Zasadzinski, J. A., Davis, H. T. and Scriven, L. E., Phil. Mag., to be submitted (1982).

38. Kaler, E. W., Falls, A. H., Davis, H. T., Scriven, L. E. and Miller, W. G., J. Colloid Interf. Sci., to appear (1982).

39. Talmon, Y., J. Microsc. 125, 227 (1982).

40. Biais, J., Mercier, M., Bothorel, P., Clin, B., Lalanne, P. and Lemanceau, B., J. Microsc. 121, 169 (1981).

41. Brügeller, P. and Mayer, E., Nature 288, 569 (1980).

42. Mayer, S. E. and Brüggeler, P., Nature 298, 715 (1982).

43. Dubochet, J. and McDowall, A. W., J. Microsc. 124, RP3 (1981).

44. Swann, P. R., private communication (1982).

45. Knapek, E. and Dubochet, J., J. Molec. Biol. 141, 147 (1980).

46. Young, T., Phil. Trans. R. Soc. (London, 1805) 95, 65.

47. Laplace, P., Traité de Mécanique Céleste (Courcier, Paris, 1806) Vol. 4, Suppl. to Book 10.

48. Gibbs, J. W., Trans. Conn. Acad. 3, 108 (Oct. 1875-May 1876); ibid. 3, 343 (May 1877-July 1878); reproduced in The Scientific Papers of J. Willard Gibbs (Longmans Green, & Co., New York, 1906) Vol. 1, 55.

49. Lord Rayleigh, Phil. Mag. [ser. 5] 33, 209 (1892); reproduced in Scientific Papers (Dover, New York, 1964) 513.

50. van der Waals, J. D., Z. Phys. Chem. 13, 657 (1894).

51. Davis, H. T. and Scriven, L. E., Adv. Chem. Phys. 49, 357 (1982).

52. Bongiorno, V. and Davis, H. T., Phys. Rev. A 12, 2213 (1975).

53. Yang, A. J. M., Fleming III, P. D. and Gibbs, J. H., J. Chem. Phys. 64, 3732 (1976).

54. Bongiorno, V., Scriven, L. E. and Davis, H. T., J. Colloid Interf. Sci. 57, 462 (1976).

55. Carey, B. S., Scriven, L. E. and Davis, H. T., J. Chem. Phys. 69, 5040 (1978).

56. Davis, H. T. and Scriven, L. E., J. Chem. Phys. 69, 5215 (1978).

57. McCoy, B. F. and Davis, H. T., Phys. Rev. A 20, 1201 (1979).

58. Carey, B. S., Ph.D. thesis, University of Minnesota (1979).

59. Carey, B. S., Scriven, L. E. and Davis, H. T., AIChE J. 24, 1076 (1978).

60. Carey, B. S., Scriven, L. E. and Davis, H. T., AIChE J. 26, 705 (1980).

61. Guerrero, M. I. and Davis, H. T., Ind. Eng. Chem. Fund. 19, 309 (1980).

62. Davis, H. T., Scriven, L. E. and Carey, B. S.. in Proceedings of the Second International Conference on Phase Equilibria and Fluid Properties in the Chemical Industry, Berlin (DECHEMA, Frankfurt, 1980) 589.

63. Teletzke, G. F., Ph.D. thesis, University of Minnesota (1983).

64. Benner Jr., R. E., Ph.D. thesis, University of Minnesota, in progress (1983).

65. Falls, A. H., Scriven, L. E. and Davis, H. T., J. Chem. Phys. 75, 3986 (1981).

66. Falls, A. H., Scriven, L. E. and Davis, H. T., J. Chem. Phys., in press (1982).

67. Teletzke, G. F., Scriven, L. E. and Davis, H. T., J. Colloid Interf. Sci. 87, 550 (1982).

68. Benner Jr., R. E., Scriven, L. E. and Davis, H. T., in Structure of the Interfacial Region, Faraday Symposium No. 16 (The Royal Society, London, 1982) in press.

69. Percus, J. K. and Yevick, G. J., Phys. Rev. [ser. 2] 110, 1 (1958).

70. van Leeuwen, J. M. J., Groeneveld, J. and de Boer, J., Physica 25, 792 (1959).

71. Meeron, E., J. Math. Phys. 1, 192 (1960).

72. Morita, T. and Hiroike, K., Prog. Theor. Phys. 23, 1003 (1960).

73. Rushbrooke, G. S., Physica 26, 259 (1960).

74. Verlet, L., Nuovo Cimento 18, 77 (1960).

75. Mier y Terán, L., Falls, A. H., Scriven, L. E. and Davis, H. T.. in Proceedings of the Eighth Symposium on Thermophysical Properties, ed. J. V. Sengers, (American Society of Mechanical Engineers, New York, 1982) Vol. 1, pp. 45.

76. Telo da Gama, M. M. and Evans, R., Mol. Phys. 41, 1091 (1980).

77. Telo da Gama, M. M. and Evans, R., in Structure of the Interfacial Region, Faraday Symposium No. 16 (The Royal Society, London, 1982) in press.

78. Ebner, E., Saam, W. F., and Stroud, D., Phys. Rev. A 14, 2264 (1976).

79. Tolman, R. C., J. Chem. Phys. 17, 333 (1949).

80. Ono, S. and Kondo, S., in Handbuch der Physik, ed. S. Flügge, S., (Springer, Berlin, 1960) Vol. 10, 134.

81. Kurnik, R. T. and Reid, R. C., Fluid Phase Equilibria 8, 93 (1982).

82. Holm, L. W., Trans. AIME 216, 225 (1959).

83. Holm, L. W., J. Pet. Tech. 28, 76 (1976).

84. Holm, L. W. and Josendahl, V. A., J. Pet. Tech. 26, 1427 (1974).

85. Antonov, G., J. Chim. Phys. 5, 372 (1907).

86. Widom, B., J. Chem. Phys. 62, 1332 (1975).

87. Teletzke, G. F., Scriven, L. E. and Davis, H. T., J. Chem. Phys., in press (1982).

88. Teletzke, G. F., Scriven, L. E. and Davis, H. T., J. Chem. Phys., submitted (1982).

89. Seeto, Y., Puig, J. E., Scriven, L. E. and Davis, H. T., J. Phys. Chem., submitted (1982).

90. Zisman, W. A., in Contact Angle, Wettability and Adhesion, ed. R. Gould, Adv. Chem. Ser. 43, 1 (1963).

91. Cahn, J. W., J. Chem. Phys. 66, 3667 (1977).

92. Reed, R. N. and Healy, R. N., SPE preprint #8262, presented at the Annual Fall Technical Meeting of the Society of Petroleum Engineers, Las Vegas (1979).

93. Moldover, M. R. and Cahn, J. W., Science 207, 1073 (1980).

94. Kwon, O'D., Beaglehole, D., Webb, W. W., Widom, B., Schmidt, J. W., Cahn, J. W., Moldover, M. R. and Stephenson, B., Phys. Rev. Lett. 48, 185 (1982).

95. Barker, J. A. and Henderson, J. R., J. Chem. Phys. 76, 6303 (1982).

96. Dzyaloshinskii, I. E., Lifshitz, E. M. and Pitaevskii, L. P., Sov. Phys. JETP 37, 161 (1960).

97. Mahanty, J. and Ninham, B. W., Dispersion Forces (Academic Press, New York, 1976).

XV. SURFACTANT MICROSTRUCTURES: SYNOPSIS OF PH.D. THESIS OF E. W. KALER

The material reported here is taken from the synopsis of E. W. Kaler's Ph.D. thesis which can be obtained from University Microfilm International at the University of Michigan.

Surfactant molecules are amphiphiles, that is, they possess opposed portions that are water-loving (e.g. ionic groups) and oil-loving and water-hating (e.g. long hydrocarbon chains). Because of this dual nature, they are uniquely able to organize in solution and at interfaces into structures with molecular or larger scales. These schizophrenic molecules are everywhere in nature. They form the basis of biological membranes and are found in almost all foods. Their surface activity and their ability to solubilize effectively large portions of oil in water, water in oil, and sometimes both in one phase means that surfactants are also at the heart of an uncountable number of industrial processes. The best commercial and scientific use of natural and synthetic surfactants requires a complete understanding of how surfactants form structure and how those structures affect the bulk and interfacial macroscopic properties of mixtures and solutions containing them.

The problems addressed in this thesis have their origin in previous work directed by Professors H. T. Davis and L. E. Scriven with contributions from Professors W. G. Miller and S. Prager. Earlier Ph.D. candidates J. C. Hatfield, E. I. Franses, and J. E. Puig pioneered at Minnesota with researches aimed at understanding the types of structures present and possible in surfactant solutions which generate ultralow ($< 10^{-3}$ dyne/cm) interfacial tensions between oil and water. Their success in identifying surfactant mixtures that produce ultralow tensions and, as a result, possess interesting microstructure led directly to the studies of vesicles and micelles presented here. In parallel investigations, Hatfield and K. E. Bennett explored the properties of microemulsions formed with the same surfactants which were found to produce ultralow interfacial tensions between oil and water. Their electrical conductivity measurements and Bennett's viscosity and phase behavior observations paved the way for the SAXS studies of microemulsions that are at the heart of this thesis.

Several experimental techniques were employed by Franses, Puig, Bennett and Hatfield. One of Hatfield's ventures was a new tool — fast-freeze cold-stage transmission electron microscopy — which was subsequently developed by Y. Talmon. Talmon's technique allows direct visualization of rapidly frozen surfactant samples, but the method suffers from artifacts caused both by freezing and by electron beam damage. Thus the stage was set for two acts: one was introduction of new noninvasive techniques capable of yielding more detailed information about surfactant structures than those that were in use; the second was simultaneous provision of a way to identify the artifacts generated in electron microscopy. Two noninvasive ways to examine the organization in surfactant solutions are small-angle x-ray scattering (SAXS) and quasi-elastic light-scattering (QLS). This thesis describes the application of these techniques to microemulsions, mixed micelles and vesicular dispersions.

Microemulsions have been defined as thermodynamically stable, optically isotropic liquid phases containing hydrocarbon, water (or brine) and surfactant

(1). Usually, though not always, an alcohol or other amphiphilic cosurfactant is necessary for microemulsion formation. The amphiphilic nature of the surfactant forces it to locate as a more or less two-dimensional sheet or envelope between three-dimensional water-rich and hydrocarbon-rich regions in the microemulsion and thus imposes some intermolecular order and heterogeneity. The length scale of the inhomogeneities can vary from the length of the surfactant molecule upwards, but the long-range order is stochastic and microemulsions are of low viscosity. Microemulsions have come under increasing study recently because their ability to produce ultralow interfacial tensions ($< 10^{-3}$ dyne/cm) between oil and water makes them attractive candidates for enhanced oil recovery processes.

Lacking in the above definition of microemulsion is any description of the form of the microstructure present. At low volume fractions of dispersed oil (or water), there seems little doubt that microemulsion is a solution of swollen (inverted) micelles (2,3). At higher volume fractions of the dispersed component, however, interpretation of the experimental data becomes ambiguous and the microemulsion structure is not well known. At least two views of the structure at intermediate oil-water ratios have been put forth.

One representation of the structure holds that as the volume fraction of oil (or water) in the microemulsion is increased, the swollen (inverted) micelles present at low concentrations in either an oil-in-water (o/w) or water-in-oil (w/o) microemulsion simply pack together. In this view, at a composition near an oil-water ratio of one, the microemulsion abruptly inverts from one structure to another (Fig. 1). Despite the simplicity of this view, and its wide-

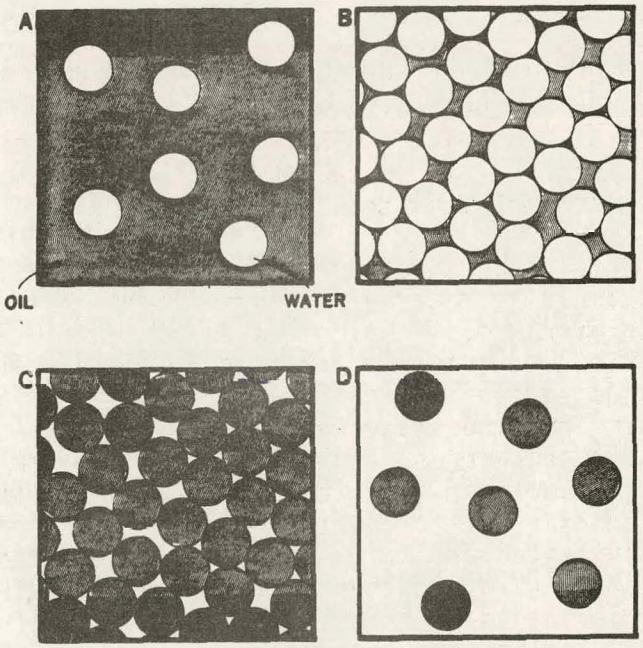

Fig. 1. Possible changes in microemulsion structure as the oil-to-water ratio decreases. A) dilute w/o droplets. B) concentrated w/o droplets. C) inversion to concentrated o/w droplets. D) dilute o/w droplets.

spread acceptance (2,4-9), examination of a schematic phase diagram (Fig. 2) reveals its crucial inadequacy. The unsuitability of a model calling for an abrupt transition is made evident by the presence of the one-phase corridor between the water-rich and oil-rich corners of the diagram (dashed line in Fig. 3), the presence of which implies that there is a continuous progression of fluid structures from swollen micelles in one corner to swollen inverted micelles in the other. In addition, there is no evidence for an abrupt structural inversion in our measurements, or in careful measurements by others.

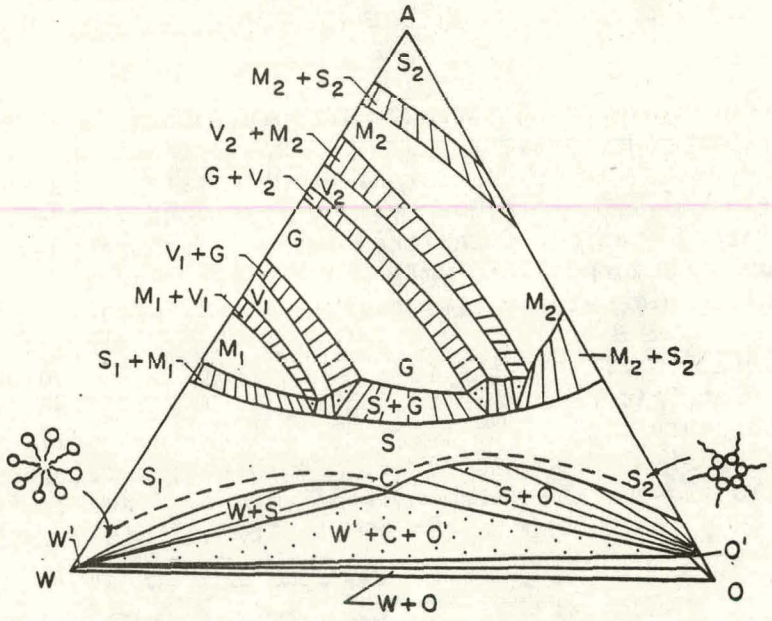

Fig. 2. A schematic phase diagram showing the continuous path (dashed line) from water-rich microemulsion (S_1) to oil-rich microemulsion (S_2).

Another view examined here which obviates the necessity for an abrupt structural inversion is one that admits bicontinuous microemulsion structures over a wide range of intermediate water-oil ratios. Such bicontinuous structures (10) contain oil-rich and water-rich domains that are sample spanning but that divide and intertwine chaotically so that the microemulsion has no long-range geometric order. The oil-rich and water-rich domains in these equilibrium microstructures are assumed to be stabilized by sheet-like surfactant-rich regions at the boundaries between domains. That microemulsion viscosities are often low (11) suggests that the hypothesized bicontinuous structures are fragile and easily deformed. In this view, the oil-rich and water-rich domains are dynamic and fluid arrangements that continually deform and may even form and reform. Nonetheless, the sheet-like surfactant regions impose topological order in the microemulsion by separating the oil-rich and water-rich domains. Because chaotically bicontinuous states can easily break down into micelle-like dispersions as the water-oil ratio becomes much different from unity, the bicontinuous view provides the simplest explanation of the observed continuous transition in microemulsion structure from disjoint swollen micelles at low volume fractions of oil to disjoint swollen inverted micelles at high oil concentrations. Fig. 3 illustrates how microemulsion microstructure would evolve when bicontinuous states are present, and Fig. 4 is a representation of a bicontin-

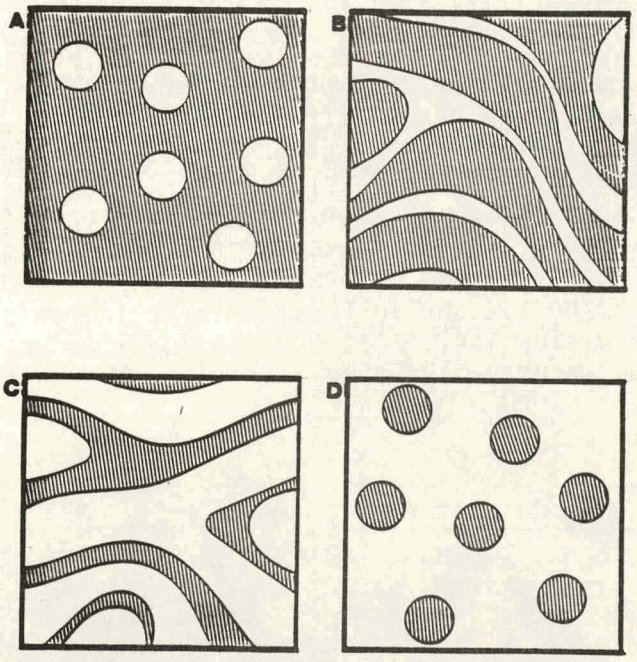

Fig. 3. Possible changes in microemulsion structure as the oil-to-water ratio decreases (compare Fig. 1). A) dilute w/o droplets. B) oil-rich bicontinuous structure. C) water-rich bicontinuous structure. D) dilute o/w droplets.

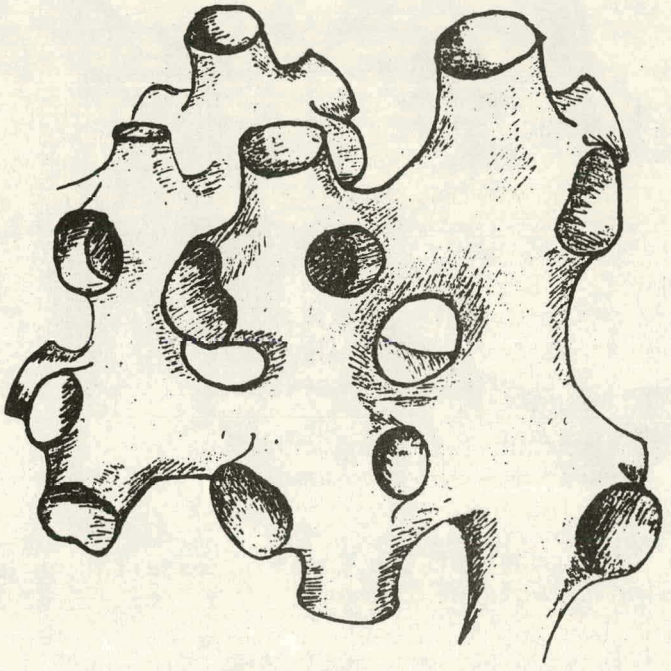

Fig. 4. Conception of an irregular, multiply-connected bicontinuous surface.

uous structure. Because the hypothesis of bicontinuous structures includes the idea of disjoint micellar structures when the oil-to-water ratio is far from one, operationally the question lies in identifying the width of the transition zone between disjoint and bicontinuous structures.

An attempt to quantify the concept of bicontinuous microemulsion structure was first made by Talmon and Prager (12). For simplicity, they used a completely random geometry of oil-rich and water-rich domains constructed with the aid of a Voronoi tessellation. The Voronoi model (Fig. 5) naturally and conveniently represents all three types of possible structure as the oil-to-water ratio varies. Talmon and Prager's success in accounting qualitatively for microemulsion phase behavior was followed by electrical conductivity calculations (13) for the Voronoi tessellation, and by calculations of the interfacial structure of microemulsion (14). The Voronoi model is an extreme representation of bicontinuous structure because it is totally random.

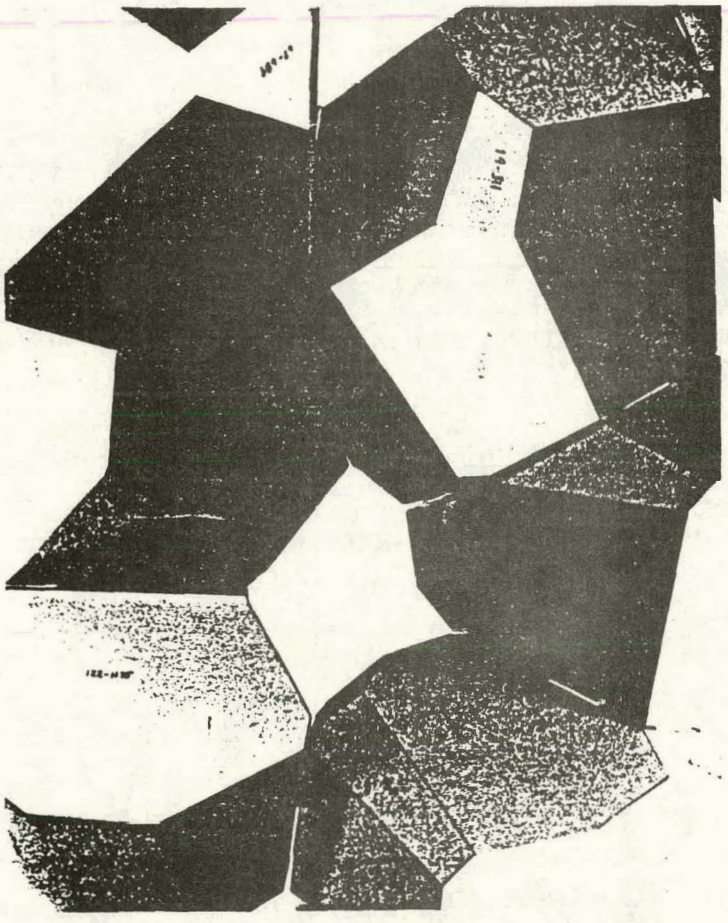

Fig. 5. Photograph of a model of the Voronoi tessellation used to represent microemulsion structure. Compare with Fig. 4.

The Voronoi model has also been used to predict both the static and dynamic scattering expected from a bicontinuous microemulsion. The predictions,

which are in Chapter 3, establish that many of the scattering results heretofore interpreted in terms of swollen micellar structures (6,9) can be accounted for equally well by bicontinuous structures and the micellar structures into which they evolve.

The idea that bicontinuous structures exist in microemulsions at oil-water ratios near unity is discussed further in Chapters 5 and 6. The results for a swollen-micelle arrangement, represented as a solution of interacting, monodisperse spherical structures with a hard-sphere interaction law augmented by a mean-field attraction term, are compared with the results of the Voronoi model described above. The Voronoi representation calls naturally for disjoint polydisperse micellar structures at volume fractions of the disperse phase below 0.16 (the percolation threshold). However, the degree of polydispersity in the Voronoi model is not large (13), and calculations show (15,16) that including the same amount of polydispersity in the hard-sphere model yields a result only slightly different from that gotten for a monodisperse system. Furthermore, inclusion of an adjustable swollen micelle size distribution would increase the already considerable number of parameters available in the swollen-micelle representation.

Chapters 5 and 6 also contain electrical conductivity and SAXS results from measurements on microemulsions formed from a pure alkyl aryl sulfonate (sodium 4-(1'-heptylnonyl)benzenesulfonate) and from a commercial mixture of petroleum sulfonates. A comparison of a prediction from the Voronoi model and the results of SAXS experiments on microemulsions made with both the pure and the commercial surfactant is shown in Fig. 6. The key results along with the various predictions of the models are summarized in Table 1.

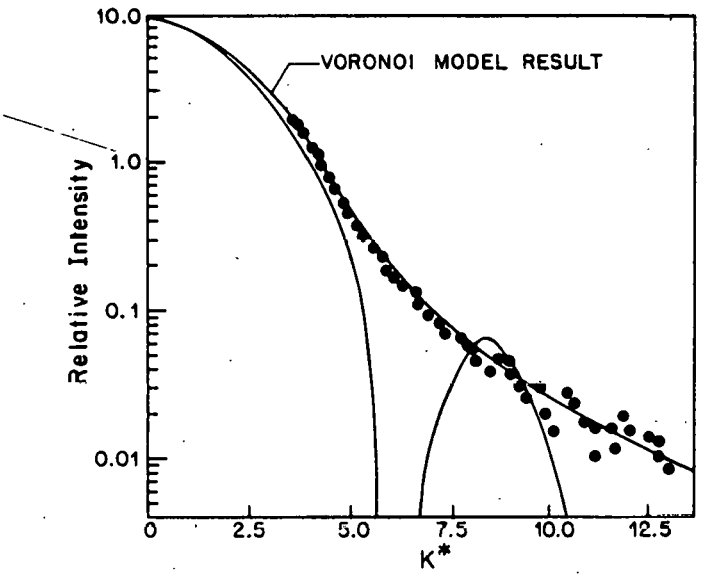

Fig. 6 A) Scattering curve predicted from the Voronoi model with data points from an SHBS microemulsion containing 46 wt% dodecane and 49 wt% water. The scattering curve from a single sphere of the same apparent size is shown for comparison.

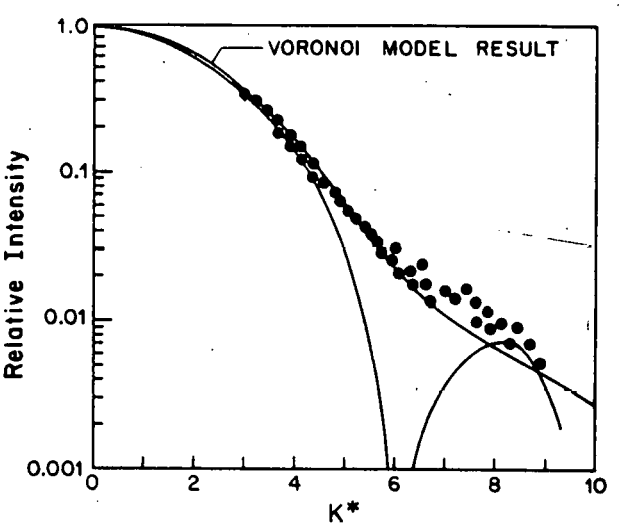

Fig. 6. B) Voronoi scattering curve and data points from a TRS 10-80 microemulsion containing 70 wt% octane and 25 wt% water.

TABLE I MEASUREMENT or OBSERVATION	PURE SURFACTANT		MIXED SURFACTANT	
	MONODISPERSE HARD-SPHERE MODEL	VORONOI MODEL WITH BICONTINUOUS STRUCTURES*	MONODISPERSE HARD-SPHERE MODEL	VORONOI MODEL WITH BICONTINUOUS STRUCTURES*
Electrical conductivity-percolation threshold and ϕ dependence	INCONSISTENT	CONSISTENT	INCONSISTENT	CONSISTENT
SAXS - scattering curves	INCONSISTENT without an adjustable polydispersity function	CONSISTENT at intermediate volume fractions	INCONSISTENT without an adjustable polydispersity function	CONSISTENT at intermediate volume fractions
- $I(0)/Q$ vs. ϕ	CONSISTENT for $\phi_D < 0.5$	CONSISTENT OVERALL	CONSISTENT for $\phi_D < 0.5$	INCONCLUSIVE
- R_{ga} vs. ϕ	CONSISTENT For $\phi_D < 0.15$	CONSISTENT OVERALL	CONSISTENT for $\phi_D < 0.2$	INCONCLUSIVE
- $I(0)/Q - R_{ga}^3$	INCONSISTENT	CONSISTENT	INCONSISTENT	CONSISTENT
Phase behavior	INCONCLUSIVE	CONSISTENT	INCONCLUSIVE	CONSISTENT

SYSTEMS EXAMINED BY OTHERS

MEASUREMENT	PURE SURFACTANT	
	MONODISPERSE HARD-SPHERE MODEL	VORONOI MODEL WITH BICONTINUOUS STRUCTURES*
QLS - scattering curves with nonexponential decay 1)	INCONSISTENT	CONSISTENT
- K-dependent diffusion coefficient 1)	INCONSISTENT	CONSISTENT
SANS and QLS 2)	CONSISTENT with an adjustable polydispersity function	INCONSISTENT
Radioactive tracer diffusion 3)	INCONSISTENT	CONSISTENT
Electrical conductivity 4)	CONSISTENT	CONSISTENT

* AND POLYDISPERSE DISCRETE STRUCTURES

Note that the comparison is of models that differ in two respects: size distribution of discrete elements, and presence of bicontinuous structures.

1) Bellocq et al. (1980). Ref. 9
2) Cebula et al. (1981). Ref. 4
3) Lindman et al. (1980). Ref. 18
4) Clausse et al. (1982). Ref. 17

Table 1 Comparison of the two representations of microemulsion structure with the experimental results.

From these results, we conclude that in multiphase microemulsions there are large composition regions where the Voronoi model — a completely random representation of polydisperse discrete structure that evolves into mostly bicontinuous structure at oil-water ratios around unity — agrees well with the experimental data. The available hard-sphere *monodisperse* swollen micellar representations can not correlate the same results; however, there are likely regions where a model of *polydisperse* disjoint micelles may be accurate. The discussion in Chapters 1, 5 and 6 develops the idea that the bicontinuous structures are chaotic and have no long-range geometric order, but retain the topological order imposed by the amphiphilic nature of the surfactant. They are much like disordered viscous isotropic liquid crystals. Elucidation of microemulsion structure must wait, however, fuller understanding of the molecular forces which dictate how surfactants arrange themselves in solution.

To build the base of experimental data on which such an understanding of surfactant molecular forces can rest, Chapters 7 and 8 describe studies of two simpler types of surfactant microstructure: vesicles and mixed micelles.

The results of a study of the vesicles formed by sonication of aqueous dispersions of liquid crystals of the double-tailed surfactant sodium 4-(1'-heptylnonyl)benzenesulfonate by several techniques are reported in Chapter 8. Vesicles are solvent-filled spheroidal shells consisting of one or several bilayers. They are valuable models for biological membranes and may serve as delivery vehicles for drugs. Corroboration of the results of several experimental techniques, particularly electron microscopy, reveals the sources of artifacts which routinely obscure the observations reported by others.

The main results are 1) the average diameter of the vesicles prepared in water is about 450Å. 2) The average size decreases when prepared in NaCl or at higher surfactant concentrations. 3) The presence of a few large liquid crystallites in the dispersion, as detected by fast-freeze cold-stage transmission electron microscopy, is shown to bias severely the measurement of vesicle sizes by quasielastic light scattering techniques. 4) The commonly used techniques of gel permation chromatography and ultrafiltration are shown to be ineffective in separating liquid crystals from SHBS vesicle dispersions. 5) The spontaneous, irreversible reversion of vesicles to liquid crystallites as the dispersions age is documented and proves that SHBS vesicles are not equilibrium structures in water or brine.

Chapter 7 details the results of a study of a mixed micellar solution that is unique in that the micelles occur in a mixture containing a surfactant that produces micelles alone (SDS) and one that forms liquid crystals alone (SHBS). The principal findings are that 1) addition of SHBS to SDS increases the micelle molecular weight. 2) Mixed micelles are cylindrical (prolate) at SDS/SHBS weight ratios of 10/1 and 5/1 in 0.3M and 0.6M NaCl, but may be disk-like (oblate) at an SDS/SHBS ratio of 3/1 in 0.3M NaCl. 3) Addition of SHBS to SDS lowers the critical micelle concentration and the critical micellization temperature in both 0.3M and 0.6M brine.

The thesis concludes with an appendix describing a state-of-the-art small-angle x-ray camera assembled at the University of Minnesota. It is equipped

with a position-sensitive detector and a sample cell suitable for measurements on temperature-sensitive liquid samples. The appendix also contains a description of a complete FORTRAN library of SAXS data analysis routines and examples of their use.

The results laid out in this thesis shed some light on the mysteries of surfactant microstructure, but much remains to do. The Voronoi model used to represent the bicontinuous microemulsion states is only one possible realization of bicontinuous structure. D. M. Anderson is now working to relate other models of bicontinuous structures to the results of measurements on microemulsions in order to test further the idea of bicontinuous microemulsion phases. Just as the Voronoi model is only one possible representation of bicontinuous structure, the multiphase microemulsions studied experimentally occur in only one portion of a phase diagram. Further experimental investigation, particularly using SAXS, of the one-phase microemulsions studied by others would be useful. In addition, understanding how microemulsions relate to the liquid crystal phases formed at higher surfactant concentrations, the subject of investigations being made by A. Papaionnou and W. F. Michels — likely will provide valuable insights into how and why microemulsions form.

Similar questions remain about the simpler vesicular and micellar systems. How vesicles form and how and why they revert to liquid crystallites are questions that can only be answered when fuller understanding of the intermolecular forces governing surfactants is in hand. These same forces presumably dictate the size and shape of micelles in solution. Continuing cold-stage microscopy work (J. A. Zasadzinski) may provide the final resolution of the questions of surfactant structures — an artifact-free three-dimensional image. These and other results provide the test for present theories and point the way for future understanding of surfactant microstructures.

References Cited in Section XV

1. Danielsson, I. and Lindman, B., Colloids and Surface 3, 391 (1981).

2. Gulari, E., Bedwell, B. and Alkhafaji, S., J. Colloid Interface Sci. 77, 202 (1980).

3. Zulauf, M. and Eicke, H.-F., J. Phys. Chem. 83, 480 (1979).

4. Cebula, D. J., Ottewill, R. H., Ralston, J. and Pusey, P. N., J. Chem. Soc., Faraday Trans. 1 77, 2585 (1981).

5. Dvolaitzky, M., Gruyot, M., Lagues, M., Le Pesant, J. P., Ober, R., Sauteray, C. and Taupin, C., J. Chem. Phys. 69, 3279 (1982).

6. Ober, R. and Taupin, C., J. Phys. Chem. 84, 2418 (1980).

7. Cazabat, A. M., Langevin, D. and Pouchelon, A., J. Colloid Interface Sci. 73, 1 (1980).

8. Agterof, W. G. M., van Zomeren, J. A. J. and Vrij, A., Chem. Phys. Lett. 43, 363 (1976).

9. Bellocq, A. M., Fourche, G., Chabrat, J. P., Letamendia, L., Rouch, J. and Vaucamps, C., Opt. Acta 27, 1629 (1980).

10. Scriven, L. E., in Micellization, Solubilization and Microemulsions, ed. K. L. Mittal (Plenum, New York, 1977) 877.

11. Bennett, K. E., Hatfield, J. C., Davis, H. T., Macosko, C. W. and Scriven, L. E., in Microemulsions, ed. I. D. Robb (Plenum Press, New York, 1982) 65.

12. Talmon, Y. and Prager, S., J. Chem. Phys. 69, 2984 (1978).

13. Winterfeld, P. H., Ph.D. Thesis, University of Minnesota (1981).

14. Talmon, Y. and Prager, S., J. Chem. Phys. 76, 1535 (1982).

15. Vrij, A., J. Chem. Phys. 71, 3267 (1979).

16. van Beurten, P. and Vrij, A., J. Chem. Phys. 74, 2744 (1981).

17. Clausse, M., Heil, J., Peyrelasse, J. and Boned, C., J. Colloid Interface Sci. 87, 584 (1982).

18. Lindman, B., Kamenka, N., Kathopoulis, T. M., Brun, B., Nilsson, P. G., J. Phys. Chem. 84, 2485 (1980).

XVI. FLUID MICROSTRUCTURES, PHASE AND TENSION BEHAVIOR OF AMPHIPHILE-HYDROCARBON-WATER-SALT SYSTEMS: SYNOPSIS OF PH.D. THESIS OF J. E. PUIG

The material reported here is taken from J. E. Puig's Ph.D. thesis which can be obtained from University Microfilm International at the University of Michigan.

Introduction

Surfactants can form a wealth of fluid microstructures with water, oil, and various additives. In water most surfactants form closed equilibrium aggregates called micelles, above what is known as the Krafft temperature and above what is termed the critical micellization concentration (1-3). Certain double-tail surfactants, e.g. phospholipids, at low concentrations in water form lamellar liquid crystals and closed nonequilibrium aggregates called vesicles, but not micelles (4-6). At higher concentrations surfactants can form a variety of liquid crystalline states, or mesophases, such as hexagonal, lamellar, and cubic phases (6-9). In organic solvents surfactants can form inverse micelles (10,11) and liquid crystalline phases (12,13). Under certain conditions, surfactants can solubilize substantial amounts of water and hydrocarbon to form microemulsions, although the presence of a cosolvent is often required (14-19). However, amphiphiles which do not qualify as surfactants, e.g. alcohols, can also solubilize substantial amounts of water and hydrocarbon in isotropic solutions (20-24). Moreover, it has been shown (21,22) that the patterns of phase behavior of surfactant-oil-brine systems of the sort employed in immiscible microemulsion flooding processes for enhancing oil recovery (18) are reproduced by certain alcohol-hydrocarbon-brine systems. Evidence is presented in Chapter 4 that indicate that alcohol-hydrocarbon-brine systems also imitate the main features of the tension behavior of microemulsions systems (18).

The phase and tension behavior of aqueous-oleic systems are modified dramatically by surfactants as well as by the microstructures which they form. In the absence of surfactants, water and oil are immiscible and the interfacial tensions between them is typically 20 to 50 dynes/cm. By adding a surfactant some oil can be solubilized into the aqueous phase and vice versa; the interfacial tension usually drops to values of a few dynes/cm. However, under very narrow circumstances, ultralow tensions (less than 0.01 dyne/cm) are obtained (25-29). One mechanism to recover residual oil from underground reservoirs requires such ultralow tensions (26,30,31). Ultralow tensions can be readily obtained with commercial petroleum sulfonates; these are relatively inexpensive complex mixtures of anionic surfactants. However, ultralow tensions are extremely sensitive to surfactant structure and concentration, concentration of electrolytes and cosolvents, temperature, and other factors (26,28,29,33,34). Against these parameters, interfacial tension between oil and aqueous preparations of petroleum sulfonates goes through a sharp and deep minimum. In Chapters 5 to 7 of the thesis I present evidence that shows that ultralow tensions in surfactant systems are brought about not by surfactant monolayer adsorption (which had been the general belief), but by certain equilibrium microstructured phases which are microemulsions or surfactant-rich third phases perhaps related to liquid crystalline phases. The evidence includes that adduced by E. I. Franses in earlier research (35), which I have extended in several directions. The

scientific investigation described here to elucidate the origins of ultralow tensions in surfactant systems is the result of a group effort that started in the summer of 1972 under the direction of H. T. Davis and L. E. Scriven, who were subsequently joined by W. G. Miller. C. D. Manning (36) and Y. Seeto (37) with their work on tensiometry and effects on interfacial tension of order of mixing and age of surfactant preparations, and J. C. Hatfield (38) with his research on microemulsions, laid the foundations for subsequent investigation. The structure on which my research rests was built by E. I. Franses (35) with his work on phase behavior and interfacial tension of surfactant systems representative of surfactant waterflooding processes. Important contributions to the framework were also made by Y. Talmon, P. K. Kilpatrick, E. W. Kaler, A. H. Falls, F. D. Blum, and P. S. Russo.

One of the major drawbacks of surfactant flooding is the retention of surfactants by reservoir rocks (39,40). If retention is excessive, surfactant is depleted from the injected slug — this being a volume of surfactant preparation which is usually but a fraction (5 to 50%) to the reservoir pore volume — as it moves through the rock; consequently, the slug loses the ability to lower interfacial tension (32,39,40) and, hence, to mobilize residual oil. So it is important to determine how surfactants are retained by porous rock as well as to find means to reduce retention. The mechanisms by which surfactants are lost to the reservoir are well-known (41-43). What is new is my finding that the amount of surfactant retained is related to the types and sizes of the surfactant-rich microstructures in the injected preparations (Chapter 8). By pretreating the surfactant preparations to reduce mean size of surfactant-rich microstructures, losses by physical entrapment are reduced dramatically.

The thesis focuses on the fluid microstructures and closely related states that are involved in surfactant waterflooding. I present a concerted study of a petroleum sulfonate surfactant system representative of surfactant waterflooding and of pure surfactant systems that mimic it. I review in Chapters 5 to 8 and summarize in Chapter 9 the relationships between surfactant-rich microstructures and their compositions, recovery of residual oil from short Berea sandstone cores, and surfactant retention in such cores. In Chapter 4 I test the hypothesis that the phase and tension behavior of surfactant-oil-brine systems which form microemulsion phases in equilibrium with aqueous and oleic phases are characteristic of all amphiphile-oil-brine systems. The organization of the thesis is shown in Table 1.

In the remainder of this chapter I give the background of the thesis, summarize the major findings, and describe the strategy for the thesis research.

Fluid Microstructures

Interfacial phenomena are involved in important ways in engineering processes (e.g. oil recovery, food processing) and products (e.g. detergents and emulsifiers) as well as biological mechanisms (e.g. transport processes of living organisms) and materials (e.g. biomembranes). Intimately associated and often directly responsible for interfacial properties are what we call fluid microstructure. A fluid microstructure is a region in a fluid in which densities and/or compositions vary appreciably over distances of the order of magnitude of the range of intermolecular interactions (44). Examples of fluid microstruc-

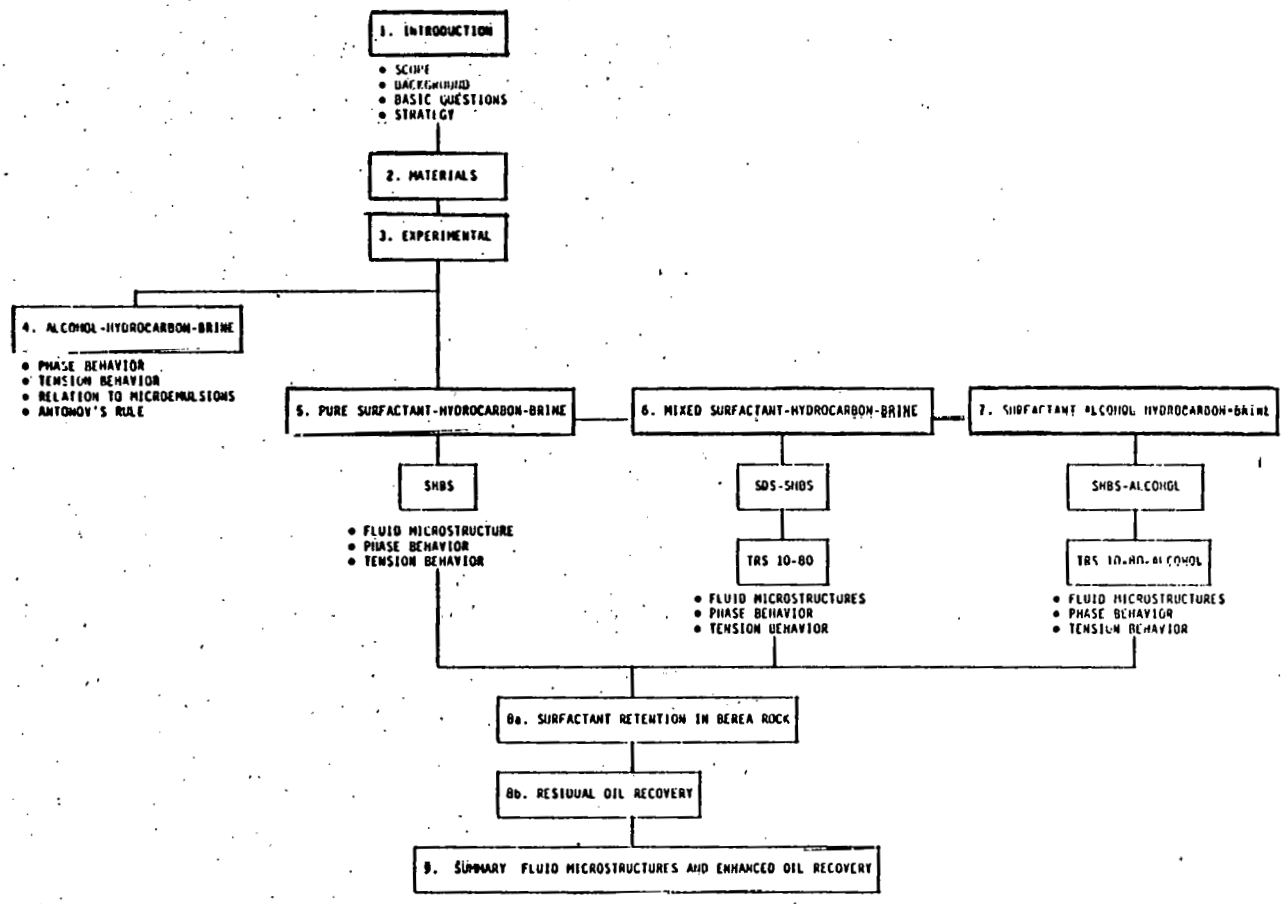

Table 1 Organization of the thesis.

tures include fluid-fluid interfaces, the fluid side of fluid-solid interfaces, thin-film states of fluid materials, micelles and other equilibrium and non-equilibrium colloidal particles of fluid character.

Of particular relevance to this research are those fluid microstructures which amphiphiles form with water and organic solvents, e.g. micelles, microemulsions, liquid crystals and related mesophases, and the like.

Amphiphiles: Surfactants

Amphiphiles are substances in which the molecules possess both hydrophilic (water soluble) and oleophilic (oil soluble) moieties joined by covalent bonds. According to IUPAC (45), surfactants are substances which lower the surface

tension of the medium in which they are dissolved and/or the interfacial tension with other phases. It is generally accepted (1,3,46) that surfactant molecules must have amphiphilic or dual nature. Because of this amphiphilic character, surfactants are adsorbed at interfaces, lower interfacial tension, and aggregate in bulk phases. However, not all amphiphiles are surfactants. For instance, alcohol and amines are amphiphiles which are adsorbed at interfaces and lower interfacial tension of water/air and water/oil interfaces (47,48); they also associate in chains in aqueous and oleic bulk phases (49,50); but they are not regarded as surfactants. Laughlin (51) emphasizes that tension lowering and amphiphilic character are not sufficient; he reserves the term surfactant for molecules which also form micellar aggregates and liquid crystals in the presence of varying amounts of water. However, there are surfactants which do not form micelles in water, although they do form liquid crystalline phase (6,35). Kilpatrick (23) is investigating the transition zone that separates surfactants from "simple" amphiphiles. In this thesis I take as surfactants those amphiphiles which are able, or which I presume to be able, to associate in sheet-like structures in aqueous and organic bulk phases as well as at interfaces, their hydrophilic moieties lying on one side of the sheets and the oleophilic moieties on the other (52).

Depending on the polar group, surfactants are classified as ionic, which may be anionic or cationic, nonionic, and zwitterionic. The increasing practical importance of and scientific interest in surfactants is demonstrated by the many reviews and books published in the last twenty years (46,53-57).

Micelles

Surfactants in solution are often association colloids, that is, they tend to form micelles, meaning aggregates of colloidal dimensions existing in equilibrium with the molecules or ions from which they are formed (45). The word micelle, from the latin micella meaning small bit, was introduced by McBain (58) to describe the formation of globular colloidal particles in solutions of soaps.

While the concept of micelle formation has general acceptance as the cooperative self-association of amphiphiles, it is also used somewhat unsystematically in reference to other types of aggregation (59), for example the cooperative or noncooperative association into small aggregates, and even the noncooperative association into big aggregates that a number of dye compounds exhibit. The term micelle has also been employed to describe microscopic or submicroscopic particles of a second phase (34,60,61), nonequilibrium biological aggregates or vesicles (62), and the basic structural units of liquid crystalline phases (63). We prefer a more restricted definition of micelle (35): "A micelle is a stable, disjoint, cooperative, topologically ordered, closed, equilibrium colloidal aggregate of amphiphilic molecules." The topological ordering of micelles in water is the hydrated polar heads on the outside facing toward the surrounding solvent and the hydrophobic chains on the inside forming the core which is liquid-like (64). In organic solutions micelles have inverse structure, i.e. the polar groups form the core whereas the hydrophobic chains face outward toward the solvent; so they are referred as inverse micelles.

Micelles first appear within narrow ranges of surfactant concentration, i.e. there is a relatively small range of concentrations separating the limit below which virtually no micelles are detectable and the limit above which virtually all additional surfactant forms micelles (2). Many properties of surfactant solutions, if plotted against concentration, appear to change at a different rate above and below this range (Fig. 1). By extrapolating the loci of such a property above and below this range until they intersect, a value known as the critical micellization concentration, or c.m.c., is obtained (2). Because the values obtained using different properties are not quite identical, the method by which a c.m.c is determined should be clearly stated.

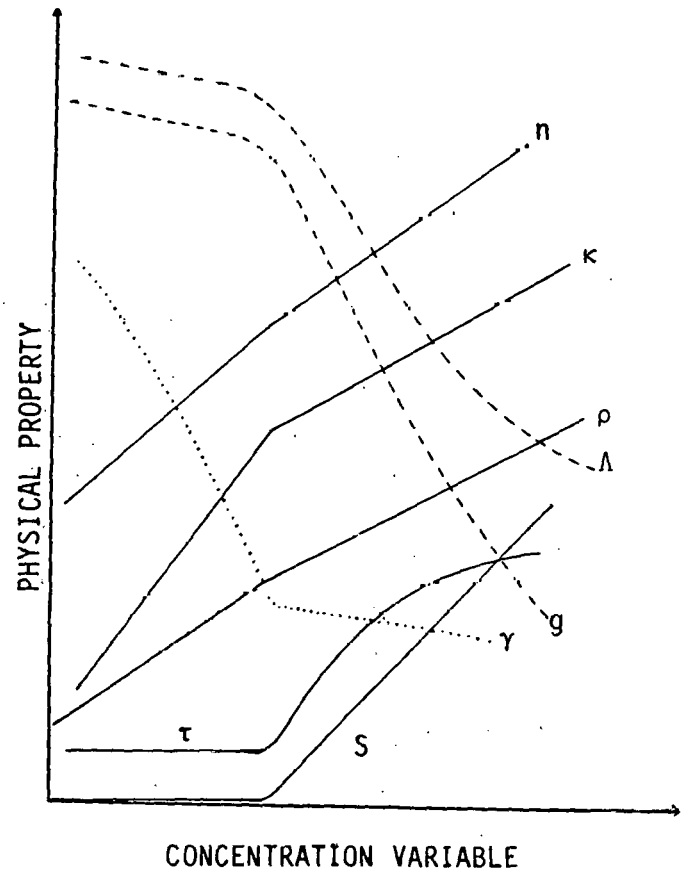

Figure 1. Change of physical properties with concentration variable in vicinity of c.m.c.: n-refractive index, κ-electrical conductance, ρ-density, Λ-equivalent conductivity, g-osmotic coefficient, σ-surface tension, τ-turbidity and S-solubility of organic compound (from (1)).

The existence of a c.m.c. is reflected in a change in the concentration dependence of various properties of the solution over a narrow range. The reverse is, however, not necessarily true. For instance, the concentration dependence of a physicochemical property of a surfactant solution can and in many instances does vary abruptly at the solubility limit. If the solubility limit is low and the particles of the second phase are submicroscopic, the sol-

ubility limit can be mistaken, and it has been mistaken (34,61), for the c.m.c. phenomenon. The distinction is important. At a solubility limit a new phase appears, the chemical potential of which is independent of its amount and its state of dispersion. In contrast, beyond the c.m.c. a characteristic population of the equilibrium fluid microstructures known as micelles appears, the chemical potential of which depends on the concentration of surfactant monomers in solution, and continues to vary, though only slightly, with further increase in total surfactant concentration. Hence it is important to determine that indeed below the c.m.c. the solution is mainly monomeric whereas above it the number of micelles — micelles as defined above — increases rapidly with concentration.

At surfactant concentrations that are slightly above the c.m.c. the micelles give evidence of being spherical (65), or at least globular. As the concentration is increased, certain properties of the solution indicate a change in the micellar structure, probably primarily due to interaction between the micelles, e.g. alterations in the electrical double-layers of the normal micelles of anionic surfactants (8). At still higher concentrations the micelles become cylindrical or perhaps take on lamellar character (63,66,67) and, ultimately, when more or less random orientation of the micelles becomes impossible, a phase transition from micellar solution to liquid crystal or related mesophases intervenes.

Liquid Crystalline Phases

Liquid crystals represent a number of states of matter in which the degrees of molecular order lie intermediate between the almost perfect long-range positional and orientational order of solid crystals and the statistical long-range disorder of ordinary isotropic amorphous liquids (7). Liquid crystalline phases are also known as mesophases, a term introduced by Friedel (68). Mesomorphism can be induced by increasing the temperature of certain pure compounds or by adding suitable solvents to them. Temperature-induced liquid crystals are known as thermotropic liquid crystals, and those which form by addition of solvent are known as lyotropic liquid crystals.

Amphiphilic compounds frequently form lyotropic liquid crystalline phases, either at room temperature or at higher temperatures, by incorporating into their structures considerable amounts of water and/or organic solvents. Many amphiphiles can also form thermotropic liquid crystals.

Certain substances which are not amphiphiles, in particular nonpolar and moderately polar compounds with fairly rigid "rod"- or "lath"-like molecules, and in some instances globular molecules, can also form lyotropic and thermotropic liquid crystals. Non-amphiphilic mesophases are beyond the scope of this thesis; the interested reader is referred to the books of Gray (69), Gray and Winsor (7), and de Gennes (70).

The most common and well-established of lyotropic liquid crystalline phases are the lamellar, the hexagonal, and the viscous-isotropic phases. The classification is based on the type of low-angle X-ray diffraction patterns obtained form each phase (71-73).

The lamellar phase, also known as neat phase, has the structure illustrated in Fig. 2A. The surfactant molecules are arranged in fluid, parallel bilayers separated by solvent (water) layers. The layers extend over large distances, commonly of the order of microns or more. The water layers can vary from about 8Å to more than 100Å depending on the water content, while the surfactant layer thickness is generally about 10-30% less than the length of two all-trans surfactant chains (6,74,75). This structure is consistent not only with many X-ray studies (71,73,74,76,77), but also with electron micrographs (78), NMR linewidths and chemical shifts (79), and optical textures in the polarizing microscope (80-82).

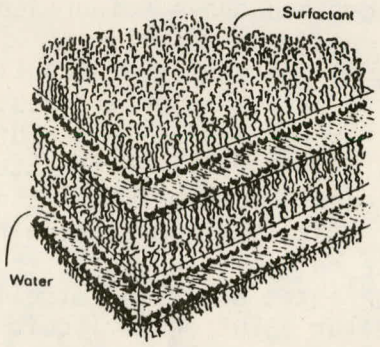

(A)

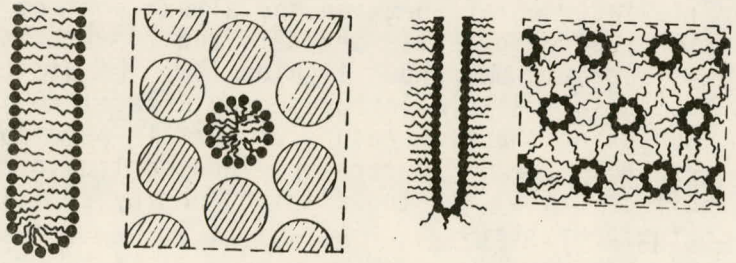

(B) (C)

Figure 2. Representation of (A) lamellar liquid crystalline phase; (B) normal hexagonal phase; (C) reversed hexagonal phase (from 83).

There are two well-established structures for the hexagonal liquid crystalline phase: the normal hexagonal or middle phase (Fig. 2B), and the inverse hexagonal phase (Fig. 2C). The hexagonal phase consists of rod-shaped micelle-like units of indefinite length packed in a hexagonal array and separated by a continuous water region. In the inverse hexagonal phase, the hydrocarbon chains occupy the space between the hexagonally-packed water cylinders of indefinite length. The normal and the inverse hexagonal phases as well as the lamellar phase can be identified by their characteristic textures in the polarizing microscope (80-82).

The existence of viscous-isotropic mesophases, also known as cubic phases, is established beyond doubt. However, their phase structures are not as well-established as those of the hexagonal and lamellar phases (6,9,84). Viscous-isotropic phases are optically isotropic phases of very stiff consistency — high viscosity — which give X-ray diffraction patterns in the low-angle region usually consistent with a three-dimensional crystalline cubic pattern (73). There are at least two types of cubic phase structure, and these can occur in the normal (i.e. water continuous) or reverse (i.e. oil continuous) form. One proposed structure for these phases is normal or inverted globular micelle-like aggregates in some type of cubic array (73). Figure 3A shows an example of a face-centered structure (8). Another type of structure (Fig. 3B) has short surfactant rods joined to form a continuous network (85,86). The main evidence for these structures is X-ray data backed up by NMR spectroscopic measurements, but their validity has been questioned (9,84,87). Fontell (9,84) has suggested several alternative structures, notably bicontinuous structures (see Fig. 3C) first proposed by Scriven (88,89). Incidentally, Scriven (90) has raised the possibility that geometrically disordered but topologically ordered bicontinuous viscous isotropic phases are what birefringent lamellar liquid crystals of SHBS form on addition of oil, i.e. what we call surfactant-rich third phases (Chapter 5), and that these can be continuously converted to microemulsion by addition of alcohol (Chapter 7).

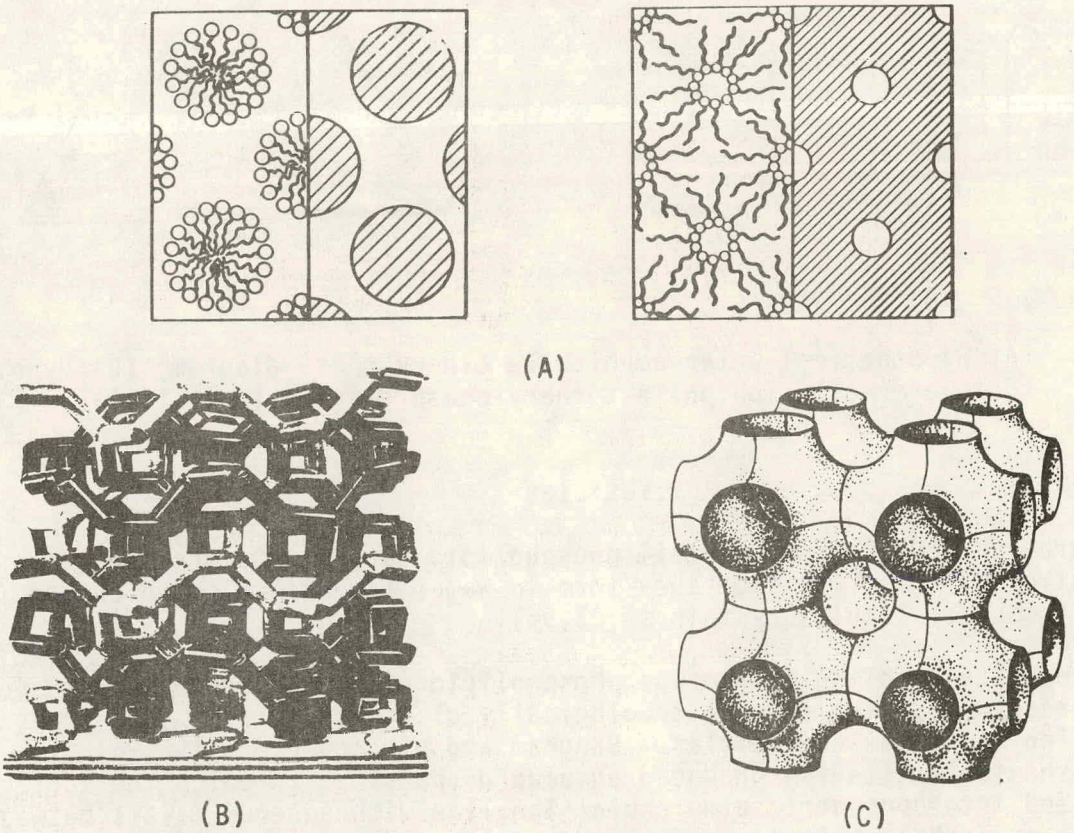

Figure 3. Representation of (A) face-centered structure of normal and reversed forms of cubic phase (91); (B) continuous network of surfactant-rods structure of cubic phase (85); (C) bicontinuous structure (88,89).

At constant temperature, as the surfactant concentration is increased in water-surfactant binary systems, one usually encounters the sequence: isotropic micellar solution — hexagonal phase — lamellar phase — reversed hexagonal phase — low-water phases (crystalline solid, isotropic solution or melt), but other liquid crystalline phases may be interspersed between these phases. Figure 4A is a hypothetical water surfactant binary phase diagram (89). The nomenclature is that of Winsor (63). Notice that each mesophase is a separate phase and that a two-phase region must separate two adjacent mesophases. Phase behavior of water and surfactant becomes even more interesting scientifically — and much more complicated to unravel — when oil or other nonpolar fluid is also present. Notably Winsor (63) and Ekwall (75) have studied in detail binary and ternary systems of surfactant, water, and/or oil. Figure 4B, which is idealized, suggests the complexity that water-surfactant-oil ternary systems can achieve.

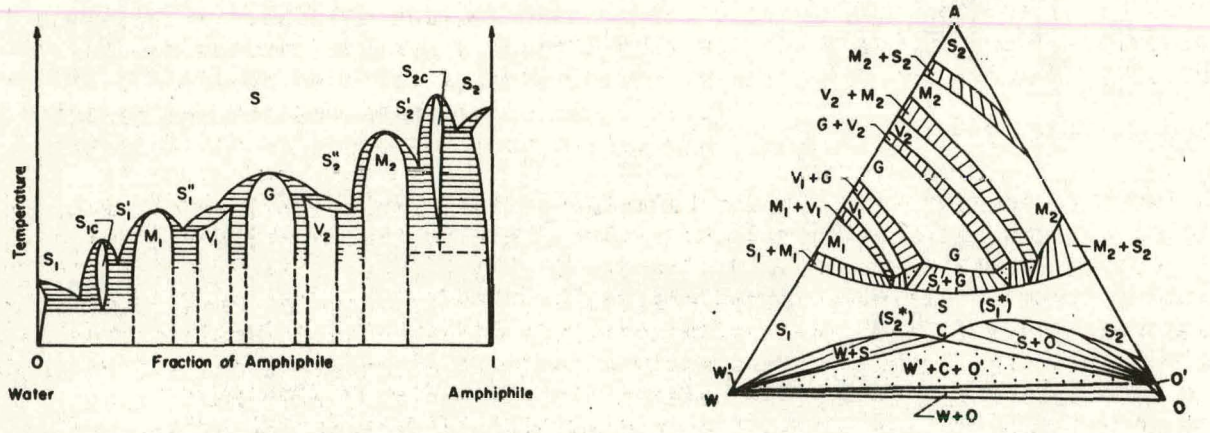

(A) (B)

Figure 4. (A) Hypothetical water-amphiphile binary phase diagram; (B) Hypothetical water-oil-amphiphile ternary phase diagram (from (89)).

Vesicles

Naturally occurring double-tail phospholipid surfactants are not known to form micelles (6,92). Instead, they form in water biphasic dispersions of lamellar (smectic) liquid crystals (6,93,94).

Appropriate handling of aqueous phospholipid systems produces dispersions of the surfactant in the form of topologically closed structures that are variously called liposomes or vesicles. Bangham and his coworkers (95,96) by gentle mechanical agitation produced aqueous dispersions in which the surfactant is organized into concentric bimolecular lamellae with aqueous layers between successive surfactant bilayers. These dispersions are very heterogeneous and contain many particles easily observable by light microscopy. The multilayer onion-like aggregates in these dispersions are generally referred to as liposomes. Liposomes have many physical properties of the bulk smectic mesophase

from which they originate; hence, liposomes can be considered to be bulk smectic phase with a concentric lamellar organization that perhaps represents a tendency toward minimization of the area of contact between hydrophobic groups of the surfactant and water.

Prolonged exposure of the coarse dispersions of liposomes to ultrasonic radiation breaks up the larger multilamellar particles into smaller, unilamellar spheroidal particles, or vesicles (97-99). In the sonicated dispersions most of the surfactant is found in small spheres having diameters of 20-30 nm and consisting of a single bilayer enclosing an aqueous phase. There are few if any smaller particles. The minimum diameter appears to be an intrinsic property of the surfactant-solvent system, and, perhaps is related to constraints on packing of surfactant molecules (100).

Vesicles have also been prepared from naturally occurring materials and analogs by means other than sonication. These include molecular dissolution in an organic solvent followed by injection through a syringe into an aqueous solution (101-103), and formation of mixed micelles followed by removal of the micellizing agent (104,105). Vesicles prepared by these methods are reported always as being larger than the minimum-size vesicles produced by sonication.

The thermodynamic and dynamic behavior of the surfactant in minimum-sized vesicles differs not only from that of surfactant in the bulk smectic phase and in liposomes, but also from that in larger unilamellar vesicles (94,106-108). The thermodynamic stability of dispersions of vesicles has not been conclusively determined. Once formed, dispersions of vesicles held above the so-called gel-liquid crystalline transition temperature can be concentrated, and are reported to be stable for days (98,107). However, Franses et al. (109) found that although vesicular dispersions of a phospholipid surfactant and of a synthetic alkylarylsulfonate surfactant (SHBS) remain apparently stable for weeks, and in some circumstances even for months, they slowly revert to the consolidated liquid crystals. Our results with dispersions of SHBS and of TRS 10-80 (a commercial petroleum sulfonate surfactant) which are presented in Chapter 5 support the conclusion of Franses et al. (109) that small, unilamellar vesicles are not thermodynamically stable with respect to the bulk liquid crystalline phase from which they are formed by sonication. We examine in Chapter 5 the stability of dispersion of vesicles with respect to preparation and salinity history, and to contact with hydrocarbons.

Microemulsions and Solubilization

By titrating with an alcohol an emulsion of oil and water stabilized by a surfactant, Schulman et al. (14,110,111) obtained isotropic, transparent solutions they christened microemulsions and thought to be in thermodynamic equilibrium. According to Schulman and his followers (17,112-114) microemulsions are emulsion — macroemulsions is the implication — with unique properties. Another school, however, considers micromeulsions prepared in this way to be solutions of normal or inverse swollen micelles (18,63,91,115,116). Although the microstructures and properties of microemulsions are far from established, the author subscribes to the second view, at least when the ratio of oil to water is either

very low or very high. There are problems with the micellar solution model when the ratio is around unity, as is brought up below.

In this thesis, by microemulsion we mean a low viscosity, isotropic, optically transparent or translucent, topologically ordered microstructured phase in thermodynamic equilibrium which contains substantial concentrations of two ordinarily immiscible fluids (e.g. water and oil), surfactants, and sometimes other additives (117). The requirement of topological ordering in this definition is intended to exclude isotropic solutions of water, oil, and alcohol that have been referred to elsewhere (20,118) as "detergentless microemulsions," because for them there is no convincing evidence of swollen micelles (119) nor is there evidence that low molecular weight alcohols micellize or form sheet-like microstructures in either water or oil. However, certain isotropic solutions of surfactant, alcohol, hydrocarbon, and brine which are sometimes considered to be microemulsions, have been proved to be molecular solutions (120). Hence the term microemulsion generally (and operationally) denotes a fluid, isotropic phase that is in thermodynamic equilibrium and consists of surfactants, alcohol, water, oil, and other additives, because there is not yet an unambiguous means for determining the microstructure of microemulsions when the proportions of oil and water are comparable.

Microemulsions have been employed in surfactant-based enhanced oil recovery processes (40). Many of the surfactant-oil-brine systems of the sort employed in microemulsion flooding exhibit a characteristic pattern of phase behavior in which the microemulsion phase progresses from being the lower ($\underline{2}$), to being the middle (3), and then the upper phase ($\overline{2}$) as the salinity is increased (18,121, 122). There is general agreement (18,63,115,116) that at low salinity the lower-phase microemulsion is a water-continuous solution of oil-swollen micelles and that at high salinity the upper-phase microemulsion is an oil-continuous solution of water-swollen micelles. The microstructures at intermediate salinities, where the middle microemulsion phase takes up substantial amounts (even equal amounts) of both oil and water, are not known yet. Scriven (88,89) suggested that in this intermediate region a microemulsion is a submicroscopically bicontinuous interspersion. Some evidence has come forth that supports the hypothesis of the bicontinuous microstructure (38,123-127).

Many alcohol-hydrocarbon-brine systems, i.e. systems without surfactant, also exhibit the phase progression of microemulsion systems as the salinity is increased, i.e. the $\underline{2}$-3-$\overline{2}$ phase progression (21,22). The similarities in phase behavior of the two kinds of systems corroborates the speculation that the patterns of phase behavior of microemulsion systems are characteristic of all amphiphile-hydrocarbon-brine systems. Our findings (Fig. 5 and Chapter 4) with alcohol-hydrocarbon-brine systems reveal that the tension behavior of microemulsion systems (18,121) is not unique and may also be characteristic of all amphiphile-hydrocarbon-brine systems. Hence, phase and tension behavior alone do not provide sufficient criteria to indicate a microemulsion. Transport properties are a more sensitive probe of microstructure than equilibrium properties, especially phase and tension behavior. Because it appears that the microstructures of microemulsions are not characteristic of all amphiphile-hydrocarbon-brine systems, transport-property behavior may provide more useful criteria for deciding whether or not a phase is a microemulsion.

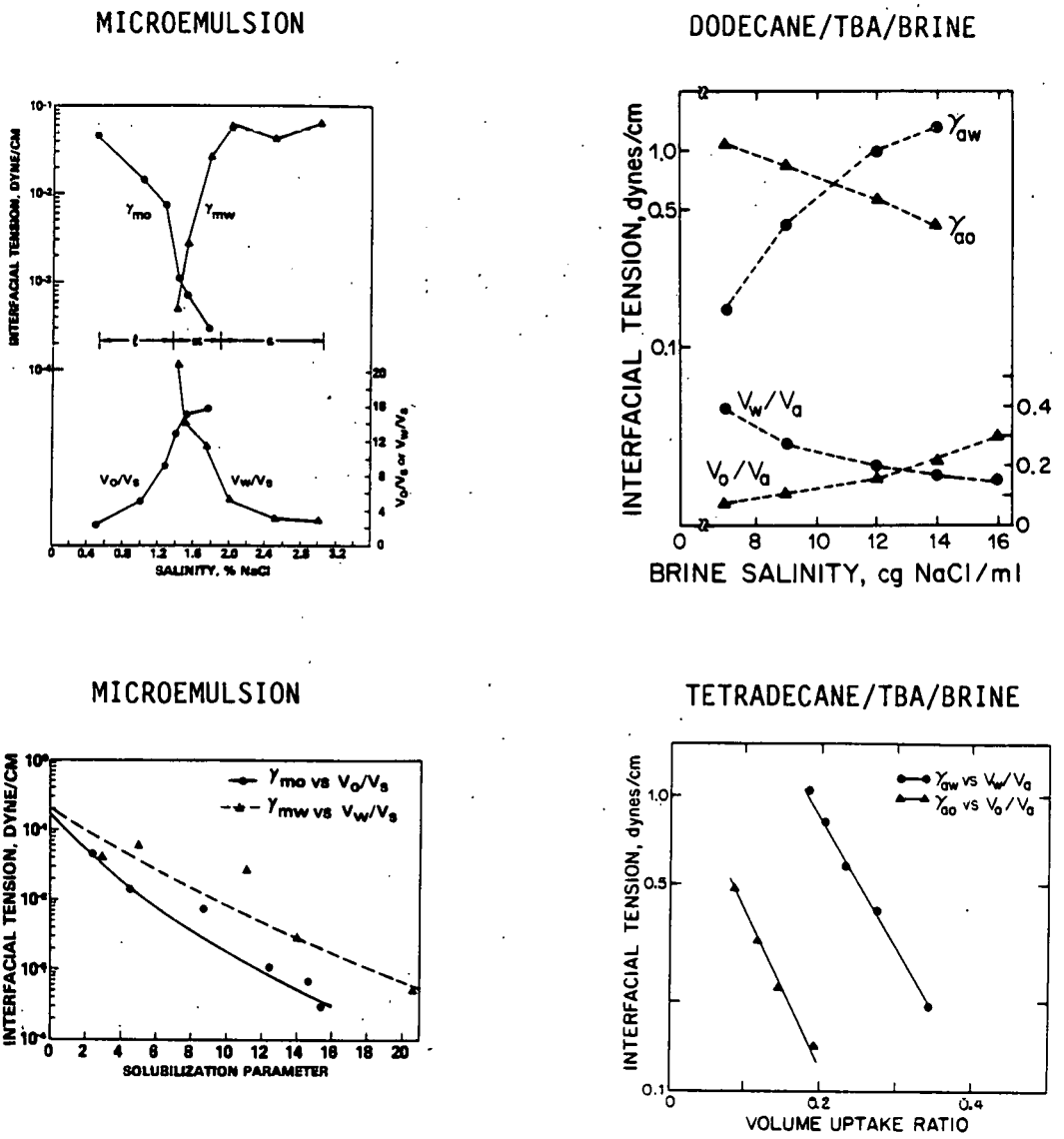

Figure 5. Interfacial tension and volume uptake versus brine salinity or interfacial tension versus volume uptake ratio for microemulsion (surfactant-oil-brine) systems (129) and for alcohol-hydrocarbon-brine systems (24).

Oil Recovery Processes

Oil recovery processes, as their name implies, bring oil from underground deposits in porous rock formation, or reservoirs, through wells to the earth's surface. These processes have been classified into primary, secondary, and tertiary or enhanced recovery operations (128).

The target of primary oil production is all of the oil originally in place in a deposit. Primary oil recovery uses energy existing in the reservoir to

drive the oil through the reservoir to producing wells. The driving energy can come from gas that evolves from solution in the oil, expansion of free gas, expansion of large amounts of water in and communicating with the reservoir, influx of water from a connecting subterraneous aquifer, or gravity forces. Eventually the natural energy drive dissipates. When this happens, energy must be supplied to the reservoir to produce any additional oil.

The target of secondary oil production is oil that remains after the energy sources of primary production have been exhausted. In secondary oil recovery, energy is supplied to a reservoir by injecting gas or water under pressure through selected wells. Managed properly this stimulates the movement of oil toward producing wells and leads to additional recovery at economic rates. Waterflooding is the principal secondary recovery method and accounts for about half the current United States daily production (128,130,131).

Conventional primary and secondary recovery are expected to produce ultimately about one-third of the oil discovered in exploitable deposits (132). In the United States, about 420 billion barrels of crude oil have been discovered (132). Thus nearly 300 billion barrels will be left in currently known reservoirs. This residual oil is the target for enhanced oil recovery operations.

Enhanced Oil Recovery: Surfactant Flooding

Presently a number of tertiary recovery methods aimed at recovering residual oil are being investigated (39,40,128,133-139). These processes involve the sequential injection of a number of fluids which are designed either to increase the portion of reservoir being contacted (increased sweep efficiency) or to mobilize oil better than water does in those portions of the reservoir contacted during waterflooding (increased microscopic displacement efficiency). In many cases, residual oil is trapped in the rock pores as disconnected blobs or ganglia. This is true of water-wet reservoirs, but of only some portion of oil-wet reservoirs and of those of mixed-wettability. One sure way to mobilize residual oil is by reducing the capillary forces holding it in the pores or by eliminating those forces completely (26,30,31,140-142). This can be accomplished by lowering drastically the interfacial tension down to the range of millidyne/cm — or causing oil/water interfaces to disappear altogether — by injecting surfactants into the reservoir. Nevertheless, there are other mechanisms by which residual oil can be mobilized by a surfactant flooding (143,144).

Two design philosophies of enhanced oil recovery by surfactant flooding exist. In one, the chemical slug is designed to be miscible with reservoir oil and brine, i.e. capillary forces are completely eliminated; the goal is what is termed miscible displacement of oil (141,142). The second is to attain, rather than miscibility, ultralow interfacial tensions between the injected-slug fluid and resident oil (26,27,121). However, miscibile and immiscible surfactant displacement are closely related (18,143-145). Miscible displacements break down into immiscible displacements because of surfactant retention, mixing with brine and oil at the front and rear of the bank, etc. (18,41,146).

Regardless of whether the surfactant is formulated to achieve "miscibility"

with reservoir fluids or to displace residual oil by reducing interfacial tension, it is important that three criteria be satisfied (39): (1) the surfactant as injected must be capable of mobilizing residual oil; (2) the ability to displace oil must be maintained as the surfactant progresses from injection to producing wells in the reservoir; and (3) certain mobility relationships must be satisfied in order to avoid bypassing much of the target oil.

Surfactant Waterflooding: Ultralow Tensions. Nonequilibrium Effects

The importance of ultralow tensions (less than 0.01 dyne/cm) between residual oil and displacing surfactant formulations as the means of achieving high capillary number — which measures the ratio of Darcy flow forces of oil mobilization to capillary forces of oil entrapment — displacement is well recognized (26,31). That this is feasible in the surfactant waterflooding range, i.e. at surfactant concentrations less than those which characterize the microemulsion flooding range, and usually in the absence of cosurfactants or cosolvents that typify microemulsions, is well established (26,27,32). Information in the technical and patent literature concentrates on commercial petroleum sulfonate surfactant systems (39,130,147). These surfactants have been selected because: (1) they can produce ultralow tensions against oil at low or moderately low concentrations; (2) they are relatively inexpensive; (3) they are potentially available in large quantities; and (4) they are not "adsorbed" on the rock, i.e. they are not retained, to an untenable degree. However, petroleum sulfonates can be "salted out" of solution by the levels of salinity found in many reservoirs and they can be precipitated by multivalent cations (e.g. calcium, magnesium) — two phenomena that uncontrolled can destroy the effectiveness of surfactant-based flooding.

Interfacial tensions in surfactant waterflooding formulations, i.e. the tensions between oil and dilute preparations of commercial petroleum sulfonates, depend strongly on surfactant concentration (26,27,29,148), surfactant equivalent weight and equivalent weight distribution (28,29,32,148-150), salt type and concentration (25-27), oil type (30,151), cosolvent nature and concentration (152,153), when cosolvent is used and so on. The required ultralow tensions for a successful surfactant waterflooding typically occur only in some narrow range of these variables: Figure 6, which exemplifies this situation, is the often-seen bull's eye of interfacial tension in commercial petroleum sulfonate systems for surfactant waterflooding (26).

Even with surfactant formulations capable of producing ultralow tensions, the tensions measured in the laboratory depend on the way the systems are prepared (29,147,154). Moreover, the tension is found to vary with time (154-156).

Cayias et al. (155) reported that the tension increases with the time that a stock aqueous preparation of TRS 10-80, a typical petroleum sulfonate surfactant, remains stored before it is diluted with brine to the particular concentration examined. These authors called this effect "aging," and found it to be reproducible, and concluded that it may be due to an unidentifiable physical cause, rather than chemical degradation. Even after diluting the stock preparation with brine, the interfacial tension against hydrocarbons of the resulting preparation changes with time (154,157).

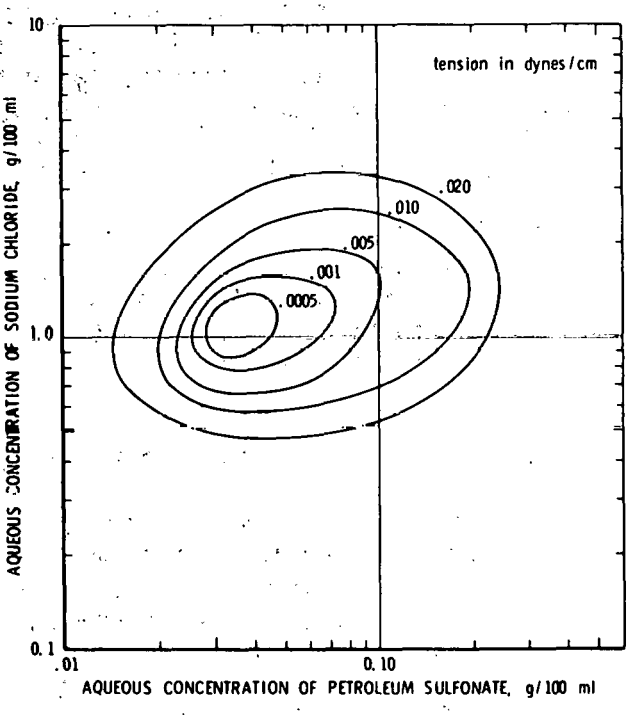

Figure 6. Equitension lines of oil-water interfacial tensions of petroleum sulfonate (from (26)).

Dunlap and Foster (147) and Dunlap and Brandner (29) found that the order of mixing of surfactant and salt in water affects the observed tensions against oils, the visual appearance of the preparations, and the surfactant losses in tests of flows through porous media. Lorenz et al. (158) observed strong order-of-mixing effects on turbidity, electrical conductivity, and viscosity of surfactant preparations.

Manning (36) noticed that steady values of tensions against hydrocarbons of aqueous preparations of nonionic surfactants can vary as much as two orders of magnitude depending on the number of days the two phases were precontacted prior to the tension measurements. Seeto (37) reported similar striking dependence with alkylarylsulfonate surfactants.

Wellington (159), Puig et al. (154), and Hall (156) all find that the interfacial tension against oil of pure and commercial alkylarylsulfonate surfactants varies strongly in time during measurement in the spinning drop tensiometer. Similarly, tension is also observed to vary in time in the sessile drop tensiometer (154). Each of these researchers has observed the formation in the tensiometer of highly viscous, nonbirefringent or birefringent surfactant-rich materials which appear to be related to the dramatic lowering of interfacial tension.

Reproducible tension measurements can be made, nevertheless, by observing a fixed experimental protocol (34,160). Tensions measured this way with a given surfactant correlate strongly with semi-empirical assignment of carbon numbers to a wide range of hydrocarbons (33,151,161). The correlation extends across related sulfonate surfactants and is a potentially useful means of characterizing low-tension formulations. Understanding this correlation and its relationship to nonequilibrium effects of tension, may shed light on the mechanisms of ultralow tensions in the low-surfactant concentration regime.

Time effects, order-of-mixing effects, and frequent inconsistency and lack of reproducibility of tension data indicate that basic understanding of the low tension phenomenon and the factors responsible for nonequilibrium effects is crucial to interpreting correctly laboratory and field data and to rationally designing processes for surfactant waterflooding.

Surfactant Waterflooding: Surfactant Retention

Surfactant retention in reservoir rocks is a major factor limiting effectiveness of oil recovery by surfactant flooding processes. For successful surfactant waterflooding, a surfactant formulation must not only be able to mobilize residual oil by achieving the required ultralow tensions: it also must propagate through the reservoir without losing this ability. If surfactant retention is excessive, i.e. if surfactants are depleted by reservoir rocks, interfacial tensions become high enough to retrap residual oil in the remainder of the reservoir (32,40,43).

Several mechanisms responsible for surfactant retention have been described (32,41-43,162-167). These include adsorption on pore walls and associated minerals, physical trapping within pores and at pore throats, precipitation, partitioning of surfactants into a residual oil phase and other resident fluids, and entrapment of microemulsions and other surfactant-rich phases. It is plain that determining means to diminish surfactant retention is crucial for optimizing surfactant waterflooding processes.

Petroleum sulfonates are complex mixtures of surfactants with wide ranges of equivalent weights (168). When preparations of petroleum sulfonates flow through porous media, surfactant components can be retained selectively (32,165); selective retention of surfactants can lead to loss of ultralow tensions. Gale and Sandvik (32) reported that components at the high end of the equivalent weight distribution of petroleum sulfonates, which by themselves are quite insoluble in water and produce turbid particulate dispersions, are essential to lowering of interfacial tensions. However, such high equivalent weight surfactants are strongly retained by porous rock. Adding low equivalent weight surfactants, which by comparison are very soluble in water and are retained little, brings the higher equivalent weight components into solution and reduces retention. However, the tension may no longer be ultralow (32,167). It is evidently for this reason that selective retention of higher equivalent weight surfactants may result in poor oil recovery.

Ultralow tensions against oils have been frequently associated with turbid

preparations of surfactants (26,32,147,169,170). Although the state of the surfactant in these preparations was not reported, there is now convincing evidence that the turbidity arises from submicron- and micron-size particles dispersed in the aqueous phase. Careful, systematic work (5,35,154,156,157) with pure and commercial alkylarylsulfonate surfactants proves that many of the preparations of surfactants that produce low tensions and are turbid — or under some circumstances are transparent — which were thought to be micellar solutions, are in fact dispersions of liquid crystallites. Because the typical sizes of liquid crystallites and other dispersed particles in turbid preparations may be larger than throats in the pores of reservoir rocks, and in the Berea rock specimens that are used as laboratory representatives (cf. refs. (35) and (171)), large retention of surfactant may occur and does occur when such dispersions are injected, for example into Berea cores (42,167,170). It has been found that retention of turbid preparations can be reduced by adding low equivalent weight cosurfactants (32) or cosolvents (42,170) to bring the dispersed surfactant into solution — which also decreases turbidity. However, the tension of the resulting solution against oil may no longer be ultralow. In Chapter 8 I propose a novel technique to reduce drastically the retention of turbid dispersions of liquid crystals without diminishing their ability to produce low tensions, and without changing their composition. The technique is to generate an ultradispersion of tiny vesicles by sonication of the originally turbid liquid crystalline dispersions. Because vesicles are small compared to pore dimensions, it is to be expected that this treatment reduces retention and in Chapter 8 I provide evidence that this is so. Thus, by creating vesicles of the tension-lowering high equivalent-weight surfactants, it may be possible to reduce the amounts of lower equivalent weight material used, to avoid excessive losses by retention, and yet to deliver the surfactant to the interfaces between residual oil and brine where it is needed to produce the ultralow tensions required for mobilizing the oil.

The Origins of Ultralow Tensions

One of the main purposes of this research is to elucidate the origins of ultralow tensions in surfactant-oil-brine systems of the sort encountered in surfactant waterflooding.

It is well-known that ultralow tensions (less than 0.01 dyne/cm) occur between two phases provided they are sufficiently close to a critical point, since by definition the two phases become identical and the interfacial tension reaches zero at their critical point. Liquid-vapor critical points, solution critical points, and plait points are commonly observed critical points.

The gradient theory of interfaces (52) explains how ultralow tensions are achieved between two phases that have near-critical interfaces. The inputs of the theory are the Helmholtz free energy density $f_0(n)$ of homogeneous fluid and what are known as influence parameters $c_{\alpha\beta}$ of inhomogeneous fluids — this being measures of the free energy stored in fluid component density gradients. The gradient theory reveals that interfacial tension depends on (1) the topography of the homogeneous free-energy surface f_0 in component density or in composition space; and (2) the values of influence parameters $c_{\alpha\beta}$ which gauge the effective

range of intermolecular effects that are peculiar to the inhomogeneous fluids in fluid microstructures such as interfaces.

The local microstructure in surfactant-oil-brine systems is governed by the intermolecular forces among the molecules: thermal motion, short range repulsive forces, nondirectional forces, dipolar and quadrapolar forces, hydrogen bonding forces, ionic forces, etc. Interfacial tensions in surfactant systems are also controlled by these intermolecular forces among the molecules. Gradient theory provides answers to how the intermolecular forces which dictate the local geometry, control the interfacial tension.

The physics can be illustrated simply with an approximation from the theory for a one-component fluid, according to which the interfacial tension is (52):

$$\gamma \approx \sqrt{\frac{c}{2}} \sqrt{\Delta\omega_{max}(n)}\ (n_\ell - n_g) \qquad (1)$$

where c is the influence parameter, $\Delta\omega_{max}$ is the maximum value of the thermodynamic potential difference which simply stated is the height of the free energy curve $f_o(n)$ above the line tangent to the free energy surface at the coexisting bulk densities, n_g and n_ℓ. The modern theory of critical phenomena (172,173) teaches that the maximum value of $\Delta\omega(n)$ and the difference $n_\ell - n_g$ approach zero as temperature (or any other field variable) approaches the critical value T_c according to the relations

$$\Delta\omega_{max} \propto (T_c - T)^{0.95} \quad , \quad n_\ell - n_g \propto (T_c - T)^{0.34} \qquad (2)$$

From Eq. (1) it follows that near a critical point, the interfacial tension is small owing to the flatness of the free energy surface and to the closeness of the densities of the coexisting phases. However, the flattening of the free energy surface is associated with a critical exponent of about three times that of the density difference. Thus, the flatness of the f_o curve is the dominant factor, not the convergence of densities, in near-critical low tension behavior. This fact explains how the low tensions observed between apparently quite different phases can nevertheless be the result of near-critical phenomenon (174; see also Chapter 7).

Near-critical compositions are likely to be involved in enhanced oil recovery by CO_2 or gas injection or other so-called miscible flooding techniques. And from a body of compelling evidence (52,122,174-176) it seems likely that near-critical interfaces provide the mechanism of enhanced oil recovery by microemulsion flooding. A picture of this is that in microemulsion systems, surfactant induces the ultralow tensions by providing on the free energy surface a dale that connect to the oil-rich and water-rich valleys by relatively flat passes.

Surfactants can also lower the interfacial tension of oil-water systems by

adsorbing at the oil-water interface, perhaps adsorbing so strongly as to form there a monolayer. In this circumstance the surfactant provides a graded zone that shields oil from water and in which the transition from oil to water may be sufficiently gradual or tailored to reduce tension one order of magnitude. Though this mechanism was widely suggested by surface chemists in the past decade as an explanation for the ultralow tensions which represent reductions by three, four, and five orders of magnitude, no body of evidence has accumulated that it is ever responsible.

So notwithstanding that monolayer formation, aided perhaps by surface-active micelles, has repeatedly been suggested (26,169,177) as the mechanism of ultralow tension in surfactant waterflooding formulations, i.e. between oil and alcohol-free dilute surfactant preparations, the facts have proved otherwise. On the basis of extensive investigations of model pure surfactants and of a commercial petroleum sulfonate, in parallel, we found (5,157,167, and Chapters 5 and 6 of this thesis) that ultralow tensions are observed only in the presence of a surfactant-rich third phase. The independent results of Hall (156) support our findings. The third phase — which forms when the surfactant in the form of liquid crystals in the aqueous phase absorbs decane — can be nonbirefringent (167; see also Chapter 5), streaming birefringent, or even birefringent (156; see also Chapter 6). In all cases, however, the third phase is quite viscous.

If the third phase is a fluid, i.e. if it lacks geometric order (notwithstanding that it may have topologically ordered fluid microstructure), then it seems likely that the low tension mechanism is the same as that of microemulsion — the low tensions of near-critical behavior. On the other hand, if the third phase is a liquid crystalline phase, then it is not clear whether it can become near-critical with isotropic fluid phases. For unless there is a continuous breakdown of the liquid crystalline geometric structure as a certain state is approached, it cannot become identical with a fluid phase at that critical state. Thus, if continuous free energy surfaces connecting fluid and liquid crystalline phases exist at all, a new dimension, the degree of geometric order, must be added to the thermodynamic space on which the free energy is defined (52). In any event, the structure of surfactant-rich third phase is a very important issue to be resolved. In Chapters 5 and 6 I present preliminary work to elucidate the microstructures of the third phase.

Basic Questions Attacked in Thesis

Understanding the relationships in surfactant waterflooding formulations among surfactant-rich microstructures, phase behavior, tension behavior, surfactant retention, and residual oil recovery from porous rock raises the following questions:

i) What types of surfactant-rich microstructures form in surfactant waterflooding formulations? What are their roles, if any, in the achievement of ultralow tensions? What are their roles in the mechanisms of surfactant retention by porous rock?

ii) How are ultralow tensions produced between oil and dilute preparations of surfactants? What is the structure of ultralow tension interfaces? — Are ultralow tensions an extreme case of surfactant adsorption in strictly two-phase systems of oil and water, or do they require a third phase to cover the oil-water interface? If the latter, how is the mechanism of ultralow tension in surfactant waterflooding related to that in immiscible microemulsion flooding?

iii) What causes the strong dependence of interfacial tension on surfactant type and concentration? On surfactant equivalent weight and equivalent weight distribution? On salt type and concentration? On alkane carbon number?

iv) What causes the time and order of mixing effects so often seen in laboratory tests? In the light of these effects, are ultralow tensions at low surfactant concentrations nonequilibrium properties or are they equilibrium properties? Under what conditions can ultralow tensions be reproduced?

v) How is phase behavior related to interfacial tensions, nonequilibrium or equilibrium as the case may be, in surfactant-oil-brine systems?

Many of these questions were partially answered, and some were quite clearly answered by the work of Franses (35). The goal of this thesis is to answer the rest and to provide more detailed, more comprehensive analysis of the central issues.

Strategy Used

In planning a systematic scientific study of this sort, the complexity of the formulations of surfactant waterflooding processes has to be borne in mind. Crude oil, resident brines of underground reservoirs, and petroleum sulfonates, all are complex multicomponent mixtures that are characterized inadequately for basic physicochemical studies. Experience suggests that systems of representative pure surfactants, pure hydrocarbon, distilled water, and pure salts would display much of the behavior of commercial systems thereby exposing the practically important aspects to thorough scientific study.

What is needed, therefore, are systematic studies with systems of well-characterized model surfactants which imitate the behavior of commercial systems. The strategy adopted was to make parallel studies of systems made with a representative commercial petroleum sulfonate, TRS 10-80, and with a pure alkylaryl-sulfonate surfactant, sodium 4-(1'-heptylnonyl)benzenesulfonate (SHBS or Texas No. 1). This surfactant was used alone or in combination with the micellar surfactant, sodium dodecylsulfate (SDS) or one of several low molecular weight alcohols. SHBS was selected because (1) it is isomerically pure; (2) it is available in relatively large quantities; (3) when dispersed in brine at low concentrations it can produce ultralow tensions against hydrocarbons (Chapter 5); and it can form a middle microemulsion phase with alkanes, brine, and alcohol (122); and Chapter 7 of this thesis).

It turned out to be possible to reproduce with well characterized systems every feature that I and my associates considered significant in the behavior

of systems containing the commercial surfactant. This is true not only of phase behavior and interfacial tensions (Chapters 5, 6, and 7), but also of core floods with Berea rock (Chapter 8). The basic case developed is condensed in Chapter 9.

To investigate the possibility that the patterns of interfacial tension in microemulsion systems disclosed by Healy et al. (18,121,129) as well as structural properties are also characteristic of all amphiphile-oil-brine systems, I present in Chapter 4 phase behavior, interfacial tension, viscosity, and electrical conductivity of alcohol-hydrocarbon-brine systems which mimic the phase behavior of microemulsions. The leading hypothesis is that the patterns of phase behavior and interfacial tension of microemulsion systems are universal to amphiphile-oil-brine systems, but that the microstructures of microemulsions are unique.

In addition to investigation in surfactant-oil-brine systems the origins of ultralow tensions, fluid microstructures, retention of surfactant by Berea rock, and the ability to displace residual oil from short Berea cores, I am also concerned in developing the spinning drop technique for the routine, accurate measurement of ultralow tensions. In Appendix A I present designs of less expensive, improved spinning drop interfacial tensiometers for measurements of ultralow tensions in gyrostatic equilibrium, which is the sine qua non of the technique. In Appendix B I present an analysis, by means of the rigorous ray-tracing method of geometric optics, of the spinning drop to estimate the optical magnification factor required to compensate for the cylindrical lens effect of the sample tube during measurement of the spinning drop diameter — which is needed to calculate interfacial tension.

References Cited in Section XVI

1. Shinoda, K., Nakagawa, T., Tamamushi, B. I. and Isemura, T., Colloidal Surfactants. Some Physicochemical Properties (Academic Press, New York, 1963).

2. Mysels, K. J. and Mukerjee, P., Pure & Appl. Chem. 51 1083 (1979).

3. Lindman, B. and Wennerström, H., Topics in Current Chemistry 87, 3 (1980).

4. Tausk, R. J. M., Karmiggelt, J., Oudshoorn, C. and Overbeek, J. Th. G., Biophys. Chem. 1, 175 (1976).

5. Franses, E. I., Davis, H. T., Miller, W. G., Scriven, L. E., in Chemistry of Oil Recovery, Eds., R. T. Johansen and R. L. Berg, ACS Symposium Series 91 (A.C.S., Washington, D.C., 1979) 35.

6. Tiddy, G. J. T., Physics Reports 57, 1 (1980).

7. Gray, G. W. and Winsor, P. A., Liquid Crystals & Plastic Crystals, Vol. 1 (Ellis Horwood Ltd., Chichester, 1974) 1.

8. Ekwall, P., in Advances in Liquid Crystals, Vol. 1, Ed., G. H. Brown (Academic Press, New York, 1975) 1.

9. Fontell, K., Mole. Cryst. Liq. Cryst. 63, 59 (1981).

10. Eicke, H. F., in Micellization, Solubilization and Microemulsions, Vol. 1, Ed., K. L. Mittal (Plenum Press, New York and London, 1977) 429.

11. Kertes, A. S., in Micellization, Solubilization and Microemulsion, Vol. 1, Ed., K. L. Mittal (Plenum Press, New York and London, 1977) 445.

12. Ekwall, P. and Stenius P., in Surface Chemistry and Colloids, Ed. M. Kerker, International Review of Science, Physical Chemistry Series Two, Vol. 7 (Butterworths, London, 1975) 215.

13. Skoulious, A., Ann. Phys. 3, 421 (1978).

14. Hoar, T. P. and Schulman, J. H., Nature 152, 102 (1943).

15. Friberg, S., J. Am. Oil Chem. Soc. 48, 578 (1971).

16. Friberg, S., Buraczewska, I. and Ravey, J. C., in Micellization, Solubilization, and Microemulsions, Vol. 2, Ed. K. L. Mittal (Plenum Press, New York and London, 1977) 901.

17. Prince, L. M., ed., Microemulsion. Theory and Practice (Academic Press, New York, 1977).

18. Reed, R. L. and Healy, R. N., in Improved Oil Recovery by Surfactant and Polymer Flooding, Eds., D. O. Shah and R. S. Schechter (Academic Press, New York, 1977) 383.

19. Kilpatrick, P. K., Gorman, C. A., Davis, H. T., Miller, W. G. and Scriven, L. E., J. Phys. Chem., to be submitted (1982).

20. Smith, G. D., Donelan, C. E. and Barden, R. E., J. Colloid Interf. Sci. 60, 488 (1977).

21. Knickerbocker, B. M., Pesheck, C. V., Scriven, L. E. and Davis, H. T., J. Phys. Chem. 83, 1984 (1979).

22. Knickerbocker, B. M., Pescheck, C. V., Davis, H. T. and Scriven, L. E., J. Phys. Chem. 86, 393 (1982).

23. Kilpatrick, P. K., Ph.D. Thesis, in progress, University of Minnetsota (1983).

24. Puig, J. E., Hemker, D. L., Gupta, A., Davis, H. T. and Scriven, L. E., J. Phys. Chem., submitted for publication (1982).

25. Dunlap, P. M., Brandner, C. F. and Townsend, H. L., U.S. Patent 3,467,190 (1969).

26. Foster, W. R., J. Pet. Tech. 25, 205 (1973).

27. Hill, H. J., Reissberg, J. and Stegemeier, G. L., J. Pet. Tech. 25, 186 (1973).

28. Wilson, P. M., Murphy, C. L. and Foster, W. R., paper SPE 5812 presented at the Improved Oil Recovery Symposium of the Soc. of Pet. Eng. of AIME, Tulsa, Okla., March 22-24 (1976).

29. Dunlap Wilson, P. M. and Brandner, C. F., J. Colloid Interf. Sci. 60, 473 (1977).

30. Taber, J. J., Soc. Pet. Eng. J. 9, 3 (1969).

31. Melrose, J. C. and Brandner, C. F., J. Can. Pet. Tech. 13, 54 (1973).

32. Gale, W. W. and Sandvik, E. I., Soc. Pet. Eng. J. 13, 191 (1973).

33. Morgan, J. C., Schechter, R. S. and Wade, W. H., in Improved Oil Recovery by Surfactant and Polymer Flooding, Eds., D. O. Shah and R. S. Schechter (Academic Press, New York, 1977) 101.

34. Doe, P. H., El-Emary, M., Wade, W. H. and Schechter, R. S., J. Am. Oil Chem. Soc. 54, 570 (1977).

35. Franses, E. I., Ph.D. Thesis, University of Minnesota (1979).

36. Manning, C. D., M.S. Thesis, University of Minnesota (1976).

37. Seeto, Y., M.S. Thesis, University of Minnestoa (1977).

38. Hatfield, J. C., Ph.D. Thesis, University of Minnesota (1978).

39. Gilliland, H. E. and Conley, F. R., Proc. 9th World Petrol. Congr. 4, 259 (1976).

40. Gogarty, W. B., J. Pet. Tech. 28, 93 (1976).

41. Healy, R. N., Reed, R. L. and Carpenter Jr., C. W., Soc. Pet. Eng. J. 15, 87 (1975).

42. Novosad, J. and Baxter, L. A., Research Report RR-42, Petroleum Recovery Institute, Calgary, Alberta (1979).

43. Glover, C. J., Puerto, M. C., Maerker, J. M. and Sandvik, E. L., Soc. Pet. Eng. J. 19 183 (1979).

44. Davis, H. T. and Scriven, L. E., Annual Research Report to Department of Energy, DOE/BC/10116-20 (1979).

45. IUPAC Manual of Symbols and Terminology, Pure Appl. Chem. 31, No. 4, 577 (1972).

46. Rosen, M. J., Surfactants and Interfacial Phenomena (Wiley-Interscience, New York, 1978).

47. Bartell, F. E. and Davis, J. K., J. Phys. Chem. 45, 1321 (1941).

48. Donahue, D. J. and Bartell, F. F., J. Phys. Chem. 56, 480 (1952).

49. McDonald, M. P., in Ordered Fluids and Liquid Crystals, Eds., R. S. Porter and J. F. Johnson, Adv. in Chemistry Series 63 (A.C.S., Washington, D.C., 1967) 125.

50. Tucker, E. E. and Becker, E. D., J. Phys. Chem. 77, 1783 (1973).

51. Laughlin, R. G., in Advances in Liquid Crystals, Vol. 3, Ed., G. H. Brown (Academic Press, New York, 1978) 41.

52. Davis, H. T. and Scriven, L. E., paper SPE 9278 presented at the 55th Annual Fall Technical Conference and Exhibition of the Society of Petroleum Engineers of AIME, Dallas, TX, Sept. 21-24 (1980).

53. Schick, M. J., Ed., Nonionic Surfactants (Marcel Dekker, New York, 1967).

54. Elworthy, P. H., Florence, A. T. and MacFarlane, C. B., Solubilization by Surface-Active Agents (Chapman and Hall Ltd., London, 1968).

55. Jungermann, E., Ed., Cationic Surfactants (Marcel Dekker, New York, 1970).

56. Linfield, W. M., Ed., Anionic Surfactants, Part I, Surfactant Science Series, Vol. 7 (Marcel Dekker, New York, 1976).

57. Lucassen-Reynders, A., Ed., Anionic Surfactants (Marcel Dekker, New York, 1981).

58. McBain, J. W., Trans. Farad. Soc. 9, 99 (1913).

59. Wennerstrom, H. and Lindman, B., Physics Reports (Review Section of Physics Letters) 52, 1 (1979).

60. Szabo, M. T., paper SPE 6772 presented at the 52nd Annual Fall Technical Conference and Exhibition of the Society of Petroleum Engineers of AIME, Denver, CO, Oct. 9-12 (1977).

61. Shah, D. O., Improved Oil Recovery Research Program, Semi-Annual Report to Department of Energy, June (1978).

62. Tanford, C., The Hydrophobic Effect. Formation of Micelles and Biological Membranes (Wiley-Interscience, New York.

63. Winsor, P. A., Chem. Rev. 68, 1 (1968).

64. Mukerjee, P., Cardinal, J. R., Desai, N. R., in Micellization, Solubilization, and Microemulsions, Vol. 1, Ed., K. L. Mittal (Plenum Press, New York and London, 1977) 241.

65. Hartley, G. S., in Micellization, Solubilization, and Microemulsions, Vol. 1, Ed., K. L. Mittal (Plenum Press, New York and London, 1977).

66. Mazer, N. A., Benedek, G. B. and Carey, M. C., J. Phys. Chem. 80, 1075 (1976).

67. Mazer, N. A., Carey, M. C. and Benedek, G. B., in Micellization, Solubilization, and Microemulsions, Vol. 1, Ed. K. L. Mittal (Plenum Press, New York and London, 1977) 359.

68. Friedel, M. G., Annls. Phys. 18, 273 (1922).

69. Gray, G. W., Molecular Structure and the Properties of Liquid Crystals (Academic Press, London and New York, 1962).

70. De Gennes, P. G., The Physics of Liquid Crystals (Clarendon Press, Oxford, 1974).

71. Husson, P. F., Mustacchi, H. and Luzzati, V., Acta Cryst. 13, 668 (1960).

72. Luzzati, V., Mustacchi, H., Skoulious, A. and Husson, F., Acta Cryst. 13, 660 (1960).

73. Fontell, K., in Liquid Crystals and Plastic Crystals, Vol. 2, Eds., G. W. Gray and P. A. Winsor (Ellis Horwood Ltd., Chichester, England, 1974) 80.

74. Luzzati, V., Mustacchi, H. and Skoulious, A., Disc. Faraday Soc. 25, 43 (1958).

75. Ekwall, P., Mandell, L. and Fontell, K., J. Colloid Interf. Sci. 33, 215 (1970).

76. Luzzati, V. and Husson, F., J. Cell. Biol. 12, 207 (1962).

77. Rogers, J. and Winsor, P. A., J. Colloid Interf. Sci. 30, 247 (1969).

78. Balmbra, R. R., Clunie, J. S., Corkill, J. M. and Goodman, J. F., Trans. Faraday Soc. 58, 1661 (1962).

79. Flautt, T. J. and Lawson, K. D., in Ordered Fluids and Liquid Crystals, Eds., R. S. Porter and J. F. Johnson, Adv. in Chemistry Series 63 (A.C.S., Washington, D.C., 1967) 26.

80. Rosevear, F. B., Amer. Oil Chem. Soc. J. 31, 628 (1954).

81. Rosevear, F. B., J. Soc. Cosmetic Chemists 19, 581 (1968).

82. Hartshorne, N. H. and Stuart, A., Crystals and the Polarizing Microscope, (E. Arnold Ltd., London, 1970).

83. Fontell, K., Mandell, L. and Ekwall, P., Act. Chem. Scan. 22, 3209 (1968).

84. Fontell, K., Prog. Chem. Fats other Lipids 16, 145 (1979).

85. Luzzati, V. and Spegt, P. A., Nature 215 710 (1967).

86. Luzzati, V., in Biological Membranes, Physical Fact and Function, Ed., D. Chapman (Academic Press, New York, 1968) 1.

87. Gray, G. W. and Winsor, P. A., in Lyotropic Liquid Crystals and the Structure of Biomembranes, Ed., S. Friberg, Adv. Chem. Ser. 152 (A.C.S, Washington, D.C., 1976) 1.

88. Scriven, L. E., Nature 263, 123 (1976).

89. Scriven, L. E., in Micellization, Solubilization, and Microemulsions, Vol. 2, Ed., K. L. Mittal (Plenum Press, New York, 1977) 877.

90. Scriven, L. E., private communication (1981).

91. Ekwall, P., Mandell, L. and Fontell, K., Mol. Cryst. and Liq. Cryst. 8, 157 (1969).

92. Small, D. M., J. Am. Oil Chem. Soc. 45, 108 (1968).

93. Ladbrooke, B. D. and Chapman, D., Chem. Phys. Lipids 3, 304 (1969).

94. Papahadjopoulos, D., Ed., Liposomes and their Uses in Biology and Medicine, (New York Academy of Science, N.Y., 1978).

95. Bangham, A. D., Standish, M. M. and Watkins, J. C., J. Mol. Biol. 13, 238 (1965).

96. Bangham, A. D., Hill, M. W. and Miller, N. G. A., in Methods in Membrane Biology, Vol. 1, Ed., E. D. Korn (Plenum Press, New York, 1969) 1.

97. Huang, C., Biochemistry 8, 344 (1969).

98. Huang, C. and Thompson, T. E., Methods Enzymol. Biomembranes 32, 485 (1974).

99. Barenholz, Y., Gibbes, D., Litman, B. J., Goll, J., Thompson, T. E. and Carlson, F. D., Biochemistry 16, 2806 (1977).

100. Papahadjopoulos, D. and Kimelberg, H. K., in Progress in Surface Science, Vol. 4, Ed., S. G. Davison (Pergamon Press, New York, 1973) 141.

101. Batzri, S. and Korn, E. D., Biochim. et Biophys. Acta 298, 1015 (1973).

102. Brunner, J., Skrabal, P. and Hauser, H., Biochim et Biophys. Acta 455, 322 (1976).

103. Kremer, J. M. H., Esker, M. W. J., Pathmamanoharan, C. and Wiersema, P. H., Biochemistry 16, 3932 (1977).

104. Deamer, D. and Bangham, A. D., Biochim. et Biophys. Acta 443, 629 (1976).

105. Rhoden, V. and Goldin, S. M., Biochemistry 18, 4173 (1979).

106. Levine, Y. K., Prog. in Biophys. 24, 1 (1972).

107. Suurkuusk, J., Lentz, B. R., Barenholz, Y., Biltonen, R. L. and Thompson, T. E., Biochemistry 15, 1393 (1976).

108. Lee, A. G., Prog. Biophys. Molec. Biol. 29(1), 3 (1975).

109. Franses, E. I., Talmon, Y., Scriven, L. E., Davis, H. T. and Miller, W. G., J. Colloid Interf. Sci. 86, 449 (1982).

110. Schulman, J. H. and Riley, D. P., J. Colloid Sci. 3, 383 (1948).

111. Schulman, J. H. and Friend, J. A., J. Colloids Sci. 4, 497 (1949).

112. Carey, M. C. and Small, D. M., Am. J. Med. 49, 590 (1970).

113. Gerbacia, W. and Rosano, H. L., J. Colloid Interf. Sci. 44, 242 (1973).

114. Prince, L. M., J. Colloid Interf. Sci. 52, 182 (1975).

115. Winsor, P. A., Solvent Properties of Amphiphilic Components (Butterworths, London, 1954).

116. Shinoda, K. and Friberg, S., Adv. Colloid & Intef. Sci. 4, 218 (1975).

117. Scriven, L. E., What are Microemulsions?, Plenary Lecture, American Chemical Society 55th Colloid & Surface Science Symposium, Cleveland, OH, June 16 (1981).

118. Borys, N. F., Holt, S. L. and Barden, R. E., J. Colloid Interf. Sci. 71, 526 (1979).

119. Rossen, W. R., Ph.D. Thesis, University of Minnesota (1982).

120. Shah, D. O., Walker, R. D., Hsieh, W. C., Shah, N. J., Dwivedi, S., Nelander, J., Pepinsky, R. and Deamer, D. W., paper SPE 5815 presented at the Improved Oil Recovery Symposium of the Soc. Pet. Eng. of AIME, Tulsa, Okla., March 22-24 (1976).

121. Healy, R. N., Reed, R. L. and Stenmark, D. C., Soc. Pet. Eng. J. 16, 147 (1976).

122. Bennett, K. E., Phelps, C. H. K., Davis, H. T. and Scriven, L. E., Soc. Pet. Eng. J. 21, 747 (1981).

123. Lagües, M., Ober, R. and Taupin, C., J. Physique Lett. 39, L-487 (1978).

124. Lagües, M., J. Physique Lett. 40, L-331 (1979).

125. Lagourette, B., Peyrelasse, J., Boned, C. and Clausse, M., Nature 281, 60 (1979).

126. Dvolaitzky, M., Lagües, M., LePesant, J. P., Ober, R., Sauterey, C. and Taupin, C., J. Phys. Chem. 84, 1532 (1980).

127. Bennett, K. E., Hatfield, J. C., Davis, H. T., Macosko, C. W. and Scriven, L. E., in Microemulsions, Ed., I. D. Robb (Plenum Press, New York, 1981) 65.

128. National Petroleum Council, Enhanced Oil Recovery (1976).

129. Healy, R. N. and Reed, R. L., Soc. Pet. Eng. J. 14, 491 (1974).

130. Ahearn, G. P., J. Am. Oil Chemists' Soc. 46, 540A (1969).

131. Craig, F. F., Jr., The Reservoir Engineering Aspects of Waterflooding, Soc. Pet. Eng. Monograph, Vol. 3 (1971).

132. American Petroleum Institute, Reserves of Crude Oil, Natural Gas Liquids, and Natural Gas in the United States and Canada as of December 31, 1977, vol. 32 (1978).

133. Johnson, C. E., J. Pet. Tech. 28, 83 (1976).

134. Shah, D. O. and Schechter, R. S., Eds., Improved Oil Recovery by Surfactant and Polymer Flooding (Academic Press, New York, 1977).

135. Gogarty, W. B., paper SPE 7041 presented at the SPE Fifth Symposium on Improved Methods for Oil Recovery, Tulsa, Okla., April 16-19 (1978).

136. Stalkup, F. I., paper 7042 presented at the SPE Fifth Symposium on Improved Methods for Oil Recovery, Tulsa, Okla., April 16-19 (1978).

137. Chang, H. L., paper SPE 7043 presented at the SPE Fifth Symposium on Improved Methods for Oil Recovery, Tulsa, Okla., April 16-19 (1978).

138. Prats, M., paper SPE 7044 presented at the SPE Fifth Symposium on Improved Methods for Oil Recovery, Tulsa, Okla., April 16-19 (1978).

139. Taber, J. J., Pure & Appl. Chem. 52, 1323 (1980).

140. Taber, J. J., Kamath, I. S. K. and Reed, R. L., Soc. Pet. Eng. J. 1, 39 (1961).

141. Gogarty, W. B. and Tosch, W. C., J. Pet. Tech. 20, 1407 (1968).

142. Holm, L. W., in Improved Oil Recovery by Surfactant and Polymer Flooding, Eds., D. O. Shah and R. S. Schechter (Academic Press, New York, 1977) 453.

143. Larson, R. G., Davis, H. T. and Scriven, L. E., paper SPE 8840 presented at the First Joint SPE/DOE Symposium on Enhanced Oil Recovery, Tulsa, Okla., April 20-22 (1980).

144. Larson, R. G., Davis, H. T. and Scriven, L. E., J. Pet. Tech., 34, 243 (1982).

145. Larson, R. G., Soc. Pet. Eng. J. 19, 411 (1979).

146. Holm, L. W., J. Pet. Tech. 23, 1475 (1971).

147. Dunlap, P. M. and Foster, W. R., U.S. Patent 3,468,377 (1969).

148. Puig, J. E., Franses, E. I. and Miller, W. G., J. Colloid Interf. Sci. 22, 37 (1982).

149. Cayias, J. L., Schechter, R. S. and Wade, W. H., J. Colloid Interf. Sci. 59, 31 (1977).

150. Wade, W. H., Morgan, J. C., Jacobson, J. K. and Schechter, R. S., Soc. Pet. Eng. J. 17, 122 (1977).

151. Cayias, J. L., Schechter, R. S. and Wade, W. H., Soc. Pet. Eng. J. 16, 351 (1976).

152. Wade, W. H., Morgan, J. C., Schechter, R. S., Jacobson, J. K. and Salager, J. L., Soc. Pet. Eng. J. 18, 242 (1978).

153. Woodbury, N. A., Puig, J. E., Davis, H. T., Scriven, L. E. and Miller, W. G., J. Disp. Sci. Tech. to be submitted (1982).

154. Puig, J. E., Franses, E. I., Davis, H. T., Miller, W. G. and Scriven, L. E., Soc. Pet. Eng. J. 19 71 (1979).

155. Cayias, J. L., Hayes, M. E., Schechter, R. S. and Wade, W. H., J. Pet. Tech. 28, 985 (1976).

156. Hall, A. C., Colloids and Surfaces 1, 209 (1980).

157. Franses, E. I., Puig, J. E., Talmon, Y., Miller, W. G., Scriven, L. E. and Davis, H. T., J. Phys. Chem. 84, 1547 (1980).

158. Lorenz, P. B., Kayser, M. B., Hsieh, M. A. and Tham, M. K., Abstract of paper, Proceeding of 52nd Colloid and Surface Science Symposium, Eds. E. L. Fuller, Jr. and H. G. Corbett, Nat. Tech. Inform. Serv., U.S. Dept. of Commerce, May (1978); Solution Chemistry of Surfactants, 2, 903 (1979).

159. Wellington, S., private communication (1977).

160. Anderson, D., Bidner, M. S., Davis, H. T., Manning, C. D. and Scriven, L. E., SPE paper 5811 presented at the Society of Petroleum Engineers Symposium on Improved Oil Recovery, Tulsa, Oklahoma, March 22-24 (1976).

161. Cash, R. L., Cayias, J. L., Fournier, G. R., Jacobson, J. K., LeGear, C. A., Schares, T., Schechter, R. S. and Wade, W. H., in Detergents in the Changing Scene, American Oil Chemist's Society, Champaign, Il, 1-9 (1977).

162. Trushenski, S. P., Dauben, D. L. and Parrish, D. R., Soc. Pet. Eng. J. 14, 633 (1974).

163. Hurd, B. G., paper SPE 5818 presented at the Improved Oil Recovery Symposium of SPE of AIME, Tulsa, Okla., March 22-24 (1976).

164. Trogus, F. J., Sophany, T., Schechter, R. S. and Wade, W. H., Soc. Pet. Eng. J. 17, 337 (1977).

165. Bae, J. H. and Petrick, C. B., Soc. Pet. Eng. J. 17, 353 (1977).

166. Lawson, J. B. and Dilgren, R. E., Soc. Pet. Eng. J. 18, 75 (1978).

167. Puig, J. E., Franses, E. I., Talmon, Y., Davis, H. T., Miller, W. G. and Scriven, L. E., Soc. Pet. Eng. J. 22, 37 (1982).

168. Sandvik, E. I., Gale, W. W. and Denekas, M. O., Soc. Pet. Eng. J. 17, 184 (1977).

169. Ahearn, R. N. and Gale, W. W., U.S. Patent 3,302,716 (1976).

170. Batycky, J. P. and McCaffery, F. G., Research Note No. 6, Petroleum Recovery Institute, Calgary, Alberta; paper No. 78.29.26 presented at the 29th Annual Meeting of CIM, Calgary, June 13-16 (1978).

171. Dullien, F. A. L. and Dhawan, G. K., J. Colloid Interf. Sci. 52, 129 (1975).

172. Stanley, H. E., Introduction to Phase Transitions and Critical Phenomena (Clarendon Press, Oxford University Press, 1971).

173. Ma, S., Modern Theory of Critical Phenomena (W. A. Benjamin, Inc., 1976).

174. Fleming III, P. D., Vinatieri, J. E. and Glinsmann, G. R., J. Phys. Chem. 84, 1526 (1980).

175. Fleming III, P. D. and Vinatieri, J. E., AIChE J. 25, 493 (1979).

176. Fleming III, P. D. and Vinatieri, J. E., J. Colloid Interf. Sci. 81, 319 (1981).

177. Chan, K. S. and Shah, D. O., J. Disp Sci. Tech. 1, 55 (1980).

PUBLICATIONS FROM PROJECT

Vesicles and Liposomes

P1. Falls, A.H., Davis, H.T., Scriven, L.E. and Talmon, Y., "Imaging vesicular dispersions with cold-stage electron microscopy," Biochimica et Biophysica Acta 693, 364-378, (1982).

P2. Kilpatrick, P.K., Blum, F.D., Davis, H.T., Falls, A.H., Kaler, E.W., Miller, W.G., Puig, J.E., Scriven, L.E., Talmon, Y. and Woodbury, N.A., "Alcohol effects on transitions in liquid crystalline dispersions," pp. 143-172 in *Microemulsions*, ed. by Robb, I.D., Plenum Publishing Corporation, New York (1982).

P3. Miller, W.G., Blum, F.D., Davis, H.T., Franses, E.I., Kaler, E.W., Kilpatrick, P.K., Nietering, K.J., Puig, J.E. and Scriven, L.E., "Fluid microstructures of sodium 4 - (1' - heptylnonyl) benzenesulfonate mixtures," Proceedings of International Symposium on Solution Behavior of Surfactants, Lund University, Lund, Sweden, July 1982. Edited by K.E. Mittal (1983).

P4. Puig, J.E., Scriven, L.E., Davis, H.T. and Miller, W.G., "Fluid microstructures and enhanced oil recovery," American Institute of Chemical Engineering Journal 78, 1-27 (1982).

P5. Bennett, K.E., Davis, H.T. and Scriven, L.E., "Microemulsion phase behavior: Four-phase progressions in five-component mixtures," J. Physical Chemistry 86, 3917-3919 (1982).

Microemulsions

P6. Kaler, E.W., Bennett, K.E., Davis, H.T. and Scriven, L.E., "Toward understanding microemulsion microstructure: a small-angle x-ray scattering study," Journal of Chemical Physics (to appear 1983).

P7. Papaioannou, A.T., Bennett, K.E., Davis, H.T., Macosko, C.W. and Scriven, L.E., "Microemulsion rheology measured," Paper B-15, 54th Annual Meeting of the Society of Rheology, Evanston, IL (October 1982). Abstract only.

P8. Rossen, W.R. and Kohn, J.P., "Behavior of microemulsions under compression," SPE Reprint #11210, New Orleans Meeting, Sept. 26-29, 1982.

Phase Behavior and Interfacial Tensions

P9. Frances, E.I. and Miller, W.G., "Molecular motion and phase behavior of a double-tail sulfonate surfactant by NMR," J. Colloid and Interface Science (submitted for publication).

P10. Kilpatrick, P.K., Davis, H.T. and Scriven, L.E., "Critical loci and the evolution of multiphase equilibria in ternary liquid systems," Session on Thermodynamics and Critical Phenomena, 75th Annual Meeting of the AIChE, Los Angeles, CA (Nov. 1982). Manuscript available.

P11. Kilpatrick, P.K., Scriven, L.E. and Davis, H.T., "Thermodynamic modelling of quaternary systems: oil-brine-surfactant-alxohol," SPE Reprint #11209 New Orleans Meeting, Sept. 26-29, 1982.

P12. Larson, R.G., Scriven, L.E. and Davis, H.T., "Monte Carlo simulation of model amphiphile-oil-water systems," Journal of Chemical Physics (submitted).

P13. Nitsche, J.M., Teletzke, G.F., Scriven, L.E. and Davis, H.T., "Phase behavior of binary mixtures of water, carbon dioxide and decane predicted with a lattice model," Session on Modelling the Properties of Liquid Mixtures, 75th Annual Meeting of the AIChE, Los Angeles, CA (Nov. 1982). Manuscript available.

P14. Rossen, W.R., Brown, R.G., Davis, H.T., Prager, S. and Scriven, L.E., "Thermodynamic modelling of pseudoternary phase behavior," SPE Journal 22, 945-961 (1982).

Fluids and Thin Films at Solid Surfaces

P15. Tirrell, M.V., Aubert, J.H., Adolf, D. and Davis, H.T., "Dynamic properties of macromolecules near interfaces," IUPAC, Proceedings 28th Macromolecular Symposium, Amherst, MA, July 12-16, 1982.

P16. Tirrell, M.V., Aubert, J.A., Adolf, D. and Davis, H.T., "Molecular theory of momentum transport in polymeric liquids near fluid-solid interfaces," 75th Annual Meeting of the AIChE, Los Angeles, CA (Nov. 1982). Abstract # 55d.

P17. Teletzke, G.F., Davis, H.T. and Scriven, L.E., "How liquids spread on solids," Journal of Colloid and Interface Science (submitted).

P18. Teletzke, G.F., Davis, H.T. and Scriven, L.E., "Wetting hydrodynamics," Journal of Fluid Mechanics (submitted).

P19. Teletzke, G.F., Scriven, L.E. and Davis. H.T., "Wetting transitions: First order or second order?," J. Chemical Physics 77, 5794-5798 (1982).

Molecular Theory of Fluid Microstructures

P20. Davis, H.T., "Capillary waves and interfacial structure," Proceedings of Symposium on Waves on Fluid Interfaces, Mathematics Research Center, University of Wisconsin, Madison, WI, Oct. 18-20, 1982.

P21. Davis, H.T. and Scriven, L.E., "Stress and structure in fluid interfaces," Advances in Chemical Physics 49, 357-454 (1982).

P22. Falls, A.H., Scriven, L.E. and Davis, H.T., "Adsorption, structure, and stress in binary interfaces," Journal of Chemical Physics (to appear).

P23. Kerins, J.E. and Boiteux, M.," Thermodynamic properties of inhomogeneous fluid," Physica A (submitted for publication).

Instrumentation and Techniques

P24. Bennett, K. E., Davis, H. T., Macosko, C. W. and Scriven, L. E., "Multiphase rolling ball viscometer," Patent Disclosure (to be submitted).

P25. Falls, A. H., "Transmission electron microscope observations of dislocations in hexagonal ice," pp. 552-553 in 40th Annual Proceedings of the Electron Microscopy Society of America, ed. by Bailey, G. W., Washington, DC (1982).

P26. Falls, A. H., Wellinghoff, S. T., Talmon, Y. and Thomas, E. L., "A transmission electron microscopy study of hexagonal ice," Journal Materials Science (to appear 1983).

P27. Franses, E. I., Scriven, L. E., Miller, W. G. and Davis, H. T., "Interpreting the appearance of dispersed systems. Part I. Model dispersions of polymer latex spheres," Journal of the American Oil Chemists' Society (to appear May 1983).

P28. Franses, E. I., Scriven, L. E., Miller, W. G. and Davis, H. T., "Interpreting the appearance of dispersed systems. Part II. A guide for surfactant systems," Journal of the American Oil Chemists' Society (to appear May 1983).

P29. Perlov, G., Talmon, Y. and Falls, A. H., "An improved transfer module and variable temperature control for a simple commercial cooling holder," Ultramicroscopy (submitted for publication).

P30. Talmon, Y., "Frozen hydrated specimens," Proceedings of the 10th International Congress on Electron Microscopy, Hamburg, Germany (Aug. 1982). Abstract only.

Flow and Transport in Porous Media and Composite Materials

P31A Davis, H. T., "Transport in disordered composite media," IUPAC 28th Macromolecular Symposium Proceedings, p. 739, 12-16 July 1982, Amherst, MA.

P31B Scriven, L. E., "Physics of structure and transport in porous media", General Lecture, Proceedings of the Ninth U.S. National Congress of Applied Mechanics, p. 57, 21-25 June 1982, Ithaca, NY.

P32. Heiba, A. A., Sahimi, M. and Scriven, L. E., "Percolation theory of two-phase relative permeability," SPE Reprint #11015, New Orleans Meeting, Sept. 26-29, 1982.

P33. Hughes, B. D., Montroll, E. W. and Shlesinger, M. F., "Fractal random walks," J. Statistical Physics 28, 111-126 (1982).

P34. Hughes, B. D. and Sahimi, M., "Random walks on the Bethe lattice," J. Statistical Physics 29, 781-794 (1982).

P35. Hughes, B. D. and Shlesinger, M. F., "Lattice dynamics, random walks, and nonintegral effective dimensionality," J. Math. Phys. 23, 1688-1692 (1982).

P36. Pathak, P., Davis, H. T. and Scriven, L. E., "Dependence of residual nonwetting liquid on pore topology," SPE Reprint #11016, New Orleans Meeting, Sept. 26-29, 1982.

P37. Sahimi, M., Davis, H. T. and Scriven, L. E., "Dispersion in disordered porous media," Chemical Engineering Communications (accepted for publication).

P38. Sahimi, M., Heiba, A. A., Hughes, B. D., Davis, H. T. and Scriven, L. E., "Dispersion in flow through porous media," SPE New Orleans Meeting, Sept. 26-29, 1982. Manuscript available.

P39. Sahimi, M., Hughes, B. D., Scriven, L. E. and Davis, H. T., "On Pólya random walks, lattice Green functions, and the bond percolation threshold," Journal Physics A (accepted for publication).

Mechanisms and Simulation

P40. Benner, R. E. and Scriven, L. E., "Adaptive subdomaining for solution of one-dimensional problems by the finite element method," Presented at the 30th Anniversary Meeting of SIAM, Stanford, CA, July 19-23, 1982. Manuscript available.

P41. Larson, R. G., Davis, H. T. and Scriven, L. E., "Elementary mechanisms of oil recovery by chemical methods," Soc. Pet. Eng. J. (February 1982), 243-258.

Theses

P42. Falls, A. H., "Electron microscopy and molecular theory of microstructured fluids," Ph.D. Thesis, University of Minnesota, 1982.

P43. Kaler, E. W., "Surfactant microstructures," Ph.D. Thesis, University of Minnesota, 1982.

P44. Puig, J. E., "Fluid microstructures, phase and tension behavior of amphiphile-hydrocarbon-water-salt systems," Ph.D. Thesis, University of Minnesota, 1982.

P45. Rossen, W. R., "Multicomponent phase behavior in an external field," Ph.D. Thesis, University of Minnesota, 1982.

Vesicles and Liposomes

P1. *Imaging vesicular dispersions with cold-stage electron microscopy, Biochimica et Biophysica Acta 693, 364-378 (1982).*

A fast-freeze, cold-stage transmission electron microscopy technique which can incorporate in situ freeze-drying of the sample is described. Its use in elucidating structure in unstained and stained, hydrated and freeze-dried, aqueous vesicular dispersions of biological and chemical interest is demonstrated with vesicles of L-α-phosphatidylcholine (bovine phosphatidylcholine) and of the synthetic surfactant sodium 4-(1'-heptylnonyl)benzenesulfonate (SHBS). The contrast features observed in transmission electron microscope images of frozen, hydrated samples are identified and explained with the dynamical theory of electron diffraction. Radiolysis by the electron beam is shown to increase contrast in vesicle images and to change their structure and size. Micrographs illustrate the freeze-drying of a dispersion in the microscope; the process causes vesicles to shrink and collapse.
By A. H. Falls, H. T. Davis, L. E. Scriven and Y. Talmon.

P2. *Alcohol effects on transitions in liquid crystalline dispersions, pp. 143-172 in Microemulsions, ed. by Robb, I. D., Plenum Publishing Corporation, New York (1982)*

We report the solubilization of a lamellar liquid crystalline aqueous dispersion of a pure double-tail surfactant, SHBS (sodium 4-(1'-heptylnonyl)benzenesulfonate), by a number of low molecular weight alcohols: t-butanol, n-butanol, n-pentanol, and n-hexanol. The mechanism of solubilization is deduced from ^{13}C NMR spectroscopy and involves the positioning of alcohol molecules in the bilayers. The process of solubilization results in an aqueous isotropic solution in which there are probably small aggregates of alcohol-solvated surfactant molecules as indicated by conductimetry. The phase transformation from biphasic dispersion to isotropic solution is studied by spectroturbidimetry, conductimetry, small-angle x-ray scattering, ^{13}C and ^{23}Na NMR spectroscopy, and fast-freeze cold-stage transmission electron microscopy. Addition of NaCl to isotropic alcohol-SHBS-water solutions results in the separation of two fast-settling phases, the upper one with some microstructure. Microemulsion formation results from addition of decane to some of these systems; the effect of salinity on domain size in these microemulsions is discussed.
By P. K. Kilpatrick, F. D. Blum, H. T. Davis, A. H. Falls, E. W. Kaler, W. G. Miller, J. E. Puig, L. E. Scriven, Y. Talmon and N. A. Woodbury.

P3. *Fluid microstructures of sodium 4-(1'-heptylnonyl)benzenesulfonate mixtures, Proceedings of International Symposium on Solution Behavior of Surfactants, Lund University, Lund, Sweden, July 1982. Edited by K. E. Mittal (1983).*

The phase behavior of sodium 4-(1'-heptylnonyl)-benzenzenesulfonate, SHBS, in water or brine from 20 to 90°C is dominated by a broad biphasic region consisting of a lamellar liquid crystalline phase in equilibrium with a dilute isotropic SHBS solution. In the isotropic phase the SHBS is not micellar, though conductimetry and nmr spectroscopy indicate weak, concentration dependent aggregation. At 25°C the

lamellar phase is approximately 100° above the gel-liquid crystal phase transition temperature and the sulfonate head group undergoes rapid though anistropic motion. The lamellar phase is very fluid and easily deformable, whether dispersed in the saturated aqueous phase or as the bulk lamellar phase. Mechanical agitation and other sample preparation techniques give closed shell liposome dispersions; the mean size and size distribution depend markedly on the sample history. Sonication of a dilute dispersion leads to long lived, nonequilibrium vesicles. Addition of a suitable cosurfactant, sodium dodecylsulfate, leads to a mixed micellar solution while the addition of a cosolvent, e.g. n-pentanol, leads to a non-micellar solution.

Many preparations of SHBS-H_2O(NaCl)-(cosolvent, cosurfactant) show ultralow tension against hydrocarbon. In formulations in which the tension measurements depend on time and preparation technique, an opaque, viscous, thin, surfactant-rich third phase forms at the oil-water interface. The microstructures present in this low volume fraction surfactant-rich middle phase are unknown. The tension behavior, however, correlates with the nature of the microstructure present in the precontacted aqueous surfactant dispersion. Formulations containing alcohols which produce low, equilibrium tensions that do not depend on the method of preparation yield a low-viscosity, translucent middle phase, a microemulsion. The microemulsion middle phase is shown in this case to be continuous in both water and oil; it is not a swollen micellar microstructure.

By W. G. Miller, F. D. Blum, H. T. Davis, I. E. Franses, E. W. Kaler, P. K. Kilpatrick, K. J. Neitering, J. E. Puig and L. E. Scriven.

P4. *Fluid microstructures and enhanced oil recovery, American Institute of Chemical Engineers Journal 78, 1-27 (1982)*

Ultralow interfacial tensions between oil and water are caused not by monolayer adsorption but by a film of surfactant-rich third phase—either viscous meterial derived from liquid crystalline dispersions, or less viscous equilibrium microemulsion. The sometimes transparent dispersions, which had been overlooked before, become ultradispersions of vesicles upon sonication, and can be dissolved by certain alcohols.

These and other findings are summarized from a concerted study of a petroleum sulfonate surfactant system representative of surfactant waterflooding, and of pure surfactant systems that mimic it. Reviewed are the relationships between surfactant-rich microstructures and their compositions, recovery of residual oil from short sandstone cores, and surfactant retention in such cores. Vesicular surfactant delivery is examined.

By J. E. Puig, L. E. Scriven, H. T. Davis and W. G. Miller.

Microemulsions

P5. *Microemulsion phase behavior: Four-phase progressions in five-component mixtures, J. Physical Chemistry 86, 3917-3919 (1982)*

The phase behavior of microemulsions of brine, hydrocarbon, alcohol, and a pure alkylarylsulfonate—sodium 4-(1'-heptylnonyl)benzenesulfonate (SHBS or Texas No. 1)—was investigated under conditions where four equilibrium liquid phases are present. Systematic progressions from three phases to four phases (two microemulsion phases) to three phases with

changing temperature and salinity are reported for the first time. The observed sequences of phase splits are described in terms of inferred phase diagrams. The collapse of a four-phase tie tetrahedron into a critical tie triangle is disucssed.
By K. E. Bennett, H. T. Davis, and L. E. Scriven.

P6. *Toward understanding microemulsion microstructure: A small-angle x-ray scattering study, Journal of Chemical Physics (to appear 1983)*

The microemulsion phases formed in solutions of octane, commercial surfactant and alcohol with various brines are examined with small-angle x-ray scattering (SAXS), electrical conductivity and viscosity techniques. Models based on monodisperse populations of swollen micelles or microemulsion "droplets" adequately represent the SAXS data at low volume fractions of brine. Introduction of hard-sphere interactions with the Percus-Yevick approximation allows us to model the composition dependence of the radius of gyration and isothermal compressibility up to volume fractions of brine near a percolation threshold for electrical conductivity. For brine volume fractions above the percolation threshold, a mean field attractive interaction term is needed to model the variation of isothermal compressibility; however, the same theory fails to model the composition dependence of the apparent radius of gyration. But predictions from a model for a bicontinuous microemulsion structure that is geometrically irregular yet topologically ordered and that evolves continuously into swollen (inverted) micellar solutions at low volume fraction of water (oil) are in good agreement with the SAXS and electrical conductivity data over a wide range of brine volume fractions.
By E. W. Kaler, K. E. Bennett, H. T. Davis and L. E. Scriven.

P7. *Microemulsion rheology measured, Paper B-15, 54th Annual Meeting of the Society of Rheology, Evanston, IL (October 1982). Abstract only.*

A microemulsion is a thermodynamically stable, microstructured fluid phase that incoporates substantial amounts of hydrocarbon, water, and surfactant, as well as salt usually and alcohol often. Viscosities of microemulsions from both a pure and a commercial alkyl aryl sulfonate surfactant were measured as functions of salinity, hydrocarbon chain length, surfactant concentration, and temperature. The multiphase rolling ball viscometer gave good estimates of viscosities of the one or more phases in the sealed samples. Shear-rate dependence of selected samples was accurately found with a cone-and-plate rheometer equipped with an environmental chamber to control temperature and evaporative loss.

At fixed shear rate or shear stress, microemulsion viscosity often goes through two maxima as salinity is raised and the microemulsion phase evolved from water-continuous to oil-continuous. The maxima are 5- to 500-fold higher than the pure hydrocarbon and pure brine viscosities, and remain at nearly the same salinity over a five-fold variation in surfactant concentration—despite marked changes in microemulsion appearance, salinity coordinates of phase boundaries, and the types of phase transitions observed at those boundaries. Microemulsions around the viscosity maxima are not Newtonian: under shear their viscosity fell as much as six-fold from a zero-shear value as low as ten mPa·s (centipoise). Yet away from the maxima microemulsions appear to be sub-

stantially Newtonian.

In several microemulsions shear-history effects were found even though temperature, gaseous environment, and experimental procedure were carefully controlled.

By A. T. Papaioannou, K. E. Bennett, H. T. Davis, C. W. Macosko and L. E. Scriven.

P8. *Behavior of microemulsions under compression, SPE Reprint #11210, New Orleans Meeting, Sept. 26-29, 1982*

Compression to reservoir pressures alters microemulsion phase behavior, on which the success of enhanced oil recovery by microemulsion flooding depends. For convenience, however, phase behavior studies are often conducted at atmospheric pressure. Extrapolating phase behavior from atmospheric to reservoir pressures requires the volumetric properties of each phase under compression, in particular the isothermal compressibility as a function of pressure and composition.

We present the compressibility at up to 160 bar (158 atm) of several systems of oil and water with surfactants and protosurfactants. We fit the compressibility to simple models for its pressure and composition dependence. The pressure dependence fits the Tait equation in this pressure range; selected high pressure data indicate how the compressibility deviates at much higher pressures. The composition dependence is nearly linear in volume-fraction composition, increasing with oil fraction and decreasing with water fraction. More data are needed to verify this dependence.

A simple compressibility cell, first described here, allows both rapid determination of compressibility and direct determination of the phase boundary under compression. We observed both phase separation and coalescence of distinct phases with increasing pressure.

We do not address here the effect of dissolved gases such as methane, which at high pressures can also affect microemulsion phase behavior.

By W. R. Rossen and J. P. Kohn.

Phase Behavior and Interfacial Tensions

P9. *Molecular motion and phase behavior of a double-tail sulfonate surfactant by NMR, J. Colloid and Interface Science (submitted for publication)*

^{13}C and ^{1}H NMR were used to study the behavior of the double-tail surfactant sodium 4-(1'-heptylnonyl)benzenesulfonate in chloroform, water, chloroform/water, decane, and water/decane. All carbon and proton resonances are observed as sharp resonances only if the surfactant is above a limiting mass fraction and in an isotropic solution. For the lamellar liquid crystalline phase formed by surfactant and water, T_1, measurements and linewidths indicate a pronounced motional gradient resulting from anisotropic motion as the ionic head group is approached. Whereas the chain ends are quite mobile, the motion at and close to the benzene ring is substantially hindered. This behavior is observed at surfactant concentrations from 2 to 70 wt % and at temperatures from 25 to 80°C. The surfactant molecular motion is slow in the highly viscous surfactant/decane phase. This phase undergoes a transition around 50°C yielding a much more fluid phase in equi-

librium with an isotropic solution containing ~9 wt % surfactant. The surfactant molecular motion in the surfactant/water liquid crystalline phase becomes faster when either decane or chloroform is solubilized in the surfactant bilayers.
By E. I. Franses and W. G. Miller.

P10. *Critical loci and the evolution of multiphase equilibria in ternary liquid systems, Session on Thermodynamics and Critical Phenomena, 75th Annual Meeting of the AIChE, Los Angeles, CA (Nov. 1982). Manuscript available.*

First explored by Korteweg in 1889, critical loci—plait point loops and higher order critical points—are the key to systematic computation of multiphase equilibria from equations of ternary solution state. We analyze and compare the ways in which critical loci can be computed from equations of state. We also illustrate the utility of critical loci by unfolding from them all patterns of phase behavior.
By P. K. Kilpatrick, H. T. Davis and L. E. Scriven.

P11. *Thermodynamic modelling of quarternary systems: oil-brine-surfactant-alcohol, SPE Reprint #11209, New Orleans Meeting, Sept. 26-29, 1982*

The modelling of quaternary systems is necessary in an accurate treatment of oil-brine-surfactant-alcohol mixtures. Two previous approaches have proven useful in the correlation and prediction of phase split and composition data for these systems, both relying on the pseudoternary approximation. One method, attractive because of its simplicity and ease of implementation, is to take limited data and interpolate and extrapolate them with a mathematical model which retains thermodynamic consistency. This method succeeds in modelling phase volume splits but fails to quantify phase compositions because alcohol-surfactant mixtures are poor pseudocomponents. The alternative approach is to fit the limited data to the parameters of a thermodynamic equation of state. This method is not quite as simple as the use of a mathematical model but yields an abundance of free energy-related thermodynamic information which makes it more attractive. The quaternary version of a thermodynamic model is preferred as it provides for unequal partitioning of alcohol and surfactant in different phases in equilibrium. A molecularly-based free energy model is also preferred because it links directly the forces of constituent molecules to patterns of phase, interfacial, and wetting behavior.

A systematic scheme for the computation of phase behavior in a quaternary system begins with the determination of phase equilibria on the ternary faces and proceeds by numerical continuation through the higher dimensional composition space. The calculation is expedited by knowledge of the limits of thermodynamic stability—the spinodal surfaces—and all critical points, which serve as beacons to guide the computations in penetrating the tetrahedron. Multiphase equilibria are searched out by both parametric and compositional continuation. The result provides the basis for understanding the patterns of three- and four-phase equilibria in oil-brine-surfactant-alcohol systems.
By P. K. Kilpatrick, L. E. Scriven and H. T. Davis.

P12. *Monte Carlo simulation of model amphiphile-oil-water systems, Journal of Chemical Physics (submitted)*

A square-lattice model of amphiphile-oil-water systems is developed in which oil and water molecules occupy single sites and amphiphiles occupy chains of sites. Energies and free energies estimated by Monte Carlo sampling of configuration space show that when the head, or water-loving portion, of the amphiphile has no tendency to hydrate or surround itself with water, as opposed to surrounding itself with other heads, the capability of even long amphiphiles to solubilize repellant oil and water into a single phase is weak. Although the Monte Carlo free energies deviate markedly from those given by quasi-chemical theory, the deviation of the phase behavior is modest. Computer drawings of typical equilibrium configurations show highly irregular interfaces, apparently owing to capillary waves. *By R. G. Larson, L. E. Scriven and H. T. Davis.*

P13. *Phase behavior of binary mixtures of water, carbon dioxide and decane predicted with a lattice model, Session on Modelling the Properties of Liquid Mixtures, 75th Annual Meeting of the AIChE, Los Angeles, CA (Nov. 1982). Manuscript available.*

Simple equations of state, such as the Peng-Robinson or Soave equations, generally perform well in predicting vapor pressures of hydrocarbons, but perform poorly when applied to such hydrogen-bonded compounds as water or ammonia. Moreover, even for nonpolar substances, calculated liquid densities are often inaccurate. Recently, a new lattice-based equation of state has been proposed by Klientjens and Konigsveld. The parameters of the model relate to the size and attractive energy of molecular segments and to the coordination number of the molecule. It has been applied with excellent results to some pure hydrocarbons, ammonia and water.

In this paper the new equation of state is used to model the phase behavior of pure carbon dioxide, water, and decane, and of the mixtures carbon dioxide-water and carbon dioxide-decane. For the single component systems, it is shown to be significantly more accurate than the Peng-Robinson equation, yet only slightly more complicated to use. Four parameters must be determined for most pure substances, and five for water, compared with three for Peng-Robinson. For binary mixtures two or three mixture parameters, fit to the binary critical line, lead to a more accurate description of phase behavior than that achieved by the Peng-Robinson equation, with two mixture parameters. The minimum amount of data needed for application is discussed for both equations. The Kleintjens-Konigsveld equation requires only slightly more data than does the Peng-Robinson equation.

The new equation is the first theoretical model that works well for nonpolar and hydrogen-bonded fluids.
By J. M. Nitsche, G. F. Teletzke, L. E. Scriven and H. T. Davis.

P14. *Thermodynamic modelling of pseudoternary phase behavior, SPE Journal 22, 945-961 (1982) [also the cover of the SPEJ December 1982 issue]*

Phase behavior is the fulcrum at which the chemistry and physics of surfactant and solvent systems govern the engineering and economics of chemical flooding. Salient behavior is represented by pseudoternary diagrams that account for polar, nonpolar, and amphiphilic components. The common 2,3,2, phase-split progression—induced, for example, by

salinity change in microemulsion systems—is required by thermodynamic principles. Although such progressions can be simulated semiempirically, modeling them with a suitable free-energy function or an equation of mixture state is more reliable for interpolating and extrapolating limited data on phase splits and coexisting phase compositions for use in mechanism-based computer simulation of laboratory experiments and field applications.

Simple equations of mixture state prove inadequate but lead to the promising new linearly screened Flory-Huggins (LSFH) equation, which accounts for simultaneous association of amphiphile with oil and water and aggregation of surfactant amphiphile into curved sheetlike structures that separate water-rich from oil-rich regions. From this equation for a ternary mixture are calculated representative sets of diagrams with continuous progressions of tielines and binodals, plait points, tie-triangles, and three-phase regions with their critical endpoints. Several overlapping regions of metastable one-and two-phase equilibria are identified. Free-energy surfaces are pictured, and the free-energy factor that jointly controls interfacial tension (IFT) is computed. Ultralow tensions are favored by low-relief free-energy surfaces; so also are long-lived metastable states. The exponentially screened Flory-Huggins (ESFH) equation, superior in some ways to the linearly screened version, also is discussed briefly.

Computational methods are described for fitting the six parameters of the ternary equation to data as well as for predicting phase behavior from given parameters.

By W. R. Rossen, R. G. Brown, H. T. Davis, S. Prager and L. E. Scriven.

Fluids and Thin Films at Solid Surfaces

P15. *Dynamic properties of macromolecules near interfaces, IUPAC, Proceedings 28th Macromolecular Symposium, Amherst, MA, July 12-16, 1982.*

Macromolecules which find themselves in interfacial zones experience spatially inhomogeneous interactions. Spatial distributions of chain segments are therefore different in interfacial regions than in bulk fluid phases. This difference may manifest itself as a segment density profile in the direction normal to the interface and/or as altered distributions of chain conformations (even at constant total segment density) in the interfacial zone. These inhomogeneities exist at equilibrium in interfacial regions and profoundly alter the dynamics of nonequilibrium processes occurring near interfaces. In this paper we report on our studies of these problems by two different theoretical methods and by model experiments, confining ourselves here to studies of dilute and semidilute polymer solutions.

By M. V. Tirrell, J. H. Aubert, D. Adolf and H. T. Davis.

P16. *Molecular theory of momentum transport in polymeric liquids near fluid-solid interfaces, 75th Annual Meeting of the AIChE, Los Angeles, CA (Nov. 1982). Abstract #55d.*

Fluid interfaces are not mathematical surfaces but zones of continuous density and/or composition variation. The pressure tensor is not isotropic in these zones of density variation and this influences the local momentum transport. With a thermodynamic model for the polymeric liquid we can calculate the density profile, and thus

the pressure tensor as a function of position via gradient theory. The details of this theory are presented. Once known the pressure tensor can be used in Cauchy's equations of motion to solve fluid mechanical problems in interfacial zones, without the need for assumptions of uncertain validity which arise when the interface is treated as a single mathematical surface. The theory is applied to the problem of a polymeric liquid in a thin slit. The connection is then made between this work and our previous work on the same problem using a bead-and-spring kinetic model of the polymer.
By M. V. Tirrell, J. H. Aubert, D. Adolf and H. T. Davis.

P17. *How liquids spread on solids, Journal of Colloid and Interface Science (submitted)*

A theory of the wetting of solids by liquids is put forward. The theory accounts for capillary pressure gradient, gravitational potential gradient, surface tension gradient, disjoining pressure gradient driving forces of flow in thick thin-films and of surface diffusion in thin thin-films. Disjoining pressure stems from the way intermolecular forces aggregate in submicroscopically thin films. For thick thin-films of slowly varying thickness the lubrication approximation to velocity distributions is appropriate. With this approximation the spontaneous, unsteady, two-dimensional spreading of liquid is shown to be governed by a nonlinear convective-diffusion equation for the evolution of the film thickness profile. The predictions of the theory agree with Marmur and Lelah's (1980, 1981) observations of water drops spreading on glass and with Bascom, Cottington and Singleterry's (1964) and Ludiksson and Lightfoot's (1971) observations of oils spreading on high energy surfaces. The theory is used to analyze Deryagin and co-workers' (1944, 1957, 1970) blowing-off experiments designed to measure thin-film rheology. The theory is also used to buttress the proposition that much contact angle hysteresis is due simply to slow attainment of equilibrium.
By G. F. Teletzke, H. T. Davis and L. E. Scriven.

P18. *Wetting hydrodynamics, Journal of Fluid Mechanics (submitted)*

Fluid films so thin as to be inhomogeneous in density or composition—typically less than 1 micrometer thick and hence invisible even with the light microscope—are subject to anisotropic stress states peculiar to their microstructure. The resultant fluid microstructure forces can be incorporated in the Navier-Stokes equation (or approximations) in order to analyze flows where such thin-films are important, as in wetting of solid, which is actually the displacement of one fluid by another and so involves the apparent contact line where fluid, liquid, and solid seem to meet.

Integrodifferential equations are derived for the shape and shape evolution of thin-films. With the lubrication approximation to velocity profiles a theory of forced, steady, two-dimensional displacement is developed. There are two regimes, depending on capillary number $\mu U/\sigma$. At low speed the dynamic apparent contact angle retains its static value. If the displaced fluid perfectly wets the solid an equilibrium thin-film remains; if not, there is no continuous thin-film. At high speed a hydrodynamically entrained film is left behind regardless of equilibrium wetting characteristics. These predictions accord

with experiment. Implications are discussed, including the submicroscopic origins of seeming slip at apparent contact lines.
By G. F. Teletzke, H. T. Davis and L. E. Scriven.

P19. *Wetting transitions: First order or second order?, J. Chemical Physics 77, 5794-5798 (1982)*
A generalization of Sullivan's recently proposed theory of the equilibrium contact angle, the angle at which a fluid interface meets a solid surface, is investigated. The generalized theory admits either a first-order or second-order transition from a nonzero contact angle to perfect wetting as a critical point is approached, in contrast to Sullivan's original theory, which predicts only a second-order transition. The predictions of this computationally convenient theory are in qualitative agreement with a more rigorous theory to be presented in a future publication.
By G. F. Teletzke, L. E. Scriven and H. T. Davis.

Molecular Theory of Fluid Microstructures

P20. *Capillary waves and interfacial structure, Proceedings of Symposium on Waves on Fluid Interfaces, Mathematics Research Center, University of Wisconsin, Madison, WI, Oct. 18-20, 1982*
Thermal fluctuations drive capillary waves or two-dimensional deformations of the planar interface out of the interfacial plane. The result is that the interfacial zone becomes more diffuse. The capillary wave dispersion of the interfacial zone increases as $\sqrt{\ell n A}$ in the absence of gravity as as $\sqrt{\ell n(\gamma/\Delta\rho g)}$ in the presence of gravity. A is the area transverse to the interface, γ the interfacial tension, g the acceleration of gravity, and $\Delta\rho$ the density difference of the bulk phases. $\sqrt{\gamma/\Delta\rho g}$ is frequently referred to as the capillary length.
Because of residual coherence even in randomly driven capillary waves, the density at one point in the interfacial zone is correlated with the density at another point in the interfacial zone. In the interfacial zone the density-density correlations are long-ranged, the characteristic range being the smaller of $\sqrt{\gamma/\Delta\rho g}$ or $\sqrt{A}$. Thus in the absence of gravity (either an interface in outer space where $g = 0$ or a liquid-liquid interface with densities matched so that $\Delta\rho = 0$) density correlations extend across the entire interfacial zone. The magnitude of the long-ranged transverse density correlations is inversely proportional to the interfacial tension, a fact that is exploited in light-scattering determination of tension. Perpendicular to the interface, the density correlations are short-ranged, that is, if density measured in the interfacial zone is independent of density measured in the bulk phase just outside the interfacial zone.
The picture given here of an interface and its capillary wave fluctuations has in recent years emerged from the statistical mechanical theory of inhomogeneous fluid. A versatile and mathematically appealing approximate theory of inhomogeneous fluid is the so-called gradient free energy theory. In what follows, it is used to expose the current status of the molecular theory of interfacial structure and capillary waves. The major implications of gradient theory are supported by rigorous statistical mechanical principles.
By H. T. Davis.

P21. *Stress and structure in fluid interfaces, Advances in Chemical Physics 49, 357-454 (1982)*

Modern theory of interfaces and capillarity has its roots in the works of Rayleigh and of Van der Waals and his followers. Rayleigh argued that density across an interface is continuous, contrary to the discontinuous structure assumed by Young and by Laplace. Both Rayleigh and Van der Waals derived versions of the gradient theory of interfaces, which theory has been the most revealing and practical tool used during the last two decades of theoretical analysis of inhomogeneous equilibrium fluid. Van der Waals' work, much more complete than any others of the time, was based on statistical thermodynamics, the starting point being an approximate free energy of inhomogeneous fluid that is a functional of the fluid density distribution.

Gradient theory, rediscovered by Cahn and Hilliard, led to an understanding of the mechanism of spinodal decomposition. The behavior of fluids near the critical was an early subject of gradient theory. And Fisk and Widom obtained from gradient theory scaling laws familiar to the current theory of critical phenomena.

The next major advancement in the fundamental theory of interfaces came some fifty years after the Van der Waals era. This was what we have designated herein as the mechanical theory of inhomogeneous fluid. Interfacial tension derives directly from fluid stress and is therefore a mechanical quantity whose definition does not depend on the existence of thermodynamic laws. Kirkwood and Buff and Kirkwood and co-workers derived molecular theoretical expressions for the stress tensor of inhomogeneous fluid and related interfacial tension rigorously, for the first time, to intermolecular forces and the distribution functions of inhomogeneous fluid. The distribution functions can in principle be determined from the equations of hydrostatic equilibrium (i.e., the Yvon-Born-Green equations).

In the early sixties, the techniques of functional differentiation were exploited in several seminal papers that provide the statistical thermodynamic basis for relating equilibrium properties of inhomogeneous fluids to density distributions and direct correlation functions of the type introduced originally by Orstein and Zernike. From this theory, a rigorous formula for interfacial tension emerges similar in form to the original Rayleigh-Van der Waals gradient formula. The exact elements of the gradient theory of density distributions and correlation functions have been related, with the aid of the general theory, to certain homogeneous fluid quantities. An important aspect of the density functional theory is that no particular assumptions are made concerning the nature of the intermolecular interactions. In fact, in formulas for the thermodynamic functions of inhomogeneous fluid, molecular forces do not appear explicitly—all information is carried by direct correlation functions of inhomogeneous fluid.

As is unfortunately almost always the case with rigorous results for nonideal fluids, neither the exact mechanical nor exact density functional thermodynamical theory yields tractable results for actually computing fluid properties. Nevertheless, rigorous theory does provide the right starting point for introducing simplifying approximations and in fact can be suggestive of approximating models. Indeed, the general equations of inhomogeneous fluid have been rendered tractable by such intuitive assumptions as discontinuous interfaces and locally homogen-

eous correlation functions and by such systematic approximations as truncated virial expansions and gradient theory.

In this paper we attempt to put into perspective the present state of rigorous theory of the existence and stability of inhomogeneous fluid structures, of the derivation and application of tractable models, and of the physical interpretation of interfacial structure and thermodynamics. Over the past two decades, activity in the theory of fluid interfaces has exploded. Although we try to cover the major ideas and results, we cannot hope to provide a balanced discussion of the works of everyone involved. For a broader review of the literature than that provided here we recommend the older article by Ono and Kondo and the recent articles by Widom, Croxton, and Jhon and Dahler, Rowlinson, and Evans.

By H. T. Davis and L. E. Scriven.

P22. *Adsorption, structure, and stress in binary interfaces, Journal of Chemical Physics (to appear)*

The physics of fluid-fluid interfaces is investigated with the gradient theory of inhomogeneous fluid. The theory is used to predict component density and principal pressure (negative of stress) profiles in flat and curved interfaces formed in carbon dioxide and decane mixtures. In some cases the component density (and total density) profiles are not monotonic, with CO_2 being prominently surface active. In composition regions near where a perfect-wetting third phase splits out, the composition and pressure profiles are especially structured, a thin-film appearing which is akin to the perfect-wetting phase and which almost separates two distinct interfaces. This precursor to the third phase gives rise to Antonov's rule for the interfacial tension between the two phases that are nearly in equilibrium with the third, perfect-wetting phase. Below a perfect-wetting transition temperature, T_{cw}, such thin-films do not arise near compositions of the three phase region.

Curvature of sufficiently small drops or bubbles significantly affects adsorption at interfaces. The theory predicts that the Young-Laplace equation as traditionally applied overestimates the pressure drop across the interface in some cases (as found earlier in the case of one-component drops), but underestimates the pressure drop across interfaces related to perfect-wetting structures. The minimum work of forming critical nuclei is predicted.

By A. H. Falls, L. E. Scriven and H. T. Davis.

P23. *Thermodynamic properties of inhomogeneous fluid, Physica A (submitted for publication)*

A general method, the method of variation under extension, is presented for expressing the thermodynamic properties of an inhomogeneous fluid as functionals of the local number density when given a density functional for the total thermodynamic grand potential of the fluid. The method is demonstrated in detail for the van der Waals square-gradient density functional and for the nonlocal density functional which arises in the theory of fluids with long-ranged pair potentials or in the mean-field theory of penetrable-sphere models. As specific examples, we consider the planar and spherical interface between two fluid phases, the line of contact of three fluid phases, the contact line be-

tween two surface phases and the planar interface between a solid and fluid.
By J. E. Kerins and M. Boiteux.

Instrumentation and Techniques

P24. *Multiphase rolling ball viscometer, Rev. Sci. Inst. (to be submitted)*
A literature survey and the preliminary draft of a publication have been prepared for the multiphase rolling ball viscometer developed by Karl Bennett of the Minnesota group. The device is cheap, fast, and sufficiently accurate to be used as a microemulsion screening tool.
By K. E. Bennett, H. T. Davis, C. W. Macosko and L. E. Scriven.

P25. *Transmission electron microscope observations of dislocations in hexagonal ice, pp. 552-553 in 10th Annual Proceedings of the Electron Microscopy Society of America, ed. by Bailey, G. W., Washington, DC (1982).*
Despite the power of TEM in elucidating microstructure in solids, there have been relatively few studies of ice. The reasons are the difficulty of preparing thin specimens and of creating an environment in the microscope that can accommodate them. Another problem is the sensitivity of ice to an electron beam.

With the cold-stage system developed by Talmon et al., suitable ice specimens can be prepared and imaged. The idea is to capture a layer of water between two polyimide film-coated grids and to freeze the assembly by plunging it into boiling nitrogen. The frozen sample is put into a JEOL 100CX cooling-holder and transferred into the microscope where its temperature is maintained at 110 K.

The crystal structure of ice specimens that are prepared with this technique is hexagonal. These samples contain dislocation defects whose appearance is similar to those in metals. Dislocations in ice, however, cannot always be conclusively identified because the cold-stage tilts about just one axis and because grid bars and trap grids, which shield the specimen from contaminants and thermal radiation, can block diffracted beams when the stage is tilted. Also, at 93 K, on the order of 1.5 μg of ice are lost for every coulomb of 100 kV electrons striking a sample; only a few dark-field images can be recorded before radiolysis significantly alters the sample.

A slip plane can be identified from the angle it makes with the plane of the sample surface. The tangent of this angle is the extinction distance of the operating reflection divided by the distance between thickness fringes. The most probable slip direction can then be assigned and compared to the projected direction of the dislocation line in the image to determine the screw/edge nature of the defect. A large magnitude of the projection of the Burgers vector onto the diffraction vector, $\mathbf{b}\cdot\mathbf{g}$, provides a check on the indexing of the system.

Figs. 1a and 1b are a $(11\bar{2}0)$ dark-field/bright-field pair of micrographs taken from a crystal near a break in the film. Screw dislocations are evident in two slip systems: $(10\bar{1}0)[1\bar{2}10]$ and $(0\bar{1}10)[\bar{2}110]$. The angle these slip planes make with the sample plane is measured as $\arctan[(\xi_{11\bar{2}0}=1300\text{Å})/570\text{Å}] = 66°$; the calculated angle is 65°. The dislocation lines in the figures are about 48° and -38° from $[11\bar{2}0]$. These angles compare favorably with angles of ±43° which are calculated by assuming that the defects are screw dislocations. Fig. 1b shows

cavities that form during radiolysis. These cavities do not appear to interact preferentially with dislocations; other features, e.g., surfaces or grain boundaries, may have more influence on nucleation and growth of radiation-induced voids in thin films of ice. Fig. 2 shows dislocations in the basal plane of ice. Because they are several μm in length and the film is less than 1 μm thick, these defects lie in the sample plane, which is (0001). Most of the dislocation lines in Fig. 2 are parallel to $[11\bar{2}0]$ or $[\bar{2}110]$ and thus are likely to be (a/3) $\langle 11\bar{2}0\rangle$ dislocations of mostly screw character.

Fast-freeze, cold-stage TEM is fast becoming a major technique for visualizing microstructure in unstained aqueous structured liquids. Fig. 3 is an example. Because water is a component of microstructured fluids important in biological and chemical processes, it is essential to understand the morphology of ice in order to understand the structures that occur in frozen hydrated structured fluids such as liquid crystalline phases and vesicular dispersions.
By A. H. Falls.

P26. *A transmission electron microscopy study of hexagonal ice, Journal Materials Science (submitted for publication)*

The morphologies of fast-frozen, thin-film samples of pure and dilute solutions of salts and surfactants in hexagonal ice are investigated with transmission electron microscopy. The cold-stage microscopy technique is described briefly and limitations imposed by the equipment and the sample itself are discussed. Ice grains, grain boundaries, dislocations, and stacking faults are imaged before radiolysis from the electron beam can alter their structures. The technique shows that screw dislocations in the ice basal plane are common, in accord with observations from x-ray topography and etch-replication microscopy. It also makes visible nonbasal dislocations in hexagonal ice, including dislocations in first prismatic planes, nonprismatic dislocation loops, and stacking faults on first pyramidal planes; heretofore, these defects have not been confirmed experimentally. Implications of the work for cold-stage microscopy of microstructured fluids are mentioned.
By A. H. Falls, S. T. Wellinghoff, Y. Talmon and E. L. Thomas.

P27. *Interpreting the appearance of dispersed systems. Part I. Model dispersions of polymer latex spheres, Journal of the American Oil Chemists' Society (to appear May 1983)*

Measurements of total absorbance at wavelengths 350 to 780 nm of aqueous dispersions of polymer latex microspheres of diameters 0.091 μm, 0.254 μm, 0.325 μm, and 1.10 μm were used to interpret systematic observations of them. Light scattering dissymmetries and scattering ratios of dispersions of the 0.091 μm microspheres were measured at varying concentration and path length at 546 nm and 436 nm. Spectrotubidimetry and observations were also made in binary mixtures of the above particle sizes and in dispersions of microspheres with added dye, the sodium salt of methyl red.

For absorbance due to scattering, A_{scat}, exceeding 0.05 but not 2, the absorbance and its wavelength dependence yield reliable estimates of particle size, even though the dissymmetry and the scattering ratio do not. Observations of nonabsorbing systems under ordinary illumi-

nation are most reliably interpreted when $0.1<A_{scat}<1$. That the Tyndall effect, or a variant of it when absorption is important, is visible implies that particles smaller than 0.1 μm are present. In Part II the results are used to devise rules for interpreting the appearance of dispersed surfactant systems, with due regard for path length, particle size, particle concentration, and multiple scattering.
By E. I. Franses, L. E. Scriven, W. G. Miller and H. T. Davis.

P28. *Interpreting the appearance of dispersed systems. Part II. A guide for surfactant systems, Journal of the American Oil Chemists' Society (to appear May 1983)*

We first analyze how color and transparency are perceived. Drawing on principles of light scattering investigated in Part I, we suggest simple rules and procedures in a diagnostic form for visually observing fluid surfactant systems to estimate sizes of dispersed particles. Rules and procedures are organized into a guide, the use of which we illustrate by observing certain important surfactant systems. We conclude that it is possible to estimate particle sizes in the Rayleigh, Rayleigh-Debye-Gans, and Mie scattering regimes from such observations alone.
By E. I. Franses, L. E. Scriven, W. G. Miller and H. T. Davis.

P29. *An improved transfer module and variable temperature control for a simple commercial cooling holder, Ultramicroscopy (submitted for publication)*

A new cold stage transfer module was designed for the commercially available cooling holder of the JEOL JEM 100CX electron microscope. In the new CSTM the entire loading of the specimen is carried out under liquid nitrogen. This gives a frost-free transfer during which the temperature of the sample does not exceed 120 K. Straightforward modifications to the commercial cooling holder permit continuous selection of specimen temperature between 100 K to 450 K. The sample can be heated or cooled at rates of up to 7 K/s. These modifications did not impair the resolution of this holder which is better than 1.5 nm. This work illustrates a relatively simple way of modifying a commercial cooling holder into a true cold stage system.
By G. Perlov, Y. Talmon and A. H. Falls.

P30. *Frozen hydrated specimens, Proceedings of the 10th International Congress on Electron Microscopy, Hamburg, Germany (Aug. 1982). Abstract only.*

Frozen hydrated specimens are specimens of biological, organic or inorganic origin which have been thermally fixed by rapid freezing, and transferred to the electron microscope for examination without elimination of water. In the broader sense this definition may include other volatiles in the specimen such as organic solvents. The amount of water in these specimens may be a few weight percent e.g., water of hydration in organic crystals, to over 75% in thin sections of animal and plant tissue, and over 99% in water in suspensions of phospholipids, synthetic surfactants or polymer latexes. Frozen hydrated specimens have been examined by conventional transmission electron microscopy (STEM), scanning electron microscopy (SEM), X-ray microprobe, and in the high voltage electron microscope.

Electron microscopists have studied frozen hydrated specimens for over twenty-five years now (see an early account of work in the area by Fernández-Moran); fast freezing is well accepted as the best method for the preservation of ultrastructure of water-containing systems; there is at least one cold stage/cold transfer unit commercially available for a CTEM/STEM instrument, and another for SEM work. Nevertheless the technique is not a routine one yet, the number of research groups working in this field is small, and most papers published still involve development of the technique with some "sample results". But it is encouraging that scientists from different disciplines (biology, physics, physical chemistry and engineering) have contributed in recent years to the understanding of properties and behavior of frozen hydrated specimens.

The purpose of this paper is to describe some of the peculiarities of frozen hydrated specimens: their special characteristics, the problems they pose to the microscopist, ways to overcome these problems, and questions that are still open.

By Y. Talmon.

Flow and Transport in Porous Media and Composite Materials

P31A *Transport in disordered composite media, IUPAC 28th Macromolecular Symposium Proceedings, p.739, 12-16 July 1982, Amherst, MA*

In this work a composite medium is one whose subparts, which can be regular or irregular in shape, are small compared to sample dimensions. The subparts are materials with known thermodynamic, mechanical, and transport properties. In a disordered composite the subparts are chaotically distributed.

Transport in a composite medium depends on the transport properties of its subparts and on its morphology. The geometry—the size and shape—of the subparts and the topology—the way the subparts are connected to each other—are coequals in determining morphological state.

A common idealization of a disordered composite is to imagine that the subparts are identical, space filling polyhedra, chaotically assigned to be the various materials of the composite. For example, space can be subdivided into cubic cells and the cells randomly assigned with probabilities $\phi_1, \ldots, \phi_M$ to be any one of M materials, where ϕ_i is the volume fraction of material i. Such an idealization represents the disordered distribution of materials in a regular (periodic) subdivision (tessellation) of space. More disordered is a chaotic distribution of different materials in a randomly tessellated space. Voronoi polyhedra provide a convenient random tessellation of space. These space filling polyhedra have a wide distribution of sizes, shapes, and faceting and, therefore, are templates for generating composites having high geometric and topological disorder. The connectedness of a tessellation is conveniently measured by the coordination number z, namely, the number of faces of the basic building blocks of the tessellation. $z = 6$ is a cubic tessellation, but in the Voronoi system z is a random variable with an average value of 15.54.

The purpose of this paper is to investigate the effects of morphological disorder on transport—diffusion and conduction—in binary composites (i.e., $M = 2$). Chaotic distributions in regular tessellations are compared with chaotic distributions in random tessellations. Geo-

metrical versus topological factors are considered.

If the materials have widely differing transport properties, the overall transport behavior of the composite is a strong function of the relative proportions of the materials, on dimensionality, and on the average coordination number of the tessellation. Regular and irregular tessellations behave quite similarly as long as the average coordination numbers are the same. The implication of this is that simpler and cheaper models of porous media may yield quite adequate estimates of overall properties.

By H. T. Davis.

P31B *Physics of structure and transport in porous media, General Lecture, Proceedings of the Ninth U.S. National Congress of Applied Mechanics, p. 57, 21-25 June 1982, Ithaca, NY*

Pores change the mechanics of and transport in otherwise solid materials. The properties of porous media, like chaotic composites more generally and solid states disordered at molecular or atomic level, depend as much on the connectivity, or topology, of their microstructure as on its size and shape, or geometry, and material or constitution. Permeable porous media are bicontinuous, a topology requiring three-dimensional experimental analysis and theoretical modeling of matrix and pore space. A systematic new procedure finds the network topological equivalent of each and provides means for mapping local geometric and material properties onto these interpenetrating networks.

No real porous medium has been so analyzed yet, but realistic, polyhedral granular models are being studied by modern computer-aided methods. The models are based on Voronoi random tessellation of space and Voronoi-like tessellations with prescribed biases or correlations. For theoretical modeling of transport the simplest versions are the corresponding networks and their approximations by regular networks and by regular and irregular trees. Published analytical theory of percolation and conduction in topologically regular trees is instructive. A few analytical results are available for two-dimensional regular networks. Beyond them are various Monte Carlo simulations, recently extended to irregular trees and networks and applied to diffusion, conduction, elasticity, microcracking, permeability, and convective dispersion, and to the distribution and flow of immiscible fluids in pore space.

A recent advance in Monte Carlo simulation with the transport equation solved by means of finite element basis functions for Voronoi tessellations, which opens the way to as accurate a statistical theory of porous media as desired—or affordable. To reduce the size of samples simulated requires devising accurate boundary conditions for them where they would interface the larger specimen, and selecting a statistical method for averaging over them. Most attractive is the self-consistency condition of effective medium and coherent potential approximations, not as that condition has been used in continuum theory, because permeable pore space is neither isolated rounded inclusions nor long straight tubes nor separated lamellae, but rather as it is invoked in theories of transport on disordered lattices, an active subject in solid state physics. Samples as small as single lattice bonds may lead to an adequate approximation. But generalizations to bond pairings and extended clusters that are currently under study are the most promising way to the goal of a

statistical physics of macroscopic behavior, which by accounting for microscopic topology, as well as geometry and constitution, unifies structure and all manner of transport in porous media.
By L. E. Scriven.

P32. *Percolation theory of two-phase relative permeability, SPE Reprint #11015, New Orleans Meeting, Sept. 26-29, 1982*

Fluid distributions and flow through the pore space of reservoir rock depend not only on pore sizes and shapes but also on local pore connectivity, i.e. topology. This topology can be described in terms of the network concept of coordination, which is central in most of the development to date of the percolation theory of transport in chaotic media, a theory advanced by Larson et al. for multiphase flow in porous media.

The transport-path accessibility function from percolation theory, we find, summarizes the topological aspects of porespace important to describing the capillarity-controlled spatial distributions of two fluids; and the transport-path conductivity function, we find, summarizes the topological aspects of porespace important to describing the creeping flow of two fluids, each continuously connected in a distinct set of channels. From these functions, and statistical distributions of pore configurations, we derive general formulas for the drainage and imbibition relative permeabilities of two phases, one of which is completely wetting. Imputs required for calculations are a network analog of pore connectivity, or the coordination number of its Cayley or Bethe tree approximation (for which the accessibility and conductivity functions can be evaluated in closed form); and distributions of flow-controlling and inventory-controlling pore dimensions.

Results for Bethe tree approximations to pore topology, and for several simple statistical distributions of pore dimensions, agree well with all the features of oil and water relative permeabilities reported for Berea sandstones—including not only the shapes of the curves but also the lack of hysteresis in water relative permeability and the presence of hysteresis in oil relative permeability. The inputs to the theory can be adjusted to fit limited experimental data for purposes of interpolation and extrapolation. Alternatively they can be determined from automated microscopic examination of suitable spatial sections of core samples, with the aid of methods recently used by Pathak et al.

The theory is so founded that it can be extended in consistent ways to two-phase relative permeabilities when neither phase is completely wetting, and to three-phase relative permeabilities.
By A. A. Heiba, M. Sahimi, L. E. Scriven and H. T. Davis

P33. *Fractal random walks, J. Statistical Physics 28, 111-126 (1982)*

We consider a class of random walks (on lattices and in continuous spaces) having infinite mean-squared displacement per step. The probability distribution functions considered generate fractal self-similar trajectories. The characteristic functions (structure functions) of the walks are nonanalytic functions and satisfy scaling equaitons.
By B. D. Hughes, E. W. Montroll and M. F. Shlesinger.

P34. *Random walks on the Bethe lattice, J. Statistical Physics 29, 781-794 (1982)*

We obtain random walk statistics for a nearest-neighbor (Pólya) walk on a Bethe lattice (infinite Cayley tree) of coordination number z, and show how a random walk problem for a particular inhomogeneous Bethe lattice may be solved exactly. We question the common assertion that the Bethe lattice is an infinite-dimensional system.
By B. D. Hughes and M. Sahimi.

P35. *Lattice dynamics, random walks, and nonintegral effective dimensionality, J. Math. Phys. 23, 1688-1692 (1982)*

Definitions of the nonintegral effective dimensionality of recursively defined lattices (fractal lattices) may be based on scaling properties of the lattices, or on the qualitative behavior of cooperative phenomena supported by the lattices. We examine analogs of these definitions for regular (i.e., periodic) lattices supporting long-range interactions. In particular, we show how to calculate a harmonic oscillator effective dimension, a scaling dimension, and a random walk effective dimension for simple cubic lattices with a class of long-range interactions. We examine the relationship between these three dimensions for regular lattices, and conjecture a constraint on the analogs of these dimensions for fractal lattices.
By B. D. Hughes and M. F. Shlesinger.

P36. *Dependence of residual nonwetting liquid on pore topology, SPE Reprint #11016, New Orleans Meeting, Sept. 26-29, 1982*

Fluid distributions and flow through the porespace of reservoir rock depend not only on pore sizes and shapes but also local pore connectivity. This can be characterized in terms of the network concept of coordination but is more appropriately described by the topological invariant called *genus*, which is the basic measure of the multiplicity of paths through the pore network. The larger the genus per unit volume, the larger the number of alternative paths available for fluid connection and flow. Genus is the number of distinct holes in a holey structure such as porous rock.

Model rocks of a series of pore structures were prepared by controlled sintering of model sediments of three different grain shapes and two grain sizes. The morphology of each core was found by serial sectioning and recording all the relevant dimensions and connections. From features on representative two-dimensional sections the statistics of genus and other relevant properties of the three-dimensional structures were calculated by means of mathematical relations known for random structures.

Residual saturations when oil was displaced by water, and vice versa, were measured in each core before it was sectioned. The experiments were made at low capillary numbers, and by the Penn State method.

The measured residual saturations of nonwetting liquid in model rocks synthesized from grains of the same size but different shapes correlate remarkably well with genus per unit volume. Pore topology, heretofore unstudied, is as crucial as pore geometry in determining residual nonwetting saturations. The higher the genus, the more alternate routes are available for oil drainage, the larger the average number of choke-off and break-off events it takes to isolate blobs of oil, and so the lower the residual saturation.
By P. Pathak, H. T. Davis and L. E. Scriven.

P37. *Dispersion in disordered porous media, Chemical Engineering Communications (accepted for publication)*

We report results of Monte Carlo investigations of dispersion in one- and two-phase flow through disordered porous media represented by square and simple cubic networks of pores of random radii. Dispersion results from the different flow paths and consequent different transit times available to tracer particles crossing from one plane to another in a porous medium. Dispersion is found to be diffusive for the process simulated, i.e., a concentration front of solute particles can be described macroscopically by a convective-diffusion equation. Dispersivity in the direction of mean flow, i.e., longitudinal dispersivity, is found to be an order of magnitude larger than dispersivity transverse to the direction of mean flow. In two-phase flow, longitudinal dispersivity in a given phase increases greatly as the saturation of that phase approaches its percolation threshold; transverse dispersivity also increases, but more slowly. As the percolation threshold is neared, the backbone of the sublattice occupied by the phase becomes increasingly tortuous, with numerous subloops which provide alternative particle paths that are evidently highly effective in dispersing a concentration front of tracer particles.

By M. Sahimi, H. T. Davis and L. E. Scriven.

P38. *Dispersion in flow through porous media, SPE New Orleans Meeting, Sept. 26-29, 1982. Manuscript available.*

Dispersion is a consequence of flow. It results from the different paths and speeds and the consequent range of transit times available to tracer particles convected across a permeable medium. The kinematic mechanism stems from the connectivity structure of porespace; the dynamic mechanism, from the effect of pore shape and size on flow. Molecular diffusion can modify both. In many circumstances these mechanisms lead to distributions of macroscopic average solute or tracer concentration that are diffusive, i.e. that can be modeled by the convective diffusion equation, dispersion coefficients taking the role of diffusivity.

For cases of diffusive mixing locally at pore junctions and no appreciable diffusion between, a simple network approximation is appropriate. Square and simple cubic networks of variable pore segments, with average flow in one of the pore directions, are useful idealizations. Dispersion in one- and two-phase flow through these networks is studied here by the Monte Carlo strategy of replicated computer experiments. This strategy is combined, with considerable computational savings, with the percolation theory of fluid distributions in two-phase flow. Network topology and pore geometry and thus the two basic mechanisms are precisely controlled.

The results show that dispersion is diffusive in the cases simulated. Longitudinal (mean flow direction) dispersivity is an order of magnitude greater than dispersivity in transverse directions. In two-phase flow, longitudinal dispersivity in a given phase rises greatly as the saturation of that phase approaches residual, i.e. its percolation threshold; transverse dispersivity also increases, but more slowly. As the threshold is neared, the backbone of the subnetwork occupied by the phase becomes increasingly tortuous, with local mazes spotted

along it that are highly effective dispersers.

All of the findings accord qualitatively with most available data, except that dispersivities in reality are not constant but increase slowly with macroscopic average flow rate, which may stem from molecular diffusion that is lost from the network approximation used.
By M. Sahimi, A. A. Heiba, B. D. Hughes, H. T. Davis and L. E. Scriven.

P39. *On Pólya random walks, lattice Green functions, and the bond percolation threshold, Journal Physics A (accepted for publication)*

Based on numerical evidence, we conjecture a connection between the bond percolation threshold of Bravais lattices in three or more dimensions and the value at the origin of a lattice Green function related to the probability of return to the origin for a Pólya random walk.
By M. Sahimi, B. D. Hughes, L. E. Scriven and H. T. Davis.

Mechanisms and Simulation

P40. *Adaptive subdomaining for solution of one-dimensional problems by the finite element method, presented at the 30th Anniversary Meeting of SIAM, Stanford, CA, July 19-23, 1982. Manuscript available.*

Uniform distribution of integral error over variable subdomains is an attractive criterion by which to subdivide a domain for the Galerkin/finite element method when localized steep gradients and high curvatures are to be resolved. The uniform integral error criterion is developed here into an adaptive technique for one-dimensional problems and linear basis functions. Newton iteration is used to update simultaneously the nodal values and the node positions; continuation is similarly used as parameter values are varied or time advanced. Three illustrative problems are solved: (1) convective diffusion with an exponential boundary layer, for which the analytical solution is known and compared with results of uniform subdomaining and adaptive subdomaining; (2) gradient theory of Peng-Robinson fluid between parallel walls, which features thin-film states and fluid interface behavior that require highly non-uniform discretization for accurate determination of stability and bifurcation; and (3) Buckley-Leverett theory of two-phase Darcy flow in porous media, which features the development of a shock front in time. The new adaptive technique resists entanglement of the nodal mesh without requiring special restrictions on nodal movement.
By R. E. Benner and L. E. Scriven.

P41. *Elementary mechanisms of oil recovery by chemical methods, Soc. Pet. Eng. J. (February 1982), 243-258*

Basic mechanisms of oil recovery by introducing chemical agent act either by altering fractional flow relations, as by lowering interfacial tension or raising viscosity, or by changing phase behavior, as by making oil partially soluble in an aqueous phase (solubilization) or water soluble in the oleic phase (swelling). These mechanisms are catalogued. Simplified idealizations of them are analyzed with graphical constructions of Buckley-Leverett type for saturation and concentration profiles during representative linear displacements starting with waterflood residual. Emulsification mechanisms with nonequilibrium fluid states are shown to be amenable to similar an-

alysis of processes involving combinations of mechanisms as in practical chemical flooding is illustrated.

Whereas microscopic displacement efficiency measures local mobilization of oil, *process performance efficiency* measures the rate at which oil is recovered from the flow paths the process actually travels. In its ideal limit, each mechanism discussed is 100% efficient in the microscopic sense, but can be much less efficient in the process performance sense.

By R. G. Larson, H. T. Davis and L. E. Scriven.

Theses

P42. *Electron microscopy and molecular theory of microstructured fluids, Ph.D. thesis, University of Minnesota, 1982*

This thesis describes advances in understanding fluid microstructure. In Part I, fast-freeze, cold-stage transmission electron microscopy is deveoped to image supramolecular structure in liquids. Because microstructured fluids often contain water, ice and frozen aqueous solutions are studied first. Hexagonal ice contains dislocations and stacking faults. Basal dislocations are most common, but nonbasal dislocations and loops also exist; heretofore, these have not been experimentally identified.

Applications of the technique to dispersions of surfactants illustrate how it is used to elucidate fluid microstructures important in biology, medicine, chemistry, and polymer science. Micrographs, backed by other experimental probes, show that freezing preserves aqueous surfactant dispersions. Images of frozen, hydrated specimens of them are interpreted with theories of electron diffraction. Artifacts of irradiating, staining, and freeze-drying samples are identified. Cold-stage microscopy successfully follows the effects of alcohols on dispersed lamellar phases, detects the presence of liquid crystallites in vesicular dispersions, and helps prove that vesicles of some surfactants are not equilibrium structures in brines.

Artifacts, however, obscure interpretation of images of micellar solutions and microemulsions. Such systems appear to rearrange when they solidify. Frozen microemulsions also crosslink when bombarded by electrons. Ways are suggested to overcome these problems in future research.

In Part II, the physics of fluid-fluid interfaces is investigated with molecular theories of inhomogeneous fluid. Because traditional calculations are inadequate, a modern, computer-aided functional analysis is developed to handle the nonlinear integral and differential equations of statistical mechanical models that describe equilibrium and nonuniform fluid. These are solved for component density and principal pressure profiles in flat and curved interfaces containing one and two components.

In some cases, interfacial density profiles are not monotonic; instead, one of the components is prominently surface active. In composition regions where a perfect-wetting third phase arises, a thin-film, which is akin to the perfect-wetting phase, can appear on binary interfaces.

Curvature of sufficiently small drops or bubbles affects adsorption at interfaces. The Young-Laplace equation as traditionally applied can either overestimate or underestimate the pressure jump across spherical

interfaces. Minimum works of forming critical nuclei are predicted. *By A. H. Falls.*

P43. *Surfactant microstructures, Ph.D. thesis, University of Minnesota, 1982.*

Studies of microemulsions, vesicles and mixed micelles formed by ionic surfactants or surfactant mixtures are reported. The chief experimental tools were small-angle x-ray scattering (SAXS) and quasi-elastic light scattering (QLS). A modern SAXS facility incorporating a position-sensitive detector is described.

Many equilibrium microemulsion phases can solubilize hydrocarbon and water in all proportions in a continuous progression of states without any visibly abrupt transition. When the volume fraction of oil ϕ_0 in the microemulsion is nearly zero or unity, the microemulsion structure almost certainly consists of either micelles swollen with oil (at small ϕ_0) or inverted micelles swollen with water (at ϕ_0 near 1). Contending pictures of the mid-range progression of microstructures are that swollen micelles pack together as their sizes and numbers increase, or that swollen micelles fuse into chaotic and dynamic bicontinuous structures of low viscosity. A model that calls for totally random bicontinuous structures for volume fractions of oil or water between 0.16 and 0.84 was used to predict the SAXS intensity curve and the QLS autocorrelation function for microemulsions. These predictions compare well with the SAXS measurements of microemulsions formed with the pure alkyl aryl surfactant sodium 4-(1'-heptylnonyl)benzenesulfonate and with the QLS measurements of others. However, there is a limited composition range over which the SAXS measurements on microemulsions made with a commercial mixture of alkyl aryl sulfonates (Witco TRS 10-80) are better correlated with a model of microemulsion as disjoint interacting swollen micelles.

Vesicles form upon sonication of aqueous dispersions of SHBS in either water or NaCl brine. The vesicles are less than 500Å in diameter and apparently consist of single SHBS bilayer shells surrounding an aqueous core. They are thermodynamically unstable and eventually revert to the bulk smectic phase. Reversion is hastened by flow through a porous medium.

QLS studies of mixed micelles present in solutions of SHBS and sodium dodecylsulfate (SDS) show that the micelles have prolate shapes in NaCl brines and are larger than pure SDS micelles.
By E. W. Kaler.

P44. *Fluid microstructures, phase and tension behavior of amphiphile-hydrocarbon-water-salt systems, Ph.D. thesis, University of Minnesota, 1982*

The fluid microstructures formed in water or brine by sodium 4-(1'-heptylnonyl)benzenesulfonate (SHBS), by SHBS mixed with sodium dodecylsulfate (SDS) or with a low molecular weight alcohol, and by a commercial petroleum sulfonate (TRS 10-80) representative of surfactant waterflooding are described. Upon addition of hydrocarbon these surfactant-rich microstructures can produce surfactant-rich third phases; in some cases, these are microemulsion phases. Those that are not microemulsions may be related to mesophases; they are highly viscous and can be nonbirefringent, streaming birefringent, or even birefringent. The relationships between surfactant-rich microstructured fluids and their compositions, phase and tension behavior with hydrocarbons, efficacy

to recover residual oil from short Berea cores, and surfactant retention were investigated.

Ultralow tensions by which petroleum recovery can be enhanced by surfactant-based flooding processes are caused not by monolayer adsorption but by surfactant-rich third phases that are microemulsions or viscous substances derived from liquid crystalline dispersions.

The high surfactant retention and pressure build-up typical of flow of liquid crystalline dispersions through porous rock can be drastically reduced by sonicating the surfactant dispersion beforehand, a novel treatment which further disperses liquid crystalline material into vesicles. The same effect is achieved by dissolving the liquid crystallites by adding a short-chain alcohol or a micellar surfactant such as SDS.

In tests with short Berea cores, high recovery of residual oil was achieved with low surfactant retention by injecting sonicated vesicular dispersions of suitable composition, or else alcohol-solubilized surfactant solutions, again of suitable composition.

Alcohol-hydrocarbon-brine systems that split into two or three liquid phases follow the same patterns of phase and interfacial tension variations as do surfactant-oil-brine systems in which one or two phases are microemulsions. The tensions are much higher, however. Antonov's rule was verified for several of these three-phase systems.

Improved spinning drop tensiometers for measuring interfacial tension at gyrostatic equilibrium were built. It was shown by the ray-tracing method of geometric optics that when drop and tube walls are concentric the image, a virtual one, is formed concentric with drop and tube.

By J. E. Puig.

P45. *Multicomponent phase behavior in an external field, Ph.D. thesis, University of Minnesota, 1982*

Two problems in solution thermodynamics are addressed. First, a pseudoternary free energy model is developed for surfactant/oil/water microemulsion systems used in enhanced-oil-recovery processes. This model readily generates phase behavior patterns like those observed experimentally, and the free energy surface topography reveals a partly thermodynamic basis for extreme sensitivity, long-lived metastable equilibria, slow equilibration, and low interfacial tensions. Fitting the model parameters to data and generating phase diagrams from the model are discussed.

Second, an experimental technique for gathering thermodynamic data, equilibrium ultracentrifugation, is developed and applied to amphiphile/oil/water mixture. Its development led to four topics treated here: 1) The theory of multicomponent, multiphase equilibrium in an external, e.g., centrifugal, field. The degree of field-induced stratification in a mixture depends on volume and density properties and on the mixture equation of state; consequently the equation of state can be determined from this stratification. Stratification is greatest, and the technique most powerful, in near-critical mixtures and microemulsions. Conversely, field-free phase behavior determined by centrifugation can be in error because field-induced stratification can markedly affect the number of interfaces observed. Colloidal particle mass determined from equilibrium centrifugation can be in error because solu-

tion nonideality and particle mass have similar effects on equilibrium stratification. 2) The theory of approach to equilibrium in an external field, or sedimentation velocity. Colloidal particle mass determined from sedimentation velocities can be in error because solution nonideality and particles mass have similar effects on sedimentation-velocity patterns. 3) The practice of preparative ultracentrifugation and sample fractionation to determine field-induced stratification and the equation of state, applied here to three systems of oil and water with amphiphile. An extensive error analysis demonstrates the accuracy of the technique and identifies three remaining problems: slow equilibration, remixing of the sample before fractions are obtained, and the lack of an adequate volumetric model for correlating needed volumetric data. 4) Auxiliary measurements of the compressibility of oil/water/amphiphile mixtures. These data are required for analyzing sedimentation-equilibrium results and also for predicting the effect of pressure on microemulsion phase behavior.
By W. R. Rossen.

☆U.S. GOVERNMENT PRINTING OFFICE:1984 -746 -081/2555 REGION NO. 4